UNIVERSITÀ DEGLI STUDI DI PALERMO
Dottorato di ricerca in Scienze della Terra – Indirizzo Geochimica
Dipartimento di Scienze della Terra e del Mare (DiSTeM)
Sez. Chimica e Fisica della Terra

THE NATURE AND SOURCE OF MAJOR MAGMATIC VOLATILES: OPEN-VENT DEGASSING VOLCANOES IN THE CENTRAL AMERICAN VOLCANIC ARC

DOTTORE
PHILIPPE ROBIDOUX

COORDINATORE
FRANCESCO PARELLO

TUTOR
ALESSANDRO AIUPPA

CICLO XXVI
2016

Title: The nature and source of major magmatic volatiles: open-vent degassing volcanoes in the Central American Volcanic Arc

Philippe Robidoux

© PHILIPPE ROBIDOUX

ABSTRACT

Major volatiles play an important role in subduction zone magmatism, from magma generation in the mantle, to crustal ascent and evolution, until its dramatic expression during a volcanic eruption. In the attempt to add a piece of information on source and behavior of major volatiles in arc volcanism, I here report on the geochemistry of H_2O, CO_2, S and Cl in two volcanic systems in NW Nicaragua (Central America), San Cristóbal and Telica.

The observational approach is based upon combination of some of the most recent techniques in volcanic gas monitoring and petrology. I here explore quiescent and eruptive degassing processes by combining both volcanic gas and melt inclusion approaches. Field gas measurements were primarily obtained via the Multi-Component Gas Analyzer system (Multi-GAS) technique, complemented with additional remote sensing observations via open-path Fourier Transform IR (OP-FTIR) spectroscopy, ultraviolet differential optical absorption spectroscopy (UV-DOAS). These techniques together allowed characterizing compositions and fluxes of CO_2, H_2O, S and Cl in the central crater plumes of both quiescent degassing volcanoes. These measurements contribute to our understanding of the current structure and state of the shallow plumbing systems that feed the surface gas emissions.

The targeted San Cristóbal and Telica volcanoes are also investigated by characterizing, for the first time, the volatiles contents (CO_2, H_2O, S and Cl, F) in their melt inclusions. Using a series of laboratory instrumental facilities, such as electron microprobe, micro FTIR spectroscopy, Raman spectroscopy and Nano secondary ions mass spectroscopy (NanoSIMS), I show that olivine- and pyroxene-hosted melt inclusions can reveal crucial information on pre-eruptive magma conditions at both San Cristóbal and Telica. I propose that polybaric degassing and crystallization models can suitably describe major volatile abundance and behavior during magmatic evolution. These results are synthesized in 3D illustrative sketches that represent the crustal structure of San Cristóbal and Telica volcano-magmatic systems.

Water is the primary agent during magmatic fragmentation and strongly influences eruptive style. CO_2, the second most abundant volatile in magmas, is generally more difficult to quantify in melt inclusion studies, but its role in volcanic processes is revealing more and more important as volcanological research advances. I therefore spend major attention in this study to charactering the carbon content in San Cristóbal and Telica primitive magmas. CO_2, apart from being an excellent chemical tracer of magmatic degassing processes, is one of the most important triggers of explosive eruptions in basic to intermediate magmas.

The volatile contents of Central American magmas show wide regional-scale variations. It is shown here that gas signature (carbon abundance) of Central American volcanic gases correlates with petrological tracers of magma compositions, and specifically with the trace element proxies of slab-fluid contribution to the mantle wedge. This brings novel constraints on carbon source in volcanic arc regions. I also show, using noble gas isotope compositions of fluid inclusions in olivine-pyroxene crystals, that a common mantle fluid signature persists along the entire Nicaragua volcanic segment. Controls on magma generation are, instead, better reconstructed using incompatible trace elements; these data reveal that the degree of mantle melting and sedimentary fluid incorporation are higher in Nicaragua than in other sectors of the arc. We find that local variations exist also at the scale of a single magma system. These variations, at different spatial and temporal timescales, prove that regional compositional heterogeneities exist underneath volcanic arcs.

PUBLICATIONS

Conde, V., **P. Robidoux**, G. Avard, B. Galle, A. Aiuppa, A. Muñoz, (2014). Measurements of SO_2 and CO_2 by combining DOAS, Multi-GAS and FTIR observations: a case study from Turrialba and Telica volcanoes, *International Journal of Earth Sciences, June 2014, p.1437-3254*

Aiuppa, A., **P. Robidoux**, G. Tamburello, V. Conde, B. Galle,G. Avard, E. Bagnato, J. M. DeMoor, M. Martinez, A. Munoz, (2014). The Costa Rica – Nicaragua volcanic segment: along arc variations in volcanic gas chemistry and improved CO_2 budget, *Earth and Planetary Science Letter, October 13, p.134-147*

Manuscripts in preparation

Robidoux, P., Aiuppa, A., Rotolo, S., Hauri, E., Rizzo, A., Frezzotti, M.L., (2016). The volatile content of mafic to intermediate magmas from San Cristóbal volcano, Nicaragua, Manuscript in preparation for *Lithos*

Robidoux, P., Aiuppa, A., Hauri, E., Rizzo, A., Lanzo, G., Rotolo, S., (2016). Geochemistry and petrology of magmas produced during explosive eruptions at Telica, Manuscript in preparation for *Lithos*

Robidoux, P., Frezzoti, M., Hauri, E., Aiuppa, A., (2016). A C-O-H-S fluid system in shrinkage bubbles of melt inclusions, Manuscript in preparation for *Journal of Petrology*

Aiuppa, A., **P. Robidoux**, T. Fisher, (2016). Along-arc and inter-arc variations in volcanic gas CO2/S signature, manuscript in preparation for *Earth Science Review*

Robidoux, P., J. Roberge and C. Urbina Adams (2016). A geostatistical method and interpolation model applied for the study of trace element signatures for the Chichinautzin Volcanic Field in Mexico, Manuscript in preparation for *International Geology Review*

Conference contribution

Robidoux, P., M.L. Frezzotti, E.H. Hauri, A. Aiuppa: *Low-temperature superficial chemical changes and post-entrapment effects alter CO_2 budget estimation in vapor bubbles of glass inclusions*; Poster Presentation, AGU Meeting 2015, San Francisco, United States (December 2015)

Robidoux, P., A. Aiuppa, S. Rotolo, E. H. Hauri, M.L. Frezzotti, G. Giudice, *Refining the approach for volcanic CO_2 output estimation at San Cristóbal volcano*, Oral Presentation , Goldschmidt 2015, Pragua, Czeq. Rep. (August 2015)

Aiuppa, A., **P. Robidoux**, and T. Fischer, *Along-arc and inter-arc variations in volcanic gas CO_2/S signature*, EGU General Assembly 2015, Vienna, Austria (May 2015)

Robidoux, P., A. Aiuppa , S. Rotolo, G. Giudice, R. Moretti, V. Conde, B. Galle and G. Tamburello*: Open-vent degassing of CO_2 from typical andesitic volcanoes in the Central American Volcanic Arc; study case at San Cristobal and Telica*; Oral Presentation, AGU Meeting 2014, San Francisco, United States (December 2014)

Robidoux, P., Aiuppa A., Rotolo S., Conde V., Galle B., Giudice G., Moretti R., Avard G., Muñoz A., 2014, *Investigating the CO_2 budget and source from active volcanoes in the Central American Volcanic Arc*. Poster Presentation, Yellowstone National Park (USA), First Deep Carbon Observatory (DCO) Summer School (July 13-18, 2014)

Robidoux, P., Aiuppa A., Conde V., Galle B., Giudice G., Avard G., Angélica Muñoz A., 2014, *First volcanic CO_2 budget estimate for three actively degassing volcanoes in the Central American Volcanic Arc*, Poster Presentation, EGU General Assembly 2014, Vienna, Austria (May 1, 2014)

Robidoux P., Roberge J., Guilbaud M.N., Reyes Luna P. C., Justo Espinosa L. R., Briseno A.A., 2012, *Variation in volatile content from three monogenetic cones in the Chichinautzin Volcanic Field, México: Implication in the degasification and the eruption style*, Poster Presentation , Goldschmidt 2012, Montréal, Canada (June 28, 2012)

Robidoux P., Roberge J., Urbina Oviedo C.A., 2011, *A geostatistical method applied to the geochemical study of the Chichinautzin Volcanic Field in Mexico*, Poster Presentation , AGU Annual Meeting, San Francisco, (see also Reunión Anual 2011 de la Unión Geofísica Mexicana (UGM), Puerto Vallarta, Jalisco, México)

Stéphanie,

Un Amour qui a nourri une Passion

ACKNOWLEDGEMENT

First, I thank my advisor, Alessandro Aiuppa, for inviting me to work on incredible projects and to participate in numerous scientific field missions and meetings dedicated to the study of volcanic gases worldwide. Through several field seasons I have learned about the volcanology and methodology to monitor active volcanoes, especially in Italy, where I had the opportunity to entirely live the culture. Overall, I thank Sandro for his encouragement, support and patience. I also thank Gaetano Giudice at INGV-Palermo for his guidance, who introduced me to an impressive world of technology and genuine approaches. I specially retain a lot from his creativity; this is the motor of science and improvement !

Special thanks to Silvio Rotolo (DISTEM) and his former students, Maria Luce Frezzotti (U. Milano), Andrea Rizzo (INGV-Palermo), Eric Hauri (Carnegie Institution), Andrea Cavallo (INGV-Roma), Franco Furnari (DISTEM), Giovanni Lanzo (DISTEM), Sergio Calabrese (DISTEM) for helping me through all the laboratory experience.

The members of the INGV students/staff (Vincenzo Francofonte, Andrea Maestro, Marcello Bitteto, Andrea Di Piazza, etc.), who provided me with a friendly and cooperative working environment. Without exception, all members I have met there are incredible funny and special co-workers.

All my colleagues, specially Giancarlo Tamburello, Maria Pedone (Piccirida), Claudio Inguaggiato, Emmanuella Gennaro, Silvia Milazzo, Lisa Gagliano, Pierangelo Romano, etc. They all followed me since the beginning of the PhD.

Our partners in Central America: INETER-Nicaragua and OVSICORI-Costa Rica and the DCO community, Vladimir Conde and Bo Galle from Chalmers U. Technology, Gothenburg (Sweden). Thanks to Gilles Lévresse for helping with mFTIR (CGEO-UNAM).

Special thanks to some of my former professors at UNAM (Prof. Yuri Taran), UQAM (Prof. Daniele Pinti) and McGills University (Prof. Anthony E. Williams-Jones) who continue to show interest in my career.

To all the members of the Dipartimento di Scienze della Terra e del Mare (DiSTeM) who created a welcoming environment.

TABLE OF CONTENTS

LIST OF FIGURES

INTRODUCTION

Volcanoes represent a key step in the transfer of major volatiles from the Earth interior to its surface. To investigate the role, behavior and fate of volatiles in volcano-magmatic systems, research focuses on three general depth zones: 1) eruption, and shallow magma interaction levels with atmosphere and hydrosphere, 2) crustal stagnation and differentiation of magma and 3) root zone where magma is generated and rises in the mantle.

The tectonic setting where lithospheric plates share contact with each other determine the environment and transport mechanisms of volatile budget from one reservoir to another. Plate margins can be divergent (mid-ocean ridges, rift zones) or convergent (subduction zones) and each correspond to distinct mechanisms of volatile transport.

Subduction zones exhibit a number of particularities; volatiles are contributed by marine sediments and hydrothermally altered rocks in the deep seafloor. Over geological time scales of Myrs, inorganic and organic fluids rich in water, carbon (S, Cl, F, etc.) are transported at depth by subduction, and released by the subducting slab surface into the mantle. A fraction of the mass of each volatiles returns to the exosphere through the nearby arc volcanoes driven by subduction. Volatile elements participate into magmatic processes at variable pressures and temperatures, and are finally exhaled at surface by volcanism.

Onland, at the convergent margins, there is variety of natural hazards caused by volcanism. Volcanoes are numerous, but the diversity of their eruptive style often includes explosive eruptions. Paradoxically, a large part of the global population live in the surroundings of active volcanoes because of many advantages (fertile volcanic soils, ore deposits, volcanic raw material, geothermal energy, tourism, etc.). Despite of these natural benefits, however, many developing countries with insufficient social/economical resources struggle with the lack of scientific and risk management resources, and lack of efficient and fully volcano monitoring networks.

1.1 Objective

In this thesis, I explore the sources and behavior of major volatiles like H_2O, CO_2, S and Cl in two volcanic systems from NW Nicaragua (Central America).

Volatiles play a crucial role in mantle melting, magma differentiation and eruption style during magma evolution from the mantle to the surface. For this reason, I integrate here multiple aspects of volatiles evolution, from close to the surface and at the deeper levels of the magma feeding system. A special attention is reserved to CO_2, which owing to relatively less reactivity compared to H_2O, SO_2, or HCl is considered as an optimal chemical tracer of magmatic degassing processes (Symonds et al. 2001).

In the aims of studying a typical volcanic arc setting that is densely populated, we are targeting a series of active open-vent strato-volcanoes in Central American Volcanic Arc (CAVA). Those volcanoes represent magma of basaltic to andesitic compositions and they are continuously emitting a plume at the central crater which facilitate the investigation for estimating total output gas budget. Two of these volcanoes are at the moment among the most

active in CAVA; San Cristóbal and its neighbor Telica. San Cristóbal have erupted ash clouds at few hundred meter high in June 12, 2015 and several explosions occur almost each years since 2009 with fluctuating seismic activity and SO_2 gas fluxes at the central plume. At Telica, on September 26, 2015, a series of strong explosions sent ash cloud to 3 km high and also shows frequent signs of activity (GVP, 2014). Considering the increasing information on the gases emitted by their quiescent degassing regime (Galle et al., 2010; Conde et al., 2013; Conde et al., 2014; Aiuppa et al., 2014; Conde, 2015; Conde et al., 2015) additional work need to furnish background information on their respective volatile content in primary magma (Sadofsky et al., 2008; Wehrman et al., 2011). We therefore focus on these two volcanoes to build a degassing model which can integrates data on volatiles from melt inclusion and temporal variation of gases from the central crater plume.

For realizing such investigation, a multidisciplinary melt inclusion/gas monitoring approach is proposed, which combines (1) field instrumentations and (2) laboratory facility, as described below.

1.1.1 Field instrumentations

A variety of novel gas sensing techniques have recently assisted volcanic plumes, such Multi-Component Gas Analyzer systems (Multi-GAS, Shinohara, 2005 Aiuppa et al., 2005a), open-path FTIRs (Oppenheimer et al. 1998; Duffell et al. 2003; Sawyer et al. 2011), ultraviolet differential optical absorption spectrometers (UV-DOAS; Platt, 1994), correlation spectrometers (COSPEC; Hoff and Millan, 1981), light detection and ranging (LIDAR; Svanberg 2002), and tunable laser system (Humphries et al., 2008). These instrumental methods can all provide complementary information on gas behavior through time series at superficial levels. Periodic gas sampling campaigns, using evacuated-flasks to directly sample crater fumaroles gases, still continue today, and remain the only source for analyzing the maximum of compounds for tracing gas changes and genesis (Giggenbach, 1975; Giggenbach and Matsuo, 1991; Fischer, 1998).

Among those techniques designated to measure volcanic gas plume concentrations and its variation over time, I studied the field deployment and data acquisition of manufactured Multi-GAS from Insituto Nazionale de Geofisica e Vulcanologia of Palermo (INGV – Palermo). It is a practical economic instrument that targets small time scale variations of H_2O, CO_2, SO_2 and H_2S with a system of pneumatic tubes and electrochemical/ IR sensors. During the PhD work thesis, with INGV-Palermo colleagues, I used the Multi-GAS and helped to install its components with telecommunication devices to remote automatically a volcanic plume (Stromboli, Etna, etc.) or used the instrument as a portable captor to trace spatial changes in a fumaroles field (e. g. Solfatara Puzzoli).

During the Observation of Volcanic and Atmospheric Change (NOVAC) missions in Nicaragua and Costa Rica (2013 – 2014), with INGV assistance from Italy, field work was integrated as an important chapter for my thesis. I helped Prof. Bo Galle and Dr. Vladimir Conde (Department of Earth and Space Sciences, Chalmers University of Technology) to install the Multi-GAS instruments in tandem with a OP-FTIR that were brought to measure a large set of gas species in the plume (H_2O CO_2, H_2O, S species and HCl, F). Also, during the 2013-2014 period, I helped the NOVAC colleagues to install, repair and activate a UV-DOAS station network at different volcanoes (3 at Telica, 3 at Turrialba; 2 at San Cristóbal, 3 at Masaya) that were scanning the plume for calculating temporal change in SO_2 fluxes. Those mission field work have been organized in collaboration with governmental agencies specialized for natural hazards in Nicaragua (Instituto Nicaragûense de Estudios Territoriales; INETER) and Costa Rica

(Instituto de Investigación Observatorio Vulcanológico y sismológico de Costa Rica; OVSICORI-UNA).

1.1.2 Laboratory facility

Melt inclusions in mafic minerals have been widely used for probing volatile behavior in deep regions of magmatic plumbing systems. During the last 50 years, this aspect of petrology have been mainly developed by new instruments in laboratories, for example by the development of the heating stage technique (e.g. Sobolev et al., 1971). First detailed work on the genesis and trapping of melt inclusions were summarized in (Sobolev and Kostyuk, 1975; Roedder and Weiblen, 1970, Roedder, 1979, 1984). More recently in the 1990s, the development of advanced micro-analytical techniques (electron microprobe, secondary ion microprobe spectroscopy, IR microspectroscopy, Raman spectroscopy, etc.) has helped researchers to use melt inclusions as one of the best tools in petrology (summarized in Lowenstern, 1995; Sobolev, 1996; Frezzotti, 2001; Schiano, 2003; Wallace, 2005; De Vivo and Bodnar, 2008; Kent, 2008; Métrich and Wallace, 2008, etc.).

To provide an extend of petrologic information on abundance and degassing behavior of volatile species at San Cristóbal and Telica, a series of important pyroclasts and lava from important eruption since Holocene have been analyzed. We have chosen the melt inclusion approach to cover the whole composition of primitive to mostly evolved magma that participated to past and recent eruptions, because they represent initial trapped melts and volatiles at different depths and pressures of the volcano-magma system. Glass inclusions from San Cristóbal and Telica volcanoes were analyzed for major elements and volatiles (CO_2, H_2O, S and Cl, F) by electron microprobe at INGV-Roma with the help of Andrea Cavallo and Piergiorgio Scarlato, for water (H_2O, OH^-) and carbon (CO_3^{2-}, CO_2) species by mFTIR at Università Degli Studi di Palermo (UNIPA) with Prof. Silvio Rotolo and Dr. Giovanni Lanzo. CO_2, H_2O, S and Cl by Nano - secondary ion microprobe spectroscopy (NanoSIMS) were being measured for a set of impressive small scale inclusions (10-50 µm in size) with Dr. Erik Hauri at Carnegie Institution (Washington, D.C., U.S.). Because of the special attention given to CO_2, we also used detailed microRaman spectroscopy with Prof. Maria-Luce Frezzotti and Dra Simona Ferrando at Università degli stud de Torino (UNITO) for measuring CO_2 density in < 4 – 20 µm diameter shrinkage vapor bubble in the attempt to correct CO_2 loss that leak the inclusions to the bubble. Fluid inclusions (FI) from mineral separates from the same materials were also analyzed for their Ne-He and Ar noble gas isotopes by mass spectrometry with Dr. Andrea Rizzo, with the aim of tracing the origin of fluids from magmas feeding the reservoir beneath, while Laser- Light Amplification by Stimulated Emission of Radiation (ICPMS) instruments was used with Dr. Antonio Paonita and Dra. Claudia Doriano to measure trace and rare earth elements signatures in some inclusions. The objective is to trace the origin of their respective primitive melts in addition to major, trace and rare earth elements measured on bulk rock samples made with Antonio Furnari (UNIPA) by using wavelength-dispersive X-ray fluorescence (XRF) and ICPMS (Act Labs, Ancaster, Canada).

1.2 Combining melt inclusion/gas monitoring approach

In different volcanic arc settings, models have been proposed to explore quiescent and eruptive degassing processes, by combining both volcanic gas and melt inclusion approaches; for example at Stromboli and Etna in Italy (Burton et al., 2007b; Aiuppa et al., 2011). Integrated

petrological-gas studies are now implemented to obtain comprehensive information on volatile behavior in magmatic systems. On the one hand, melt inclusions are trapped at different depth by crystal during magma crystallization, and can therefore record the whole degassing story of melts during ascent and eruption. In turn, gas observations, eventually assisted by new instrumental techniques such Multi-Component Gas Analyzer systems (Multi-GAS, Aiuppa et al., 2005a), can provide complementary constraints on gas behavior at superficial levels (Allard et al., 1997; Shinohara et al., 2003; Allard et al. 2005). Examples of these multi-disciplinary studies performed with the Multi-GAS include also Yasur and Ambrym in the Vanuatu arc (e.g. Métrich et al. 2011; Allard et al., 2015). A similar integrated gas-petrological approach is used in this thesis to characterize Telica and San Cristóbal volcanoes.

1.3 Organization

Using similar philosophy as in previous mentioned work, this thesis includes three central chapters (C. 4, 5), where each corresponds to different submitted/ published manuscripts. The publication 1 and 2 are found as external appendices (A, B).

1.3.1 Summary Publication n. 1

Conde, V., **P. Robidoux**, G. Avard, B. Galle, A. Aiuppa, A. Muñoz, 2014, Measurements of SO_2 and CO_2 by combining DOAS, Multi-GAS and FTIR observations: a case study from Turrialba and Telica volcanoes, *International Journal of Earth Sciences, June 2014, p.1437-3254*

This work is presented in chapter 4.1 and present the CO_2/SO_2 ratio that were obtained by a fully-automated Multi-GAS instrument, developed at the Istituto Nazionale di Geofisica e Vulcanologia (INGV), Sezione di Palermo. The Multi-GAS approach represents a excellent tool for showing time series changes in gas compositions, but it measures only a section of the whole volcanic plume. For this reason, this ratio is even more representative of the whole volcanic plume when comparing with a performing cross-crater open path Fourier transform infrared spectroscopy (FTIR) measurements (Oppenheimer et al. 1998; Sawyer et al. 2011; Duffell et al. 2003; Conde et al., submitted). Finally, stationary and mobile Multi-GAS measurements combined with OP-FTIR technique and DOAS are determined to be the main field approach for this project. Putting all together, it is even more representative of the whole temporal and spatial changes in gas plume compositions which was one of the principal element of discussion (Conde et al., 2014). Those gas flux measurements of CO_2 and SO_2 were measured with the participation of NOVAC and INGV-Palermo in collaboration with governmental agencies OVSICORI-UNA (Costa Rica) and INETER (Nicaragua) during the campaign 2013 at Turrialba, Telica and San Cristóbal. As mention previously (cfe 3), the strategy to calculate CO_2 fluxes depends on the results from Multi-GAS sensors to obtain CO_2/SO_2 ratio of the plume which is multiplied by the SO_2 flux rate given from a UV-DOAS instrument. At Turrialba and Telica, OP-FTIR were used to validate Multi-GAS ratios and to allows the measurement of the concentration of volcanic gas species that have spectral signatures in the infrared region (e.g. CO_2, SO_2, HCl, HF, CO, COS).

1.3.2 Summary Publication n. 2

Aiuppa, A., **P. Robidoux**, G. Tamburello, V. Conde, B. Galle,G. Avard, E. Bagnato, J. M. DeMoor, M. Martinez, A. Munoz, 2014, The Costa Rica – Nicaragua volcanic segment: along arc variations in volcanic gas chemistry and improved CO_2 budget, *Earth and Planetary Science Letter, October 13, p.134-147*

This work is presented in chapter 4.2 where we investigated the volcanic gas plumes of Turrialba, Poás, and Rincón de la Vieja (all in Costa Rica) and of San Cristóbal and Telica (both in Nicaragua) by using the Multi-GAS, whose first volcano applications emerged in the mid-2000s (Aiuppa et al., 2005; Shinohara, 2005), is a compact unit constructed by assembling different commercial IR (for CO_2 and H_2O) and electrochemical (for SO_2 and H_2S) gas sensors. The same sensor assemblage as in Aiuppa et al. (2009, 2010, 2011) was used in the present study. We employed two distinct types of Multi-GAS. At Turrialba, Poás, San Cristóbal, and Telica, we temporarily deployed a fixed, fully autonomous version of the Multi-GAS, similar to the systems used in other permanent networks (e.g., Stromboli; Aiuppa et al., 2009). The fixed Multi-GAS, powered by a 12-V lead-acid battery connected to a photovoltaic module, ran unattended at Turrialba from March 12 to March 19, 2013; at Telica from March 27 to April 5, 2013; at San Cristóbal from April 11 to 16, 2013; and at Poás during April 16–18, 2013. At all volcanoes the fixed Multi-GAS was deployed at a location within the active crater(s) area, from tens to a few hundreds of meters from the main degassing vent(s), which ensured frequent fumigation by the plume. The instrument was programmed to measure the concentrations of various gases (H_2O, CO_2, SO_2, and H_2S) in the plume at a sampling rate of 0.1 Hz, in cycles lasting for 30 minutes (four to eight daily cycles were performed, depending on power availability).

1.3.3 Summary Publication n. 3

Robidoux, P., Aiuppa, A., Rotolo, S., Hauri, E., Rizzo, A., Frezzotti, M.L., (2016). The volatile content of mafic to intermediate magmas from San Cristóbal volcano, Nicaragua, Manuscript in preparation for *Lithos*

This work is presented in chapter 5.1 and targets the abundance, source and behaviour of volatiles in magmas of San Cristóbal, in the NW-sector of the Nicaragua volcanic arc segment. This volcano was previously un-studied for volatile contents in primary melts (Sadofsky et al., 2008; Wehrman et al., 2012). Here, volatile contents were measured in melt inclusions of mafic crystals, for tracking the degassing style and volatile signature of the most primitive volatile-rich melts. In the framework of the thesis, glass inclusions were analyzed for major elements and volatiles (CO_2, H_2O, S and Cl) by electron microprobe at INGV-Roma (Italy), mFTIR at UNIPA (Italy) and NanoSIMS at Carnegie Institution (Washington, D.C., U.S.). A set of inclusions (10-50 µm in size) was also analyzed by microRaman (U. Torino, Italy) in the attempt to correct for CO_2 loss to shrinkage bubbles. Results are used in the attempt of reconstructing volatile-related magmatic processes and their variations since Holocene periods at San Cristóbal. The main targets are (A) the crustal plumbing system and (B) the conditions of the magma feeding source. In addition, trace elements in whole rocks and noble gases analysis from fluids inclusions in olivines were integrated to this study to identify the magma origin in the mantle.

1.3.4 Summary Publication n. 4

Robidoux, P., Aiuppa, A., Hauri, E., Rizzo, A., Lanzo, G., Rotolo, S., (2016). Geochemistry and petrology of magmas produced during explosive eruptions at Telica, Manuscript in preparation for *Lithos*

This work is presented in chapter 5.2 and focuses on the magmas feeding the explosive eruptions of Telica, a volcano located about 10 km SE from the San Cristóbal volcanic complex. Like at San Cristóbal, I explore with similar instrumentation to chapter 5.1 the conditions at which magma ascend and stagnate in the crust and evolve through differentiation in the plumbing system, but by focusing on a vulcanian eruption of high explosivity represented by Scoria Telica Superior. I report here the first volatile abundances in Telica melt inclusions that are clearly identified in literature for their eruptive episodes, and I additionally use trace and rare earth elements from single melt inclusions to track the source of the primitive melts. I search for correlations between regional trace and rare earth element tracers with volatile contents. An attempt is also made to model the evolution of crystal assemblages and liquid with MELTs software (Gualda and Ghiorso, 2015) and identify regional patterns resumed in Patino et al. (2000) by tracking the origin of volatile flux components from the subducted slab to the mantle wedge beneath Telica.

Chapter 2 - Geological Background

The Central American Volcanic Arc (CAVA) represents a chain of volcanoes that extends along the Pacific coast line between Guatemala and Costa Rica. This volcanic arc is the result from the northeasterly Cocos Plate's subduction beneath the Caribbean Plate. The rate of subduction ranges from 6 cm/yr off southern Guatemala to 9 cm/yr off southern Costa Rica (Demets, 2001). The volcanoes of CAVA are geographically distributed along a NW-trending 1,100 km long corridor between latitude 10° and 15° (Fig. 1).

As in many arcs, there are two regions of magmatism, the volcanic front and the back-arc (Patino et al., 2000). The volcanic front is composed of Quaternary volcanoes of diverse morphology, such as complex composite volcanoes, calderas and numerous small cinder cones that are not necessary close with the neighboring polygenetic volcanoes (Walker et al., 2001; Kutterolf et al., 2007). The Holocene and Pleistocene age back-arc volcanism mainly lies east of the volcanic front along the Caribbean Sea lowlands in Honduras, Nicaragua, and Costa Rica (Patino et al., 2000; Carr et al., 2007).

2.1 Tectonic context of CAVA

This study is focalized on Costa Rica and Nicaragua, on the southern segment of the Central American Volcanic Arc (CAVA). Volcanoes are aligned along an active margin which is the consequence of Cocos plate subduction beneath the Caribbean plate since the late Cretaceous.

Nicaragua and Costa Rica exhibit different subduction parameters (Fig. 1). For instance, the angle of slab dip varies between 61 to 65 ° below the volcanic front of Nicaragua (Syracuse and Abers, 2006; Auger et al., 2006; MacKenzie et al., 2008). Within this context, convergence rates of Cocos plate below Nicaragua is 74 mm/yr (Ehrenborg, 1996; DeMets et al., 2001). Contrast exists also at mantle levels between NW Nicaragua and Costa Rica. The Vp/Vs anomaly that defines a change between rigid crust and viscous mantle lies at 80 km depth in NW Nicaragua under the arc, but farther SE, it lies at 40 – 50 km and is aligned with the location of the arc front in Costa Rica (Fig. 2 a-b). This may force magma to migrate toward the thinner crust in southern Nicaragua, rather than ascending vertically (Mackenzie et al., 2008).

In comparison to Nicaragua, Costa Rica is characterized by shallower dips (35 to 65 °) and slightly thicker crust (>40 km) compared to central Nicaragua (<34 km) (Fig. 2 a-b; Shaw et al., 2003; Syracuse and Abers, 2006; MacKenzie et al., 2008). Based on geophysical constraints relating Bouguer gravity to regional elevation, the crustal structure of Costa Rica is made of superimposed Tertiary and Quaternary volcanic sequences, resulting in a thick crust of intrusive and extrusive arc magmas accumulated over 45 km (Carr et al., 1990; Carr et al., 2003). The oceanic subducted plate beneath Costa Rica and western Panama is significantly younger, convergence rates are slower (84 mm/yr), and it contains the Galapagos hot spot track marking on the seafloor (Werner et al., 1999, 2003; Hoernle et al., 2008; Gazel et al., 2009).

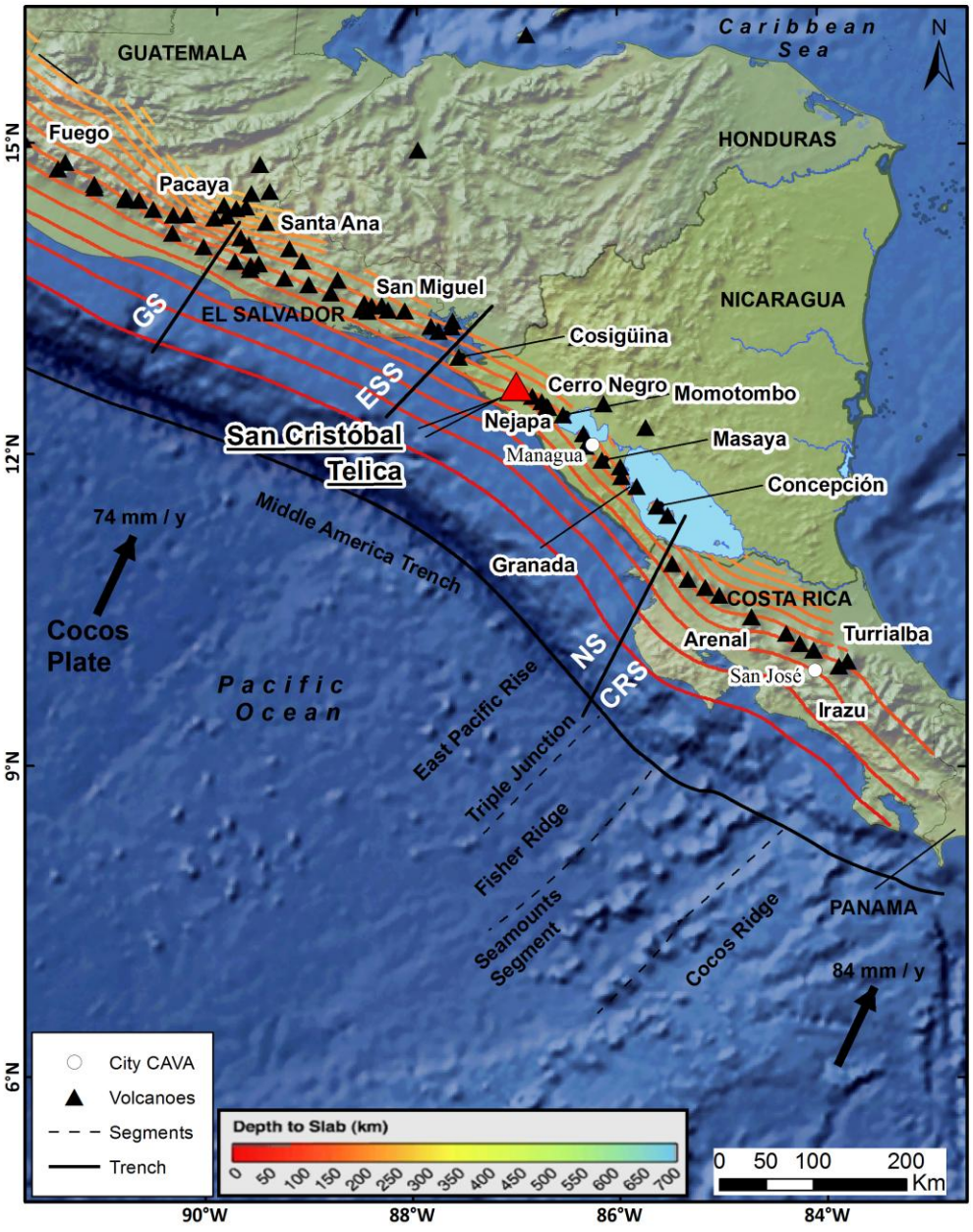

Fig. 1 CAVA region. Map of the subduction zone integrating arc segments from El Salvador (ESS), Nicaragua (NS) and Costa Rica (CRS). Arrows indicate the direction of motion of the Cocos Plate and the convergence velocities relative to the Caribbean Plate (in millimeters per year) after DeMets (2001). Topography effect is representing the 1:10m Natural Earth II with Shaded Relief and Water; file "CleanTOPO2" released by Smith and Sandwell in 1997 with contour shape files from ESRI and mapped with ArcGIS, Arc Map 10.1; World Map. Plate segments and trench structures are interpreted from the bathymetry imagery in Von Huene et al. (2000).

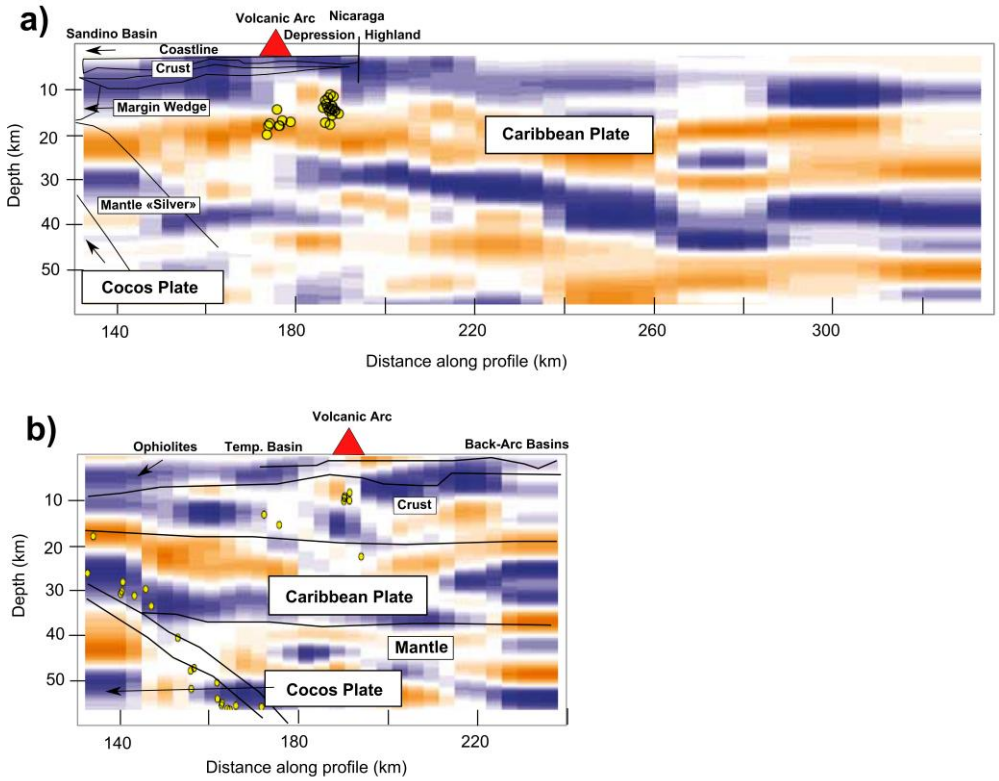

Fig. 2 Tectonic profile behind CAVA. Modified from Mackenzie et al. (2008). a) Interpolated receiver functions for Nicaraguan , slab depth (Vp/Vs and tomography from Mackenzie et al., 2008). Colored lines show interfaces from refraction survey (Walther et al., 2000). b) Interpolated receiver functions for Costa Rican line. Colored lines show main interfaces from refraction survey (Sallares et al., 1999).

In Nicaragua, the tectonic setting determines an high transfer of slab fluids into a relatively small asthenospheric volume (Carr et al.,1990). Geochemical studies have shown that most of the lavas are normal mid-ocean ridge basalts (N-MORB) produced by high degrees of partial melting of a mantle largely contaminated by serpentinite-derived fluids rising from the subducted plate (e.g. Carr, 1984; Carr et al.,1990; Patino et al., 2000; Ranero et al., 2003; Grevemeyer et al., 2007; Ivandic et al., 2008; Heydolph et al., 2012).

2.2 Structural geology

Convergence between the young Cocos plate (< 25 Myrs) and the Caribbean plate along the Middle America Trench is the principal contributor to regional faulting and deformation between Nicaragua and Panama. Oblique subduction at particularly high convergence rates (DeMets et al., 2003) results in NW-directed trench-parallel block motion (Lafemina et al. 2002); the obliquity angle varies due to changes in strike of the trench, from essentially zero in southern Costa Rica to more than 15° in Nicaragua (Barckhausen et al., 2001).

The general parallel motion to the American Trench, is obvious for most of the region, and according to Lafemina et al. (2009) may partially explain the oblique convergence and variable effects of mechanical coupling between subducting and overriding plates between north of Nicaragua (Nicoya Point) and south of Costa Rica (Osa Point). This motion may also be linked to upper plate expressions of deformation (Protti et al., 1995; Lafemina et al., 2009). This trench-parallel motion is also observed in central Costa Rica, where plate convergence is normal to the trench, and according to GPS surveys the Nicaraguan forearc movement is even faster (>80 mm/yr) (DeMets, 2003; Lafemina et al., 2009).

On land, the main deformation structures since Pleistocene-Holocene include three active fault trends: N45° – 65°W right-lateral strike-slip faults, N30° – 45°E left-lateral strike-slip faults, and N15°W – N10°E normal faults (Carr, 1976; Weyl, 1980; Manton, 1987; Weinberg, 1992). Several volcanoes in Nicaragua are associated with these N–S striking extensional structures which cross the volcanic front. This is particularly of interest, because their mechanism can control the volcanic plumbing system permeability by opening or closing fractures that allow magma ascent and degassing and also by accelerating magma transport through the crust (Carr et al., 2003). From structural field mapping, in Nicaragua, NE striking faults dominate the forearc and arc (Carr, 1976; Weyl, 1980), while in El Salvador, Guatemala, and Costa Rica, there is more evidence of NW striking right-lateral faults (Carr, 1976; Marshall et al., 2000). These NW-striking faults are thought to be associated with segment breaks along the Central American volcanic arc (Stoiber and Carr, 1973; Carr, 1976).

Overall, the general N-striking faults show normal to oblique offset and bound N-striking grabens, such as the Managua graben in Nicaragua (Girard and van Wyk de Vries, 2005), the Gulf of Fonseca and the Guatemala City graben (Stoiber and Carr, 1973). N-S alignments of volcanic vents, like the Cerro La Mula–Cerro Negro alignment (McBirney and Williams, 1965; Weinberg, 1992), are common along the volcanic front, but large transverse extensional structures occur only at the right steps between the volcanic lines. This is specially accentuated in the region of the Nicaragua Depression (Fig. 3) with its NW–SE trending and 45-km-wide structures affected by many still seismically active strike-slip fault and grabens (Weyl, 1980; Hradecký et al., 2007). Large part of the Depression is occupied by the Managua Lake, the ignimbrite plateau of Tipitapa, the Nicaragua Lake, and by the Coyol Neogene lavas and ignimbrites between the San Cristóbal and Cosigüina volcanic complexes (Hradecký et al., 2007).

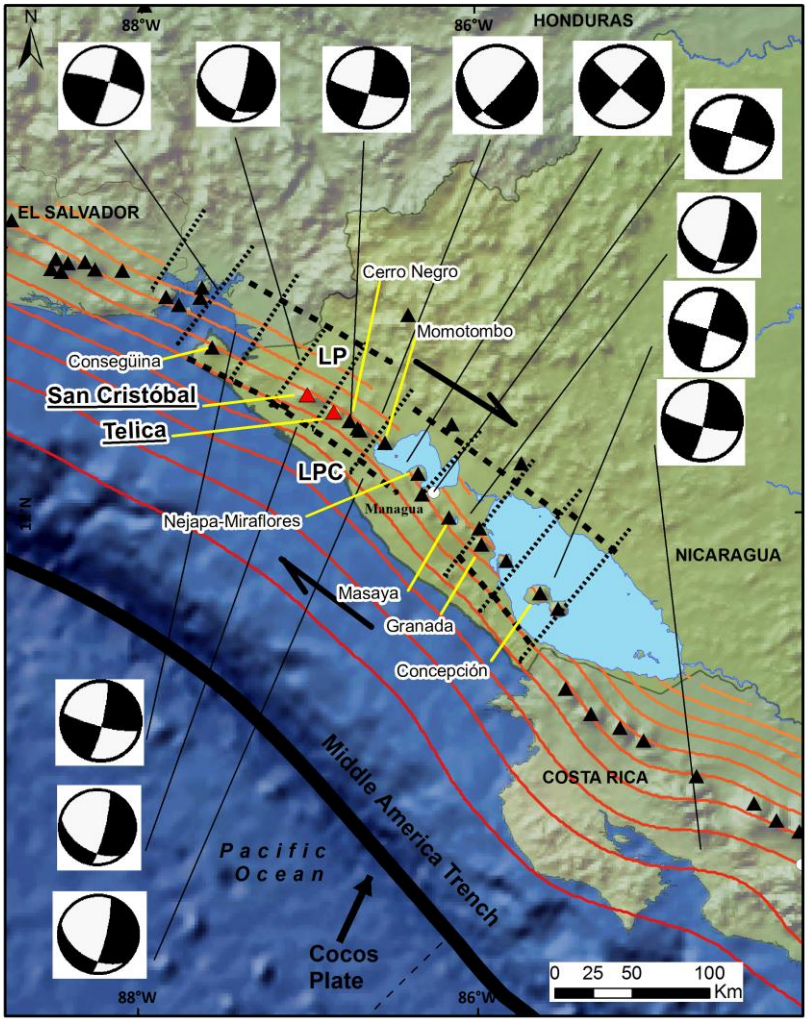

Fig. 3 Structural regional map of Nicaragua. Structural lineaments and focal mechanisms are from Lafemina et al. (2002). Digital elevation model is from figure 1. Focal mechanisms of historical strike-slip earthquakes are from Molnar and Sykes (1969), White (1991), and Harvard centroid moment tensor catalog (see Lafemina et al., 2002).

The geomorphologic depression observed in Nicaragua was apparently formed since Plio-Pleistocene (Weinberg, 1992). In the Nicaragua segment, the crust thickness varies between 25 km beneath the volcanic front to 34 km inland (Syracuse and Abers, 2006; Auger et al., 2006; MacKenzie et al., 2008). Recent GPS measurements show that the fore arc is translating NW at 15 mm/yr with only a few mm/yr at most of arc-normal extension (Turner et al., 2007), and may be accommodated by bookshelf-type faulting on arc-normal strike-slip fault systems (La Femina et al., 2002) which would lead to little crustal thinning. Still, many uncertainties remain on if the depression was caused by opening rifting (and if it continues to occur), and if the crustal thinning

structure occurred before the formation of the depression structure itself and the modern volcanic arc (Weinberg, 1992; Walther et al., 2000).

2.3 Petrology

Volcanic rocks at the volcanic front of Nicaragua and Costa Rica are generally classified as basalts, basaltic andesites and andesites (Saginor et al., 2007). In the Costa Rica back-arc, most of the basalts are alkali-rich (K_2O, Na_2O) and south of Costa Rica (Fig. 4), it is frequent to find alkali basalts and adakites.

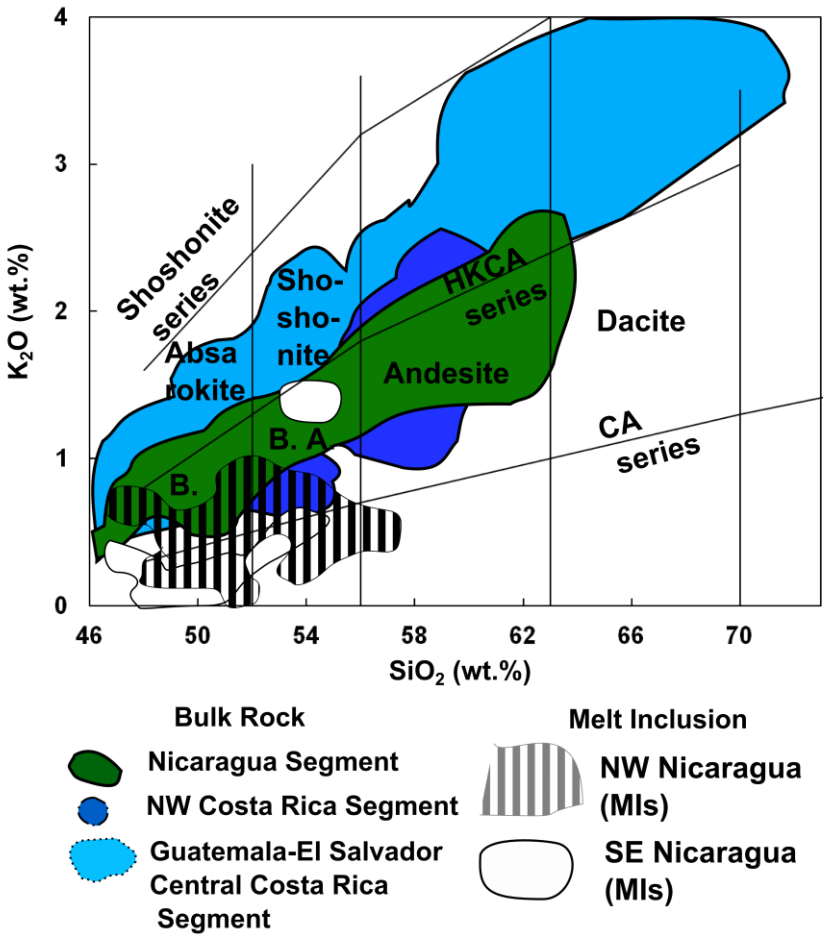

Fig. 4 Geochemical classification diagram (Peccerillo and Taylor, 1976). Modified from Saginor (2008). Colored polygon represent the field of compositions from data of Carr et al. (2003) and Saginor et al. (2008).

According to the Zr/Y classification of Pearce (1999), most samples have tholeitic affinity in Nicaragua and Costa Rica, while the rocks in El Salvador to Guatemala are between tholeiitic and transitional (Fig. 5).

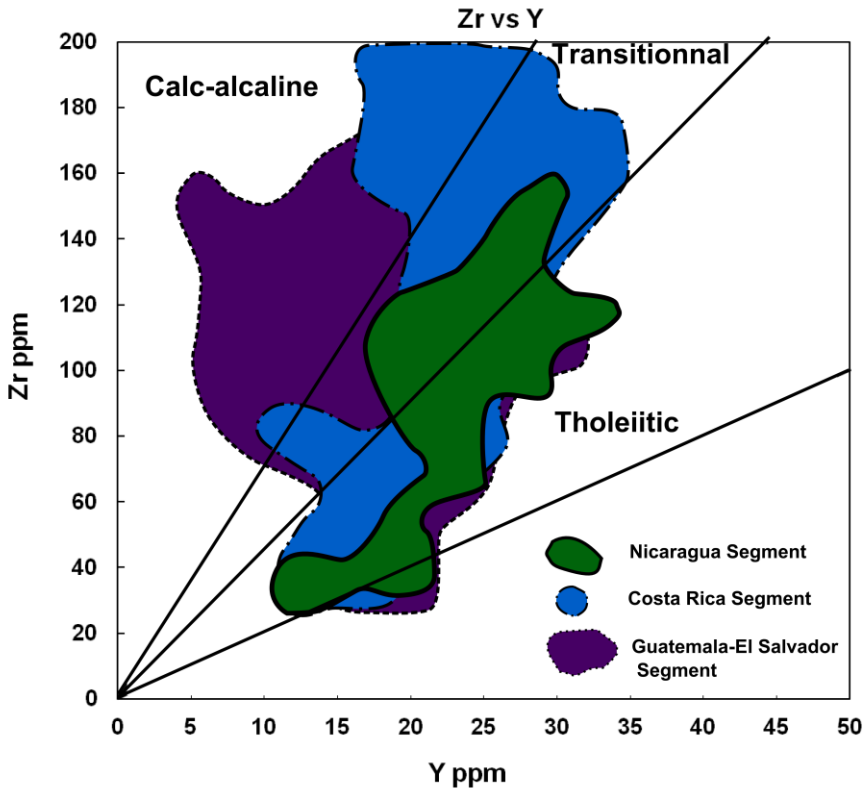

Fig. 5 Zr vs Y volcanic series of CAVA. Tholeiitic-transitionnal-alcaline series are illustrated with polygon of Guatemala-Salvador, Nicaragua, Costa Rica. Data are compiled with GEOROC and Geochemical Earth Reference Model (GERM).

Their primary melts, investigated using melt inclusions (Sadofsky et al., 2008; Werhman et al., 2011), demonstrate large heterogeneities of the sources on local and regional scales, which may be related to variable contributions of various slab, crustal and mantle components involved in magma genesis (Fig. 6a). Sadofsky et al. (2008) observed i of water and major and trace elements (e.g. Ti, Y and Na; Ba/La, B/La) indicating melting of a mantle wedge with fluids rich in Barium, Boron and H_2O (serpentinite-derived) beneath the central (Nicaraguan) part of the arc. In SE Nicaragua and Guatemala LREE are richer in glass inclusions and in Costa Rica, highly incompatible elements are showing higher contents (e.g. Nb, La) (Sadofsky et al., 2008).

Generally in CAVA, the trace and rare earth element geochemistry of bulk rocks show N-MORB profiles in Nicaragua to Guatemala, and minor differences between LREE (La) and HREE (Yb-Lu). In contrast, Costa Rica samples from Turrialba in Bolge et al. (2009) show steeper REE normalized trends, and are more enriched in incompatible light REE, as seen MORB-normalized spidergrams from melt inclusion analysis of Sadofsky et al. (2008) (Fig. 6bc). The thickness of the crust overlying the mantle wedge has been shown to correlate with the extent of melting (Plank and Langmuir, 1998) and therefore may play an important role by increasing the degree of melting for producing the magma bodies in CAVA (high La/Yb ratios).

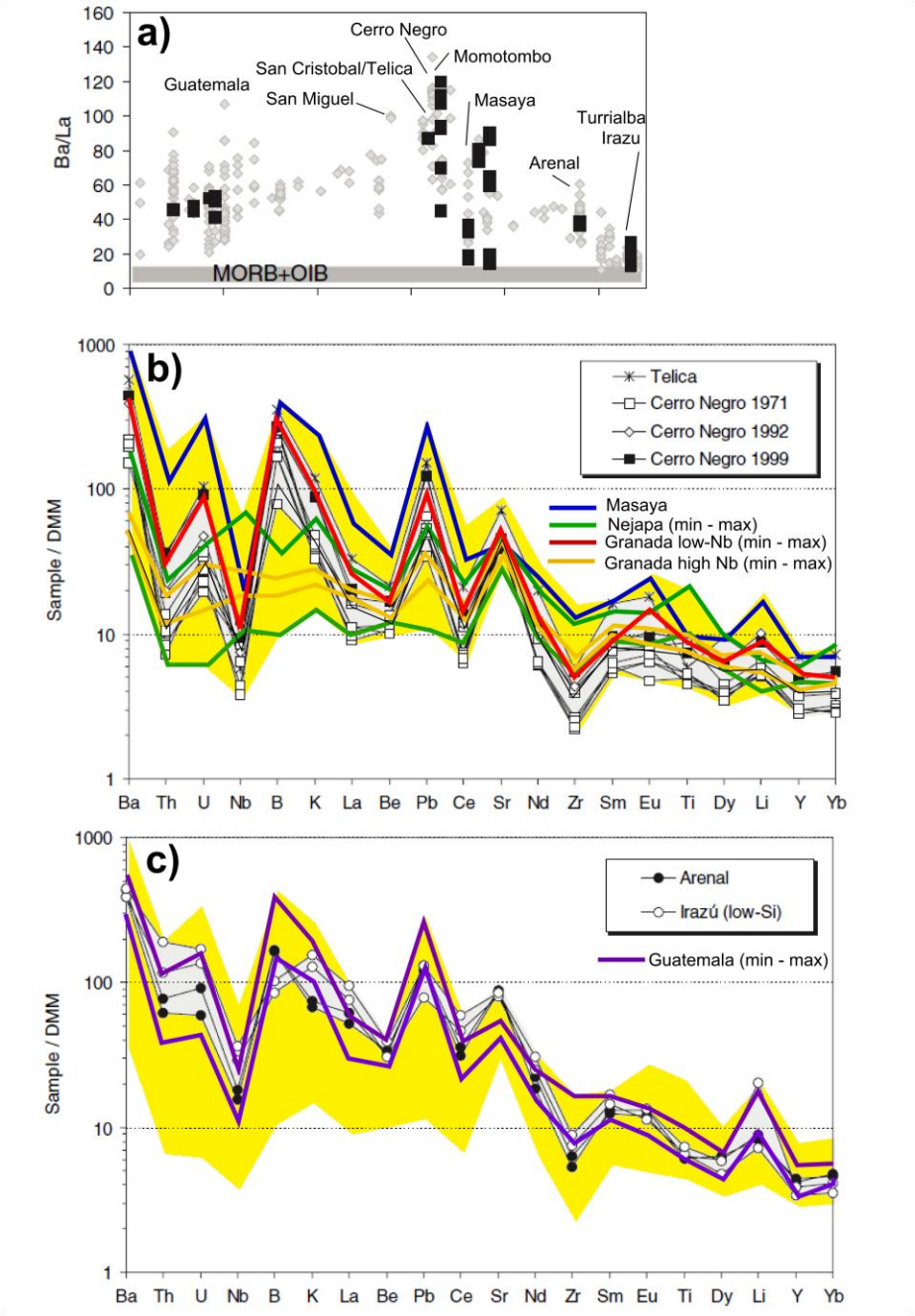

Fig. 6 Trace and rare earth elements in CAVA. a) Ba/La ratios of incompatible in melt inclusions plotted versus distance along the arc (see Sadofsky et al., 2008). Filled symbols denote data from Sadofsky et al., (2008), small gray diamonds denote compositions of primitive to moderately evolved whole rocks with SiO_2\54 wt%. Horizontal lines illustrate typical trace element ratios in mid-ocean-ridge basalts (MORB) and ocean-island basalts (OIB) (Chaussidon and Jambon 1994; Hofmann 1988; Sun and McDonough 1989). CAVA Spidergram are represented Incompatible trace elements in melt inclusions normalized to the composition of depleted MORB mantle (DMM; Salters and Stracke 2004). Yellow field illustrates the entire compositional range of the melt inclusions from Central America. b) Nicaragua. Minimum (min) and maximum (max) normalized values are defining the limit for some volcanoes c) Costa Rica. Purple lines define the min-max values from Guatemala (Atitlán, Agua, Fuego, Santa Maria).

Generally in CAVA, the trace and rare earth element geochemistry of bulk rocks show N-MORB profiles in Nicaragua to Guatemala, and minor differences between LREE (La) and HREE (Yb-Lu). In contrast, Costa Rica samples from Turrialba in Bolge et al. (2009) show steeper REE normalized trends, and are more enriched in incompatible light REE, as seen MORB-normalized spidergrams from melt inclusion analysis of Sadofsky et al. (2008) (Fig. 6bc). The thickness of the crust overlying the mantle wedge has been shown to correlate with the extent of melting (Plank and Langmuir, 1998) and therefore may play an important role by increasing the degree of melting for producing the magma bodies in CAVA (high La/Yb ratios).

Many researchers have also emphasized the importance of slab fluids in the genesis of CAVA magmas, based on petrology and geochemistry of the rocks (Carr et al., 1984; Leeman et al.,1994; Patino et al., 2000; Eiler et al., 2005; Barnes et al., 2008; Bolge et al., 2009; Heydolph et al., 2012) and stable gas isotopes (Shaw et al., 2003; Zimmer et al., 2004; Elkins et al., 2006; Hilton et al., 2010). The Ba/La ratio has been indicated as a good tracer of regional variations in slab-fluid contributions (Fig. 6a), in addition to Boron and beryllium isotopes that show particularly high values in Nicaragua (see also Zr/Nb, U/Th; Heydolph et al., 2012). According to Van Keken et al. (2011), the Nicaragua subducted plate exhibit Intermediate thermal structure, and dehydrates at various depth levels. Cl - isotopes evidence fluid contribution from serpentinites in the Nicaragua arc (Barnes et al., 2009), and seismic evidence exists for significant serpentinization of the mantle due to normal faulting in the forearc (Ranero et al., 2003; Ivandic et al., 2008). Dehydration of much of the subducted crust below the hot wedge is also consistent with changes in observed boundaries in migrated scattered wave imaging (MacKenzie et al., 2010). The exact depth of magma generation is still uncertain, but considering the prevailingly low Dy/Yb ratios, it is very likely that this occurs shallower than the garnet-peridotite stability field (Heydolph et al., 2012), or <60–75 km (e.g. Green and Ringwood 1970).

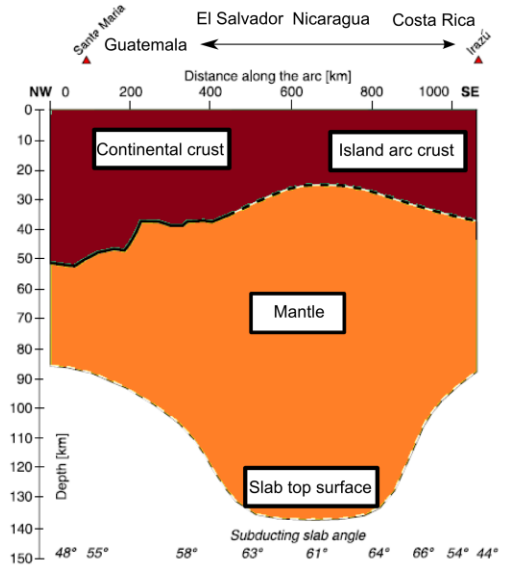

Fig. 7 Along-arc profile below CAVA. Modified from Wehrman et al. (2011). The profile is extending ~1000 km, illustrating the variations in the depth to the surface of the subducting slab, crustal thickness, mantle wedge thickness and composition of the overlying crust. Slab depth and Guatemalan crustal thickness are from Syracuse and Abers (2006); crustal thicknesses of Nicaragua and Costa Rica are from MacKenzie et al. (2008).

Another interesting feature in geochemical variations along the Nicaragua segment is the effect of crustal thickness and the presence of the graben structures. Apparently, thin crust (<34 km) in this region of CAVA would influence lower degrees of crustal contamination and the earlier mentioned high degree of fusion (Fig. 7) as recorded by trace elements (Carr, 1984; Plank and Langmuir, 1988; Patino et al., 2000; Shaw et al., 2006). Geometry of faulting in this region is probably important for magma-crustal interaction, but it is still uncertain how it affects magma signature, As observed by Plank et al. (2002), most Miocene (7–25 Ma), volcanic rocks are encountered both NE of the Depression and on the western coastal hills, and both group of rocks share many of the geochemical trends of the modern arc (Carr et al. 2007).

2.4 Major Volatiles in CAVA

2.4.1 Volcanic gases

Volcanoes are a significant sources of major gases such as H_2O, SO_2, CO_2, H_2S, HCl, and HF into the atmosphere. The development of remote sensing techniques over the years has allowed to make estimates of global volcanic emissions, but in Central America (as in most volcanic regions) the volcanic gas dataset is large but still far from being complete (Stoiber and Jepsen, 1973; GVP, 2014; Andres and Kasgnoc, 1998; Burton et al., 2000; Williams-Jones et al., 2003; Shaw et al., 2003–2006; Rodriguez et al., 2004; Zimmer et al., 2004; Mather et al., 2006; Witt et al., 2008; Hilton et al., 2010; GVP, 2011; Conde et al. 2013; Conde et al. 2014; Aiuppa et al., 2014).

CO_2 has received primary attention in this work. Quiescent and active plume CO_2 degassing from open-conduit volcanoes is an important contribution to earth degassing, but much still needs to be done to fully understand budget and source in volcanic arcs (Burton et al., 2013 and references therein). CO_2 has complex history within the earth geochemical cycles; because of its volatile behavior, CO_2 is fractionated into vapors by rising magmas, and outgassed into the atmosphere via volcanoes and faults (Wilson, 1989). Sub-aerial volcanism produces ~100-500 Mt/yr of CO_2 worldwide (Burton et al., 2013) and there is still no clear characterization of its origin and exchange process in the subduction zone environment (Dasgupta et al. 2013; Manning, 2014). Siebert and Simkin (2002) mention that considering all volcanoes worldwide, 50-70 erupt explosively each year an ~150 produce a gas emission with open-vent degassing. Unfortunately, only 22% of these degassing volcanoes have been measured for their CO_2 flux (Brantley and Koepenick 1995; Burton et al., 2013).

In Central America, the actual reported SO_2 flux data cover at least 13 active volcanoes between Guatemala and Costa Rica (Fig. 8) Overall, the range of measured fluxes is large, between 30 to 1,540 T/d of SO_2, and as for CO_2 depends largely on the degassing system of each volcano (Mather et al., 2006; Shinohara et al., 2013a). Most of the data have been obtained via COSPEC or DOAS measurements (Stoiber 1971-1977; Delmelle, 1999; William-Jones et al., 2003; Rodriguez et al., 2004; Mather et al., 2006).

For CO_2, the techniques used are the most diverse; diffuse CO_2 fluxes have been obtained in soil surveys, such as at Cerro Negro (Shaw et al. 2003; Lucic et al. 2014), and many others, but the plume CO_2 fluxes have been calculated indirectly from SO_2 fluxes and fumarole compositions. The latter have been studied by direct sampling for major gas compositions (Hazlett 1977; Simkin et al., 1981; Williams, 1983; Menyailov et al., 1986; Gemmel, 1987) and isotope species (Shaw et al., 2003-2006; Vaselli et al. 2010), covering volcanoes (from NW to SE

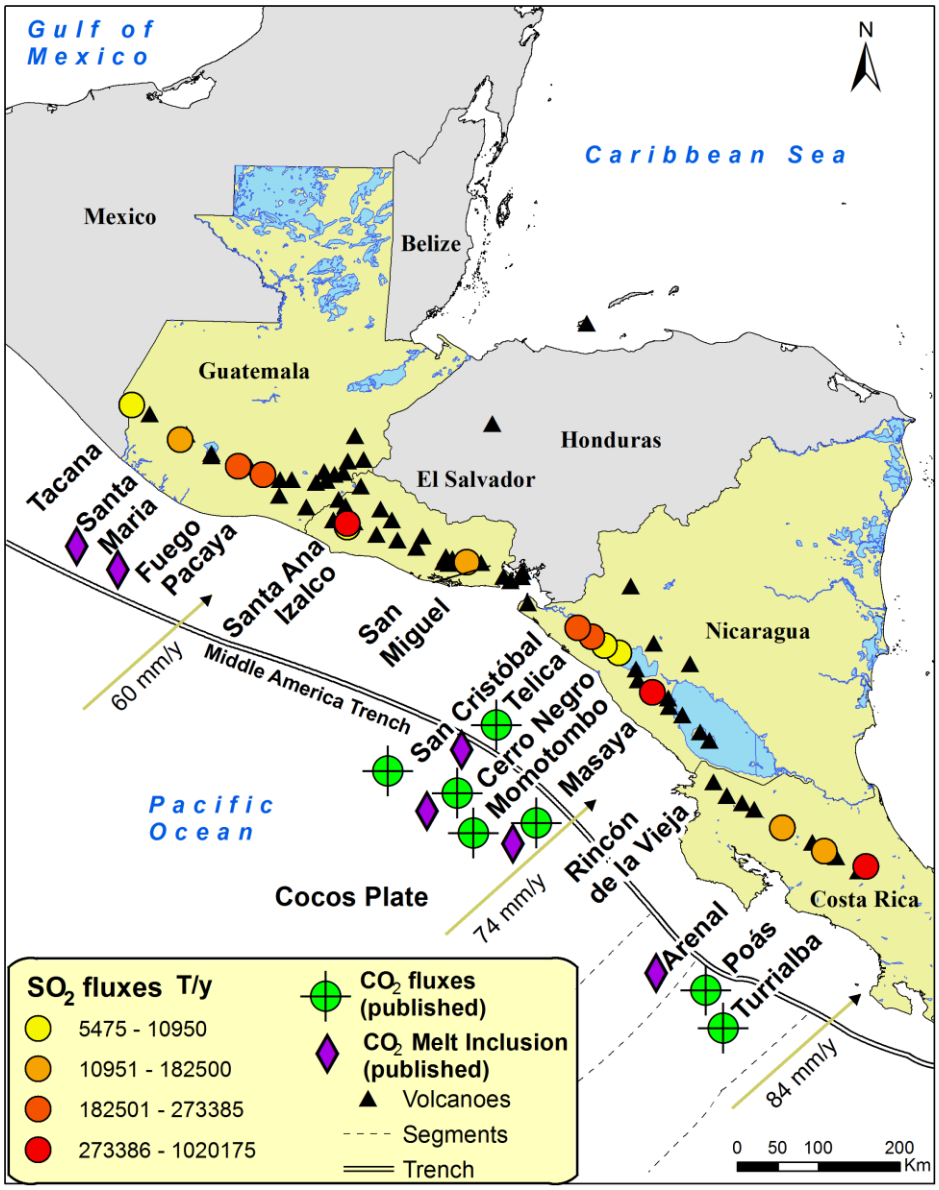

Fig. 8 SO_2 flux map of CAVA. The map represent the subduction zone in Nicaragua and Costa Rica. SO_2 fluxes are represented by tones per years (T/y) (e.g. Mather et al., 2006; Aiuppa et al., 2014). Published work on melt inclusion are indicated at each volcano by a purple crystal symbol. CO_2 fluxes are only representing published works in Nicaragua and Costa Rica covered by Aiuppa et al. (2014) but also takes into account Turrialba CO_2 soil survey (IAVCEI, 2003), Telica CO_2 Soil survey (Dionis et a., 2010), Momotombo fumarole sampling (Menyailov et al., 1986), Cerro Negro COSPEC (GVP, 2011) and CO_2 soil survey (Lucic et al., 2014), Masaya CO_2 soil survey and COSPEC measurements (Delmelle et al., 2002; Lewicki et al., 2003; GVP, 2011) and its OP-FTIR survey (Burton et al., 2000). The convergence velocities relative to the Caribbean Plate (in millimeters per year) after DeMets (2001).

CAVA) such as; San Cristóbal, Telica, Cerro Negro, Momotombo, Masaya (Nicaragua), and also Rincón de la Vieja, Poás, Arenal, Irazu, Turrialba (Costa Rica). Several studies have determined volcanic CO_2 emissions from hydrothermal vents, hot springs, fumaroles or wells (e.g. Snyder et al., 2001; Hilton et al., 2002; Shaw et al., 2003; de Leeuw et al., 2007). Natural emissions from fore-arc seafloor venting have been estimated by observations (e.g. Kulm and Suess, 1990; Fryer et al., 1999), or by using numerical modeling (e.g. Connolly, 2005; Gorman et al., 2006). Yet, in CAVA, the highest CO_2 fluxes have been measured on Masaya volcano from volcanic plume OP-FTIR spectroscopy observations (Burton et al. 2000), yielding an interval of 2,765-3,110 t/d (between 1998 and 1999). This number can be compared with the diffuse CO_2 emissions over the whole Masaya Caldera Complex, measured with CO_2 soil gas: 1,728 t/d (Pérez et al., 2000). At Telica, Conde et al. (2014) used a field technique assemblage of OP-FTIR, DOAS and Multi-GAS to estimate CO_2 fluxes at 166+/-76 t/d. The operation was settled in March 2013 during quiescent degassing activity. Also during March-April 2013, in Turrialba (Costa Rica), they reported values of 1,094+/-631 t/d also for a period of passive degassing (Aiuppa et al., 2014).

At the scale of the entire arc segment, using fumarolic CO_2/SO_2 ratios in tandem with SO_2 fluxes, Elkins et al. (2006) estimated a CO_2 flux of ~156,747 t/d by for the Nicaragua segment. A much lower flux (~25,320 t/d) was quoted by the same authors based on ^3He fluxes and $CO_2/^3He$ fumarolic ratio. In comparison, volcanic gas CO_2/S compositions and extrapolated SO_2 fluxes led Hilton et al. (2002) and Mather et al. (2006) to assess the CAVA CO_2 output at 3618 t/d and 2296–5010 t/d, respectively.

2.4.2 Volatile from melt inclusions

Individual volcanoes were investigated for eruptive CO_2 release via melt inclusion analyses such as: Fuego (Roggensack, 2001b), Cerro Negro (Roggensack et al., 1997), Irazú (Benjamin et al., 2007), Arenal (Wade et al., 2006), and variations in melt inclusion CO_2 contents across the Guatemalan arc segment were described by Walker et al. (2003). The amount of available data on melt inclusions in olivine crystals from Central America has increased over the two recent decades. Sadofsky et al. (2008) and Wehrmann et al. (2011) provide a comprehensive view of the wide ranges of dissolved H_2O and CO_2 in MIs, measured by secondary ion mass spectrometry. In these studies, specifically olivine samples were taken from historic mafic tephra (Fig. 9; Fig. 10).

Sadofsky et al. (2008) also analyzed major elements, Cl and S of glass inclusions and hosted olivines. Their instrument was a CAMECA SX50 electron microprobe at IFM-GEOMAR, but trace elements, fluorine and hydrogen concentrations (for water) were determined using a CAMECA ims4f ion microprobe (secondary ion mass spectrometry or SIMS) at the Institute of Microelectronics and Informatics (Yaroslavl, Russia). Samples were collected at Santa Maria, Fuego, Atitlán, Agua in Guatemala; at Telica, Cerro Negro, Nejapa, Masaya, Granada in Nicaragua; at Arenal and Irazú in Costa Rica.

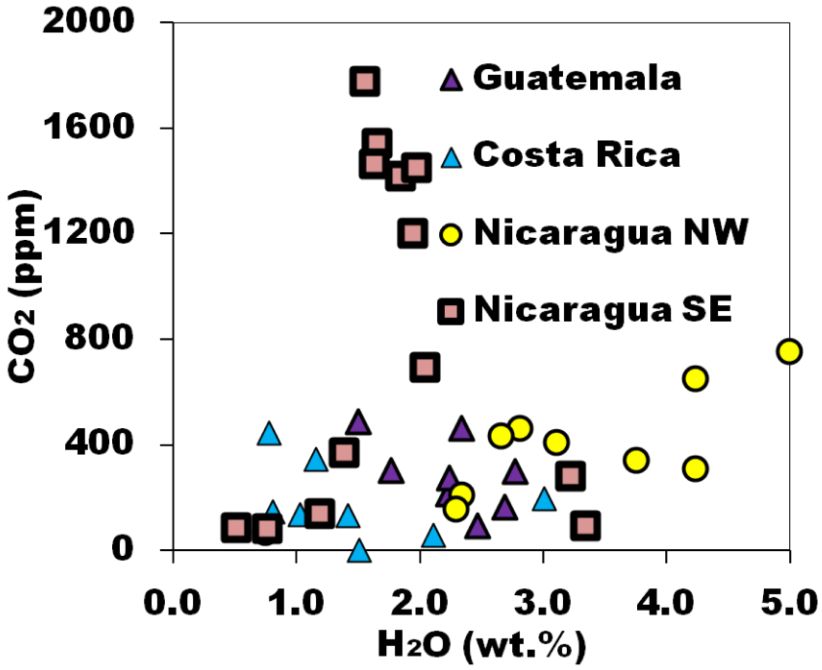

Fig. 9 CO_2 versus H_2O in melt inclusions of CAVA.

In Wehrmann et al. (2011), the inclusions had been analyzed with the same facilities, but major elements (wt %), F (ppm), nonvolatile trace elements (ppm) and host olivine compositions (wt %) were also referred to Sadofsky et al. (2008). The samples were representing the same volcanoes with exception of Fuego (Guatemala) and Telica (Nicaragua). Combining both studies, the ranges of major volatile concentrations are respectively 203 to 2,278 ppm (S), 298 to 3,704 ppm (Cl) and 100 to 3,159 ppm (F). H_2O and CO_2 concentrations vary respectively between 0.51 to 5.20 wt% and below detection limits to 1,777 ppm (Fig. 10).

For water contents in melt inclusions from CAVA mafic magmas, the first studies using have demonstrated a wide range of H_2O contents, from below 1 wt.% in back-arc volcanoes from Guatemala (Walker et al., 2003) to 6 wt.% at Cerro Negro volcano in Nicaragua (Roggensack et al., 1997; Portnyagin et al., 2012). In Guatemala, mafic melt inclusions contain less water with an average of ~2 wt.% for Pacaya and ~4 wt.% for Fuego (Sisson and Layne, 1993; Roggensack, 2001b; Walker et al., 2003). In Costa Rica, the first volcano investigated was Arenal (Wade et al., 2006), which contains up to 4 wt.% water, then Benjamin et al. (2007) added data from Irazú with their highest water contents varying between 3.2 to 3.5 wt%. Most recently, Turrialba (Costa Rica) has also been investigated; melt inclusions in olivine phenocrysts of old eruptive products have been found to contain up to 2.4 wt% H_2O, 54 ppm CO_2 and ~ 2,200 ppm Cl (Di Piazza; unpublished data), and ~2,500 ppm S (Wehrmann, unpublished data in Conde et al., 2013).

Melt inclusions from Guatemalan back-arc basalts notably have high CO_2 contents (>900 ppm CO_2). CO_2 concentrations increase up to 1,039 ppm at Cerro Negro in Nicaragua (Roggensack et al., 1997). At Fuego, CO_2 reaches 1,249 ppm, but it is quite variable (Roggensack, 2001b). Further south, at Arenal, tephra layers reveal high concentrations of volatile species (3,000 ppm S and Cl), but relatively low CO_2 contents in the range of 50 – 300 ppm (Roggensack et al., 2001b). The MIs with the highest water concentrations are the most mafic (Wade et al., 2006). Benjamin et al. (2007) measured olivine-hosted melt inclusions data indicated volatile-rich compositions from Irazú, with > 200 ppm CO_2, > 2,500 ppm S, > 2,200 ppm Cl and > 1,800 ppm F.

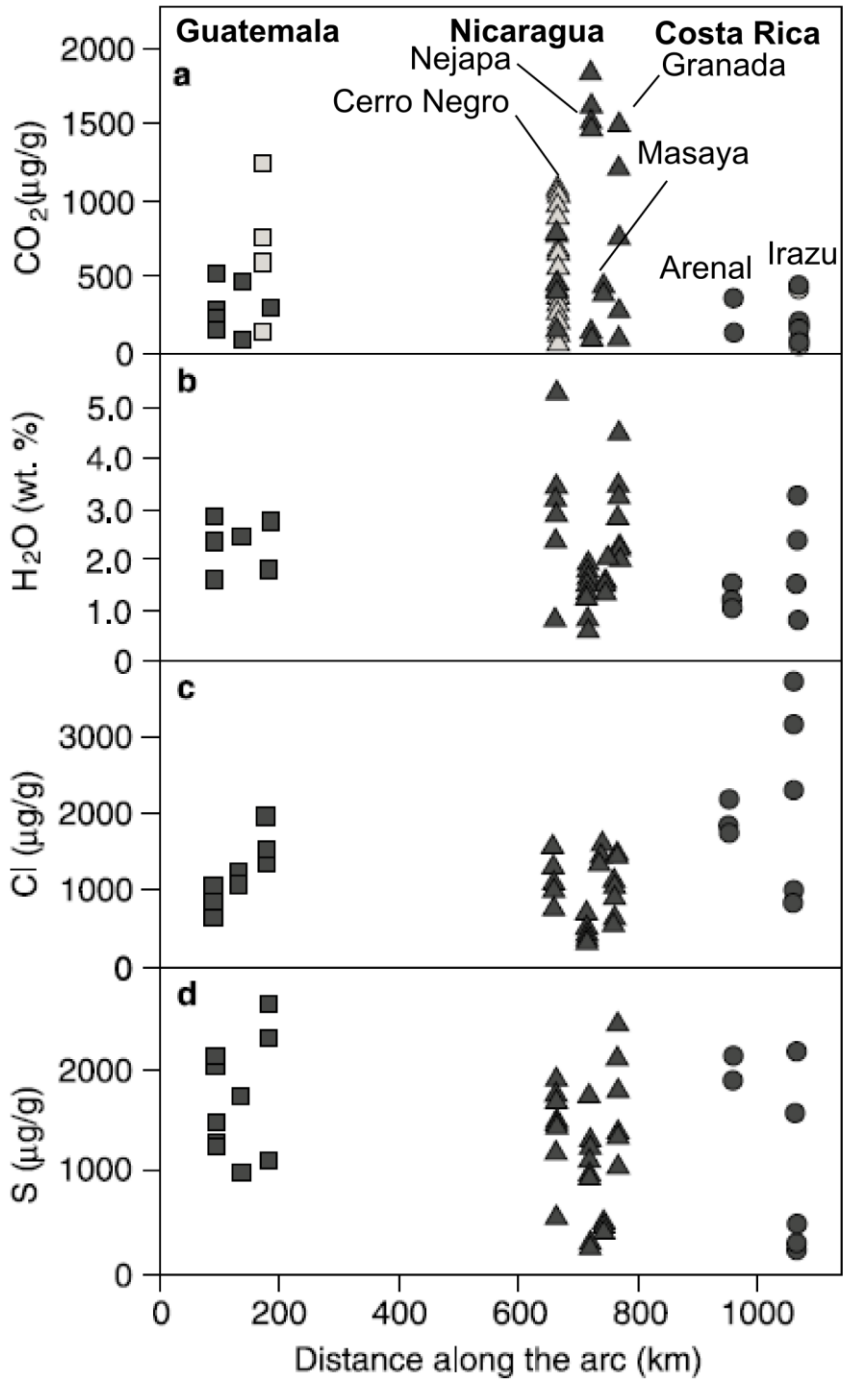

Fig. 10 CAVA along-arc variations in volatile content. Modified from Wehrmann et al. (2011). Melt inclusion volatile compositions versus distance along the arc from Guatemala to Costa Rica for (a) CO_2, (b) H_2O, (c) Cl, (d) S; dark gray symbols from Wehrmann et al. (2011); light gray symbols show additional data from Roggensack et al. (1997) and Roggensack (2001a, 2001b) for Guatemala and Nicaragua and from Wade et al. (2006) and Benjamin et al. (2007) for Costa Rica.

Chapter 3 - Methods

3.1 Estimating degassing budgets

Our strategy for estimating CO_2 fluxes in based upon multiplying the CO_2/SO_2 ratio in plumes by the co-acquired SO_2 flux (Oppenheimer et al. 2011; Burton et al., 2013). Recent technological advances have allowed to real-time monitoring CO_2/SO_2 ratios by using Multi-sensor Gas Analyzer System (Multi-GAS) (Shinohara 2005; Aiuppa 2006; Aiuppa et al. 2007) or with OP-FTIR spectrometers (Burton et al., 2007a). Our approach is resumed in figure 11. The Multi-GAS-derived CO_2/SO_2 ratios are multiplied with results of in-parallel SO_2 flux measurements, made by using scanning UV-DOAS instruments (Galle et al. 2010), to derive CO_2 fluxes. Scanning UV-DOAS have been proved their utility in variety of context (Galle et al. 2002; Edmonds et al. 2003; Galle et al. 2010; Burton et al. 2009).

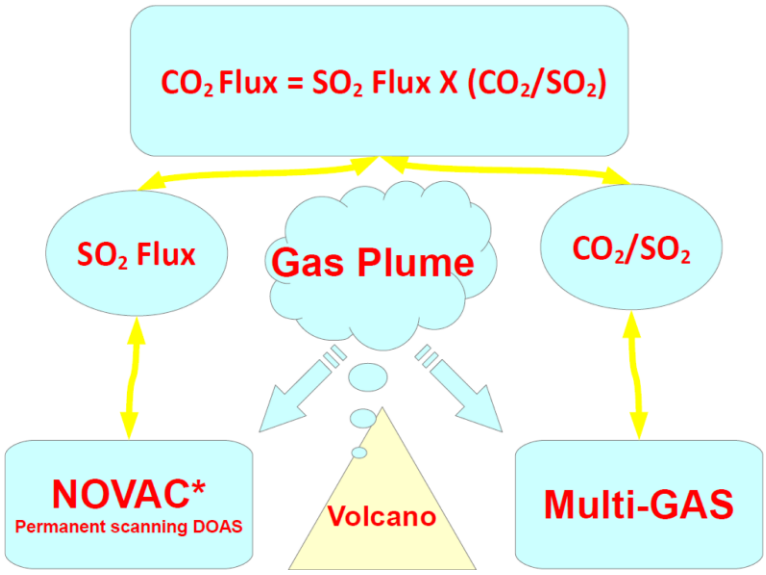

Fig. 11 CO_2 flux measurement strategy.

3.1.1 Multi-GAS

The fully-automated Multi-GAS instrument, developed at the Istituto Nazionale di Geofisica e Vulcanologia (INGV), Sezione di Palermo, is designed to measure temporal changes of major gases at a frequency of few seconds. The Multi-GAS, illustrated in figure 12, integrates an infrared spectrometer for CO_2 sensing (Gascard II, calibration range 0 – 3000 ppmv; accuracy ±2%; resolution, 0.8 ppmv), along with specific electrochemical sensors for the measurement of SO_2 (CityTechnology, sensor type 3ST/F, calibration range, 0 - 200 ppmv, accuracy, ±5%, resolution, 0.1 ppmv) and H_2S (SensoriC, sensor type 2E, calibration range, 0 – 200 ppmv, accuracy, ±5%, resolution, 0.1 ppmv). H_2O concentrations were also calculated from records of temperature and relative humidity (Galltec sensor, measuring range, 0 – 100 % Rh, accuracy, ±2%), using a time-average pressure of 670 mBar at Turrialba and 912 mBar at Telica.

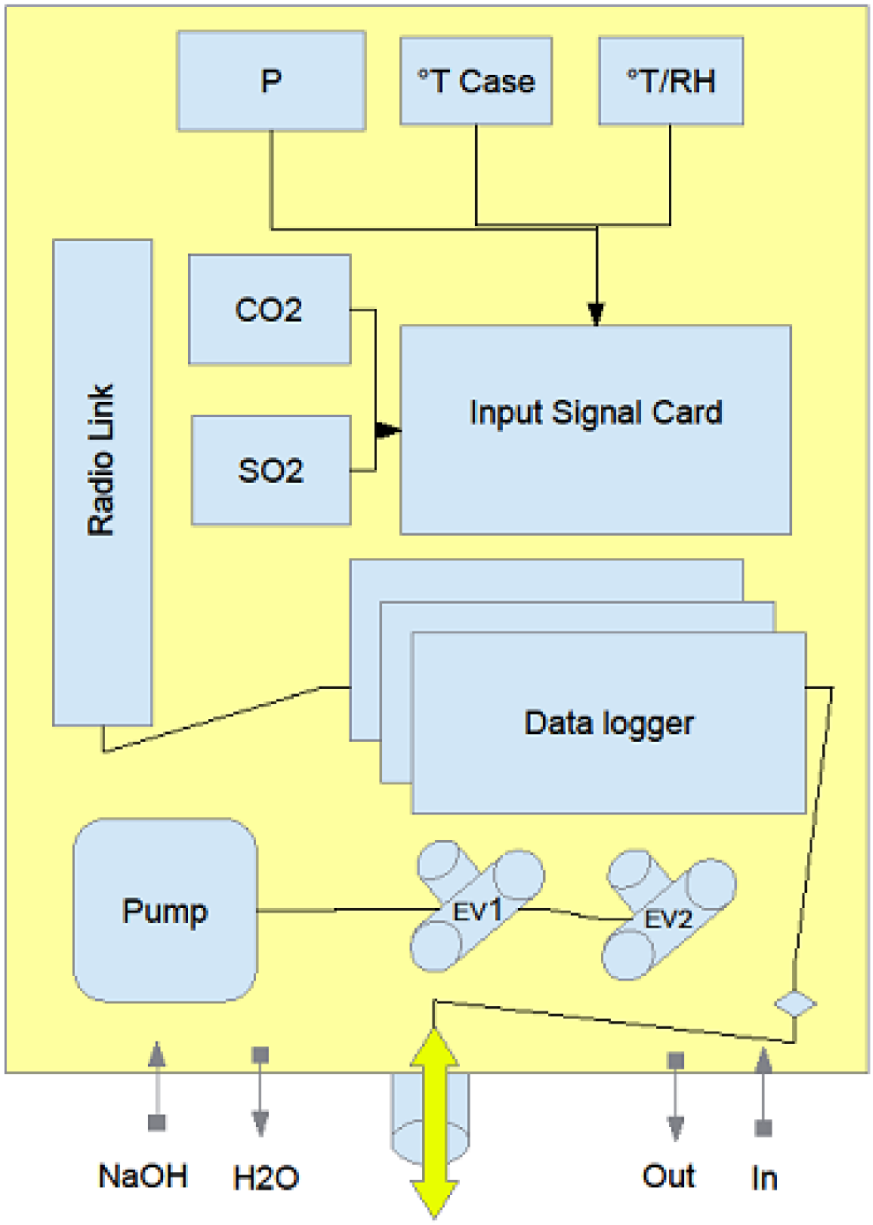

Fig. 12 Multi-GAS components.

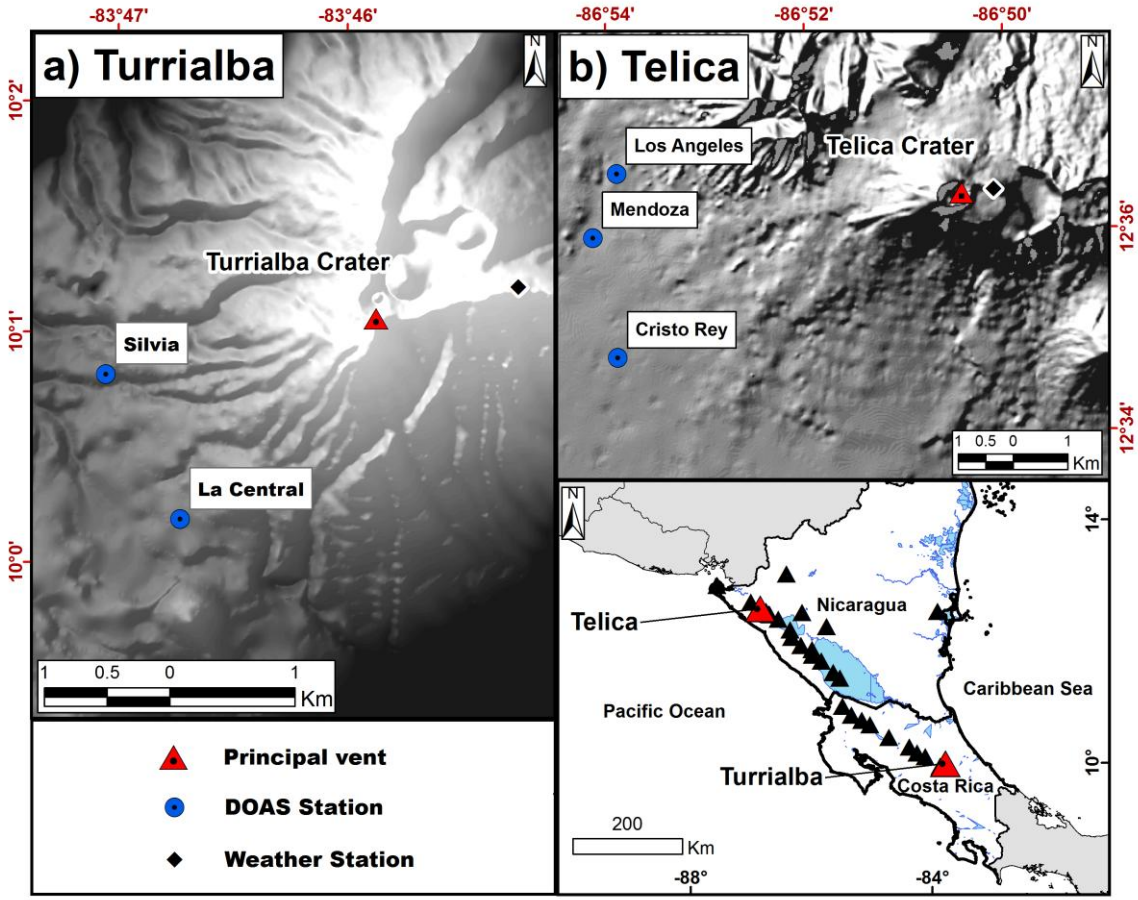

Fig. 13 UV-DOAS regional deployment at a) Turrialba, b) Telica.

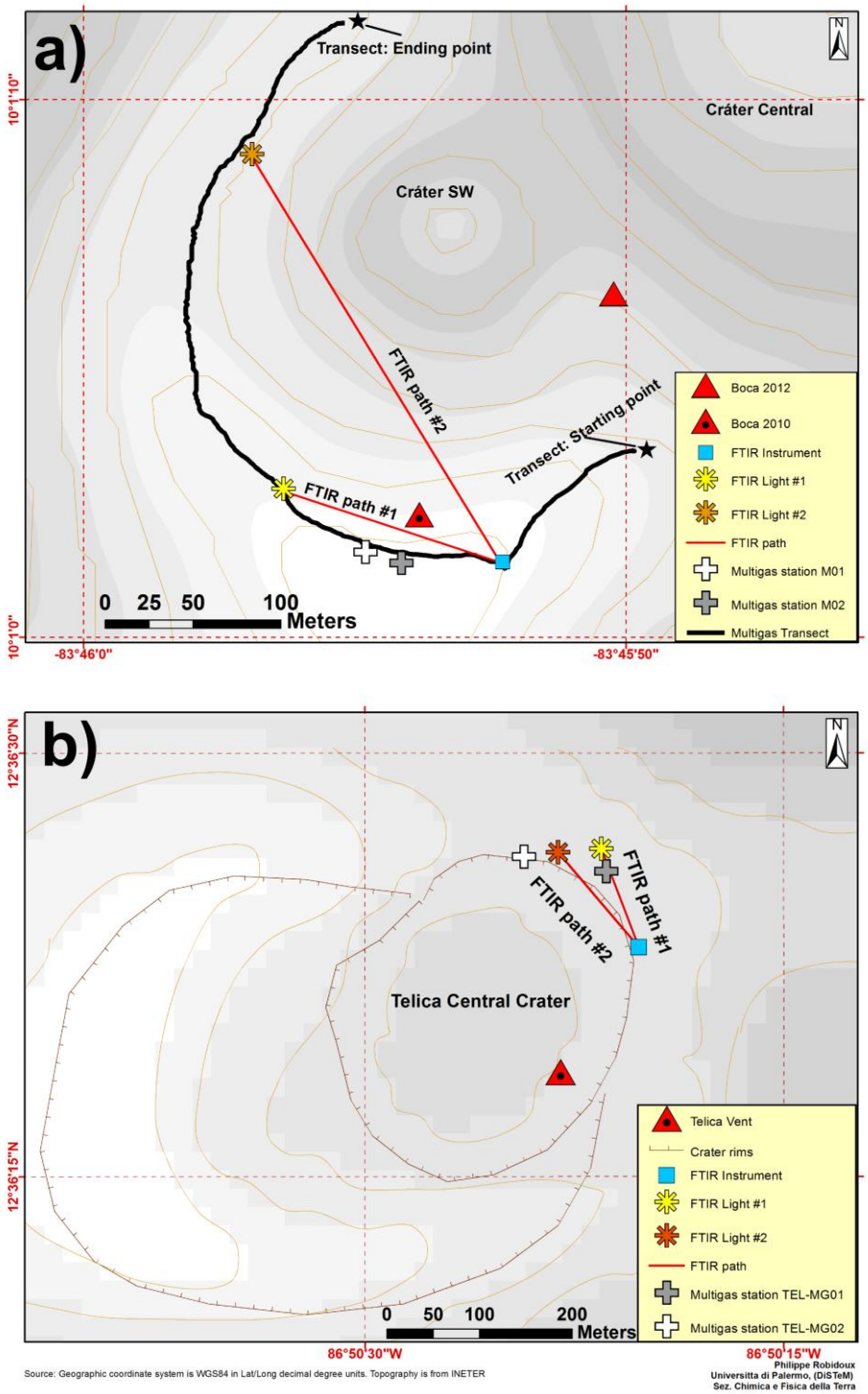

Fig. 14 Multi-GAS and OP-FTIR summit crater deployment at a) Turrialba, b) Telica

During our 2013 field campaign, the Multi-GAS was first installed on the southern rim of the active west crater of Turrialba (Fig. 13a; Fig. 14a), during March 17-19, and was temporarily deployed roughly 10 m south of the main vent Boca 2010. A similar deployment was made on the north rim of the active crater of Telica on March 23. During the period from March 27 to April 8, the Multi-GAS was installed closer to the north rim of the crater of Telica and running continuously/simultaneously with the distant mini scanning DOAS stations at Los Angeles, Mendoza and Cristo Rey (Fig. 13b; Fig. 14b). At San Cristóbal, the instrument was operating continuously in simultaneous with two stationary DOAS at Hill and Suiza (Fig. 15).

The Multi-GAS was set to perform measurements during sampling periods of 30 min to 2 hours. During each measurement interval, the plume gas was pumped into the sensor's housing and a data-logger board captured the output signals from the sensors at 0.1 Hz rate. The Multi-GAS was powered by a 12 V lead battery connected to a photovoltaic module, and the main box with sensors was protected inside a waterproof box (30 × 20 × 15 cm). At the end of each cycle, a radio link operated automatic data transfer from the remote Multi-GAS to a temporary base station on the flank of the volcano (Fig. 16). Overall, the instrument acquired a total of 12.5 hours of observations.

In addition to the static measurements, a small, compact, portable version of the Multi-GAS instrument was used to perform sequences of walking transects around the outer rim of the West Turrialba Crater. During the walking traverses, the inlet tube of the Multi-GAS was kept 50 cm from the ground to capture plume gas while avoiding any soil contribution. In total, 12 traverses were done between 9-19 March (Fig. 14a). At Telica, 8 traverses were done between 21 – 23 March (Fig. 14b).

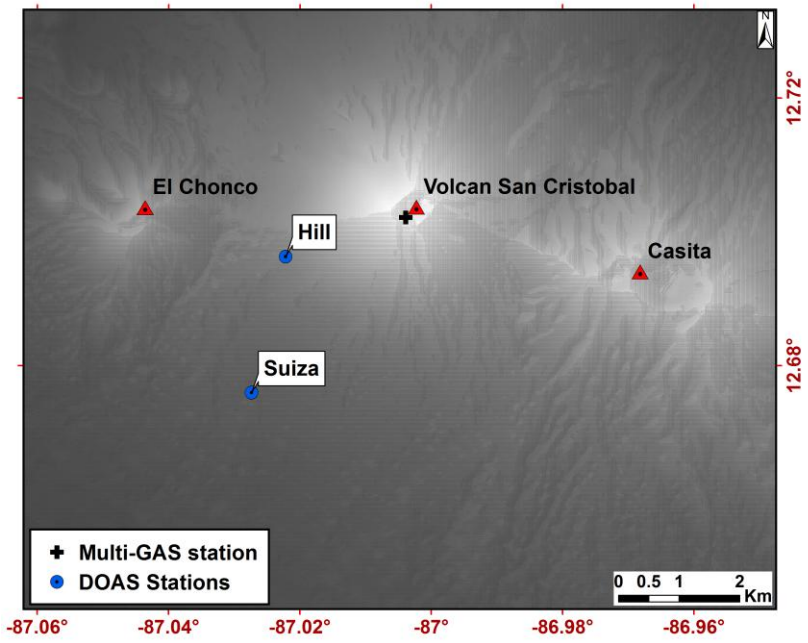

Fig. 15 UV-DOAS regional deployment at San Cristóbal.

In addition to the static measurements, a small, compact, portable version of the Multi-GAS instrument was used to perform sequences of walking transects around the outer rim of the West Turrialba Crater. During the walking traverses, the inlet tube of the Multi-GAS was kept 50 cm from the ground to capture plume gas while avoiding any soil contribution. In total, 12 traverses were done between 9-19 March (Fig. 14a). At Telica, 8 traverses were done between 21 – 23 March (Fig. 14b).

The acquired concentration data (from both fixed and portable Multi-GAS instruments) were processed using a custom-made Ratiocalc software (Tamburello, 2015). Air background corrected concentrations were first calculated by subtracting ambient air concentrations for H_2O and CO_2 from the raw data. Any temperature-dependent sensors' baseline drift was also removed by simple baseline fitting with polynomial functions.

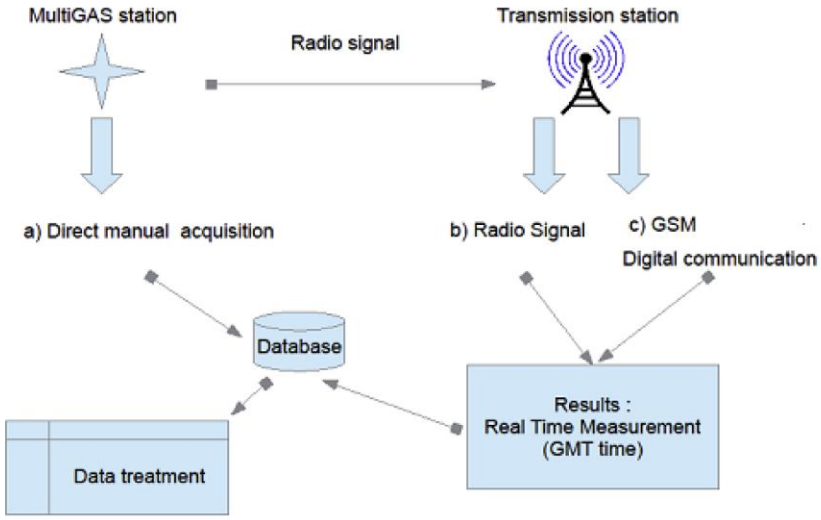

Fig. 16 Multi-GAS data acquisition

These corrected data were then used to derive gas-gas scatter plots, and finally to derive CO_2/SO_2 molar ratios in the plume by taking the gradient of the best-fit regression lines (e. g. Fig. 17). To explore the time-variability of plume compositions, a number of such scatter plots were sequentially created by Ratiocalc (by scanning the available dataset), each from data acquired during individual time windows of a few minutes long. A time-series for such "time averaged" CO_2/SO_2 gas ratios of our data is shown in Conde et al. 2014 and Aiuppa et al. (2014) (see following chapters). Measurement intervals were considered null (e.g., no ratio was calculated) when CO_2 and SO_2 concentrations were below fixed threshold values (e.g., $SO_2 < 3$ ppmv). In such diluted plumes, the error in gas ratios becomes in fact larger than typically ($<\pm$ 20%) obtained in denser plumes. The short-term (0.1 Hz) variability of CO_2/SO_2 ratios was also explored by calculating the point-to-point ratio between simultaneously measured CO_2 and SO_2. While the error in such higher rate measurements can be as high as 50%, we yet observe an overall good match between "point-to-point" and "time averaged".

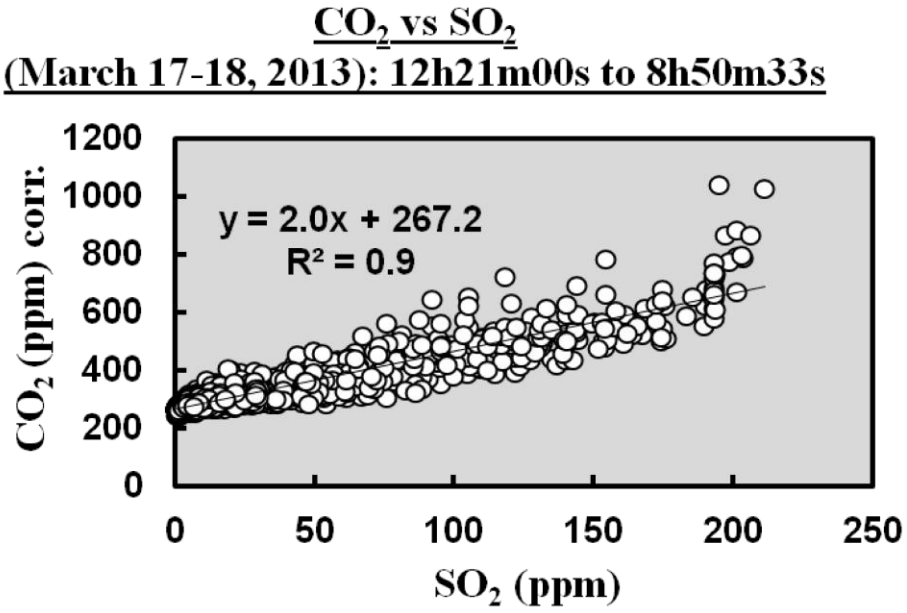

Fig. 17 Multi-GAS best-fit regression lines example of Ratio Calc (CO_2 vs SO_2). Data from Turrialba campaign (2013).

3.1.2 Scanning UV-DOAS

For measuring SO_2 fluxes we used scanning dual-beam Mini-DOAS spectrometers developed within the EU projects Development of Optical Remote Sensing Instruments for Volcanological Applications (DORSIVA) (Galle et al., 2006) and NOVAC (Galle et al., 2010). This instruments allow to derive column amounts of SO_2 from the retrieved spectra (acquired at regular angular steps) by applying DOAS (Differential Optical Absorption Spectroscopy; Fig. 18ab) (e.g. Plank and Stutz, 2008). The scanning Mini-DOAS instrument collects scattered sunlight and scans the sky over 180 degrees downwind of the volcano. The principle for calculation of the gas concentration is the Beer Lambert law, which describes attenuation of light interacting with matter. The Beer-Lambert Law describes the absorption of radiation ($I_0(\lambda)$ and $I(\lambda)$) as it passes through a layer of a thickness L, where the species (in this case SO_2, with an absorption cross section $\sigma(\lambda)$) to be measured is present at a concentration c (Platt, 1994).

The fixed NOVAC stations are installed according to the predominant wind direction (mostly eastern wind), at sites on the periphery of volcanoes with easy access for technical operations (see complete setting in Galle et al. 2009; Conde et al., 2013; Conde et al., 2014) (Fig. 13ab, 14ab, 15). The SO_2 flux can be obtained by multiplying the integrated gas columns with the estimated plume (wind) speed. This is obtained from direct measurements with a weather station deployed next to the crater rim. Based on validation experiments, the measurement error is expected to be around ±25% under good weather conditions (clear sky and high visibility), and around ± 50% - 100% under moderate to bad weather conditions (Galle et al., 2010; Rivera et al., 2009) .

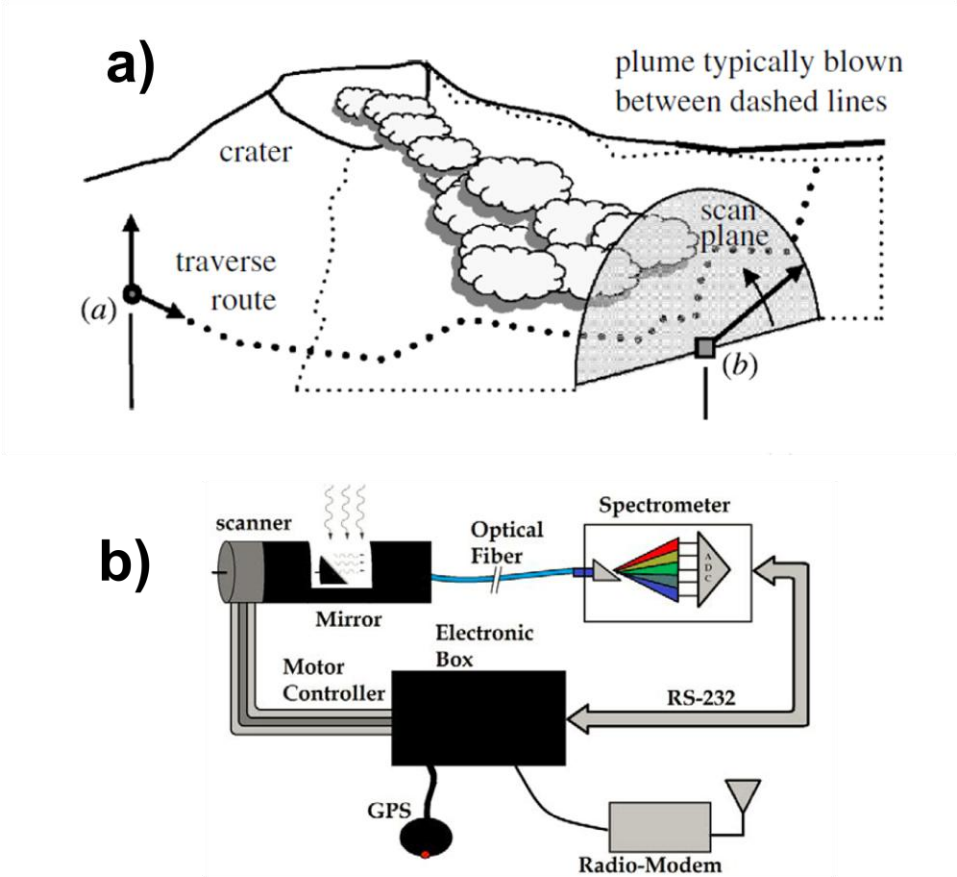

Fig. 18 UV-DOAS function. Major parameters: scanning angle, wind direction and plume interception area with its specific geometry (planar or conical) a) Field UV-DOAS modified form Tamburello (2011) and Mc Gonigle et al. (2005b), b) UV-DOAS components from the instrument (modified from Conde, 2012).

3.1.3 OP-FTIR

At Turrialba and Telica volcanoes, we also used OP-FTIR spectrometers to characterise plume emissions. Infrared spectroscopy has been used for the first time in a volcanic plume in 1969 by Naughton et al. (1969), during a lava fountain on Kīlauea, Hawai'i. Later, the principle was developed by laboratory and industrial application (Brown et al., 1992) and the open-path Fourier transform infrared (OP-FTIR) spectroscopy was for the first time applied to study of volcanic gas at Unzen (Mori et al., 1993; Mori and Notsu 1997) is a widely-utilized tool to measure in situ volcanic gas compositions (e.g. Oppenheimer et al., 1998; Burton et al., 2000). In our study, OP-FTIR measurements were made close to the main vent of Turrialba and Telica (Fig. 14 a-b). The measurements were impossible at San Cristóbal due to the difficulty for transporting the material to the main summit (Conde et al., 2014).

As IR source, we used an incandescent lamp, which was placed at specific positions depending on the crater rim topography and plume transport direction/velocity. As explained in

Conde et al. (2014), at Turrialba, the lamp was placed at two distinct positions, leading to twodifferent light paths: path1 and path2, with lengths of 136 and 275 meters respectively (Fig.14 b). Each light path represents the individual contribution of the two main vents (Boca 2010 and Boca 2012) to the total volcanic plume composition. At Telica, the plume has a single origin; thus the lamp remained fixed during the period of measurements.

3.2 Estimate volatiles contents in primitive melts

Volatiles contents in melt inclusions (MIs) in phenocrysts have been used worldwide in various volcanic arc settings (Wallace, 2005). MIs are common tools in petrology because they give direct information on those physical parameters (P, T and melt composition) that control crystallization and evolution of magmatic systems (Anderson, 1982; Sisson and Grove, 1993; Roggensack et al., 1997; Cashman, 2004; Houghton and Gonnerman, 2008). MIs allow estimating pre-eruptive magmatic volatile contents, and complement direct measurements of exsolved gases provided by gas monitoring and remote sensing techniques (LI-COR infrared analyzer, distant OP-FTIR, DOAS, Multi-GAS, COSPEC, etc.). Knowledge of the original volatile contents in magmas also allows estimation of the magma mass required to produce an observed gas flux. It also permits quantitative comparison of geological time scale fluxes with geophysical and volcanological observations. Measurements of original volatile contents are therefore of great interest.

3.2.1 Melt inclusion formation

Melt inclusions are small volumes of melt trapped in crystals of different sizes. During magmatic ascent, these entrapped immiscible silicate structures are preserving dissolved volatiles species and other elements, thus recording pre-eruptive magma compositions (Fig. 19; Métrich and Wallace, 2008; Wallace, 2005). During cooling, the inclusions form glasses by quenching, but then, they can be affected by physical and chemical changes which are commonly described as post-entrapment crystallization (PEC) and diffusion effects (Sobolev and Kostyuk, 1975; Roedder, 1984; Nielsen et al., 1998; Gaetani and Watson, 2000). These effects have been largely identified, but quantified in few works for elemental diffusion, for example by Danyushevsky et al. (2000b; 2002b; 2011). To avoid interpreting composition modified by secondary processes, correction by experimental reheating to trapping temperature have been proposed by Soboloev and Kostyuk (1975), Nielsen et al. (1998) and Danyushevsky et al. (2002b). Still, during heating experiment and even for certain natural studied inclusions, it is frequent that a boundary layer is formed between glass and host crystals because of elemental diffusion processes (Roedder, 1984).

Melt inclusions are formed in crystals when the development of the atomic structure is irregular and when some processes interfere with crystal growth. In any cases, it is a relatively slow growth of part of a crystal that allows local re-entrant of melt forming in an area that is perfect for deposition, while the crystal itself tries to keep it original shape while growing (Bodnar, 2003). On the basis of petrographic observations and analogies with fluid inclusions (Roedder (1979, 1984; Sobolev and Kostyuk, 1975), we summarize tree important mechanisms: (1) skeletal or other irregular growth forms due to strong undercooling or non-uniform supply of nutrients, (2) formation of reentrants by resorption followed by additional crystallization, and (3) wetting of the crystal by an immiscible phase or attachment to another small crystal (e.g. Métrich and Wallace, 2008). The material entrapped can be solid, liquid, or gas or even a multiphase mix.

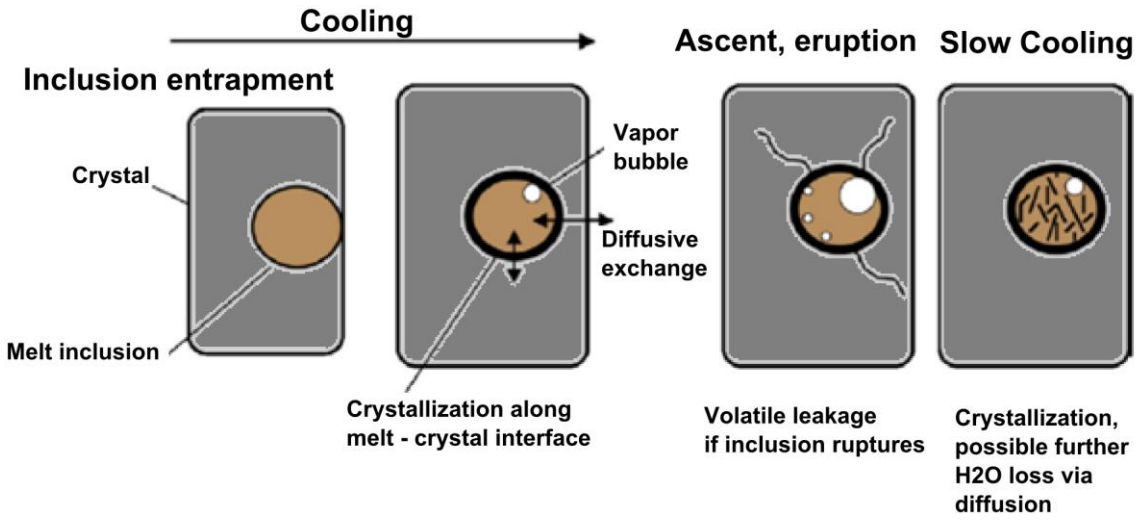

Fig. 19 Post entrapment modification of melt inclusions. Modified from Wallace (2005).

Melt inclusions are formed in crystals when the development of the atomic structure is irregular and when some processes interfere with crystal growth. In any cases, it is a relatively slow growth of part of a crystal that allows local re-entrant of melt forming in an area that is perfect for deposition, while the crystal itself tries to keep it original shape while growing (Bodnar, 2003). On the basis of petrographic observations and analogies with fluid inclusions (Roedder (1979, 1984; Sobolev and Kostyuk, 1975), we summarize tree important mechanisms: (1) skeletal or other irregular growth forms due to strong undercooling or non-uniform supply of nutrients, (2) formation of reentrants by resorption followed by additional crystallization, and (3) wetting of the crystal by an immiscible phase or attachment to another small crystal (e.g. Métrich and Wallace, 2008). The material entrapped can be solid, liquid, or gas or even a multiphase mix.

As the magma system is cooling down, secondary physical processes as crystal sinking, magma deformation or sometimes formation of hourglass inclusions affect the major element composition of initially trapped melt (Bodnar, 2003; Métrich and Wallace, 2008). Many problems have been identified, including diffusion of volatiles and major elements out of the glass (see Baker, 2008). For example, Fe-loss and FeO-MgO re-equilibration in olivine-host melt inclusion is one of the most investigated issue, because it particularly affects the Fe contents of many melt inclusions in olivines (Danyushevsky, 2000b). Finally, other secondary texture are frequently reported such as annealing effect, outer radius contact with wall crystallization, presence of shrinkage bubbles, cracking and late diffusion exchange. These are additional factors acting during secondary physical processes and PEC, but they are difficult to quantify.

3.2.2 How to measure volatile contents in glass inclusions

In laboratory, glass inclusions are investigated with «qualitative» petrographic tools to obtain information on texture, presence of liquid/vapor phase, mineral phases, oxydes, etc. (Sobolev and Kostyuk, 1975; Roedder, 1979-1984; De Vivo and Bodnar, 2008). Many geological and quantitative properties can also be retrieved via laboratory experiments on the glass. This aspect of the dissertation is not explored into details, but it is possible to investigate physical behavior of glass inclusions under physical stress, such as temperature effects with

calorimetry/dilatometry (e.g. Bottinga, 1984b), quenching rates and effects of volatile contents and speciation (Dingwell and Webb, 1989; Dingwell, 1990), density (expansivity/compressibility; e.g. Lange and Carmichael, 1987-1990; Kress and Carmichael, 1991; Webb et al., 1992; Smithells, 1998), viscosity/viscoelasticity (e.g. Hummel et al. 1985; Gottsman et al., 2002), enthalpy (heat capacity; e.g. Adam and Gibbs, 1965; Stebbins et al., 1982-1983-1984; Richet et al., 1982; Richet and Bottinga, 1985; Neuville et al., 1993), conductivity, etc. (see also Liu et al., 1988; Dingwell and Webb, 1989; Dingwell, 1990; Knoche et al., 1992). All of these physical characteristics give precious information on entrapment conditions and they are closely tied to change of magma composition.

A panoply of work in the domain of melt inclusions concerns investigation of «intensive» magmatic variables (Blundy and Cashman, 2008), such as solubility and speciation of volatiles, diffusivities of elements, oxydo-redox conditions, concentration of major trace and rare earth elements and even sometimes isotopes. Of course, the volatiles content itself is the central aspect of this thesis. Volatile concentrations are mainly governed by (1) solubility, (2) pressure and (3) temperature which are the three principal magmatic variables used in this work to study the complexity of the magmatic plumbing systems.

The first to recognize melt inclusions as potential records of magma genesis was probably Sorby (1858), but until the 19th century, no attempt has been made to reveal the presence of volatiles in these micro geologic systems. In fact, the first attempts to measure volatile contents in melt inclusions were made by Sobolev et al. (1971), while using heating stage experiments (resumed in Sobolev and Kostyuk, 1975; Roedder, 1979-1984). Until the advent of new micro-analytical techniques in the 1980s (electron microprobe, ion microprobe, mFTIR, etc.), results long remained ambiguous, and dependent upon experimental determination of P-T intensive parameters in solubility models (Burnham and Davis, 1971-1974). Melt inclusion were suspiciously considered because of the frequent presence of a boundary layer between the melt and the crystal, testifying evidence of elemental diffusion (e.g., Watson et al., 1982; Faure and Schiano, 2005; Baker et al., 2008). Textural properties often indicated that melt inclusions had been affected by PEC. Later on, in the 1990s, high P-T rapid quenching experiments with rapid-quenched pressure vessels (e.g. Ihinger, 1991; Holloway et al., 1992b) and piston cylinders (e.g. Baker, 2004; Moore et al., 2008a) were introduced to investigate volatile solubilities, and to reproduce the closed-system environment entrapped by melt inclusions.

In natural glass inclusions, hydrogen and carbon species were first investigated with vibrational micro-spectroscopy in the infrared and near-infrared. These techniques have allowed researchers to obtain information on H_2O and CO_2 contents and speciation (e.g., OH^- versus molecular H_2O; Stolper, 1982; CO_3^{2-} versus molecular CO_2; Mysen et al., 1975). The advances in micro-spectroscopic techniques, and the collection of natural and experimental glasses worldwide, motivated use of micro Fourier Transform Infrared – «mFTIR» spectroscopy and micro Raman spectroscopy in a wide range of silicate compositions, form basalts to rhyolite (e.g. Devine et al., 1995). Later on, Hauri et al. (2002-2006) were able to use ion probe with calibrated glass in tandem with electron microprobe «EMPA» to measure H and C in a variety of glass silicate compositions.

Sulfur and chlorine in glass inclusions have been investigated for the first time with electron microprobe by Métrich and Clocchiatti (1989). Techniques were developed to analyse S and Cl using electron and secondary ion microprobe spectrometry, or «SIMS» (e.g. Hervig and Williams, 1988; Hauri et al., 2002). Fluor was also included in the list of analyses after methods taking into account iron and matrix effects were introduced (e.g., Hauri et al., 2002; Davis et al., 2003; Witter and Kuehner, 2004).

In the following years, the new micro-analytic techniques were applied at many volcanoes from various tectonic contexts. In subduction zones, first studies targeting H_2O, CO_2, S, Cl, F in melt inclusion aimed at evaluating P-T conditions and nature of the trapping melts, in combination with petrological investigations (Anderson, 1982; Harris et al., 1984; Sisson and Layne, 1993; Métrich et al., 2001; Walker et al., 2003; Cervantes and Wallace, 2003b). Such approaches, and the growing quantity of regional studies in volcanic arcs, were then summarized (e.g. Sisson and Layne, 1993 Lowenstern, 1995; Sobolev, 1996; Frezzotti, 2001; Schiano, 2003; Wallace, 2005; De Vivo and Bodnar, 2008; Métrich and Wallace, 2008), and permitted to diffuse in a common language the methodology of melt inclusions, and to better understand the role of volatiles in primitive melt generation. In subduction zones, work resume well the exercice of tracking the origin of volatiles from the mantle and their transport to the roots of magmatic systems (Wallace, 2005; Sadofsky et al., 2008; Johnson, 2008; Johnson et al., 2010; Roberge, 2009; Vigouroux, 2011). For completing these types of investigations, commonly SIMS (e.g. Shimizu and Hart, 1982; Dunbar et al., 1992; Hinton, 1995) or LA-ICPMS analysis (e.g. Taylor et al., 1997 Durrant, 1999; Halter et al., 2002) are used to measure major,trace and rare earth elements (REE) inside the glasses (Kent et al., 2002a; Kent et al., 2004b). Trace and REEs can be correlated to volatile concentrations, and used to give information on magma genesis and evolution in volcanic arcs (Kamenetsky et al., 1997; Danyushevsky et al., 2000a; Cervantes and Wallace, 2003b; Rowe et al., 2009; Benjamin et al., 2007; Wade et al., 2007; Portnyagin et al., 2007; Johnson et al., 2009; Sadofsky et al., 2008; Vigouroux et al. 2008; Wehrman et al. 2011; Wehrman et al., 2014; Portnyagin et al., 2014).

Chapter 4 - Volcanic gases from the plume of quiescent degassing volcanoes in CAVA

In this chapter, we present the summary of publications on volcanic gases from the plume of quiescent degassing volcanoes in CAVA integrated to the dissertation. I resume the field methodology that was proposed to quantify the budget of CO_2 and study the CO_2/SO_2 major gas ratios for different volcanoes in Nicaragua and Costa Rica. The body of the investigation is presented as two publications (**publication no. 1**, **publication no. 2**) where I participated as second author; one was published as Conde et al. (2014) and the second as Aiuppa et al. (2014).

Mainly, the CO_2 flux from volcanic plume is inferred as the product of the CO_2/SO_2 ratio and the SO_2 flux (Oppenheimer et al. 2011; Burton et al., 2013). Recent technological advances resumed above have allowed to integrate CO_2/SO_2 and to allow real-time monitoring of CO_2 fluxes by using Multi-sensor Gas Analyzer System (Multi-GAS) (Shinohara 2005; Aiuppa 2006; Aiuppa et al. 2007).

4.1 Publication n. 1

See External Appendices (A)

Conde, V., **P. Robidoux**, G. Avard, B. Galle, A. Aiuppa, A. Muñoz, 2014, Measurements of SO_2 and CO_2 by combining DOAS, Multi-GAS and FTIR observations: a case study from Turrialba and Telica volcanoes, *International Journal of Earth Sciences, June 2014, p.1437-3254*

4.2 Publication n. 2

See External Appendices (B)

Aiuppa, A., **P. Robidoux**, G. Tamburello, V. Conde, B. Galle,G. Avard, E. Bagnato, J. M. DeMoor, M. Martinez, A. Munoz, 2014, The Costa Rica – Nicaragua volcanic segment: along arc variations in volcanic gas chemistry and improved CO_2 budget, *Earth and Planetary Science Letter, October 13, p.134-147*

Chapter 5 – Multidisciplinary melt inclusion/gas monitoring approach: study cases

In this chapter, I explore the sources and behavior of major volatiles like H_2O, CO_2, S and Cl in two volcanic systems from San Cristóbal and Telica volcano, NW Nicaragua (Central America). We target active open-vent strato-volcanoes previously studied for the volcanic gases from the plume of quiescent degassing volcanoes. I present here two investigations that we be used to build a degassing model that integrate data on volatiles from melt inclusion and temporal variation of gases from the central crater plume.

In one hand, we present gas observations assisted by Multi-Component Gas Analyzer systems. On the other hand, with laboratory facility (mFTIR, EMPA, NanoSIMS, Raman Spectroscopy, etc.), we measure the volatile content of melt inclusions hosted in olivine and pyroxene crystals from several explosive eruptions and later estimate the depth at which magma evolve in the crust The body of the investigation is presented as two publications (**publication n.3**, **publication n.4**) where I participated as first author.

5.1 Publication n. 3

Robidoux, P., Aiuppa, A., Rotolo, S., Hauri, E., Rizzo, A., Frezzotti, M.L., (2016). The volatile content of mafic to intermediate magmas from San Cristóbal volcano, Nicaragua, Manuscript in preparation for *Lithos*

Robidoux, P., Aiuppa, A., Rotolo, S., Hauri, E., Rizzo, A., Frezzotti, M.L., (2016). The volatile content of mafic to intermediate magmas from San Cristóbal volcano, Nicaragua, Manuscript in preparation for *Lithos*

ABSTRACT

San Cristóbal volcano, in north-west Nicaragua, is one of the most active and young basaltic-andesitic strato-volcanoes of the Central American Volcanic Arc (CAVA). Here, we provide novel constraints on the volcano's magmatic plumbing system, by presenting the first direct measurements of major volatile contents in mafic to intermediate glass inclusions from Holocene to recent (1971) volcanic activity.

Olivine-hosted (Fo>80) glass inclusions from Holocene scoria tephra layers contain moderate H_2O (0.1–3.3 wt.%), S and Cl (>2,500 ppm) contents, and define the mafic (basaltic) end-member component. Historical scoria-tephra layers exhibit more evolved olivines (Fo~69-72) that contain distinctly lower volatile contents (0.1 – 2.2 wt.% H_2O, S >760 ppm and Cl > 1140 ppm), and represent a more evolved (basaltic-andesite) magmatic term. All glass inclusions are relatively poor in CO_2 (maximum CO_2 content measured by NanoSIMS of 530 ppm), suggesting pre- to post-entrapment CO_2 loss to a magmatic vapour. We use results of Raman spectroscopy, obtained on a population small (<20 µm) inclusions with CO_2-bearing shrinkage bubbles (3-12µm), to correct for post-entrapment CO_2 loss to bubbles, and to assess an original minimum CO_2 content in San Cristóbal parental melts of ~1,200 ppm.

H_2O-CO_2 solubility models constrain the degassing pathway of magmas, which includes a deep CO_2 degassing step (only partially preserved in the melt inclusion record), followed by coupled H_2O-S degassing plus ~26% crystal fractionation in a vertically elongated plumbing system (magma volatile saturation depths from ~195 MPa to <10 MPa). The degassing models are additionally constrained by compositions of present-day open-vent gas emissions from San Cristóbal, which we characterized as dominated by H_2O (~92 mol%), followed by CO_2 (~6mol %) and SO_2 (~3.8mol %).

The inferred volatile content evolutions in San Cristóbal magmas are interpreted to reflect (i) during the Holocene eruptive cycles, the fast emplacement of basaltic magma batches, saturated in volatiles (in the 2.2 – 5.2 km depth range)(ii) followed (in Historical times) by ascent of more slowly-moving, differentiated, and volatile-poor basaltic andesites, having longer residence times in the shallowest (< 2.9 km) coolest regions of the magmatic plumbing system.

The first measurements of noble gases (He-Ne-Ar) isotopic compositions in fluid inclusions of olivine and pyroxene crystals are combined with bulk rock major and trace rare earth elements. The $^3He/^4He$ ratios of Holocene and Historic rocks are in the same range (7.01-7.20 Ra), indicating a common mantle source for both magmas and the lack of temporal evolution. We characterize this magmatic source as a relatively shallow (>19-26 km) Primitive Pacific MOR-mantle ($^3He/^4He$=7.01–7.20 Ra), influenced to variable extents by distinct slab fluid components for basalts (Ba/La ~76; U/Th ~0.8) and basaltic andesites (Ba/La~86 and U/Th~1.0).

1. Introduction

San Cristóbal (Fig. 1) is a large (~ 107 km^3) and relatively young (~320±120 ka) strato-volcano, located in the Cordillera *de los Marabios,* on the north-western margin of the Nicaragua volcanic arc segment (Carr et al. 2007). Since the Holocene, San Cristóbal activity has been dominated by frequent cycles of lava emissions, intermittent strombolian to moderate vulcanian explosions generating important fallout and pyroclastic deposits, and eventually some rare pumice-bearing sub-plinian eruptions (Hazlett, 1977; Hazlett, 1987; Havlicek et al., 1999-2000). The erupted volcanics include basalts, basaltic andesites and dacites (Martinez and Viramonte, 1971; Hazlett, 1977; Hazlett, 1987; Carr, 1984; Carr et al.,1990; Patino et al., 2000; Bolge et al., 2009; Heydolph et al., 2012). Central America includes many examples of continuously (passively) degassing

open-vent mafic arc volcanoes (e.g., Aiuppa et al., 2014). In this category, San Cristóbal volcano is following, since 1971, a period of reactivation, possibly interpreted as a new magmatic cycle, and is today one of the most active basaltic-andesitic strato-volcanoes in Nicaragua (Fig. 1a).

Overviews on the main petrologic processes active at San Cristóbal have been offered by (Hazlett, 1977; Hazlett, 1987; Carr, 1984), and work has been carried out to relate the magmatic source to fluid contributions from subducting plate, using geochemical tracers (e.g. B/La, Leeman et al.,1994; Ba/La, Patino et al., 2000; $^{18}\delta O$, Eiler et al., 2005; $\delta^{37}Cl$, Barnes et al., 2008; Zr/Nb, Bolge et al., 2009; Sr-Nd-Pb isotopes, Heydolph et al., 2012) and volcanic gas information (e.g. Shaw et al., 2003; Zimmer et al., 2004; Elkins et al., 2006; Hilton et al., 2010; Aiuppa et al., 2014).

Surprisingly however, no petrologic information exists on abundance and degassing behaviour of volatile species and, to date, no effort has been made to explore the variability and nature of primitive volatile assemblage conditions in the San Cristóbal pluming system, during past and present-day volcanic activity. Also, $^3He/^4He$ ratio information, useful to constrain the features of magmatic/mantle source, are only available for a few low-temperature fumarole samples and yield lower values (5.65-5.74 Ra; Shaw et al., 2003; Elkins et al., 2006) than the maximum values at volcanoes in Nicaragua (Snyder et al., 2003; Shaw et al., 2003; Elkin et al., 2006; Leeuw et al., 2007) which are usually over 7.0 (except Conseguina; 3.37 Ra; Shaw et al., 2003). Such ratio cannot be considered representative of the pristine He isotope signature. Filling these information gaps is important, given the key role volatiles play in subduction zones mantle melting, magma differentiation and eruption style during ascent in the crust (e.g. Sisson and Grove, 1993; Roggensack et al., 1997; Cashman, 2004; Houghton and Gonnerman, 2008).

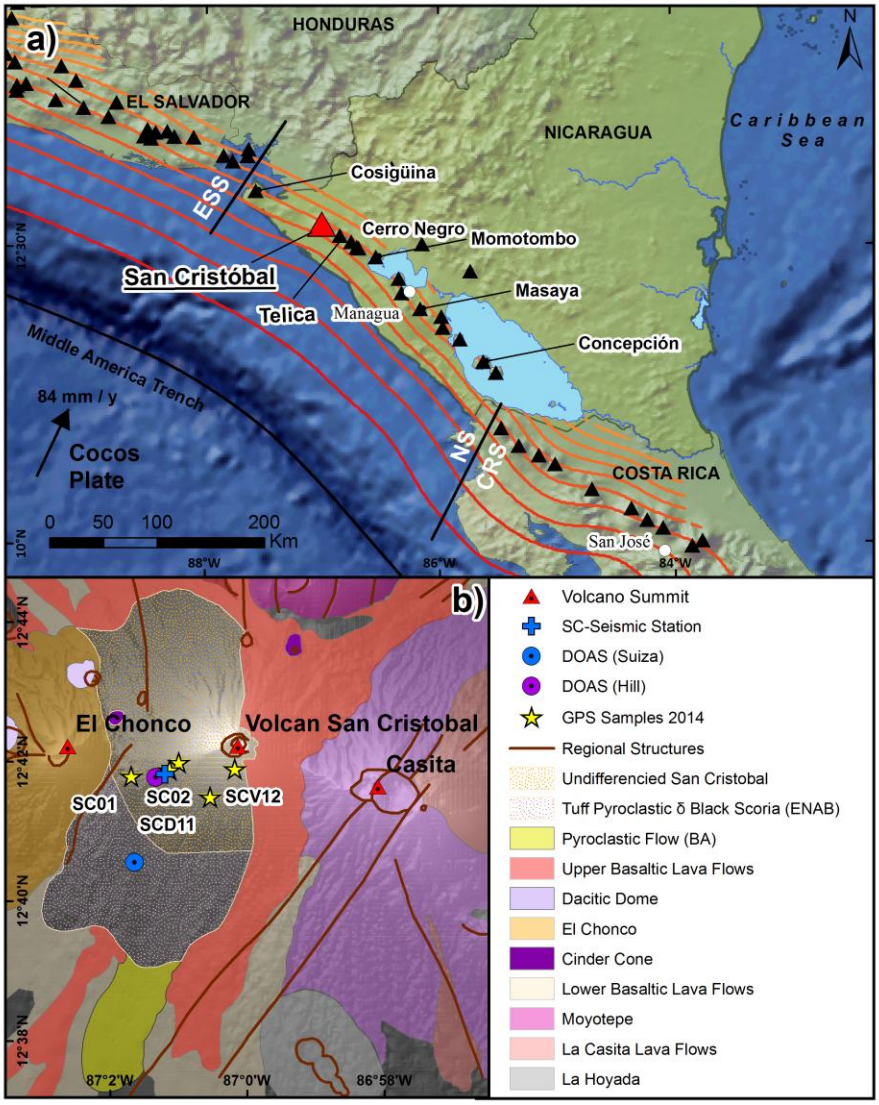

Figure 1 – Regional map of Nicaragua and San Cristóbal. a) Map of the subduction zone integrating arc segments from El Salvador (ESS), Nicaragua (NS) and Costa Rica (CRS). Arrows indicate the direction of motion of the Cocos Plate and the convergence velocities relative to the Caribbean Plate (in millimeters per year) after DeMets (2001). Topography effect is representing the 1:10m Natural Earth II with Shaded Relief and Water; file "CleanTOPO2" released by Smith and Sandwell in 1997 with contour shape files from ESRI and mapped with ArcGIS, Arc Map 10.1; World Map. Plate segments and trench structures are interpreted from the bathymetry imagery in Von Huene et al. (2000). **b)** Map of the main lithostratigraphy in the San Cristóbal-El Chonco-Casita area based on the work of the Geological Tcheque Republic Survey (Havlicek et al., 2000; Hradecký et al., 2007) and R. Hazlett (1977 - 1987). The instrument setting for monitoring San Cristóbal is also shown. DOAS stations are represented by circles with a single dot in the centre. MultiGAS stations are demonstrated in Aiuppa et al. (2014).

Recently, integrated petrological-gas studies have been implemented to obtain comprehensive information on volatile behavior in magmatic systems. Melt inclusions in mafic minerals have been widely used for explaining variation of volatile contents in deep regions of magmatic plumbing systems (e.g., Lowenstern, 1995; Sobolev, 1996; Frezzotti, 2001; Schiano, 2003; Wallace, 2005; De Vivo and Bodnar, 2008; Métrich and Wallace, 2008, etc.), while gas observations, eventually assisted by new instrumental techniques such Multi-Component Gas Analyzer systems (Multi-GAS, Aiuppa et al., 2005), can provide complementary constraints on gas behavior at superficial levels (Allard et al., 1997; Shinohara et al., 2003; Witter et al., 2005; Allard et al. 2005). Examples of these multi-disciplinary studies performed with Multi-GAS include Stromboli and Etna in Italy (e.g. Aiuppa et al., 2007; 2010), Yasur and Ambrym in the Vanuatu arc (e.g. Métrich et al. 2011; Allard et al., 2015). On the other hand, the investigation of $^{3}He/^{4}He$ ratio in gases and rocks revealed very useful to assess the features of the mantle source and of magma degassing beneath a volcano (e.g., Correale et al., 2012; Di Piazza et al., 2015; Rizzo et al., 2015). The study of $^{3}He/^{4}He$ ratio in rocks erupted over a volcano history is also important to assess the evolution of a magmatic system (e.g., Martelli et al., 2014).

San Cristóbal is an ideal site to bring new natural samples and test a similar combined petrological-gas monitoring approach to major volatile studies. Here, we first explore the abundance, source and behaviour of volatiles in San Cristóbal magmas, in the attempt of reconstructing volatile-related magmatic processes and their variations since Holocene periods. Our main targets are(1) the characterization of San Cristóbal crustal plumbing system and (2) the conditions of the magma feeding source. Glass inclusions from San Cristóbal volcano are analyzed for the first time for major elements and volatiles (CO_2, H_2O, S and Cl) by electron microprobe, mFTIR and NanoSIMS. A set of inclusions (10-50 μm in size) was also analyzed by microRaman in the attempt to correct for CO_2 loss to shrinkage bubbles. This petrological information is combined with novel volcanic gas plume observations with the aim of deriving a general model for H_2O-CO_2-S behavior in the magmatic plumbing system, and its variation over time. In addition, for recognizing sources and processes of magma generation, major, trace and rare earth elements were measured on bulk rock samples and compared with the other magma found along the CAVA. The first measurements of He, Ne and Ar noble gas isotopes in fluid inclusions (FI) from mineral separates from the same materials are also presented, with the aim of tracing the origin of fluids from magmas feeding the reservoir beneath San Cristóbal.

2. The Central American Volcanic Arc (CAVA)

The Central American Volcanic Arc represents a chain of volcanoes extending along the Pacific coast line between Guatemala and Costa Rica. This volcanic arc is the result of the northeasterly subduction of the Cocos Plate underneath the Caribbean Plate. The rate of subduction ranges from 6 cm/yr off southern Guatemala to 9 cm/yr off southern Costa Rica (Demets, 2001). The active CAVA volcanoes are geographically distributed along a NW-oriented, 1,100 km long corridor between latitudes 10° and 15°N, and is composed of Quaternary edifices of diverse morphology including composite volcanoes, calderas and monogenetic cinder cones (Mc Birney and Williams, 1965; Walker et al., 2001; Kutterolf et al., 2007) (Fig. 1a). In Nicaragua, the crust is relatively thin, from 25 km beneath the volcanic front to 34 km inland, and the angle of slab dip ranges 65 to 75 ° below the volcanic front (Syracuse and Abers, 2006; Auger et al., 2006; MacKenzie et al., 2008).

2.1 San Cristóbal volcano

San Cristóbal is a basaltic-andesitic stratovolcano located at 12°70' lat. N. and 87°00' long. W., at the NWend of the Volcanic Chain of Nicaragua. It is located at the NW end of the Cordillera Marrabios Range, a volcanic complex which also includes (from NW to SE) Casita (a composite volcano east of San Cristóbal flanks),Telica, Santa Clara, Cerro Negro, Las Pilas and Momotombo. The San Cristóbal peak, or El Viejo, has a symmetrical morphology, is the highest cone in Nicaragua (1,745 ma.s.l.), and culminates with a 500 m X 600 m wide crater (Fig.1b).

The San Cristóbal and Casita volcanoes are part of a larger complex that also includes older satellite volcanoes from the Pleistocene to Holocene, partially eroded and covered with laharic/mudflow deposits and volcanic alluvium like Moyotepe (composite basaltic andesite cone), Apastepe (tuff cone) and Chonco (composite dacite cone). The Caldera La Pelona was formed by the only probable plinian eruption in the volcanic complex since the Plio-Pleistocene (Martinez and Viramonte, 1971). San Cristóbal and Casita complex also includes Pleistocene to Holocene secondary cinder cones, maars and scoria cones with their associated lavas (Hazlett, 1977; Hazlett, 1987).

The composition of Pleistocene to Historic San Cristóbal pyroclastic deposits ranges from basaltic to andesitic (Havlicek et al., 2000; Heydolph et al., 2012). These deposits are well-sorted layers of ash, scoria and pumice from long-lived strombolian to moderately vulcanian activity. Volcanic bombs and blocks dominate the proximal deposits (Hazlett, 1987). Deposits are constituted of lithics and recycled materials fragmented by shallow depth hydro-volcanic eruptions (GVP, 2014).

The lava flow sequences on the volcano flanks (Fig. 1b), mainly of basaltic to basaltic-andesitic composition (Martinez and Viramonte, 1971; Hazlett, 1977; Hazlett, 1987; Carr, 1984; Carr et al.,1990; Feigenson et al., 2004; Bolge et al., 2009; Heydolph et al., 2012), testify recurrent effusive activity during the Quaternary period, most recently during the 16-17th century (Mooser et al., 1958; Hazlett, 1977). The majority of the San Cristóbal magmatic eruptions have been explosive in nature, however, and have concentrated at the central crater (Stoiber (1911-2001); Hazlett, 1987; Havlicek et al., 1999-2000). Explosive eruptions with Volcanic Explosivity Index (VEI) of 1 to 3 have been reported since the 16-17th century eventually producing important pumice layers (Hazlett, 1987; Stoiber (1911-2001); GVP, 2013). The absence of morphological and/or structural evidence for summit ring structures, and the lack of volumetric (~ 10 km^3) ash fall deposits at large distance (> 50 km), point against the occurrence of paroxysmal explosive eventsof plinian type (Hazlett, 1977; Schmincke, 2003). Fumarolic activity has been reported during the early 16-17th centuries at San Cristóbal and Casita volcanoes (Mooser et al., 1958 in Hazlett, 1977). Overall, both edifices are considered as potential sources for lahar and landslides (Vallance et al., 2004).

2.2 Recent eruptive activity

After almost three centuries of dormancy, degassing activity restarted on San Cristóbal summit crater on May 3, 1971 (Hazlett, 1977). Intense gas emissions and small explosions continued through May, June and July (Stoiber, 1971). This degassing activity persisted until

March 1976, when strong jet-like plume activity started, accompanied by significant increase in fumaroles' temperature, major collapses inside the crater and subsidence with small seismic activity (Stoiber, 1977; e.g. Stoiber (1976a-b)). A major violent explosion finally occurred on March 16, 1976. Since then, and until present, quiescent degassing and intense explosive phreatic events have alternated at the summit crater (Fig. 2a-b; Fig. 3a-b). According to satellite observations from the Washington Volcanic Ash Advisory Center (VAAC) and its Satellite Analysis Branch (SAB), NE-trending winds control tephra distribution and plume dispersal during both explosive events and quiescent degassing (GVP, 2014).

Different agencies and local observers have provided detailed reports on the post-1971 period of activity, including Darmouth College, Instituto Nicaraguense de Energía, Instituto de Investigaciones Sísmicas (IIS), Instituto Nicaraguense de Recursos Naturales (IRENA), and Instituto Nicaragüense de Estudios Territoriales (INETER). They reported volcanic activity alternating short-lived periods of high gas emission, moderate ash and gas explosions (VEI = 1-2), seismicity (ML ~ 1-5) and volcanic tremor, interspersed within longer periods of smaller explosions and regular passive degassing (see Fig. 2a-c).

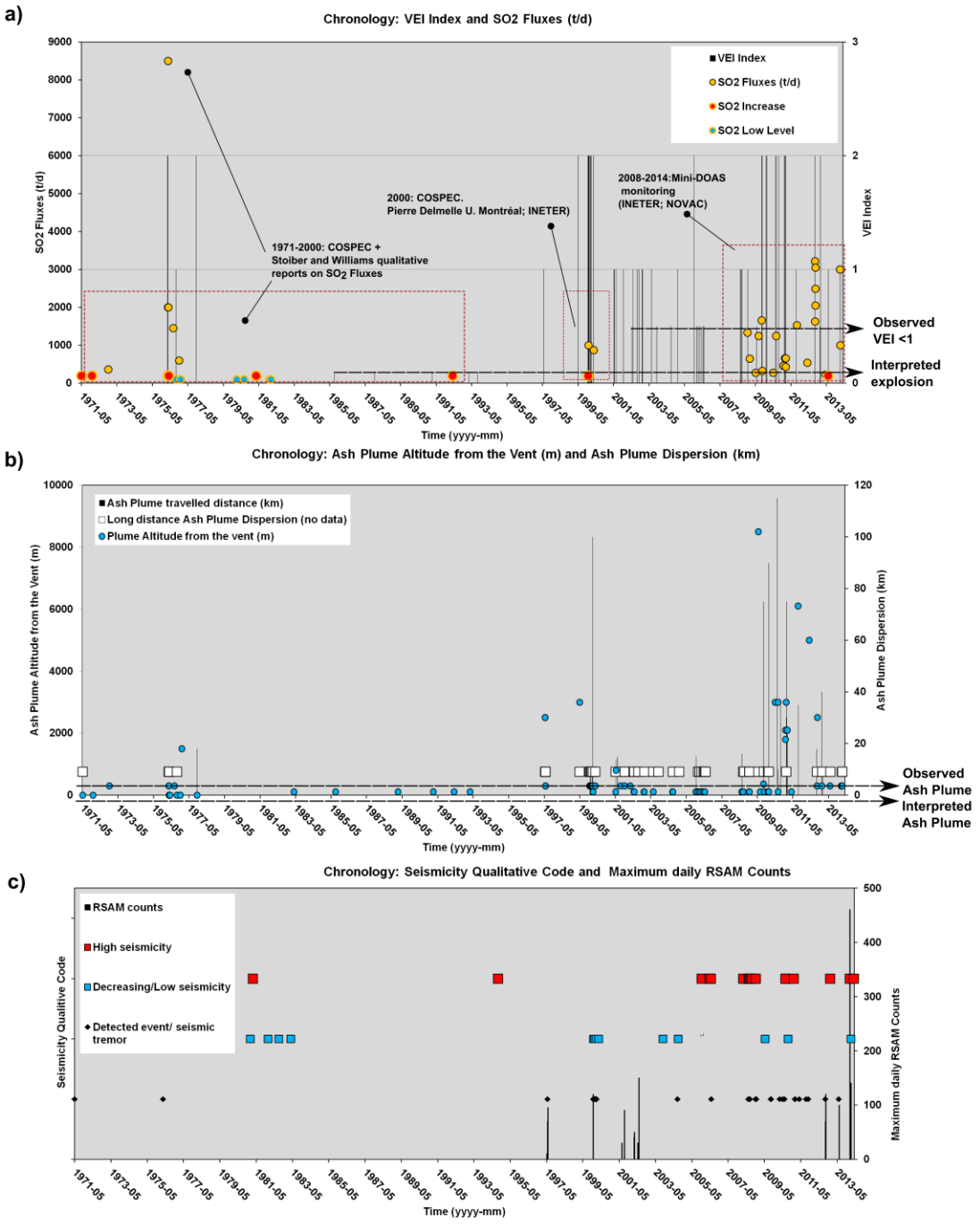

Figure 2 – Chronology of the volcanic activity at San Cristóbal. a) Chronology of Volcanic Eruptive Index (VEI) and a condensate of archived observations coupled with SO_2 fluxes at San Cristóbal since 1971 (GVP, 2014), b) Chronology of eruptive events with ash plume altitude (m) and dispersion from the vent (Km), c) Chronology of seismicity decrease and increase based on daily RSAM.

2.3 Past geochemical surveys at San Cristóbal

Plume SO_2 flux emissions have been quantitatively investigated for the first time at San Cristóbal with the Correlation Spectrometer (COSPEC) by Stoiber (1977) between 1972 and 1976 and by INETER and partners in later years. The SO_2 flux was generally found to vary between <300 and 3050 tons/day (Stoiber, 1977; Hazlett, 1977; Gemmel, 1987; Galle et al., 2009; Aiuppa et al., 2014), but emissions of up to 8,500 tons/day have been measured by hot gas venting (temperatures of ~500-600 °C) after the eruption of March 16, 1976, which may have resulted from opening of the system caused by the eruption, allowing deep sulfur-rich magma to more freely degas and escape (Stoiber, 1977; Hazlett, 1977). Fumarolic condensates collected at 566 – 582°C by Gemmel (1987) were mainly formed of Cl-SO_4 (> 1000 ppm), rock-forming elements (Si-Ti-Al-Fe: > 10 ppm;K-Na-Mg-F-Sn-Zn: > 1ppm), plus a multitude of minor constituents (< 1 ppm). Direct sampling of the summit crater's fumaroles indicated that SO_2 (65.4%) dominated over CO_2 (33.9%) (see Stoiber data in GVP, 2013). Low temperature (95.6 °C) fumaroles were investigated for helium and carbon isotopes by Shaw et al. (2003). These fumaroles showed relatively low $^3He/^4He$ isotope compositions (R_c/R_a : 5.65-5.74 ± 0.09; where R_c is the air-corrected $^3He/^4He$ ratio in the sample and R_a is the $^3He/^4He$ of air), and moderately higher $CO_2/^3He$ ratios (26-38 ± 2 X 10^9) relative to average Nicaragua gases. Since the 2000s, the crater plume has been frequently scanned for the SO_2 flux by UV spectrometers (Fig. 1a) of the NOVAC (Network for Observation of Volcanic and Atmospheric Change). These observations outputted SO_2 fluxes of 860±490 tons/day (Galle et al., 2010; see Conde, 2015 and references therein). Periods of increasing SO_2 (tons/day) emissions were generally marking a new cycle of explosive events (1971-1977; 1997-1999; 2008-2011; 2012-2013). Plume CO_2 fluxes estimation via CO_2/SO_2 (4.2±1.3) measured with Multi-GAS multiplied by SO_2 fluxes measured by UV-DOAS have been calculated at 523±263 tons/day for the first time by Aiuppa et al. (2014) during April 2013.

3. Sampling and Methods

3.1 Volcanic gas plume measurements

The major volcanic gas species (H_2O, CO_2, SO_2) in the San Cristóbal plume were measured using a Multi-Component Gas Analyzer System (Multi-GAS). The Multi-GAS was first applied in the mid-2000s for near-vent volcanic gas observations (Aiuppa et al., 2005; Shinohara, 2005). It is a compact unit constructed by assembling different commercial IR (for CO_2 and H_2O) and electrochemical (for SO_2 and H_2S) gas sensors. The same sensor assemblage as in Aiuppa et al. (2014) was used in this study. A fixed Multi-GAS, powered by a 12-V lead-acid battery connected to a photovoltaic module, was temporarily deployed (from April 11 to 16, 2013) in the San Cristóbal active crater area. This site (Fig. 1b) was tens of meters from the main degassing vent(s), but was frequently fumigated by the plume. The instrument was programmed to measure the concentrations of various gases (H_2O, CO_2, SO_2) in the plume at a sampling rate of 0.1 Hz, in cycles lasting for 30 minutes (four to eight cycles were performed daily). H_2S and Cl sensors were not mounted on-board this Multi-GAS to keep the instrument simple and compact.

The acquired concentration data were processed using the Ratiocalc software (Tamburello, 2015) to calculate ratios between individual volatiles. The CO_2/SO_2 ratio dataset was already discussed in Aiuppa et al (2014); we here extend this previous work by implementing H_2O/CO_2 ratios.

Time	"n"	H_2O/CO_2	CO_2/SO_2	CO_2	H_2O	SO_2
Bulk Plume						
Starting Time						
2013-04-11 08:51:18						
2013-04-11 16:46:12	95	15.7	2.8	0.06	0.92	0.02
2013-04-11 16:53:42	50	13.2	4.6	0.07	0.92	0.02
2013-04-11 17:01:57	55	12.4	2.5	0.07	0.90	0.03
2013-04-11 17:09:54	53	9.6	3.9	0.09	0.88	0.02
2013-04-12 04:56:42	97	20.4	3.6	0.05	0.94	0.01
2013-04-12 10:46:39	125	28.4	5.2	0.03	0.96	0.01
2013-04-12 12:56:24	105	25.0	4.4	0.04	0.95	0.01
2013-04-12 14:58:39	85	12.2	3.3	0.07	0.90	0.02
2013-04-12 15:14:06	75	11.1	3.4	0.08	0.90	0.02
2013-04-12 23:00:36	85	6.9	4.2	0.12	0.85	0.03
2013-04-13 01:03:09	73	28.2	3.3	0.03	0.96	0.01
2013-04-13 03:13:30	90	21.4	4.1	0.04	0.94	0.01
2013-04-13 04:52:39	72	15.5	3.9	0.06	0.92	0.02
2013-04-13 05:03:45	74	41.6	4.5	0.02	0.97	0.01
Ending Time						
2013-04-15 07:04:12						

Table 1 - Compositions of San Cristóbal volcanic gas plume (in mol%). The compositions for the bulk plume (essentially contributed by persistent passive degassing) was derived with RatioCalc software (See Aiuppa et al., 2014).

In brief, scatter plots of co-acquired H_2O vs. CO_2 and CO_2 vs. SO_2were created, and the volatile ratios were calculated from the slopes of the best-fit regression lines. For H_2O and CO_2, background-air corrected concentrations were used throughout. Results are shown in Table 1, where "time averaged" ratios in observational windows of 10-120 min each were calculated as in Aiuppa et al (2014). The windows selected for processing, and their respective durations, were chosen so as to have a number of readings ("n" in Table 1) assuring correlations of R^2>0.7 in H_2O vs. CO_2 and CO_2 vs. SO_2 scatter plots.

3.2 Description of field sites for rock sampling

The studied samples for petrology consist of crystal-rich scoriae and ash fall deposits. Each sample was weighed and treated for granulometry, liquid densimetry, then hand-picking for final separation of olivine, feldspar and pyroxene phenocrysts. The chosen deposits (samples SC2012, SC02B, SC5K, SC5C, SC11D; see supplementary materials) all mark significant episodes of reactivation of the San Cristóbal main crater (El Viejo).

Sample SC2012 corresponds to fine to medium coarse ashes of dark to grey tones collected at La Hacienda Roja, at 2 km SW from the summit crater after the January 2013eruption. It is composed of 75% scoria fragments, 10-15% altered plagioclases and 10-15% rounded lithic fragments, but very few olivine and pyroxene crystals.

The layer SC02B (Fig. 3c; Electronic Appendix 1) was deposited during the March 1976 eruption (VEI = 2), and was identified in the field under a thin oxidized reworked soil layer which used as a chronological marker for post 1997-1999 events (A. S. Ceballos; personnal

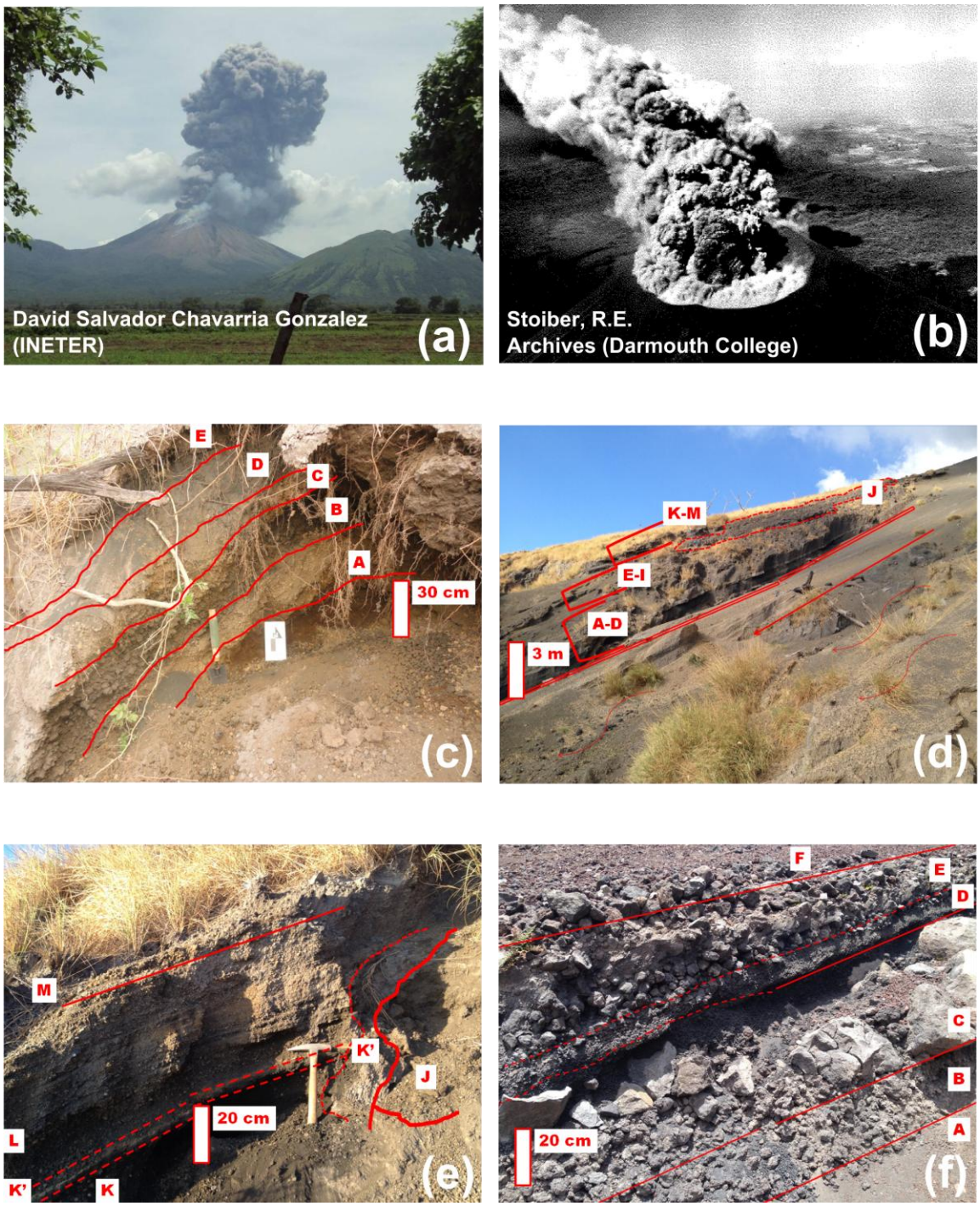

Figure 3 – Field photography. a) Phreatic eruption of April 4, 2014 (Photo Courtesy of D. Chavarria), b) Vulcanian eruption of March 9, 1976 (Photo courtesy of Darmouth College – R.E. Stoiber Archives), c) Outcrop SC02 near Seismic Station, d) Outcrop SC5 and a typical fluvial and lahar corridor pathway on SW flanks of San Cristóbal, e) Top of outcrop SC5, f) Outcrop SC11 on S flanks of San Cristóbal (avalanche deposit with typical jigsaw puzzle structure of the bloc).

communication, 2014). Scoria of the 1971-1977 sequence (SC02B) are medium to coarse lapilli, and have dark grey to black color. Coarse ashes of dark to grey tones contain most of the selected loose olivine phenocrysts, have almost no trace of clinopyroxene and small amounts (<5%) of lithic fragments, mostly beige-golden pumice fragments.

SC5K is a layer of coarse ashes and small lapilli-sized scoriae that contains several lithic fragments, including abundant pumices of different colors (<15%). SC5K is topping the whole SC5 outcrop, composed of several volcanic and volcanoclastic layers deposited during the Holocene to 16-17th century period (Fig. 3d; Electronic Appendix 1-2).

The SC5K layer shows laminated structures, washed from thin ashes, and could represent a series of reworked, mixed coarse ashes (Fig. 3e, Electronic Appendix 1-2) emitted between 1680 and 1684-1685, eventually mixed with coarse ashes from the 1971-1977 eruptive cycle transported by repeated series of lahar and diluvial rain. SC5K is found below the 1997-1999 soil marker and above a layer of the spatter agglutined lava bombs «SC5J» that may represents a source of ejected material from a terminal summit eruption. Considering its weathering conditions, it is younger than any lava flow of «categorie A» identified in Hazlett (1977) and thus, SC5J and subsequently SC5K are not older than 450 ± 50 yrs B.P. (Mooser et al., 1958; A. S. Ceballos, D. Chavarria, R. Hazlett, pers. comm.).

Other sequences (SC5 and SC11) from Holocene were also incorporated in this study. SC5C is a layer of coarse ashes and homogenous lapilli-sized scoria of dark tone. It represents a part of the ENAB deposit described in Havlicek et al. (2000) that covers the N, W and SW flanks of San Cristóbal for 2-5 km (Fig. 1b).

SC11 is in direct contact with an altered lava flow of «categorie B» identified in Hazlett (1977) and located 600 m south of the crater rim (Fig. 3f; Electronic Appendix 3). The sequence initiates with a layer of coarse scoriae and bombs and a thick avalanche block layer which corresponds to the BA deposit previously described by Havlicek et al. (2000). The studied sample in this sequence is SC11D which is made of glassy porous medium to large lapilli-sized scoriae and unconsolidated coarse ash

Older units like SC5C and SC11D contain very few lithics (<2%)(Electronic Appendix 2) except for SC11C, which is constituted of homogenous large grey crystalline blocks, probably associated with a dome collapse deposit (Electronic Appendix 3).

3.3 Petrography and mineral chemistry

Analytical methods

Whole-rock major element compositions were determined by wavelength-dispersive X-ray fluorescence (XRF) (Rigaku ZSX Primus) at DiSTeM (Table 2). The powder duplicate were analyzed for trace and REE with fusion ICP/MS (WRA4B2) at Ancaster (Actlabs: Code 4B2-Std).

Major elements, Cl, and S contents in glass inclusions, groundmass glasses and crystals were determined using a JXA-8200 WD/ED combined electron microprobe (EMPA; at INGV-Roma). The analytical conditions were 6.3 nA beam current, acceleration voltage of 15 kV, 5 □m beam diameter. The counting time for glass inclusions were 10'' on peak and background were 10 sec. and 5 sec., respectively). Table 3 lists average matrix glass compositions of the studied samples, while Table 4 presents EMPA compositions for 41 different glass inclusions, from 20 different olivine crystals and 2 clinopyroxenes. Sixty-five additional EMPA spot measurements were performed on 28 olivines (core and rim),12 spots on 6 clinopyroxenes and 8 spots on 4 diverse plagioclases to determine their chemistry.

The compositions of glass inclusions in olivines were corrected for post-entrapment crystallization and for Fe-loss by using Petrolog3 code (Danyushevsky and Plechov, 2011) fixing a Fe-Mg distribution between olivine and liquid ($K_D^{Fe\text{-}Mg}{}_{ol\text{-}liq}$) = 0.30 ± 0.04 (Roedder and Emslie, 1970; Toplis, 2005). In this method, an olivine component is incrementally added at 0.01% level until the melt inclusion reaches the equilibrium Kd value with the host olivine. The inclusions were preserved in Fe-rich olivines, but most of them had FeO > 1-4 % higher than their host rocks, and were corrected until their FeO_T was restored to follow the MgO v. FeO_T trend of the whole rock.

Material	Ashes	Scoria	Scoria	Spatter/Scoria	Scoria	Scoria
Age	2012-01-25	March 1976	15th Cent.-1977	Historic	Holocene	Holocene
Sample	SCO1A	SCO2B	SC5K	SC5J	SC5C	SC11D
Long.	N12°41'47.587"	N12°41'53.221"	W87°00'59.8"	W87°00'59.8"	W87°00'59.8"	W87°00'32.6"
Lat.	W87°01'41.727"	W87°01'7.867"	N12°41'59.3"	N12°41'59.3"	N12°41'59.3"	N12°41'29.8"
SiO_2	52.31	52.85	50.18	49.84	47.48	48.44
TiO_2	0.70	0.88	0.92	1.06	0.85	0.98
Al_2O_3	18.43	16.51	18.48	18.00	20.10	18.24
Fe_2O_3	10.32	11.00	10.92	11.16	10.68	11.57
MnO	0.17	0.21	0.21	0.21	0.19	0.21
MgO	2.94	3.88	4.03	3.47	4.66	4.77
CaO	10.48	10.33	9.78	9.63	11.74	10.48
Na_2O	2.82	2.41	2.80	2.94	2.18	2.60
K_2O	0.42	0.50	0.66	0.74	0.42	0.57
P_2O_5	0.13	0.14	0.20	0.23	0.14	0.18
L.O.I.	0.22	0.81	0.29	0.98	0.76	0.51
Total	98.72	98.71	98.19	97.27	98.43	98.02
Mg# (FeOT)	0.36	0.41	0.42	0.38	0.46	0.45
V, ppm	250	308	292	310	314	325
Cr	< 20	< 20	< 20	< 20	< 20	< 20
Co	26	29	22	21	26	26
Ni	< 20	< 20	< 20	20	20	< 20
Cu	150	190	160	210	200	220
Zn	200	100	90	110	80	90
Ga	19	19	20	20	19	19
Rb	11	13	14	15	9	11
Sr	592	572	562	541	523	498
Y	16	21	21	24	16	19
Zr	42	50	49	57	34	41
Nb	2	2	< 1	1	< 1	< 1
Ba	509	594	601	646	407	484
La	5.8	7.5	7.5	8	4.6	5.9
Ce	12.7	16.6	16.2	18	10.5	13.6
Pr	1.93	2.52	2.52	2.8	1.78	2.2
Nd	9.2	12.7	12.5	14.1	9	11
Sm	2.6	3.4	3.4	4.1	2.6	3.2
Eu	0.92	1.08	1.07	1.24	0.86	1.01
Gd	2.6	3.5	3.5	4	2.6	3.4
Tb	0.5	0.6	0.6	0.7	0.5	0.6
Dy	3	3.9	3.7	4.4	2.9	3.6
Ho	0.6	0.8	0.8	0.9	0.6	0.7
Er	1.8	2.3	2.1	2.7	1.7	2.2
Tm	0.26	0.34	0.33	0.41	0.25	0.33
Yb	1.7	2.2	2.1	2.6	1.7	2.2
Lu	0.28	0.36	0.33	0.39	0.25	0.33
Hf	1.1	1.3	1.5	1.8	1	1.3
Ta	< 0.1	< 0.1	< 0.1	< 0.1	< 0.1	< 0.1
Pb	< 5	< 5	< 5	< 5	< 5	< 5
Th	0.8	1	0.9	0.9	0.5	0.6
U	0.6	0.7	0.7	0.8	0.5	0.6
Ba/La	87.8	79.2	80.1	80.8	88.5	82.0
U/Th	0.8	0.7	0.8	0.9	1.0	1.0
La/Yb	3.4	3.4	3.6	3.1	2.7	2.7

Table 2 - Bulk analysis of rock samples at San Cristóbal. Major elements analysis performed on the wavelength - dispersive X - ray fluorescence (XRF) (Rigaku ZSX Primus) at DiSTeM (U. Palermo). Major elements were determined on glass disks prepared from 9:1 mixtures of Li-tetraborate and rock powder that had been heated and oxidized during loss on ignition (LOI) determination. Fe_2O_3 was calculated as total iron. LOI values are loss on ignition measurements at 1,100 °C for 1 h on replicate powders dried for 24 h at 110 C. These LOI values have not been corrected for oxygen uptake upon conversion of FeO to Fe_2O_3 in the furnace. Trace elements analyses by ICP-MS (inductively coupled plasma mass spectroscopy) were performed at ActLabs in Ancaster (Canada) with FUS-MS Code 4B2-Std (1-10) Trace Elements Fusion ICP/MS(WRA4B2).

No. Spot	SiO_2	TiO_2	Al_2O_3	FeO	MnO	MgO	CaO	Na_2O	K_2O	P_2O_5	S	Cl	F	Total	S/Cl
	(wt.%)										(ppm)	(ppm)	(ppm)	(wt.%)	
Frag. No.	**Bulk matrix spots: SC02Bbulk**														
1	51.51	1.44	13.89	13.19	0.29	4.05	8.14	3.39	1.21	0.34	n.d.	1130	n.d.	97.57	
2	52.45	1.70	13.85	13.78	0.33	3.99	7.87	3.29	1.22	0.36	n.d.	900	n.d.	98.95	
3	52.23	1.36	13.85	13.24	0.25	4.04	8.03	3.52	1.20	0.39	n.d.	850	n.d.	98.19	
4	53.03	1.43	13.48	13.36	0.21	3.87	7.97	3.33	1.22	0.34	112	1220	n.d.	98.37	0.1
5	52.41	1.44	13.62	13.79	0.18	4.02	7.98	3.39	1.28	0.34	92	980	n.d.	98.57	0.1
6	52.94	1.48	14.10	12.34	0.31	4.04	8.43	3.87	1.29	0.36	n.d.	1150	n.d.	99.30	
7	52.39	1.33	14.37	12.63	0.35	3.67	8.07	3.64	1.06	0.36	32	960	n.d.	97.96	0.0
8	51.83	1.52	13.91	13.29	0.31	3.99	8.43	3.12	1.12	0.37	n.d.	1160	n.d.	97.97	
Average	**52.35**	**1.46**	**13.88**	**13.20**	**0.28**	**3.96**	**8.11**	**3.44**	**1.20**	**0.36**				**98.36**	
Stdev 1σ	**0.51**	**0.11**	**0.27**	**0.50**	**0.06**	**0.13**	**0.21**	**0.23**	**0.08**	**0.02**					
Frag. No.	**Olivine Border: SC02B15glass1**														
1	53.56	1.40	14.32	12.71	0.30	3.89	7.73	3.09	1.07	0.28	372	770	n.d.	98.54	0.5
2	53.52	1.30	13.71	13.35	0.33	3.82	8.15	2.90	1.12	0.38	128	1090	n.d.	98.73	0.1
Frag. No.	**Bulk matrix spots: SC02Bbulk**														
1	52.71	1.36	14.06	12.96	0.35	3.55	7.66	3.46	1.28	0.38	100	800	n.d.	97.75	0.1
Frag. No.	**Olivine Border: SC5k2glass**														
1	50.18	1.30	14.87	12.76	0.28	3.82	8.20	3.42	1.04	0.27	1186	1220	n.d.	96.57	1.0
2	49.52	1.22	14.74	12.16	0.33	3.70	8.31	3.56	0.98	0.19	1190	1130	n.d.	95.09	1.1
3	51.44	1.18	13.43	13.20	0.33	3.79	8.16	3.40	1.17	0.31	929	1100	n.d.	96.73	0.8
Frag. No.	**Olivine Border: SC5Cr1glass**														
1	51.00	1.42	13.30	14.36	0.34	4.04	8.96	3.23	1.14	0.32	196	1070	n.d.	98.11	0.2
2	50.25	1.57	13.45	15.08	0.29	3.98	9.11	2.71	1.14	0.31	132	930	n.d.	97.91	0.1
Frag. No.	**Plagioclase Border: SC5Cr4glass**														
1	50.59	1.36	14.24	13.21	0.26	3.72	9.21	3.09	1.05	0.33	n.d.	1120	n.d.	97.06	
Frag. No.	**Olivine Border: SC11Dr1glass**														
1	51.36	1.88	12.19	14.54	0.37	3.02	7.20	3.32	1.44	0.34	68	1180	n.d.	95.66	0.1

Table 3 – Electron microprobe analyses of San Cristóbal matrix volcanic glass. Sulphur contents (ppm) are converted from original SO_3 (wt.%).

Inclusion Phenocryst	SC2012A2	SC2012A	SCO2B1a	SC02B4a	SC02B4b	SC02B6aI	SC02B5a
Phenocryst chemistry (Fo)	-	-	71	71	71	69	72
Cpx (Ens)	70.4	70.4	-	-	-	-	-
Inclusion shape and size	i, 44X24	i, 52X30	e-i, 74X40	e-i, 72X45	e-i, 72X46	e, 140X90	e, 60X47
Assemblage order	A1/A1	A1/A1	A1/A2	A2/A2	A2/A2	A2/A3	A1/A1
Order	Primary	Primary	Primary	Secondary	Secondary	Primary	Primary
Type	Fully enclosed	Fully enclosed	Fully enclosed	Reentrant	Reentrant	Fully enclosed	Fully enclosed
Bubble (vol %)	-	-	-	-	-	-	-
SiO2	54.5	55.0	52.1	50.5	56.9	56.0	51.6
TiO2	1.2	1.1	1.1	1.4	1.3	1.9	1.1
Al2O3	13.1	13.8	16.0	15.2	11.9	15.3	15.8
FeO*	13.4	12.9	12.7	14.3	13.3	9.1	12.7
MnO	0.3	0.3	0.2	0.4	0.3	0.2	0.2
MgO	4.5	4.4	4.5	4.9	4.6	3.1	4.6
CaO	8.6	8.1	8.4	8.3	7.4	9.0	8.8
Na2O	3.2	3.4	3.7	3.6	2.9	3.6	3.9
K2O	1.2	1.1	0.9	1.1	1.0	1.4	1.0
P2O5	0.3	0.3	0.3	0.4	0.3	0.4	0.2
TOT	100	100	100.0	100.0	100.0	101	100.0
T (°C) by KP	1133	1124	1126	1134	1128	1070	1128
H2O (wt.%) nSIMS	0.13	0.96	-	1.9	-	-	-
CO2 (ppm) nSIMS	17	150	-	123.6	-	bdl	-
Cl (ppm) EMPA	1530	1490	1280	1590	1110	1340	1280
Cl (ppm) nSIMS	-	-	-	-	-	-	-
S (ppm) EMPA	575	721	633	364	160	449	717
S (ppm) nSIMS	-	-	-	-	-	-	-
CPX Thermobar. (Mpa) by KP	420	609	-	-	-	458	-
Sat. Press. (Mpa) by PPL	44	761	-	-	-	206	-

Inclusion Phenocryst	SC02B7a	SC02B8a	SC02B13a	SC02B13b	SC02B13_A4	SC02B18a	SC02B18b
Phenocryst chemistry (Fo)	71	70	71	72	72	70	70
Cpx (Ens)	-	-	-	-	-	-	-
Inclusion shape and size	e, 100X56	e, 73X46	e, 121X108	e, 90X51	e, 70X60	i, 130X60	i, 116X80
Assemblage order	A1/A2	A1/A1	A1/A3	A1/A3	A2/A3	A1/A3	A3/A3
Order	Primary	Primary	Primary	Primary	Primary	Primary	Secondary
Type	Fully enclosed	Fully enclosed	Fully enclosed	Fully enclosed	Fully enclosed	Fully enclosed	Reentrant
Bubble (vol %)	-	-	4.3	-	-	-	-
SiO2	53.6	51.7	52.8	53.5	52.7	54.2	52.3
TiO2	1.3	1.2	0.6	1.3	0.6	1.5	1.2
Al2O3	14.7	15.5	15.6	15.3	15.5	15.0	15.4
FeO*	12.3	13.3	12.9	11.8	13.2	11.9	13.2
MnO	0.3	0.3	0.3	0.2	0.3	0.3	0.3
MgO	4.2	4.2	4.3	4.1	4.5	4.3	4.1
CaO	8.8	8.4	9.1	8.8	8.7	7.7	9.0
Na2O	3.5	4.0	3.6	3.7	3.8	3.6	3.3
K2O	1.0	0.9	0.5	0.9	0.5	1.2	1.0
P2O5	0.3	0.3	0.2	0.3	0.2	0.3	0.2
TOT	100.0	100.0	100.0	100.0	100.0	100.0	100.0
T (°C) by KP	1121	1122	1124	1118	1127	1123	1120
H2O (wt.%) nSIMS	-	-	-	1.2	-	-	-
CO2 (ppm) nSIMS	-	-	-	57.3	-	-	-
Cl (ppm) EMPA	1025	1905	1425	1195	1455	1160	1255
Cl (ppm) nSIMS	-	-	-	-	-	-	-
S (ppm) EMPA	278	1376	1684	1125	1592	443	481
S (ppm) nSIMS	-	-	-	-	-	-	-
CPX Thermobar. (Mpa) by KP	-	-	-	-	-	-	-
Sat. Press. (Mpa) by PPL	-	-	-	-	-	-	-

Inclusion Phenocryst	SC02Br3a	SC02Br3z	SC02Br5a	SC02Br5bI	SC02Br5c	SC5k1a	SC5k2a
Phenocryst chemistry (Fo)	72	71	65	65	65	70	69
Cpx (Ens)	-	-	-	-	-	-	-
Inclusion shape and size	e, 21X15	s, 60X58	s-i, 35X30	s, 46X34	44X33	e-i, 70X40	e, 70X40
Assemblage order	A1/A3	A1/A3	A2/A3	A2/A3	A1/A3	A1/A1	A1/A1
Order	Primary	Primary	Primary	Primary	Primary	Primary	Primary
Type	Fully enclosed	Fully enclosed	Fully enclosed	Fully enclosed	Fully enclosed	Fully enclosed	Fully enclosed
Bubble (vol %)	2.3	2.6	2.6	-	-	-	-
SiO2	57.8	55.4	54.8	54.6	54.9	55.5	53.6
TiO2	1.0	0.9	1.1	1.1	1.2	1.4	1.3
Al2O3	15.5	16.5	17.4	17.1	16.5	14.6	15.1
FeO*	8.4	9.9	9.2	9.8	10.5	11.2	12.2
MnO	0.2	0.3	0.3	0.2	0.3	0.2	0.3
MgO	3.2	3.7	2.6	2.8	2.9	3.9	4.0
CaO	8.6	7.8	9.2	8.9	8.1	7.6	8.1
Na2O	3.5	3.8	3.9	4.1	4.2	3.9	4.1
K2O	1.4	1.6	0.8	0.8	1.0	1.2	1.0
P2O5	0.4	0.2	0.5	0.6	0.3	0.4	0.4
TOT	100	100	100	100	100	100.0	100.0
T (°C) by KP	1068	1058	1019	1027	1042	1115	1117
H2O (wt.%) nSIMS	0.9	-	1.4	nd	-	-	-
CO2 (ppm) nSIMS	0	-	89	nd	-	-	-
Cl (ppm) EMPA	980	1295	1300	1110	1150	1253	1505
Cl (ppm) nSIMS	-	-	-	-	-	-	-
S (ppm) EMPA	493	328	917	621	885	1011	1404
S (ppm) nSIMS	-	-	-	-	-	-	-
CPX Thermobar. (Mpa) by KP	505	551	242	241	323	-	-
Sat. Press. (Mpa) by PPL	111	-	362	96	-	-	-

Inclusion Phenocryst	SC5Kr1a	SC5Kr1b	SC5Kr2a	SC5Kr2b	SC5Cr6a	SC5Cr6b
Phenocryst chemistry (Fo)	69	69	69	69	74	73
Cpx (Ens)	-	-	-	-	-	-
Inclusion shape and size	e, 43X26	e, 41X23	e-i, 42X24	i, >50X40	s-i, 28X25	e, 21X12
Assemblage order	A1/A2	A1/A2	A1/A2	A2/A2	A1/A3	A2/A3
Order	Primary	Primary	Primary	Secondary	Primary	Primary
Type	Fully enclosed	Fully enclosed	Fully enclosed	Reentrant	Fully enclosed	Fully enclosed
Bubble (vol %)	1.5	1.5	4.3	2.1	4.2	-
SiO2	53.8	55.3	54.5	53.0	50.7	49.8
TiO2	1.2	1.3	1.0	1.2	1.0	0.8
Al2O3	15.6	15.4	15.6	16.1	16.7	17.3
FeO*	11.3	10.6	11.3	11.8	11.4	11.7
MnO	0.3	0.3	0.2	0.3	0.3	0.2
MgO	3.9	3.6	3.8	3.9	4.8	4.7
CaO	8.8	8.2	8.5	8.8	10.6	11.7
Na2O	3.7	3.9	3.8	3.6	3.2	3.1
K2O	1.0	1.1	1.0	1.0	0.7	0.5
P2O5	0.3	0.3	0.3	0.2	0.5	0.2
TOT	100	100	100	100	100	100
T (°C) by KP	1081	1080	1081	1076	1095	1095
H2O (wt.%) nSIMS	1.6	1.5	1.6	1.6	2.4	-
CO2 (ppm) nSIMS	71	202	41	44	527	-
Cl (ppm) EMPA	905	1025	1375	1370	1195	1025
Cl (ppm) nSIMS	-	-	-	-	-	-
S (ppm) EMPA	523	853	575	717	927	1075
S (ppm) nSIMS	-	-	-	-	-	-
CPX Thermobar. (Mpa) by KP	439	528	507	462	445	264
Sat. Press. (Mpa) by PPL	489	777	385	369	1366	-

Inclusion Phenocryst	SC5Dr1a	SC5Dr1aa	SC5Dr1b	SC5Dr1bb	SC5Dr1bbb	SC5Dr1c	SC5Dr3a
Phenocryst chemistry (Fo)	78	77	78	77	78	77	79
Cpx (Ens)	-	-	-	-	-	-	-
Inclusion shape and size	s, 25X23	s, 16X11	e, 25X18	e, 12X8	e, 24X16	e, 17X13	e, 54X36
Assemblage order	A1/A3	A1/A3	A1/A3	A1/A3	A1/A3	A2/A3	A1/A2
Order	Primary	Primary	Primary	Primary	Primary	Primary	Primary
Type	Fully enclosed	Fully enclosed	Fully enclosed	Fully enclosed	Fully enclosed	Fully enclosed	Fully enclosed
Bubble (vol %)	4.2	4	5.4	4.2	4.3	13	4.3
SiO2	43.2	45.4	45.4	45.9	44.1	44.3	47.0
TiO2	0.9	1.1	1.1	1.0	1.1	1.1	1.4
Al2O3	17.3	22.4	21.8	19.9	21.4	21.9	19.6
FeO*		9.7	10.3	10.9	11.3	10.9	10.6
MnO	0.2	0.1	0.2	0.3	0.2	0.2	0.2
MgO	8.4	4.6	4.8	5.1	5.3	5.0	5.5
CaO	10.0	13.3	13.0	13.5	13.3	13.4	10.8
Na2O	2.2	2.8	2.8	2.9	2.6	2.7	3.2
K2O	0.4	0.4	0.4	0.4	0.4	0.4	1.1
P2O5	0.2	0.3	0.2	0.1	0.2	0.1	0.5
TOT	100	100	100	100	100	100	100
T (°C) by KP	1192	1111	1118	1118	1145	1138	1117
H2O (wt.%) nSIMS	-	-	-	-	-	-	-
CO2 (ppm) nSIMS	-	-	-	-	-	-	-
Cl (ppm) EMPA	1290	1550	1740	1220	975	1505	1260
Cl (ppm) nSIMS	-	-	-	-	-	-	-
S (ppm) EMPA	1818	2395	2333	1838	1991	1959	765
S (ppm) nSIMS	-	-	-	-	-	-	-
CPX Thermobar. (Mpa) by KP	636	241	121	137	134	254	425
Sat. Press. (Mpa) by PPL	-	-	-	-	-	-	-

Inclusion Phenocryst	SC11Dr1g	SC11Dr1h	SC11Dr1i	SC11D1a	SC11D2a	SC11Dr1b	SC11Dr1z
Phenocryst chemistry (Fo)	78	78	80	79	77	78	77
Cpx (Ens)	-	-	-	-	-	-	-
Inclusion shape and size	e, 18X12	e, 17X11	e, 19X12	e, 32X28	e, 22X14	e, 25X18	e, 60X52
Assemblage order	A1/A2	A1/A2	A1/A2	A1/A2	A1/A1	A1/A2	A3/A3
Order	Primary	Primary	Primary	Primary	Primary	Primary	Primary
Type	Fully enclosed	Fully enclosed	Fully enclosed	Fully enclosed	Fully enclosed	Fully enclosed	Fully enclosed
Bubble (vol %)	5.4	5.2	5.8	-	-	7.3	>10?
SiO2	45.4	46.1	46.3	46.9	52.8	47.0	45.6
TiO2	0.9	0.9	1.3	0.9	0.8	1.1	0.9
Al2O3	23.0	21.0	20.6	18.7	19.8	20.6	18.6
FeO*	9.3	9.7	9.4	12.2	6.7	9.6	12.9
MnO	0.3	0.0	0.2	0.2	0.1	0.2	0.3
MgO	4.5	4.6	5.1	6.5	3.3	4.7	6.2
CaO	13.0	14.1	13.9	12.0	12.1	13.4	12.3
Na2O	2.9	2.9	2.6	2.3	2.7	2.9	2.5
K2O	0.5	0.4	0.4	0.3	1.2	0.4	0.4
P2O5	0.3	0.2	0.2	0.1	0.3	0.1	0.3
TOT	100	100	100	100	100	100	100
T (°C) by KP	1107	1102	1114	1142	1009	1098	1143
H2O (wt.%) nSIMS	2.6	2.2	2.2	3.3	2.6	-	-
CO2 (ppm) nSIMS	310	369	350	406	117	-	-
Cl (ppm) EMPA	1520	1380	1180	1147	1340	1425	1305
Cl (ppm) nSIMS	-	-	-	-	-	-	-
S (ppm) EMPA	1850	1975	1536	1995	835	2105	1929
S (ppm) nSIMS	-	-	-	-	-	-	-
CPX Thermobar. (Mpa) by KP	130	220	196	-	-	-	339
Sat. Press. (Mpa) by PPL	606	599	594	1206	741	-	-

Table 4 – Electron microprobe analyses of San Cristóbal glass inclusions. Sulphur contents (ppm) are converted from original SO_3 (wt.%).The chemical composition was corrected for post-entrapment effects PEC by using Petrolog3 (Danyushevsky and Plechov, 2011). The major element composition was recalculated on a volatile free basis. FeO*, total FeO. Chemical composition from host phenocrysts are the closest analyzed spot to the MIs and they are written with Fo, forsterite content (mol %) in the olivine and «CPX Ens», for magnesium number of clinopyroxenes calculated with model of Morimoto M. (1988). Saturation pressures in megapascals (MPa) by «PPL» are calculated from H_2O and CO_2 contents of the melt inclusions using the solubility model of Papale et al. (2006). An online version of the Papale's solubility model (http://ctserver.ofmresearch.org/Papale/Papale.php) was used for these calculations. Temperatures by '«KP» are calculated using equation (16) in Putirka (2008) from spreadsheet of Putirka (2008) and considered as a maximum thermometer input values for subsequent calculations. Inclusion shapes are resumed as ''s'', spherical shape; ''e'', elliptical shape; ''I'', irregular shape. ''A'' is for textural assemblage order among other inclusions assemblage found in the same crystal.

Similarly, melt inclusions hosted in clinoyroxene phenocrysts were corrected for post-entrapment crystallization, adding cpx component to the melt inclusions until the equilibrium $K_D^{Fe\text{-}Mg}{}_{cpx\text{-}liq}$ (0.26 ± 0.04) was reached.

3.4 Volatile contents in glass inclusions

Carbon and water in double-faced polished glass inclusions of > 20-30 µm were analyzed (at DiSTeM) by micro Fourier transform IR spectroscopy (mFTIR) using a Hyperion 1000/2000 microscope (Bruker), equipped with a Tensor 27 IR source (Bruker), an MCT detector cooled with N_2 and a KBr beamsplitter. The clean and dry air from the bench and microscope was constantly purged with a CO2RP015 CO_2 remover/air dryer with maximum outlet flow rate of 1.5 L/min.

Volatile abundances were calculated using the Beer-Lambert Law: $C = MA / \rho d\varepsilon$, where M is the molar mass (g/mol), A is the absorbance at the band of interest, ρ is room temperature density of the glass (g/L), d is thickness of the glass inclusion (cm^{-1}) and ε is the molar absorption coefficient (absorptivity, L / mol cm). Water concentrations listed in Table 5 were measured considering the total H_2O peak at 3,550 cm^{-1}, which corresponds to the fundamental OH^- stretching vibration (Stolper, 1982; Ihinger et al., 1994). We used a molar absorption coefficient (ε) of 63 ± 3 L/mol cm (Dobson, D. et al., unpublished data, Dixon et al., 1995 a). The samples' absorbance signals also registered clear $H_2O_{mol.}$peaks, representing the symmetrical bending mode at 1,635 cm^{-1}.The average first standard deviation uncertainty (1σ) in total H_2O concentration calculated by considering each parameters of Beer-Lambert Law, was ±0.3 wt.%. Carbon dioxide concentrations were determined by measuring the double peak of CO_3^{2-} at 1,515 and 1,435 cm^{-1} with a background subtraction procedure similar to Newman and Stolper (2000) and Roberge et al. (2005). The absorption coefficient ε (1,515 cm^{-1}) was calculated using the equation $\varepsilon_{1525} = 451 - 342$ (Na/Ca+Na), according to Dixon and Pan (1995 a-b), and values ranged between 379 and 397 L/mol cm. The double peak of CO_3^{2-} was quantified in 2 over 12 detected carbonate peaks, because of large estimated uncertainty (Table 6).

CO_2, H_2O, S and Cl concentrations were also determined using a Cameca NanoSIMS 50/50L ion probe at Carnegie Institution of Science. The polished crystals and standard samples were pressed into indium inside 25 mm diameter Al-metal disks mounts adopting the procedure of Hauri et al. (2002). Samples and standards were analyzed in a vacuum chamber (pressure of < $5 \cdot 10^{-9}$ Torr). A primary voltage of ~8 kV was applied to the primary $^{133}Cs^+$ source. Measurements were realized using a pre-sputtering time of 180 s using a 20X20 μm^2 beam and a 3.8 to 10 µm squared aperture window (depending on inclusion surface). The NanoSIMS 50L was calibrated using a set of natural basaltic and andesitic glasses: 1654, 1833-11, 1833-1, 1846-12, 519, A288opx, CM58ol, GRR1012ol, Herasil, IndiaEn, KBH-1opx, KenyaEn, KLV-23ol, ROM177ol, ROM250-13ol, ROM250-2ol, ROM273opx, WOK28-3 (Hauri et al., 2002, 2006; H. E. Hauri, pers. comm.). To quantify the volatile element concentrations, intensities of the secondary ions $^1H^-$, $^{12}C^-$, $^{32}S^-$, $^{35}Cl^-$ were measured and normalized to the intensity of $^{28}Si^-$ (Electronic Appendix 4). Two main reference materials (D30-1, 519 in Fine and Stolper, 1986 and Hauri et al., 2002) were measured two to three time per day during the 4 day analytical run and prove highly reproducible with a repeatability of 7.2 % (D30-1, 1σ, N=8) and 9.1 % (519, 1σ, N=8) relative for CO_2. For CO_2, H_2O, S and Cl the relative errors are respectively 13.8 %, 7.1%, 11.4% and 14.8% (Table 7).

Samples	Thickness (μm)	Density (g/L)	Molecular H2O 3,550 cm-1		
SC02B			Abs.	H2O (wt%)	1 σ (wt%)
SC02B1a	48	2.583	0.450	1.1	0.2
SC02B3a	56	2.559	0.301	0.6	0.2
SC02B4a	42	2.529	0.168	0.5	0.3
SC02B4b	42	2.586	0.163	0.5	0.2
SC02B5a	30	2.575	0.379	1.3	0.3
SC02B5b	30	2.575	0.247	0.9	0.3
SC02B6a	40	2.604	0.469	1.3	0.2
SC02B6b	40	2.604	0.274	bdl	-
SC02B7a	35	2.604	0.136	0.5	0.2
SC02B8a	30	2.544	0.274	1.0	0.3
SC02B9a	26	2.559	0.675	2.3	0.3
SC02B12a	18	2.580	0.272	1.6	0.5
SC02B13a	22	2.548	0.304	1.3	0.8
SC02B13b	22	2.553	0.259	1.1	0.8
SC02B13c	22	2.543	0.413	2.0	0.8
SC02B15a	22	2.559	0.140	0.8	0.4
SC02B18a	37	2.525	0.614	1.9	0.2
SC02B18b	37	2.615	0.165	0.4	0.3

Samples	Thickness (µm)	Density (g/L)	Molecular H2O 3,550 cm-1		
			Abs.	H2O (wt%)	1 σ (wt%)
SC02B SC5K					
SC5K1a	39	2.518	0.485	1.4	0.2
SC5K2a	43	2.565	0.282	0.8	0.2
SC5K4a	25	2.541	0.257	1.0	0.3
SC5K9a	30	2.541	0.203	0.8	0.3
SC5K1G	49	2.541	0.718	1.6	0.2
SC5K2G	42	2.541	0.296	0.8	0.2
SC5K3G	42	2.541	0.675	1.9	0.2
SC5K5aG	37	2.541	0.410	1.2	0.2
SC5K5bG	37	2.541	0.224	0.7	0.2
SC5C					
SC5C5a	33	2.562	0.287	1.0	0.3
SC5C1a	33	2.562	0.090	0.3	0.3
SC5C1b	33	2.562	0.085	0.4	-
SC5C4a	49	2.562	0.105	0.3	-
SC5C4b	49	2.562	0.150	0.4	0.3
SC5C4c	49	2.562	0.250	0.6	0.2
SC5C6a	40	2.562	0.240	0.7	0.4
SC5C6b	40	2.562	0.312	0.9	0.3
SC5C7a	38	2.562	0.240	0.7	0.2
SC5C1G	36	2.562	0.392	1.2	0.2
SC5C7aG	32	2.562	0.206	0.8	0.3
SC5C7BG	32	2.562	0.232	bdl	-
SC5C5G	58	2.562	0.233	0.4	0.2
SC5C4G	35	2.562	0.241	2.1	0.3

Table 5 – Fourier transform infrared spectroscopic data for H_2O in San Cristóbal glass inclusions. The uncertainty for thickness has great influence on the water content (± 0.2 wt.%.) compare to their molar absorption coefficient (± 0.06 wt.%) and their density (± 0.04 wt.%). Direct thickness measurement estimated with the digital displacement gauges by measuring the vertical displacement between the focused surfaces of the wafer and this procedure was repeated 3 times. Crystal samples of various size/ thickness were selected because they were subject to various errors reproduction and they were put on mFTIR stage for a second run by using another Hyperion Bruker mFTIR spectrometer at Laboratorio de fluidos corticales, Centro de Geociencias Campus Juriquilla (México). The second spectrometer permitted to use the Interference fringes method from Nichols and Wysoczanski (2007), because of the possibility to test the reflectance mode with a pure golden plate background (Wysoczanski and Tani, 2006). The thicknesses determined by this method agree with an average error of 12 % (6 µm) for the selected samples estimated with digital displacement gauges.

Samples	Thickness (µm)	Density (g/L)	CO32-		CO2	
			1,435 cm-1 Abs.	1,515 cm-1 Abs.	Avg. (ppm)	1 σ (ppm)
SC02B						
SC02B4a	42	2.529	0.026	0.019	bdl	-
SC02B5a	30	2.575	0.026	0.033	bdl	-
SC02B13b	22	2.553	0.023	0.010	bdl	-
SC02B13c	22	2.553	0.025	0.021	bdl	-
SC02B18a	37	2.525	0.030	0.029	358	79
SC5K	-	-	-	-	-	-
SC5C						
SC5C5a	30	2.562	0.024	0.021	bdl	-
SC5C4b	49	2.562	0.021	0.032	bdl	-
SC5C4c	49	2.562	0.032	0.036	bdl	-
SC5C5G	58	2.562	0.015	0.025	bdl	-
SC5C4G	35	2.562	0.015	0.016	216	71

Table 6 – Fourier transform infrared spectroscopic data for CO_2 in San Cristóbal glass inclusions. See Table 5 for H_2O absorbtion values. CO_2 in mid-IR is assumed to be the average of both1,435 cm^{-1} and 1,515 cm^{-1} peak absorbencies. The average uncertainty for the reproducibility of the CO_3^{2-} absorbance in the 12 detected peaks can change the concentration by ± 44 ppm and the uncertainty for thickness by ± 86 ppm when using Beer-Lambert Law. Uncertainty in the absorption coefficient ε (± 3 ppm) and density (± 5 ppm) are playing a less important role.

3.5 Raman Spectroscopy

A subset of inclusions was selected for testing the extent of CO_2 migration into shrinkage bubbles, considering their frequent occurrence among different assemblages of inclusions. Bubbles selected for Raman spectroscopy occupied ~ < 10 vol% of glassy, spherical-ellipsoidal shaped fully-enclosed inclusions, with no post-entrapment daughter crystals, oxides and crystallization on the inclusion walls. In view of these textural characteristics, we argue CO_2 in these shrinkage bubbles was exsolved from the host melt inclusion, and can be re-introduced in the glass by mass balance calculations (e.g. Roedder, 1979; Skirius et al., 1990; Anderson and Brown, 1993; Cervantes et al., 2002; Métrich and Wallace, 2008; Hansteen and Klügel, 2008; Hartley et al., 2014; Moore et al., 2014; Moore et al., 2015; Wallace et al. 2015; Lowenstern, 2015).

Inclusion NanoSIMS	CO2 (µg/g)	H2O (wt%)	S (µg/g)	Cl (µg/g)
2012				
SC2012A2	17	0.13	59	270
SC2012A	150	0.96	357	1479
SC02B				
SC02B4a (diff spot)	124	1.91	818	1349
SC02Br3a	0	0.75	143	900
SC02Br3c	2	0.76	37	573
SC02Br5a	89	1.36	152	907
SC02B6b	7	0.58	314	1199
SC02B13z (MI#b)	57	1.25	568	1160
SC02B13y ((MI#b)	31	1.24	463	957
SC5K				
SC5Kr1_2	71	1.63	689	1042
SC5Kr1_B	202	1.51	457	1134
SC5Kr2a1	40	1.73	485	1380
SC5Kr2a2	41	1.59	462	1221
SC5Kr2B1	44	1.62	608	1234
SC5k3Ga	-	0.98	270	-
SC5k3Gb (=MI#SC5K3G)	-	1.88	-	-
SC5k3GbII (=MI#SC5K3G)	191	2.16	1676	1971
SC5k5Ga	34	2.06	409	1522
SC5K5Gb	175	1.79	456	1195
SC5K9Ga	87	1.65	566	1059
SC5K9GaII	88	1.62	550	1021
SC5K9GGlass	16	0.13	29	1168

Inclusion NanoSIMS	CO2 (µg/g)	H2O (wt%)	S (µg/g)	Cl (µg/g)
SC5C				
SC5C1a	408	2.27	805	815
SC5C1b	376	2.68	-	1194
SC5C1c	111	2.37	978	1177
SC5C6I	245	2.63	692	1587
SC5C7Ga	47	1.57	275	1372
SC5C7Gb	92	1.63	486	982
SC5C7Glass	-	0.17	81	560
SC5Cr6	527	2.36	1160	1134
SC11D				
SC11Dr1_2	386	2.91	1918	1375
SC11Dr1d	305	2.03	1755	1351
SC11Dr1g	310	2.25	2532	2210
SC11Dr1h	369	2.01	2043	1430
SC11Dr1i	350	2.05	1946	1452
SC11D1a	406	3.31	2401	1446
SC11D2	117	2.63	625	1531
STD 519	12.9	7.0	10.9	13.9
STD D30	14.8	7.3	11.9	15.6
Total STD DEV.	13.8	7.1	11.4	14.8

Table 7 – NanoSIMS 50L data for CO_2 – H_2O – S – Cl in San Cristóbal glass inclusions.
No data are determined for « - ».

We initially identified a population of 100 olivine phenocrysts for each of the studied layers (SC11D, SC5C, SC5K, and SC02B) and we noted that the fraction of olivines with closed glass inclusions with a shrinkage bubble, was 12%, 15%, 3% ,4 %, in each of the 4 layers, respectively. The selected olivine crystals with bubble-bearing glass inclusion were prepared in CrystalBond™ on single side-polished sections for Raman spectroscopy. The micro-Raman spectrometer was a Horiba Jobin Yvon HR800 instrument of LABRAM HRVIS at the Laboratorio di spettroscopia MicroRaman in Dipartimento di Scienze della Terra (University of Torino). The instrument was applied exclusively for CO_2 density measurements (Table 8) following instrumental setting and approach from Frezzotti et al. (2012) and calculation method of Wang et al. (2011). Density results and correction of the samples with the presence of a shrinkage bubble are explained in Electronic Appendix 5.

Sample	Fermi diad v+ (cm-1)	Fermi diad v+ (cm-1)	Δ (cm-1)	Fluid Density (Raman) g/cm3	Fluid Density (IGL) g/cm3
SC02Br5a	1289.62	1392.99	103.37	0.2672	0.1212
SC5Kr1a*	1288.02	1391.41	103.39	0.2750	0.1582
SC5Kr1b*	1288.02	1391.41	103.39	0.2750	0.4120
SC5k3Gb	1288.02	1391.41	103.39	0.2750	0.3290
SC5Cr6	1289.62	1392.99	103.37	0.2672	0.2932
SC11Dr1-2	-	-	-	-	-
SC11Dr1d	-	-	-	-	-
SC11Dr1g	-	-	-	-	-
SC11Dr1i	-	-	-	-	-

Table 8 – Fluid density of the bubble in glass inclusion by Raman spectroscopy. No data are determined for « - ». Procedure explained in Electronic Appendix 5,6,7.

3.6 Noble gas isotopes from mineral separates

The elemental and isotope composition of He, Ne, and Ar was measured in fluid inclusions (FI) hosted in the olivine and pyroxene crystals at Istituto Nazionale di Geofisica e Vulcanologia, Sezione di Palermo (INGV-Palermo). Olivine and pyroxene crystals were separated from the 0.5 - 1 mm fraction of the ashes and scoria layers by using a heavy liquid (sodium polytungstate), and then carefully handpicked under a binocular microscope. The selected crystals were cleaned following internal protocol (e.g., Di Piazza et al., 2015), then each group of samples (0.1 - 1.3 g) was placed inside stainless-steel bowls and installed in a crusher capable of loading up to six samples at the same time. Noble gases trapped inside fluid inclusions were released by in-vacuo single-step crushing. This procedure is the most conservative in order to analyze a fluid composition that reflects that of the magmatic/mantle source, because minimizes the contribution of cosmogenic ^{3}He and radiogenic ^{4}He possibly grown/trapped in the crystal lattice (e.g., Kurz, 1986; Hilton et al., 1993, 2002). Gas released from the mechanical fragmentation of crystals was cleaned in an ultra high vacuum purification line, which means that all the species of the gas mixture except noble gases were removed. Helium isotopes (^{3}He and ^{4}He) and ^{20}Ne were measured separately by two different split-flight-tube mass spectrometers (Helix SFT-Thermo). The values of the ^{3}He/^{4}He ratio are expressed as R/Ra (where Ra is the ^{3}He/^{4}He ratio of air, which is equal to $1.39 \bullet 10^{-6}$). The analytical uncertainty of the He isotopic ratio is generally <11%. The R/Ra values were corrected for atmospheric contamination based on the ^{4}He/^{20}Ne ratio (e.g. Sano and Wakita, 1985) and are expressed hereafter as Rc/Ra values. Argon isotopes (^{36}Ar, ^{38}Ar and ^{40}Ar) were analyzed by a multicollector mass spectrometer (GVI Argus), with an analytical uncertainty generally <1.5% (Table 9). The uncertainty in the determinations of He, Ne, and Ar elemental contents was less than 5%. Typical blanks for He, Ne and Ar were $<10^{-14}$, $<10^{-16}$ and $<10^{-14}$ mol, respectively. Further details about the sample preparation and analytical procedures are available in e.g. Di Piazza et al. (2015).

Sample ID	Sample detail	Phase	Weight	[He]	[Ne]	^{40}Ar	R/Ra	He/Ne
			g	mol/g	mol/g	mol/g		
SC5K	Historic - 1976	Ol	0.117	7.02E-14	3.76E-15	1.30E-12	6.34	18.7
SC11D	Holocene	Ol	0.281	4.60E-14	2.13E-15	1.89E-13	6.91	21.6
SC11D (1)	Holocene	Ol -Scoriaa	0.600	6.30E-14	3.28E-15	3.16E-13	6.97	19.2
SC11D (2)	Holocene	Ol -Scoriaa	0.373	3.49E-14	3.45E-15	6.87E-13	6.82	10.1
SCO2B	1976 eruptive cycle	Ol	1.000	1.42E-14	6.61E-16	4.01E-13	7.11	374
SCO2B	1976 eruptive cycle	Cpx	0.500	1.59E-14	1.77E-15	2.55E-13	6.25	226

Sample ID	Rc/Rab	Error tot +/-	^{40}Ar/^{36}Ar	Error	^{38}Ar/^{36}Ar	Error
				%		%
SC5K	6.44	0.389	301	0.279	0.194	0.191
SC11D	7.01	0.401	301	0.805	0.209	0.206
SC11D (1)	7.07	0.234	300	0.217	0.194	0.192
SC11D (2)	7.02	0.582	303	0.249	0.195	0.193
SCO2B	7.20	0.408	304	0.301	0.185	0.184
SCO2B	6.45	0.750	300	0.481	0.193	0.192

Table 9 – Chemical and isotopic compositions of noble gases from fluid inclusions entrapped in olivine and pyroxene phenocrysts. Crystals with glassy and/or altered surfaces were found and therefore segregated in different batch of analysis of SC11D for validating the reproducibility and judging the effect of scoria contamination.

4. Results

4.1 The H_2O–CO_2–SO_2 composition of San Cristóbal plume

During the observation period (from April 11 to 16, 2013), while the volcanic plume CO_2/SO_2 ratio was frequently determined (see Aiuppa et al., 2014), the volcanic H_2O signal was more difficult to resolve from the large, atmospheric H_2O background. We therefore report in Table 1 the results of the only 14 simultaneous detections of CO_2/SO_2 and H_2O/CO_2 ratios (all obtained between April 11 and 13). Our measured H_2O/CO_2 ratios ranged from 6.9 to 41.6, with a mean value of 18.7±9.4. The co-acquired CO_2/SO_2 ratios ranged 2.8 to 5.2 (with a mean value of 3.8±0.7).

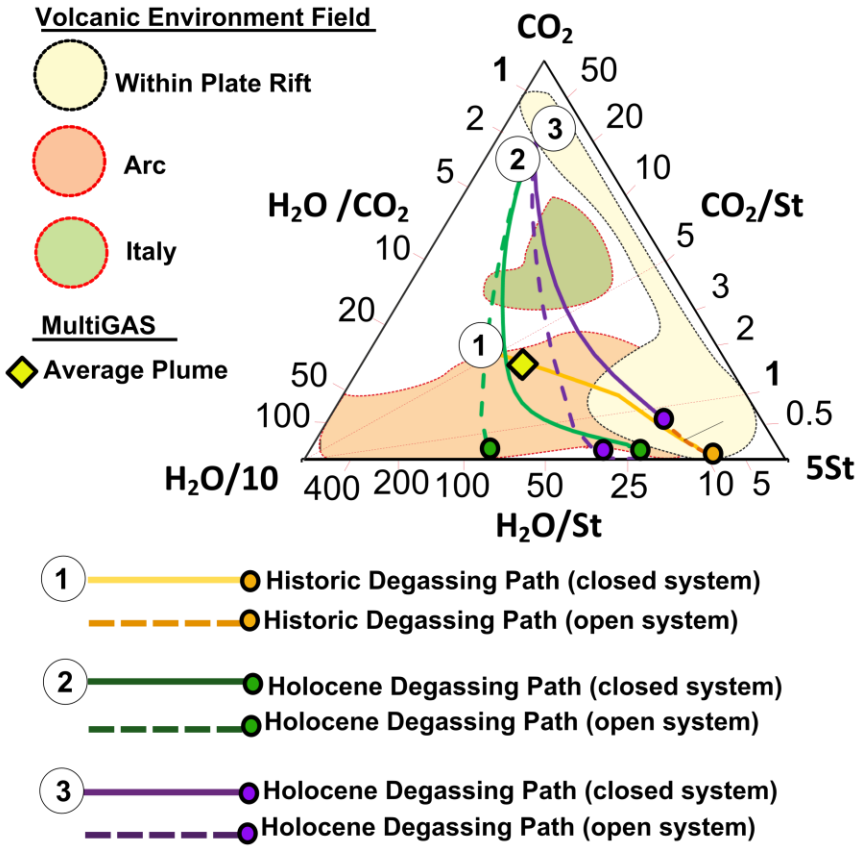

Figure 4 – H_2O–CO_2–SO_2 plot. Plume gas compositions of Multi-GAS are shown with diverse degassing trend from melt inclusion volatile assemblages in the vapour by using SolEx program (Witham et a., 2012). The average quiescent degassing plume composition from April 11-16 (2013) is shown. To facilitate the interpretation of each group of samples in the solubility model and also because they have similar magma compositions, basalts from SC5C and SC11D were grouped together has «Holocene» and basaltic andesites from SC02B and SC5K as «Historic» samples. The degassing paths in closed and open system (1), (2) and (3) are also presented in figure 11-12.

From these ratios, and assuming minor contribution from gases such as H_2, H_2S and HCl, we obtained the molar proportions in the plume of the major volcanic components (H_2O, CO_2 and SO_2). Results (Table 1) demonstrate that San Cristóbal plume gas is dominated by H_2O (85-97 mol%; mean of 92%), followed by CO_2 (2-12 mol%; mean of 6%) and SO_2 (3-5 mol%; mean of 3.8%). Figure 4 shows these compositions in a $H_2O/10$-CO_2-$5S_t$ ternary plot.

4.2 Whole-rock geochemistry

Whole-rock compositions range from basaltic to basaltic-andesitic (SiO_2: 48.7-52.8 wt%; K_2O: 0.55-1.71 wt%, Fig. 5a). The least evolved sample is SC5C,an high alumina basalt with 48.7 wt% SiO_2 (and 4.7 % MgO) and relatively low total alkali content ($Na_2O + K_2O$= 2.7 wt%); the most evolved sample among those sampled is SCO1A (SiO_2= 52.9 wt%, MgO= 2.8 wt%). Younger samples of ashes and scoria lapilli (1970s to 16th-17th century: SC02B and SC5K) are more evolved, with 53.6-54.3 wt% SiO_2 and total alkalis between 3.0-3.3 wt%. The bulk rock samples from the 1976-2012 series (# SC01A-SC02B) are much poorer in K_2O (0.47 wt%) compared to older Holocene scoriae.

In the literature the most evolved rocks analyzed from San Cristóbal is an andesite lava flow (SiO_2= 62 %, Hazlett ,1977). Recently analyzed scoriae and ashes from 1971-2012 and lava samples from literature also belong to the calc-alkaline series, according to K_2O vs. SiO_2 diagram (Villamonte, 1971; Carr et al., 1984; Hazlett, 1987; Heydolph et al., 2012) (Fig. 5a).

In figure 5b, Holocene bulk rocks appear richer in MgO (4.7 – 4.9 wt%) than Historic samples (3.0 – 4.2 wt%). In figure 5b-c-d-f, compatible oxides are similar for all samples, as for example in CaO (10.0 – 12.1 wt%), Al_2O_3 (17.0 – 20.6 wt%), but also TiO_2 (0.7 – 1.1 wt%) and FeO (9.3 – 10.7 wt%). CaO, Al_2O_3 and MgO (Fig. 5c-d-e) show negative dependences on SiO_2, indicating that fractional crystallization played a central role for magma evolution at San Cristóbal. Fractionation vectors show that plagioclase was dominant among the fractionating mineral assemblage (Fig. 5c to e).

The primitive mantle-normalized (Mc Donough and Sun, 1995) REE bulk-rock trends are rather flat, with a small LREE enrichment(La/Yb_N=1.8 to 2.4). The La/Yb_N ratio slightly increases from the oldest (Holocene) to the most recent (SC5K to 1970s samples) layers, but it is still in the typical array of arc tholeiites and in line with observations at nearby volcanoes of Nicaragua (Heydolph et al., 2014; Carr et al., 1984) and in south-east El Salvador (Table 2, Fig. 6a). The Eu anomaly, if any, is low (Eu/Eu*= 1.07 -0.92), slightly more pronounced for basaltic andesites.

The San Cristóbal samples are enriched in large ion lithophile elements (Cs, Rb, Ba, La, etc) relative to N-MORBs, and they overlap the E-MORB range. Most samples have low contents of high field strength elements (Ta, Nb, Zr, Hf), in particular, the high negative anomaly in Ta-Nb (Fig 6b) and, for a slightly lesser extent, also for Zr, Hf and Ti. Negative anomalies of the above HFS elements are typical of subduction-related magmas and are peculiar of all the magmas erupted in the Nicaragua segment (Bolge et al., 2009; Heydolph et al., 2012).The San Cristóbal lava samples (including basaltic andesites and one high alumina basalt) exhibit similar patterns compared to our scoria (Carr and Rose, 1987; Hazlett, 1988; Bolge et al., 2009; Heydolph et al. 2012). The basaltic lavas, in particular, have profiles in the spidergram similar to our most primitive samples (SC5C, SC11D). Additionally, as seen in figure 6b, the most differentiated products (effusive of explosive) emitted at San Cristóbal peaks at higher values for sediment fluid-related elements as Ba, U, K and Sr.

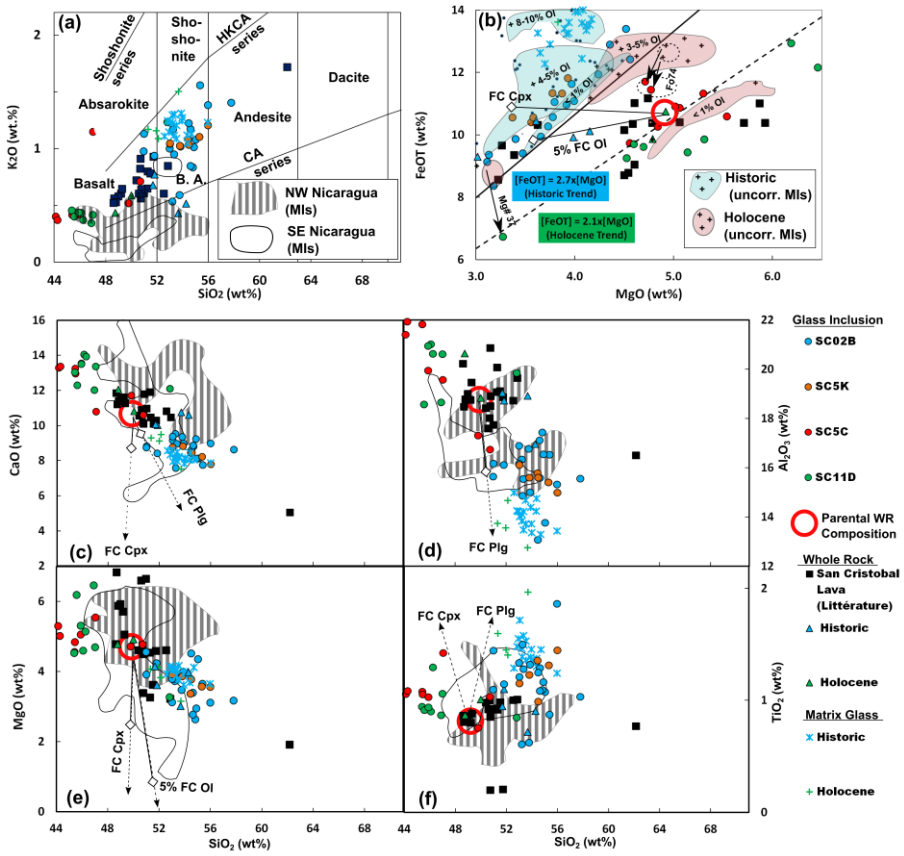

Figure 5 – Diagram of major elements at San Cristóbal for analyzed melt inclusions, whole rock from scoria and matrix glasses including whole rock data from lava series in the literature. The melt inclusions hosted- olivines (MIs) are the rounded shapes with white interior representing the SE and stripped interiors from NW Nicaragua (Roggensack et al., 1997; Wehrman, 2005, Tesis; Atlas, Z. Tesis, 2008; Sadofsky et al.,2008; Wehrman et al., 2011; Portnyagin et al., 2012). In literature, whole rock from San Cristóbal are represented by the black squares (Martinez and Viramonte, 1971; Hazlett, 1977; Hazlett, 1987; Carr, 1984; Carr et al.,1990; Bolge et al., 2009; Heydolph et al., 2012a). In this study, whole rock data from historic samples are symbolized by blue interior triangles: SCD1, SCV12, SCO1A, SC02B, SC5K, SC5J, and from Holocene samples as green interior triangles (SC5C, SC11D). The red contour circles are the proposed primitive models for crystallized fractionation (FC) where the length of each vector (arrows) is stopping for 15% crystallization by a white interior lozenge for each proposed mineral phase (5% values are exceptions written for olivine). a) K_2O vs. SiO_2 classification rock diagram from Peccerillo and Taylor (1977), b) FeOT vs. MgO trending of melt inclusion with uncorrected (blue and red interior rounded shapes) and corrected MIs with their fraction of olivine added (% Ol) for post-entrapment processes by using Petrolog 3. FeO_T is restored to the FeO_T v. MgO trend of the whole rock (condition of respecting the Kd = 0.3 ± 0.04; Toplis, 2005) and illustrated by the regression lines and their respective equations for Historic rocks (blue interior rectangle) and Holocene rocks (green interior rectangle). One inclusion of Mg#35 and two inclusions from a Fo74 olivine host from Holocene are corrected at different values from the general tending. c) CaO v. SiO_2. d) Al_2O_3 v. SiO_2. e) MgO v. SiO_2. f) TiO_2 v. SiO_2.

With the exception of sample SC01A (discarded for comparisons because it is rich in fine grained lithic material), the Ba/La ratio, a tracer for slab-derived fluids contribution in the mantle source region, (Leeman et al., 1994; Reagan et al., 1994), Ba/La is very high, in the range 79-88 (Table 2), more than twice higher than the mean of Central American volcanoes (Ba/La= 31; references in figure 6), although Nicaraguan volcanoes characteristically all depart towards higher Ba/La values (mean Ba/La= 62) (compilation in Ruscitto, 2011). To compare between the different layers in the stratigraphy, we calculated the Ba/La from the primitive mantle-normalized values (N) and the Ba/La_N ratio is slightly higher in Holocene samples (>8.1) than in historical rocks (<7.8).

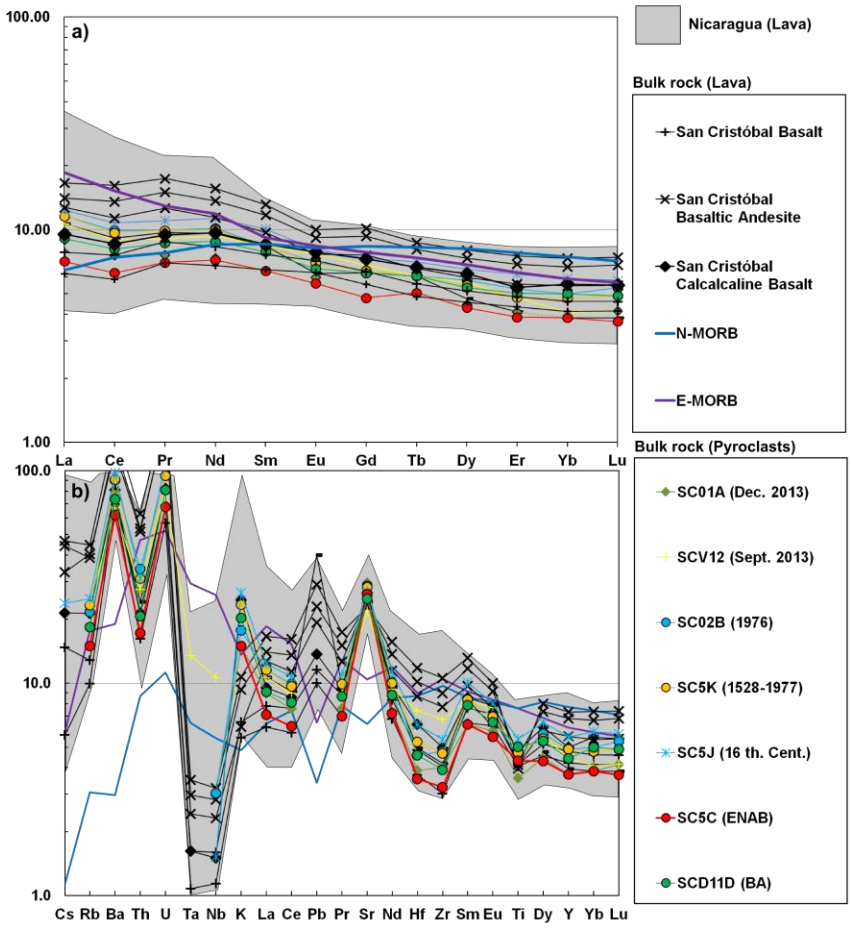

Figure 6 – Spidergrams for trace and rare earth elements in bulk rock scoria at San Cristóbal including whole rock data from literature. Original values are normalized to the Pyrolite sample from Mc Donought et Sun (1995) representing primitive mantle. In San Cristóbal bulk whole rock of ash and scoria products are represented with lava samples analyzed from literature (see Carr, 1984; Carr et al.,1990; Bolge et al., 2009; Heydolph et al., 2012a) and the minimum and maximum normalized samples in Nicaragua (see regional literature data references in Walker et al., 1984-2007-2009; Carr et al., 1984-1990-2007; Reagan et al., 1994; Noll et al., 1996; Picket et al., 1997; Chan et al., 1999; Patino et al., 2000; Feigenson et al., 2004; Bolge et al., 2009; Hoernle et al., 2008; Heydolph et al., 2012). N-MORB and E-MORB are from Gale et al. (2013). a) La-Lu serie. b) Trace and rare elements from heavier to lighter.

U/Th_N ratios are also consistently higher in Holocene (>3.9) samples than in historic rocks (<3.4). Samples with abundant lithic fragments (SC01A) mark irregularities compared to the other historic samples.

4.3Petrography

The studied rocks are variably porphyritic (phenocryst abundance from 45 to 55 vol. %) with phenocrysts of plg >ol >cpx> mt. Fragments are frequently highly vesicular and groundmass is generally microcrystalline to glassy, but some scoria fragments can have high microcrystalline density with equigranular plagioclase in the matrix. In historic samples (SC02B, SC5K), frequent intergrowths including these four phases have been observed (Fig. 7a). In SC5C and SC11D, fragments are less microcrystalline, highly vesicular and contain more phenocrystals of plagioclase and olivine, but clinopyroxenes are rarely seen, and are absent in sample SC5J.

Olivines phenocrysts are euhedral to subhedral (Fig. 7 b-d) and show lower forsterite (Fo mol %) contents in historic scoria samples than in Holocene ones, often with normal zoning (Fig. 8). SC02B phenocryst cores (number of spots «n» = 19; Fo_{66-71}) are slightly more magnesian than the rims (n = 3; $Fo_{64–66}$). Olivine of Fo_{69} enclosed inside Cpx (Mg/Mg+ Fe = 0.72) prove to be a late stage of crystallization (Fig. 7a). In SC5K, the core (Fo_{69-71};n = 8) shows similar composition to the rim (n = 3; Fo_{66-71}). The proportion of olivine crystals with lower MgO closer to the rim composition, rather than the core, is greater for historic samples (6/6) than Holocene (3/6). Holocene magmas like SC5C do not record relevant core-rim zoning (core n = 7; $Fo_{69–74}$) (rim n = 3; Fo_{72-73}), but the olivine crystals at the top of the SC5C sequence (SC5D) are more primitive (n = 8; Fo_{78-80}). SC11D has a primitive composition with Fo_{77-80} in the core (n = 8) and Fo_{76-79} (n =3) in the rim.

Of the100 olivines in each layer (in this order: SC11D, SC5C, SC5K, SC02B), the frequency of olivines that contain glass inclusions are: 46, 67, 100, 100 respectively. Olivines with pure closed glass inclusions containing a shrinkage bubble are respectively 12, 15, 3 ,4.

Clinopyroxene phenocrystals are euhedral, to subhedral, some having sharp edges and direct matrix-rims contact (Fig. 7c). They are classified as augite and core to rim zoning is almost absent : (n = 12) and has $Ens_{41.7-43.6}$ $Wo_{39.1-41.3}$ with Mg/Mg+Fe between 0.70-0.74 in SC02B and 0.67-0.71 in samples from 2012 (Fig. 8).

Plagioclase phenocrysts are characterized instead by very Ca-rich cores (An91) opposed to less calcic rims (An71) and often appear crowded, specially along the outer shells, by primary concentric, recrystallised, glass inclusions. Most of the plagioclase phenocrysts have dusty bands with sieve textured cores (Fig. 7b).

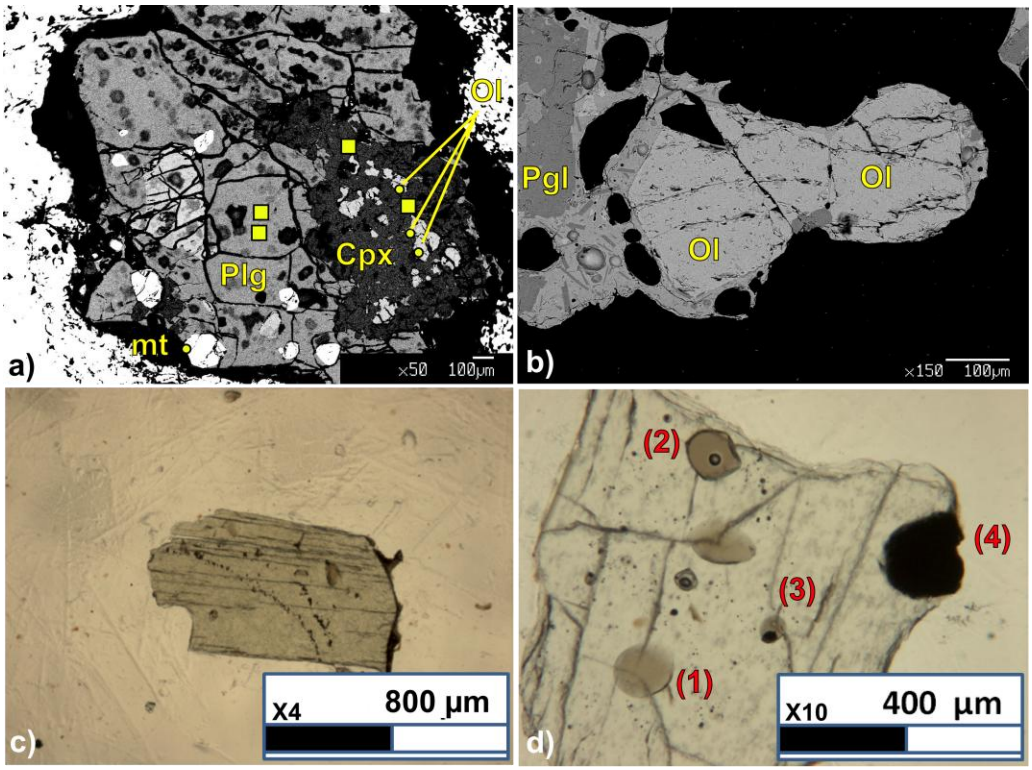

Figure 7 – Mineralogy. EMPA photography of a) cogenetic plagioclase-clinopyroxene (Plg-Cpx) with solid inclusions of olivine crystals (Fo_{69}) and Ti-magnetites. Clinopyroxene are augite ($Wo_{41}En_{42}Fs_{16}$; Mg number = 0.72) and plagioclase are calcium rich and unzoned (An_{88}) b) twin microphenocryst of olivine (Fo_{70}) in a matrix of microlithic plagioclase. **Transmitted light photography** from c) clinopyroxene phenocrystals containing typical concentric series of glass inclusions and d) olivine phenocrystal sample SC02B18 with diverse glass inclusion textural assemblages: (1) Glassy (hourglass or completely closed), (2) Homogenous ~2-8 % vapor bubble, (3) Heterogenous with ~2-8 Vol.% vapor bubble/visible oxide, (4) crystallized inclusion + dominant solid oxide phase.

4.4 Glass inclusions and matrix glass compositions

Historic uncorrected melt inclusions generally follow the same FeO_T vs MgO trend of the corresponding whole-rocks (FeO_T/MgO ratio of 2.7; described by 4 bulk-rock samples with < 4.0 % MgO) (Fig. 5b). Nineteen out 26 inclusions required > 3-10% olivine addition for Post-Entrapment Correction (PEC) to reach equilibrium Kd as explained above (Fig. 5b). Eleven out 17 Holocene uncorrected inclusions required> 3-10 % olivine addition to reach equilibrium at a FeO_T/MgO ratio of 2.1 (the typical ratio of bulk-rock samples). The PEC includes 3 anomalous inclusions in figure 5b which plot close to the trend of evolved historic samples, owing to their more differentiated nature (Olivine of Fo_{73} in SC5Cr6). Glass inclusions and matrix glasses are generally richer in FeO_T compared to the bulk-rock samples of the same age category and thus, do not show signs of Fe-loss (Danyushevsky and Plechov, 2011). 8 Holocene samples were following the FeO_T/MgO ratio of 2.1 slightly below the regression line, but they were not corrected for a second run of calculation for Fe-loss to prevent their Kd of being out of the normal range of equilibrium (Kd = 0.30 ± 0.4).

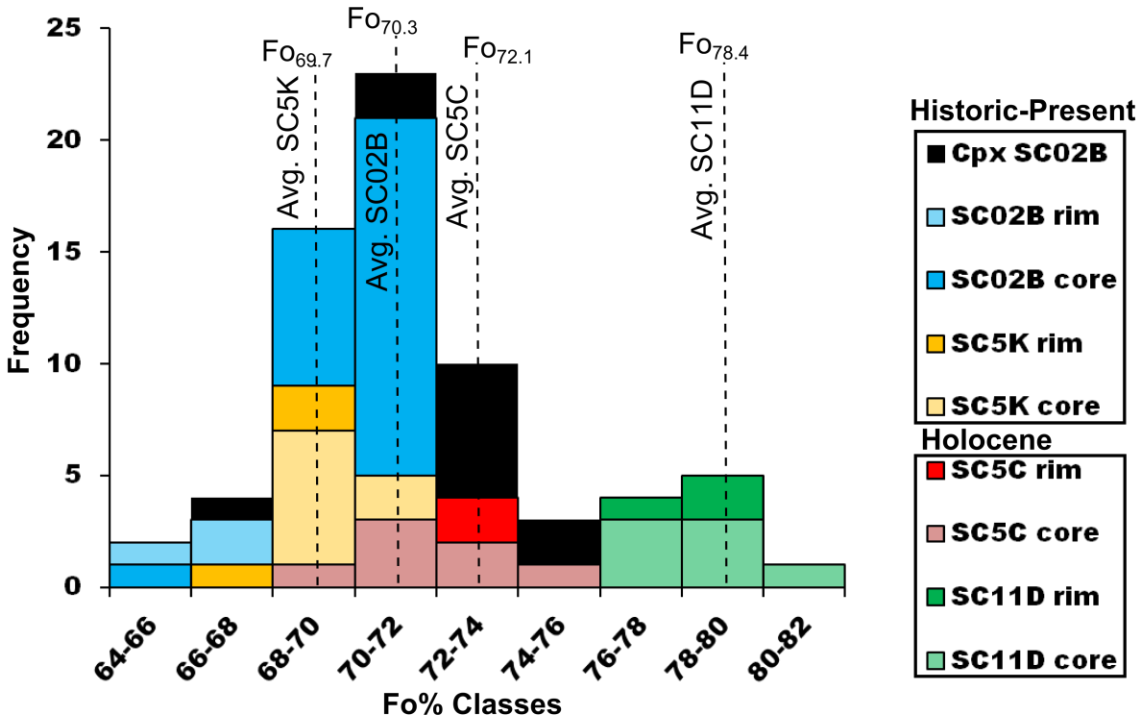

Figure 8 – Histogram of forsterite content and magnesium number from phenocrystals of olivines and clinopyroxenes in tephra ofSan Cristóbal. Mineral spots were performed by electron microprobe analyses at INGV-Roma. Average «Avg.» forsterite contents for olivines and magnesium number from clinopyroxene are calculated with Morimoto (1988).

Glass inclusions are richer in K_2O in historic samples (0.9 – 1.5 wt%) than in Holocene samples (0.3 – 1.2 wt%)(Fig. 5a). All matrix glasses compositions are richer in K_2O than their corresponding glass inclusions and bulk-rocks; for other oxides, no substantial differences are noted between Holocene and historic matrix glass samples. As for SiO_2, glass inclusion are richer in Historic samples (51 – 56 wt%) compared to Holocene samples (43 – 53 wt%). SiO_2 is higher in all matrix glass samples (52 – 56 wt%) and matrix glasses from pumice fragments (63 – 73 wt%), indicating that K_2O and SiO_2 are reliable magma tracers for differentiation at San Cristóbal (Fig. 5a). Considering the classification boundary of Peccerillo & Taylor (1976) for primary glass inclusions, Holocene magmas (SC11D, SC5C) are basalts and they are rich in compatible elements. Historic to present-day magmas (SC5K, SC02B, SC2012) are generally basalts to andesite, and are poorer in compatible elements than bulk-rocks. The pumice fragments and one lava flow (the Cola de Iguana Flow in Hazlett, 1977) are dacites with much lower MgO, CaO and Al_2O_3 (Fig. 5 c-d-e).

4.5 Volatiles contents

Water concentrations (as H_2O_{tot}) were quantified with mFTIR in 18 glass inclusions from sample SC02B (0.3 – 2.3 wt.%), 9 from SC5K (0.7 – 1.6 wt.%), 14 from SC5C (0.3 – 2.1 wt.%). No measurement is available for SC11D, where the majority of olivine crystals contained glass inclusions less than 30 µm in size (Table 5). CO_2 concentrations were quantified with mFTIR in only 2 samples (216, 358 ppm), although an absorption peak for dissociated carbon (CO_3^{2-}) was detected in 12 samples, similarly to observations made in rocks of similar composition (King and Holloway, 2002) (Table 6).

The range of water contents determined by NanoSIMS in glass inclusions of historic samples were also quantified in SC02B (0.6 – 1.9 wt.%) and SC5K (0.3 – 2.16 wt.%) (Table 7). Higher water contents were observed in Holocene samples, such as in SC5C (0.2 – 2.7 wt.%) and SC11D (2.0 – 3.3 wt.%). These results are similar, or only slightly higher, than seen by mFTIR. The difference in the size of the aperture window of both instruments, and the possible effect of post entrapment crystallization for the larger inclusions selected for mFTIR, could explain this difference. A minimum value of 0.13 wt.% H_2O was obtained for the glassy rims around an olivine crystal from SC5K, which could only be detected due to the lower NanoSIMS detection limit (<0.1 wt.%) relative to mFTIR (0.3 wt.%) (Table 7). For this reason, only water contents determined by NanoSIMS were conserved for using in solubility models (section 5.2).

The ranges of detected CO_2 contents (determined by NanoSIMS) were lower in glass inclusions of historic samples: 17 – 150 ppm in SC02B, and 16 – 202 ppm in SC5K. Moderately high CO_2 contents were observed in Holocene samples: 92 – 527 ppm in SC5C, and 117 – 406 ppm in SC11D. The highest CO_2 contents broadly correspond to higher H_2O contents. For instance, the average CO_2 content of Holocene samples (347 ppm) is 4 times higher than for Historic samples (88 ppm); similarly, the H_2O content is on average twice as much higher in Holocene samples than in Historic samples (2.3 wt.% vs.1.3 wt.%).

Historic and Holocene glass inclusions contain comparable S and Cl (Table 4, 7).We here only discuss EMPA results, which were obtained on same surface and analytical conditions as the major elements. For glasses inclusion of Historic samples, EMPA provides an average S content in SC02B of 556 ppm (excluding SC02B13, richer in all volatiles) and a 160 – 1684 ppm S range for all inclusions. EMPA demonstrates similar sulfur contents in SC5K (270 – 1675 ppm) and SC02B (160 – 1684 ppm). Scoria from Holocene samples (SC5C, SC11D) contain on average 1571 ppm S (from 625 to 2532 ppm), and the mean value for basaltic glasses (holocene + historical) is 1380 ppm.

Matrix glasses in SC02B (n=8) contain 36 to 300 ppm S (Table 3). The matrix glass (n=8) from pumice fragments found in layer SC02B have similar sulfur contents(68 – 368 ppm), and between 32 – 132 ppm S was found in a pumice fragment from SC5K (n=4). The glassy border rims of olivines (n=8) contain from 128 to 1189 ppm S in SC5K (Table 3). Scoriae from Holocene olivine samples (SC5C, SC11D) contain 68 to 196 ppm S (n=5) in their matrix glasses, close to the phenocrystals (Table 3)

Scoriae from Historic samples (SC2012, SC02B, SC5K) contain on average 1137 ppm Cl in their glass inclusions (range: 270 – 1971 ppm; Table 4). In scoriae from Holocene samples (SC5C, SC11D), olivines contain on average 1308 ppm (560 to 2210 ppm Cl; Tables 4, 7).

Matrix glasses in SC02B groundmass contain 850 to 1220 ppm Cl, and 100 – 1650 ppm Cl was detected close to the border of olivine phenocrystals (Table 3). The glassy border rims of olivines contain from 770 to 1220 ppm Cl in SC5K. The matrix glass (n=8) from pumice fragments found in layer SC02B have higher chlorine contents(540 – 3100 ppm), and one spot showed 132 ppm in a pumice fragment from SC5K (n=4). The pumice fragments are the only glasses with detected fluorine and overall their range (n=12) vary between 790 – 3600 ppm F. Holocene samples have their matrix glass containing 930 to 1180 ppm Cl (Table 3).

According to the comparative analysis of glass inclusion from NanoSIMS data, major volatiles are definitively present in larger contents in Holocene samples, relative to historic samples. Substantial differences between the two sets of samples are also observed for volatile ratios. In historic to present-day samples, including results from both EMPA and NanoSIMS, the H_2O/CO_2, CO_2/S, H_2O/S and H_2O/Cl ratios in glass inclusions are 3-60, 0.1-0.8, 0.1-1.2, and 1.3-20.6. S/Cl ratios range 0.1-1.6 for melt inclusions, while they range 0.1-0.3 and 0.5 - 1.0 in matrix glasses and around olivine crystal glassy rims, respectively. In Holocene samples, by considering only NanoSIMS results, the H_2O/CO_2, CO_2/S, H_2O/S and $H_2O/Clor$ S/Cl ratios are 4-33, 0.-0.5, 0-1.7, 0.9-5.7 and 0.3-2.8.

4.5 Raman-corrected CO_2 contents

Several glass inclusions contained shrinkage bubbles, representing 0.4 – 2.2 (Vol.%) of the inclusion volumes. We selected 9 of such spherical/ellipsoidal glass inclusions (among those for which NanoSIMS CO_2 data were available), in which we characterized the shrinkage bubbles for their CO_2 content, using Raman. Only 5 out of the 9 samples had shrinkage bubbles yielding clear CO_2 signals in the Raman spectra (see Electronic Appendix 5). No fermi diads were detected for any bubble in SC11D (>4.5 Vol.%), so the presence of CO_2 was not confirmed in these samples.

The average bubble fluid density, when successfully obtained by Raman, was 0.272±0.004 g/cm^3in samples SC02B, SC5K and SC5C (Table 8). The volume of each bubble was calculated from the bubble diameter, determined by imagery from the MicroRaman high resolution petrografic optic microscope Olympus BX41 (±1 µm). The CO_2 mass in the bubble was then calculated from the specific density, and ranged from $1.66 \cdot 10^{-11}$ to $3.99 \cdot 10^{-10}$ g (see Electronic Appendix 5).The mass of CO_2 in each bubble was also independently estimated using the ideal gas law (IGL) (see Electronic Appendix 5) and overall, resulted in the same range of Raman values (see Electronic Appendix 5).

The CO_2 mass contained in each shrinkage bubble was added to the mass of CO_2 in the host glass inclusion (this obtained from glass density and volume (Ochs and Lange, 1999), and the CO_2 content measured by the NanoSIMS) to obtain a total mass of CO_2 (glass inclusion + shrinkage bubble; uncertainty ±26%). The obtained total CO_2concentrations - 718 to 1940 ppm (±516 ppm)- were sensibly higher that in the original (uncorrected) glass inclusions (71 – 527 ppm)(see Electronic Appendix 5).

4.6 Noble gases isotopes in fluid inclusions

Olivine and pyroxene phenocrysts trap primary and secondary FIs during their growth in magmatic conditions. The entrapment pressure of these inclusions is generally related to the main zones where magma is stored and crystallizes or to its ascent within a volcanic plumbing system. Thus, FIs potentially preserve the pristine composition of fluids originally dissolved in silicate melts, including noble gases. These trace gases (especially $^{3}He/^{4}He$ ratio) are useful in order to define the origin of fluids and for evaluating mantle, magmatic and crustal processes. This means that their investigation is important for evaluating the characteristics and the structure of a volcanic plumbing system, as well as for recognizing crustal processes (e.g., crust assimilation, magma aging) acting sometimes to modify the pristine composition of magma. Also, the study of noble gases is useful to investigate the evolution of a magmatic system over time and for assessing the characteristics of magma before it erupts (e.g., Martelli et al., 2014; Rizzo et al., 2015). This becomes crucial above all when fumarolic gases are not fully representative of the pristine magmatic source due to the presence of shallow post-magmatic modifications (i.e., interaction with hydrothermal systems, atmospheric contamination)(e.g., Capasso et al., 2005; Rizzo et al., 2009).

In this study we performed 6 analyses of He, Ne and Ar in the samples (layers SC02B, SC5K and SC11D) from which was possible to separate an amount of olivine and pyroxene (only for SC02B) crystals sufficient for the isotopic analyses. Data are presented in Table 9.

The ^{4}He concentrations [He] measured in FIs from olivines of scoria and ash samples vary from $1.42 \cdot 10^{-14}$ mol/g to $7.02 \cdot 10^{-14}$ mol/g (Fig. 9). The lowest He contents are observed in sample SC02B, while SC5K is typically the most [He] rich. Clinoyroxene crystals were only found in sufficient quantity in SC02B, and the resulting ^{4}He concentration was $1.59 \cdot 10^{-14}$ mol/g, comparable to that of co-genetic olivine crystals (Fig. 9). Ne and Ar in olivines have ranges of $6.61 \cdot 10^{-16} – 3.76 \cdot 10^{-15}$ mol/g and $1.89 \cdot 10^{-13} – 1.30 \cdot 10^{-12}$ mol/g respectively. Ne and Ar are found at comparable levels of $1.77 \cdot 10^{-15}$ and $2.55 \cdot 10^{-13}$ mol/g in clinopyroxenes of SC02B. $^{40}Ar/^{36}Ar$ results returned values of 300 to 304 in all samples, substantially comparable with the typical atmospheric signatures ($^{40}Ar/^{36}Ar$ = 295.5). Coherently, the $^{4}He/^{20}Ne$ ratio varied in the 9–21 range in SC5K and SC11D, while the highest values (226-373) were recorded in SC02B (the atmospheric $^{4}He/^{20}Ne$ is 0.318). Either the $^{40}Ar/^{36}Ar$ or the $^{4}He/^{20}Ne$ ratios indicate that gases released from fluid inclusions are strongly contaminated by an atmospheric-derived component. Similar evidences were found by Fischer et al. (2005) in olivines from Cerro Negro (Nicaragua) and were attributed to the seawater stored in subducted sediments. This means that Ne and Ar signatures could testify the presence of an atmospheric-derived component in the mantle beneath San Cristóbal, or a contamination at crustal levels.

The Rc/Ra values (n = 5) vary between 6.44 and 7.20 (6.95±0.30) in olivines, while the only clinopyroxenes measurement (SC02B) has a Rc/Ra of 6.45 (±0.75) (Fig. 9). The two lowest values (6.44 Ra and 6.45 Ra) were found in olivines of SC5K and in clinopyroxenes of SC02B. We also point out gas samples from Nicaragua volcanoes, analysed by (Elkins et al., 2006), yielded $^{3}He/^{4}He$ lower than 6.8 Ra, likely unrepresentative of the magmatic source and resulting from significant addition of crustal ^{4}He to the gases. Thus, in order to assess the He isotopic signature of the pristine magmatic source, we prefer to discard these values.

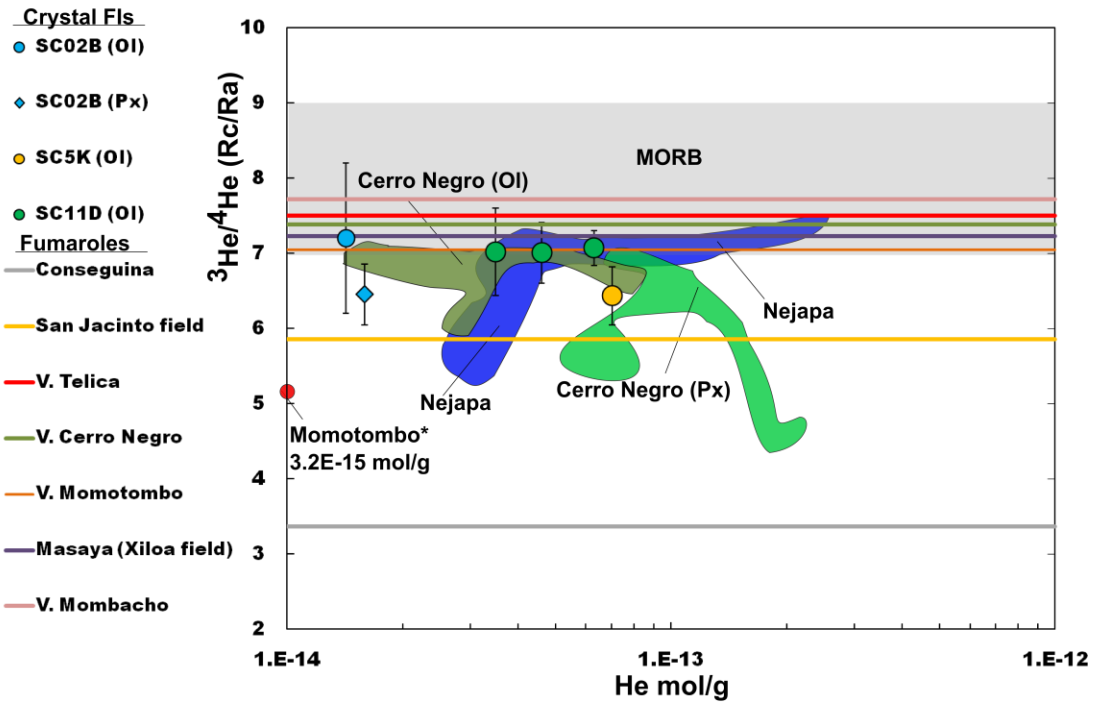

Figure 9 – Rc/Ra ratio vs. He concentration (mol/g). Fluid inclusion (FIs) hosted olivines (circles) and clinopyroxenes (lozenge) from this study are compared to the interval Rc/Ra of 7–9 from Graham (2002) represented by continuous lines. Summit fumaroles collected in 2002 from Shaw et al. (2003) are represented by the small (minimum) and large (maximum) tilted line. Colored polygons of Cerro Negro (Ol-Px) and Nejapa represent the contour of all Rc/Ra ratio vs. He concentration (mol/g) presented in Shaw et al. (2006).

The range of $^{3}He/^{4}He$ can be restricted to 7.01-7.20 Ra. This range is close to the lower limit of Pacific MORB (Graham, 2002), but is in the typical range of arc volcanoes worldwide (8±1 Ra; Hilton et al., 2002) and in the nearby Costa Rica (Di Piazza et al., 2015). The Rc/Ra values found in San Cristobal fluid inclusions are higher than previously reported in crater and flank fumaroles of this volcano, that vary between 5.65 – 5.74 (±0.8 – 0.9) (Shaw et al., 2003; Elkins et al., 2006).

5. Discussion

In the following sections, we make use of our novel results to infer the volatile signature of parental magmas at San Cristóbal, and to quantitatively explore the degassing processes that controlled variations of magmatic volatile abundances over the recent volcano's history. Our results are interpreted in the attempt to provide novel constraints on mechanisms and depths of magma storage/transport in the volcanic plumbing, and to characterize the mantle source feeding volcanism in the NW Nicaragua.

5.1 Volatiles content and magma composition

San Cristóbal melt inclusion compositions, when compared in the framework of available melt inclusion data for CAVA volcanism, suggest low to moderate H_2O-CO_2 abundances. Water contents in San Cristóbal magmas, varying widely from 0.5 to 2-3%, are comparable to those measured in Guatemala melt inclusions (1.5 – 2.8 %) (Roggensack et al., 2001b; Walker et al., 2003; Wherman et al., 2011) and Costa Rica (0.2 – 3.9 %) (Wade et al., 2006; Benjamin et al., 2007; Wherman et al., 2011), but are distinctly lower than those observed at other Nicaragua volcanoes, such as Telica (3%), Granada (1.9 – 5.0%) and Cerro Negro (1971-1995) (0.5 – 6.1 %) (Roggensack et al., 1997; Atlas, 2008; Sadofsky et al., 2008; Wehrman et al., 2011; Portnyagin et al., 2012). The uncorrected (see section 5.2) range of CO_2 contents in San Cristóbal melt inclusions (47 – 408 ppm CO_2) are lower than the rnange of CAVA melt inclusions (21 - 2342 ppm CO_2) (76 on 126 inclusions with measurable CO_2). San Cristóbal basaltic samples (< 52 % SiO_2) have average water contents (2.2 ± 0.7 wt. % H_2O) nearly twice as much higher than the average for basalt andesites (> 52% SiO_2; 1.3 ± 0.5 wt.% H_2O), which suggests that volatiles are effectively lost as magmas evolve and differentiate. We argue San Cristóbal magmas are already saturated with a H_2O-CO_2 vapor phase at intermediate to low crustal levels, so that these volatiles are lost to gas before melt inclusion trapping. Volatile saturation occurs when the sum of partial pressures of the gas species exceeds the confining pressure which is probably low to moderate considering the solubility models in section 5.3 (Holloway, 1976). Following the same line of reasoning, no H_2O enrichment with time between Holocene and historic eruptions may be indicating that gas saturation occurred previously in basaltic Holocene magmas. Low CO_2 contents of closed glassy inclusions prove that saturation levels were probably corresponding to low-moderate carbon contents, most of this CO_2 probably formed bubbles already getting separated from the melt before melt inclusion trapping so their contents are lower than it should be.

Average S contents in San Cristóbal melt inclusions slightly lower and variable compare to CAVA melt inclusion average (966 ±613 vs. 1200±80 ppm S), but the basalts are far richer in S than the basaltic andesite (1316±621 vs. 755±507 ppm S). Chlorine average contents are slightly higher than the CAVA average (1522 ± 490 vs. 1141± 100 ppm), but again the basalts are moderately enriched compared to the basaltic andesites (1522±490 vs. 1143±412 ppm Cl). We find no textural evidence of Cl abundance in melt being limited by a solid phase or immiscible Cl-rich brine (e.g. Luhr, 1990; Wallace and Carmicheal, 1992; Carroll and Webster, 1994; Webster et al., 1999).

Our results conclusively indicate a clear dependence of volatile abundance in San Cristóbal magmas on major element composition (Fig. 10). To interpret this effect, the respective roles of (1) crystallization and (2) degassing in controlling volatile enrichment/depletion in melts have to be quantified. In figure 10, we use either K_2O or Mg# as traces of magma differentiation.

K_2O has very low abundance in the majority of mafic melts belonging to the subalkaline series and is commonly used as an index of crystal fractionation due to its incompatibility in magmas during crystallization (e.g. Sisson & Layne, 1993; Blundy & Cashman, 2005; 2008; Atlas et al., 2006; Wade et al., 2006; Benjamin et al., 2007; Spilliaert et al., 2006a; Vigouroux et al., 2008; Johnson et al., 2008; 2010; Ruscitto, 2012; Métrich et al. 2011, 2014). K_2O-normalized volatile abundances suggest two distinct trends for our melt inclusions: the H_2O/K_2O, S/K_2O and Cl/K_2O ratios (Fig. 10a-b-c) in Holocene samples follow vertical lines of descent, while historic samples follow flatter trends. We conclude that poorly evolved, volatile-richer inclusions for Holocene eruptions (SC11D, SC5C) have their volatile behaviors mainly determined by degassing, while more differentiated volatile-poor inclusions from Historic eruptions (SC5K, SC02B) are controlled by degassing plus crystallization.

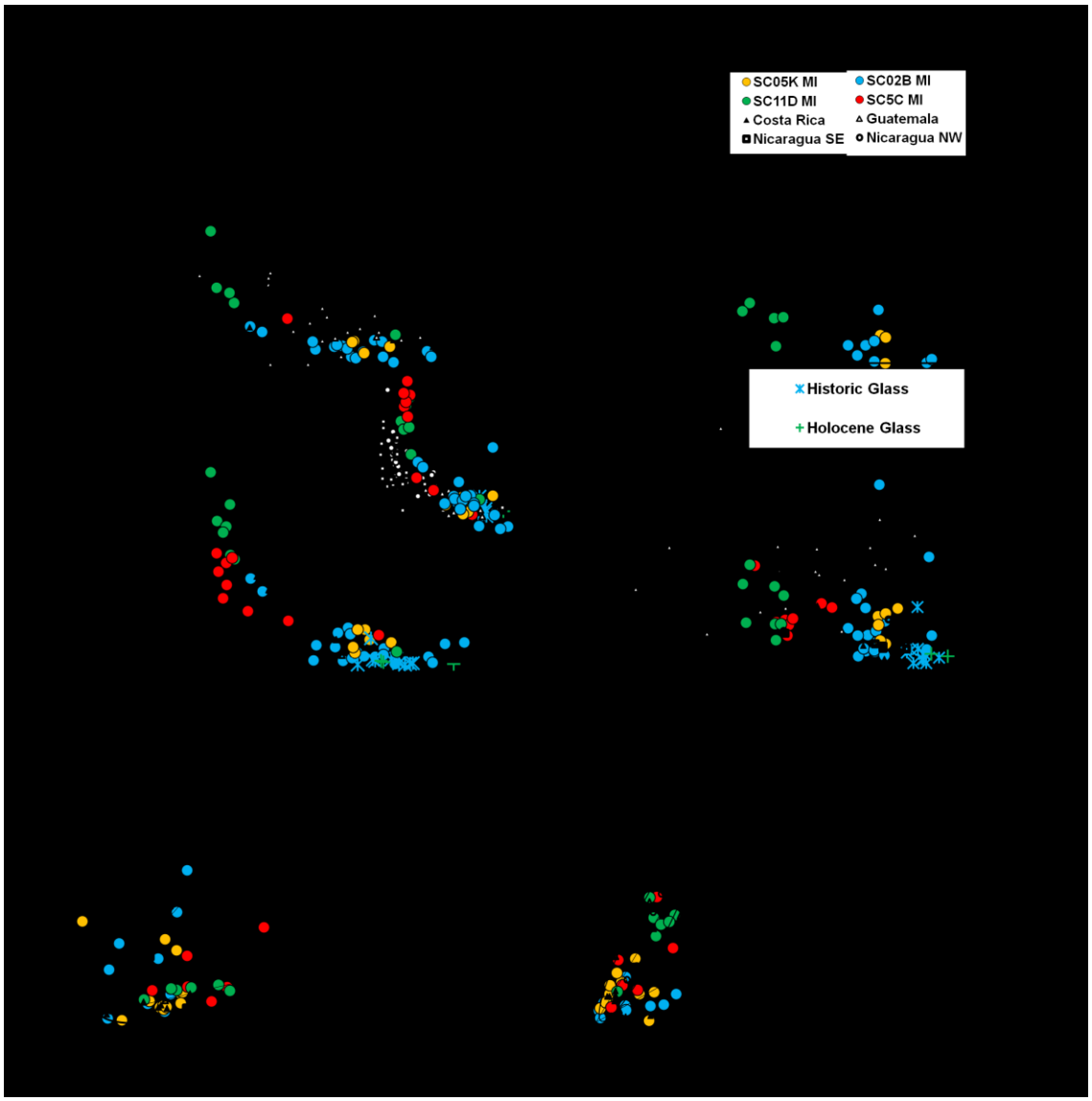

Figure 10 – Volatile vs. indices of melt inclusion differentiation form major elements. PEC restored melt inclusion from this study (colored circles) are compared with a compilation of melt inclusion data from literature and confronted with hypothetical evolution of vapor-undersaturated crystallization (horizontal, no degassing) and degassing-only (vertical, no crystallization).B is for basaltic MI and BA for basaltic andesite MI. Telica and Cerro Negro (1992-1995) represent NW Nicaragua segment (Roggensack et al., 1997; Sadofsky et al.,2008; Portnyagin et al., 2012). Nejapa, Granada, Masaya represent the SE segment of Nicaragua (Wehrman, 2005; Sadofsky et al., 2008; Atlas, 2008; Wehrman et al., 2011; Portnyagin et al., 2012). Some melt inclusions from Guatemala are represented for Fuego (Roggensack, 2001b), Pacaya and surrounding monogenetic cones (Walker et al., 2003) and Santa Maria - Atitlan - Agua (Wehrman et al., 2011) and finally Irazu and Arenal the segment of Costa Rica (Wade et al., 2006; Benjamin et al., 2007; Wehrman et al., 2011). a) H_2O/K_2O vs. K_2O b) CO2 vs. Mg#, c) S/K_2O vs. K_2O, d) Cl/K_2O vs. K_2O, e) S/Cl vs. Mg#, f) CO_2/S vs. H_2O/Cl, g) S/Cl vs. CO_2/H_2O.

S/Cl or CO_2/S ratios in melt inclusions (Fig. 10e-f), which are often assumed to inversely correlate with pressures in closed or open system degassing conditions (Spilliaert, 2006a),

decrease with decreasing Mg# contents, mirroring the H_2O/K_2O, S/K_2O and Cl/K_2O vs. K_2O trends (Fig. 10a-c). S/Cl with CO_2/H_2O also define certain tendencies, well illustrated for basalt and basaltic andesite melt inclusions from San Cristóbal and Cerro Negro. As for CO_2 (discussed in 5.2), no clear association was found with Mg# (Fig. 10d) or any other major elements, but his relative amount appear richer than sulfur and water in monogenetic cones from Guatemala (Walker et al., 2003). CO_2 ratios (with sulfur and water) is also higher for Nejapa and Granada where all volatiles are found with higher concentrations (Fig. 10f-g).This is generally the case in CAVA, and without surprise well illustrates the CO_2 behavior in mafic magma in general, in which the two first order parameters controlling CO_2 degassing are pressure and, to a lesser extent, temperature (Dixon et al., 1995a; Papale, 1999; Brooker et al., 2001; King and Holloway, 2002; Iacono-Marziano et al., 2012) CO_2-rich melt inclusions in Nicaragua have exceptionally been found in some primitive (low K_2O/high Mg#) magmas at Granada and Nejapa, reflecting distinct deep magma sources and fast ascent through the crust (Sadofsky et al., 2008; Wehrman et al., 2011).

5.2 CO_2 contents of melt inclusions and corrections for the shrinkage bubble

Clearly, CO_2 contents do not correlate with changes in magma composition (Fig. 10d). Although a carbonate group (CO_3^{2-}) absorption peak was apparent in most mFTIR spectra CO_2 was below detection limit (50 ppm) inessentially all (but 2) of the larger glass inclusions characterized with mFTIR (as high as ~300 ppm), and very low in the smaller (<20 µm) inclusions studied with the NanoSIMS (< 527 ppm). The overall low CO_2 contents are common features of arc basalts and andesites (Dixon et al., 1995a; Sano and Williams, 1996; Wallace, 2005; Lowenstern, 2001), in which CO_2 separates into a vapor phase at mid- to deep-crustal depths, e.g. prior to glass inclusion entrapment (Lowenstern, 2001; Wallace, 2005; Métrich and Wallace, 2008). The composition of the quiescent plumes released by open-vent basaltic to andesitic arc volcanoes (e.g., Masaya) is consistent with deep CO_2-rich gas feeding from deeply stored magma (Giggenbach, 1992; Wallace, 2005). The open-vent degassing plume of San Cristóbal shares the same characteristics (moderately high CO_2 fluxes and CO_2/SO_2 ratios in the plume; Aiuppa et al., 2014), which likely reflects CO_2 loss from deeply stored magma. The CO_2 fraction lost by degassing, owing to its low solubility in silicate melts (Blank and Brooker, 1994), is a major drawback to trace the original (parental) melt CO_2 concentrations from melt inclusions (Métrich and Wallace, 2008).

Apart from early (pre-entrapment) exsolution in the vapor (Holloway, 1976), sin- to post-entrapment CO_2 partitioning into shrinkage bubbles is an additional cause of low CO_2 contents in melt inclusions (Lowenstern, 2001). We here attempt to evaluate, and correct for, this latter process by using a methodology inspired by recent technical advances in Raman Spectroscopy. The separation of CO_2 from the melt to vapor occurs at depths and necessitate experimentally high cooling rates (Mangan and Sisson, 2000), but this phenomenon is known to be traced by the evidence of a CO_2-bearing shrinkage bubbles (Lowenstern, 1995). If a bubble in the inclusion reflects the existence of coexisting melt/vapor phase during inclusion entrapment, then CO_2 represents the magmatic vapor that was co-precipitated with the melt in a mixed inclusion (Roedder, 1984; Lowenstern, 2001). If this assumption reveals to be true for our samples, we can therefore use mass balance calculations to re-add the mass of CO_2 from the bubble to the measured mass of CO_2 in the glass. Our approach reminds those of similar recent studies, in which pre- to post-entrapment CO_2 loss to shrinkage bubbles has been corrected for using trace elements (Hartley et al., 2014) and/or a combination of Raman and experimental heating techniques (Moore et al. 2015; Wallace et al. 2015).

Raman spectroscopy (cfr. 4.5) proved the presence of CO_2 in 5 bubbles, and allowed to calculate total (glass + bubble) CO_2 contents in the inclusions of 718-1940 ppm, i.e. well above what the NanoSIMS detected in the corresponding glasses (71 – 527 ppm). Interestingly, these Raman-based total CO_2 contents are in overall agreement with those obtained using the IGL method (Electronic Appendix 5). We therefore consider a *minimum* total CO_2 content of 1186±480 (the mean+1 SD of the 5 samples) as representative of San Cristóbal magmas, but no systematic differences exist between bubble-bearing and bubble-free melt inclusions in CO_2 contents (~400 – 500 ppm). We still argue this estimate represents a lower range for the parental (un-degassed) San Cristóbal melt, because pre-entrapment CO_2 loss remains unaccounted for. Migration of CO_2 to the shrinkage void, alone, is insufficient to explain the low CO_2 contents in the entire population of glass inclusions, the majority of which do not record the presence of a shrinkage bubble. Taking our measured volcanic gas CO_2/SO_2 ratio of 3.8 (range 2.8-5.1) (cfr 4.1) as representative of time-averaged CO_2/S signature of the source magmas, and with a parental melt S content of ~1300 ppm (cfr. 5.1), we evaluate a hypothetical total content of ~5000 ppm (range, 3000-6800 ppm) for San Cristóbal magmas. This is a factor ~3-4 times higher than the Raman-derived maximum value of 1940 ppm, indicating that pre-entrapment CO_2 loss is likely to be significant at San Cristóbal.

5.3 Deep and superficial magmatic volatile evolutions

In order to evaluate the conditions of magma storage, ascent and degassing at San Cristóbal, the volatile contents in glass inclusions and their major element concentrations were compared against the results of model simulations of volcanic degassing. To characterise the shallower part of the plumbing system, the melt inclusion-based model results were also compared against compositions of major gas species in the volcanic gas plumes, as derived from Multi-GAS observations.

We used the saturation code SolEx (Whitam et al. 2012) to model the degassing path of San Cristóbal magmas, and to calculate the equilibrium compositions of coexisting melt and vapour phase in a range of pressure and temperature conditions relevant to the system (Fig. 4; 11-12). The SolEx software has the advantage of allowing saturation models to be derived in the H_2O-CO_2-S-Cl system. SolEx calculations take into account the compositional dependence of melt-fluid partition coefficients for these species.

Three sets of model runs were carried out (Figs. 4,11,12). Run (1) was initialized using the highest volatile assemblage registered in historic melt inclusions, and are therefore taken as representative of the degassing history of basaltic andesites. In particular, the inclusion selected to initialize simulations (closed and open system) corresponds to sample #SC5K3G, which contains 2.16 wt. % H_2O, 191 ppm CO_2, 1675 ppm S, and 1970 ppm Cl. Simulations were generated at redox conditions equal to NNO = 0 and at T = 1120°C, and starting from a initial pressure of 90 MPa; this is the inclusion entrapment pressure, calculated from the co-dissolved best representative H_2O and CO_2 contents of our samples using the SolEx model (a very similar pressure would be obtained for same composition using the model of Papale et al. (2006)). From the initial pressure of 90 MPa, the degassing paths were generated by step-by-step decompression in either closed- (continuous line) or open-system (dashed line) conditions. Results of these simulations are shown in Figure 11a.

The majority of the measured historical glass inclusion compositions plot to the left of the model curves, indicating either a lower (1.5-1.7 wt.%) parental melt H_2O content, and/or that natural melts evolve in a vapor-buffered system. In fact, it is noteworthy to observe that the majority of the glass inclusion samples are comprised in figure 11a within the 20 and 40 mol% CO_2 isopleths, a range two to four times higher than the gas compositions measured in the plume by the Multi-GAS (H_2O/CO_2 ratios of 7 – 41), corresponding to 2 and 12 mol% CO_2 in the gas. We conclude, therefore, that the basaltic andesite magmas sampled by historical eruptions may well have evolved in a relatively shallow (<70 MPa, but mostly ≤50 MPa; Fig. 11a) mafic reservoir, flushed by a more deeply sourced (CO_2-rich) gas bubbles compare to those quiescently degassed by San Cristobal during our 2013 survey. The model-predicted (model (1)) gas compositions are compared against measured volcanic gas composition in Fig. 4. This comparison suggests the volcanic gas plume sampled in 2013 has a composition consistent with that formed by equilibrium magma-gas separation in the 55-85 MPa pressure range.

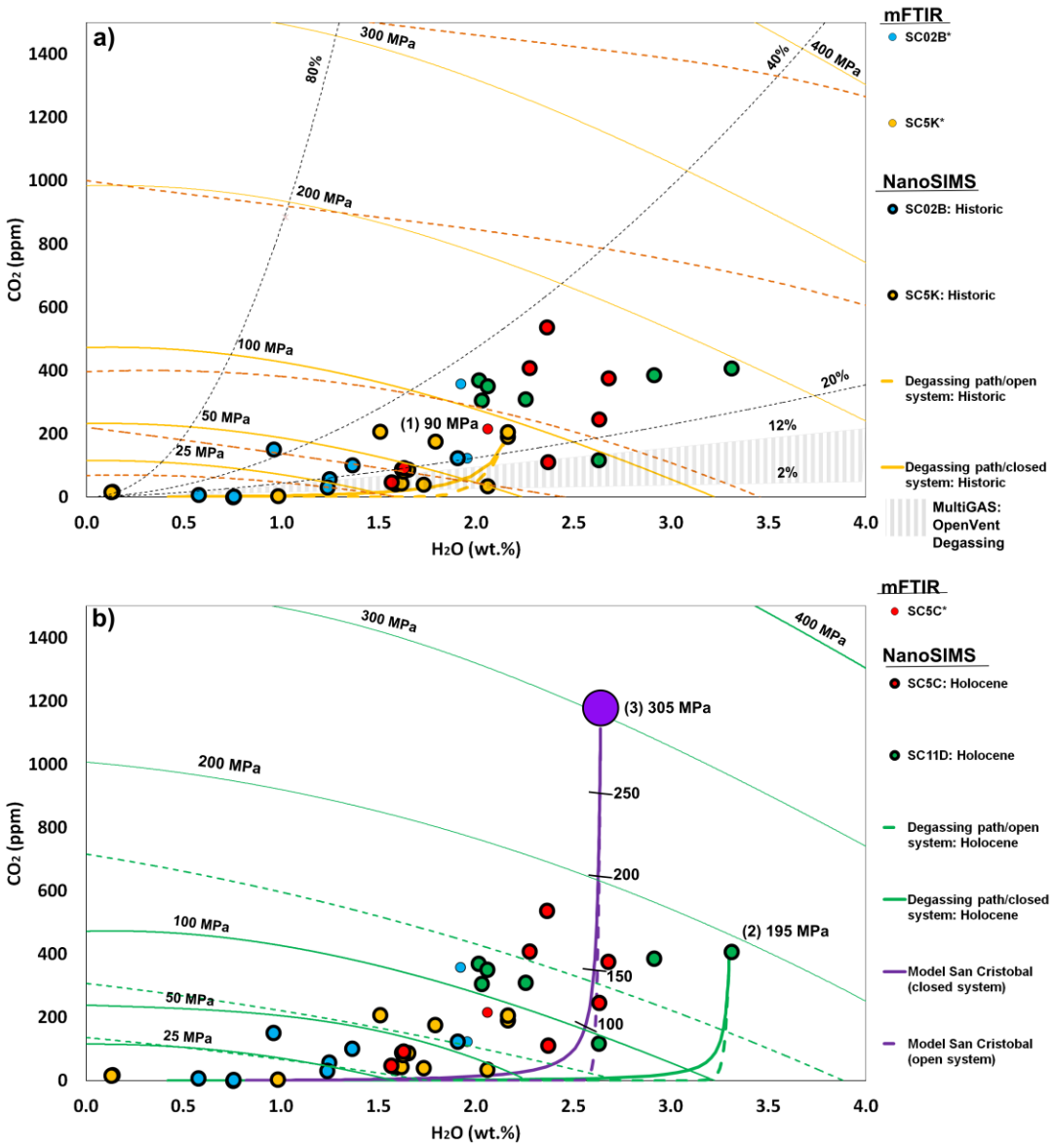

Figure 11 – CO_2 vs. H_2O of melt inclusions from San Cristóbal. a) The volatile contents from NanoSIMS (large circles) and mFTIR data (small circles) are plotted along isobars (complete lines) and isopleths (tilted lines) built with the model of Whitam et al. (2012). a) for basaltic andesite compositions, degassing paths are proposed in closed (tilted yellow line) and open system (continuous yellow line) for a starting pressure condition of (1) 90 Mpa for matching the maximum quantity of data. The grey stripped area represent the interval of CO_2/H_2O ratios of 2-12mol% in the vapor from Multi-GAS plume data. b) proposed degassing model for basalt samples of San Cristóbal starting at (2) 195 MPa in a closed (tilted green line) and an open system (continuous green line). The general degassing model of San Cristobal (3) (305 MPa) initiate with the purple interior dot in a closed (continuous purple line) and open system (tilted purple line) which correspond to CO_2 contents average (~1187 ppm) of the corrected inclusions by Raman spectroscopy.

A second set of model runs (2) was performed in order to reproduce the conditions of basaltic Holocene magmas. The starting conditions for runs (2) (closed system represented by a line and open system by tilted line) were taken from composition of inclusion #SC11D1A: 3.31 wt.%

H_2O, 406 ppm CO_2, 2401 ppm S, 1446 ppm Cl (NNO = 0; T = 1145 °C). The initial pressure was 195 MPa (consistent entrapment pressures were obtained from the models of Papale et al. (2006) and Whitam et al. (2012)). In such conditions, the obtained degassing model trends (closed system (tilted line) and open system (continuous line) in figure 11b) show rapid CO_2 depletion in the melt at constant H_2O (3.31 wt.%) until ~ 100 MPa pressure, followed by H_2O degassing at lower pressure. These model trends do not satisfactorily match the evolution of natural samples (Fig. 11b). The majority of the Holocene melt inclusion samples is, instead, best reproduced by model trends of (3) (closed system represented by continuous line) – (open system represented by a dashed line), which used the same conditions as in runs before (SC11D1A major element composition; Delta NNO = 0; 1145 °C) except for a distinctly lower H_2O content (2.5 wt.%; the average water composition of basalts in SC11D) but higher CO_2 content (1187 ppm; the mean shrinkage bubble-corrected content; cfr 5.2). As a matter of fact, even considering the model trend (3) to fit historical samples (eventually with slightly lower starting H_2O content suggesting diffusive processes) the recalculated entrapment pressures for these samples would be comparable to those obtained from model trend (1). From this agreement, we conclude that a CO_2-richer, more deeply sourced magmatic system (relative to the historic period) has been feeding San Cristóbal activity during the Holocene, while historical samples were generated from a magma residing at shallower depths of the plumbing system. Still, the scattered datapoints suggest that a number of processes are operating at various timescales beneath San Cristóbal which would affect their relative H_2O-CO_2 contents.

Glass inclusions cluster along two distinct groups in a CO_2 vs S plot (Fig. 12a). A first group, representing the majority of the glass inclusions, plots below the CO_2/S_t ratio of 0.35 and includes both historic samples with medium (~ 800 ppm) sulphur contents and Holocene samples with high sulphur contents (>1,600 ppm S). Following the regression line, a CO_2/S_t ratio of 0.16 would represent the majority of the samples. The closed system degassing path (1) for basaltic-andesitic melts (Historic samples) matches well the majority of these CO_2/S_t< 0.35 data, and proves that CO_2 and S are simultaneously lost in the vaporfor P< 100 MPa (Dixon et al., 1995b). A second group of melt inclusions plot at higher (~ 0.35) CO_2/S_t ratios, and are not well matched by either historical (1) or Holocenic (2-3) model trends.

An overall good match between model and natural evolution trends is seen in the S vs. H_2O plot (Fig. 12b), particularly for H_2O> 1.5 wt %, but for < 800 ppm S, a certain mismatch appears, with the model underestimating the natural S contents under the saturation sulfide line from Arenal volcano which has a similar volatile assemblage and melt inclusion compositions (Wade et al., 2006). The degassing trend for Holocene (2-3) in figure 12b, as for the natural samples, shows a spectacular drop of the sulfur content around 60-40 MPa; from 1,600 to 450 ppm S. This behavior is likely to reflect fast ascent of magma in the crust and degassing, rather than changes in redox state conditions (Spilliaert et al., 2006b; Wade et al., 2006). This can be explained because olivine has a rather narrow Fo content (~Fo_{77-80}) and melt inclusion do not show relevant changes of Mg# (~45-50). With such hypothetical rapid ascent, we believe that for a certain interval of depths (40-90 MPa), melts were already trapped in olivines while the level of oxidation necessary for sulfate precipitation was still not reached. This later conclusion was better supported for the studied inclusions of Arenal and Irazu, which record an important sulfur drop for P <150 MPa in oxidized, H_2O-rich melt inclusions (3.0 – 3.5 wt. %H_2O) (Wade et al., 2006; Benjamin et al., 2007).

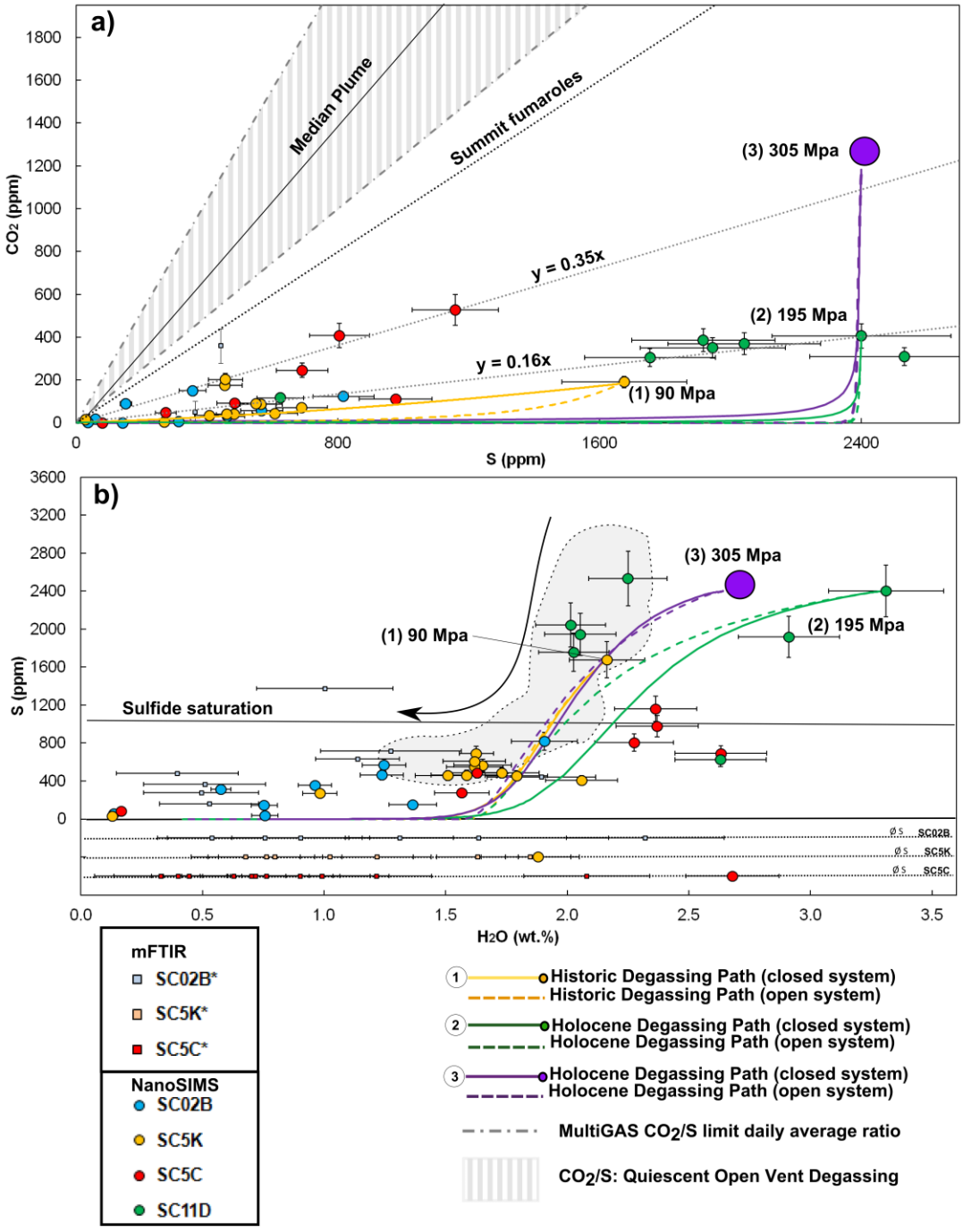

Figure 12 – Binary diagram of volatiles with degassing path of melt inclusions from San Cristóbal. The volatile contents from NanoSIMS (circles) are plotted with their errors. a) CO_2 vs S diagram shows (1) closed-open degassing path initiating at 90 MPa and (2) 195 MPa with a regression line linked to a group of low (0.16) and high (0.35) CO_2/St from melt inclusions. Fumaroles data from Stoiber (1972) are plotted for comparison with data of the Multi-GAS with range of CO_2/St ppmv ratio converted in weight ppm in the vapor. b) S vs. H_2O diagram idem to a) for degassing paths. Water contents measured by mFTIR with missing sulfur variables are plotted along and below the horizontal axis. The sulfide saturation continuous line and the grey rounded shape area passing by the data of Arenal melt inclusion volatiles contents are both from Wade et al. (2006).

5.4 Plumbing system developed with two magma compositions

Two slightly different magma products have been erupted during the San Cristóbal eruptive history: basalts vs. basaltic-andesites. According to the model-simulated H_2O-CO_2 solubilities in basaltic-andesites (model trend (1), Fig. 11a), SC02B and SC5K magmas have a maximum inferred saturation depth around ~3.0 km (Fig. 13a) (we use an average rock density of 2.700 kg/m^3 in the calculations here and below). More precisely, considering, all individual pressures estimates from the available H_2O-CO_2 couples (we averaged results of solubility models of Papale et al (2006) and Witham et al., (2012)), the 1976-to present glass inclusions record saturations depths (0.17 – 2.9 km) that includes the SC5K eruptive cycle range with most samples under 2.0 with 3 samples between 2.9 – 3.4 km. Considering the estimated range of pressures for a similar plume and equilibrium magma-gas composition (see section 5.3), shallow gas separation from magma during the 2013 quiescent degassing phase could occur below 2 km below the actual crater. Those levels may represent a shallow ponding zone where basaltic andesite magma feeding plume gases resides and degasses. In contrast with the historic systems, Holocene magmas, based on model trend (3), appear to have evolved at deeper levels (2.2 and 5.2 km) according to glass inclusion data from BA and ENAB deposits (SC5C; SC11D).

To maximize the possible depth conditions at which the melt inclusions are trapped in the system below San Crystobal, we considered also the model of SolEx for the general degassing path of San Cristobal (3), starting for an average of Raman-corrected CO_2 melt inclusions.

In this case only, the initial pressures of saturation would have an equivalent depth of at least 11.5 km, but even thought, independently on the presence of the shrinkage bubble (Fig. 13b), the saturation depths mentioned previously must be viewed as minimum values for each eruptive cycle (see section 5.2). Other independent methods support deeper magmatic depths: using some spot analysis of coexisting glass and crystals in SC02B sample (n = 8), we infer equilibrium pressures respectively of ~400 MPa (at 1147 °C) and ~220 MPa (1138°C) for the clinopyroxene-liquid and plagioclase-liquid use of the geo-thermobarometers from Putirka (2008). These crystal-liquid thermobarometers overall corresponds to an interval of depth up to 16 km, which constrain the minimum depths of magma differentiation. A deep crustal plumbing system below San Cristóbal is also supported by the wide depth range (1 – 15 km) of epicenters of volcano-tectonic (VT) seismicity reported by INETER (GVP, 2013). Additionally, lower crustal conditions are supported by long-period (LP) earthquakes for local magnitude (M_L ~ 1 – 4) below 5 km. Gas explosions, landslides and block falls on surface are often registered by seismometers and confirmed by local observers during recent rise of volcanic activity during the 2000s. Any batch of magma formed in the mantle below San Cristóbal has to penetrate a 24.6 ± 3.5 km thick average rock succession before reaching the surface (MacKenzie et al., 2008).

In this case only, the initial pressures of saturation would have an equivalent depth of at least 11.5 km, but even thought, independently on the presence of the shrinkage bubble (Fig. 13b), the saturation depths mentioned previously must be viewed as minimum values for each eruptive cycle (see section 5.2). Other independent methods support deeper magmatic depths: using some spot analysis of coexisting glass and crystals in SC02B sample (n = 8), we infer equilibrium pressures respectively of ~400 MPa (at 1147 °C) and ~220 MPa (1138°C) for the clinopyroxene-liquid and plagioclase-liquid use of the geo-thermobarometers from Putirka (2008). These crystal-liquid thermobarometers overall corresponds to an interval of depth up to 16 km, which constrain the minimum depths of magma differentiation

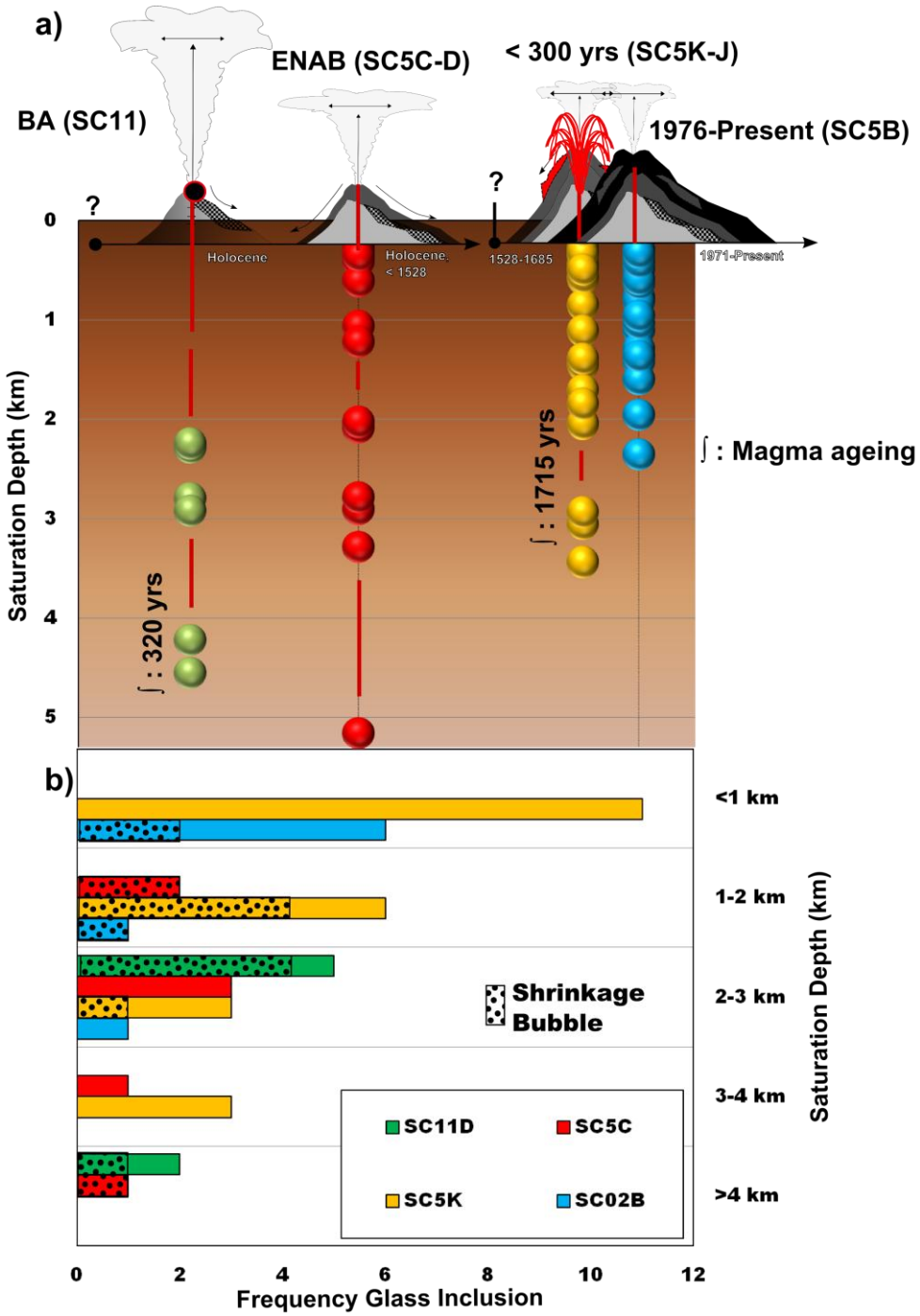

Figure 13 – Model of saturations depth at each eruptions. a) Saturation depth calculated with average from model of Papale et al. (2006) and Witham et al. (2012). b) Frequency diagram with distribution of saturation depth equivalent for each eruptions and the frequency of samples with shrinkage bubble.

The net difference in saturation pressure conditions between basalts and basaltic andesites supports polybaric fractional crystallization behavior. We used fractionation models, based upon major and trace element bulk rock compositions, to test if historic basaltic-andesites magmas can be derived from a primitive magma source similar to that drained during Holocene eruptions. The most primitive bulk rock composition (SC11D) was used as parental magma; from this, mass balance calculations using major elements compositions were initialized attempting at reproducing the composition of the most evolved basaltic andesite (SC02B). Results (Electronic Appendix 6) demonstrate that a primitive magma can produce SC02B-type melt after 28 wt % of crystallization of a solid composed of plagioclase olivine and magnetite (SSR = 0.49). Those values are consistent with the evolution of major elements in addition to the calculated vectors of % mass crystallized graphically represented by the tie-line between the bulk composition of the parent rock and the evolved groundmass composition (Fig. 5 c-d-f). The resulted daughter liquid represented by the end of the white lozenge match most of the natural groundmass samples. The model also predicts that the major fractionating phase is plagioclase (69 wt % of total solid mass), followed by olivine (20 %) and Ti-magnetite (12 %) well consistent with the strong decrease in alumina, and less pronounced in MgO, CaO with silica increase (figure 5 b-e)..

The results obtained with major elements composition were later tested for a selection of trace elements, (Sr, Ba, La, Ce, Zr) assuming Rayleigh fractional crystallization. The bulk D was calculated according to the mineral assemblage previously mentioned and using Kd values from basaltic-andesite systems (references in Electronic Appendix 7). Overall, the match of trace elements calculation is very satisfying for the most incompatible elements of the set, La, Ce and Zr, while it is less close for Sr (the most compatible element of the chosen set), likely depending on the large variation of existing Kd values for plagioclase, critical in the calculations because it is the most abundant mineral phase. The less satisfactory fit of Sr may also be due to the fact that some of the plagioclase crystals may be cumulates in origin, while other crystals (Olivine, Pyroxene, etc.) are not.

Comparison with the primitive samples and differentiated samples show that SC5K and SC02B have an increase in trace elements (Ba, La, Zr, Ce) that fit well with simple fractionation (solid line in figure 14 a-b). The historic samples of bulk tephra show natural enrichments in some elements (La, Zr, Ce) that fit the calculated enrichment caused by simple fractionation and appear to represent a large set of data from Nicaragua magmas that were erupted as basalts to -basaltic andesites (> 2.5 MgO %). According to major and trace element calculations, it is possible to assess that modeling the FC process allow to consider a parent-daughter relationship between SC11D and SC02B: Mineral zoning patterns reasonably exclude relevant episodes of magma mixing and/or assimilation of country rocks along the ascent route.

To further support the inference of a polybaric evolution of magma in the plumbing system of San Cristóbal, we focus on the He content measured in fluid inclusions from historical (SC02B) and Holocene (SC11D) samples. We highlight that SC11D displayed from 2.5 to 4.5 times more He than SC02B (Fig. 9 and Table 9). With the assumption of a common composition of parental magma and a comparable frequency of fluid inclusions per crystal, the He content should be strictly related to entrapment pressure and thus with the degassing/evolution extent. This means that, even for He content, Holocene samples reflect a deep provenance of magma in the plumbing system relatively to those historical.

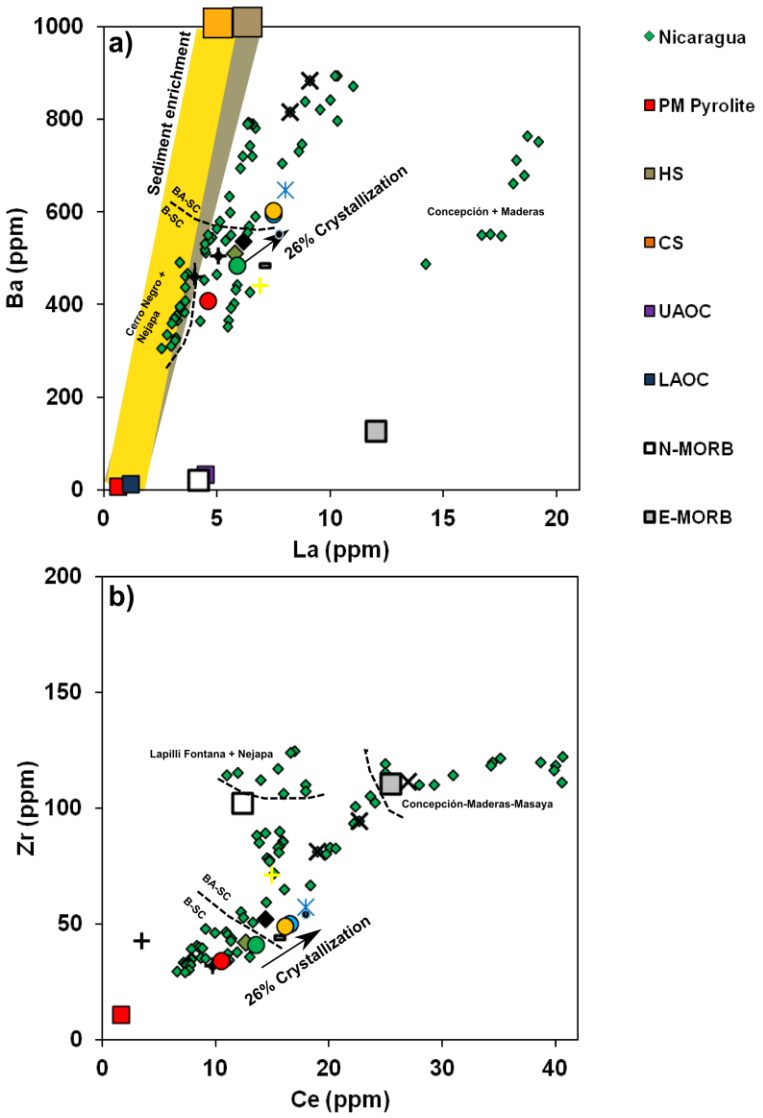

Figure 14 – Trace element analysis of bulk tephra. Trace and rare earth elements comes from the Geochemical Database by Carr et al. (2013) including Carr and Rose (1987) CENTAM database, but only basalts «B» and basaltic andesite «BA» (< 52 wt.% SiO2) with MgO > 2.5 wt.% are considered for comparisons. Dotted line represent compositional limits for certain volcanoes including the limit between basalts of San Cristóbal B-SC and basaltic andesites from San Cristóbal BA-SC that concord well with literature data. HS is for Hemipelagic sedimends, CS for carbonate sediments, UAOC is for upper altered oceanic crust and LAOC the lower section listed in Patino et al. (2000) and PM is the primitive mantle from Mc Donought et al. (1995). Vector for fractional crystallization of a parental melt is drawn with the arrow. Sediment enrichment line is drawn from the UAOC / PM end pole to the end pole of sediments HS and CS from Patino et al. (2000). See symbol of bulk rock samples from San Cristóbal in figure 6.

SC02B and SC5K can be thus considered the result of fractional crystallization of a magma similar in composition to the basalt that fed the Holocene activity (SC11D). The evidence of the

lack of appreciable compositional changes from Holocene to historical time comes also from the $^{3}He/^{4}He$ ratios measured in fluid inclusions (Fig. 9). Indeed, there is no difference in the Rc/Ra values measured in SC11D from Holocene (7.01-7.07 Ra) compared to the most recent SC02B sample (7.20 Ra) (Table 9). But this doesn't mean that a continuous spatial and temporal evolution occurred in the plumbing system with the same batch of magma. More reasonably, it appears that no important temporal changes occurred in the source of San Cristóbal since Holocene. Additionally, no long-term chronological and spatial changes seem to have occurred during the building of the San Cristóbal. In this respect, there is no apparent correlation with mineral abundances (determined with the basis of 1000 count modal analyses of thin sections) and neither with the compositions versus the age categories of lavas in Hazlett (1977) that could support systematic changes in the magma evolution dynamics, and feeding rate from the deep sourced magma reservoir over time (Mc Birney and Williams, 1965; Hazlett, 1977).

We thus propose a scenario with the evidences that historic magma record (1) longer magma residence times for olivine in shallow feeding dyke during the last stage of evolution and that (2) magma differentiation was caused by fractional crystallization via high cooling rates:

(1) The observed textures in melt inclusions of olivines are linked to numerous heterogeneous inclusion assemblage with large inclusions and the concentric clusters of inclusions in both olivines and augites phenocrystals (Fig. 7d; e.g. Roedder, 1979). The important presence of oxide phases in inclusion assemblages may, in turn, be a textural indices to support late water loss by diffusion and explain our low < 2.5 wt.% H_2O inclusions (e.g. Roedder, 1979; Sobolev and Danyushevsky, 1994; Hauri et al., 2002; Gaetani et al., 2012).

(2) The frequent normally chemically zoned olivine and plagioclase crystals (in figure 8) may be explained by fast cooling rates and insufficient time for major elements to diffuse during fractional crystallization. It may have affected a population of crystals growing closer to the cooler periphery wall rocks (Danyushevsky et al., 2002b), laterally in a vertical mush column plumbing system (models of Sin and Detrick, 1992; Marsh, 1998). The olivines without a chemical zonation rather represent an equilibrium state in a fractionated melt for slow cooling magma at the center of a magma body. In comparison, the high-Fo olivines from Holocene samples are not zoned (Fig. 8) and probably were separated from the magma faster than the melt changes its composition. This is all supported by their degassing trend in 5.3, unusual differentiated glass rims and their slightly more differentiated groundmass compositions (> 51 wt. % SiO_2) for SC11D and SC5C (Fig. 5; Table 3).

5.5 Source of magmas and volatiles beneath San Cristóbal

Along-arc variations in CO_2/S ratios in MIs and volcanic gases concur to support a CO_2-richer composition of volcanism in Nicaragua, relative to Costa Rica (Wehrmann et al., 2011; Aiuppa et al., 2014). As mentioned in section 5.2, no natural CO_2-rich (> 1000 ppm) glass inclusion has been found in the San Cristóbal volcanics. However, our glass inclusion data – after correction for the presence of CO_2 in the shrinkage bubbles - indicate that the original CO_2 contents in the San Cristóbal parental melts can be as high as ~1200 ppm (range, 708 - 1940 ppm CO_2), close to the compositions of the CO_2-richest basaltic melt inclusions from Central Nicaragua (Granada and Nejapa magmas, maximum detected CO_2 contents of 1450 and 1780

ppm, respectively; Wehrmann et al., 2011). These Granada and Nejapa CO_2-rich magmas are close to the average N-MORB (Gale et al., 2013) as for their trace and REE compositions, so that no clear pattern exists between the levels of CO_2 enrichment and the abundances of trace element proxies for slab fluid contributions (Sadofsky et al., 2008; Wehrman et al., 2011).

In contrast to CO_2, water contents in melt inclusions variations exhibit more systematic correlations with Ba/La or B/La ratios (Sadofsky et al., 2008), and are therefore better proxies for fluid contributions from subducted sediments. As a matter of fact, the San Cristóbal basaltic glass inclusions that are richest in H_2O also are observed in rocks with the highest bulk rock Ba/La ratios. Similarly, the highest sulphur and chlorine contents in San Cristóbal inclusions are found hosted in basalts with high Ba/La ratios. Apparently, the mantle source beneath San Cristobal seems to share very similar features (S- and Cl-rich) to other volcanic systems in Nicaragua.

Several geochemical markers, including the generally high U/Th (0.7 – 1.0) or Ba/La (79.2 - 87.8) ratios, concur to indicate a strong influence of slab fluids (e.g., fluids from subducted sediments and/or serpentinized oceanic crust) to magma genesis at San Cristóbal. These fluids may participate in the generation of Nicaragua magmas and may increase the degree of partial melting. This case is well reflected by the low La/Yb_N ratios (Fig. 15 a), which make San Cristóbal (this study) and Nicaragua (Carr et al., 1990; Abers et al., 2003; Eiler et al., 2005) magmas compositionally distinct with restricted low La/Yb_N values compare to those nearby Guatemala and Costa Rica that display higher and variable values (Carr et al., 1990; Plank and Langmuir, 1998; Plank et al., 2002). The high Sm/Nd_N ratios (0.82 – 0.96; where Nd_N is after normalization to the primitive mantle of Mc Donought et al., 1995), and the concurrently low La/Yb_N ratios (1.5 – 2.4), support high degree of mantle melting underneath San Cristóbal, which is compatible with a thin crust below the region of Cordillera *de los Marabios* (Mackenzie et al. 2008). The exact depth of magma generation is still uncertain, but considering the prevailingly low Dy_N/Yb_N ratios (1.7-1.8) of San Cristóbal bulk rocks, it is very likely that this occurs at depths shallower than the garnet-peridotite stability field (Feigenson and Carr, 1993; Heydolph et al., 2012), or <60-75 km (e.g. Green and Ringwood 1970).

The Ba/Th vs. U/La plot of figure 15b and the Ba/La vs. distance along the arc plot of figure 16a establish the well-recognised regional patterns in CAVA magmas, and once more indicate that NW Nicaragua magmas, including those of San Cristóbal, rather reflect the signature of hemipelagic (HS) compare to carbonatic (CS) sediments (e.g. Carr, 1984-1990; Morris, 1990; Leeman et al., 1994; Reagan et al., 1994; Chan et al., 1999; Patino et al., 2000; Feigenson et al., 2004; Bolge et al., 2009; Heydolph et al. 2012). The compositional array of Nicaraguan lava points to a magmatic end-member with far higher Ba/Th, U/La and Ba/La ratios relative to lavas in Costa Rica and the Guatemala-El Salvador segment (Patino et al., 2000). The most primitive San Cristóbal magmas (SC11D, SC5C, and basalts from literature) plot the closest to the CS – HS poles (Fig. 15b), indicating magma generation in the presence of a compositionally heterogeneous sedimentary input.

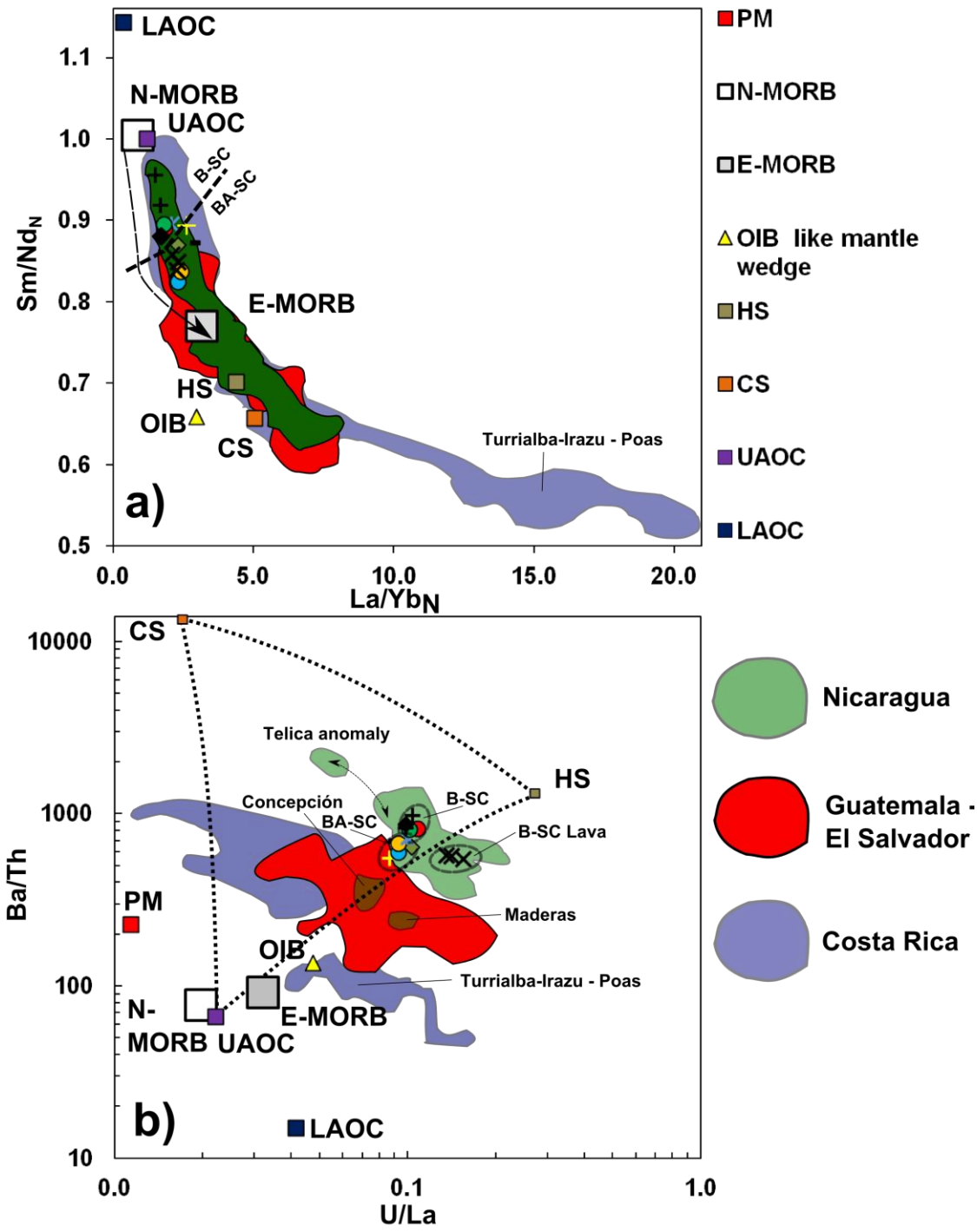

Figure 15 – Normalized to primitive mantle plots. See figure 14 for description symbols and references for whole rock data in literature. **a) Sm/Nd vs. La/Yb and b) Ba/Th vs. U/La.**

A dominant slab-fluid imprint to magmas of the San Cristóbal (NW Nicaraguan) district is also supported by stable isotope (N_2, C) and compositional systematics in volcanic gases (e.g. Fischer et al., 2002; Shaw et al., 2003; Zimmer et al., 2004; Elkins et al., 2006; Hilton et al., 2010; Aiuppa et al., 2014; Di Piazza et al., 2015), by regional studies of sediment input at the trench (e.g. Plank et al., 2002; Freundt et al. 2014), and seismological investigations (e.g. Rüpke et al., 2002; Abers et al., 2003; Ranero et al., 2003; Syracuse et al., 2006; Grevemeyer et al., 2007).

The He isotopic composition measured in fluid inclusions from San Cristobal is in the range 7.01 – 7.20 Ra (Fig. 9; Fig. 16). These values are within the common range of arc volcanoes worldwide (8±1 Ra; Hilton et al., 2002), but higher than the mean arc value of 5.7 Ra. Indeed, $^3He/^4He$ of 7.01 – 7.20 Ra correspond to the highest ratios ever measured before at this volcano. Before this study, the only two measurements performed in 2002 in gases collected from low temperature crater fumaroles yielded values of 5.65 and 5.74 Ra (Shaw et al., 2003; Elkins et al., 2006). As inferred by Elkins et al. (2006), $^3He/^4He<6.8$ Ra cannot be considered representative of the He isotopic signature of Nicaraguan magmas, while they probably reflect shallow contamination of magmatic fluids by radiogenic, crustal-derived, ^4He. One possibility is that these fumaroles are fed by a hydrothermal aquifer in which gas-water-rock interactions contaminated the pristine signature of magmatic fluids. Although, high- and low-temperature crater fumaroles generally reflect the magmatic signature of $^3He/^4He$ (e.g., Paonita et al., 2012; Di Piazza et al., 2015), in some circumstances crater fumaroles may be affected by shallow contaminations leading to wrong conclusions (e.g., Capasso et al., 2005; Rizzo et al., 2009). In these cases, as for San Cristobal, the study of fluid inclusions becomes crucial to assess the $^3He/^4He$ signature of mantle source. The range of $^3He/^4He$ values measured at San Cristobal appears comparable to the maximum ratios measured from north to south in FIs from Cerro Negro and Nejapa (7.11 Ra and 7.49 Ra, respectively; Shaw et al., 2006), and in fumaroles from Telica (7.50 Ra; Shaw et al., 2003; Elkins et al., 2006)(Figs. 9 and 16b), Cerro Negro (7.38 Ra; Shaw et al., 2003; Elkins et al., 2006; Lucic et al., 2014), Momotombo (7.05 Ra; Snyder et al., 2003), Masaya (7.23 Ra; Shaw et al., 2003; Elkins et al., 2006). Only fumaroles from Mombacho show appreciably higher $^3He/^4He$ values (7.72 Ra; Shaw et al., 2003; Snyder et al., 2003; Elkins et al., 2006). All these Nicaraguan volcanoes have a MORB-like mantle signature of $^3He/^4He$ (8±1 Ra; Graham, 2002).

The comparison of $^3He/^4He$ with Ba/La data (Fig. 16) allows further considerations on the influence of sediments and slab fluids along the Nicaraguan segment of CAVA. It is well known that the maximum Ba/La ratios are measured in the NW part of Nicaragua, indicating the dominant component of subducted sediments (Eiler et al., 2005, Hoernle et al., 2008, Sadofsky et al., 2008; Gazel et al., 2009). The pattern of Ba/La along Nicaragua displays a gradual decreasing trend toward SE, with the lowest values measured at Concepción and Maderas volcanoes. These volcanoes show Ba/La within the OIB-like range, typical of Costa Rican segment influenced by the subduction of Galapagos Seamounts that overwhelm the signal coming from the sediments themselves (e.g., Gazel et al., 2009). From north to south, $^3He/^4He$ ratios show a rather homogeneous signature (7.05-7.50 Ra) up to Masaya volcano (Fig. 16b), bur rather appear decoupled from Ba/La. From Mombacho volcano there seems to be a slight tendency to an increase of the $^3He/^4He$ ratios, considering that fumaroles from this volcano showed the highest $^3He/^4He$ ratios of Nicaragua. Unfortunately there are no He isotope data from Concepción and Maderas volcanoes to confirm this tendency. For proving consistency at regional scale, additional volcanoes need to be investigated for noble gases in fluid inclusions (Concepción, Maderas, Masaya, Mombacho, Momotombo, and Telica).

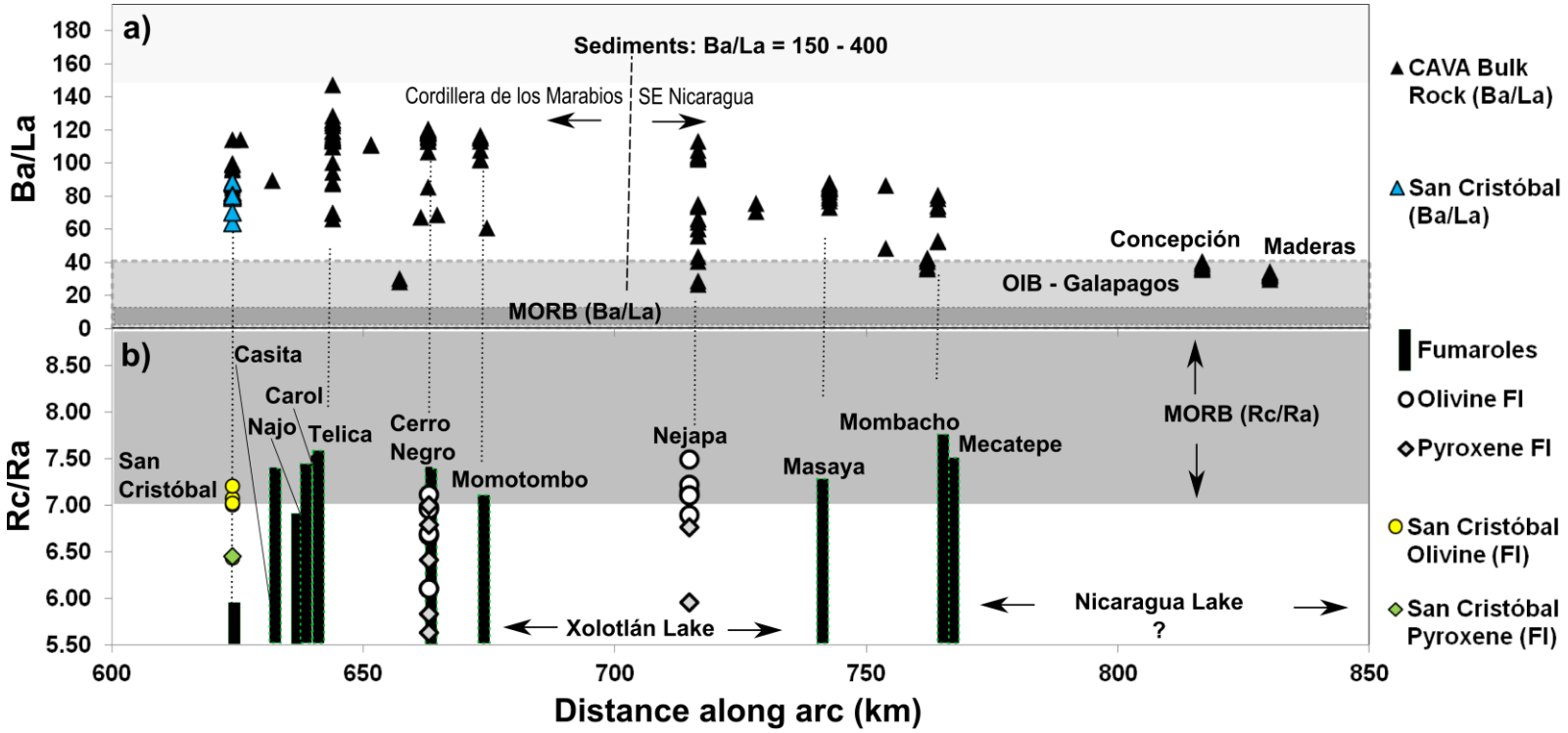

Figure 16 – Plots of Ba/La (a), and Rc/Ra (b) ratios vs distance (km) along the arc from the border between NW and SE Nicaragua. Ba and La data are from figure 14. MORB Ba/La ratios are including UAOC and LAOC (Ba/La calculated between 7 – 10) and explained in figure 14. OIB- Galapagos Ba/La ranges are from Gazel et al. (2009). Data of Rc/Ra measured in gases from CAVA volcanoes (black bar) are from Snyder et al. (2003), Shaw et al., (2003), Elkins et al. (2006), de Leeuw et al. (2007), while Rc/Ra data from fluid inclusions FI are from Poreda and Craig (1989), Fisher et al. (2005) and Shaw et al. (2006). A gap of Rc/Ra data along Nicaragua Lake is recorded with «?». Concepción and Maderas, two islands in the middle of the Nicaragua Lake have Ba/La data which represent the extreme SE of Nicaragua. Rc/Ra data from Conseguina, (extreme NW of Nicaragua) are not shown because they are lower than our fixed minimum of 5.5.

Conclusions

The combination of volatile content and major element data from melt inclusion hosted in olivine phenocrystals of major tephra deposits allowed us to investigate the primitive composition of magmas for different past explosive eruptions at San Cristóbal volcano in Nicaragua. Gas relative abundance from the central plume supported information on shallow degassing processes while volatile contents from the melt inclusion study characterized outgassing behaviours for the deepest part of the plumbing system. Noble gases from fluid inclusions of the same investigated group of olivine crystals allowed us to characterize the nature of fluids from the diverse batches of magma sourced in the mantle in combination with major, trace and REE from the bulk rock. The most relevant conclusions are summarized as follows:

1. The volatile contents assemblage from melt inclusion studied with NanoSIMS and mFTIR reveal moderate H_2O-CO_2 contents coming from scoria and ash deposits of the Holocene BA an ENAB eruptions while microprobe analysis of those melt inclusions indicate S-Cl rich contents and primitive basaltic magma compositions. On the other hand, historic eruptions illustrate basaltic andesite magmas depleted in their volatile contents. Supported by the degassing trend of CO_2-H_2O-S and the geochemistry from the studied phenocrystals and associated liquids, the progressive volatile lost from the trapped melt inclusion in several eruptive cycles are controlled by the lower magma ascent rate conditions and increasing degassing effect combined with polybaric crystal fractionation. 26% of fractional crystallization of Plg > Ol > Cpx > Mt seems to have affected the historic basaltic andesite magmas produced at San Cristóbal and may be coherent with larger time residence in the plumbing system in comparison with basaltic samples from Holocene deposits.

2. CO_2 is present in shrinkage bubble of glass inclusions detected by Raman spectroscopy and may indicate richer original carbon content in the most primitive melt (> 1300 ppm CO_2) before being lost during magma ascent by degassing. Further studies need to prove the conditions at which CO_2 migrated into the bubble and if the CO_2 mass represent 100% of the fraction dissolved in the vapor (1) during or (2) after entrapment of the melt. Actually the solubility models indicate minimum saturation pressures of the trapped melt along a 1-5 km deep plumber system (<195MPa). The pre-entrapment volatile lost (CO_2-H_2O-S-Cl) in the vapour occurred in this region of the crust and was caused by increasing crystallization induced by rapid magma cooling rates for some olivine crystals evolving closer to the wall rocks. Because of its low solubility in melts, CO_2 is already quickly released in the vapour phase and apparently could not be demonstrated to vary in function of changes in magma composition inside the plumbing system.

3. The gas mixture investigated with the combination of MultiGAS and UV-DOAS instruments from the central plume may appear symptomatic of the important SO_2-CO_2 losses that occurs in a superficial buffer controlled vapour system (< ~75 MPa). At the superficial level of the plumbing system of San Cristóbal, actually water seems to control the inner plume variation and may be due to introduction of meteoric water and interaction with water reservoirs.

4. The $^{3}He/^{4}He$ ratios measured in fluid inclusions of olivine crystals vary in a narrow range (7.01-7.20 Ra), with no differences between Holocene and Historic samples. This means that the magmatic source remained constant over this period and did not suffer any crustal contamination within the plumbing system. These Rc/Ra values are the highest ever measured at San Cristóbal, since previous measurements in crater and flank fumaroles vary between 5.65 Ra and 5.74 Ra, suggesting shallow contamination by radiogenic ^{4}He.

5. At regional scale, the range of $^{3}He/^{4}He$ values measured at San Cristobal is comparable to the maximum ratios measured in most of the volcanoes along the NW-SE segment of Nicaraguan arc. Only fumaroles from Mombacho show appreciably higher $^{3}He/^{4}He$ values (7.72 Ra; Shaw et al., 2003; Snyder et al., 2003; Elkins et al., 2006), namely in the part of the segment where Ba/La ratios decreases significantly. All these Nicaraguan volcanoes have a MORB-like mantle signature of $^{3}He/^{4}He$ (8±1 Ra; Graham, 2002), indicating that the contribution of radiogenic ^{4}He from the subducted sediments is low. Trace and REE complete the regional picture by showing conditions of high degree of partial melting for those volcanoes along Cordillera de los Marabios, but they are influenced by incorporation of fluid sediments at different degree from the slab by considering the heterogeneous temporal and spatial Ba/La data repartition.

BIBLIOGRAPHY

- Abers, G.A., T. Plank, B. R. Hacker (2003). The wet Nicaraguan slab. Geophys. Res. Lett.30
- Aiuppa, A., Federico, C., Giudice, G., Gurrieri, S., (2005). Chemical mapping of a fumarolic field: La Fossa Crater, Vulcano Island (Aeolian Islands, Italy). Geophys. Res. Lett., No. 32, (13), L13309
- Aiuppa, A., P. Robidoux, G. Tamburello, V. Conde, B. Galle,G. Avard, E. Bagnato, J. M. DeMoor, M. Martinez, A. Munoz, (2014). The Costa Rica – Nicaragua volcanic segment: along arc variations in volcanic gas chemistry and improved CO_2 budget, Earth and Planetary Science Letters, Vol. 407, p. 134-147
- Atlas, Z. D., (2008). Volatiles in melt inclusions from Mexican and Nicaraguan volcanoes: implications for complex degassing processes, Open Access Dissertations, Paper 142, p. 1 -131
- Auger, L. S., G. Abers, K. Fisher, M. Protti, V. Gonzales, and W. Strauch, (2006). Crustal thickness variations beneath the Central American Volcanic Arc, Eos Trans. AGU, 87, (52), Fall Meet. Suppl., Abstract T23C-0517
- Benjamin, E. R. T. Plank, J. A. Wade, K. A. Helley, E. H. Hauri, G. E. Alvarado (2007). High water contents in basaltic magmas from Irazù volcano, Costa Rica, J. Volcanol Geotherm. Res., Vol. 168, p. 68 - 92
- Bolge L. L., M.J. Carr, K.I. Milidakis, F.N. Lindsay, M.D. Feigenson, (2009). Correlating Geochemistry, Tectonics, and Volcanic Volume Along the Central American Volcanic Front, Geochemistry Geophysics Geosystems, Vol. 10, Issue 12, p. 1-15
- Blank, J. G., and R. A. Brooker ((1994). Experimental studies of carbon dioxide in silicate melts solubility, speciation and stable carbon isotope behavior. In: Carroll M. R., J. R. Holloway (eds) Volatiles in magmas. Rev. Mineral, Vol. 30, p. 157 - 186
- Brooker, R. A., S. C. Khon, J. R. Holloway, (2001). Structural controls on the solubility of CO2 in silicate melts Part I: bulk solubility data, Chem. Geol., Vol. 174, p. 225 - 239
- Capasso, G. Carapezza, M. L., C. Federico, S. Inguaggiato, A. Rizzo (2005a). Geochemical monitoring of the 2002-2003 eruption at Stromboli volcano (Italy): precursory changes in the carbon and helium isotopic composition of fumarole gases and thermal waters, Bull. Volcanol., Vol. 68, p. 118 - 134
- Carr, M. J. (1984). Symmetrical and segmented variation of physical and geochemical characteristics of the Central American volcanic front, J. Volcanol. Geotherm. Res., No. 20, p. 231-252
- Carr, M. J., and W. I. Rose, (1987). CENTAM - A data base of Central American volcanic rocks, J. Volcanol. Geoth. Res., Vol. 33: (Stoiber Volume), p. 239 - 240
- Carr, M.J., M.D. Feigenson, and E.A. Bennett, (1990). Incompatible element and isotopic evidence for tectonic control of source mixing and melt extraction along the Central American arc, Contrib. Mineral. Petrol., No. 105, p. 369-380
- Carr, M. J., I. Saginor, G. E. Alvarado, L. L. Bolge, F. N. Lindsay, K. Milidakis, B. D. Turrin, M. D. Feigenson, and C. C. Swisher III, (2007). Element fluxes from the volcanic front of Nicaragua and Costa Rica, Geochem. Geophys. Geosyst., Vo 8, No. 6, p. 1-22
- Danyushevsky, L. V., S. M. Eggins, T. J. Falloon, and D. Christie (2000b), H2O abundance in depleted to moderately enriched mid-ocean ridge magmas, Part I:

Incompatible behaviour, implications for mantle storage, and origin of regional variations, J. Petrol., Vol. 41, p. 1329 – 1364
- Danyushevsky, L. V. and P. Plechov, (2011). Petrolog3: integrated software for modeling crystallization processes. Geochemistry, Geophysics, Geosystems, Vol. 12
- Di Piazza, A. A. L. Rizzo, F. Barberi, M.I. Carapezza, G. De Astis, C. Romano, F. Sortino (2015). Geochemistry of the mantle source and magma feeding system beneath Turrialba volcano, Costa Rica, Lithos, Vol. 232, p. 319 - 335
- Dixon, J. E., E. M. Stolper, and J. R. Holloway (1995). An experimental study of water and carbon dioxide solubilities in mid-ocean ridge basaltic liquids, Part I, Calibration and solubility models, J. Petrol., Vol. 36, p. 1607–1631
- Dixon, J. E., and E. M. Stolper (1995). An experimental study of water and carbon dioxide solubilities in mid-ocean ridge basaltic liquids, Part II, Applications to degassing, J. Petrol., Vol. 36, p. 1633 – 1646
- Dixon, J. E. and V. Pan (1995). Determination of the molar absorptivity of dissolved carbonate in basanitic glass, American Mineralogist, Vol. 80, p. 1339 - 1342
- Danyushevsky, L. V. and P. Plechov (2011). Petrolog3: Integrated software for modeling crystallization processes, Geochemistry Geophysics Geosystems, Vol. 12, No. 7, p. 1 - 32
- Demets, C., (2001). A New estimate for present-day Cocos–Caribbean plate motion: implications for slip along the Central American Volcanic Arc, Geophys. Res. Lett., No. 28 (21), p. 4043-4046
- Eiler, J.M., M. J. Carr, M. Reagan, M., E. Stolper (2005). Oxygen isotope constraints on the sources of Central American arc lavas. Geochem. Geophys. Geosyst, 6
- Feigenson, M.D. and M. J. Carr (1993). The source of Central American lavas: inferences from geochemical inverse modeling. Contrib Mineral Petrol, Vol. 113, p. 226 - 235
- Feigenson M. D., M.J. Carr, S.V. Maharaji, S. Juliano, L.L. Bolge, (2004). Lead Isotope Composition Of Central American Volcanoes: Influence Of The Galapagos Plume ; Geochemistry Geophysics Geosystems, No. 5, Issue 6, p. 1-14
- Fine and Stolper (1986). Dissolved carbon dioxide in basaltic glasses: Concentrations and speciation. Earth and Planetary Science Letters, Vol. 1976, p. 263 – 278
- Fischer, T.P., N. Takahata, Y. Sano, H. Sumino, D. R. Hilton, (2005). Nitrogen isotopes of the mantle: insights from mineral separates. Geophysical Research Letters, Vol. 32, L11305
- Frezzoti, M. L., F. Tecce, A. Casagli (2012). Raman spectroscopy for fluid inclusion analysis, Journal of Geochemical Exploration, Vol. 112, p. 1 - 20
- Galle B., M. Johansson, C. Rivera, Y. Zhang, M. Kihlman, C. Kern, T. Lehmann, U. Platt, S. Arellano, S. Hidalgo, (2010). Network for Observation of Volcanic and Atmospheric Change (NOVAC)-A global network for volcanic gas monitoring: Network layout and instrument description, J. Geophys. Res. 115, D05304
- Gale, A., Dalton, C. A., Langmuir, C. H., Su, Y. & Schilling, J. G. (2013). The mean composition of ocean ridge basalts. Geochemistry, Geophysics, Geosystems, Vol. 14, No. 3, p. 489 – 518
- Gemmell, J. B., (1987). Geochemistry of metallic trace elements in fumarolic condensates from Nicaraguan and costa Rican volcanoes, J. Volcanol. Geotherm. Res., No. 33, p. 161 – 181
- Giggenbach, W.F. (1992). Isotopic shifts in waters from geothermal and volcanic systems along convergent plate boundaries and their origins. Earth Planet. Sci. Lett., Vol. 113, p. 495 - 510

- Giggenbach,W.F., Sano, Y.,Wakita, H., (1993). Isotopic composition of helium, and CO2 and CH4 contents in gases produced along the New Zealand part of a convergent plate boundary. Geochimica et cosmochimica acta, Vol. 57, No. 14, Vol. 3427 - 3455.
- Global Volcanism Program, National Museum of Natural History (GVP). Retrieved 2014, http://volcano.si.edu/
- Graham, D.W. (2002). Noble gas isotope geochemistry ofmid-ocean ridge and ocean island basalts: Characterization of mantle source reservoirs. Reviews in Mineralogy and Geochemistry, Vol. 47, No. 1, p. 247 - 317
- Hartley, M.E., Maclennan, J., Edmonds, M., and Thordarson, T. (2014). Reconstructing the deep CO2 degassing behaviour of large basaltic fissure eruptions. Earth and Planetary Science Letters, Vol. 393, p. 120 - 131
- Hauri, H. E., J. Wang, J. E. Dixon, P. L. King, C. Mandeville, S. Newman (2002). Chemical Geology, Vol. 183, p. 99 – 114
- Hauri, H. E., A. M. Shaw, J. Wang, J. E. Dixon, P. L. King, C. Mandeville (2006). Matrix effects in hydrogen isotope analysis of silicate glasses by SIMS, Chemical Geology, Vol. 235, p. 352 - 365
- Havlicek, P., P. Hradecky, M. Hrubes, B. Mlcoch, M. Opletal, J. Sebesta (CGU), N. Buitrago, W. Strauch, (1999). Estudio Geológico Y Reconocimiento De La Amenaza Natural - Zona Chinandega-Leon , Nicaragua. Praga-Managua 1999, Resumen Ejecutivo (Servicio Geológico Checo, CGU, en cooperación con Instituto Nicaragüense de Estudios Territoriales, INETER), 23 p.
- Havlicek, P., P. Hradecky, M. Hrubes, P. Kyel, B. Mlcoch, S. Mrazova, Z. Novak, M. Opletal, A. Prichystal, J. Sebesta, J. Seveik, M. Bustillo, Z. Rizo, (2000). Estudio Geológico Y Reconocimiento De La Amenaza Geológica En El Área De León - La Paz Centro Y Malpasillo, Praga-Managua 2000, Reporte Final (Servicio Geológico Checo, CGU, en cooperación con Instituto Nicaragüense de Estudios Territoriales, INETER), 244 p.
- Hazlett, R.W. (1977). Geology and Hazards of the San Cristobal Volcanic Complex, Nicaragua, Darmouth College, June 1977, 212 p.
- Hazlett, R.W. (1987). Geology of the San Cristobal Volcanic Complex, Nicaragua, J. Volcanol. Geotherm. Res., Vol. 33, p. 223-230
- Heydolph, K., K. Hoernle, F. Hauff, P. van den Bogaard, M. Portnyagin, I. Bindeman, D. Garbe-Schonberg, (2012). Along and across arc geochemical variations in NW Central America: Evidence for involvement of lithospheric pyroxenite, Geochimica et Cosmochimica Acta, No. 84, p.459-491
- Kilinc, A., , I.S.E Carmichael, M. Rivers, M., and R. O. Sack, (1983). The Ferric–Ferrous Ratio of Natural Silicate Liquids Equilibrated in Air, Contrib. Mineral. Petrol., Vol. 83, p. 136 - 140
- Hradecký, P., J. Šebesta et. al., (2007). Mapa de la Cadena volcánica Nicaragúense 1:200.000, Czech Geological Survey, iSBN 978-80-7075-671-3
- Iacono-Marziano, G., Morizet, Y., Trong, E. L. and Gaillard, F. (2012). New experimental data and semi empirical parameterization of H2O–CO2 solubility in mafic melts. Geochimica et Cosmochimica Acta, Vol. 97, p. 1 – 23
- Ihinger, P. D., Hervig, R. V. & McMillan, P. F. (1994). Analytical methods for volatiles in glasses. In: Caroll, M. (ed.) Volatiles in Magmas. Reviews in Mineralogy. Mineralogical Society of America, Washington, DC, Vol. 30, p. 67 – 121
- King, P. L. and J. R. Holloway (2002). CO2 solubility and speciation in intermediate (andesitic) melts: The role of H2O and composition, Geochimica et Cosmochimica Acta, Vol. 66, No. 9, p. 1627 - 1640

- Kutterolf, S., A. Freundt, W. Pérez, H. Wehrmann, H.-U. Schmincke, (2007). Late Pleistocene to Holocene temporal succession and magnitudes of highly-explosive volcanic eruptions in west-central Nicaragua J. Volcanol. Geotherm. Res., No. 163, p. 55-82
- Lowenstern, J. B. (1995). Applications of silicate melt inclusions to the study of magmatic volatiles. In: Thompson JFH (ed) Magmas, fluids and ore deposits. Mineral Assoc. Canada Short Course 23, p. 71 - 99
- Lowenstern, J. B. (2001). Carbon dioxide in magmas and implications for hydrothermal systems, Mineralium Deposita, No. 36, p. 490 – 502
- Lucic, G., J. Stix, B. S. Lollar, G. L.-Couloume, A. Munoz, M. I. Carcache (2014). The degassing character of a young volcanic center: Cerro Negro, Nicaragua, Bull. Volcanol., Vol. 76, p. 3 - 23
- Ochs, F. A. and R. A. Lange (1999). The density of hydrous magmatic liquids, Science, Vol. 283, p. 1314 - 1317
- Leeman, W.P., Carr, M.J., Morris, J.D., (1994). Boron geochemistry of the Central American volcanic arc: constraints on the genesis of subduction-related magmas, Geochim. Cosmochim. Acta, Vol. 58, p. 149 - 168
- Mangan, M. and T. Sisson (2000). Delayed, disequilibrium degassing in rhyolite magma: decompression experiments and implications for explosive volcanism, Earth Planet Sci Lett, Vol. 183, p. 441 – 455
- Martelli, M., A. L. Rizzo, A. Renzulli, F. Ridolfi, I. Arienzo, A. Rosciglione (2014). Noble-gas signature ofmagmas froma heterogeneousmantle wedge: the case of Stromboli volcano (Aeolian Islands, Italy), Chemical Geology, Vol. 368, p. 39 - 53
- Martinez, M., J. G. Viramonte, (1971). Geologia de la Cordillera Marrabios, Catastro e Inventario de Recursos Naturales, Managua, Nicaragua
- MacKenzie, L., G. A. Abers, K. M. Fisher, E. M. Syracuse, J. M. Protti, V. Gonzales, and W. Strauch (2008). Crustal structure along the southern Central American volcanic front, Geochem. Geophys. Geosyst., No. 9, Q08S09
- McBirney, A. R., Williams, H., (1965). Volcanic History of Nicaragua, University of California Publ. in Geol. Sci., Vol. 55, p. 1-73
- Martinez, M. and J. G. Viramonte (1971). Geologia de la Cordillera Marrabios, Catastro e Inventario de Recursos Naturales, Managua
- Métrich, N., A. Bertagnini, P. Landi, and M. Rosi, (2001). Crystallization Driven by Decompression and Water Loss at Stromboli Volcano (Aeolian Islands, Italy), Journal of petrology, Vol. 42, No. 8, p. 1471-1490
- Métrich, N. and P. J. Wallace (2008). Volatile abundance in basaltic magmas and their degassing paths tracked by melt inclusions, Rev. Mineral. Geochem., Vol. 69, p. 363 - 402,
- Métrich, N., P. Allard, A. Aiuppa, P. Bani, A. Bertagnini, H. Shinohara, F. Parello, A. Dimuro, E. Garaebiti, O. Belhadj, and D. Massare, (2011). Magma andVolatile Supply to Post-collapse Volcanism and Block Resurgence in Siwi Caldera (Tanna Island,Vanuatu Arc), Journal of petrology, Vol. 52, No. 6, p. 1077-1105
- Moore, L., Gazel, E., Tuohy, R., Lloyd, A., Esposito, R., Steele-MacInnis, M., Hauri, E.H., Wallace, P. J., Plank, T., and Bodnar, R.J. (2015). Bubbles matter: An assessment of the contribution of vapor bubbles to melt inclusion volatile budgets. American Mineralogist, Vol. 100, p. 806 - 823

- Mooser, F., H. Meyer-Abich, A.R. McBirney, (1958). Catalogue of the Active Volcanoes of the World including Solfatara Fields, Part VI, Central America, Int'l Volc. Assoc., Napoli, Italy
- Moretti, R., P. Papale (2004).On the oxidation state and volatile behaviour on multicomponent gas–melt equilibria. Chemical Geology, Vol. 213, p.265 - 280
- Newman, S., E. Stolper and R. Robert, (2000). H2O and CO2 in magmas from the Mariana arc and back arc systems, Geochemistry Geophysics Geosystems, Vol. 1, No. 1, p. 1 – 24
- Papale, P. (1999). Modeling of the solubility of a two-component H2O + CO2 fluid in silicate liquids, Am. Mineral, Vol. 84, p. 477 - 492
- Papale, P., Moretti, R. & Barbato, D. (2006). The compositional dependence of the saturation surface of H2O-CO2 fluids in silicate melts. Chemical Geology, Vol. 29, p. 78 - 95
- Patino, L. C., M. J. Carr, and M. D. Feigenson, (2000). Local and regional variations in Central American arc lavas controlled by variations in subducted sediment input, Contributions to Mineralogy and Petrology, No. 138.3, p. 265-283
- Plank, T., Langmuir, C.H., (1988). An evaluation of the global variations in the major element chemistry of arc basalts. Earth Planet. Sci. Lett., Vol. 90, Issue (4), p. 349 – 370
- Plank, T., Balzer, V., Carr, M., (2002). Nicaraguan volcanoes record paleoceano-graphic changes accompanying closure of the Panama gateway. Geology, Vol. 30, No. 12, p. 1087 - 1090
- Portnyagin, M. V., K. Hoernle, N. L. Mironov (2014). Contrasting compositional trends of rocks and olivine-hosted melt inclusions from Cerro Negro volcano (Central America): Implications for decompression-driven fractionation of hydrous magmas, International Journal of earth Sciences, October 2012, Vol. 103, Issue 7, p. 1963 – 1982
- Putirka, K. (2008). Thermometers and Barometers for Volcanic Systems. In: Putirka KD, Tepley III G.J. (eds) Minerals, Inclusions and Magmatic Processes. Reviews in Mineralogy and Geochemistry, Vol 69. Mineralogic Society of America, p. 61-120
- Reagan, M.K., Morris, J.D., Herrstrom, E.A., Murrell, M.T., (1994). U series and Be isotope evidence for an extended history of subduction modification of the mantle below Nicaragua. Geochim. Cosmochim. Acta, Vol. 58, p. 4199 – 4212
- Rizzo, A., F. Grassa, S. Inguaggiato, M. Liotta, M. Longo, P. Madonia, L. Brusca, G. Capasso, S. Morici, D. Rouwet, F. Vita, (2009). Geochemical evaluation of observed changes in volcanic activity during the 2007 eruption at Stromboli (Italy). Journal of Volcanology and Geothermal Research, Vol. 182, p. 246 - 254
- Rizzo, A., Barberi, F., Carapezza, M.L., Di Piazza, A., Francalanci, L., Sortino, F., D'Alessandro, W., (2015a). New mafic magma refilling a quiescent volcano: evidence from He–Ne–Ar isotopes during the 2011–2012 unrest at Santorini, Greece. Geochemistry, Geophysics, Geosystems, Vol. 16, Issue 3, p. 798 - 814
- Roberge, J., Wallace, P., White, R. V., M. F. Coffin, (2005). Anomalous uplift and subsidence of the Ontong Java Plateau inferred from CO2 contents of submarine basaltic glasses, Geological Society of America, Geology, Vol. 33, No. 6, p. 501 - 504
- Roedder, P. L., and R. F. Emslie (1970). Olivine-liquid equilibrium, Contrib. Mineral. Petrol., Vol. 29, p. 275 – 289
- Roedder, E. (1979). Origin and significance of magmatic inclusions, Bull. Minéral., 102, p. 487-510
- Roedder, E. (1984). Fluid Inclusions. Rev. Miner., Vol. 12, 644 p.

- Roggensack, K., R. L. Hervig, S. B. McKnight, and S. N. Williams (1997). Explosive basaltic volcanism from Cerro Negro: Influence of volatiles on eruptive style, Science, No. 277, p. 1639 – 1642
- Roggensack, K. (2001b). Unraveling the 1974 eruption of Fuego volcano (Guatemala) with small crystals and their young melt inclusions, Geology, no. 29, p.911 – 914
- Sadofsky, S. J., M. V. Portnyagin, K. Hoernle, and P. van den Bogaard (2008). Subduction cycling of volatile and trace elements through the Central American Volcanic Arc: Evidence from melt inclusions, Contrib. Mineral. Petrol., Vol. 155, p. 433 – 456
- Sano, Y., S. N. Williams (1996). Fluxes of mantle and subducted carbon along convergent plate boundaries, Geophys. Res. Lett., Vol. 23, p. 2749 - 2752
- Shinohara, H., (2005). A new technique to estimate volcanic gas composition: plume measurements with a portable multi-sensor system. J. Volcanol. Geotherm. Res., No. 143, p. 319 - 333
- Shaw, A.M., Hilton, D.R., Fisher, T.P., Walker, J.A., Alvarado, G.E., (2003). Contrasting He–C relationships in Nicaragua and Costa Rica: insights into C cycling through subduction zones. Earth and Planetary Science Letters, No. 214, p. 419–513
- Shaw, A.M., D. R. Hilton, T.P. Fisher, J. A. Walker, G. A. M. de Leew, (2006). Helium isotope variations in mineral separates from Costa Rica and Nicaragua: assessing crustal contributions, timescale variations and diffusion-related mechanism. Chemical Geology, Vol. 230, p. 124 - 139
- Schmincke, H. - U., (2004). Volcanism, Springer, 325 p.
- Snyder, G., R. Poreda and U. Fehn, (2003). Sources of nitrogen and methane in Central American geothermal settings: Noble gas and 129I evidence for crustal and magmatic volatile components, G3, Vol. 4, No. 1, 14 January 2003, p. 1 - 28
- Spilliaert, N., P. Allard, N. Métrich, A. Sobolev (2006a). Melt inclusion record of the conditions of ascent, degassing and extrusion of volatile-rich alkali basalt during the powerful 2002 flank eruption of Mount Etna (Italy). J. Geophys. Res. 111: B04203
- Spilliaert, N., N. Métrich, P. Allard, (2006b). S–Cl–F degassing pattern of water-rich alkali basalt: modeling and relationship with eruption styles on Mount Etna volcano. Earth and Planetary Science Letters, Vol. 248, p.772 – 786
- Stoiber, R.E. (1971). San Cristobal volcanic activity, Smithsonian Institute Center for Short-Lived Phenomena, Event, No. 99-71, 21 Dec.
- Stoiber, R.E. (1976a). San Cristobal (El Viejo) volcanic activity, Smithsonian Institute Center for Short-Lived Phenomena, Event Card No. 16-76, 15 Mar.
- Stoiber, R.E. (1976b). San Cristobal volcanic activity, Smithsonian Institute Center for Short-Lived Phenomena, Event No. 71-76, 1 Sept.
- Stoiber, R.E. (1977). Data relative to temperature, SO2, and Cl content of condensates from fumaroles at San Cristobal and Cerro Negro volcanoes, unpublished data, Darmouth College
- Stoiber, R.E. (1911-2001). From the Papers of Richard E. Stoiber, Rauner Special Collections, Rauner Manuscript ML-98, Dartmouth College Library
- Symonds, R. B., Gerlach, T. M., and Reed, M. H., (2001), Magmatic gas scrubbing: implications for volcano monitoring, in Allard, P., H. Shinohara, and P. Wallace, eds., Magma degassing through volcanoes; A tribute to Werner F. Giggenbach: J. Volcanol. Geotherm. Res., Vol. 108, p. 303-341
- Stolper, E. (1982), Water in silicate glasses: An infrared spectroscopic study, Contrib. Mineral. Petrol., Vol. 81, p. 1 – 17

- Syracuse, E. M., and G. A. Abers, (2006). Global compilation of variations in slab depth beneath arc volcanoes and implications, Geochem. Geophys. Geosyst., No. 7, Q05017
- Tamburello, G., (2015). Ratiocalc: Software for processing data from multicomponent volcanic gas analyzers, Computers & Geosciences, Vol. 82, p. 63 - 67
- Toplis, M. J. (2005). The thermodynamics of iron and magnesium partitioning between olivine and liquid: Criteria for assessing and predicting equilibrium in natural and experimental systems, Contrib. Mineral. Petrol., Vol. 149, p. 22 – 39
- Vallance, J.W., S.P. Schilling, G. Devoli, M.E. Reid, M.M. Howell, (2004). and D.L. BrienUSGS, Lahar Hazards at Casita and San Cristóbal Volcanoes, Nicaragua, USGS Open-File Report 01-468, p. 1-24
- Wade, J.A. T. Plank, W. G. Melson, G. J. Soto, A. H. Hauri (2006). Volatile content of magmas from Arenal volcano, Costa Rica, J. Volcanol Geotherm. Res., Vol 157, p. 94 - 120
- Walker, J. A., L. C. Patino, J. C. Michael and M. D. Feigenson, (2001). Slab control over HFSE depletions in central Nicaragua, Earth and Planetary Science Letters, No. 192, p.533-543
- Wallace, P. J. (2005). Volatiles in subduction zone magmas: concentrations and fluxes based on melt inclusion and volcanic gas data, J. Volcanol. Geotherm res., Vol. 140, p. 217 – 240
- Wallace, P. J., V. S. Kamenetsky and P. Cervantes (2015). Melt inclusion CO2 contents, pressures of olivine crystallization, and the problem of shrinkage bubbles, American Mineralogist, Vol. 100, p. 787 – 794
- Wang, X., Ming-Chou, I., Hu,W., Burruss, R.C., Sun, Q., Song, Y., (2011). Raman spectroscopic measurements of CO2 density: experimental calibration with high-pressure optical cell (HPOC) and fused silica capillary capsule (FSCC) with application to fluid inclusion observations. Geochimica et Cosmochimica Acta, Vol. 75, p. 4080 – 4093
- Wehrmann, H., Hoernle, K., Portnyagin, M., Wiedenbeck, M., Heydolph, K., (2011). Volcanic CO2 output at the Central American subduction zone inferred from melt inclusions in olivine crystals from mafic tephras. Geochem. Geophys. Geosyst., Vol. 12, p. 1 - 16, Q06003
- Witham, F., J. Blundy, S. C. Kohn, P. Lesne, J. Dixon, S. V. Churakov, and R. Botcharnikov (2012). SolEx: a model for mixed COHSCL-volatile solubilities and exsolved gas compositions in basalt, Computers & Geosciences, Vol. 45, p. 87 - 97

ELECTRONIC APPENDIX 1

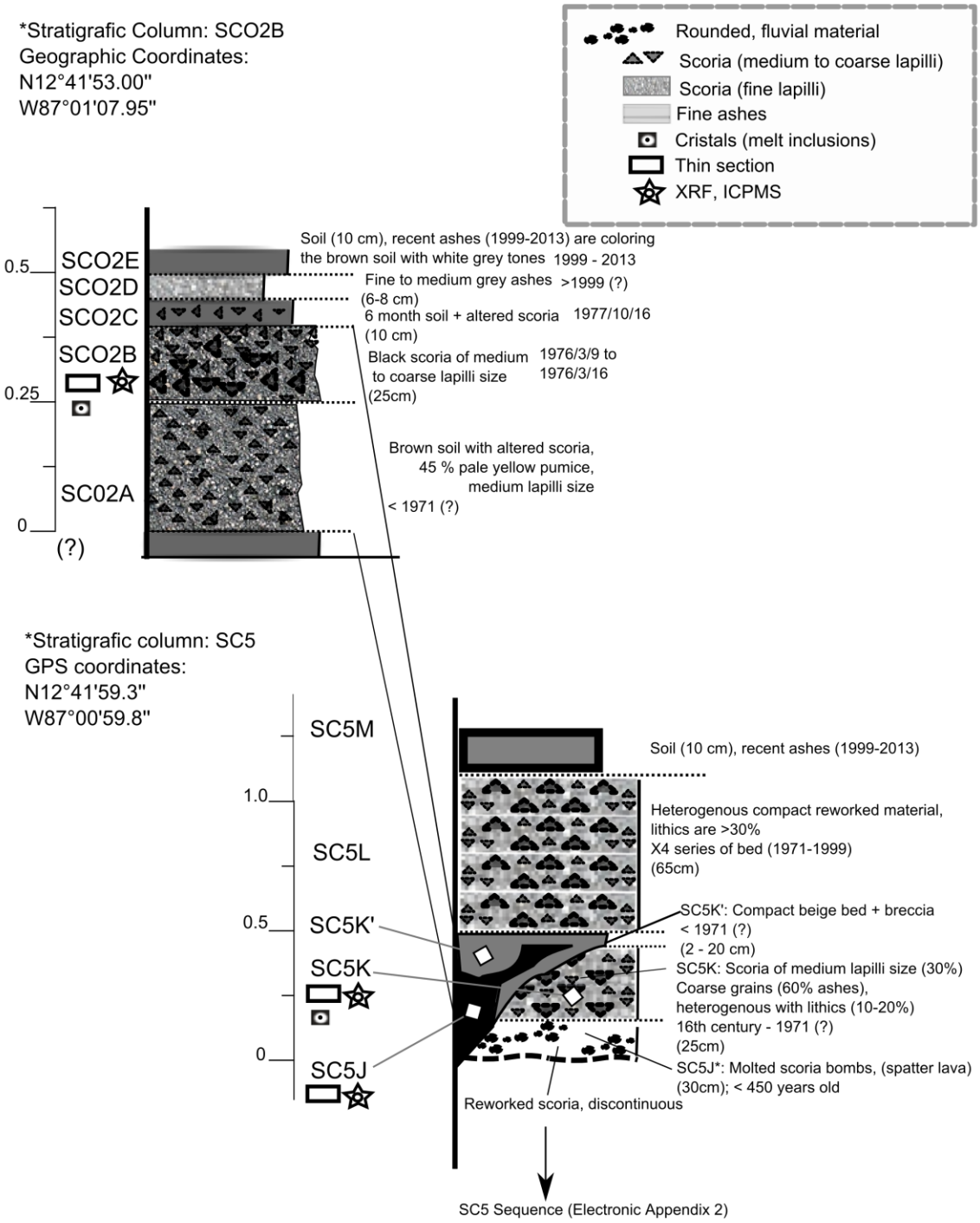

ELECTRONIC APPENDIX 2

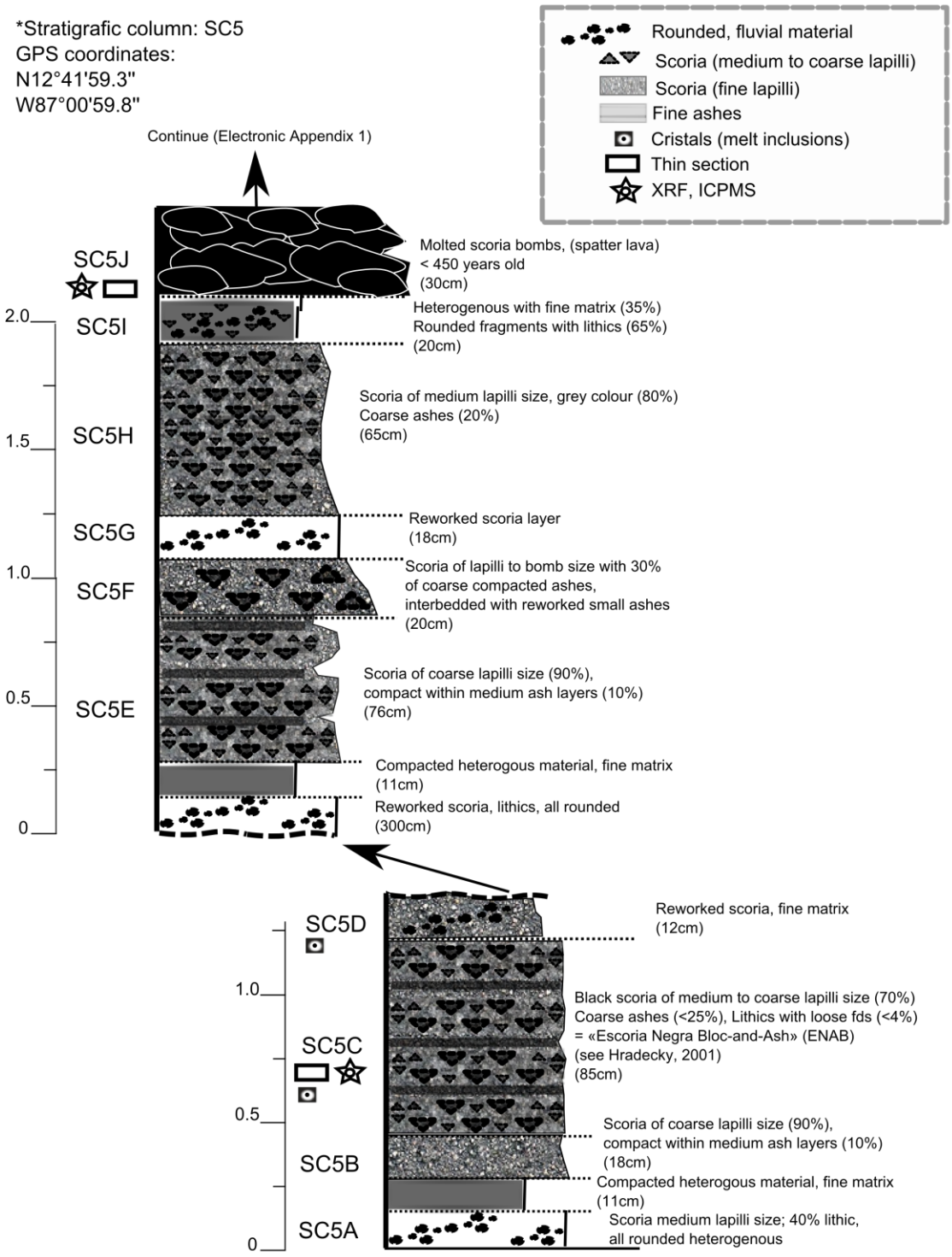

ELECTRONIC APPENDIX 3

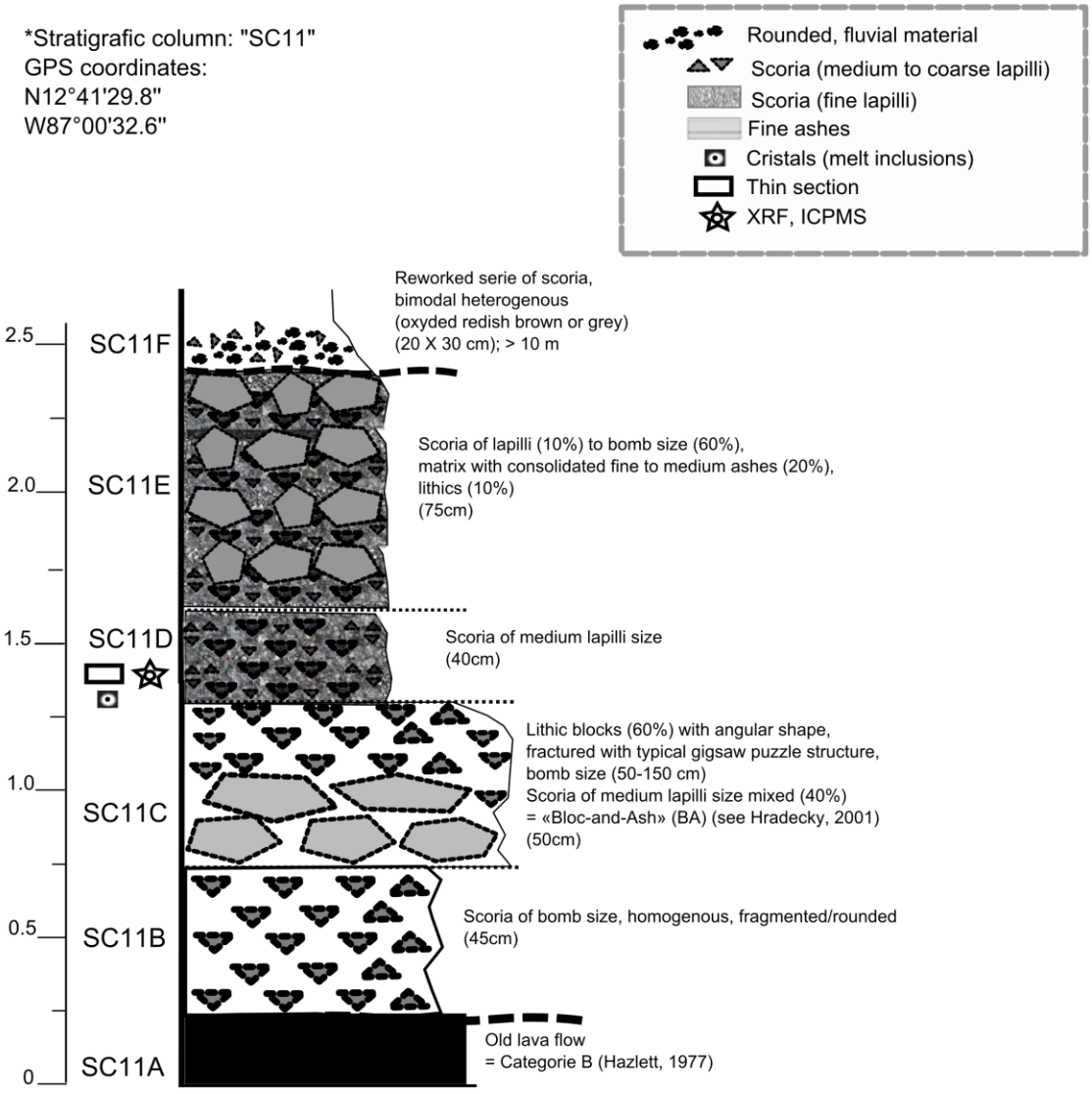

ELECTRONIC APPENDIX 4

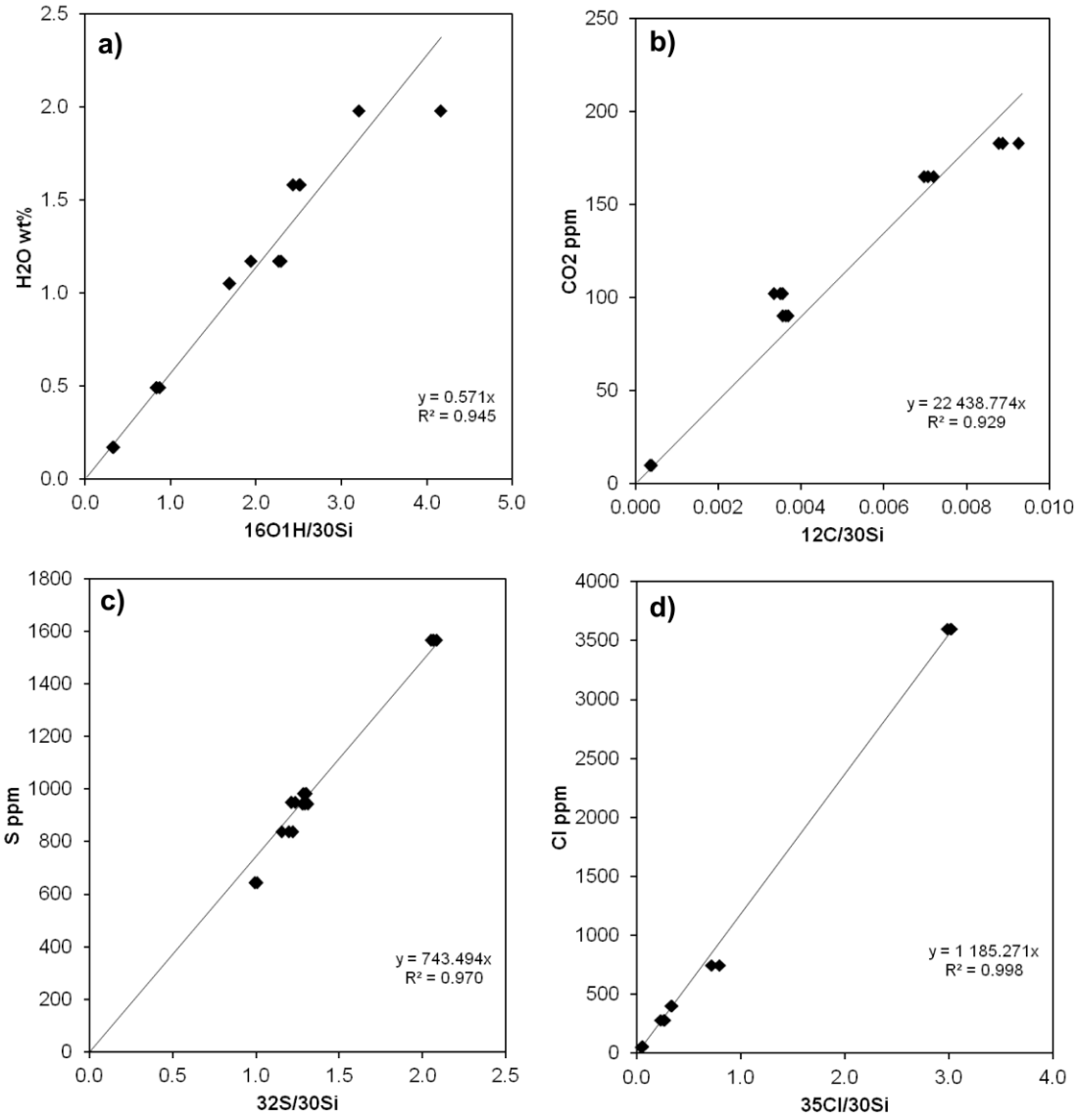

ELECTRONIC APPENDIX 5

INTRODUCTION

The CO_2 mass bubbles «m» in inclusion can be converted with the resulted number of moles «n» estimated by using the perfect gas law (PV= nRT). Raman spectroscopy is used in this paper to test if whether or not the CO_2 is present in the shrinkage bubble and also as a second approach for calculating the CO_2 mass from the shrinkage bubbles.

Section 1. Estimaiton of Ideal Gas Law parameters

By using the PV=nRT approach, the bubble environment is considered as an ideal closed vapor H_2O-CO_2 system where volatiles already diffused from the glass to the shrinkage bubble during cooling. Pressure P is the saturation pressure from the chosen solubility model (Papale et al., 2006). The volume V is the measure from a sphere using MicroRaman high resolution petrografic optic microscope Olympus BX41 (1 μm). R is the constant from perfect gases. The temperature T is associated to the closure temperature of the cooling petrological system as defined by Dodson et al. (1973) (see figure 1 a-b; Table 1).

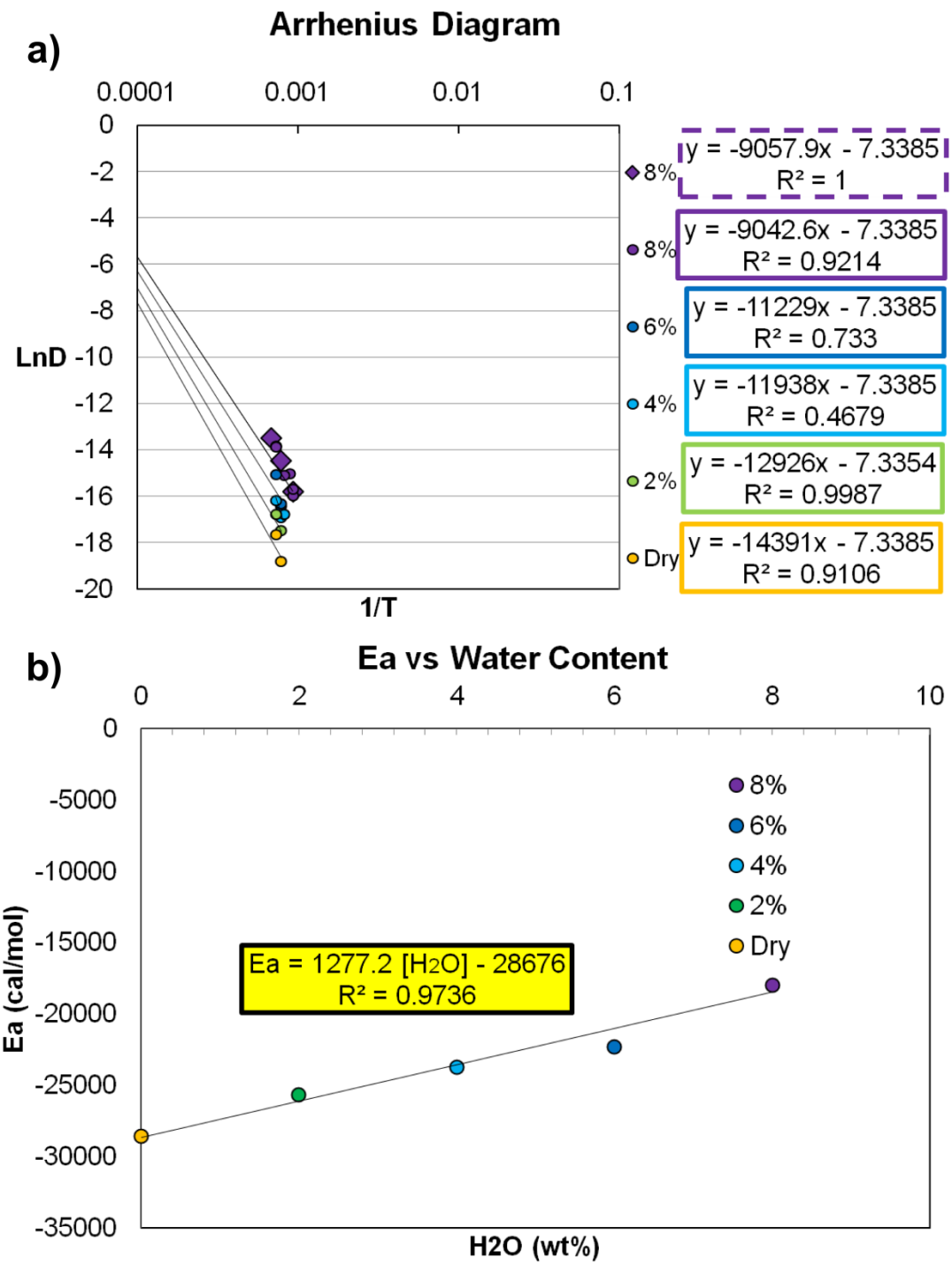
a)
Arrhenius Diagram
0.0001
0.001
0.01
0.1
0
-2
-4
-6
-8
-10
-12
-14
-16
-18
-20
LnD
1/T
8%
8%
6%
4%
2%
Dry
y = -9057.9x - 7.3385
R² = 1
y = -9042.6x - 7.3385
R² = 0.9214
y = -11229x - 7.3385
R² = 0.733
y = -11938x - 7.3385
R² = 0.4679
y = -12926x - 7.3354
R² = 0.9987
y = -14391x - 7.3385
R² = 0.9106
b)
Ea vs Water Content
0
2
4
6
8
10
0
-5000
-10000
-15000
-20000
-25000
-30000
-35000
Ea (cal/mol)
H2O (wt%)
8%
6%
4%
2%
Dry
Ea = 1277.2 [H2O] - 28676
R² = 0.9736

ELECTRONIC APPENDIX 5 (next)

Figure 1 :

a) To estimate the closure temperature Tc inserted in «PV = nRT», it is recommended to choose the appropriate diffusion rate constant for CO_2 in the diffusion equation of Dodson et al. (1973):

$T_c = E_a / \ln (A\ t\ D_{CO2}/r^2)$

Where:

R: Gas constant = 1.9872 cal/mol K

E_a: Activation energy for diffusion (cal/mol)

A: Numerical geometric constant for the volume of a sphere (55)

D_{CO2}: Diffusion pre-exponential factor from Watson et al. (1991) = 0.0006354 cm^2/s

r: Diffusion length scale (inclusion diameter in cm)

t: Diffusion time constant (below) = 341.5 s

Using the diffusion equation assumes that composition of silicate glass has no effect on D_{CO2} (Nowak and Screen, 2003; Nowak et al., 2004; Baker, 2005) and that the CO_3^{2-} species (as detected by mFTIR in San Cristobal samples) have similar diffusion rates with CO_2 (Sierralta et al., 2002). Therefore, the use of D_{CO2} for diffusion model can be considered. Closure temperature Tc were calculated by using a modified equation of Watson et al. (1991) for CO_2 diffusion. By plotting the closure temperatures Tc and experimental D_{CO2} in the Arrhenius diagram, different functions were adapted to fit the best linear correlation between Ln and 1/T from Watson (1991) experiments (figure a).

b) The slope of the diagram for different water concentrations in the glass (glass inclusion) were plotted in a binary diagram to test their correlation. A general equation was then attributed where activation energy of diffusion *Ea* (Cal/Mol) depends on the water content of the glass (wt.%) with $Ea_{CO2} = 1277.2\ C_{[H2O]} - 28676$ ($R^2 = 0.9736$).

ELECTRONIC APPENDIX 5 (next)

Samples	Inclusion [H_2O] wt%	°T °C	Bubble Lenght cm	Closure Temperature °C
SC02Br5a	1.36	1114	1.31E-03	597
SC5Kr1a	1.63	1107	7.60E-04	530
SC5Kr1b	1.51	1107	4.60E-04	489
SC5k3Gb	2.16	1107	1.01E-03	536
SC5Cr6a	2.36	1130	5.80E-04	475
SC11Dr1a	2.91	1132	3.70E-03	651
SC11Dr1d	2.03	1132	8.63E-04	524
SC11Dr1g	2.25	1132	4.00E-04	448
SC11Dr1i	2.05	1132	4.00E-04	455

Table 1:

The table 1 shows the water contents necessary to calculate the closure temperature °C. The water content (wt%) from each glass inclusion determined by NanoSIMS is inserted in the modified Watson (1991) equation in figure 1a. Initial temperature of the cooling system (°C) represents the best approximation of the initial magmatic conditions for olivine and clinopyroxene crystallization (see equation 16 in Putirka et al., 2008). The bubble length (cm) represents the diffusion length scale in Dodson equation. The result is the closure temperature (°C).

ELECTRONIC APPENDIX 5 (next)

Section 2. Estimaiton of fluid density in the bubble

Fluid density is calculated using the equation of Wang et al.(2011). CO_2 fluid density depends on the distance between the Fermi doublet (Δ) which can be calculated with diverse functions of Δ (cm^{-1}) depending on the experimental works (Rosso and Bodnar; 1995; Kawakami et al., 2003; Yamamoto and Kagi, 2006; Song et al., 2009; Fall et al., 2011). For San Cristóbal samples, the relation was best suited for the equation of Wang et al. (2011). The position of the Fermi bands (around 1288 and 1393 cm^{-1}) were determined with Fityk 0.9.8 by fitting Lorenzian curves to the Raman spectras retrieved from the Raman instrument with Labspec 5. Raman spectra were obtained with a 1800 mm^{-1} collected grating and for improving the precision of CO_2 density calculations, a collection times of 180 seconds was programmed for the instrument.

The error in the peak fitting procedure was used to estimate the precision of Δ which englobes the densimeter precision. The densimeter can measure a range of density between 0.0472-1.0060 g/cm^3 (σ = 0.0253 g/cm^3) and the average precision for Δ was 0.007 cm^{-1} in San Cristóbal bubbles with corresponding density errors of 0.04 g/cm^3 (see results in table 2).

ELECTRONIC APPENDIX 5 (next)

	Sample		SC02Br5a	SC5Kr1a	SC5Kr1b	SC5k3Gb	SC5Cr6	SC11Dr1g
Bubble	**Bubble width/depth**	**(cm)**	1.48E-03	7.75E-04	4.91E-04	1.02E-03	5.86E-04	4.02E-04
	Bubble lenght	**(cm)**	1.31E-03	7.61E-04	4.61E-04	1.01E-03	5.81E-04	4.00E-04
	Bubble volume	**(cm3)**	5.39E-10	2.30E-10	5.10E-11	5.39E-10	1.02E-10	2.09E-10
MI	**Inclusion lenght**	**(cm)**	5.22E+01	4.30E+01	4.14E+01	5.20E+01	3.20E+01	1.80E-03
	Inclusion width/depth	**(cm)**	3.90E+01	2.60E+01	2.57E+01	3.90E+01	2.70E+01	1.20E-03
	Inclusion volume	**(cm3)**	4.15E-08	1.52E-08	1.43E-08	4.14E-08	1.22E-08	2.04E-09
	Bubble/Melt	**Ratio**	1.3	1.5	0.4	1.3	0.8	10.3
Glass	**volume**[a]	**(cm3)**	4.10E-08	1.50E-08	1.43E-08	4.09E-08	1.21E-08	1.99E-09
	Density	**(g/cm3)**	2.53E+00	2.51E+00	2.51E+00	2.48E+00	2.52E+00	2.52E+00
	Glass Mass[b]	**(g)**	1.04E-07	3.76E-08	3.59E-08	1.01E-07	3.05E-08	5.02E-09
	CO_2 Mass in the glass[c]	**(g)**	9.28E-12	2.67E-12	7.24E-12	1.93E-11	1.61E-11	1.55E-12
	m CO_2 Bubble (PV=nRT)	**g**	6.54E-11	3.64E-11	2.10E-11	1.77E-10	3.00E-11	1.37E-11
	m CO_2 Bubble (Raman)	**g**	1.44E-10	6.32E-11	1.40E-11	1.48E-10	2.73E-11	0
	Diff.	**%**	121	74	-33	-16	-9	-
	Corr. CO_2 Mass MI	**g**	7.46E-11	3.90E-11	2.82E-11	1.97E-10	4.61E-11	1.55E-12
	Uncorr. [CO_2]	**ppm**	89	71	202	191	527	310
	Corr. [CO_2]	**ppm**	718	1037	787	1940	1506	310
	Added CO_2	**ppm**	628	966	585	1748	979	0

ELECTRONIC APPENDIX 5 (next)

Table 2:

a) The glass volume = inclusion volume − bubble volume.

b) The glass mass is the glass density determined by Ochs and Lange (1987) multiplied by the volume of the glass inclusion.

c) The CO_2 mass in the glass is the uncorrected CO_2 content (or its fraction) multiplied by the glass mass where the CO_2 content is measured by NanoSIMS.

Section 3. Estimation of the CO_2 mass in the bubble

The total CO_2 mass in inclusion = glass CO_2 mass + bubble CO_2 mass (Table 2), depending on the Ideal Gas Law (IGL) «PV=nRT» for the bubble CO_2 mass estimation. The IGL method is only considered for correcting the CO_2 glass inclusion content if the «Raman» bubble CO_2 mass estimation is not under/over estimating the same result. To verify if both methods are consistent, the % of difference (Diff. in %) in function of the «Raman» CO_2 bubble mass estimation is calculated. If the «Raman» CO_2 mass estimation of the bubble is slightly different (difference of ± 30%), the CO_2 correction is applied by using the «Raman» CO_2 bubble mass estimation.

The «Raman» CO_2 mass estimation of the bubble is calculated by multiplying the CO_2 shrinkage bubble density (g/cm^3) by its volume (cm^3). Such method necessitated re-adding CO_2 from a typical shrinkage bubble of < 10.0 Vo% (bubble/inclusion) into 5 inclusions by using simple mass balance estimation (Table 2), but its presence needed to be confirmed with MicroRaman spectroscopy. 9 inclusions were tested by this medthod, but SC11Dr1g (in example in table 2) among 4 other crystals of layer SC11D did not showed Fermi dias bands for CO_2 so its presence remains uncertain.

Using the different steps of section 1, 2,3, only 5 calculated CO_2 mass results from the bubble coincided well with the CO_2 mass measured using the MicroRaman approach.

ELECTRONIC APPENDIX 6

Composition	Density ($g\ cm^{-1}$)	Mass fraction	SiO_2 wt.%	TiO_2	Al_2O_3	FeO*	MnO	MgO	CaO	Na_2O	K_2O	P_2O_5	Sum
Parent	2.6	1	49.4	1.0	18.6	10.6	0.2	4.9	10.7	2.7	0.6	0.2	98.8
Ol	3.4	-5.9	38.6	0.0	1.3	21.4	0.4	38.4	0.8	0.0	0.0	0.0	100.9
Cpx	3.2	-3.3	50.1	0.5	2.8	10.0	0.4	14.7	19.2	0.3	0.0	0.0	98.0
Plg	2.7	-14.3	46.0	0.0	32.6	0.8	0.0	0.0	16.5	1.7	0.1	0.0	97.7
Mt	5.2	-2.8	0.1	7.3	5.5	84.8	0.0	0.0	0.0	0.0	0.0	0.0	97.9
Daughter		F* = 73.7	53.0	0.7	18.7	9.4	0.2	2.9	10.5	2.9	0.4	0.1	98.8
RSD			0.026	0.076	0.014	0.030	0.003	0.003	0.006	0.086	0.063	0.007	0.31

Note: Parent is the most primitive bulk rock sample SC11D containing the highest H2O-CO2 contents in Fo>80 mol.%. and Daughter is the more differentiated bulk rock sample SC02B that is also the closest to the matrix glass composition. Melt densities are calculated after Ochs and Lange (1987). RSD is residual squared difference between the parent and daughter composition. The crystal assemblage as input represent the average crystal composition from layer SC02B. According to the calculations made by XL FRAC software (Stormer and Nicholls, 1978) 26 % is fractionated by weight of the minerals (liquid fraction , F*= 73.7%) that occurs in the inferred parental magma with the given composition. In detail, the fractionated mineral assemblage consists of (% by weight): plg= 54 % ; oliv= 22 % ; cpx= 13 % ; mt = 11 %.

ELECTRONIC APPENDIX 7

The results of major elements in Electronic Appendix 8 are tested for selected trace elements, (Sr, Ba, La, Ce, Zr) assuming Rayleigh fractional crystallization. The bulk D was calculated according to the mineral assemblage derived using Kd values from basaltic-andesite systems (references below).

Elements	D_{bulk}	Parental melt SC11D (ppm)	Derivative melt SC02B (ppm)	Calculated derivative melt
		(ppm)		
Sr	1.11	498	572	482
Ba	0.57	484	594	551
La	0.10	7.7	7.5	7.7
Ce	0.07	13.6	16.6	18.0
Zr	0.08	41	50	54

According to major and trace element calculations, is possible to assess that modeling the FC of 24% crystals allow to consider a parent-daughter relationship between the magma that produced SC11D and SC02B.

References

Dostal et al., Geo. Cos. Acta, v 47, 525, 1983

Drake and Weill, Geo. Cos. Acta, v 39, 689, 1975

Ewart and Griffin, Chem. Geo., v 117, 251, 1994

Larsen, Lithos, v 12, 303, 1979

Nielsen et al., Contrib. Mineral. Petrol., v 110, 488, 1992

Philpotts and Schnetzler, Geo. Cos. Acta, v 34, 307, 1970

ELECTRONIC APPENDIX 8

Eruption	2012-01-25		March 1976				
Unit	SC2012	SC2012	SCO2B	SCO2B	SCO2B	SCO2B	SCO2B
MI Sample	SC2012A2	SC2012A	SCO2B1a	SC02B4a	SC02B4b	SC02B6aI	SC02B5a
No. (#spot/average)	Average	113.00	2.00	10.00	12.00	160.00	13.00
SiO_2	51.40	53.49	49.30	51.36	54.01	52.74	48.48
TiO_2	1.24	1.09	1.07	1.41	1.30	1.67	1.04
Al_2O_3	13.06	14.14	15.14	15.77	11.58	13.73	14.82
FeO*	12.24	12.12	11.97	13.99	11.88	13.18	11.90
MnO	0.26	0.30	0.20	0.36	0.29	0.27	0.22
MgO	3.44	3.42	4.23	3.97	3.09	3.26	4.31
CaO	7.34	7.10	7.92	8.63	7.21	8.08	8.30
Na_2O	3.22	3.48	3.46	3.73	2.85	3.21	3.63
K_2O	1.24	1.12	0.88	1.10	0.93	1.24	0.93
P_2O_5	0.30	0.29	0.32	0.40	0.30	0.37	0.23
Cr_2O_3	0.00	0.00	0.00	0.03	0.00	0.00	0.01
NiO	0.00	0.00	0.05	0.00	0.13	0.00	0.03
TOT	93.74	96.55	94.54	100.73	93.56	97.75	93.89

ELECTRONIC APPENDIX 8 (next)

Eruption	March 1976						
Unit	SCO2B	SCO2B	SCO2B	SCO2B	SCO2B	SCO2B	SCO2B
MI Sample No.	SC02B7a Average	SC02B8a Average	SC02B13a Average	SC02B13b Average	SC02B13_A4 Average	SC02B18a Average	SC02B18b Average
SiO_2	51.16	49.53	50.43	50.89	50.23	52.88	51.47
TiO_2	1.23	1.19	0.56	1.20	0.56	1.48	1.14
Al_2O_3	13.99	15.06	15.03	14.58	15.09	14.65	15.22
FeO*	11.76	12.38	12.12	11.23	12.09	11.58	13.02
MnO	0.29	0.29	0.30	0.18	0.30	0.28	0.26
MgO	4.01	3.40	3.72	3.82	3.40	4.20	4.02
CaO	8.39	8.19	8.79	8.41	8.44	7.47	8.84
Na_2O	3.33	3.92	3.50	3.53	3.69	3.46	3.22
K_2O	0.95	0.89	0.49	0.89	0.53	1.15	0.98
P_2O_5	0.31	0.30	0.20	0.28	0.20	0.31	0.24
Cr_2O_3	0.024	0	0.0055	0.018	0.0365	0.0125	0.0245
NiO	0.012	0	0.011	0.0465	0.0235	0	0.0165
TOT	95.45	95.14	95.16	95.09	94.57	97.47	98.45

ELECTRONIC APPENDIX 8 (next)

Eruption	March 1976					15th Cent.-1977	
Unit	SCO2B	SCO2B	SCO2B	SCO2B	SCO2B	SC5K	SC5K
MI Sample No.	SC02Br3a 23	SC02Br3z Average	SC02Br5a Average	SC02Br5bI 16	SC02Br5c 17	SC5k1a Average	SC5k2a Average
SiO_2	53.87	54.48	49.53	51.12	50.14	53.37	50.88
TiO_2	0.93	0.86	0.92	0.95	1.00	1.36	1.23
Al_2O_3	14.06	16.27	14.66	14.98	14.24	14.07	14.32
FeO*	10.55	9.63	13.75	14.20	13.28	10.81	11.54
MnO	0.19	0.29	0.36	0.27	0.38	0.21	0.27
MgO	3.26	3.56	3.28	3.51	3.82	3.71	3.78
CaO	7.81	7.63	7.79	7.79	7.02	7.33	7.69
Na_2O	3.17	3.72	3.32	3.59	3.63	3.75	3.90
K_2O	1.27	1.53	0.70	0.74	0.87	1.13	0.98
P_2O_5	0.34	0.24	0.41	0.55	0.22	0.34	0.35
Cr_2O_3	0	0	0	0	0	0.018	0.011
NiO	0	0	0	0	0	0.007	0.003
TOT	95.45	98.20	94.72	97.70	94.60	96.10	94.95

ELECTRONIC APPENDIX 8 (next)

Eruption	15th Cent.-1977				Holocene - ENAB	
Unit	SC5K	SC5K	SC5K	SC5K	SC5C	SC5C
MI Sample No.	SC5Kr1a Average	SC5Kr1b Average	SC5Kr2a Average	SC5Kr2b 10	SC5Cr6a Average	SC5Cr6b Average
SiO_2	51.08	53.04	52.04	50.34	47.26	46.15
TiO_2	1.13	1.23	0.92	1.07	0.93	0.67
Al_2O_3	14.35	14.42	14.50	14.96	15.06	15.35
FeO*	13.01	11.79	12.37	12.33	12.36	12.86
MnO	0.31	0.30	0.25	0.33	0.28	0.20
MgO	4.06	3.82	4.15	4.20	5.15	5.28
CaO	8.13	7.70	7.87	8.15	9.55	10.40
Na_2O	3.44	3.68	3.53	3.33	2.87	2.73
K_2O	0.94	1.03	0.96	0.97	0.64	0.46
P_2O_5	0.26	0.27	0.27	0.23	0.47	0.21
Cr_2O_3	0.0005	0	0	0	0	0
NiO	0	0	0	0	0	0
TOT	96.72	97.27	96.86	95.91	94.55	94.32

ELECTRONIC APPENDIX 8 (next)

Eruption	Holocene - ENAB						
Unit	SC5D	SC5D	SC5D	SC5D	SC5D	SC5D	SC5D
MI Sample	SC5Dr1a	SC5Dr1aa	SC5Dr1b	SC5Dr1bb	SC5Dr1bbb	SC5Dr1c	SC5Dr3a
No.	47	49	Average	51	Average	Average	Average
SiO_2	41.41	43.62	42.59	41.45	42.25	42.29	46.40
TiO_2	0.89	0.99	0.95	0.89	0.98	1.00	1.43
Al_2O_3	17.44	20.53	19.64	17.23	19.83	20.21	19.64
FeO*	13.25	12.98	12.52	12.49	13.09	12.86	9.84
MnO	0.19	0.12	0.20	0.26	0.25	0.23	0.21
MgO	7.80	4.42	4.63	4.89	5.11	4.92	4.78
CaO	10.00	12.17	11.68	11.72	12.33	12.32	10.83
Na_2O	2.18	2.58	2.52	2.48	2.43	2.50	3.17
K_2O	0.38	0.38	0.40	0.36	0.37	0.34	1.15
P_2O_5	0.16	0.24	0.17	0.10	0.22	0.11	0.51
Cr_2O_3	0	0	0	0	0	0	0
NiO	0	0	0	0	0	0	0
TOT	93.70	98.03	95.28	91.86	96.85	96.79	97.97

ELECTRONIC APPENDIX 8 (next)

Eruption	Holocene BA- SC11D						
Unit	SC11D	SC11D	SC11D	SC11D	SC11D	SC11D	SC11D
MI Sample No.	SC11Dr1g 71	SC11Dr1h 67	SC11Dr1i Average	SC11D1a Average	SC11D2a Average	SC11Dr1b Average	SC11Dr1z Average
SiO_2	40.57	42.32	43.68	44.69	49.69	44.47	43.18
TiO_2	0.81	0.79	1.19	0.85	0.77	0.97	0.87
Al_2O_3	19.71	18.45	18.94	18.04	18.05	18.82	17.67
FeO*	11.19	12.08	12.19	11.42	9.51	12.10	11.67
MnO	0.28	0.07	0.20	0.21	0.13	0.24	0.29
MgO	4.16	4.38	4.23	5.41	3.18	4.34	5.83
CaO	11.19	12.35	12.80	11.62	11.02	12.22	11.71
Na_2O	2.45	2.58	2.36	2.20	2.48	2.61	2.38
K_2O	0.39	0.38	0.34	0.33	1.12	0.38	0.38
P_2O_5	0.22	0.20	0.16	0.09	0.30	0.13	0.30
Cr_2O_3	0	0	0	0	0	0	0
NiO	0	0	0	0	0	0	0
TOT	90.96	93.59	96.07	94.87	96.25	96.28	94.27

ELECTRONIC APPENDIX 9

Id Mount#1	Filename	STD Name	CO_2 (µg/g)	H_2O (wt%)	S (µg/g)	Cl (µg/g)
Standard fragment	**D30-1**					
SampleA_4		STD519_1	149	0	896	57
SampleA_15		STD519_2	157	0	876	54
SampleA_35		STD519_3	146	0	925	58
SampleB_59		STD519_12	182	0	850	52
		χ	158	0	887	55
		RSD	16	0	32	3
		Rel. Err. %	10	3	4	5
Standard fragment	**519-4-1**					
SampleA_3		STD D30_1	36	1	1359	657
SampleA_14		STD D30_2	36	1	1502	746
SampleA_34		STD D30_3	29	1	1346	693
SampleB_58		STD D30_12	42	2	1597	832
		χ	36	1	1451	732
		RSD	5	0	121	76
		Rel. Err. %	15	6	8	10

Id Mount#2	Filename	STD Name	CO_2 (µg/g)	H_2O (wt%)	S (µg/g)	Cl (µg/g)
Standard fragment	**D30-2**					
SampleB_3		STD519	158	0	1024	60
SampleB_20		STD519_2	150	0	876	46
SampleB_22		STD519_3	156	0	889	49
SampleB_36		STD519_4	165	0	944	50
		χ	157	0	933	51
		RSD	6	0	67	6
		Rel. Err. %	4	5	7	12
Standard fragment	**519-4-2**					
SampleB_1		STD D30_1	37	2	1665	847
SampleB_19		STD D30_2	38	1	1363	639
SampleB_21		STD D30_3	37	2	1641	821
SampleB_35		STD D30_4	35	2	1649	819
		χ	37	1	1579	782
		RSD	1	0	145	96
		Rel. Err. %	3	5	9	12

ELECTRONIC APPENDIX 10

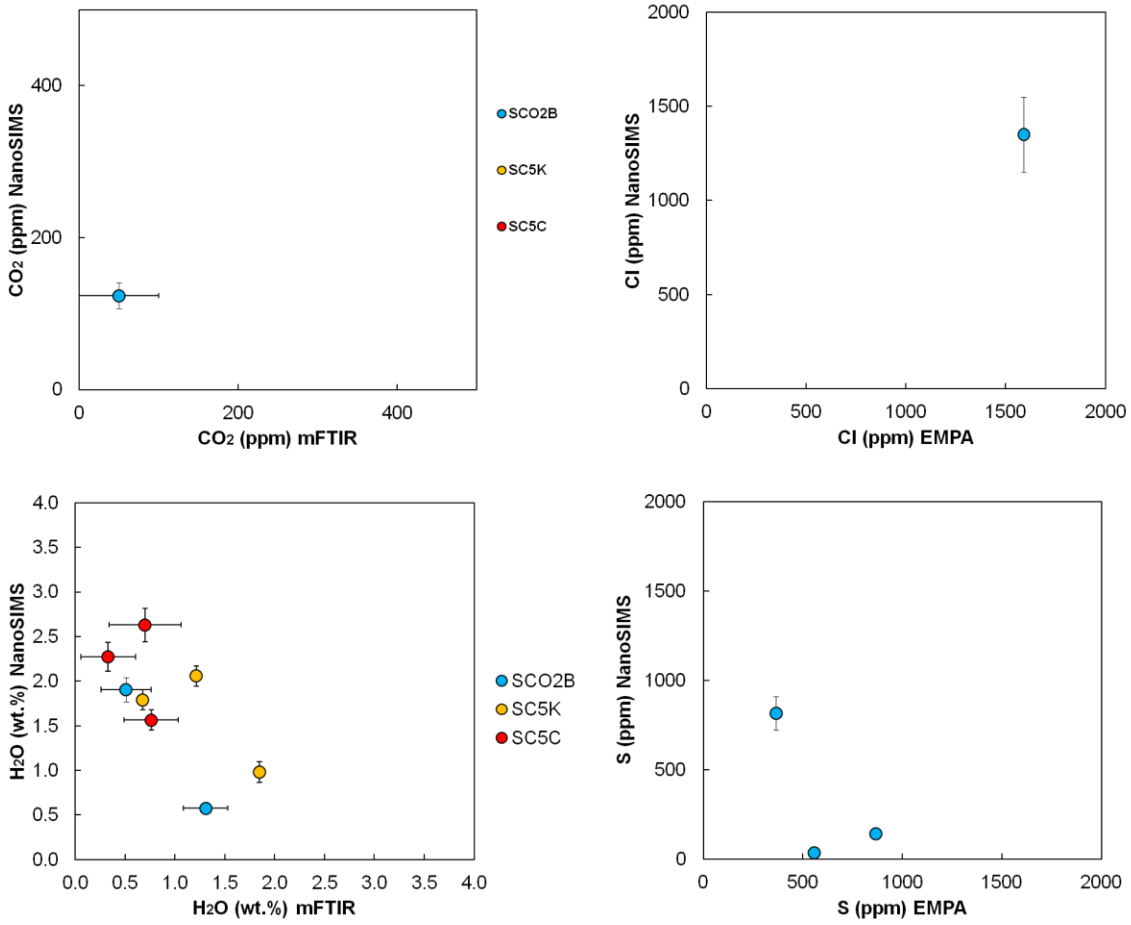

5.2 Publication n. 4

Robidoux, P., Aiuppa, A., Hauri, E., Rizzo, A., Lanzo, G., Rotolo, S., (2016). Geochemistry and petrology of magmas produced during explosive eruptions at Telica, Manuscript in preparation for *Lithos*

Robidoux, P., Aiuppa, A., Hauri, E., Rizzo, A., Lanzo, G., Rotolo, S., (2016). Geochemistry and petrology of magmas produced during explosive eruptions at Telica, Manuscript in preparation for *Lithos*

Abstract

Telica volcano, in north-west Nicaragua, is a young strato-volcano of intermediate magma composition producing frequent vulcanian to phreatic explosive eruptions. The volcano has increasingly been targeted by gas and geophysical observations in recent years, but additional investigation is required to better constrain the petrology of magmas. In the attempt to refine the current understanding of the plumbing system and magma characteristics, we report on major and volatile element compositions of melt inclusions trapped in olivine and pyroxene crystals from some stratigraphically significant tephra deposits of Telica. These deposits include the products of some important vulcanian eruptions (VEI > 2-3), such as the Scoria Telica Superior (STS) deposit (2000 – 200 yrs BP) and pyroclasts from the post-1970s eruptive period (1987; 2011). Based on NanoSIMS measurements, we show that olivine-hosted (Fo>80) glass inclusions (10 – 50 µm in size) fall into 2 distinct clusters: a group of H_2O-rich (1.8 – 5.2 wt.%) inclusions, similar to those of nearby Cerro Negro volcano, and a second group of CO_2-rich (360 – 1,700 ppm CO_2) inclusions, previously found only in few volcanic centers of the Central American Volcanic Arc (Nejapa, Granada). Based on model calculations, we find that CO_2 dominates the magmatic vapor phase at equilibrium with the majority of the inclusions (X_{CO2}> 62 - 95%). CO_2, sulfur (generally < 2,000 ppm) and H_2O are lost to the vapor phase during deep decompression (<400 MPa) and early crystallization of magmas. In contrast, chlorine exhibits a wide concentration range (400 – 2,300 ppm Cl) in primitive olivine-entrapped melts (likely suggesting variable contributions of salty slab-derived fluids), and is typically enriched in the most differentiated melts (1,000 – 3,000 ppm). In such low-pressure (<50-60 MPa) and volatile-poor (H_2O < 0.3 – 1.7 wt.%; CO_2< 23 – 308 ppm) conditions, recorded in glass inclusions, chlorine enrichment is often associated with inverse zonation in both pyroxenes (Mg# from 0.69 to 0.76) and plagioclases (An80 to An88), possibly indicating mixing during late fractional crystallization stages. By combining recently published reports on Telica volcanic gases with our EMPA results for S-Cl contents in matrix glasses/evolved pyroxene inclusions, we estimate vapor/melt partition coefficients for Cl and S of D_{Cl}= 0.2 to 2 and D_S= 4 to 6. We argue these coefficients are representative of the felsic (andesitic-dacitic) end-member melts of the recent (post 1980s) Telica activity. We also present new data of He-Ne-Ar isotopic compositions of fluid inclusions in the same suite of rocks to assess the origin of Telica magmas. According to $^3He/^4He$ measurements, the primitive liquids are formed at shallow depths (>19-34 km) and they show MORB-like characteristics ($^3He/^4He$ =7.39 – 7.57 Ra), similarly to the other volcanic centres of Nicaragua and to Central America Volcanic Arc (CAVA). Trace and Rare Earth (REE) elements indicate that original magmas derive from an heterogeneous mantle wedge, influenced to variable extents by distinct slab fluid components.

1. Introduction

Telica is one of the most active opent-vent degassing volcanoes of basaltic-andesite composition in the Central American Volcanic Arc (CAVA). Seismic and degassing activity have closely been examined,as the volcano recently (during the 2000s) entered a phase of intense

strombolian to vulcanian activity, and minor freatomagmatic events (Geirsson et al., 2013; Rodgers et al., 2015). Research (Navarro, 1994;Havlicek et al. 1999, 2000; Novák and Přichystal, 2006) indicates that a large-scale vulcanian eruption, larger in magnitude than those recently observed, would be expected to significant impact NW Nicaragua, claiming for improved volcanic hazard assessment studies.The last of such large scale events (Volcanic Explosive Index, VEI: 3-4) occured in 1529, but the only remaining deposit, clearly identified in the field, is attributed to the Scoria Telica Superior (STS), the youngest sequence of the Telica Superior Group (Hradecký et al., 2007).

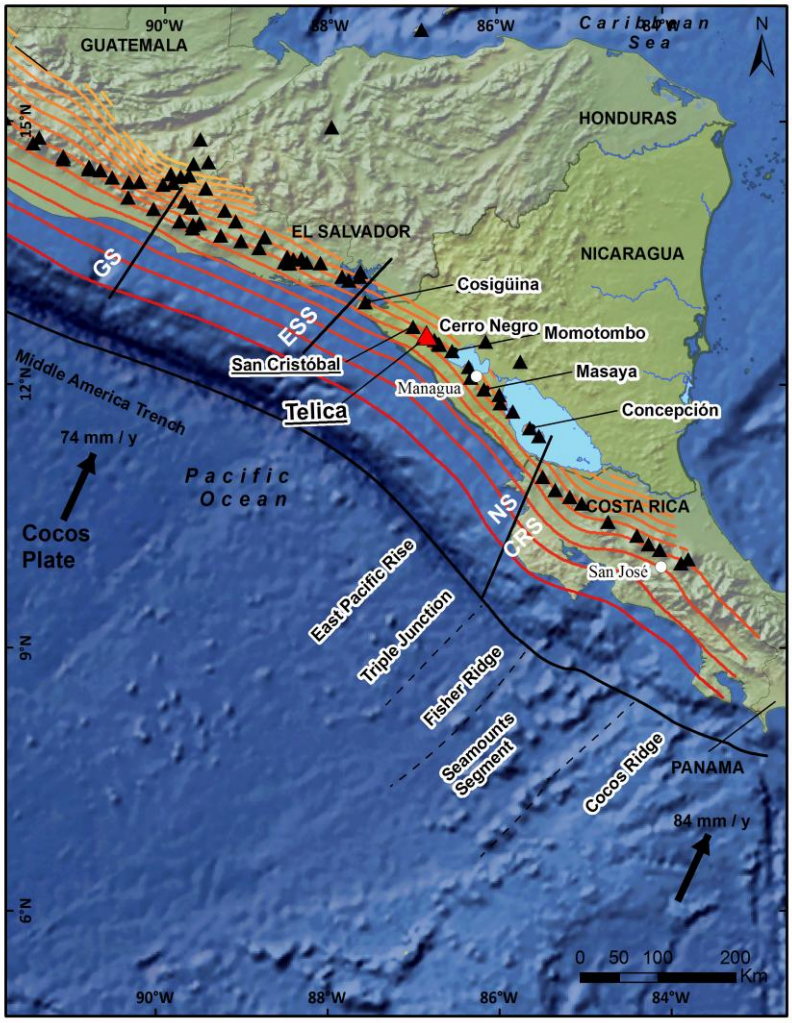

Figure 1 – Regional map of Central American Volcanic Arc (CAVA). a) Map of the subduction zone integrating arc segments from El Salvador (ESS), Nicaragua (NS) and Costa Rica (CRS). Arrows indicate the direction of motion of the Cocos Plate and the convergence velocities relative to the Caribbean Plate (in millimeters per year) after DeMets (2001). Topography effect is representing the 1:10m Natural Earth II with Shaded Relief and Water; file "CleanTOPO2" released by Smith and Sandwell in 1997 with contour shape files from ESRI and mapped with ArcGIS, Arc Map 10.1; World Map. Plate segments and trench structures are interpreted from the bathymetry imagery in Von Huene et al. (2000).

Regional geological mapping studies in the area were conducted by the Czech Geological Survey – CGS (Hradecký et al., 2007). Havlicek et al. (1999, 2000) examined stratigraphy and bulk rock compositions of Telica pyroclastic deposits. These studies allowed assessing the depositional areas of STS and post-1970s explosive activity, and identified the key compositional features of Telica magma (and older structures). Lava and scoria samples of different emission centers, all contemporaneous to the present-day Telica complex, helped defining the compositional range (from basaltic to basaltic andesite; Carr and Rose, 1987; Patino et al., 2000), while the regional study of Carr (1984) highlighted the peculiar geochemical (trace elements and REE) signature of Telica (and NW Nicaragua) magmas, relative to CAVA. More recently, Sadofsky et al. (2008) and Wehrmann et al. (2012, 2013) discussed regional patterns of major/trace/REE compositions and volatile abundances of CAVA melt inclusions, but included only one Telica sample in their datasets. Therefore, our current knowledge of pre-eruptive volatiles in Telica magmas is much uncompleted, and prevents us from obtaining a better understanding of the volcano's plumbing system.

Here, we present a first comprehensive melt-inclusion characterization of pre-eruptive volatiles in Telica magmas, which we use, in analogy with previous work (e.g. Roedder, 1979, 1984; Lowenstern, 1995; Sobolev, 1996; Frezzotti, 2001; Schiano, 2003; Cashman, 2004; Wallace, 2005; De Vivo and Bodnar, 2008; Métrich and Wallace, 2008; Blundy and Cashman, 2008) to probe the volcano's magmatic plumbing system.To this aim, we interpret volatile contents in melt inclusions based on results of equilibrium saturation models that reproduce numerically magmatic degassing trends, and therefore yield conditions of magma storage, ascent and decompression. These models are confined by, and complemented with, results of recent volcanic gas studies (Conde et al., 2014; Aiuppa et al., 2014). We also attempt at identifying the peculiarities in the magmatic source underneath Telica by comparing our derived ranges of volatile (H_2O, CO_2, S, Cl) contents in magmas with similar results obtained in other segments of the arc (Roggensack et al., 1997; Wade et al., 2006; Benjamin et al., 2007; Atlas, 2008; Sadofsky et al. 2008; Portnyagin et al., 2012 and Wehrmann et al. 2012). For recognizing sources and processes of magma generation beneath the volcano, major, trace and REE bulk rock compositions are also compared with those of other CAVA magmas. Conjointly, fluid inclusions (FI) from mineral separates are analyzed for their Ne-He and Ar noble gas isotopes to better trace the origin of fluids in magmas feeding the reservoir beneath Telica. Overall, our results contribute an inside look at the volatile evolution along the Telica deep to shallow plumbing system. We investigate, in particular, the processes responsible for triggering the large STS eruption, and attempt at determining what this eruption tells for interpreting the recent (historical to actual) evolution of volcanism at Telica.

2. Geological and volcanological background

2.1Telica volcano in the Central American Volcanic Arc (CAVA)

The Telica is a 1,061m.a.s.l. high basaltic-andesitic stratovolcano located at 12°60' lat. N. and 86°85' long. W. in the central part of the Cordillera Los Maribios, 20 km east of the Pacific Coast (Havlicek et al., 1999). This Cordillera is composed of a NW-SE-trending chain of volcanoes within the Nicaragua Depression, including (from NW to SE) Conseguina, San Cristóbal/Casita, Telica,La Rota, Cerro Negro, El Hoyo, Asososca and Momotombo (Mc Birney

and Williams, 1965; Walker et al., 2001). Like the majority of those neighborhood, Telica exhibits a typical strato-volcano shape and its summit (actually the highest point near the city of León) hosts a 250X150 m wide crater (Havlicek et al.,2000).

The Cordillera de Los Maribios extends along the Pacific coast line between Guatemala and Costa Rica, along a 1,100 km long corridor between latitude 10° and 15° (Fig 1). The volcanic arc is the result of the northeasterly Cocos Plate's subduction beneath the Caribbean Plate, with a rate of subduction ranging from 6 cm/yr off southern Guatemala to 9 cm/yr off southern Costa Rica (Demets, 2001).A series of NE-trending left-lateral strike–slip faults and deformation structures (Lafemina et al. 2002) are determined by oblique subduction of the Cocos plate against the Caribbean (DeMets et al., 2001). Slab dip measures 65-75 ° below the volcanic front (Syracuse and Abers, 2006;Auger et al., 2006; MacKenzie et al., 2008).In Nicaragua, crust thickness varies from 25 km beneath the volcanic front to 34 km inland. Thickness of the crust overlying the mantle wedge has been shown to control the extent of melting (Plank and Langmuir, 1998).

From Late Cretaceous to Holocene, magmatism in Nicaragua has occurred in two distinct regions, the volcanic front and the back-arc (Mc Birney and Williams, 1965). Throughout the Early and Middle Tertiary, volcanism migrated progressively from the Central Nicaraguan Highlands toward SW of the arc front (Mc Birney and Williams, 1965; Ehrenborg, 1996). The volcanic front is composed of Quaternary volcanoes of diverse morphology (complex composite volcanoes, calderas and numerous small cinder cones; Walker et al., 2001; Kutterolf et al., 2007). Holocene to Pleistocene back-arc volcanism mainly concentrates east of the volcanic front, along the Caribbean Sea lowlands in Honduras, Nicaragua, and Costa Rica (Patino et al., 2000; Carr et al., 2007).

2.2 The Telica Complex

Telica volcano is part of the Telica Complex,composed of a series of voluminous pyroclastic deposits and surrounded by extinct satellite cones from Plio-Pleistocene (Fig. 2). In a geo-chronological scale, the Telica Complex encloses the Group of Pre-Telica Caldera, the group of satellite volcanoes, and the Group of Telica (Havlicek et al., 2000).

The Pre-Telica Caldera Group (Neogene-Pleistocene) is probably covering parts of the Tamarindo volcanic Formation (14.7-11.7 Myrs),a narrow band of basaltic to andesitic lavas inter-layered with thick ignimbrite deposits and volcaniclastic sediments outcropping along Nicaragua's Pacific coast (McBirney and Williams, 1965; Plank et al., 2002; Saginor et al., 2011). The Pre-Telica Caldera Group represents a large caldera that originated blocky pyroclastic flows alternating with lava flows of andesite-basaltic composition (Havlicek et al., 2000). This Pre-Telica caldera is filled by deposits from detritic flows and andesitic lavas, and it is only possible to recognize its extension from the satellites volcanoes on its borders (Havlicek et al., 2000; Hradecký et al., 2007). These satellite cones are obviously younger and include Cerro Montoso, Cerro los Portillos, Cerro de Aguero, San Jacinto and Santa Clara (Hradecký et al., 2007).

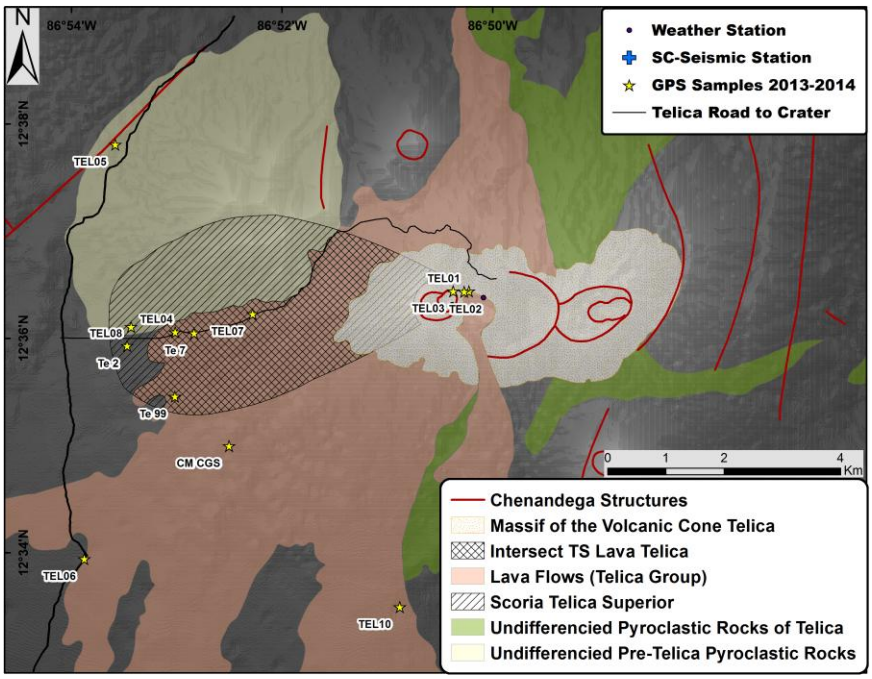

Figure 2 – Geological map of Telica. The main lithostratigraphy in the Telica area are shown based on the work of the Geological Tcheque Republic Survey (Hradecký et al., 2000) and digital topography effect (1:20m) and shapefile with the lines from the main Chenandega structures are provided by INETER (2014).

2.3 Group of Telica

According to Havlicek et al.(2000), the Group of Telica is composed of five sequences: the Scoria Telica Valles (STV), the Freatomagmatic Sequence (FS) (minimum age, 2150 +/- 150 yrs B.P.), the Scoria Najanjada Sequence (SNS), the Cañadas Sequence (CS) (younger than 2,300 yrs B.P.; Hradecký et al., 2000) and the Scoria Telica Superior (STS). The whole group is illustrated in figure 2. The group is dominated by thick scoria sequences (at least 23 m thick), covered by alluvial deposits, and inter-bedded with altered tuffs (e.g.,the Cañada Sequence), and thin altered scoria and block layers resulting from phreato-magmatic activity (Havlicek et al., 2000).

2.4 Scoria Telica superior (STS)

The most recent member of the Group of Telica is the Scoria Telica superior (STS), a deposit formed by vulcanian eruptive style covering the area between the summit Crater and Las Colimas (Fig. 2). STS is composed of six scoria layers separated by thin laminations of beige tuff, ranging in thickness from a few millimeters to centimeters. Depending on the locality, the basal sequence is overlying the Freatomagmatic Sequence (FS), the Scoria Najanjada Sequence (SNS), or the Cañadas Sequence (CS), with a sharp erosional contact. The deposit is therefore younger than 2,150 +/- 150 yrs B.P(the age of the FS deposit; Havlicek et al., 1999, 2000).

A basaltic aa-type lava flow covers the S and SE flanks of Telica for 4-5 km to cross highway No. 12 near the town of Telica (Havlicek et al., 2000). Although no age determination is available

for the lava itself, field evidence supports a time of emplacement contemporaneous to the STS (Havlicek et al., 2000; Novák and Přichystal, 2006).

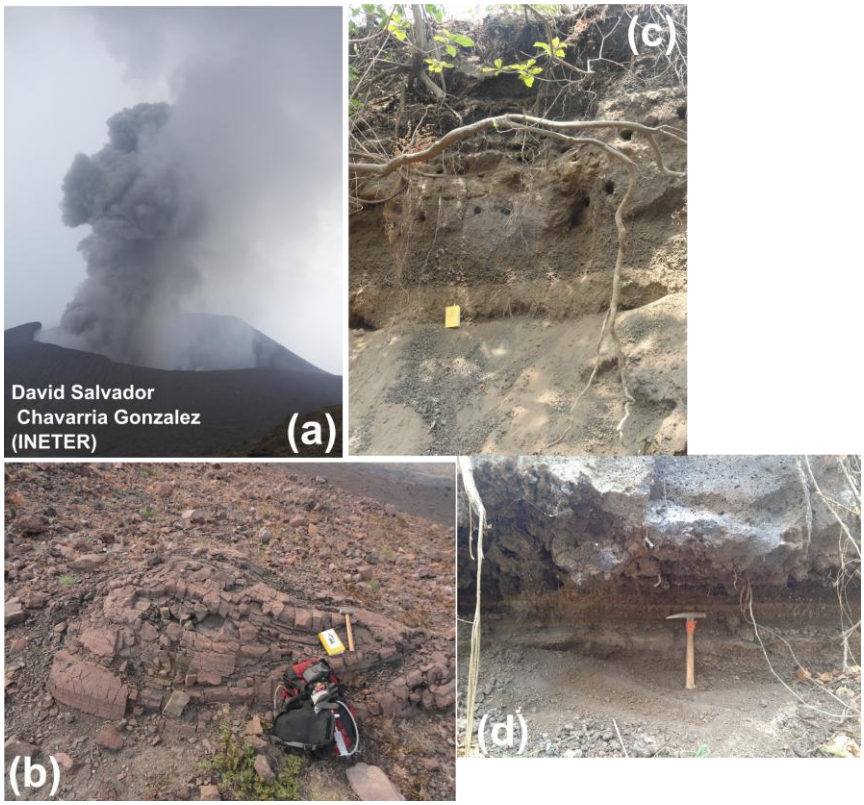

Figure 3 – Field photography. a) Phreatic eruption from a recent period of activity at Telica between May 15-21, 2011 (Photo Courtesy of D. Chavarria), b) Breadcrusted bomb from sample TEL02 emitted between February 12-20, 1982, c) Outcrop TEL04 from STS deposit, d) Outcrop TEL07 with lava flow from STS deposit.

2.5 Observed historical activity at Telica

At least 10 important eruptions of vulcanian/strombolian style have been recorded at Telica since 1527 (Novák and Přichystal, 2006). The 1982 eruption emitted a 3,7-4,3 km high column,and volcanic ash covered an area extending from León to Corinto (Navarro, 1994; Novák and Přichystal, 2006). The 1987 eruption impacted the western and northern flanks of Telica, where angular blocks of andesite-basaltic composition at least one meter in size were deposited (Novák and Přichystal, 2006). According to reports from Darmouth College geologists (cited in GVP, 2015) "*blocks and scoria 2-3 m in diameter were thrown over an area extending 200 m from the crater rim. The deposit was strongly inversely graded. Fresh bread-crusted scoria bombs up to 80 cm in diameter were widely scattered throughout the deposit*". Since 1987, several explosions of Volcanic Explosive Index (VEI) between 0 and 2 have occurred at the summit, with small to moderate phreatic explosions and increases of seismic activity (Rodgers et al., 2013, 2015; Geirsson et al. 2014).

3. Methodology

3.1 Field work

Since the 1990s, the majority of the eruptions have shown a phreato-magmatic character, and typically eject mixtures of juvenile and altered fine ashes that are frequently dispersed on the western, downwind side of the volcano (Fig. 3a). Frequently,coarse lithics fragments (blocks) are deposited on the crater area. Some of these lithic fragments, erupted during the Telica eruption(s) in 2011,were collected (samples TEL03A, TEL03B). Large bombs and lapilli-sized scoriae from the 12-20 February 1982 explosions probably represent the only remaining fresh juvenile materials from recent eruptive periods. Several of these bombs were sampled; TEL01 is an elliptic-shaped deformed bomb with dimensions of 82X52cm, with bread-crusted fractured layers aligned parallel to the long axis. TEL02 (Fig. 3b) has similar shape and structure,and impressive dimensions (392X195cm).

Rock samples were also taken from some of the most recent large-scale eruptions recorded in the stratigraphic sequence.Scoriae from the Scoria Telica Superior,STS (Group of Telica, GT), were collected at ~5.5 km west from the crater. STS is covered by a soil layer(Fig 3c), and is composed of layers of scoriae and tuff (Havlicek et al., 2000), these latter interpreted here as lahar deposits (given their resistant and compact nature, and the presence of small porous textures with frequent oxidized organic imprints and fossils). Depending on the locality, the thickness and presence of such reworked fluvial layers and lahars can vary. No charcoal or burned pieces of wood were found for dating, and attempts to date oxidized leaf imprints gave a minimum approximated limit corresponding to the 18^{th} century, at the top of the sequence (Figs. 4 a-b-c-d).

The stratigraphic section TEL04 (Fig. 3c) corresponds to pulses II to VI in the lithostratigraphic column STS «Telica Escoria Superior» of Havlicek et al. (1999)(see fig. 4d). At the bottom, TEL04B (Fig. 4c) corresponds to a finer section of the pulse no. II and it is made of coarse ashes with 3 thin ash layers. The STS section continues with a fluvial deposit eroding the top of TEL04C. This is followed by several reworked fine tuff layers, cutting off and separating several distinct layers of fine to coarse ash and lapilli-size scoriae. These tuffs, here interpreted as lahars, probably represent several single events or rainy seasons, and therefore make geochronology difficult to distinguish between each scoria layer (Fig. 4a).

In a different STS outcrop, ~4 km west from the crater of Telica, the aa lava flow unit from the same STS group is also encountered. This lava flow (sample TEL07E), clearly identified in GSC (1999), serves as the best stratigraphic marker of the entire sequence, because it shows a direct contact with pulse III from the STS scoriae. In our cross-section, the lava flow stops TEL07 (Fig. 3c),the upper stratigraphic marker for pulse no. III (Fig. 4). This section includes layer TEL07A, which is made of medium lapilli and coarse ashes (Bevacqua, 2014). The last studied layer is TEL04K and it corresponds to the pulse no. V among the whole STS sequence which is composed of coarse to medium lapilli and medium ashes.

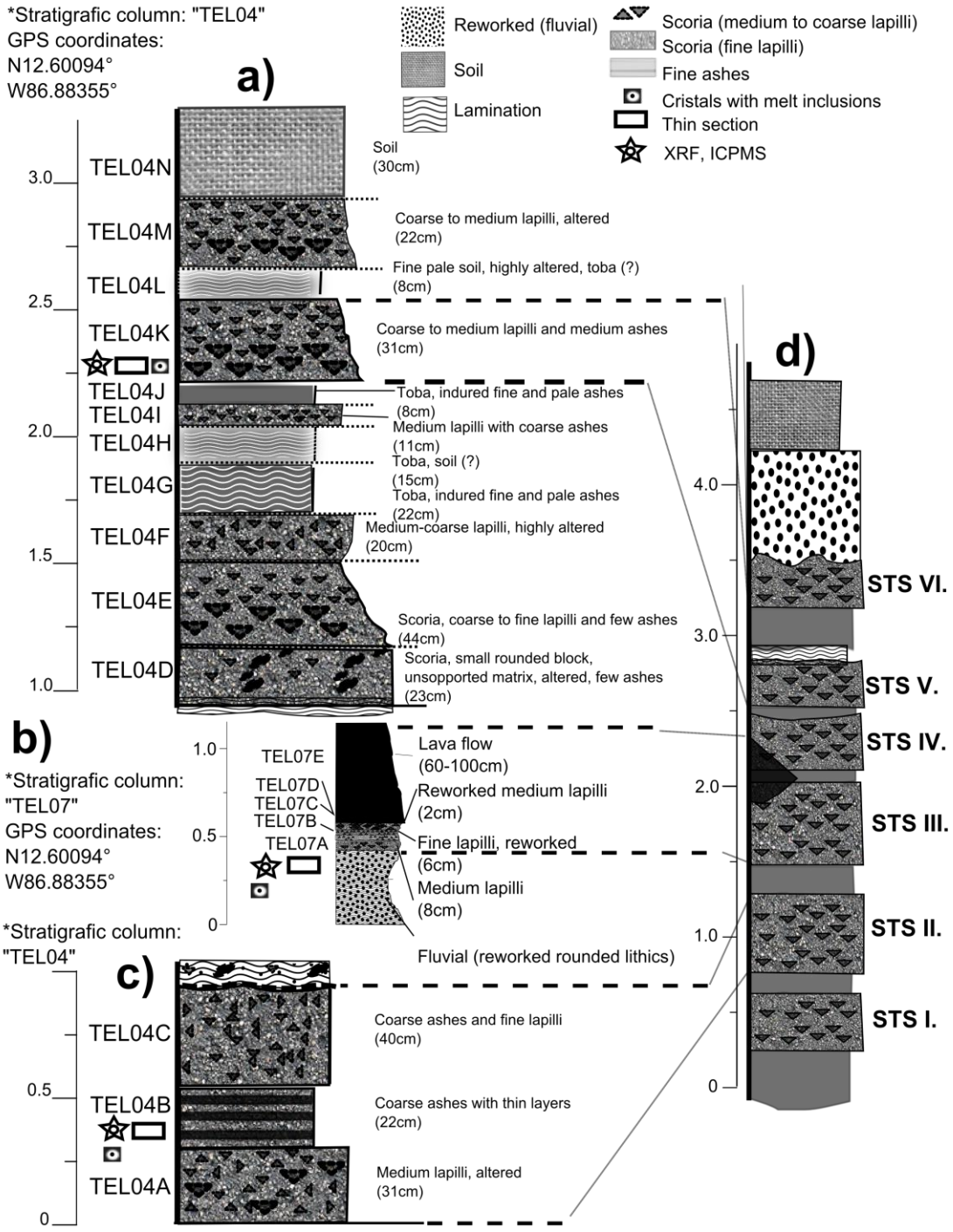

Figure 4 – Stratigraphic columns from STS deposits and selected layers for analysis. a) TEL04 (superior) that contains sample TEL04K, b) TEL04 (inferior) contains sample TEL04B, c) TEL07 contains samples TEL07A and TEL07E, d) Composite stratigraphic coloumn from Hradecký et al. (2000).

3.2 Petrography and mineral chemistry

Whole-rock major element compositions were determined by wavelength-dispersive X-ray fluorescence (WD-XRF) (Rigaku ZSX Primus) at DiSTeM (Table 1). The powder duplicate were analyzed for trace and REE with fusion ICP/MS (WRA4B2) at Ancaster (Actlabs: Code 4B2-Std).

Major elements, Cl, and S contents in glass inclusions, groundmass glasses and crystals were determined using aJXA-8200 WD/ED combined electron microprobe (EMPA; at INGV-Roma). The analytical conditions were 6.3 nA beam current, acceleration voltage of 15 kV, 5 μm beam diameter. Natural standards were used to calibrate quantitative analyses.

Table 2 lists average matrix glass compositions, while Table 3 presents EMPA compositions of 41 glass inclusions from 13 different olivine crystals and 20 clinopyroxenes. Additional 50 EMPA spots were performed on cores and rims from 18 olivines (core and rim) to determine their chemistry (Electronic Appendix 1). 27 spots on 17 clinopyroxenes were performed including SEM-EDS runs on sample TEL02 and TEL03A that were not studied for their inclusions, because mostly being crystallized (Electronic Appendix 2).

The compositions of glass inclusions in olivines were corrected for post-entrapment crystallization and for Fe-loss by using Petrolog3 code (Danyushevsky and Plechov, 2011). We used a Fe-Mg distribution coefficient between olivine and liquid ($K_D^{Fe\text{-}Mg}{}_{ol\text{-}liq}$) of 0.30 (Roedder and Emslie, 1970; Toplis, 2005). In this method, an olivine component is incrementally added at 0.01% steps until the melt inclusion reaches the equilibrium K_D value with the host olivine. The inclusions were preserved in moderate to Mg-rich olivines and all of them (17) had original FeO_T of <0.2– 2.8 %,,where FeO_T stands for total Iron (Fe^{2+} + Fe^{3+}). Those values were lower than the corresponding host rock, so they were also corrected for Fe-loss by using Petrolog3 (Fig. 5).

Material	Scoria	Scoria	Bomb	Bomb	Scoria	Scoria	Scoria	Scoria
Age	2011 - 2012	2011 - 2012	February 1982	February 1982	< 2,300 yrs BP	< 2,300 yrs BP	< 2,300 yrs BP	< 2,300 yrs BP
Sample	TELO3A	TELO3B	TELO1	TELO2	TELO4K	TEL 07E	TEL 07A	TELO4B
Long.	N12°36'26.4"	N12°36'26.4"	N12°36'26.3"	N12°36'26.3"	N12°36'03.4"	N12°01'28.2"	N12°01'28.2"	N12°36'03.4"
Lat.	W86°50'22.5"	W86°50'22.5"	W86°50'13.6"	W86°50'16.3"	W86°53'00.8"	W86°10'32.6"	W86°10'32.6"	W86°53'00.8"
SiO_2	56.11	56.95	54.90	53.50	51.45	49.58	49.63	53.61
TiO_2	0.66	0.65	0.76	0.74	0.78	1.60	0.87	0.71
Al_2O_3	16.39	16.43	17.19	17.65	16.92	16.57	17.74	17.08
Fe_2O_3	9.54	9.46	9.57	9.47	11.01	10.82	11.15	10.19
MnO	0.16	0.16	0.18	0.18	0.17	0.16	0.19	0.18
MgO	2.35	2.50	3.88	4.32	4.78	6.02	5.24	3.89
CaO	8.01	8.19	10.06	10.30	10.41	10.08	10.71	9.46
Na_2O	2.62	2.53	2.90	2.69	2.08	2.63	2.17	1.83
K_2O	1.38	1.36	1.03	0.95	0.93	0.82	0.81	0.82
P_2O_5	0.14	0.14	0.11	0.11	0.11	0.18	0.14	0.12
L.O.I.	0.72	0.76	0.78	0.72	0.60	0.00	0.00	2.70
Total	97.36	98.37	100.58	99.91	98.64	98.47	98.66	97.89
Mg# (FeOT)	0.33	0.34	0.45	0.47	0.46	0.52	0.48	0.43
V, ppm	269	278	296	300	302	270	349	255
Cr	< 20	20	40	< 20	20	130	< 20	40
Co	29	30	30	31	33	35	30	32
Ni	< 20	< 20	< 20	< 20	< 20	90	30	20
Cu	190	190	180	170	190	120	180	160
Zn	80	80	80	80	80	90	80	80
Ga	17	18	18	17	18	19	19	17
Rb	31	31	26	23	23	17	19	22
Sr	436	450	479	470	486	417	476	432
Y	21	21	20	19	19	19	18	18
Zr	88	89	73	69	68	85	59	67
Nb	3	3	3	2	2	9	1	2
Ba	884	881	742	707	681	430	614	673
La	8.9	8.4	6.9	7.1	6.9	6.7	5.7	5.9
Ce	18.6	17.8	14.8	15.2	14.9	14.7	12.6	12.9
Pr	2.66	2.62	2.25	2.29	2.24	2.28	2.02	1.99
Nd	12.3	12.3	10.9	10.8	10.8	11.8	9.9	9.6
Sm	3.4	3.4	2.9	3.1	3	3.6	2.9	2.7
Eu	0.95	0.95	0.91	0.96	0.98	1.2	0.83	0.8
Gd	3.4	3.3	3.4	3.1	3.2	3.8	3	3
Tb	0.6	0.6	0.6	0.6	0.6	0.7	0.6	0.6
Dy	3.8	4	3.6	3.7	3.6	3.8	3.3	3.5
Ho	0.8	0.8	0.7	0.7	0.7	0.7	0.7	0.7
Er	2.3	2.4	2.1	2.1	2.2	2	1.9	2
Tm	0.34	0.35	0.3	0.31	0.32	0.29	0.29	0.3
Yb	2.3	2.3	2	2.1	2.1	1.8	1.9	2
Lu	0.39	0.39	0.32	0.34	0.34	0.26	0.29	0.33
Hf	2.3	2.2	2	1.8	1.8	2.4	1.7	1.8
Ta	0.1	0.1	0.5	0.2	< 0.1	0.7	< 0.1	< 0.1
Pb	6	5	< 5	6	< 5	< 5	< 5	< 5
Th	1.7	1.8	1.4	1.4	1.3	0.8	1	1.3
U	1.4	1.5	1.1	1.1	1	0.7	0.9	1
Ba/La	99.3	104.9	107.5	99.6	98.7	64.2	107.7	114.1
U/Th	0.8	0.8	0.8	0.8	0.8	0.9	0.9	0.8
La/Yb	3.9	3.7	3.5	3.4	3.3	3.7	3.0	3.0

Table 1 - Bulk analysis of rock samples at Telica. Major elements analysis performed on the wavelength-dispersive Xray fluorescence (XRF) (Rigaku ZSX Primus) at DiSTeM (U. Palermo). Glass disks were prepared from 9:1 mixtures of Li-tetraborate and rock powder that had been heated and oxidized for determining loss on ignition (LOI). Mg# are calculated with MgO/(MgO+FeO)*100 from the bulk rock. Normalized «N» to primitive mantle trace and REE were calculated with Mc Donought (1995) and used as ratio.

Fe_2O_3 was calculated as total iron. LOI values are loss on ignition measurements at 1,100 °C for 1 h on replicate powders dried for 24 h at 110 C. These LOI values have not been corrected for oxygen uptake upon oxidation of Fe_2O_3 in the furnace. Trace elements analyses by ICP-MS were performed at ActLabs in Ancaster (Canada) with FUS-MS Code 4B2-Std (1-10) Trace Elements Fusion ICP/MS(WRA4B2).

No. Spot	SiO_2	TiO_2	Al_2O_3	FeO	MnO	MgO	CaO	Na_2O	K_2O	P_2O_5	Cr_2O_3	NiO	S	Cl	F	Total
	(wt.%)										(ppm)	(ppm)	(ppm)	(ppm)	(ppm)	(wt.%)
Frag. No.	Bulk matrix spots: TEL03Abulk															
1	61.34	1.16	13.93	9.43	0.18	0.53	3.26	3.91	3.45	0.54	0	0	140	2180		97.72
2	62.94	0.93	14.00	8.13	0.23	0.81	3.34	3.98	4.28	0.48	210	0	200	1630		99.13
3	62.16	0.87	13.59	8.37	0.13	0.70	3.42	4.25	3.57	0.47	340	640	164	1650		97.52
4	62.45	0.93	14.21	7.83	0.20	1.05	3.77	4.18	3.95	0.42	560	50	0	1750		98.99
5	62.30	0.87	14.01	8.24	0.12	0.75	3.53	4.04	3.52	0.37	0	860	8	2190		97.74
6	62.86	0.99	14.13	7.66	0.15	0.78	3.70	4.42	3.45	0.48	320	n.d.	0	1720		98.62
7	60.51	0.97	14.07	8.62	0.16	1.09	4.18	4.15	3.28	0.40	480	310	188	1720		97.42
8	62.91	0.97	13.37	8.12	0.17	2.00	3.97	3.64	4.09	0.41	0	440	0	1490		99.65
Average	**62.18**	**0.96**	**13.91**	**8.30**	**0.17**	**0.96**	**3.65**	**4.07**	**3.70**	**0.45**	**239**	**288**	**88**	**1791**		**98.40**
Stdev 1σ	**0.86**	**0.09**	**0.29**	**0.54**	**0.04**	**0.46**	**0.32**	**0.24**	**0.36**	**0.06**	**224**	**334**	**93**	**256**		**0.85**
Frag. No.	Olivine Border: TEL03B1glass															
1	52.223	0.334	2.572	9.457	0.286	14.701	18.36	0.34	0.013	0.026	150	350	749	250		98.31
Frag. No.	Olivine Border: TEL04Ko2glass															
1	51.63	2.02	15.90	10.67	0.17	4.32	8.04	2.96	1.45	0.31	n.d.	n.d.	164	730		97.46
2	51.64	2.00	15.54	10.37	0.17	3.99	8.23	2.98	1.42	0.33	n.d.	n.d.	296	760		96.66
Frag. No.	Olivine Border: TEL04K6oglass															
1	52.835	0.898	15.943	9.910	0.282	3.438	8.150	2.685	1.686	0.267	n.d.	n.d.	485	1620		96.09
Frag. No.	Olivine Border:TEL04K10cpxglass															
1	54.95	1.19	16.72	8.69	0.25	2.65	8.35	3.44	1.75	0.23	320	0	8	1430		98.22
Frag. No.	Olivine Border: TEL04K26oglass															
1	52.06	1.31	12.96	10.82	0.26	3.64	7.01	2.61	2.00	0.37	0	100	216	1530		93.02

Table 2 – Electron microprobe analyses of Telica matrix volcanic glass. Sulphur contents (ppm) are converted from original SO_3 (wt.%).

Inclusion Phenocryst	TEL04K20a	TEL04K6a	TEL04K8a	TEL04K8b	TEL04K9a	TEL04K9cI
Phenocryst chemistry (Fo)	_	-	-	-	-	-
Cpx (Ens)	75	73	72	72	75	69
Inclusion shape and size	s50X45	i65X53	e60X35	e50X30	e107X50	e90X45
Type	Fully enclosed	Fully enclosed	Fully enclosed	Fully enclosed	Fully enclosed	Fully enclosed
Bubble (vol %)	_	-	-	-	-	-
SiO_2	55.4	58.9	64.2	60.3	57.4	60.8
TiO_2	1.0	0.9	0.7	0.7	0.8	0.8
Al_2O_3	15.8	15.7	14.6	15.5	15.7	14.2
FeO*	10.8	9.2	6.2	8.0	9.3	8.7
MnO	0.2	0.1	0.2	0.2	0.3	0.2
MgO	4.2	3.0	1.8	2.3	3.6	2.9
CaO	7.6	6.8	4.5	5.3	6.9	6.6
Na_2O	3.0	2.8	3.4	3.4	3.5	3.2
K_2O	1.8	2.4	3.9	4.0	2.2	2.1
P_2O_5	0.2	0.2	0.4	0.3	0.3	0.3
Cr_2O_3	0.014	n.d.	n.d.	n.d.	0.004	n.d.
NiO	0.038	0.028	n.d.	n.d.	0.032	0.114
TOT	100	100	100	100	100	100
T (°C) by KP	1122	1093	1077	1085	1110	1098
H_2O (wt.%) nSIMS	1.37	1.68	0.62	0.00	0.98	0.00
CO_2 (ppm) nSIMS	n.d.	n.d.	n.d.	n.d.	n.d.	n.d.
S (ppm) EMPA	519	300	256	92	356	409
Cl (ppm) EMPA	1785	1960	2900	2320	2220	2070
Sat. Press. (Mpa) by PPL	140	26	167	-	12	-

Inclusion Phenocryst	TEL04K9d	TEL04K10a	TEL04K10b	TEL04K10c	TEL04K13a	TEL04K14b
Phenocryst chemistry (Fo)	-	-	-	-	-	-
Cpx (Ens)	71	70	69	76	73	67
Inclusion shape and size	e80X40	e100X50	e90X45	e85X35	e30X15	e50X25
Type	Fully enclosed	Fully enclosed	Fully enclosed	Fully enclosed	Fully enclosed	Fully enclosed
Bubble (vol %)	-	-	-	-	-	-
SiO_2	60.2	60.2	59.7	56.5	57.7	63.5
TiO_2	0.7	0.9	0.9	1.0	1.0	1.1
Al_2O_3	13.5	14.7	15.0	16.9	14.9	13.3
FeO*	10.5	8.9	8.8	9.8	10.1	7.9
MnO	0.4	0.2	0.2	0.2	0.2	0.2
MgO	3.0	2.4	2.6	3.7	3.1	1.8
CaO	6.9	5.6	5.6	7.0	6.9	5.1
Na_2O	2.7	3.5	3.7	2.8	3.8	3.4
K_2O	1.9	3.2	3.2	1.7	1.9	3.5
P_2O_5	0.2	0.4	0.4	0.2	0.3	0.3
Cr_2O_3	n.d.	0.013	0.016	n.d.	0.018	n.d.
NiO	n.d.	0.032	0.037	0.038	n.d.	0.021
TOT	100	100	100	100	100	100
T (°C) by KP	1086	1083	1090	1111	1089	1076
H_2O (wt.%) nSIMS	0.00	0.91	1.40	0.00	0.00	1.16
CO_2 (ppm) nSIMS	n.d.	n.d.	309*	n.d.	n.d.	n.d.
S (ppm) EMPA	445	46	176	705	102	n.d.
Cl (ppm) EMPA	2360	2490	2740	1950	2020	4135
Sat. Press. (Mpa) by PPL	-	11	179	-	-	-

Inclusion Phenocryst	TEL04K15a	TEL04K18c	TEL04K21aI	TEL04K22a	TEL04K22b	TEL04K25a
Phenocryst chemistry (Fo)	-	-	-	-	-	-
Cpx (Ens)	74	66	73	71	69	72
Inclusion shape and size	e60X35	e35X10	e35X15	i330X130	i110X50	e110X15
Type	Fully enclosed	Fully enclosed	Fully enclosed	Fully enclosed	Fully enclosed	Fully enclosed
Bubble (vol %)	-	-	-	-	-	-
SiO_2	60.5	63.7	57.3	59.4	59.7	62.3
TiO_2	0.7	0.7	1.1	0.8	0.7	0.8
Al_2O_3	15.1	13.0	15.2	15.4	14.8	15.3
FeO*	8.1	8.7	10.6	8.8	9.2	7.1
MnO	0.2	0.2	0.3	0.2	0.2	0.0
MgO	3.3	2.4	3.2	3.6	3.4	2.2
CaO	5.8	4.7	6.2	6.0	6.1	5.1
Na_2O	3.5	3.6	3.5	3.2	3.3	3.2
K_2O	2.4	2.8	2.3	2.4	2.3	3.7
P_2O_5	0.3	0.3	0.3	0.2	0.3	0.4
Cr_2O_3	0.016	n.d.	n.d.	0.024	0.023	0.044
NiO	0.021	0.026	n.d.	0.011	0.057	n.d.
TOT	100	100	100	100	100	100
T (°C) by KP	1104	1087	1099	1109	1106	1084
H_2O (wt.%) nSIMS	1.72	0.00	0.00	0.95	0.00	1.09
CO_2 (ppm) nSIMS	n.d.	n.d.	n.d.	n.d.	n.d.	n.d.
S (ppm) EMPA	344	110	421	340	344	0
Cl (ppm) EMPA	2595	1925	2410	2175	2130	2580
Sat. Press. (Mpa) by PPL	166	-	-	13	-	16

Inclusion Phenocryst	TEL04K25b	TEL04K18a	TEL03B1	TEL01	TEL01b	TEL01c
Phenocryst chemistry (Fo)	-	-	-	-	-	-
Cpx (Ens)	71	64	74	74.3	70.9	70.9
Inclusion shape and size	e80X20	e42X15	i90X50	i130X30	i«?»	i«?»
Type	Fully enclosed	Fully enclosed	Fully enclosed	Fully enclosed	reentrant	reentrant
Bubble (vol %)	-	-	-	-	-	-
SiO_2	61.0	66.1	65.6	60.72	59.13	68.80
TiO_2	0.5	0.6	1.0	0.94	0.85	0.75
Al_2O_3	17.7	13.1	15.7	16.42	12.94	15.41
FeO*	6.0	7.4	4.2	6.35	9.93	2.99
MnO	0.1	0.2	0.1	0.24	0.21	0.08
MgO	2.1	1.5	1.1	2.68	4.19	1.26
CaO	6.2	3.7	2.4	6.65	7.18	3.89
Na_2O	3.2	3.3	4.2	3.43	3.15	3.70
K_2O	2.8	3.8	5.0	2.26	2.23	2.85
P_2O_5	0.3	0.2	0.5	0.30	0.18	0.26
Cr_2O_3	0.004	0.007	n.d.	n.d.	n.d.	n.d.
NiO	0.013	0.034	0.026	n.d.	n.d.	n.d.
TOT	100	100	100	100	100	100
T (°C) by KP	1084	1070	1054	1139	1131	1130
H_2O (wt.%) nSIMS	0.00	1.73	0.00	0.25	0.46	n.d.
CO_2 (ppm) nSIMS	n.d.	102*	n.d.	65	17	n.d.
S (ppm) EMPA	0	72	695	332	2079	136
Cl (ppm) EMPA	2210	2840	4280	621	2215	-
Sat. Press. (Mpa) by PPL	-	279	-	29	132	-

Inclusion Phenocryst	TEL04K26a	TEL04ko1a	TEL04ko2a	TEL04ko2b	TEL04ko2c	TEL04kol4a
Phenocryst chemistry (Fo)	84	80.1	82.1	82.5	82.6	84.9
Cpx (Ens)	-	-	-	-	-	-
Inclusion shape and size	i45X20	e150X120	s35X30	s30X25	s25X20	e30X25
Type	Fully enclosed	Fully enclosed	Fully enclosed	Fully enclosed	Fully enclosed	Fully enclosed
Bubble (vol %)	-	5, 12, 12	-	-	10.0	-
SiO_2	52.7	47.96	50.81	52.17	52.21	47.12
TiO_2	2.1	0.82	2.37	2.62	2.25	0.69
Al_2O_3	17.0	16.69	18.76	20.38	20.04	18.26
FeO*	11.5	12.10	7.19	4.94	5.03	11.23
MnO	0.2	0.21	0.16	0.13	0.07	0.17
MgO	5.0	6.92	4.58	2.94	3.35	8.71
CaO	10.8	12.68	12.45	13.14	13.04	11.17
Na_2O	3.5	2.24	2.97	2.89	3.12	2.13
K_2O	0.9	0.34	0.55	0.60	0.69	0.40
P_2O_5	0.3	0.04	0.17	0.18	0.21	0.12
Cr_2O_3	0.1	n.d.	n.d.	n.d.	n.d.	n.d.
NiO	0.013	n.d.	n.d.	n.d.	n.d.	n.d.
TOT	100.0	100	100	100	100	100
T (°C) by KP	1132.0	1165	1155	1090	1101	1267
H_2O (wt.%) nSIMS	1.0	4.10	1.73	1.87	1.72	-
CO_2 (ppm) nSIMS	n.d.	36	1584	1642	1359	-
S (ppm) EMPA	941	2368	1223	1245	1254	810
Cl (ppm) EMPA	560	1844	468	484	489	1540
Sat. Press. (Mpa) by PPL	14	1031	1667	1307	1113	-

Inclusion Phenocryst	TEL04kol5a	TEL04kol6a	TEL04kol8a	TEL04b	TEL04b2a	TEL04b2b
Phenocryst chemistry (Fo)	81.1	68.5	81.4	85.2	85.5	85.1
Cpx (Ens)	-	-	-	-	-	
Inclusion shape and size	e50X35	e35X30	i210X140	s40X40	s130X125	s130X125
Type	Fully enclosed	Fully enclosed	Reentrant	Fully enclosed	Fully enclosed	Fully enclosed
Bubble (vol %)	-	-	-	9.0	9.0	-
SiO_2	47.50	50.55	46.72	47.22	50.91	49.61
TiO_2	0.87	0.86	0.77	0.50	0.54	0.67
Al_2O_3	19.65	20.44	18.73	17.79	16.39	16.70
FeO*	9.35	9.65	10.71	10.96	9.30	10.06
MnO	0.22	0.12	0.21	0.21	0.15	0.20
MgO	5.56	3.19	6.48	8.90	7.96	8.32
CaO	13.78	11.92	13.69	12.45	12.45	12.27
Na_2O	2.53	2.61	2.15	1.59	1.91	1.80
K_2O	0.38	0.55	0.43	0.28	0.29	0.28
P_2O_5	0.16	0.11	0.10	0.10	0.09	0.08
Cr_2O_3	n.d.	n.d.	n.d.	n.d.	n.d.	n.d.
NiO	n.d.	n.d.	n.d.	n.d.	n.d.	n.d.
TOT	100	100	100	100	100	100
T (°C) by KP	1187	1117	1212	1231	1270	1279
H_2O (wt.%) nSIMS	-	-	-	5.22	-	-
CO_2 (ppm) nSIMS	-	-	-	360	-	-
S (ppm) EMPA	1060	700	1050	1020	865	865
Cl (ppm) EMPA	1906	1234	1825	1450	1542	1133
Sat. Press. (Mpa) by PPL	-	-	-	1980	-	-

Inclusion Phenocryst	TEL04b2c	TEL04b2d	TEL04b3a	TEL04b5a	TEL04b8a	TEL04b8b
Phenocryst chemistry (Fo)	85.1	84.7	84.3	80.7	84.0	84.3
Cpx (Ens)			-	-	-	-
Inclusion shape and size	s135X130	s130X125	s70X70	s90X90	e50X40	e45X40
Type	Fully enclosed	Fully enclosed	Fully enclosed	Fully enclosed	Fully enclosed	Fully enclosed
Bubble (vol %)	-	11.0	?	?	?	10.0
SiO_2	48.95	48.27	48.40	48.90	48.94	48.05
TiO_2	0.64	0.57	0.70	0.71	0.58	0.61
Al_2O_3	17.37	19.27	17.32	17.82	19.15	19.18
FeO*	10.21	10.14	11.51	10.90	10.05	10.44
MnO	0.19	0.27	0.24	0.18	0.15	0.29
MgO	8.40	8.07	8.91	6.66	7.65	8.06
CaO	12.15	11.42	10.68	12.36	11.32	11.28
Na_2O	1.73	1.69	1.96	2.11	1.86	1.83
K_2O	0.27	0.28	0.26	0.28	0.24	0.23
P_2O_5	0.09	0.03	0.03	0.08	0.06	0.05
Cr_2O_3	n.d.	n.d.	n.d.	n.d.	n.d.	n.d.
NiO	n.d.	n.d.	n.d.	n.d.	n.d.	n.d.
TOT	100	100	100	100	100	100
T (°C) by KP	1281	1273	1297	1243	1264	1274
H_2O (wt.%) nSIMS	-	-	-	-	-	-
CO_2 (ppm) nSIMS	-	-	-	-	-	-
S (ppm) EMPA	895	780	950	990	985	870
Cl (ppm) EMPA	875	1754	1622	1426	1332	1039
Sat. Press. (Mpa) by PPL	-	-	-	-	-	-

Inclusion Phenocryst	t4bcpx6oa	t4bcpx6ob	t4bpx6a	t4bpx6a	t4bpx6a2
Phenocryst chemistry (Fo)	-	-	-	-	-
Cpx (Ens)	71.1	71.1	74.0	74.0	74.0
Inclusion shape and size	e60X45	e55X40	e45X35	e45X35	e50X40
Type	Fully enclosed	Fully enclosed	Fully enclosed	Fully enclosed	Fully enclosed
Bubble (vol %)	-	-	-	-	-
SiO_2	56.82	56.19	58.55	56.72	58.78
TiO_2	0.75	1.03	0.73	0.89	0.81
Al_2O_3	14.18	14.68	13.97	13.13	15.02
FeO*	11.31	10.59	9.35	11.43	8.45
MnO	0.20	0.26	0.26	0.28	0.12
MgO	4.05	3.79	3.87	4.73	3.50
CaO	7.84	8.57	7.07	8.48	6.78
Na_2O	2.88	2.86	3.26	3.33	3.53
K_2O	1.76	1.85	2.54	0.83	2.71
P_2O_5	0.21	0.17	0.39	0.18	0.32
Cr_2O_3	n.d.	n.d.	n.d.	n.d.	n.d.
NiO	n.d.	n.d.	n.d.	n.d.	n.d.
TOT	100	100	100	100	100
T (°C) by KP	1141	1138	1141	1141	1141
H_2O (wt.%) nSIMS	-	-	-	-	-
CO_2 (ppm) nSIMS	-	-	-	-	-
S (ppm) EMPA	292	425	621	977	196
Cl (ppm) EMPA	1700	1760	2220	1285	2440
Sat. Press. (Mpa) by PPL	-	-	-	-	-

Table 3 – Electron microprobe analyses of San Cristóbalglass inclusions. Sulphur contents (ppm) are converted from original SO_3 (wt.%).The chemical composition was corrected for post-entrapment effects PEC by using Petrolog3 (Danyushevsky and Plechov, 2011). The major element composition was recalculated on a volatile free basis. FeO*, total FeO.Chemical composition from host phenocrystsare the closest analyzed spot to the MIs and they are written with Fo, forsterite content (mol %) in the olivine and Ens, for magnesium number of clinopyroxenes calculated with model of Morimoto M. (1988). Saturation pressuresin megapascals(MPa) by «PPL» are calculated from H_2O and CO_2 contents of the melt inclusions using the solubility model of Papale et al. (2006). An online version of the Papale's solubility model (http://ctserver.ofmresearch.org/Papale/Papale.php) was used for these calculations and compared with' thermobarometer of hydrous clinopyroxene-liquid ±150 MPausing equation (32c) by «KP»Putirka (2008) from spreadsheet of Putirka (2005) for conditions of K_D(Fe-Mg)cpx-liq=0.27±0.03. Inclusion shapes are resumed as ''s'', spherical shape; ''e'', elliptical shape; ''I'', irregular shape. ''A'' is for assemblage order among other inclusions assemblage found in the same crystal.

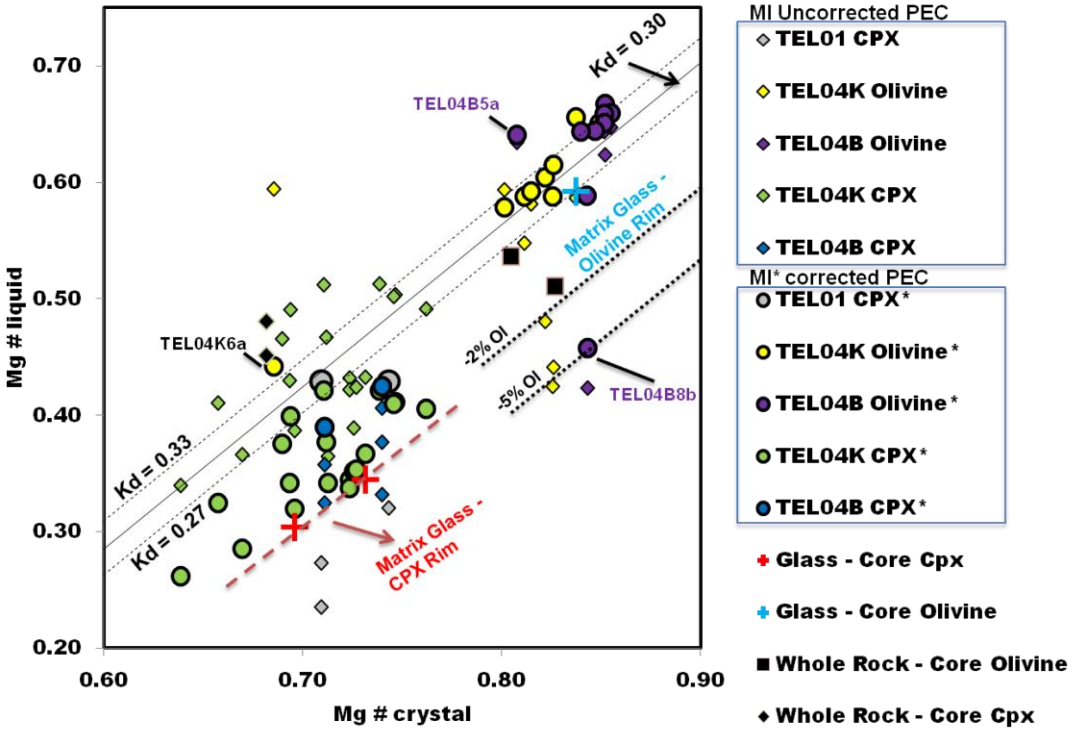

Figure 5 – Relationships between Mg# liquid and Mg# from crystals. Solid lines correspond to constant distribution coefficients of KD = 0.3. FeOT and MgO between olivine and melt (Kd= [FeO/X MgO] Xtal/[MgO/FeOT]Melt, where FeOT is total Fe in melt expressed as FeO) and were calculated:

$$XMgO_{melt} = \frac{{MgO_{Xtal}}/{40.32\ g/mol} \Big/ {FeO_{melt}}/{71.85\ g/mol}}{{MgO_{melt}}/{40.32\ g/mol}}$$

Lines were calculated for Ni-NiO = 0 and for different KD values; 0.27, 0.30, 0.33. The oxidation state of Telica melts is assumed in this work to correspond to Ni-NiO buffer and temperature calculated from Sugawara (2000). PEC corrections depended on a Fe2+/Fe3+ ratio based on model of Kilinc et al. (1983) whih was attributed for each inclusion depending on the average Fe2+/Fe3+ ratio of the corresponding layer Dotted lines denote deviation from equilibria of melt inclusions crystallized 2 and 5% of olivine after entrapment (corrected for Fe^{2+} for olivines while pyroxenes are corrected for Kd with total iron species). 3 samples of inclusion-olivine pairs show important deviation from equilibria with olivine for the majority of inclusions (TEL04Bol5a; TEL04Bol8b; TEL04Kol6a).

The inclusions were also preserved in moderate to Fe-rich clinopyroxenes. Several (15/31) inclusions had FeO_T >0.1 – 2.4 %, or higher than their host rocks, while the rest (16/31) had FeO_T< 0.1 – 7.5 %. Similarly, melt inclusions hosted in clinoyroxene phenocrysts were corrected for post-entrapment crystallization, adding cpx component to the melt inclusions until the

equilibrium $K_D^{Fe\text{-}Mg}{}_{cpx\text{-}liq}$ (0.26) was reached. An average Fe^{3+}/Fe^{2+} in the melt was attributed to each layer in which the crystal was found, by using the model of Kilinc et al. (1983) (Fig. 5).

3.3 Volatile contents in glass inclusions

Carbon and water in double-faced polished glass inclusions > 20-30 µm in size were analyzed (at DiSTeM) by micro Fourier transform IR spectroscopy (mFTIR) using a Hyperion 1000/2000 microscope (Bruker), equipped with a Tensor 27 IR source (Bruker), an MCT detector cooled with N_2 and a KBr glass beamsplitter. The clean and dry air from the bench and microscope was constantly purged with a CO2RP015 CO_2 remover/air dryer with maximum outlet flow rate of 1.5 L/min. The absorbance spectrums were corrected for the atmospheric CO_2 peak interference if necessary (2,350 cm^{-1}).

Concentrations of H_2O and CO_2 were determined from the Beer-Lambert law. Water concentrations, listed in Table 4, were obtained from the 3,550 cm^{-1}, absorption band, taking a molar absorption coefficient $\varepsilon = 63 \pm 3$ L/mol cm (Dobson, D. et al., unpublished data, cited by Dixon et al., 1995). .The average first standard deviation uncertainty (1σ) in total H_2O concentrations,was estimated at ±0.3 wt.%. Carbon dioxide concentrations were determined by measuring the doublet of CO_3^{2-} at 1,515 and 1,435 cm^{-1} with a background subtraction procedure similar to Newman and Stolper (2000) and Roberge et al. (2005). The absorption coefficient ε (1,515 cm^{-1}) was calculated using the equation $\varepsilon_{1525} = 451 - 342$ (Na/Ca+Na), according to Dixon and Pan (1995). Values ranged between 353 and 393 L/molcm for basaltic andesite glass inclusions in clinopyroxenes of TEL04K, and 401 L/molcmin the basaltic inclusions from olivines in TEL04K26. The double peak of CO_3^{2-} was quantified only in 3 over 5 detected carbonate peaks, because of large estimated uncertainty (Table 5). Density were calculated for each inclusion by using the model of Ochs and Lange (1999).

CO_2, H_2O, S and Cl concentrations were also determined using a Cameca NanoSIMS 50/50L ion probe at the Carnegie Institution of Science. The polished crystals and standard samples were pressed into indium inside 25 mm diameter Al-metal disks mounts, adopting the procedure of Hauri et al. (2002). Samples and standards were analyzed in a vacuum chamber (pressure of $< 5 \cdot 10^{-9}$ Torr). A primary voltage of ~8 kV was applied to the primary $^{133}Cs^+$ source. Measurements were realized using a pre-sputtering time of 180 s using a 20X20 μm^2 beam and a 3.8 to 10 µm squared aperture window (depending on inclusion surface). The NanoSIMS was calibrated using a set of natural basaltic and andesitic glasses: 1654, 1833-11, 1833-1, 1846-12, 519, A288opx, CM58ol, GRR1012ol, Herasil, IndiaEn, KBH-1opx, KenyaEn, KLV-23ol, ROM177ol, ROM250-13ol, ROM250-2ol, ROM273opx, WOK28-3 (Hauri et al., 2002, 2006; E. Hauri, pers. comm.). To quantify the volatile element concentrations, intensities of the secondary ions $^1H^-$, $^{12}C^-$, $^{32}S^-$, $^{35}Cl^-$ were measured and normalized to the intensity of $^{28}Si^-$ (Robidoux et al., 2016). Two main reference materials (D30-1, 519, in Fine and Stolper, 1986 and Hauri et al., 2002) were measured two to three time per day during the 4 days of analytical runs,yielding a repeatability of 7.2 % (D30-1, 1σ, N=8) and 9.1 % (519, 1σ, N=8) for CO_2. For CO_2, H_2O, S and Cl, the relative errors are estimated at respectively 13.8 %, 7.1%, 11.4% and 14.8% (Table 6).

Samples	Thickness (µm)	Density (g/L)	Molecular H2O 3,550 cm-1			Molecular H2O 1,635 cm-1		
			Abs.	H2O (wt%)	1 σ (wt%)	Abs.	H2O (wt%)	1 σ (wt%)
TEL04K								
TELO4K5a	54	2.552	0.244	0.5	0.2	0.070	0.3	0.4
TELO4K6a	23	2.515	0.343	1.7	0.4	0.097	1.1	0.4
TELO4K8a	44	2.478	0.239	1.0	0.3	0.055	0.3	0.2
TELO4K9a	33	2.556	0.292	1.0	0.3	0.097	0.8	-
TELO4K9b	33	2.552	0.281	0.9	0.3	-	-	-
TELO4K10a	54	2.528	0.500	0.9	0.2	0.076	0.3	0.2
TELO4K10b	54	2.546	0.277	0.8	0.3	0.048	0.2	0.1
TELO4K14a	28	2.552	0.153	0.6	0.3	-	-	-
TELO4K15a	30	2.479	0.453	1.7	0.4	0.065	0.6	0.3
TELO4K18a	22	2.442	0.252	1.3	0.4	0.080	1.0	0.4
TELO4K18b	22	2.552	0.381	1.9	0.4	0.080	0.9	0.5
TELO4K20a	22	2.566	0.272	1.4	0.4	-	-	-
TELO4K22a	34	2.541	0.289	0.9	0.3	0.071	0.5	0.2
TELO4K25a	57	2.479	0.542	1.1	0.2	0.135	0.6	0.2
TELO4K26a	28	2.653	0.271	1.0	0.3	0.056	0.5	-
TEL07A								
TEL07APXB	41	2.593	0.395	1.1	0.2	0.117	0.7	0.2
TEL07APX1	18	2.593	0.261	1.6	0.5	0.068	1.0	0.5
TEL07APX1bis	18	2.593	0.295	1.8	0.5	0.089	1.2	0.5
TEL07APX3	36	2.593	0.365	1.1	0.2	0.096	0.7	0.2

Table 4– Fourier transform infrared spectroscopic data for H_2O in Telica glass inclusions. The absorbtion values were measured with OPUS programs, but recertified with OriginPro 8 after a complete baseline correction of the spectrum by using the curve fitting data analysis program fityk 0.9.8 with absorbance uncertainty of ±0.1.The uncertainty for thickness has great influence on the water content (± 0.2 wt.%.) compare to their molar absorption coefficient (± 0.06 wt.%) and their density (± 0.04 wt.%). Direct thickness measurement estimated with the digital displacement gauges by measuring the vertical displacement between the focused surfaces of the wafer and this procedure was repeated 3 times. Crystal samples of various size/ thickness were selected because they were subject to various errors reproduction. They were put on mFTIR stage for a second run by using another Hyperion BrukermFTIR spectrometer at Laboratorio de fluidoscorticales, Centro de Geociencias Campus Juriquilla (México). The second spectrometer permitted to use the Interference fringes method from Nichols and Wysoczanski (2007), because of the possibility to test the reflectance mode with a pure golden plate background (Wysoczanski and Tani, 2006). The thicknesses determined by this method agreewith an average error of 12 % (6 µm) for the selected samples estimated with digital displacement gauges.

Samples	Thickness	Density	CO_3^{2-}		CO_2	
	(µm)	(g/L)	1,435 cm^{-1}	1,515 cm-1	Avg.	1 σ
TEL04K			**Abs.**	**Abs.**	**(ppm)**	**(ppm)**
TELO4K8a	44	2.478	0.027	0.053	bdl	-
TELO4K9b	33	2.552	0.084	0.012	167	112
TELO4K10b	62	2.546	0.025	0.073	554	79
TELO4K18a	22	2.442	0.010	0.023	356	255
TELO4K18b	22	2.552	0.027	0.037	701	384

Table 5 – Fourier transform infrared spectroscopic data for CO_2 in Telicaglass inclusions. See Table 5 for H_2Oabsorbtion values. CO_2 in mid-IR is assumed to be the average of both1,435 cm^{-1} and 1,515 cm^{-1} peak absorbencies.The average uncertainty for the reproducibility of the CO_3^{2-} absorbance in the 12 detected peaks can change the concentration by ± 44 ppm and the uncertainty for thickness by ± 86 ppm when using Beer-Lambert Law. Uncertainty in the absorption coefficient ε(± 3 ppm) and density (± 5 ppm) are playing a less important role.

Inclusion (NanoSIMS #)	CO_2 (µg/g)	H_2O (wt%)	S (µg/g)	Cl (µg/g)
TEL01 (Cpx)				
TEL01a	65	0.25	621	3540
TEL01b	17	0.46	2215	2677
TEL04K (Cpx)				
TEL04K10b	309	1.40	185	3180
TEL04K18a	102	1.73	82	2626
TEL04K9I*	1211	2.01	305	2139
TEL04K9II	80	1.88	293	2116
TEL04K14try	24	1.16	102	2576
TEL04K14tryb	21	0.67	45	1634
TEL04K18z	5	0.25	64	192
TEL04K (Ol)				
TEL04Ko1	36	4.07	2368	1844
TEL04Ko2a	1584	1.64	1223	468
TEL04Ko2b	1642	1.66	1245	484
TEL04Ko2c	1359	1.58	1254	489
TEL04Ko3a	334	1.80	1985	1375
TEL07 (Cpx)				
TEL07PXB	98	1.26	82	2535
TEL07APXiG2	56	0.95	59	2781
TEL04B (Ol)				
TEL04B2a	360	5.22	1513	1442
TEL04B2aII	329	4.80	1354	1281
TEL04B2	353	4.96	1464	1379
STD 519	12.9	7.0	10.9	13.9
STD D30	14.8	7.3	11.9	15.6
Total STD DEV.	13.8	7.1	11.4	14.8

Table 6 – NanoSIMS 50L data for CO_2– H_2O – S –Clin San Cristóbal glass inclusions. No data are determined for « - ». *TEL04K9I* is discarded, because of possible contamination of graphite from carbon quoting along microfractures interpreted with NanoSIMS $^{12}C^-$ mapping; 1211 ppm CO_2.

3.4 Noble gas isotopes from mineral separates

The elemental and isotope compositions of He, Ne, and Ar in fluid inclusions (FI) hosted in olivine and pyroxene crystals were measured at Istituto Nazionale di Geofisica e Vulcanologia, Sezione di Palermo (INGV-Palermo). Olivine and pyroxene crystals were separated from the already sieved 0.5 - 1 mm fraction of the ashes and scoria layers by using a heavy liquid (sodium polytungstate), and then carefully handpicked under a binocular microscope. The selected crystals were cleaned following internal protocol (e.g., Di Piazza et al., 2015), then each group of samples (0.1 - 1.5 g) was placed inside stainless-steel bowls and installed in a crusher capable of loading up to six samples at same time. Noble gases trapped inside fluid inclusions were released by in-vacuo single-step crushing. This procedure minimizes the contribution of cosmogenic ^{3}He and radiogenic ^{4}He possibly grown/trapped in the crystal lattice (e.g., Kurz, 1986; Hilton et al., 1993, 2002). Gas released from the mechanical fragmentation of crystals was purified in an ultra-high vacuum purification line. Helium isotopes (^{3}He and ^{4}He) and ^{20}Ne were measured separately by two different split-flight-tube mass spectrometers (Helix SFT-Thermo). $^{3}He/^{4}He$ ratios are expressed as R/Ra (where Ra is the $^{3}He/^{4}He$ ratio of air, or $1.39 \bullet 10^{-6}$). The analytical uncertainties of determined He isotopic ratios is generally <7%. The R/Ra values were corrected for atmospheric contamination using $^{4}He/^{20}Ne$ ratios (e.g. Sano and Wakita, 1985) and are expressed hereafter as Rc/Ra values. Argon isotopes (^{36}Ar, ^{38}Ar and ^{40}Ar) were analyzed by a multi-collector mass spectrometer (GVI Argus), with an analytical uncertainty generally <1.5% (Table 7). Uncertainty in the determined He, Ne, and Ar elemental contents was less than 5%. Typical blanks for He, Ne and Ar were $<10^{-14}$, $<10^{-16}$ and $<10^{-14}$ mol, respectively. Further details about sample preparation and analytical procedures are available in Di Piazza et al. (2015).

Sample ID	Sample detail	Phase	Weight	^{4}He	^{20}Ne	^{40}Ar	R/Ra	He/Ne
			g	mol/g	mol/g	mol/g		
TEL02	February 1982	Cpx	0.648	7.43E-14	1.83E-14	1.41E-12	7.04	4.1
TEL02	February 1982	Cpx-Scoriaa	0.325	9.13E-14	2.90E-14	1.92E-12	6.26	3.2
TEL04K	< 2,300 yrs BP	Ol	0.106	1.10E-13	4.03E-15	4.50E-13	7.37	27.4
TEL04K	< 2,300 yrs BP	Cpx	0.302	1.70E-13	6.56E-15	5.73E-13	7.34	25.9
TEL04K (1)	< 2,300 yrs BP	Ol - Scoriaa	0.265	1.65E-13	1.86E-14	2.47E-12	7.15	8.9
TEL04K (2)	< 2,300 yrs BP	Cpx-Scoriaa	0.09	1.24E-13	7.97E-15	1.72E-12	7.38	15.5
TEL04B	< 2,300 yrs BP	Ol	0.691	4.69E-14	4.50E-15	3.93E-13	7.38	10.4
TEL04B (1)	< 2,300 yrs BP	Ol	1.5	6.37E-14	9.68E-15	6.09E-13	7.28	6.6
TEL04B (2)	< 2,300 yrs BP	Ol	0.65	9.38E-14	7.27E-15	7.28E-13	6.52	12.9

Sample ID	Rc/Ra	Error tot +/-	^{40}Ar/^{36}Ar	Error	^{38}Ar/^{36}Ar	Error	He/Ar
				%		%	
TEL02	7.57	0.282	318	0.081	0.189	0.187	5.29E-02
TEL02	6.89	0.443	300	0.248	0.193	0.190	4.76E-02
TEL04K	7.45	0.443	310	0.975	0.205	0.202	2.45E-01
TEL04K	7.43	0.270	301	0.273	0.195	0.193	2.97E-01
TEL04K (1)	7.39	0.249	297	0.075	0.188	0.185	6.68E-02
TEL04K (2)	7.52	0.496	301	0.459	0.199	0.196	7.17E-02
TEL04B	7.59	0.296	306	0.160	0.190	0.187	1.19E-01
TEL04B (1)	7.61	0.245	305	0.095	0.190	0.187	1.05E-01
TEL04B (2)	6.67	0.326	301	0.259	0.198	0.196	1.29E-01

Table 7 – Chemical and isotopic compositions of noble gases from fluid inclusions entrapped in olivine and pyroxene phenocrysts. [a]Crystals with glassy and/or altered surfaces were sometimes found and therefore segregated in different batch of duplicate analysis for validating the reproducibility and judging the effect of scoria contamination.

4. Results

4.1 Whole rock geochemistry

Whole-rock compositions range from basaltic to dacitic (SiO_2: 50.9 – 58.6 wt%; K_2O: 0.84 – 1.43 wt%) and plot in the field from calc-alkaline to HK-CA rocks (Fig. 6a). The most primitive sample is the lava flow TEL07E, with 50.9 wt% SiO_2 and MgO= 6.02 wt% (table 2) with relatively low K_2O (0.82 wt%). This lava is similar in composition to the Telica basaltic lava flows available in the literature (50.8 – 53.5 wt% SiO_2; 0.9 – 1.1 wt% K_2O; e.g. Carr and Rose, 1987; Patino et al., 2000; Heydolph et al., 2012). The most evolved Telica samples were analyzed by Carr and Rose (1987), with 57.7 wt% SiO_2 and 1.9 wt% K_2O, and the Pre-Telica rocks of Havlicek et al. (2000) (67.1 wt% SiO_2 and 2.57 wt% K_2O).

The STS scoria samples have variable compositions, from 55.5 wt% SiO_2 at the bottom of the sequence (TEL04B), to 50.9 wt% SiO_2 in the middle (TEL07A), and 52.9 wt% SiO_2 at the top (TEL04K), and are therefore more evolved than the associated lava flow (TEL07E).The metric-sized bombs emitted during February 1982 (TEL01-TEL02) are evolved basaltic andesites, with 1.0% K_2O. Lithic lapilli-sized fragments emitted during May 2011 (TEL03A, TEL03B) are more evolved dacites, with 58.3–58.6 wt% SiO_2 and total alkalis between 4.0 and 4.2 wt%. They appear slightly more evolved than the juvenile-poor ashes analyzed during the same period by Geirsson et al. (2014) (55.6 – 57.6 wt% SiO_2; 0.9 – 1.2 wt% K_2O). Scoriae and ashes from the post-1970s period also spread between basalts and dacites (49.6 – 57.6 wt% SiO_2; 0.9 – 1.3 wt% K_2O). Un-eroded cones around Telica are the most primitive samples found in literature (48.8 – 50.1 wt% SiO_2; 0.6 – 0.7 wt% K_2O; Carr and Rose, 1987).

STS bulk rock samples are richer in MgO (4.0 – 6.2 wt%) than pyroclasts of the post-1970 period (2.0 – 4.4 wt%) (Fig. 6e). Similar bulk-rock compositions are observed for STS and 1982 eruption products for compatible oxides including CaO (9.8 – 11.0 wt%), Al_2O_3 (17.0 – 18.2 wt%), TiO_2 (0.8 – 1.6 wt%) and FeO (8.4 – 10.0 wt%) (see Figs.6 c-d-f). Samples from the May 2011 eruption fall outside this group. P_2O_5 concentrations show positive dependence on SiO_2 (fig. 6b), while CaO, Al_2O_3, MgO and TiO_2 are negatively correlated with SiO_2 (Fig. 6c-d-e).These negative dependences indicate crystal fractionation, as illustrated by the fractional crystallization vectors; plagioclase dominates the crystallizing mineral assemblage.

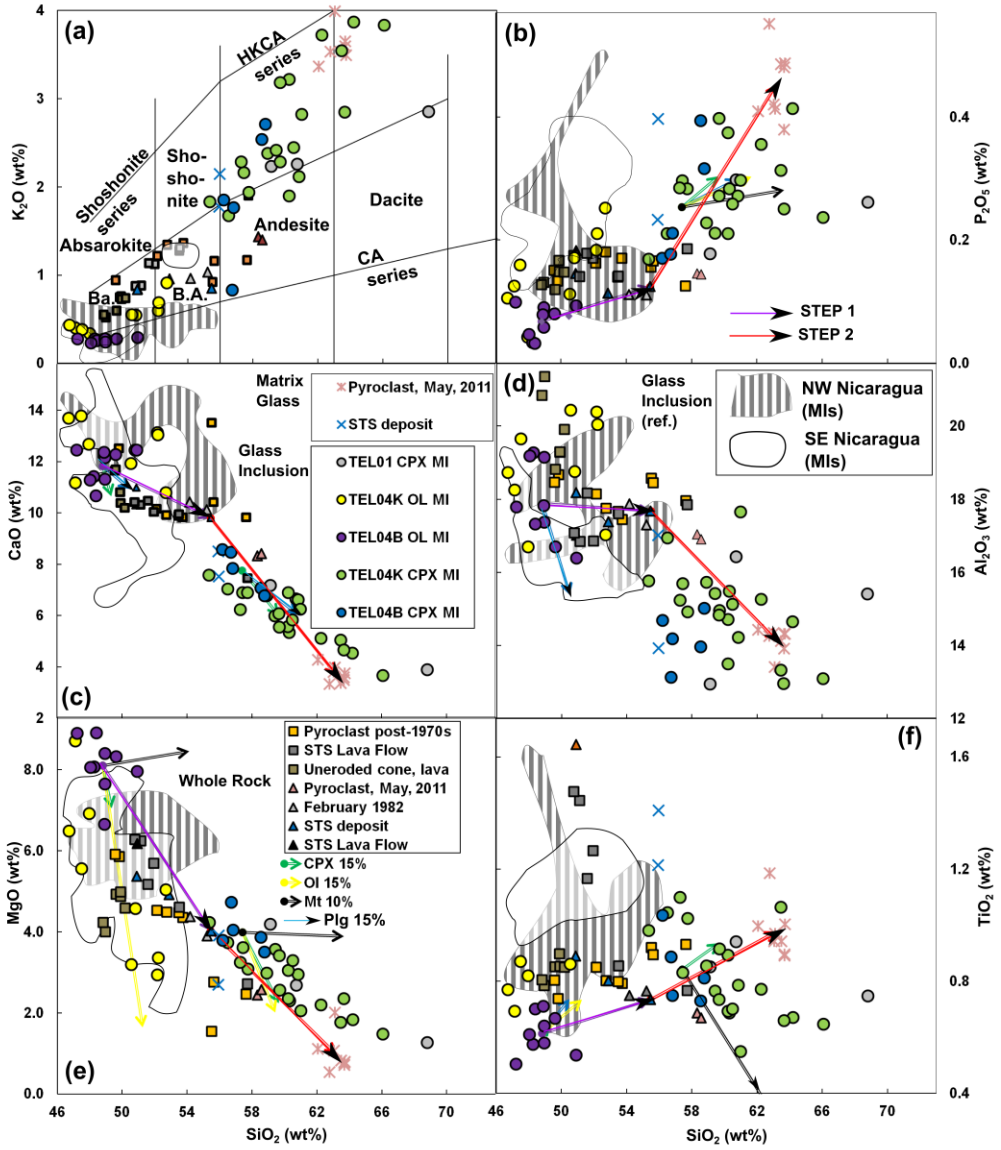

Figure 6 – Diagram of major elements at Telica for analyzed melt inclusions, whole rock from scoria and matrix glasses including whole rock data from lava series in the literature. The melt inclusions hosted- olivines (MIs) are the rounded shapes with white interior representing the SE and stripped interiors from NW Nicaragua (Roggensack et al., 1997; Wehrman, 2005, Tesis; Atlas, Z. Tesis, 2008; Sadofsky et al.,2008; Wehrman et al., 2011; Portnyagin et al., 2012). In literature, whole rock from Telica are represented by the colored squares with black frame (Carr and Rose,1987; Patino et al.,2000; Bolge et al., 2009; Heydolph et al., 2012; Geirsson et al., 2014). In this study, whole rock data are illustrated with colored triangles with black frame and grouped as: eruption of May 2011 (TEL03A, TEL03B), February 1982 (TEL01, TEL02) and STS deposits (TEL04K, TEL04B, TEL07A, TE07E). Matrix glass from scoria are illustrated with colored stars. a) K_2O vs. SiO_2 classification rock diagram from Peccerillo and Taylor (1977), b) P_2O_5 vs, c) CaO v. SiO_2. d) Al_2O_3 v. SiO_2. e) MgO v. SiO_2. f) TiO_2 v. SiO_2.

The primitive mantle-normalized (Mc Donough and Sun, 1995) REE bulk-rock trends are flat, with relatively small LREE enrichments (La/Yb_N from 2.0 to 2.6). The La/Yb_N ratio slightly increases from the oldest to the most recent layers of the STS deposit (TEL04B, 2.01; TEL07A, 2.04; TEL04K, 2.23), while post-1970 pyroclasts (TEL01, TEL02, TEL03A, TEL03B) and the STS lava flow TEL07E exhibits higher values (2.30 – 2.63). The lavas of Pre-Telica (1.10) and the un-eroded cones around Telica have the lowest La/Yb_N values (of 1.40 – 1.86) (Carr and Rose, 1987; Havlicek et al., 2000), and exhibit particularly flat LREE profiles, similar to arc tholeiitic basalts and several volcanoes of Nicaragua (Carr et al., 1984; Heydolph et al., 2012) and in south-east El Salvador (Table 1, Fig. 7a). The Eu negative anomaly is low (Eu/Eu*= 1.3 - 2.7), but clearly present in samples TEL01, TEL04B and TEL07A.

The Telica rock samples are enriched in large ion lithophile elements (LILE: Cs, Rb, Ba, La, etc.), and moderately to strongly depleted in high field strength elements (HFSE: Ta, Nb, Zr, Hf). The normalized patterns also show distinctive Ta, Nb , Ti and Zr negative anomalies (Fig. 7b) as typical in subduction-related magmatism. As a whole, the patterns exhibited by our samples are similar to those of other rocks of the Nicaragua segment (Bolge et al., 2009; Heydolph et al., 2012).

The studied rocks are variably porphyritic. Scoria fragments from STS deposit are dark to grey coloured, are highly vesicular, and show mineral assemblage similar to the rest of our samples thin section, the structure is porphyritic with a sum of 40 - 45 vol % phenocryst (plg > cpx > ol > mt) with dominant equigranular plagioclase microphenocrysts (> 5 - 12 mm) that show frequent twinning intergrowths texture (Fig. 8b). The groundmass assemblage also consists of clinopyroxene-plagioclase-olivine all with frequent magnetite inclusions. TEL04K and TEL07A have similar characteristics, but TEL04B has large phenocrysts of olivine phenocrystals (> 4 – 12 mm) and also clinopyroxene phenocrystals (~10 mm vs. 8 mm in other scoriae).

Bombs TEL01-TEL02 from the February 1982 eruption are porphyric and contain large plagioclase phenocrysts abundance (to 15 mm in length); from 6 in the rim to ~> 40 vol. % in the core of the bombs. Phenocryst assemblage has clinopyroxene dominating over olivine (Fig. 8a). Fragments are dark and frequently highly vesicular and glassy along the external parts of the bombs, and groundmass is generally microcrystalline. Samples from May 2011 eruption (TEL03A, TEL03B) are highly vesicular (vesicles >60 vol. %), crystal-poor scoriae, with similar mineral assemblage as TEL01-TEL02. Several fresh and altered plagioclase phenocrysts (to 8 mm in length) are present with frequent boxwork texture. The surface of the rock is altered with red and yellow colours.

Olivines phenocrysts are euhedral to subhedral, (Fig. 8c) with the highest Forsterite mol % in TEL04B sample (core Fo = 83.6±2.9 %, rim Fo = 82.7±2.8 %). TEL04K olivines have lower forsterite contents (core, 80.5±4.2 vs. 80.6 ±3.5 in the rims). TEL03A has the lowest Fo % (average for both core and rims, 60.2±2.1, Fig 9 a).

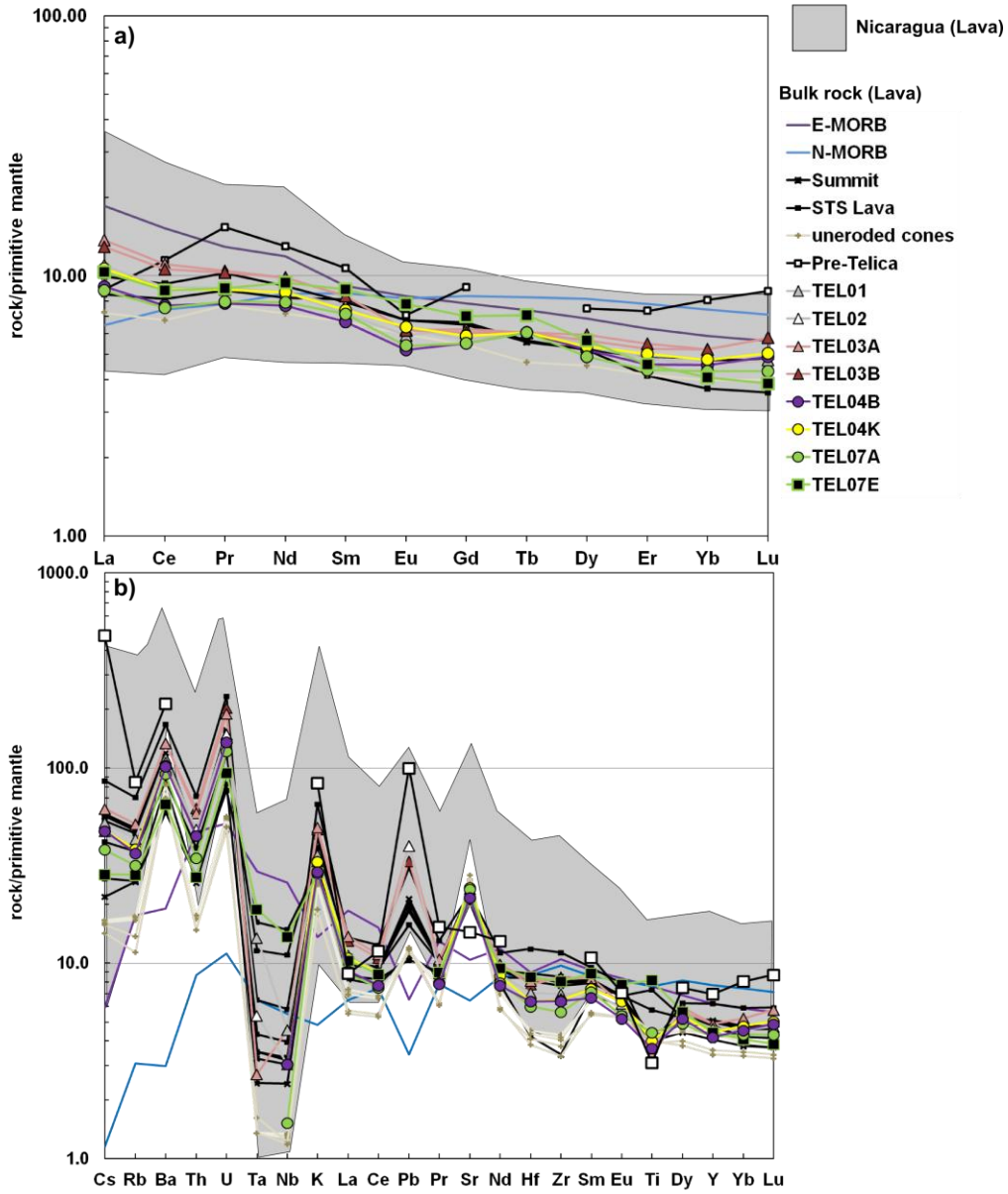

Figure 7 – Spidergrams for trace and rare earth elements in bulk rock scoria at Telica including whole rock data from literature. Original values are normalized to the Pyrolite sample from Mc Donought et Sun (1995) representing primitive mantle. In Telica whole rock of ash and scoria products are represented with lava samples analyzed from literature (see Carr and Rose, 1987; GCS, 2000; Heydolph et al., 2012; Geirsson et al., 2014) and the minimum and maximum normalized samples in Nicaragua (see regional literature data references in Walker et al., 1984-2007-2009; Carr et al., 1984-1990-2007; Reagan et al., 1994; Noll et al., 1996; Picket et al., 1997; Chan et al., 1999; Patino et al., 2000; Feigenson et al., 2004; Bolge et al., 2009; Hoernle et al., 2008; Heydolph et al., 2012). N-MORB and E-MORB are from Gale et al. (2013). a) La-Lu serie. b) Trace and rare elements from heavier to lighter.

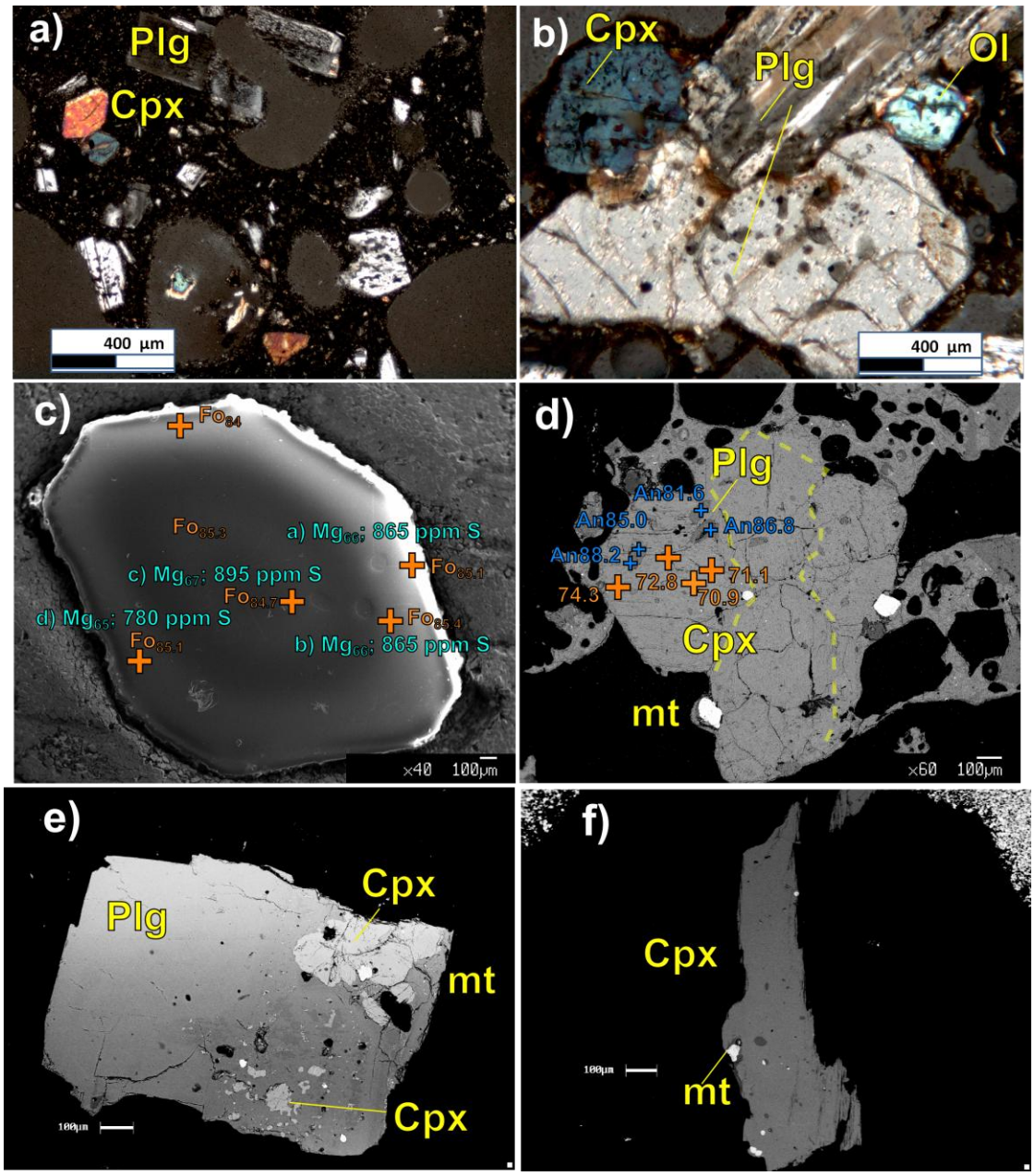

Figure 8 – Transmitted light photography of matrix glass (crossed polars, X20) from a) TEL01, bomb emitted between February 12-20, 1982. Plagioclase is separated in 2 pieces with a vesicular structure. b) TEL04K, scoria from STS with cogenetic Plg-Cpx-Ol microphenocrystals with their respective inclusion assemblages. **Mineralogy. EMPA photography (BSE)** of c) Crystal TEL04Bol2 with variable MI volatile contents and compositions, d) TEL03A augite crystals with solid inclusions of plagioclase in a highly vesiculated matrix glass, e) TEL03 crystal of plagioclase with augite inclusions, f) TEL02 augite crystal with solid plagioclase and magnetite inclusion.

4.2 Petrography and mineral chemistry

For 7 pairs of core-rim spots in the same crystal, TEL04B and TEL03B have 2/5 samples with normal zoning (at least > 2 % difference in Fo%) with the other crystal being unzoned. Inclusions found in TEL04B have large dimensions (> 30 μm), are spherical with glassy or wrinkled texture and many of these contain a bubble (Fig. 8c). These characteristics are found in many groups of inclusions following concentric patterns (Fig. 8 b). In TEL04K, glassy spherical inclusions are smaller (10 – 40 μm), but frequently larger ellipsoidal inclusions are found (20 – 50 μm), with some having slightly rounded irregular shapes (Fig. 8b). Reentrant and hourglass inclusions are found along olivine borders. Oxydes and bubbles are common, but rarely found in inclusions smaller than 20 μm.

Clinopyroxene phenocrystals are euhedral, to subhedral, some having sharp edges and direct matrix-rims contact (Fig. 8d). Crystals have dimensions between 3 to 22 mm, and are classified as augites, with some compositional range depending on the layer (Fig. 10 a-b). TEL04B shows the largest crystals (> 10 mm dimensions), with Mg/Mg+Fe of 0.71 – 0.74 and $Fs_{15.7\text{-}18.0}Wo_{39.3\text{-}41.1}$. TEL04K (10-15 mm dimensions) has composition $Fs_{13.1\text{-}22.5}Wo_{36.7\text{-}42.3}$ with Mg/Mg+Fe passing from 0.67 on the core to 0.75 on the rim for several samples with one example illustrated in figure 8d. TEL01 shows Mg number of 0.71 – 0.74 and $Fs_{15.8\text{-}18.0}Wo_{42.2\text{-}43.9}$, and TEL02 shows Mg number of 0.67 – 0.70. Three solid inclusions of augite were found in plagioclase of TEL02, with similar Mg/Mg+Fe of ~0.67 and $Fs_{19.3\text{-}20.3}Wo_{41.1\text{-}42.8}$. Phenocrystals found in TEL03A have 0.61 – 0.66 and $Fs_{20.3\text{-}23.5}Wo_{41.0\text{-}41.4}$ (Fig. 8e), while TEL03B have phenocrystals with Mg/Mg+Fe of 0.71 – 0.74 and $Fs_{16.8\text{-}17.7}Wo_{38.1\text{-}38.9}$ (Fig. 8f). It is frequent to find a complex number of inclusion typologies in the clinopyroxene crystals; we find concentric series of inclusions from the core to the rim of the crystal, with 5-15 vol.% of bubbles/inclusions and oxide phases (15 – 25 vol.%).

Plagioclase are found as abundant microliths in TEL03A, TEL03B and TEL01-TEL02 (> 40 vol.%); they are less frequent in TEL04K and TEL04B (> 25 vol.%). They are characterized by equigranular/microporphyric textures, while micro-phenocrysts have dusty bands with sieve textured cores (Fig. 8 a-b). Several are found in TEL03A with normal zoned composition, from $An_{90\text{-}96}$ (cores), to $An_{61\text{-}70}$ on the rim, but cogenetic plagioclase inclusion in clinopyroxene, instead, show Ca enrichment with clinopyroxene growth (passing from An_{82} on the core to An_{88} closer to the rim). One plagioclase found in TEL03A has $An_{57,}$ consistent with the low Mg number of coexisting pyroxene (Fig. 8f).

4.2 Glass inclusions and matrix glass composition

Corrected melt inclusion compositions (Fig. 5) generally follow the modeled Kd= 0.3 trend. Olivine re-addition for Post-Entrapment Correction (PEC) was effective in all cases except for three samples with extreme MgO contrast (low MgO content in the inclusion and high forsterite content in the host olivine, or vice-versa). In five inclusions, important corrections (of >2 % olivine) were applied (Danyushevsky and Plechov, 2011).

15/30 inclusions in pyroxene needed > 2% crystal addition to re-equilibrate their FeO_T vs MgO (Fig. 5). Pyroxene glassy rims plot along the minimum Mg# liquid vs. Mg# crystal alignment. Olivine glass rims and olivine compositions show a Kd = 0.27, in the range of equilibrium Kd as explained above.

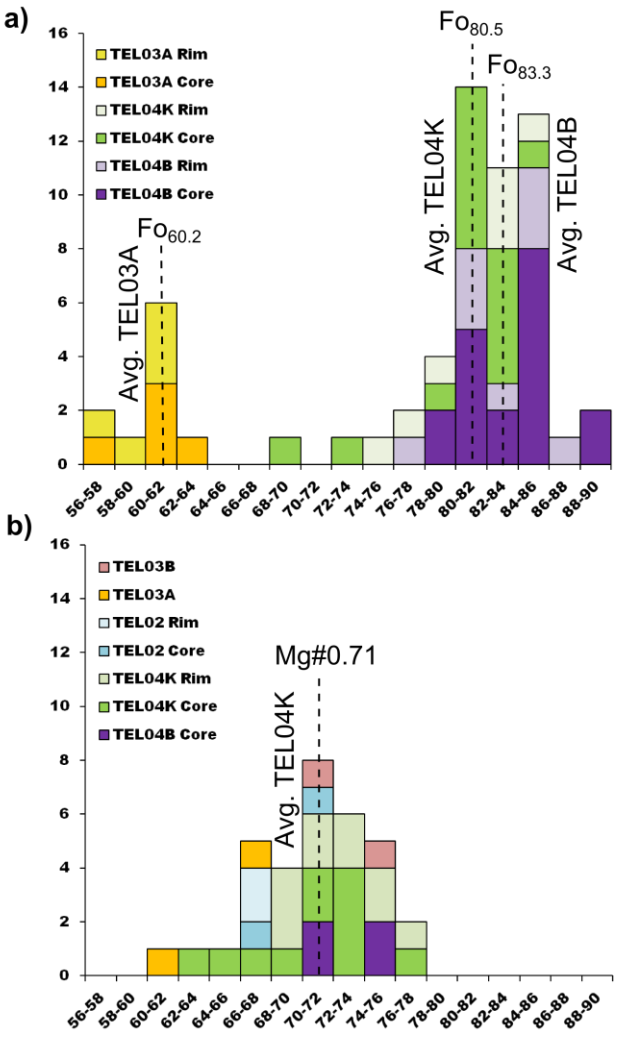

Figure 9 – Histogram of forsterite content and 100*Mg/Mg+Fe for olivines and clinopyroxenes phenocrystals in tephra of STS and late pyroclast products of Telica. a) Pyroxene, b) Olivine.

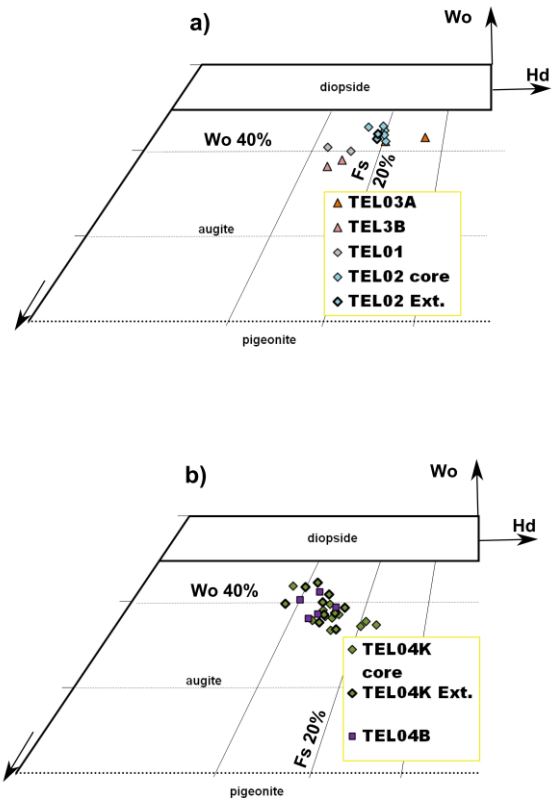

Figure 10 – Quadrilateral classification of pyroxene phenocrysts and microlites a) Pyroxene of post-1970 eruptions, b) Pyroxene of STS deposit.

Recalculated compositions from glass inclusions in clino-pyroxenes are rich in K_2O (0.8 – 4.0 wt%), and they are classified mostly as andesites, while olivine inclusions (K_2O of 0.2 – 0.9 wt%) are mostly basaltic (Fig. 6a). Similarly, olivine and pyroxene inclusions are P_2O_5-poor (0.03 – 0.41 wt%; average 0.19 wt%). Matrix glasses have high K_2O compositions (> 1.8 wt%). Glass inclusions are SiO_2-richer in pyroxenes (55 – 66 wt%) than in olivines (47 – 52 wt%). SiO_2 is higher in all matrix glass samples (>54 wt%). STS olivines (TEL04Bol, TEL04Kol) are trapping inclusions of basaltic compositions. In comparison, bulk rocks from the un-eroded cones and lava flow sampled by Rose and Carr (1988) are also classified as basalts, with lower K_2O and P_2O_5, and higher MgO, CaO and Al_2O_3 (Fig. 6 c-d-e-f).

4.3 Volatile contents

Water concentrations (as H_2O_{tot}) were quantified by mFTIR in 15 glass inclusions of sample TEL04K (0.5 – 1.9 wt.%) and 4 from TEL07A (1.1 – 1.8 wt.%). 16 measurements were obtained for the 1,635 cm^{-1} absorption peak. No measurement is available for TEL04B and in olivines (Table 4). CO_2 concentrations were quantified with mFTIR in only 3 pyroxene inclusions from TEL04K (167, 554, 356 ppm), although an absorption peak for speciated carbon as (CO_3^{2-}) ion was detected in 5 samples(Table 5).

The highest water contents (determined by NanoSIMS) in the olivine-hosted inclusions were obtained for sample TEL04B1 (5.0 ± 0.2 wt%). A range of H_2O contents were obtained in olivine-hosted inclusions from TEL07 (0.95 to 1.26 wt% H_2O), TEL04K (between 1.58 to 4.07 wt%) and TEL04K (0.25 to 2.01 wt%). Two glass inclusions in one pyroxene crystal (TEL01) were also quantified (0.25; 0.46 wt% H_2O). For each pair of mFTIR – NanoSIMS analyses on the same inclusion, the NanoSIMS-derived H_2O contents are higher than the corresponding mFTIR values. Such difference is demonstrated in Electronic Appendix 5 and probably is due to several factors; for example the spot size of mFTIR is averaging the signal for a larger surface, probably including areas of the glass that are heterogeneous in composition. Also, a small fraction of the host crystal could be interfering with mFTIR instrument signal from the glassy inclusion at few microns from the surface, because of the ellipsoidal and/or irregular shape of some inclusions. For this reason, only water contents determined by NanoSIMS were conserved for modeling (section 5.2).

Olivines of sample TEL04K contain the inclusions with the highest CO_2 contents (36 – 1,642 ppm) (determined by NanoSIMS). CO_2 contents were also determined by NanoSIMS in olivine-hosted inclusions from TEL04B (347 ± 16 ppm CO_2), TEL07 (56 to 98 ppm CO_2), and TEL04K (5 to 309 ppm CO_2).CO_2 contents are lower in glass inclusions of TEL01, but in the same pyroxene the fully enclosed inclusion has 65 ppm (the reentrant has 17 ppm).

Glass inclusions in olivine and pyroxene contain variable S and Cl contents (Table 2, 3, 6). EMPA results are only used for pyroxene; since olivine-hosted inclusions are smaller than the minimum diameter of mFTIR aperture window (< 20 µm), we rather rely on NanoSIMS data only. Pairs of pyroxene-hosted inclusions measured by both EMPA and NanoSIMS yielded consistent results (Electronic Appendix 5).

Olivine-hosted TEL04B inclusions contain 780 – 1,020 ppm S (mean 913 ±78 ppm S), or twice as much than measured in inclusions in pyroxenes (196 – 977 ppm S; mean 502 ± 310 ppm S). In TEL04K, olivine-hosted inclusions have S contents between 810 and 1,253 ppm (mean 1,213 ±220 ppm S), with the exception of the extremely high values of TEL04Kol3 (1,985 ppm S). Pyroxene-hosted inclusions of TEL04K have S contents between 72 – 705 ppm (mean 272 ±176 ppm). Lowe S contents are detected in TEL01 (332 ppm) and TEL03B (695 ppm S). Matrix glasses contain 140-216 ppm S. Overall, the primitive inclusions trapped in olivines of TEL04K (lowest wt% SiO_2) contain higher sulfur contents compare to the generally higher wt% SiO_2 from melt inclusion trapped in pyroxenes.

TEL04B inclusions contain 875 – 1,754 ppm Cl (olivines) to 1,285 – 2,440 ppm Cl (pyroxenes). In olivine TEL04B2, the 2 inclusions closest to the border have higher chlorine contents (1,542 to 1,754 ppm) than inclusions at mid-distance to the rim (1,133 ppm) or closest to the core (875 ppm); these data define a chlorine enrichment trend parallel to olivine crystal growth. In olivines of TEL04K, the 8 inclusions have 468 – 1,906 ppm Cl (1,467 ± 472 ppm Cl), while pyroxenes have between 1,785 to 2,900 ppm Cl (2,378 ± 509 ppm Cl). For glass inclusions in pyroxenes of TEL01, EMPA reveals an average chlorine content of 3030 ± 108 Cl (n = 3). In TEL03B, one inclusion has 4,285 ppm Cl. Matrix glasseschlorine contents are found with 1,480 ± 50 ppm in TEL04K and 1791 ± 256 ppm in TEL03A.

In TEL01, fluorine contents (Table 2) were detected at 2,000-2,660 ppm levels.

4.4 Noble gases isotopes in fluid inclusions

We performed 9 analyses of He, Ne and Ar compositions of fluid inclusions (FIs) extracted from olivine and pyroxene phenocrysts in samples TEL02, TEL04K and TEL04B. The results are presented in Table 7.

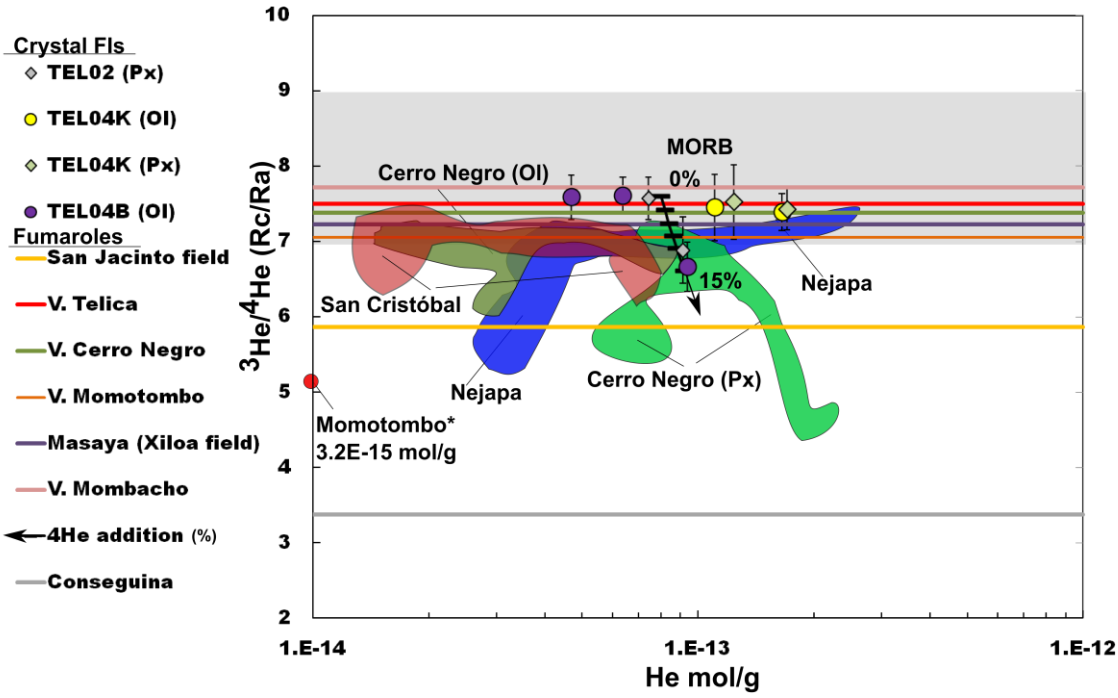

Figure 11 – He concentration (mol/g) vs R/Ra ratio. Data of fluid inclusions (FIs) hosted in Telica olivine are from this study and FIs from San Cristóbal are from Robidoux et al. (2016). Data from fumaroles of San Cristóbal, Telica, Cerro Negro and San Jacinto are measured in gases of fumaroles and thermal springs from Snyder et al. (2003), Shaw et al., (2003), Elkins et al. (2006), while Rc/Ra data from fluid inclusions FI are from Fisher et al. (2005) and Shaw et al. (2006). The grey rectangle area indicates the minimum and maximum He-isotope composition of MORB (7–9 Ra; Graham, 2002).

The ^{4}He concentrations [He] measured in FIs from olivines range from $4.69 \cdot 10^{-14}$ mol/g to $1.65 \cdot 10^{-13}$ mol/g, while in pyroxenes, [He] ranges from $7.43 \cdot 10^{-14}$ mol/g to $1.70 \cdot 10^{-13}$ mol/g (Fig. 11). The lowest He contents are observed in sampleTEL04B (olivine), while olivines and pyroxenes of TEL04K are typically the most [He] rich (Fig. 11). This is the only pair of cogenetic olivine and pyroxene that was possible to analyze and yields comparable He contents, and in the range $1.1\text{-}1.7 \cdot 10^{-13}$ mol/g. Ne and Ar in olivines have ranges of $4.03 \cdot 10^{-15}$ to$1.86 \cdot 10^{-14}$ mol/g and $3.93 \cdot 10^{-13}$ to $2.47 \cdot 10^{-12}$ mol/g, respectively. Ne and Ar are found at levels of $6.56 \cdot 10^{-15}$– $2.90 \cdot 10^{-14}$ mol/g and $5.73 \cdot 10^{-13}$– $1.92 \cdot 10^{-12}$ mol/g, respectively, in pyroxenes. ^{40}Ar/^{36}Ar ratios range 297.0 to 318.0 (±6.2), or only slightly higher than atmospheric values (^{40}Ar/^{36}Ar = 295.5). ^{4}He/^{20}Ne ratios vary in the 3–27 range, and the highest ratios were encountered in samples TEL04K, TEL04B (the atmospheric ^{4}He/^{20}Ne is 0.318). ^{4}He/^{20}Ne ratios in air-free FIs and gases are generally much higher,> 1,000 (e.g., Correale et al., 2012; Paonita et al., 2012). Overall, both ^{40}Ar/^{36}Ar and

$^{4}He/^{20}Ne$ ratios suggest that our samples are contaminated by an atmospheric-derived component, requiring correction of measured ^{40}Ar contents and $^{3}He/^{4}He$ ratios. ^{40}Ar was corrected by assuming that all ^{36}Ar measured in the sample is of atmospheric origin, and it is reported as $^{40}Ar^{*}$. We used the following formula:

$$^{40}Ar^{*} = {}^{40}Ar_{measured} - (({}^{40}Ar/{}^{36}Ar)_{air} \times {}^{36}Ar_{measured})$$

Because this correction is very sensible to $^{40}Ar/^{36}Ar$ when this ratio matches the atmospheric value ($^{40}Ar/^{36}Ar = 295.5$), we applied this correction only to samples having $^{40}Ar/^{36}Ar$ greater than 305 (Table 7). The resulting $^{4}He/^{40}Ar^{*}$ varies between 0.76 and 5.23, being this range comparable to the mantle production ratio ($^{4}He/^{40}Ar^{*}$=1–5; e.g., Ozima & Podosek, 1983; Marty, 2012) based on typical $^{232}Th/^{238}U$ and K/U values.

The correction of $^{3}He/^{4}He$ ratio was applied based on measured $^{4}He/^{20}Ne$ ratios (Giggenbach et al. 1993), as follows:

$$R/Ra = ((R/Ra)_{measured} (He/Ne)_{measured} - (He/Ne)_{air})/((He/Ne)_{measured} - (He/Ne)_{air})$$

The corrected values are reported in Table 7 and are hereafter expressed as Rc/Ra.

Olivine samples (n = 5) vary from 6.67 Ra to 7.59 Ra, while pyroxene (n = 4) from 6.89 Ra to 7.57 Ra (Fig. 11). Olivine and pyroxene crystals, although carefully polished prior to crushing, contained some minor rims of scoriaceous material that were impossible to remove; we cannot rule out, therefore, that part of our results are affected by addition of post-magmatic radiogenic ^{4}He, coming from the scoria itself, and which would have led to lowering of the initial $^{3}He/^{4}He$ ratios. To quantify this processes, we considered some duplicates and we evaluated how the addition of radiogenic ^{4}He affects olivines TEL04B and pyroxenes TEL02, which showed a simultaneous decrease of $^{3}He/^{4}He$ ratio and increase of He concentration (Fig. 11). Starting from an initial He content of $8 \cdot 10^{-14}$ mol/g (slightly greater than the He content in olivines TEL04B and pyroxenes TEL02 unaffected by this issue) and Rc/Ra=7.6 (comparable to the same ratio in olivine TEL04B and pyroxenes TEL02) we simulated a progressive addition of radiogenic ^{4}He to evaluate the effect on the $^{3}He/^{4}He$ ratio (curve in figure 11). Accordingly, the addition of ~15% of ^{4}He (i.e., $8 \cdot 10^{-15}$ mol/g and $1.2 \cdot 10^{-14}$ mol/g, respectively) is able to lower the $^{3}He/^{4}He$ ratios of pyroxenes TEL02 and olivines TEL04B, respectively, to the measured values. This leads to discard from further discussions the two $^{3}He/^{4}He$ measurements that gave 6.67 Ra and 6.89 Ra.

5. Discussion

The following sections review compositional features of Telica effusive and explosive products and explore the variation of volatile contents recorded by melt inclusions trapped in olivines and pyroxenes. A model is proposed that accounts for composition of these melt inclusions, in the specific attempt of explaining degassing processes and mechanisms of magma storage and transport in the volcanic plumbing system. Interpretation of these models leads to new hypotheses on the dynamic of explosive eruptions at Telica. Finally, the volcano's magmatic source is investigated, and compared to that feeding the activity of other CAVA volcanoes.

5.1 Stratigraphic sequence and magma composition characteristics of Telica deposits

The stratigraphic sequence characterized in this study covers several distinct magmatic episodes of the Scoria Telica Superior eruptive unit. Pulses no. 2, 3, 4 and 5 represent fallout deposits, since they appear normally graded and well sorted (Fig. 2). They are separated by net discontinuities; fluvial deposits cut off the top of pulse 2 (TEL04B), pulse 3 (TEL07A) follows fluvial deposits and is itself in direct contact with the overlying STS lava flow. Pulses 4 and 5 (TEL04K) also present sharp contacts with fine lahar layers, and are therefore separate events.

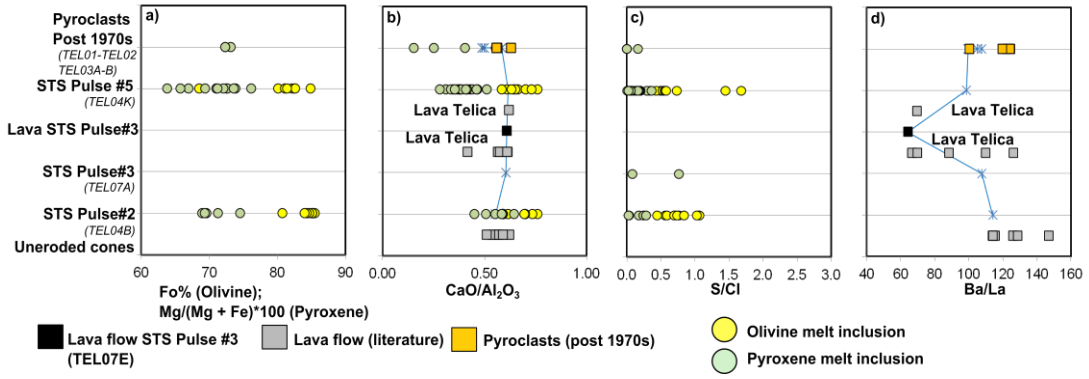

Figure 12 – Chronological geochemistry diagram. Melt trapped by olivine (yellow circle) and pyroxene (green circle) are compared with bulk rock analysis of scoria in this study (connected blue star) with lavas from literature (grey square). Lava from STS pulse #3 (TEL07E) is a black square and pyroclast from Rose and Carr (1988) are represented by an orange square. a) Fo% from olivine and pyroxene composition calculated with Mg/Mg + Fe * 100. b) CaO/Al_2O_3, c) S/Cl, Ba/La.

The different rock samples analyzed at Telica, including the most recent pyroclastic products of post 1970s activity, record similar stages of magma evolution/crystallization, as demonstrated by their overlapping crystal (Fo % content), bulk-rock (CaO/Al_2O_3), and volatile (S/Cl) compositions (Fig. 12). We do find evidence, however, of some heterogeneity in trace and REE element composition, as illustrated by variations of the Ba/La ratio (Fig. 12 d). The analyzed scoriae exhibit wide Ba/La ranges (from ~60 to 120), which may reflect some level of mantle source heterogeneity during magma generation.

Olivines crystals are systematically richer in magnesium compared to pyroxenes (Fig. 12a). Both minerals are find to trap melt inclusions being slightly less differentiated (e.g., with higher CaO/Al_2O_3) (Fig. 9a; Fig. 10 a-b) than the corresponding bulk rocks. Finally, olivines are generally less degassed (higher S/Cl) than pyroxenes in any of our products (Fig. 12c). Bombs and scoria sampled in 1987 and 2011 are also compositionally similar (Fig. 12), but present evidence for slow cooling rates, including large clast sizes (cm to metric), phenocrystals sizes (>10 mm), and the presence of crystallized inclusions.

The STS lava (Havlicek et al., 2000; Hradecký et al., 2007) probably records the last Telica's effusive event, except for a few flank lavas found on western flank (Carr and Rose, 1987; Patino et al., 2000). This lava flow unit, sampled elsewhere in literature (Carr and Rose, 1987; Patino et al., 2000; Carr Havlicek et al., 2000), marks an interesting bulk rock compositional range, with abundances of trace and rare-earth (Fig. 7, 12d) elements all being somewhat distinct from that of scoriae in STS pulse #3 that is just preceding (Fig. 12 b-d). In the scatter plots of major elements vs. silica content (Fig. 6), all lava samples from Telica (this study and literature source) share the

same evolutionary trend defined by pyroclastic deposits. This similitude in magma differentiation trend, associated with some level of heterogeneity in trace-element tracers such as Ba/La (Fig. 12d), may indicate similar crystallization processes, but possible heterogeneity in the deep mantle source (section 5.7).

5.2 Magma degassing history preserved in olivines and pyroxenes

Volatile contents in melt inclusions from both olivines and pyroxenes vary widely. Olivines are the best candidates to target the most primitive melt inclusions of Telica. One significant observation is that at least two groups of melt inclusions, with distinct volatile contents, have been trapped in Telica olivines. One group has moderate H_2O contents (1.5-2 wt%), but is high in CO_2, with maximum detected CO_2 contents (> 1700 ppm) similar to those measured in the CO_2-rich, primitive magmas of Central Nicaragua volcanoes (Granada and Nejapa; Wehrmann et al., 2011). A second group of inclusions is H_2O-rich (>4.0 - 6.1 %), similar to the hydrous magma compositions seen at nearby Cerro Negro volcano (Roggensack et al., 1997; Portnyagin et al. 2012).

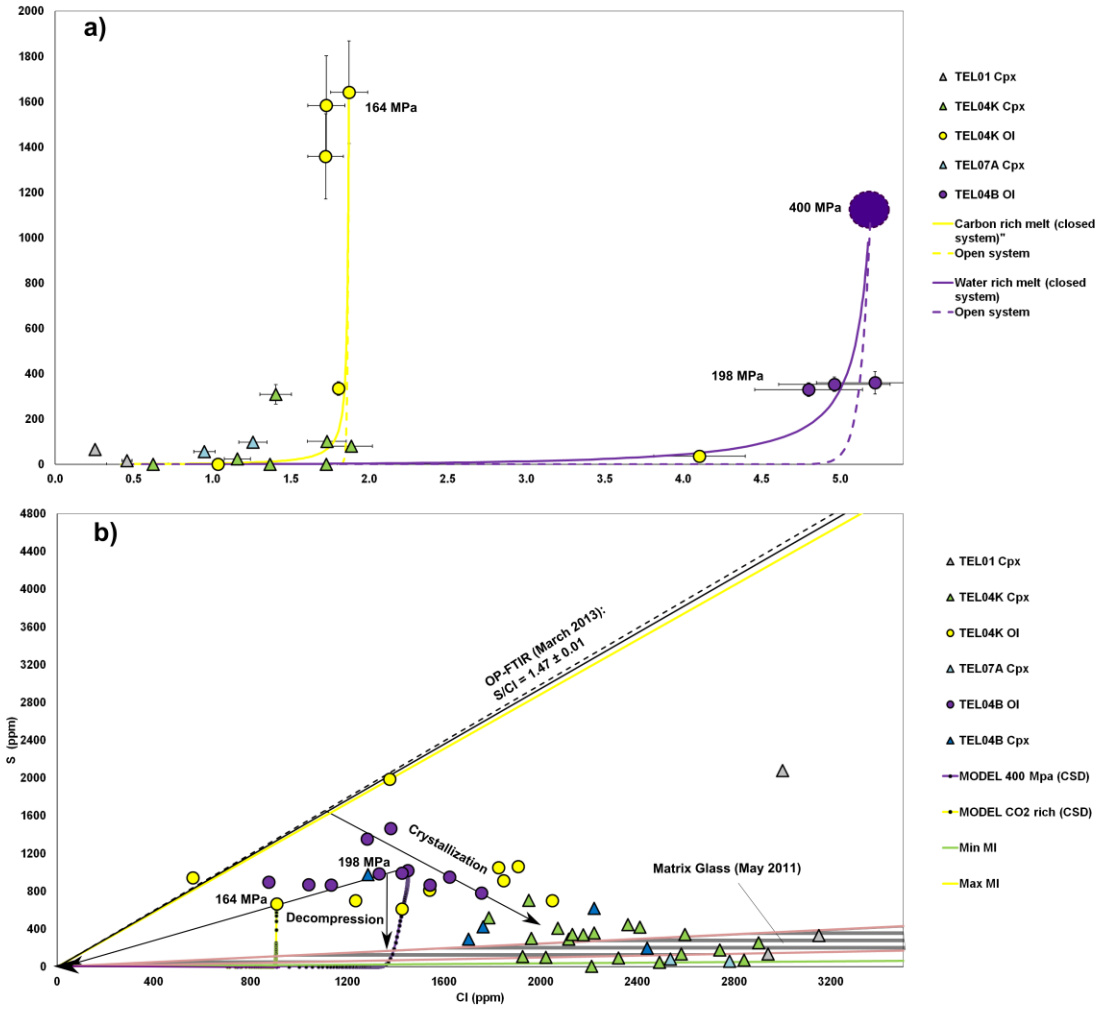

Figure 13 – Volatile contents from inclusions at Telica. a) CO_2 vs. H_2O of melt inclusions from Telica b) S vs. Cl. Open-path Fourier transform infrared (OP-FTIR) spectroscopy (e.g. Mori and Notsu 1997) data of situ volcanic gas compositions are from Conde (2015).

The simulated degassing paths, although poorly constrained by the limited number of inclusions available, reasonably fit the natural volatile contents, including the volatile-poor melts recorded by pyroxenes (Fig. 13a). It remains unclear, given the few data available, if the presence of two melt inclusion clusters means that two distinct magmas, with remarkably different H_2O-contents, have been feeding in the Telica plumbing system during the STS phase. We cannot rule out the possibility, for example, that disequilibrium degassing due to a delayed bubble nucleation in the magma (Gonnerman and Manga, 2005; Pichavant et al., 2013), or magma fluxing by CO_2-rich bubbles from a deep magmatic source (Blundy et al. 2010), are implicated in determining the H_2O-poor melt inclusion population. We exclude that mixing plays a role, given the similarity of major element and S-Cl compositions of the two melt inclusion groups.

Sulfur contents are higher in inclusions in olivines than in pyroxenes (Fig. 13b), which supports the late-stage formation of the latter minerals, eventually in a shallower volatile-depleted reservoir. In addition to distinct entrapment pressures, olivines and pyroxenes may eventually record dissimilar redox conditions (this parameters is know to affect S solubility to a large extent; Scaillet and Pichavant, 2003; Spilliaert et al., 2006b). Pyroxenes records a variety of melt inclusion formation conditions, as seen by their textures and variable compositions. The low S contents in pyroxene-hosted melt inclusions are associated with low CaO/Al_2O_3 ratios (Fig. 14a), confirming that pyroxenes are here better suited for tracking shallow crystallization and degassing (Métrich et al., 2001). In contrast, Cl, is enriched in the most differentiated inclusions in a single crystal (Fig. 8c), and increases with decreasing CaO/Al_2O_3 ratios, e.g. with magma differentiation (Fig. 14b). The contrasting degassing behavior of the two elements (Scaillet and Pichavant, 2003; Signorelli and Carroll, 2000) can be tracked from the inclusions' S/Cl ratios (Fig. 14c). This shows that melts trapped in pyroxenes are even more Cl-rich (and with lower S/Cl ratios) than recorded by matrix glass; clearly, substantial S loss (and Cl enrichment) has occurred before trapping (see results for other arc volcanoes such Augustine, Mont St-Helens (e.g. Anderson, 1974) and Galeras (Stix, 1993). Another possibility for S loss would be its precipitation as sulfide or sulfate depending on the redox conditions during melt inclusion entrapment, but these mineral phases were not observed and analytical measurements are unavailable that could support correlation between sulfur and iron inside the inclusions.

To explore degassing behavior of chlorine in magmatic systems, a common practice is to compare "petrological" and volcanic gas S/Cl ratios (Spilliaert et al., 2006b) (Fig. 14 b-c). The S/Cl (weight) ratio in Telica volcanic gases (1.47±0.01; Conde et al. 2014) is far higher than in pyroxene-hosted melt inclusions (< 0.4). If we normalize the chlorine contents of the most evolved Telica glasses (May 2011 samples: 250 – 2190 ppm) by the average chlorine content in Telica gases (Conde et al. 2014), we obtain an empirical partition coefficient D_{cl} between 0.24 to 2.1, in the range of experimentally derived coefficients for mafic melts (Webster et al., 1999; Alletti et al., 2009). A similar approach leads to higher partition coefficients for S (D_S= 3.6 – 5.5), which proves the larger gas-phase affinity of this latter element (relative to chlorine).

The solubility model of Papale et al (2006) was used to estimate the entrapment pressure conditions of both groups of inclusions, and to calculate the equilibrium compositions of coexisting melt and vapour phase along the degassing path (Fig. 13a). Two distinct degassing paths were calculated (in either closed or open system conditions), using different initial conditions. A first degassing path, representative of the population of CO_2-rich inclusions, is initialised from composition of TEL04Kol2a inclusions (1.73 wt. % H_2O, 1583 ppm CO_2), and the decompression path starts from an initial pressure of 164 MPa (at 1110 °C temperature) (Fig. 13a).The second path is initialized with inclusion TEL04Bol1 (5.22 % H_2O, 360 ppm CO_2), the initial pressure is 198 MPa (T = 1143 °C). The model degassing path could even be started at a maximum pressure of ~ 400 MPa (the entrapment pressure of an hypothetic inclusion with the highest water (5.22 wt%) and CO_2 (1641 ppm) content in our dataset), but an identical degassing trends would be obtained.

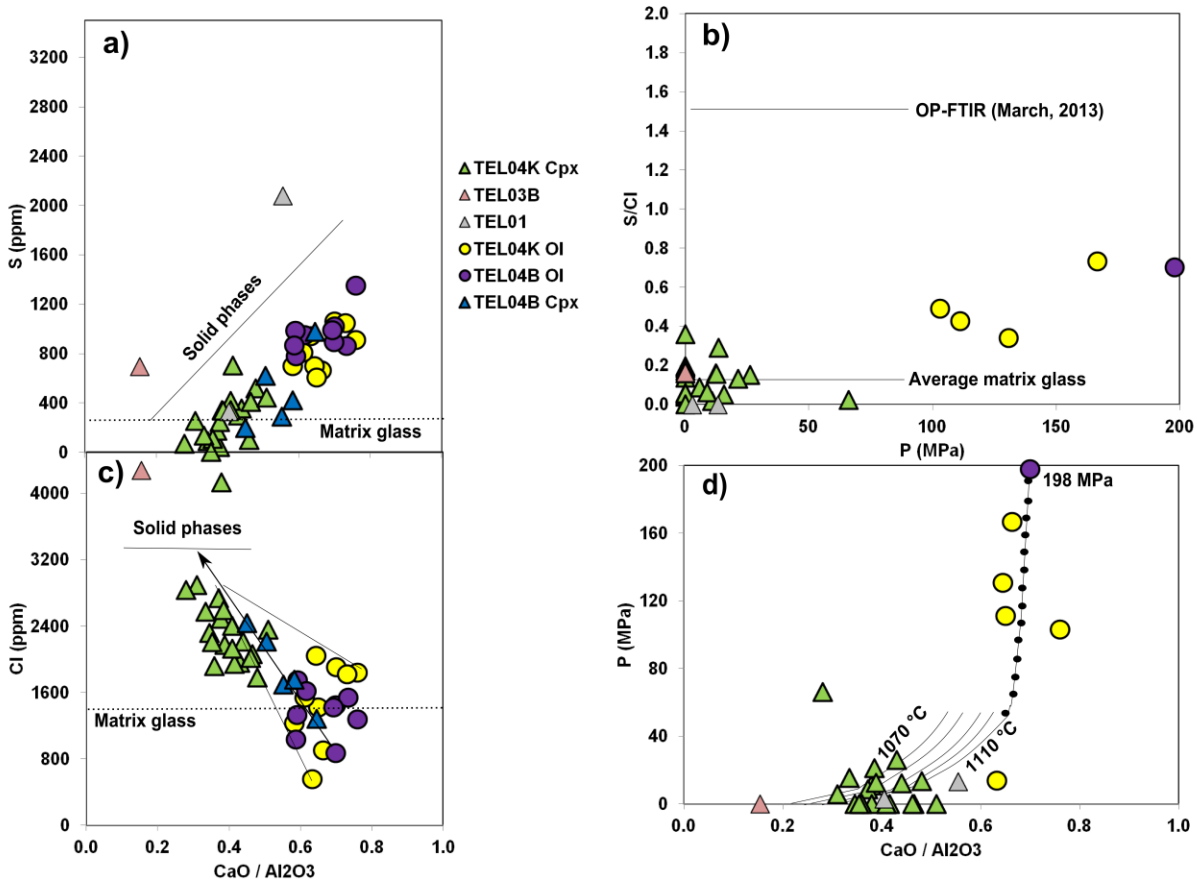

Figure 14 – Binary diagram of volatiles with degassing/crystallizing path from Telica melt inclusions. a) S vs. Cl, b) S/Cl vs P, where pressure in MPa is obtained with solubility model of Papale et al. (2006), c) Cl vs CaO/Al2O3, d) P vs CaO/Al2O3. The pressure corresponds to the melt residual compositions modeled with MELTs. The isotherms were drawn from MELT model and the pressure points were following the isothermal path at 1110 °C which was the best method to explain the melt inclusion data from olivines.

5.3 Steps in magma differentiation

Olivines are often normally zoned (Fig. 9a), and the trapped melt inclusions of both olivine and pyroxenes exhibit negative dependences of Al_2O_3 and CaO contents on SiO_2 that are likely caused by fractional crystallization (Fig. 6). To illustrate these trends, we schematically identify in Figs. 15 a-d two crystallizations steps, STEP 1 and STEP 2.

Crystallizations steps are initially graphically obtained by simply connecting together the compositional end member compositions of some selected samples (Figs. 15 a-d); these compositional tie-lines therefore only have qualitative (illustrative) nature. To provide more support to our arguments, we additionally quantitatively model steps of fractional crystallization using MELTS (Gualda and Ghiorso, 2015 and references therein). This code is used to simulate the liquid line of descent of Telica magmas, and the sequence of minerals formed on the liquidus. The starting point of the MELTS simulations was fixed using the maximum (hypothetical) volatile contents in olivine MIs (H_2O = 5.22 wt%; CO_2 = 1640 ppm), which would correspond to

an hypothetical entrapment pressure of 400 MPa (Fig. 13a). Importantly, this pressure is larger than the saturation pressures derived from truly measured MI compositions and solubility models (<164-198 MPa; fig. 13), which in turn are in good agreement with T and P constraints placed by clinopyroxene thermo-barometers (Putirka et al., 2008). These latter indicate a range of pressure of 103 to 198 MPa, and temperatures of 1090 to 1153 °C. By using an initial pressure of 400 MPa, we implicitly target the deepest parts of the plumbing system, eventually not recorded by the melt-inclusion/crystal record.

STEP 1 is represented by the tie-lines connecting compositions of (i) the most primitive melt inclusion composition (average of TEL04B) and (ii) the bulk rock composition of TEL04B (end of arrow lines), representing the resulting liquid. Several data-points cluster along this STEP 1 vector. To validate the simple vector illustration, we used MELTS to simulate the magma crystallization path in a K_2O vs. MgO wt% diagram (Fig. 15a), and determined that measured melt inclusion compositions are best reproduced by a first stage of fractional crystallization until pressures of 130 MPa, with the following mineral mass fractions: 24.8% Cpx, 22.9 % Plg,10.5 % Ol, 2.4% Mt – 40.7% Liquid.

Several glass inclusions in pyroxenes are more evolved than STEP1 stage would predict. To explain this, a second crystallization stage (illustrated by STEP 2 vector) is implicated (figure 15). In this specific case, we use the bulk rock composition of TEL03B as a proxy for the daughter liquid. By following the trendline connected until this daughter endmember, MELT crystallization would evolve until pressures of 50-60 MPa and gives the following mass fraction of minerals: 26.4% Cpx - 37.5 % Plg - 10.6 % Ol - 3.6% Mt - 18.0% Liquid. This crystallization step would contribute to the largest P_2O_5 and K_2O enrichments (Fig. 6 a-b).

Most of our bulk-rock samples, and most inclusions trapped by pyroxenes, display negative dependences of TiO_2 on SiO_2 (Fig. 6f), supporting the crystallization magnetite suggested by MELTS models (Carr and Rose, 1987; Patino et al., 2000). Overall, the wide compositional range of pyroxene-hosted inclusions records a late crystallization stage (STEP 2), and implies variable timescales of magma residence inside the feeding reservoir (Fig. 15 abcd).

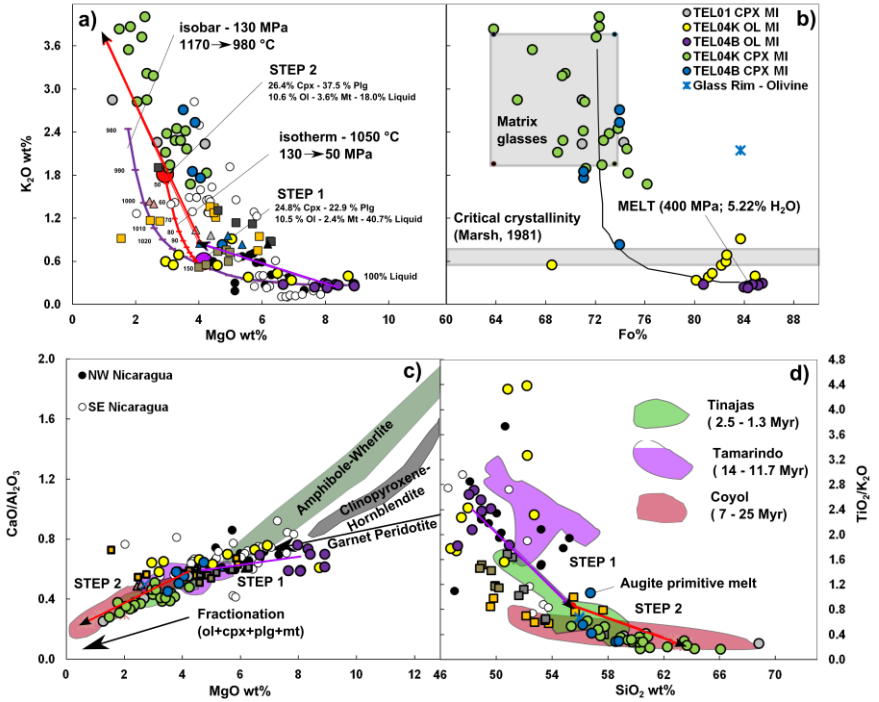

Figure 15 – Major elements crystallization models. Telica groundmass and bulk rocks from this study and literatture are symbolized in figure 6. Crystallization vectores for each supposed crystal phase are confronted with the data including two steps of melt inclusion composition evolution represented by purple arrow (STEP 1) and red arrow (STEP 2). Lava whole-rock samples from surrounding basement are from Saginor et al. (2011). a) MELTS calculations indicate that olivine crystallization explains much of the restrained range of primitive major elements (MgO, K_2O, CaO, TiO2, Al_2O_3) while the wide range of their composition is rather explained by the end of the curve tendency with effect of plagioclase±clinopyroxene crystallization. a) K_2O vs. MgO wt% with the MELTS calculations simulate a probable ascent path (varying both pressure and temperature), b) K_2O wt% vs. Fo% show temperature evolution of melt until the most evolved end member (matrix glass minimum and maximum liquid-crystal composition) with the critical chrystallinity line, c) CaO/Al_2O_3 vs. MgO wt% include experimental melting trends from amphibole-bearing wherlite (Médard et al., 2006), clinopyroxene bearing hornblendite (Pilet et al., 2008a,b) and to primary garnet lherzolite melts modeled in Gazel et al. (2011) (modified from Gazel et al., 2011). d) TiO_2/K_2O vs SiO_2 wt% and MELT model crystallization curves.

5.4 The Telica plumbing system

According to MELTS, Telica magmas (with H_2O = 5.22 wt%; CO_2 = 1640 ppm) would reach H_2O saturation at ~300 MPa. H_2O degassing and loss from the melt would trigger (degassing-driven) crystallization of (chiefly) olivines, with larger amounts of olivine crystallizing until 130 MPa pressure. The later (lower-pressure) magma crystallization and differentiation sequence is more complex. Since entrapment pressures, volatile contents and degree of differentiation are very distinct for melt inclusions trapped in olivines and pyroxenes, it is arguable that the two mineral phases did not crystallize at the same time during magma ascent, or possibly that they stabilized in two different areas of the plumbing system below Telica. These two different conditions may also be reflected by the two crystal fractionation steps, discussed above.

Overall, many line of evidences support different histories of crystal growth during magma ascent. The low, but variable volatile contents registered in pyroxenes, plus their numerous series of concentric inclusion assemblages, could testify long time of residence in the upper parts of the plumbing system, and their zoning may reflect crystal growth during ascent (Cashman and Blundy, 2000). In turn, reverse zoning may reflect heterogeneous magma and possibly mixing at shallow depths. This is likely to occur during the second step of crystallization (STEP 2; Fig. 15a), where variably degassed melts interact in the shallow depth reservoirs (<130 MPa) where pyroxenes are seen to form. According to our pressure entrapment data, we infer that most of the late crystallization sequence occurred after an equivalent crustal depth of 5 km, and most of the pyroxenes may have continued to grow and trap different, variably degassed liquids, in the 0.33 and 2.4 km depth range.

It is unclear if a large magma chamber exists below Telica, but seismic records (Rodgers et al. 2015) evidence a shallow cluster of seismic events below the summit of Telica, between 0.5 and 2 km depth (e.g. Geirsson et al., 2014). These events most probably locate the upper part of the shallow pounding zone, where the final stage of magma differentiation occurs.

5.5 Inferences on eruptive dynamics

One aspect to carefully consider is what our new data tell us for interpreting the actual eruptive stage of Telica, particularly regarding the relations between changes in magma composition and dynamics of the explosive eruptions. As seen in figure 15a, the residual liquid remaining after STEP 1-2 of fractional crystallization only makes 20 – 41% of the total magmatic mass; we argue, therefore, that the critical crystallinity conditions (liquid < 40 – 50 Vol. %; Marsh, 1981) is likely reached during the second step of crystallization. This fact is also supported by the 40 - 45 vol % fraction of matrix groundmass in the analyzed scoriae. This late crystallization stage is likely to impact eruption style at Telica, by changing magma viscosity.

For magma stalling at superficial levels in the feeding conduit systems, there is high chance for groundmass crystallization to proceed until an andesitic-dacitic mash is generated that form a viscous cap on-top of system. These crystal-rich magmas may act as sealing for the magma conduits and hydrothermal systems, eventually leading to phreatic or vulcanian eruptions depending on the participation of external water (e.g., Self et al., 1979; Fagents and Wilson,

1993). Most scoriae and blocks that are found in the products of the May 2011 eruptive phase are lithic, hydrothermally altered porphyric fragments thrown by the explosion(s) on the crater rims.

We support the idea that this evolved material is often sealing the superficial channels of the shallow hydrothermal system (Geirsson et al., 2014), leading to gas accumulation and pressure buildup (as described in Rodgers et al. 2015). The transition between open-vent degassing and closed-system conditions (Stix, 2007) may probably be influenced by the presence of this viscous sealing that play an important role for producing the frequent series of phreatic explosions. If the variable plume SO_2 fluxes over the last decades (Conde et al. 2014; Conde 2015) may reflect changes from the opening and closing of the central vent at Telica, it appears that the most frequent eruption trigger is dominated by sealing of the system. Major eruptions with fresh juvenile material are rather following long period of unrest (since 1987), but they rather represent deep recharge vs. shallow crystallization trigger for major eruptive events. For such high intensity explosions, like the major vulcanian eruptions of the STS, we additionally invoke the role of deeply sourced (> 4 – 7 km) CO_2-rich bubbles. Those magmas are also highly concentrated in sulfur and chlorine and eventually interact with superficial cooling magma. These CO_2-rich phases may trigger the explosion via their accumulation into the shallow plumbing system (<2.4 km) (Stix, 2007).

5.6 Parental melt-fluid source of Telica: sideview from noble gas of fluid inclusions

One way to verify the origin of Telica fluids, and test whether or not magmas suffered from later stage mixing, is the study of noble gases. The Rc/Ra ratios (n = 7) average 7.34±0.39 in olivines and 7.35±0.32 in clinopyroxenes; helium isotope composition appears therefore insensitive to variable crystallization history, chronology and degassing characteristics (Fig. 11). Importantly, co-genetic olivine-pyroxene pairs of TEL04K have similar ratios, likewise for their He content, which is not usual in many magmatic systems worldwide (e.g. Hilton et al., 1993, 2000; Marty et al., 1994; Shaw et al., 2006; Nuccio et al., 2008; Correale et al., 2014; Di Piazza et al., 2015; Rizzo et al., 2015), due to the late crystallization of pyroxene crystals that can, thus, reflect greater extents of degassing and suffer crustal contamination processes. Whatever this means, at Telica olivine and pyroxene crystals trapped fluid inclusions of similar composition.

As shown in figure 11, our FIs Rc/Ra ratios are similar to the highest values previously reported for fumaroles (crater and flanks) and surrounding bubbling hot springs, whose measured ranges are 7.33 to 7.5 (Shaw et al., 2003; Elkins et al., 2006). The San Jacinto gas manifestation, located east of Telica Volcano, but still linked to its fault system, shows distinctly more radiogenic He isotope composition (Rc/Ra from 5.50 to 5.86; Shaw et al., 2003; Elkins et al., 2006), probably reflecting shallow contamination by crustal-derived ^{4}He.

At larger scale in Nicaragua (e.g. Robidoux et al., 2016), this consistency of Rc/Ra ratios proves that the parental melt-fluids have similar mantle source, and that processes of differentiation in the plumbing system do not modify the He isotope signature. The ^{3}He/^{4}He ratios of our FIs and fumaroles from Telica are also consistent with the maximum values measured in other volcanic systems of Nicaragua, such as Cerro Negro (7.38 Ra), Masaya (7.23 Ra), Mombacho (7.72 Ra), Momotombo (7.05 Ra), and Nejapa (7.49 Ra) (Shaw et al., 2003, 2006; Elkins et al., 2006; Lucic et al., 2014). The He isotope signature of Telica is also comparable with that of volcanoes of the nearby Costa Rica (Di Piazza et al., 2015 and references therein). This indicates that the higher presence of slab fluids and subducted sediments in Nicaragua does not

significantly affect the He isotope signature of the mantle wedge. Nevertheless, because most of the volcanic systems along CAVA have not been studied for noble gases in fluid inclusions, it is not possible to make further speculations on a regional scale.

5.7 Origin of Telica magma

The similarity in noble gas compositions contrasts with the variations of trace and REE of bulk rocks. At Telica and other CAVA volcanoes, source heterogeneities have been identified using geochemical tracers (Carr et al., 1990; Plank and Langmuir, 1998; Patino et al., 2000; Plank et al., 2002; Abers et al., 2003; Feigenson et al., 2004; Eiler et al., 2005; Bolge et al., 2009; Heydolph et al. 2012; Wehrmann et al., 2014), but no similar inference has been made at the scale of one single eruption (e.g., for the magmatic system that produced the STS eruptions). One general observation, which finds similarly clear evidence in the neighbour volcanoes, is the generally low La/Yb_N ratios of our samples (Table 2), which suggest high degree of mantle melting. The thin crust below the region of Cordillera *de los Marabios* (Mackenzie et al. 2008) may be implicated here.

Bolge et al. (2009) and Patino et al. (2000) reported on trace element evidences of amphiboles being present in the source region of Telica magmas, but still, no amphibole has ever been detected in any of the Telica rocks. To test if our Ba/Th vs. U/Sr ratios in Telica rocks are consistent with participation of amphibole-bearing peridotites in mantle melting, (Fig. 16a) we use partition coefficients for an experimentally formed amphibole (1000°C and 1.5 GPa; Brenan et al., 1995). In fact, changes in trace element ratios (e.g., Ba/Th; or uranium contents relative to less incompatible trace elements) within co-magmatic suites can allow identifying amphibole loss from the melting assemblage (melt partition coefficient of pargasite being U = 0.009; Th = 0.017; Ba = 0.12; Sr = 0.29) (Brenan et al., 1994). We show (Fig. 16a) that our most primitive STS whole rock samples form a compositional array (including Tamarindo formation and rocks from the literature; Carr and Rose, 1988; Patino et al., 2000; Sadofsky et al., 2008) that is well consistent with the involvement of amphiboles in the magmas source region. A similar process was argued in Bolge et al. (2009) by studying the effect of amphibole on niobium.

The trace and REE signature of Telica lava can also be used to verify the extent of slab-fluid contribution to magmas. In CAVA, the lack of enrichment in U and Th indicate that an aqueous fluid, rather than an hydrous melt, are involved in fertilization of the mantle wedge (Becker et al. 2000). In this category, Ba/Th and U/La slab-fluid markers have been explored by Patino et al. (2000) for Nicaragua using bulk rocks, and by Wehrman et al. (2011) and Sadosfky et al. (2008) using melt inclusions. In Nicaragua, Ba/Th and U/La ratios are higher relative to lavas in Costa Rica and the Guatemala-El Salvador segment (Patino et al., 2000), indicating a larger contribution of subducted sediments in petrogenesis. The most primitive magmas of Telica (basalts) plot the closest to the CS – HS poles (Fig. 16b), but also show an isolated category closer to the CS pole (Telica anomaly and Tamarindo Formation), clearly supporting that magma generation below Telica occurs with a compositionally heterogeneous mantle.

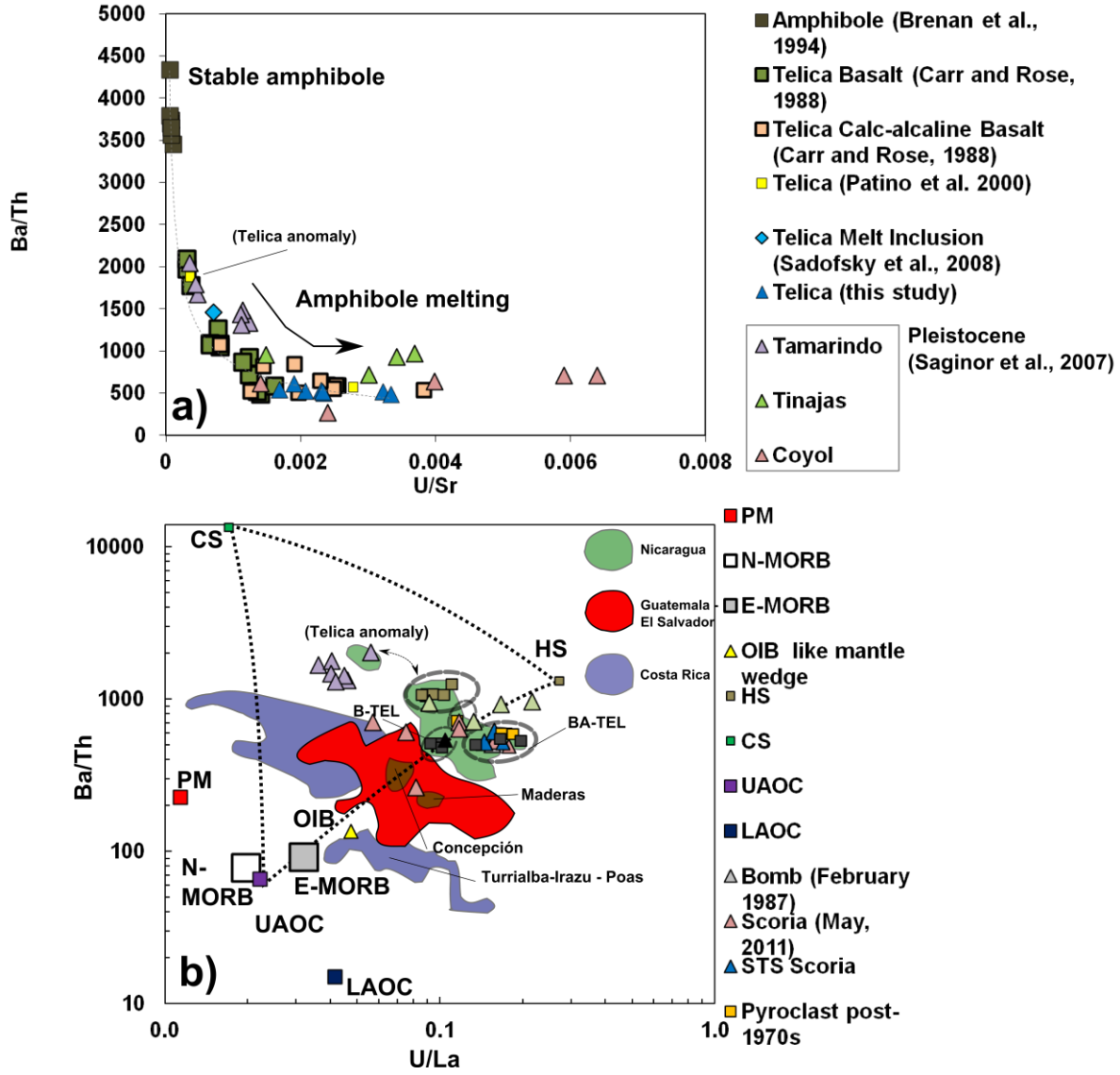

Figure 16 – Binary diagram with regional trace element signatures. See Aiuppa et al. (2014) for literature whole rock data from Nicaragua where only basalts «B» and basaltic andesite «BA» (< 56wt.% SiO2) with MgO > 2.5 wt.% are selected. Dotted line represent compositional limits for certain volcanoes including the limit between basalts and rocks more evolved than basaltic andesites from Telica BA-TEL that concord well with literature data. HS is for Hemipelagic sediments, CS for carbonate sediments, UAOC is for upper altered oceanic crust and LAOC the lower section listed in Patino et al. (2000) and PM is the primitive mantle from Mc Donought et al. (1995). Vector for fractional crystallization of a parental melt is drawn with the arrow. Sediment enrichment line is drawn from the UAOC / PM end pole to the end pole of sediments HS and CS from Patino et al. (2000). See symbol of bulk rock samples from Telica in figure 6. a) Ba/Th vs U/Sr, b) Ba/Th vs. U/La.

7. Conclusions

The combined interpretation of volatile and major element compositions of melt inclusions and whole rocks permitted to draw a model of fractional crystallization and decompression for magmas feeding vulcanian and/or effusive eruptions from Telica volcano in Nicaragua. The today gas composition of the summit crater's plume, and melt inclusion data from pyroxene of old and recent explosive eruptions, concurred to characterize the shallow levels of the plumbing system. Primitive melt inclusions trapped in olivines, in combination with noble gases is FIs and bulk rock data, allowed us to characterize the most primitive magmas and their magmatic source. The most relevant conclusions are summarized as follows:

1. The volatile contents in melt inclusions, studied via NanoSIMS, reveal two groups of H_2O-CO_2 contents in scoriae and ash deposits of the Holocenic STS eruptions. Microprobe and NanoSIMS show that melt inclusions have S-Cl contents that directly correlate to magma compositions. Olivine-hosted melt inclusions indicate high-pressures of entrapment and possible heterogeneity in the volatile source. Pyroxene from STS and 1987 eruptions show remarkable range of magma compositions, from basalts to dacites, and record shallow degassing processes linked to differentiation of residual melts, and extreme chlorine enrichments.

2. The application of solubility models to melt inclusions indicates minimum saturation pressures of the trapped melts of 4 - 7 km (<198 MPa) for olivines, and 0.3 – 2.4 km depths (from 130 MPa to <40 MPa) for pyroxenes. The model of two reservoirs at different depths evolving in two stages (STEP 1 and 2) is supported by mineral phase stability conditions, and is constrained by MELT simulations starting from a parental magma at 400 MPa, Δ NNO+ 0.88, and temperature of 1153 °C. During the first stage, volatile loss (CO_2-H_2O-S) to bubbles mainly occurs by decompression from 300 MPa down to 130 MPa. Water loss, from 5.2 to 1.8 wt.%, may cause increasing olivine and plagioclase crystallization. The constant melt composition of olivines, but their variable chlorine contents, suggest that primary liquids could have homogenised at depth, but that the fluid source was heterogeneous in Cl.
3. A shallow depth, second stage of crystallization is recorded in pyroxene melt inclusions. Rapid cooling rates may accentuate magma differentiation in such shallow (<130 MPa) levels. Inverse zoning, variable pyroxene compositions and low volatile contents in their glass inclusions may reflect a shallow area in the crust where magma mixing can occur (<2.4 km). The increasing viscosity of this differentiated material may eventually trigger tapping of the central Telica conduits, and lead to mixed phreatic/magmatic eruptions. Larger-scale vulcanian eruption likely implicate CO_2 accumulation as an additional trigger of overpressure in the central conduit, but those events are less frequent.
4. The $^3He/^4He$ ratios measured in FIs in olivines and pyroxene are within the Pacific MORB-like mantle, and agree well with maximum $^3He/^4He$ ratios found in fumaroles and fumaroles fields around Nicaragua. A surprisingly similar noble gas signature is observed for FIs in olivines and pyroxenes, independently of their crystallization story. This proves a marginal effect of magma assimilation and magma ageing processes.
5. Overall, the major, trace and rare earth elements from Telica and the Pleistocene volcanic rocks found in the basement (Coyol Group, Tamarindo Formation) share a similar magmatic source. The magmatic source underneath Telica shows high degree of partial melting, possibly see amphibole implicated in magma generation, and is variably influenced by incorporation of sedimentary fluids released from the slab.

BIBLIOGRAPHY

- Abers, G.A., T. Plank, B. R. Hacker (2003). The wet Nicaraguan slab. Geophys. Res. Lett.30
- Aiuppa, A., P. Robidoux, G. Tamburello, V. Conde, B. Galle,G. Avard, E. Bagnato, J. M. DeMoor, M. Martinez, A. Munoz, (2014). The Costa Rica – Nicaragua volcanic segment: along arc variations in volcanic gas chemistry and improved CO_2 budget, Earth and Planetary Science Letters, Vol. 407, p. 134-147
- Anderson, A.T. (1974). Chlorine, sulfur, and water in magmas and oceans. Geol. Soc. Amer. Bull., no. 85, p. 1485 – 92
- Anderson, A.T., (1975). Some basalt and andesitic gases, Rev. Geophys. Space Phys., no. 13, 37 - 55
- Atlas, Z. D., (2008). Volatiles in melt inclusions from Mexican and Nicaraguan volcanoes: implications for complex degassing processes, Open Access Dissertations, Paper 142, p. 1 -131
- Auger, L. S., G. Abers, K. Fisher, M. Protti, V. Gonzales, and W. Strauch, (2006). Crustal thickness variations beneath the Central American Volcanic Arc, Eos Trans. AGU, 87, (52), Fall Meet. Suppl., Abstract T23C-0517
- Barnes, J.D. (2009). Chlorine isotope variations along the Central American volcanic front and back arc, G3, Vol. 10, No. 11, p. 1525 – 2027
- Becker, H., K. P. Jochum, and R. W. Carlson (2000). Trace element fractionation during dehydration of eclogites from high-pressure terranes and the implications for element fluxes in subduction zones, Chem. Geol., no. 163, p. 65 – 99
- Benjamin, E. R. T. Plank, J. A. Wade, K. A. Helley, E. H. Hauri, G. E. Alvarado (2007). High water contents in basaltic magmas from Irazù volcano, Costa Rica, J. Volcanol Geotherm. Res., Vol. 168, p. 68 – 92
- Bevacqua, G. (2014). Studio delle inclusioni vetrose del Vulcano Telica (Nicaragua), Tesis esperimental di laurea di Giovanna Bevacqua, Anno 2013-2014, DISTEM, U. Palermo, Corr. S. Rotolo, G. Lanzo, 91 p.
- Blank, J. G., and R. A. Brooker ((1994). Experimental studies of carbon dioxide in silicate melts solubility, speciation and stable carbon isotope behavior. In: Carroll M. R., J. R. Holloway (eds) Volatiles in magmas. Rev. Mineral, Vol. 30, p. 157 – 186
- Blundy, J., K.V. Cashman, A. Rust, F. Witham, (2010). A case for CO2-rich arc magmas, Earth and Planetary Science Letters, Vol. 290, Issues 3–4, p. 289 – 301
- Bolge L. L., M.J. Carr, K.I. Milidakis, F.N. Lindsay, M.D. Feigenson, (2009). Correlating Geochemistry, Tectonics, and Volcanic Volume Along the Central American Volcanic Front, Geochemistry Geophysics Geosystems, Vol. 10, Issue 12, p. 1-15
- Carr, M. J. (1984). Symmetrical and segmented variation of physical and geochemical characteristics of the Central American volcanic front, J. Volcanol. Geotherm. Res., No. 20, p. 231-252
- Carr, M. J., and W. I. Rose, (1987). CENTAM - A data base of Central American volcanic rocks, J. Volcanol. Geoth. Res., Vol. 33: (Stoiber Volume), p. 239 - 240
- Carr, M.J., M.D. Feigenson, and E.A. Bennett, (1990). Incompatible element and isotopic evidence for tectonic control of source mixing and melt extraction along the Central American arc, Contrib. Mineral. Petrol., No. 105, p. 369-380

- Carr, M. J., I. Saginor, G. E. Alvarado, L. L. Bolge, F. N. Lindsay, K. Milidakis, B. D. Turrin, M. D. Feigenson, and C. C. Swisher III, (2007). Element fluxes from the volcanic front of Nicaragua and Costa Rica, Geochem. Geophys. Geosyst., Vo 8, No. 6, p. 1-22
- Carroll, M.R. and M.J. Rutherford, (1987). The stability of igneous anhydrite: experimental results and applications for sulfur behavior in the 1982 El Chichon trachyandesite and other evolved magmas, J. petrol., no. 28, p. 781 -801
- Carroll, M.R., J.D. Webster (1994). Solubilities of sulfur, noble gases, nitrogen, chlorine, and fluorine in magmas, Rev. Mineral. Geochem., No. 30, p. 231 – 279
- Cashman, K. and J. Blundy (2000). Degassing and crystallization of ascending andesite, Phil. Trans Roy Soc., no. 358, p. 1487 - 1513
- Chan, L.-H., W.P. Leeman, C.- F.You, (1999). Lithium Isotopic Composition of Central American Volcanic Arc Lavas: Implications for Modification of Subarc Mantle by Slab-Derived Fluids, Chem. Geol., No. 160, p. 255-280
- Conde, V., P. Robidoux, G. Avard, B. Galle, A. Aiuppa, A. Muñoz, 2014, Measurements of SO_2 and CO_2 by combining DOAS, Multi-GAS and FTIR observations: a case study from Turrialba and Telica volcanoes, International Journal of Earth Sciences, June 2014, p.1437-3254
- Correale, A., M. Martelli, A. Paonita, A.L. Rizzo, L. Brusca, V. Scribano, (2012). Newevidences of mantle heterogeneity beneath the Hyblean Plateau (southeast Sicily, Italy) as inferred from noble gases and geochemistry of ultramafic xenoliths. Lithos 132 – 133, p. 70 – 81
- Danyushevsky, L. V. and P. Plechov (2011). Petrolog3: Integrated software for modeling crystallization processes, Geochemistry Geophysics Geosystems, Vol. 12, No. 7, p. 1 – 32
- Demets, C., (2001). A New estimate for present-day Cocos–Caribbean plate motion: implications for slip along the Central American Volcanic Arc, Geophys. Res. Lett., No. 28 (21), p. 4043-4046
- Di Piazza, A. A. L. Rizzo, F. Barberi, M.I. Carapezza, G. De Astis, C. Romano, F. Sortino (2015). Geochemistry of the mantle source and magma feeding system beneath Turrialba volcano, Costa Rica, Lithos, Vol. 232, p. 319 - 335
- Dixon, J. E., E. M. Stolper, and J. R. Holloway (1995). An experimental study of water and carbon dioxide solubilities in mid-ocean ridge basaltic liquids, Part I, Calibration and solubility models, J. Petrol., Vol. 36, p. 1607–1631
- Dixon, J. E., and E. M. Stolper (1995). An experimental study of water and carbon dioxide solubilities in mid-ocean ridge basaltic liquids, Part II, Applications to degassing, J. Petrol., Vol. 36, p. 1633 – 1646
- Dixon, J. E. and V. Pan (1995). Determination of the molar absorptivity of dissolved carbonate in basanitic glass, American Mineralogist, Vol. 80, p. 1339 - 1342
- Ehrenborg, J. (1996). A new stratigraphy for the Tertiary volcanic rocks of the Nicaraguan highland, Geol. Soc. America. Bull., Vol. 108, p. 830 - 842
- Eiler, J.M., M. J. Carr, M. Reagan, M., E. Stolper (2005). Oxygen isotope constraints on the sources of Central American arc lavas. Geochem. Geophys. Geosyst, 6
- Elkins, L.J., T.P. Fischer, D.R. Hilton, Z.D. Sharp, S. McKnight, J. Walker, (2006). Tracing nitrogen in volcanic and geothermal volatiles from the Nicaraguan volcanic front. Geochim. Cosmochim. Acta, Vol. 70, p. 5215 – 5235
- Feigenson M. D., M.J. Carr, S.V. Maharaji, S. Juliano, L.L. Bolge, (2004). Lead Isotope Composition Of Central American Volcanoes: Influence Of The Galapagos Plume ; Geochemistry Geophysics Geosystems, No. 5, Issue 6, p. 1-14
- Fine and Stolper (1986). Dissolved carbon dioxide in basaltic glasses: Concentrations and speciation. Earth and Planetary Science Letters, Vol. 1976, p. 263 – 278

- Fischer T. P. (2008). Fluxes of volatiles (H2O, CO2, N2, Cl, F) from arc volcanoes. Geochem. J., no. 42, p. 21 – 38
- Francis, P. L. Horrocks, C. Oppenheimer, (2000). Monitoring gases from andesite volcanoes, Philosophical Transactions: Mathematical, Physical and Engineering Sciences, vol. 358, n. 1770, Causes and Consequences of Eruptions of Andesite Volcanoes (May 15, 2000), p. 1567 - 1584
- Gale, A., Dalton, C. A., Langmuir, C. H., Su, Y. & Schilling, J. G. (2013). The mean composition of ocean ridge basalts. Geochemistry, Geophysics, Geosystems, Vol. 14, No. 3, p. 489 – 518
- Geirsson, H., M. Rodgers, P. LaFemina, M. Witter, D. Roman, A. Muñoz, V. Tenorio, J. Alvarez, V.C. Jacobo, D. Nilsson, B. Galle, M.D. Feineman, T. Furman, A. Morales, (2014). Multidisciplinary observations of the 2011 explosive eruption of Telica volcano, Nicaragua: Implications for the dynamics of low explosivity ash eruptions. J. Volcanol. Geotherm. Res., No. 271, p. 55 – 69
- Giggenbach, W.F., N. Garcia, A. London, L. Rodriguez, N. Rojas, M.L. Calvache, (1990). The chemistry of fumarolic vapor and thermal-spring discharges from the Nevado del Ruiz volcanic-magmatic-hydrothermal-system, Colombia, J. Volcanol. Geotherm.Res., no. 42, p.13 - 39
- Giggenbach,W.F., Sano, Y.,Wakita, H., (1993). Isotopic composition of helium, and CO2 and CH4 contents in gases produced along the New Zealand part of a convergent plate boundary. Geochimica et cosmochimica acta, Vol. 57, No. 14, Vol. 3427 - 3455.
- Global Volcanism Program, National Museum of Natural History (GVP). Retrieved 2014, http://volcano.si.edu/
- Gonnerman, H.M., M. Manga, (2005). Nonequilibrium magma degssing : Results from modeling of the ca. 1340 A.D. eruption of Mono Craters, California, Earth and Planet. Sc. Let., No. 238, p. 1 - 16
- Graham, D.W. (2002). Noble gas isotope geochemistry ofmid-ocean ridge and ocean island basalts: Characterization of mantle source reservoirs. Reviews in Mineralogy and Geochemistry, Vol. 47, No. 1, p. 247 – 317
- Gualda, J., and M.S. Ghiorso, (2015). MELTS_Excel: A Microsoft Excel-based MELTS interface for research and teaching of magma properties and evolution. Geochemistry, Geophysics, Geosystems, 16: 315-324
- Hauri, H. E., J. Wang, J. E. Dixon, P. L. King, C. Mandeville, S. Newman (2002). Chemical Geology, Vol. 183, p. 99 – 114
- Hauri, H. E., A. M. Shaw, J. Wang, J. E. Dixon, P. L. King, C. Mandeville (2006). Matrix effects in hydrogen isotope analysis of silicate glasses by SIMS, Chemical Geology, Vol. 235, p. 352 - 365
- Havlicek, P., P. Hradecky, M. Hrubes, B. Mlcoch, M. Opletal, J. Sebesta (CGU), N. Buitrago, W. Strauch, (1999). Estudio Geológico Y Reconocimiento De La Amenaza Natural - Zona Chinandega-Leon , Nicaragua. Praga-Managua 1999, Resumen Ejecutivo (Servicio Geológico Checo, CGU, en cooperación con Instituto Nicaragüense de Estudios Territoriales, INETER), 23 p.
- Havlicek, P., P. Hradecky, M. Hrubes, P. Kyel, B. Mlcoch, S. Mrazova, Z. Novak, M. Opletal, A. Prichystal, J. Sebesta, J. Seveik, M. Bustillo, Z. Rizo, (2000). Estudio Geológico Y Reconocimiento De La Amenaza Geológica En El Área De León - La Paz Centro Y Malpasillo, Praga-Managua 2000, Reporte Final (Servicio Geológico Checo, CGU, en cooperación con Instituto Nicaragüense de Estudios Territoriales, INETER), 244 p.
- Heydolph, K., K. Hoernle, F. Hauff, P. van den Bogaard, M. Portnyagin, I. Bindeman, D. Garbe-Schonberg, (2012). Along and across arc geochemical variations in NW Central

America: Evidence for involvement of lithospheric pyroxenite, Geochimica et Cosmochimica Acta, No. 84, p.459-491
- Hilton, D.R., T.P. Fischer, B. Marty, B., (2002). Noble gases and volatile recycling at sub-duction zones. In: Porcelli, D., Ballentine, C.J., Wieler, R. (Eds.), Noble Gases in Geochemistry and Cosmochemistry. In: Rev. Mineral. Geochem., Vol.47. Mineral. Soc. Am., Washington, DC, p.319–370
- Hradecký, P., J. Šebesta et. al. (2007), Mapa de la Cadena volcánica Nicaragúense 1:200.000, Czech Geological Survey, iSBN 978-80-7075-671-3
- Ihinger, P. D., Hervig, R. V. & McMillan, P. F. (1994). Analytical methods for volatiles in glasses. In: Caroll, M. (ed.) Volatiles in Magmas. Reviews in Mineralogy. Mineralogical Society of America, Washington, DC, Vol. 30, p. 67 – 121
- Jarrard, R.D. (2003). Subduction fluxes of water, carbon dioxide, chlorine and potassium. Geochem Geophys Geosys, Vol. 4, Issue 5, p. 1 -50
- Jaupart, C., and Vergniolle, S., (1988), Laboratory models of Hawaiian and Strombolian eruptions: Nature, vol. 331, p. 58–60
- Jugo, P.J., R.W. Luth, J.P. Richards (2005b). An experimental study of the sulfur content in basaltic melts saturated with immiscible sulphide or sulfate liquids at 1300 ℃ and 1.0 GPa, J. Petrol., no. 46, p. 783 - 798
- Kilinc, A., , I.S.E Carmichael, M. Rivers, M., and R. O. Sack, (1983). The Ferric–Ferrous Ratio of Natural Silicate Liquids Equilibrated in Air, Contrib. Mineral. Petrol., Vol. 83, p. 136 - 140
- Kutterolf, S., A. Freundt, W. Pérez, H. Wehrmann, H.-U. Schmincke, (2007). Late Pleistocene to Holocene temporal succession and magnitudes of highly-explosive volcanic eruptions in west-central Nicaragua J. Volcanol. Geotherm. Res., No. 163, p. 55 - 82
- La Femina, P. C., T. H. Dixon, and W. Strauch, (2002), Bookshelf faulting in Nicaragua, Geology, No. 30, p. 751 – 754
- Leeman W. P., M.J. Carr, J.D. Morris, (1994). Boron Geochemistry of the Central American Volcanic Arc: Constraints on the Genesis of Subduction-Related Magmas, Geochim. Cosmochim. Acta, No. 58, p. 149-168
- Lhur, J.F. (1990). Experimental phase relations of water and sulfur saturated arc magmas and the 1982 eruptions of El Chichon volcano, J. Petrol., no. 31, p. 1071 - 1114
- Lucic, G., J. Stix, B. S. Lollar, G. L.-Couloume, A. Munoz, M. I. Carcache (2014). The degassing character of a young volcanic center: Cerro Negro, Nicaragua, Bull. Volcanol., Vol. 76, p. 3 - 23
- MacKenzie, L., G. A. Abers, K. M. Fisher, E. M. Syracuse, J. M. Protti, V. Gonzales, and W. Strauch (2008). Crustal structure along the southern Central American volcanic front, Geochem. Geophys. Geosyst., No. 9, Q08S09
- Martelli, M., A. L. Rizzo, A. Renzulli, F. Ridolfi, I. Arienzo, A. Rosciglione (2014). Noble-gas signature ofmagmas froma heterogeneousmantle wedge: the case of Stromboli volcano (Aeolian Islands, Italy), Chemical Geology, Vol. 368, p. 39 – 53
- Marsh, B.D. (1981). On the Crystallinity, Probability of Occurrence, and Rheology of Lava and Magma, Contrib. Mineral Petrol, No. 78, p. 85 - 98
- McBirney, A. R., Williams, H., (1965). Volcanic History of Nicaragua, University of California Publ. in Geol. Sci., Vol. 55, p. 1-73
- Métrich, N., A. Bertagnini, P. Landi, and M. Rosi, (2001). Crystallization Driven by Decompression and Water Loss at Stromboli Volcano (Aeolian Islands, Italy), Journal of petrology, Vol. 42, No. 8, p. 1471-1490

- Métrich, N. and P. J. Wallace (2008). Volatile abundance in basaltic magmas and their degassing paths tracked by melt inclusions, Rev. Mineral. Geochem., Vol. 69, p. 363 - 402
- Navarro, M. C. (1994). Peligro volcánico, volcán Telica, MS, 73 p. INETER Managua
- Noll P. D. Jr., H.E. Newsom, W.P. Leeman, J.G. Ryan, (1996). The Role of Hydrothermal Fluids in the Production of Subduction Zone Magmas: Evidence from Siderophile and Chalcophile Trace Elements and Boron, Geochim. Cosmochim. Acta, No. 60, p. 587-611
- Novák, Z. and A. Přichystal, (2006). El área volcánica de Telica (Nicaragua) y sus peligros geológicos, in: Krystalinikum, Contribution to the geology and the petrology of crystalline complexes, Moravian Museum Brno, No. 31, 2006, p. 47-66
- Newman, S., E. Stolper and R. Robert, (2000). H2O and CO2 in magmas from the Mariana arc and back arc systems, Geochemistry Geophysics Geosystems, Vol. 1, No. 1, p. 1 – 24
- Paonita, A., A. Caracausi, G. Iacono-Marziano, M. Martelli, A.L. Rizzo, (2012). Geochemical evidence for mixing between fluids exsolved at different depths in the magmatic system of Mt Etna (Italy). Geochimica et Cosmochimica Acta, No. 84, p. 380 – 394
- Papale, P., Moretti, R. & Barbato, D. (2006). The compositional dependence of the saturation surface of H2O-CO2 fluids in silicate melts. Chemical Geology, Vol. 29, p. 78 - 95
- Patino, L. C., M. J. Carr, and M. D. Feigenson, (2000). Local and regional variations in Central American arc lavas controlled by variations in subducted sediment input, Contributions to Mineralogy and Petrology, No. 138.3, p. 265-283
- Pichavant, M., I. Di Carlo, S.G. Rotolo, B. Scaillet, A. Burgisser, N. Le Gall, C. Martel, (2013). Generation of CO2-rich melts during basalt magma ascent and degassing, Contrib. Mineral Petrol., No. 166, p. 545 – 561
- Plank, T., Langmuir, C.H., (1988). An evaluation of the global variations in the major element chemistry of arc basalts. Earth Planet. Sci. Lett., Vol. 90, Issue (4), p. 349 – 370
- Plank T. and Langmuir C. H. (1998). The chemical composition of subducting sediment and its consequences for the crust and mantle. Chem. Geol., No. 145, p. 325 – 394
- Plank, T., Balzer, V., Carr, M., (2002). Nicaraguan volcanoes record paleoceano-graphic changes accompanying closure of the Panama gateway. Geology, Vol. 30, No. 12, p. 1087 - 1090
- Portnyagin, M. V., K. Hoernle, N. L. Mironov (2014). Contrasting compositional trends of rocks and olivine-hosted melt inclusions from Cerro Negro volcano (Central America): Implications for decompression-driven fractionation of hydrous magmas, International Journal of earth Sciences, October 2012, Vol. 103, Issue 7, p. 1963 – 1982
- Putirka, K. (2008). Thermometers and Barometers for Volcanic Systems. In: Putirka KD, Tepley III G.J. (eds) Minerals, Inclusions and Magmatic Processes. Reviews in Mineralogy and Geochemistry, Vol 69. Mineralogic Society of America, p. 61-120
- Reagan, M.K., Morris, J.D., Herrstrom, E.A., Murrell, M.T., (1994). U series and Be isotope evidence for an extended history of subduction modification of the mantle below Nicaragua. Geochim. Cosmochim. Acta, Vol. 58, p. 4199 – 4212
- Rizzo, A., Barberi, F., Carapezza, M.L., Di Piazza, A., Francalanci, L., Sortino, F., D'Alessandro, W., (2015a). New mafic magma refilling a quiescent volcano: evidence from He–Ne–Ar isotopes during the 2011–2012 unrest at Santorini, Greece. Geochemistry, Geophysics, Geosystems, Vol. 16, Issue 3, p. 798 - 814

- Rodgers, M., D.C. Roman, H. Geirsson, P. LaFemina, A. Muñoz, C. Guzman, V. Tenorio, (2013). Seismicity accompanying the 1999 eruptive episode at Telica Volcano, Nicaragua. J. Volcanol. Geotherm. Res. No. 265, p. 39–51
- Rodgers, M., C.D. Roman, H. Geirsson, P. LaFemina, S.R. McNutt, A. Muñoz, V. Tenorio, (2015). Stable and unstable phases of elevated seismic activity at the persistently restless Telica Volcano, Nicaragua, J. Volcanol. Geotherm. Res., No. 290, p. 63–74
- Roberge, J., Wallace, P., White, R. V., M. F. Coffin, (2005). Anomalous uplift and subsidence of the Ontong Java Plateau inferred from CO2 contents of submarine basaltic glasses, Geological Society of America, Geology, Vol. 33, No. 6, p. 501 - 504
- Robidoux, P., Aiuppa, A., Rotolo, S., Rizzo, A., Hauri, E., (2016). The volatile content of mafic to intermediate magmas from San Cristóbal volcano, Nicaragua, Lithos, (submitted).
- Roedder, P. L., and R. F. Emslie (1970). Olivine-liquid equilibrium, Contrib. Mineral. Petrol., Vol. 29, p. 275 – 289
- Roedder, E. (1979). Origin and significance of magmatic inclusions, Bull. Minéral., 102, p. 487-510
- Roedder, E. (1984). Fluid Inclusions. Rev. Miner., Vol. 12, 644 p.
- Roggensack, K., R. L. Hervig, S. B. McKnight, and S. N. Williams (1997). Explosive basaltic volcanism from Cerro Negro: Influence of volatiles on eruptive style, Science, No. 277, p. 1639 – 1642
- Ruscitto, D. (2012). Magmatic Volatile Contents And Explosive Cinder Cone Eruptions In The High Cascades: Recent Volcanism In Central Oregon And Northern California, Doctor of Philosophy Presented to the Department of Geological Sciences and the Graduate School of the University of Oregon, 182 p.
- Sadofsky, S. J., M. V. Portnyagin, K. Hoernle, and P. van den Bogaard (2008). Subduction cycling of volatile and trace elements through the Central American Volcanic Arc: Evidence from melt inclusions, Contrib. Mineral. Petrol., Vol. 155, p. 433 – 456
- Saginor I., E. Gazel, J. Michael, C. Carr, C.C. Swisher III, B. Turrin, (2011). New Pliocene–Pleistocene 40Ar/39Ar ages fill in temporal gaps in the Nicaraguan volcanic record, J. Volcanol. Geotherm. Res., No. 202, p. 143-152
- Saito, G., H. Shinohara and K. Kazahaya,(2002). Successive sampling of fumarolic gases at Satsuma-Iwojima and Kuju volcanoes, Southwest Japan. Geochem. J., no. 36, p.1 – 20
- Scaillet, B. and M. Pichavant (2003). Experimental constraints on volatile abundances in arc magmas and their implications for degassing processes, in Volcanic Degassing,, edited by C. Oppenheimer, D.M. Pyle and J. Barclay, Geol. Soc. Spec. Publ. 213, p. 23 - 52
- Shaw, A.M., Hilton, D.R., Fisher, T.P., Walker, J.A., Alvarado, G.E., (2003). Contrasting He–C relationships in Nicaragua and Costa Rica: insights into C cycling through subduction zones. Earth and Planetary Science Letters, No. 214, p. 419–513
- Shaw, A.M., D. R. Hilton, T.P. Fisher, J. A. Walker, G. A. M. de Leew, (2006). Helium isotope variations in mineral separates from Costa Rica and Nicaragua: assessing crustal contributions, timescale variations and diffusion-related mechanism. Chemical Geology, Vol. 230, p. 124 – 139
- Signorelli, S. and M.R. Carroll (2000). Solubility and fluid-melt partitioning of Cl in hydrous phonolitic melts, Geochim. Cosmochim. Acta, no. 64, p. 2851 - 2862
- Stolper, E. (1982), Water in silicate glasses: An infrared spectroscopic study, Contrib. Mineral. Petrol., Vol. 81, p. 1 – 17
- Stix J., G.J.A. Zapata, V.M. Calvache, J.G.P. Cortes, T.P. Fischer, M.D. Gomez, M.L. Narvaez, V.M. Ordonez, E.A. Ortega, C.R. Torres, and S.N. Williams, (1993). A model of degassing at Galeras volcano, Colombia, 1988–1993, Geology, No. 21, p. 963 – 967

- Stix, J. (2007). Stability and instability of quiescently active volcanoes: The case of Masaya, Nicaragua, Geology, June 2007, vol. 35, no. 6, p. 535 - 538
- Syracuse, E. M., and G. A. Abers, (2006). Global compilation of variations in slab depth beneath arc volcanoes and implications, Geochem. Geophys. Geosyst., No. 7, Q05017
- Taran Y. A., J.W. Hedequist, M.A. Korzhinsky, S.I. Tkachenko, and K.I. Shmulovich, (1995a). Geochemistry of magmatic gases of Kudryavy volcano, Iturup, Kuril islands. Geochim. Cosmochim. Acta, no. 59, p. 1741 – 1761
- Taran Y. A., A.N. Korablev and G.S. Steinberg (1995b). Chemical and isotopic composition of fumarolic gases from South Kurils volcanoes in 1992–1994. In Volcano–Atmosphere Interaction. Intl Chem. Cong. Pacific Basin Societies (Pacifichem '95). Honolulu, Hawaii
- Taran, Y.A., (2009). Geochemistry of volcanic and hydrothermal fluids and volatile budget of the Kamchatka–Kuril subduction zone, Geochimica et Cosmochimica Acta, no. 73, p.1067 – 1094
- Toplis, M. J. (2005). The thermodynamics of iron and magnesium partitioning between olivine and liquid: Criteria for assessing and predicting equilibrium in natural and experimental systems, Contrib. Mineral. Petrol., Vol. 149, p. 22 – 39
- Wade, J.A. T. Plank, W. G. Melson, G. J. Soto, A. H. Hauri (2006). Volatile content of magmas from Arenal volcano, Costa Rica, J. Volcanol Geotherm. Res., Vol 157, p. 94 - 120
- Walker, J. A., L. C. Patino, J. C. Michael and M. D. Feigenson, (2001). Slab control over HFSE depletions in central Nicaragua, Earth and Planetary Science Letters, No. 192, p.533-543
- Wallace, P. J. (2005). Volatiles in subduction zone magmas: concentrations and fluxes based on melt inclusion and volcanic gas data, J. Volcanol. Geotherm res., Vol. 140, p. 217 – 240
- Webster, D., R. J. Kinzler, and E. A. Mathez, (1999). Chloride and water solubility in basalt and andesite melts and implications for magmatic degassing, Geochimica et Cosmochimica Acta, Vol. 63, No. 5, p. 729 – 738
- Wehrmann, H., Hoernle, K., Portnyagin, M., Wiedenbeck, M., Heydolph, K., (2011). Volcanic CO2 output at the Central American subduction zone inferred from melt inclusions in olivine crystals from mafic tephras. Geochem. Geophys. Geosyst., Vol. 12, p. 1 - 16, Q06003
- Wehrmann, H., K. Hoernle, D. Garbe-Schonberg, G. Jacques, J. Mahlke, K. Schumann, (2014). Insights from trace element geochemistry as to the roles of subduction zone geometry and subduction input on the chemistry of arc magmas. Int. J. Earth Sci., Vol. 103, Issue 7, p. 1929 - 1944
- Williams, S.N, R.E. Stoiber, N.P. Garcia, A. Londono, J.B. Gemmel, D.R. Lowe, C.B. Connor (1986). Eruption of the Nevado del Ruiz volcano, Colombia, on 13 November, 1985: gas flux and fluid geochemistry, Science, no. 233, p. 964 - 967
- Zimmer, M.M., T.P. Fischer, D.R. Hilton, G.E. Alvarado, Z.D., J.A. Walker, (2004). Nitrogen systematics and gas fluxes of subduction zones: insights from Costa Rica arc volatiles. Geochem. Geophys. Geosyst., Vol. 5, Issue 5

ELECTRONIC APPENDIX 1

Sample	Zone	SiO_2	FeO	MnO	MgO	CaO	Tot. All.	Fo %
Layer TEL04B		**(wt. %)**						
t04b2aol	**Core**	39.53	13.85	0.17	46.28	0.18	100.00	85.63
t04b2bol	**Core**	39.15	14.20	0.21	46.29	0.14	100.00	85.32
t04b2col	**Core**	39.30	14.10	0.26	46.08	0.25	100.00	85.35
t04b2dol	**Core**	39.56	14.50	0.22	45.57	0.14	100.00	84.85
t04b2olcore	**Core**	40.36	13.96	0.13	45.36	0.18	100.00	85.28
t04b2olrim	**Rim**	41.85	14.64	0.22	43.13	0.17	100.00	84.01
t04b3aol	**Core**	39.66	14.81	0.21	45.14	0.18	100.00	84.46
t04b3olrim	**Rim**	39.46	14.61	0.26	45.52	0.15	100.00	84.74
t04b4aol	**Core**	43.87	10.22	0.08	45.58	0.25	100.00	88.83
t04b4olcore	**Core**	43.29	9.45	0.12	46.99	0.14	100.00	89.86
t04b4olrim	**Rim**	44.87	11.45	0.26	43.26	0.17	100.00	87.08
t04b5aol	**Core**	38.06	18.22	0.22	43.30	0.21	100.00	80.91
t04b5aolcore	**Core**	38.77	18.01	0.28	42.84	0.10	100.00	80.92
t04b5aolinter	**Inter**	38.60	17.64	0.33	43.23	0.19	100.00	81.38
t04b5aolrim	**Rim**	33.27	22.44	0.44	43.60	0.24	100.00	77.60
t04b8aol	**Core**	40.19	14.78	0.35	44.45	0.23	100.00	84.28
t04b8bol	**Core**	39.36	14.83	0.25	45.38	0.18	100.00	84.51
t04b8olrim	**Rim**	38.64	14.85	0.24	46.05	0.21	100.00	84.68
t04b9olcore	**Core**	38.65	18.06	0.23	42.88	0.18	100.00	80.89
t04b9olrim	**Rim**	39.04	17.72	0.21	42.84	0.18	100.00	81.17

ELECTRONIC APPENDIX 1 (next)

Sample	Zone	SiO_2	FeO	MnO	MgO	CaO	Tot. All.	Fo %
Layer TEL03A		**(wt. %)**						
tel03Ai13ol1	**Rim**	36.36	36.20	0.76	26.37	0.31	100.00	55.99
tel03Ai13ol2	**Core**	36.43	35.75	0.76	26.74	0.33	100.00	57.14
tel03Aol1c1	**Core**	35.65	33.11	0.73	30.20	0.25	100.00	61.93
tel03Aol1c2	**Core**	35.35	33.54	0.67	30.14	0.28	100.00	61.57
tel03Aol1rim1	**Rim**	35.94	33.17	0.74	29.77	0.28	100.00	61.54
tel03Aol1rim2	**Rim**	35.66	34.02	0.65	29.40	0.28	100.00	60.64
tel03Aol2c1	**Core**	35.63	33.39	0.70	29.96	0.27	100.00	61.54
tel03Aol2c2	**Core**	35.74	32.95	0.68	30.36	0.25	100.00	62.16
tel03Aol2rim1	**Rim**	35.56	34.42	0.71	29.07	0.24	100.00	60.09
tel03Aol2rim2	**Rim**	35.67	34.68	0.69	28.60	0.30	100.00	59.52

ELECTRONIC APPENDIX 1 (next)

Sample	Zone	SiO_2	FeO	MnO	MgO	CaO	Tot. All.	Fo %
Layer TEL04K		**(wt. %)**						
tel04b2bol	**Core**	39.12	15.72	0.25	44.68	0.23	100.00	83.52
tel04b2bolcore	**Core**	38.38	16.05	0.31	45.05	0.21	100.00	83.35
tel04b2bolrim	**Rim**	38.59	16.54	0.21	44.49	0.18	100.00	82.75
tel04o3aol	**Core**	38.27	19.13	0.23	42.14	0.22	100.00	79.70
tel04o3atry	**Core**	38.43	18.35	0.29	42.74	0.19	100.00	80.59
tel04o3olcore	**Core**	38.81	19.01	0.33	41.66	0.19	100.00	79.62
t04kol4aol	**Core**	40.89	13.91	0.29	44.74	0.17	100.00	85.15
t04kol4olrim	**Rim**	40.51	14.29	0.26	44.75	0.19	100.00	84.81
t04kol5aol	**Core**	39.10	17.51	0.29	42.90	0.19	100.00	81.37
t04kol5olrim	**Rim**	38.42	21.25	0.33	39.77	0.23	100.00	76.94
t04kol6rim	**Rim**	41.10	16.16	0.30	42.29	0.16	100.00	82.35
t04kol6tim2	**Rim**	40.50	16.03	0.35	42.90	0.22	100.00	82.67

ELECTRONIC APPENDIX 1 (next)

Sample	Zone	SiO_2	FeO	MnO	MgO	CaO	Tot. All.	Fo %
Layer TEL04K		**(wt. %)**						
t04kol7aol	**Core**	38.86	18.47	0.45	42.05	0.17	100.00	80.23
t04kol7atry1	**Core**	38.69	18.63	0.26	42.18	0.25	100.00	80.15
t04kol7atry2	**Core**	38.13	19.56	0.33	41.70	0.28	100.00	79.17
t04kol8arol	**Core**	39.29	17.26	0.23	43.03	0.20	100.00	81.64
t04kol8olcore	**Core**	39.34	17.12	0.24	43.11	0.19	100.00	81.78
t04kol8olrim	**Rim**	39.59	18.86	0.33	41.06	0.16	100.00	79.51
t4k6oaol	**Core**	36.63	27.77	0.68	34.72	0.19	100.00	69.03
t4k6xmi	**Core**	36.39	24.89	0.46	38.07	0.20	100.00	73.17
tel04K26aX	**Core**	39.30	15.44	0.23	44.52	0.29	100.00	83.71
tel04ko1aolcore	**Core**	38.46	18.45	0.34	42.47	0.27	100.00	80.41
tel04ko1aolrim	**Rim**	36.98	23.10	0.47	39.21	0.24	100.00	75.16
tel04ko2aol	**Core**	38.91	16.71	0.25	43.79	0.33	100.00	82.37
tel04ko2aolcore	**Core**	38.80	16.41	0.28	44.25	0.26	100.00	82.78
tel04ko2aoltry	**Core**	38.48	16.24	0.23	44.84	0.21	100.00	83.12
tel04ko2col	**Core**	39.04	16.38	0.21	44.15	0.21	100.00	82.77
tel04ko2olrim	**Rim**	38.91	16.15	0.18	44.50	0.27	100.00	83.09

ELECTRONIC APPENDIX 2

Sample (EMPA)	Spot	SiO_2	TiO_2	Al_2O_3	FeO	MnO	MgO	CaO	Na_2O	Cr_2O_3	Tot.
TEL04K5aX	**Core**	51.06	0.46	2.18	11.67	0.46	15.73	18.05	0.39	0.00	100.00
TEL04K6X	**Inter**	51.35	0.42	2.15	10.13	0.39	15.47	19.75	0.30	0.03	100.00
TEL04K8bX	**Core**	50.64	0.44	3.07	10.65	0.42	15.62	18.84	0.30	0.03	100.00
TEL04K9aX	**Inter**	50.27	0.42	2.60	9.59	0.34	15.76	20.72	0.26	0.04	100.00
TEL04K9cxI	**Inter**	51.04	0.28	1.73	11.89	0.54	14.81	19.33	0.36	0.03	100.00
TEL04K9dXI	**Inter**	50.51	0.32	2.29	10.87	0.40	15.11	20.21	0.28	0.01	100.00
TEL04K10axII	**Inter**	50.19	0.45	2.40	11.90	0.44	15.27	19.08	0.27	0.00	100.00
TEL04K10bX	**Core**	50.45	0.48	2.34	11.95	0.37	15.15	18.96	0.28	0.02	100.00
TEL04K10cxI	**Rim**	50.60	0.41	2.47	9.37	0.19	16.81	19.85	0.28	0.00	100.00
TEL04K13aX	**Core**	50.93	0.46	2.40	10.55	0.44	15.64	19.32	0.24	0.03	100.00
TEL04K14aX	**Core**	51.37	0.38	1.65	12.87	0.53	14.61	18.11	0.42	0.05	100.00
TEL04K15aX	**Core**	51.39	0.43	2.59	10.18	0.36	16.10	18.64	0.30	0.00	100.00
TEL04K18aX1	**Core**	50.45	0.40	1.85	14.23	0.47	14.08	18.19	0.32	0.00	100.00
TEL04K18cX1	**Core**	51.24	0.25	1.44	13.38	0.47	14.40	18.48	0.33	0.00	100.00
TEL04K19aX1	**Core**	50.88	0.50	2.79	8.41	0.11	16.17	20.89	0.23	0.03	100.00
TEL04K20aX	**Inter**	51.06	0.45	2.77	9.19	0.27	15.17	20.83	0.23	0.03	100.00
TEL04K21aIXI	**Inter**	50.85	0.50	2.91	10.68	0.32	15.93	18.52	0.29	0.00	100.00
TEL04K22aX	**Rim**	50.19	0.40	2.56	11.40	0.43	15.68	19.04	0.30	0.00	100.00
TEL04K22bX1	**Rim**	50.99	0.33	1.89	12.28	0.48	15.60	18.18	0.25	0.00	100.00
TEL04K25aX2	**Core**	51.54	0.35	2.47	10.42	0.40	15.09	19.38	0.30	0.06	100.00
TEL04K25bX	**Core**	51.07	0.44	2.46	11.15	0.39	15.44	18.75	0.31	0.00	100.00

ELECTRONIC APPENDIX 2 (next)

Sample (EMPA)	Spot	Wo (∑Fe norm)	En	Fs	Jd	Quad	Ae	PX: Mg/(Mg+Fe)
TEL04K5aX	**Core**	36.7	44.5	18.9	0.0	97.0	3.0	0.71
TEL04K6X	**Inter**	39.9	43.5	16.6	0.0	97.7	2.3	0.73
TEL04K8bX	**Core**	38.3	44.2	17.6	0.2	97.7	2.1	0.72
TEL04K9aX	**Inter**	41.7	44.1	14.2	0.0	98.0	2.0	0.75
TEL04K9cxI	**Inter**	39.3	41.9	18.8	0.0	97.3	2.7	0.69
TEL04K9dXI	**Inter**	40.8	42.5	16.7	0.0	97.9	2.1	0.71
TEL04K10axII	**Inter**	38.7	43.1	18.2	0.0	97.9	2.1	0.70
TEL04K10bX	**Core**	38.5	42.8	18.7	0.0	97.8	2.2	0.69
TEL04K10cxI	**Rim**	39.8	46.8	13.4	0.0	97.9	2.1	0.76
TEL04K13aX	**Core**	39.0	43.9	17.0	0.0	98.2	1.8	0.73
TEL04K14aX	**Core**	37.1	41.7	21.2	0.0	96.8	3.2	0.67
TEL04K15aX	**Core**	37.8	45.5	16.7	0.3	97.8	1.9	0.74
TEL04K18aX1	**Core**	37.3	40.2	22.5	0.0	97.5	2.5	0.64
TEL04K18cX1	**Core**	37.7	40.9	21.4	0.0	97.5	2.5	0.66
TEL04K19aX1	**Core**	41.8	45.1	13.1	0.0	98.3	1.7	0.77
TEL04K20aX	**Inter**	42.2	42.8	15.0	0.2	98.2	1.5	0.75
TEL04K21aIXI	**Inter**	37.6	45.0	17.4	0.2	97.8	2.0	0.73
TEL04K22aX	**Rim**	38.5	44.1	17.4	0.0	97.7	2.3	0.71
TEL04K22bX1	**Rim**	36.8	43.9	19.3	0.0	98.1	1.9	0.69
TEL04K25aX2	**Core**	39.7	43.0	17.3	0.6	97.8	1.6	0.72
TEL04K25bX	**Core**	38.1	43.6	18.3	0.1	97.6	2.3	0.71

ELECTRONIC APPENDIX 3

EMPA Sample	Spot	SiO_2	TiO_2	Al_2O_3	FeO	MnO	MgO	CaO	Na_2O	Cr_2O_3	Tot.
TEL03B1X	**Core**	50.42	0.55	2.69	11.07	0.41	15.32	19.09	0.41	0.04	100.00
TEL03B1aX	**Core**	51.42	0.42	2.38	10.29	0.38	16.06	18.87	0.18	0.00	100.00
TEL01aol	**Core**	51.49	0.45	2.43	9.59	0.36	15.56	19.89	0.24	n.d.	100.00
TEL01bol	**Core**	51.14	0.44	2.31	10.88	0.42	14.88	19.61	0.31	n.d.	100.00
TEL04Bpx6cx	**Core**	51.52	0.20	2.29	10.93	0.38	15.05	19.31	0.32	n.d.	100.00
TEL04Bpx6ax	**Core**	51.10	0.49	3.37	9.44	0.30	15.04	19.93	0.27	n.d.	100.00

SEM-EDS Sample	Spot	SiO_2	TiO_2	Al_2O_3	FeO	MnO	MgO	CaO	Na_2O	Cr_2O_3	Tot.
TEL02i1cpx1	**Core**	51.87	0.36	1.85	11.56	0.49	13.06	20.23	0.57	n.d.	100.00
TEL02i1cpx2	**Core**	51.93	0.65	2.15	10.44	0.52	13.35	20.24	0.73	n.d.	100.00
TEL02i2cpx1	**Inclusion, Plg**	51.62	0.49	2.31	11.92	0.46	13.14	19.47	0.59	n.d.	100.00
TEL02i2cpx2	**Inclusion, Plg**	51.50	0.46	2.55	11.65	0.44	13.05	19.79	0.55	n.d.	100.00
TEL02i2cpx3	**Inclusion, Plg**	51.00	0.52	3.02	11.43	0.27	12.87	20.23	0.66	n.d.	100.00
TEL02i3cpx1	**Rim**	51.42	0.55	2.65	11.51	0.33	13.34	19.59	0.61	n.d.	100.00
TEL02i3cpx2	**Rim**	51.62	0.56	2.60	11.23	0.47	13.19	19.80	0.54	n.d.	100.00
TEL03Ai13cpx1	**Core**	51.25	0.46	1.82	13.83	0.47	11.89	19.63	0.64	n.d.	100.00
TEL03Ai13cpx2	**Core**	51.26	0.48	2.42	12.08	0.35	13.19	19.53	0.69	n.d.	100.00

ELECTRONIC APPENDIX 3 (next)

EMPA

Sample	Spot	Wo (∑Fe norm)	En	Fs	Jd	Quad	Ae	PX: Mg/(Mg+Fe)
TEL03B1X	**Core**	38.9	43.4	17.7	0.0	96.8	3.2	0.71
TEL03B1aX	**Core**	38.1	45.1	16.8	0.1	98.7	1.2	0.74
TEL01aol	**Core**	40.3	43.9	15.8	0.3	98.2	1.5	0.74
TEL01bol	**Core**	39.9	42.1	17.9	0.1	97.7	2.2	0.71
TEL04Bpx6cx	**Core**	39.3	42.7	18.0	0.4	97.6	2.1	0.71
TEL04Bpx6ax	**Core**	41.1	43.2	15.7	0.9	98.0	1.2	0.74

SEM-EDS

Sample	Spot	Wo (∑Fe norm)	En	Fs	Jd	Quad	Ae	PX: Mg/(Mg+Fe)
TEL02i1cpx1	**Core**	42.3	38.0	19.7	1.5	95.7	2.8	0.67
TEL02i1cpx2	**Core**	42.7	39.2	18.1	2.4	94.6	3.1	0.70
TEL02i2cpx1	**Inclusion, Plg**	41.1	38.6	20.4	2.1	95.6	2.3	0.66
TEL02i2cpx2	**Inclusion, Plg**	41.8	38.3	19.9	2.2	95.8	2.0	0.67
TEL02i2cpx3	**Inclusion, Plg**	42.8	37.9	19.3	1.9	95.0	3.1	0.67
TEL02i3cpx1	**Rim**	41.3	39.2	19.5	2.1	95.4	2.5	0.67
TEL02i3cpx2	**Rim**	41.9	38.8	19.3	2.6	96.0	1.4	0.68
TEL03Ai13cpx1	**Core**	41.5	34.9	23.6	1.2	95.1	3.6	0.61
TEL03Ai13cpx2	**Core**	41.0	38.6	20.4	1.3	94.8	3.8	0.66

ELECTRONIC APPENDIX 4

Eruption	STS									
Unit	TEL04K	TEL04K	TEL04K	TEL04K	TEL04K	TEL04K	TEL04K	TEL04K	TEL04K	TEL04K
MI Sample	TEL04K20a	TEL04K6a	TEL04K8a	TEL04K8b	TEL04K9a	TEL04K9cI	TEL04K9d	TEL04K10a	TEL04K10b	TEL04K10c
No. (#spot/average)	Average	8			Average	19		Average	Average	
SiO_2	50.10	56.34	59.90	56.08	53.93	56.92	57.52	56.75	56.27	53.40
TiO_2	0.89	0.82	0.63	0.64	0.78	0.74	0.68	0.85	0.86	0.99
Al_2O_3	14.27	15.29	13.67	14.40	14.73	13.30	13.42	13.99	14.10	16.08
FeO*	9.77	8.74	5.80	7.51	8.71	8.16	9.77	8.37	8.27	9.23
MnO	0.22	0.12	0.22	0.17	0.27	0.18	0.34	0.21	0.21	0.20
MgO	3.83	2.58	1.71	2.12	3.39	2.75	2.17	2.05	2.41	3.45
CaO	6.85	6.18	4.23	4.96	6.48	6.19	5.74	5.06	5.24	6.58
Na_2O	2.70	2.71	3.16	3.14	3.26	2.95	2.71	3.29	3.48	2.70
K_2O	1.66	2.32	3.61	3.73	2.03	1.98	1.90	3.07	3.00	1.59
P_2O_5	0.15	0.24	0.39	0.29	0.28	0.25	0.22	0.38	0.38	0.22
Cr_2O_3	0.01	0.00	0.00	0.00	0.00	0.00	0.00	0.01	0.02	0.00
NiO	0.03	0.03	0.00	0.00	0.03	0.11	0.00	0.03	0.04	0.04
TOT	90.50	95.39	93.30	93.03	93.89	93.55	94.47	94.06	94.27	94.47

ELECTRONIC APPENDIX 4 (next)

Eruption	STS								
Unit	TEL04K	TEL04K	TEL04K	TEL04K	TEL04K	TEL04K	TEL04K	TEL04K	TEL04K
MI Sample	TEL04K13a	TEL04K14b	TEL04K15a	TEL04K18c	TEL04K21aI	TEL04K22a	TEL04K22b	TEL04K25a	TEL04K25b
No. (#spot/average)	Average	Average	Average	Average	30	Average	Average	12	17
SiO_2	56.17	60.61	58.39	60.68	55.84	56.16	56.74	59.01	59.02
TiO_2	1.02	1.02	0.68	0.63	1.08	0.72	0.70	0.73	0.53
Al_2O_3	15.02	12.72	14.60	12.36	15.04	14.58	14.10	14.47	17.08
FeO*	9.70	7.54	7.80	8.33	10.32	8.30	8.72	6.69	5.86
MnO	0.21	0.17	0.19	0.23	0.27	0.20	0.21	0.05	0.10
MgO	2.39	1.69	3.18	2.24	2.94	3.37	3.25	2.08	1.99
CaO	6.08	4.82	5.63	4.44	5.86	5.66	5.77	4.84	6.04
Na_2O	3.80	3.22	3.40	3.44	3.43	3.02	3.09	3.02	3.10
K_2O	1.97	3.39	2.36	2.72	2.26	2.28	2.17	3.53	2.73
P_2O_5	0.29	0.30	0.25	0.24	0.29	0.22	0.26	0.34	0.31
Cr_2O_3	0.02	0.00	0.02	0.00	0.00	0.02	0.02	0.04	0.00
NiO	0.00	0.02	0.02	0.03	0.00	0.01	0.05	0.00	0.01
TOT	96.66	95.49	96.51	95.32	97.32	94.55	95.09	94.79	96.78

ELECTRONIC APPENDIX 4 (next)

Eruption	STS									
Unit	TEL04K	TEL04K	TEL04K	TEL04K	TEL04K	TEL04K	TEL04K	TEL04K	TEL04K	TEL04K
MI Sample	TEL04K18a	TEL03B1	tel01	tel01b	tel01c	TEL04K26a	tel04ko1a	tel04ko2a	tel04ko2b	tel04ko2c
No. (#spot/average)	Average	Average	Average	144	149	Average	126	Average	133	129
SiO_2	64.33	62.74	60.22	58.89	66.72	50.07	45.94	48.17	48.61	48.11
TiO_2	0.63	0.97	0.96	0.90	0.73	2.02	0.80	2.21	2.36	2.03
Al_2O_3	12.76	15.06	17.24	14.51	15.44	16.26	16.38	17.52	18.35	18.07
FeO*	7.23	3.99	5.87	9.44	2.48	6.99	10.10	9.41	8.40	7.72
MnO	0.21	0.14	0.23	0.18	0.07	0.15	0.19	0.17	0.16	0.09
MgO	1.44	0.97	1.56	1.99	0.43	4.55	6.15	3.63	2.59	2.54
CaO	3.58	2.16	5.42	4.66	2.85	10.29	12.43	11.63	11.83	11.76
Na_2O	3.20	4.05	3.63	3.60	3.72	3.36	2.20	2.77	2.60	2.81
K_2O	3.73	4.79	2.40	2.58	2.88	0.87	0.33	0.51	0.54	0.62
P_2O_5	0.23	0.54	0.30	0.18	0.26	0.27	0.05	0.16	0.16	0.19
Cr_2O_3	0.01	0.00	0.00	0.00	0.00	0.07	0.00	0.00	0.00	0.00
NiO	0.03	0.03	0.00	0.00	0.00	0.01	0.00	0.00	0.00	0.00
TOT	97.37	95.43	97.83	96.92	95.58	94.90	94.59	96.17	95.59	93.93

ELECTRONIC APPENDIX 4 (next)

Eruption	STS								
Unit	TEL04K	TEL04K	TEL04K	TEL04K	TEL04B	TEL04B	TEL04B	TEL04B	TEL04B
MI Sample	t04kol4a	t04kol5a	t04kol6a	t04kol8a	tel04b	t04b2a	t04b2b	t04b2c	t04b2d
No. (#spot/average)	Average	215	Average	Average	Average	Average	Average	Average	185
SiO_2	45.49	44.76	46.85	43.70	46.40	48.80	48.78	46.91	46.55
TiO_2	0.71	0.83	0.76	0.73	0.54	0.53	0.70	0.66	0.59
Al_2O_3	18.72	18.52	17.98	17.79	18.91	16.45	17.38	17.70	19.76
FeO*	8.50	9.45	9.04	9.51	9.31	7.91	7.92	7.77	7.49
MnO	0.14	0.21	0.19	0.19	0.18	0.13	0.18	0.16	0.24
MgO	6.74	4.77	5.52	5.52	5.63	5.61	6.20	5.99	5.91
CaO	11.41	12.98	10.50	12.99	13.17	12.46	12.71	12.33	11.65
Na_2O	2.18	2.38	2.29	2.04	1.69	1.92	1.87	1.76	1.73
K_2O	0.41	0.36	0.48	0.41	0.29	0.29	0.29	0.27	0.29
P_2O_5	0.13	0.15	0.10	0.10	0.11	0.10	0.08	0.09	0.03
Cr_2O_3	0.00	0.00	0.00	0.00	0.00	0.00	0.00	0.00	0.00
NiO	0.00	0.00	0.00	0.00	0.00	0.00	0.00	0.00	0.00
TOT	94.42	94.41	93.70	92.98	96.22	94.20	96.10	93.64	94.23

ELECTRONIC APPENDIX 4 (next)

Eruption									
Unit	TEL04B	TEL04B	TEL04B	TEL04B	TEL04B	TEL04B	TEL04B	TEL04B	TEL04B
MI Sample	t04b3a	t04b5a	t04b8a	t04b8b	t4bcpx6oa	t4bcpx6ob	t4bpx6a	t4bpx6a	t4bpx6a2
No. (#spot/average)	170	Average	Average	Average	233	235	Average	Average	252
SiO_2	46.35	46.24	46.67	46.21	54.12	53.48	55.51	54.38	55.29
TiO_2	0.72	0.67	0.57	0.62	0.74	1.05	0.70	0.89	0.77
Al_2O_3	17.76	17.02	19.05	19.41	13.99	14.89	13.79	13.79	14.34
FeO*	8.45	9.82	8.01	8.05	10.68	9.85	8.71	10.82	7.88
MnO	0.21	0.17	0.12	0.26	0.18	0.23	0.25	0.27	0.11
MgO	6.55	5.95	5.93	6.25	3.33	2.66	2.95	3.01	3.03
CaO	10.89	11.80	11.22	11.37	6.91	7.21	5.86	6.39	6.06
Na_2O	2.01	2.02	1.85	1.85	2.85	2.91	3.25	3.58	3.38
K_2O	0.27	0.27	0.24	0.23	1.75	1.90	2.54	0.90	2.60
P_2O_5	0.03	0.08	0.06	0.05	0.22	0.17	0.40	0.18	0.32
Cr_2O_3	0.00	0.00	0.00	0.00	0.00	0.00	0.00	0.00	0.00
NiO	0.00	0.00	0.00	0.00	0.00	0.00	0.00	0.00	0.00
TOT	93.22	94.04	93.72	94.30	94.76	94.35	93.95	94.21	93.78

ELECTRONIC APPENDIX 5

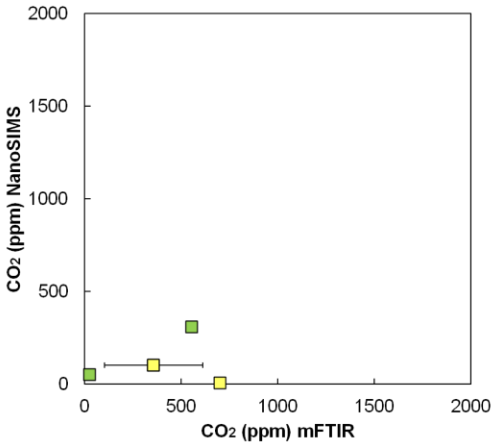

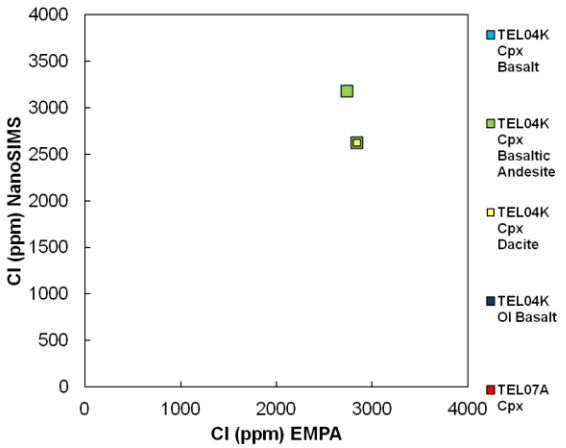

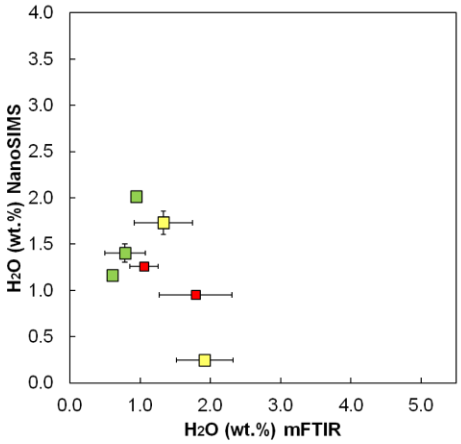

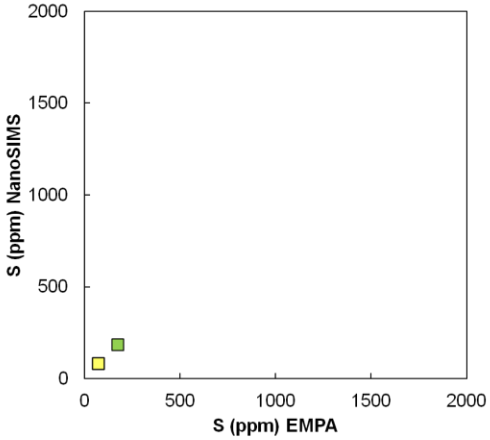

6. General discussion

The Cordillera Los Maribios, in NW Nicaragua, is a poorly characterized area where sizeable natural risk incurs due to the presence of stratovolcanoes. In fifty years, Nicaragua has assisted to several volcanic eruptions, including those of Masaya volcano, in the vicinity of the capital Managua (GVP, 2015), a major volcanic event related to Cerro Negro reactivation in 1971-1995 (Roggensack et al., 1997), the frequent major vulcanian explosions of Telica (1982, 1987; Navarro, 1994; Havlicek et al. 1999, 2000), the numerous ash emissions and seasonal lahar flows at San Cristóbal (Obando et al., 2004), and the catastrophic 1998 flank collapse and lahar disaster of Casita volcano (van Wyk de Vries et al. 2000; Kerle et al., 2003; Vallance et al., 2004).

We here bring new information on the behavior and source of major magmatic volatiles for two major Nicaraguan volcanoes, in the aim of providing new models of volcanic degassing, and to contribute to improved volcano monitoring in the region. We resume the major conclusions resulting from our volcanic gas and petrological results at San Cristóbal and Telica, with reference to three key aspects: (1) Volcanic gas output (**section 6.1**); (2) Crustal stagnation and differentiation of magmas below San Cristóbal/Telica (**section 6.2**); (3) Root zone of magma generation and implications for the mantle source of magmatism (**section 6.3**).

6.1 Volcanic gas output

Open-vent degassing is a most evident mechanism of volcanic gas dissipation from a volcanic edifice (Fig. 20). Our Multi-GAS observations allowed to investigate major gas relative abundances in volcanic plumes from both San Cristóbal and Telica. We show that gas composition when converted from their concentration (ppmV) to their relative abundance (mol%), was dominated by water H_2O at both San Cristóbal (85-97 mol%; mean of 92%) and Telica (70-98 mol%; mean of 92%). Because the instruments are placed at several tens to hundreds of meters from the source of emission, volcanic plumes are already cooler and possibly water vapor-saturated. Even though, as seen in Aiuppa et al. (2014), it was possible to approximate the magmatic major gas composition of the sourcing gas emitting vents (high temperature, >450 °C), and to assess the magmatic CO_2/S_t ratio signature of Telica (3.0 ±0.9) and San Cristóbal (4.2 ±1.3) (Fig. 21). We also estimated the volcanic outputs of CO_2 (Telica,181±35 tons/day; San Cristóbal is 523±263 tons/day) and SO_2 (Telica is 64±34 tons/day; San Cristóbal is 132±109 tons/day).

In the context of the volcanic plume CO_2 and SO_2 output, those numbers are not the highest, particularly when comparing with the voluminous system of the Masaya Caldera itself; maximum of 5,580 tons/day of SO_2 by GVP (1998) versus a maximum of 3,110 tons/day of CO_2 by Burton et al., 2000 with OP-FTIR and 3300±2500 tons/day in 2014 by Aiuppa (unpublished) with Multi-GAS/UV-DOAS. For the entire Nicaragua-Costa Rica segment, Aiuppa et al. (2014) concluded that the present-day (gas-based) CO_2outputs were 2835 ±1364 tons/day and for SO_2 they were 1886±495 tons/day. In comparison, in Japan, various fluxes estimates (persistent degassing, hot springs, cold springs, soil degassing, and eruptions) give 2,300 tons/day for CO_2 versus 2,000 tons/day of total S (Shinohara, 2013), while Mori et al. (2013) estimated a SO_2 flux of 6013 tons/day from japanese volcnaoes compiled for 1975-2006 only for plume surveys. In Kamchatka and Kurile Islands, more is known on fumarolic SO_2 fluxes and the total values could exceed >3,000 tons/day, while CO_2 exceed >2,000 tons/day (Taran, 2009).

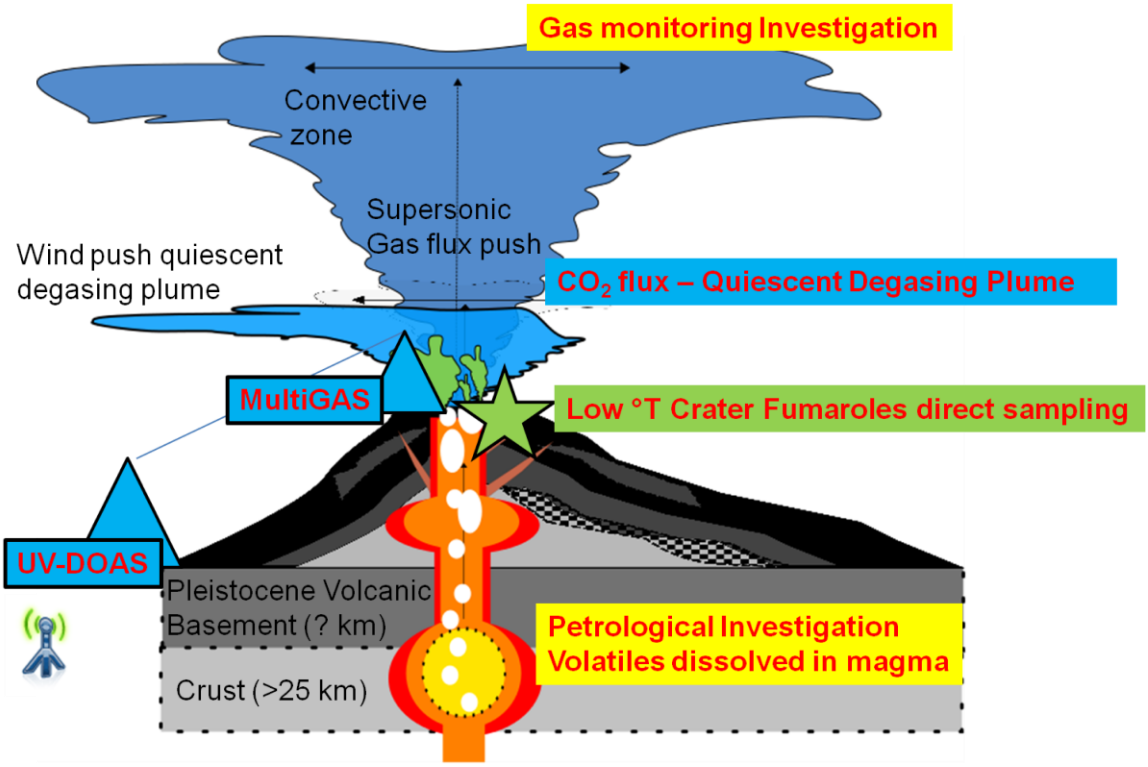

Fig. 20 The volcano gas field investigation.

Using multi-component models of volatile saturation in magmas (SolEx; Whitam et al., 2012), we reproduced the degassing paths of decompressing magmas, and compared the calculated compositions of magmatic vapors at equilibrium with magmas against the field measured gas compositions. From this comparison, we estimate depths of final gas separation from (and equilibration with) the magma (Figures 22 and 23). We propose that gases emitted from Telica and San Cristóbal originate from a magma-gas separation zone located at depths of 1.5 and 3.0 km (maximum pressures of between 55 and 85 MPa at San Cristóbal and 2. – 5.0 km for 40 to 130 MPa at Telica). These estimates gas source depths are slightly lower than the hypocenter depths of LP and LH seismicity (<2 km) (GVP, 2014, Geirsson et al., 2014; Rodgers et al., 2015). The seismic signals might represent brittle fracture zones in the volcanic edifice and/or possibly the roof of the magma reservoir which bottom could reach deeper levels at Telica. They also match the estimated pressure (depth) range estimated using the most differentiated and volatile–poor melt inclusions trapped in olivines and pyroxenes. We interpret these concurrent evidences as proves of the existence of a magma ponding zone, where magmas crystallize and degas, and vapors eventually accumulate to be finally released toward the shallow conduit system.

Our results also put novel constraints to interpret along-arc variations in CO_2/S gas ratios along CAVA (Fig. 21b). By integrating the new Telica and San Cristóbal compositions in the context of available chemistry information on high-T (>450 °C) CAVA volcanic gases (from the literatures), a regional trend appears (see Aiuppa et al. 2014) that confirms that Nicaragua volcanism has peculiar C-rich signature. The CO_2-rich composition of Nicaragua volcanism that our gas observations suggest is consistent with recent independent gas and petrological data in

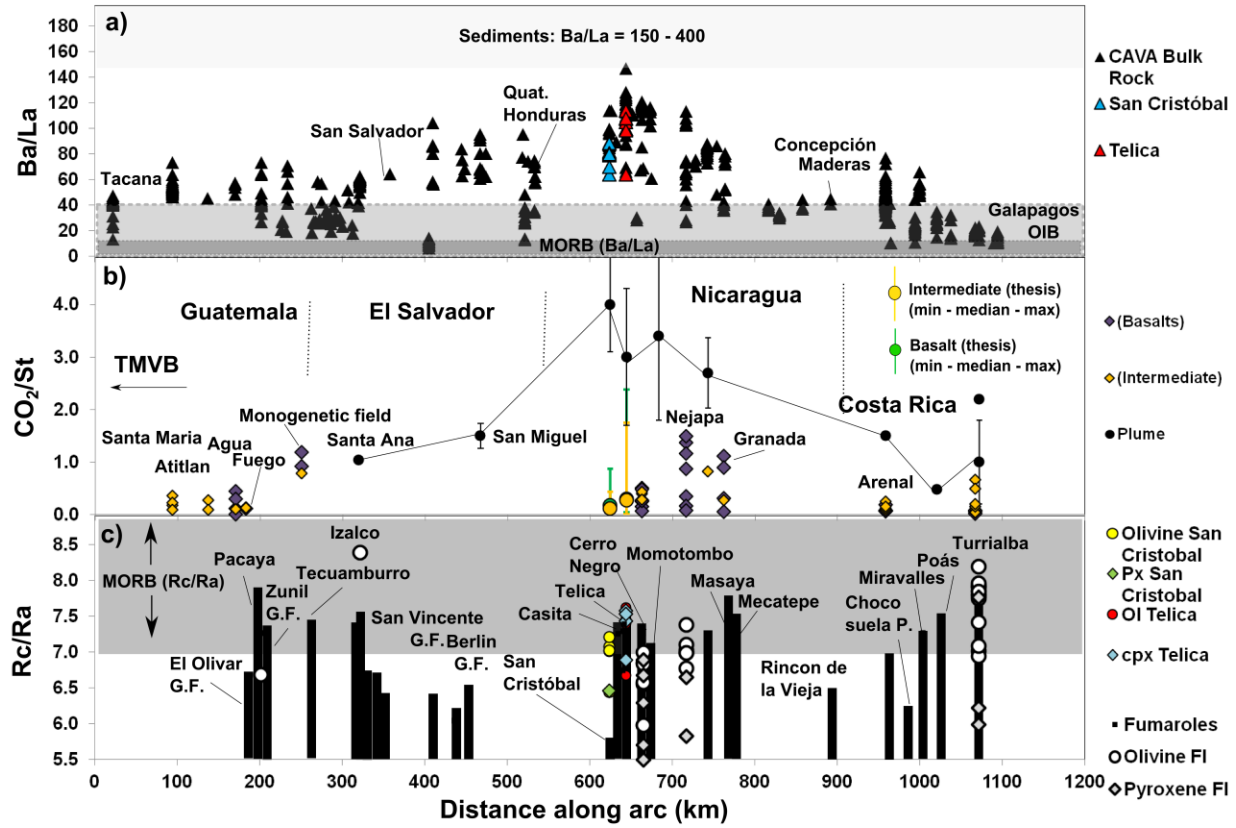

Fig. 21 Plots of Ba/La (a), CO_2/St (b) and Rc/Ra (c) ratios vs distance (km) along the arc from the border between NW and SE CAVA. Ba and La data are from the Geochemical Database by Carr et al. (2013) including Carr and Rose (1987) CENTAM database, but only basalts «B» and basaltic andesite «BA» (< 52 wt.% SiO2) with MgO > 2.5 wt.% are considered. MORB Ba/La ratios are including UAOC and LAOC (Ba/La calculated between 7 – 10) and UAOC is for upper altered oceanic crust and LAOC the lower section listed in Patino et al. (2000). OIB- Galapagos Ba/La ranges are from Gazel et al. (2009). Data of Rc/Ra measured in gases from CAVA volcanoes (black bar) are from Snyder et al. (2003), Shaw et al., (2003), Elkins et al. (2006), de Leeuw et al. (2007), Di Piazza et al. (2015) while Rc/Ra data from fluid inclusions FI are from Poreda and Craig (1989), Fisher et al. (2005), Shaw et al. (2006) and Di Piazza et al. (2015). Rc/Ra data are only shown if they are higher than our fixed minimum of 5.5.

CAVA (Hilton et al.,2002; Zimmer et al., 2004; Elkins et al., 2006; Mather et al., 2006; Wehrmann et al., 2011; Freundt et al., 2014). Importantly, this carbon enrichment (relative to sulfur) correlates well increases in those trace element petrological ratios (e.g., Ba/La, Fig. 21a; or U/Th and others) that are proxies for the involvement of slab fluids in magma petrogenesis. Doing this exercise of data compilation at the scale of several arc segments, we find that this relationship holds globally, which implies that the extreme C productivity of CAVA reflects subduction of C-rich sediments and the consequent recycling of C-rich slab fluids.

6.2 Crustal stagnation and differentiation of magma below San Cristóbal/ Telica

Application of the petrological approach to San Cristóbal and Telica rocks, based on using melt inclusions trapped in minerals, permitted to identify conditions at which volatiles evolve in the plumbing systems. By using different solubility models (Papale et al., 2006; SolEX from Whitam et al., 2012) and fractional crystallization models (XL FRAC from Stormer and Nicholls, 1978, MELTs initiated by Ghiorso and Sack,1995; Asimow and Ghiorso,1998), it was possible to identify different phases of magma differentiation and volatile loss. Our results were best explained by polybaric crystallization coupled with volatile loss associated with distinct steps in magma evolution. These models are resumed at San Cristóbal in figure 22 and at Telica in figure 23.

Because the mineral assemblage was different in both volcanoes (San Cristóbal has Ol>Px and Telica has Px>Ol), the used approach was adapted accordingly. Olivines were thus mainly used at San Cristóbal, and their inclusions revealed an impressive variability of trapping conditions from deposit to deposit, and depending on textural characteristics (shrinkage bubbles). Pyroxenes were difficult to study, because their inclusions were often crystallized, and the presence of trapped oxides overall imply a strong influence of post-entrapment effects. In comparison, Telica inclusions hosted in pyroxenes were better conserved and could be used to support information from olivines and their inclusion chemistry.

The major element compositions of bulk rocks and melt inclusions allowed to present a petrogenesis model for both San Cristóbal and Telica. We propose that San Cristóbal olivines record two different magma environments, depending on which tephra was sampled; a deep basalt saturation zone, and a shallow basaltic andesite saturation zone (Fig. 22). The Holocene tephra are more primitive, and their melt inclusions hosted in olivines mainly register basaltic melts with higher volatile contents than historical samples (mainly composed of basaltic andesites). Entrapment pressures were estimated from volatile contents and using solubility models, and at San Cristóbal have maximum values ranging from 91 MPa (3.4 km) in historical samples to 121 MPa (4.9 km) in Holocene samples. We also infer that crystallization starts at pressures of ~220 - 710 MPa (> 8-27 km). We also infer distinct magma ascent rates, being higher for basalts emitted during the Holocene eruptions (Fig. 22). At Telica, the polybaric crystallization model was interpreted as composed of two distinct phases, given the coexistence of primitive melts in olivines and evolved melts in pyroxenes (also having distinct volatile contents) (Fig. 23). The first stage of fractional crystallization is found to initiate at 200 - 400 MPa (7.6 – 15.1 km) for Scoria Telica Superior, based on volatile contents in melt inclusions from both olivines and pyroxenes, while the second stage records pressures between 50 – 130 MPa (1.9 – 5.0 km) in already differentiated (basaltic andesite to dacites) melts trapped by pyroxenes with low magnesium content (pyroxene melt saturation zone in figure 23). Overall, pyroxene crystals trap an impressive variety of magma types, volatiles contents and signs of magma mixing (mixing reservoir in figure 23), while olivines prove to have evolved in a deeper part of the plumbing system (olivine melt saturation zone in figure 23).

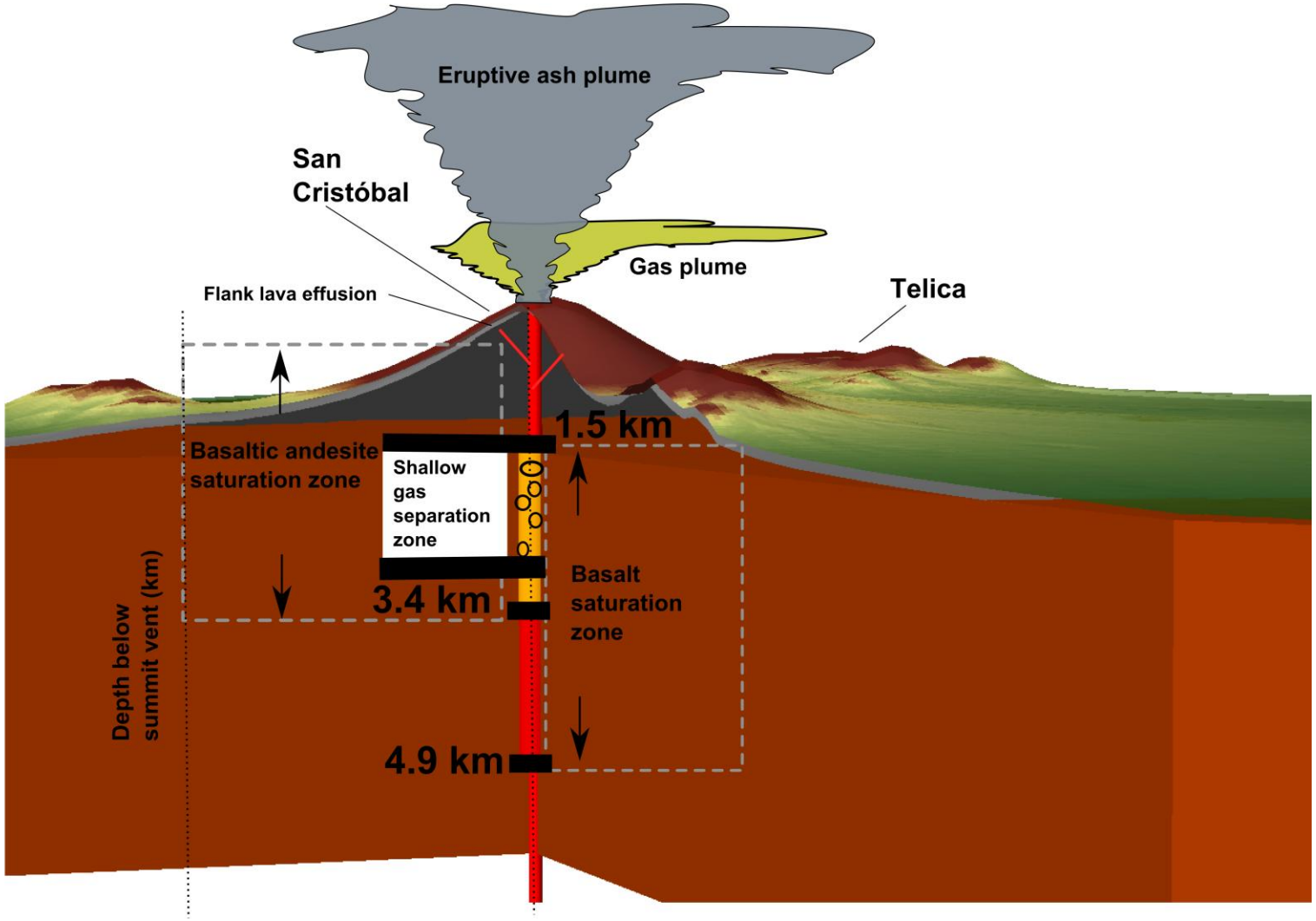

Fig. 22 San Cristóbal 3D magma reservoir model. ArcScene was used to extrude topographical raster from SRTM (30 m. resolution).

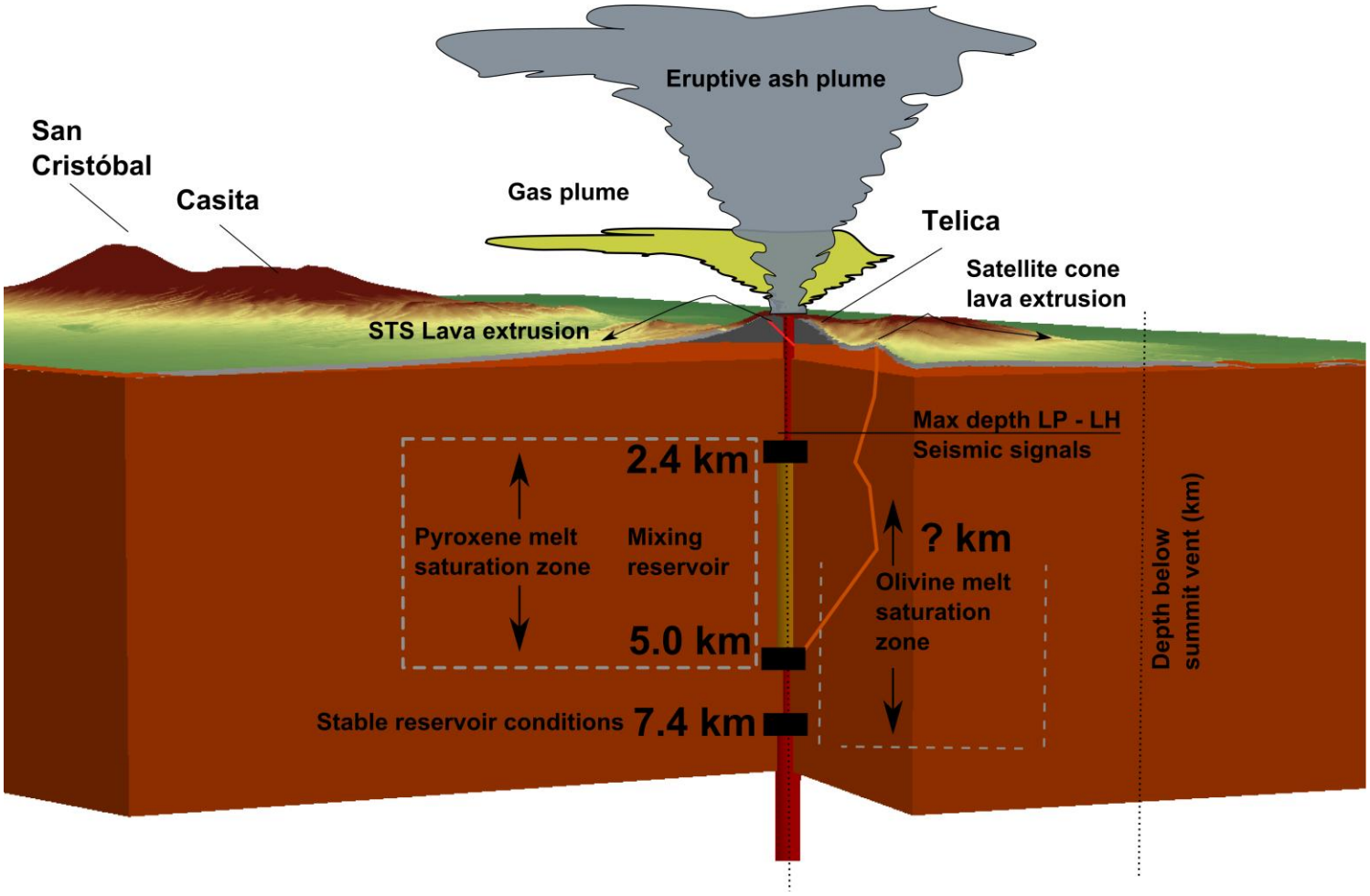

Fig. 23 Telica 3D magma reservoir model.

6.3 Root zone of magma generation and implication in source mantle of CAVA

The source of volatiles in CAVA magmatic systems is variable and find different explanations. Our study of noble gases in fluid inclusions of olivine and pyroxene crystals from the same suite of samples from San Cristobal and Telica allowed us to investigate the features of magmas feeding these volcanoes over their histories and to speculate on the mantle source beneath this segment of CAVA.

The He isotopic composition at San Cristobal varies in the narrow range 7.01–7.20 Ra (Fig. 21c). These values are the highest ratios ever measured at this volcano. Indeed, before this study, the only two measurements performed in 2002 in gases collected from low temperature crater fumaroles yielded values of 5.65 and 5.74 Ra, not representative of the local magmatic source (Shaw et al., 2003; Elkins et al., 2006). Holocene and Historic samples showed comparable $^{3}He/^{4}He$ ratios indicating that no changes occurred in the composition of San Cristóbal magmas since Holocene, and that this He isotope signature can be considered representative of the mantle beneath the volcanic system.

At Telica, the $^{3}He/^{4}He$ ratios measured in fluid inclusions of olivines and pyroxenes shows very similar Rc/Ra ratios (7.51±0.09), independently of their crystallization history, chronology and even degassing characteristics (Fig. 21c). These values are coherent with the same measurements carried out in fumarole gases (7.33-7.50 Ra; Shaw et al., 2003; Elkins et al., 2006). This consistency proves that the parental melt-fluids have a similar mantle source, and that processes of differentiation in the plumbing system do not modify the He isotope signature, likewise to that observed at San Cristóbal.

The $^{3}He/^{4}He$ ratios of our FIs at San Cristóbal and Telica fall within the range of MORB and arc volcanoes worldwide (8±1 Ra; Graham, 2002; Hilton et al., 2002), and are consistent with the maximum values measured in other volcanic systems of Nicaragua, such as Cerro Negro (7.38 Ra), Masaya (7.23 Ra), Mombacho (7.72 Ra), Momotombo (7.05 Ra), and Nejapa (7.49 Ra) (Shaw et al., 2003, 2006; Elkins et al., 2006; Lucic et al., 2014). This means that magmas from which crystallized the investigated minerals did not suffer any crust assimilation and/or magma mixing within the plumbing systems of each volcano (Fig. 21c).

In the framework of CAVA, we noticed that the He isotope signature of Nicaraguan volcanoes is also comparable with that of volcanoes of the nearby Costa Rica to the south (Di Piazza et al., 2015 and references therein) and El Salvador and Guatemala to the north (Fig. 21c; Snyder et al., 2003; Leeuw et al., 2007). Only Turrialba (Costa Rica) and Izalco (El Salvador) volcanoes show Rc/Ra values greater than 8 Ra, never measured in any other volcanic system along the arc. At the extreme NW of CAVA, the values also are particularly high, and toping at Pacaya volcano (7.9; Snyder et al., 2001). This is also comparable to the highest 3He/4He ratio measured at a fumarole of El Chichón in 1998 (8.09 Rc/Ra) (Taran et al., 1998) which fumaroles have relatively high range of values (7.4 ± 0.7 Rc/Ra; Peiffer, 2011; Peiffer et al., 2015). In comparison, other high temperature fumaroles with high Rc/Ra values are found for volcanoes (Colima / Ceboruco with 7.5; Taran et al., 2002) or geothermal fields (Los Azufres = 7.68; Peiffer et al., 2014) along the Trans Mexican Volcanic Belt (TMVB). There, Rc/Ra can often reach >7 strictly for high temperature geothermal systems (Bernard-Romero, 2008), but generally in volcanic arcs, the ratio is lower for mantle–crust interaction (Taran, 2009) in comparison to arcmagmatic gases that are generated in the mantle wedge and showing typical high values (8±1 Ra; Graham, 2002; Hilton et al., 2002).

Considering CAVA segment, the high He isotope signature could not be casual. By comparing the behavior of $^{3}He/^{4}He$ ratios along CAVA with Ba/La (Fig. 21a-c), whose values increase directly with the amount of subducted sediments and slab fluids, we hypothesize that the highest Rc/Ra values measured in Costa Rica and El Salvador could be in some ways related to the concurrent lowest and OIB-like Ba/La ratios along CAVA, but Rc/Ra vs. Ba/La are rather decoupled. Helium isotopes must represent mantle-derived gas from efficient connection between deep and shallow conducts in the crust beneath certain volcanoes (e.i. Turrialba) and/or an interaction with more complex systems of regional faults.

The behavior of CO_2/S_t along CAVA displays a pattern similar to Ba/La, indicating that many volcanoes in Nicaragua are richer in CO_2 compared to Costa Rica, El Salvador and Guatemala. Indeed, Aiuppa et al. (2014) proposed that CAVA represents one of the most productive carbon volcanic arc. This could indicate that the high presence of slab fluids and subducted sediments in the Nicaraguan segment of CAVA acts in slightly lowering the He isotope signature of the mantle wedge with the addition of radiogenic ^{4}He.

Nevertheless, because most of the volcanic systems along CAVA has not been studied for noble gases in fluid inclusions, it is not possible to make further speculations on a regional scale and the latter still remains an hypothesis to be confirmed.

The correlation with other geochemical markers worldwide will be useful for investigations in the future.

7. Conclusions

This dissertation is a volcanological contribution that aims at demonstrating the value of a combined petrological-volcanic gas approach to infer source and behavior of major volatiles in a volcanic system. The proposed degassing-petrological models for San Cristóbal and Telica volcanoes contribute to provide a quantitative interpretative framework on which volcano gas monitoring programs can be based upon. These monitoring efforts are essential in an volcanic region such as Central America, where millions of people live in the vicinity of a potentially active volcano.

I presented in this work the first determinations of water, carbon, sulfur and chlorine in melt inclusions from San Cristóbal and Telica. This information provides novel constraints essential to estimate the structure of both plumbing systems, and more explicitly the depths at which magma is stored and evolves in the crust prior to eruptions. In turn, the same volatile species, when measured at the volcano-atmosphere interface via gas observations, provide precious information on passive degassing styles and mechanisms of volatile loss of quiescent volcanoes, over temporal timescale that are inaccessible to petrological approaches. Results from gas monitoring have also been used here to estimate gas signature and output budget for both San Cristóbal and Telica, for the first time. Overall, given their complementary nature, I argue that combining gas and petrological approaches is essential to fully describing the behavior of volatiles in plumbing systems of active arc volcanoes.

The contribution of this study to our knowledge of volcanism in NW Nicaragua are multiple; thanks to the large dataset of melt inclusion compositions, I was able to explain, using natural samples, variations of compositional and intensive (pressure and temperature) parameters in time and space for each of the two studied volcanoes. We put particular accent and attention on identifying the carbon content of primitive magmas, in the assumption that deeply sourced gas is one of the most important triggers explosive eruptions from basaltic-andesitic strato-volcanoes in CAVA. The use of noble gases helped to find that even if different magma under stratovolcanoes evolve under complex conditions, they can share a common source of fluid in their primitive magma. The indices of fluid participation at various extend in the process of magma fusion derived from subducted oceanic plate supported the idea that regional compositional heterogeneity exist under subduction zones for large scales.

Such investigation hopefully will represent an ideal case of multidisciplinary approach in geochemistry for studying similar volcanic systems. Those information and data on volatile must be regarded for improving the background knowledge for quiescent degassing volcanoes and be considered for monitoring purposes and improving volcanic gas budget estimation for climatic models. Those presented degassing models have the potential to improve our knowledge of volcanic degassing style and eruptive style necessary to understand how explosive-type volcanoes can react in many circumstances.

BIBLIOGRAPHY

- Andres, R.J. A. D. Kasgnoc, (1998). A time-averaged inventory of subaerial volcanic sulfur emissions, Journal of Geophysical Research, No. 103, 25, p.251-261
- Aiuppa, A., C. Federico, G. Giudice and S. Gurrieri, (2005a), Chemical mapping of a fumarolic field: La Fossa Crater, Vulcano Island (Aeolian Islands, Italy), Geophysical Research Letters, Vo. 32, L13309-L13313
- Aiuppa, A., C. Federico, G. Giudice, S. Gurrieri, M. Liuzzo, H. Shinohara, R. Favara, and M. Valenza, M., (2006), Rates of carbon dioxide plume degassing from Mount Etna volcano, Journal of Geophysical Research, V. 111, B09207, p. 1-8
- Aiuppa, A., R. Moretti, C. Federico, G. Giudice, S. Gurrieri, M. Liuzzo, P. Papale, H. Shinohara, M. Valenza (2007), Forecasting Etna eruptions by real-time observation of volcanic gas composition, Geology, No. 35, (12), p. 1115-1118
- Aiuppa, A., C. Federico, G. Giudice, G. Giuffrida, R. Guida, S. Gurrieri, M. Liuzzo, R. Moretti, P. Papale, (2009), The 2007 eruption of Stromboli volcano: Insights from real-time measurement of the volcanic gas plume CO2/SO2 ratio, Journal of Volcanology and Geothermal Research, No. 182, p. 221-230
- Aiuppa A., M. Burton, P. Allard, T. Caltabiano, G. Giudice, S. Gurrieri, M. Liuzzo, G. Salerno, (2011). First observational evidence for the CO2-driven origin of Stromboli's major explosions, Solid Earth 2, (2), p.135-142
- Aiuppa, A., P. Robidoux, G. Tamburello, V. Conde, B. Galle,G. Avard, E. Bagnato, J. M. DeMoor, M. Martinez, A. Munoz, (2014). The Costa Rica – Nicaragua volcanic segment: along arc variations in volcanic gas chemistry and improved CO_2 budget, Earth and Planetary Science Letters, Vol. 407, p. 134-147
- Allard, P., (1997). Endogenous magma degassing and storage at Mount Etna. Geophys. Res. Lett., Vol. 24, p. 2219- 2222
- Allard, P., M.R. Burton, F. Mure, (2005). Spectroscopic evidence for a lava fountain driven by previously accumulated magmatic gas, Nature, Vol. 433, No. 7024, p. 407 – 410
- Allard P., A. Aiuppa, P. Bani, N. Métrich, A. Bertagnini, P. J. Gauthier, H. Shinohara, G. Sawyer, F. Parello, E. Bagnato, B. Pelletier, E. Garaebiti, (2015). Prodigious emission rates and magma degassing budget of major, trace and radioactive volatile species from Ambrym basaltic volcano, Vanuatu island Arc. Journal of Volcanology and Geothermal Research, vol.304, p.378-402
- Alvarado, G.E., C. Dengo, U. Martens, J. Bundschuh, T. Aguilar, B. Bonis, (2007), Stratigraphy and geologic history, in Central America. In: Bundschuh, J., Avarado, G. (Eds.), Geology, Resources and Hazards. Taylor and Francis, Leiden, p. 345-394
- Anderson, A.T., (1982). Parental basalts in subduction zones: implications for continental evolution. J. Geophys. Res., Vol. 87, p. 7047 - 7060
- Auger, L. S., G. Abers, K. Fisher, M. Protti, V. Gonzales, and W. Strauch, (2006), Crustal thickness variations beneath the Central American Volcanic Arc, Eos Trans. AGU, 87, (52), Fall Meet. Suppl., Abstract T23C-0517
- Baker, D.R., (2008). The fidelity of melt inclusions as record of melt composition, Contrib. Mineral Petrol., Vol. 156, p. 377 - 395
- Barckhausen, U., C. R. Ranero, R. von Huene, S. C. Cande, and H. A. Roeser, (2001). Revised tectonic boundaries in the Cocos plate offCostaRica: Implications for

segmentation of the convergent margin and for plate tectonic models, J. Geophys. Res., Vol. 106, No. 19, p. 207–19,220

- Barnes, J.D. (2009). Chlorine isotope variations along the Central American volcanic front and back arc, G3, Vol. 10, No. 11, p. 1525 – 2027
- Benjamin, E.R., T. Plank, J. A. Wade, K. A. Kelley, E. H. Hauri, G. E. Alvarado, (2007), High water contents in basaltic magmas from Irazú, Volcano, Costa Rica, J. Volcanol Geoth Res, No. 168, Issue 1–4, p. 68-92
- Bernard-Romero, B.R., (2008). Nuevos datos geoquímicos de yacimientos geotermales de alta temperatura del cinturón volcánico mexicano: Isótopos de helio, boro, nitrógeno y elementos traza. (Master Thesis) UniversidadNacional Autónoma deMéxico, 124 p.
- Bodnar, R.J. (2003). Introduction to fluid inclusions. In I. Samson, A. Anderson, & D. Marshall, eds. Fluid Inclusions: Analysis and Interpretation. Mineralogical Association of Canada, Short Course, No. 32, p. 1-8
- Bolge L. L., M.J. Carr, K.I. Milidakis, F.N. Lindsay, M.D. Feigenson, (2009). Correlating Geochemistry, Tectonics, and Volcanic Volume Along the Central American Volcanic Front, Geochemistry Geophysics Geosystems, Vol. 10, Issue 12, p. 1-15
- Brantley, S.L., K. W. Koepenick, (1995). Measured carbon dioxide emissions from Oldoinyo Lengai and the skewed distribution of passive volcanic fluxes, Geology 23, p.933-936
- Burton, M. R., C. Oppenheimer, L. A. Horrocks, P. W. Francis, (2000). Remote sensing of CO2 and H2O emission rates from Masaya volcano, Nicaragua. Geology 28, Vo. 10, p. 915-918
- Burton, M.R., H.M. Mader, M. Polacci, (2007b). The role of gas percolation in quiescent degassing of persistently active basaltic volcanoes, Earth Planet. Sci. Lett., No. 264, p.46 – 60
- Burton M. R., T. Caltabiano, F. Mure, G. Salerno, D. Randazzo, (2009). SO2 flux from Stromboli during the 2007eruption: Results from the FLAME network and traverse measurements, J. Volcanol. Geotherm. Res., 182, p. 214-220
- Burton, M. R., G. M. Sawyer, D. Granieri, (2013). Deep Carbon Emissions from Volcanoes, Reviews in Mineralogy & Geochemistry, Vol. 75, p. 323-354
- Carr, M. J. (1976). Underthrusting and Quaternary faulting in northern Central America, Geol. Soc. Am. Bull., Vol. 87, p. 825 – 828
- Carr, M. J. (1984). Symmetrical and segmented variation of physical and geochemical characteristics of the Central American volcanic front, J. Volcanol. Geotherm. Res., No. 20, p. 231-252
- Carr, M.J., M.D. Feigenson, E.A. Bennett, (1990). Incompatible element and isotopic evidence for tectonic control of source mixing and melt extraction along the Central American arc, Contrib. Mineral. Petrol., No. 105, p. 369-380
- Carr, M. J. and M. D. Feigenson (2003). Volcanism and geochemistry in Central America: progress and problems. Geophys., Monogr. 138, p. 153-174
- Carr, M. J., I. Saginor, G. E. Alvarado, L. L. Bolge, F. N. Lindsay, K. Milidakis, B. D. Turrin, M. D. Feigenson, and C. C. Swisher III, (2007). Element fluxes from the volcanic front of Nicaragua and Costa Rica, Geochem. Geophys. Geosyst., Vo 8, No. 6, p. 1-22
- Cashman, K. (2004). Volatile controls on magma ascent and eruption, Geophysical monograph, Vol. 150, p. 416
- Cervantes, P. and P. J. Wallace, (2003b). Role of H2O in subduction-zone magmatism: New insights from melt inclusions in high-Mg, *Geology*; Vo. 31; No. 3, p., 235-238
- Conde, V., S. Bredemeyer, E. Duarte, J. F. Pacheco, S. Miranda, B. Galle, T. H. Hansteen, (2013). SO2 degassing from Turrialba Volcano linked to seismic signatures during the period 2008–2012, Int J Earth Sci (Geol Rundsch)

- Conde, V., P. Robidoux, G. Avard, B. Galle, A. Aiuppa, A. Muñoz, G. Giudice, (2014). Measurements of volcanic SO2 and CO2 fluxes by combined DOAS, Multi-GAS and FTIR observations: a case study from Turrialba and Telica volcanoes, Int. J. Earth Sci. (Geol Rundsch), p. 1 -13
- Conde, V., (2015). Application of DOAS, FTIR and Multi-GAS for studies of evolving volcanic activity, Department of Earth and Space Sciences, Chalmers University of Technology, Gothenburg, Sweden 2015
- Conde, V. S. Bredemeyer, J. A. Saballos, B. Galle, T. H. Hansteen, (2015). Linking SO2 and seismicity by continuous wavelet transform: Implications for volcanic surveillance at San Cristobal volcano, International Journal of Earth Sciences, (accepted), p. 1 -32
- Connolly, J. A. D. (2005), Computation of phase equilibria by linear programming: A tool for geodynamic modeling and its application to subduction zone decarbonation, Earth Planet. Sci. Lett., No. 236, p. 524-541
- Danyushevsky, L.V., F.N. Della-Pasqua, S. Sokolov, (2000). Re-equilibration of melt inclusions trapped by magnesian olivine phenocrysts from subduction-related magmas: petrological implications. Contrib Mineral Petrol, Vol. 138, p. 68 - 83
- Danyushevsky, L. V., S. M. Eggins, T. J. Falloon, and D. Christie (2000b), H2O abundance in depleted to moderately enriched mid-ocean ridge magmas, Part I: Incompatible behaviour, implications for mantle storage, and origin of regional variations, J. Petrol., Vol. 41, p. 1329 – 1364
- Danyushevsky, L.V., A. W. McNeill, A. V. Sobolev, (2002b). Experimental and petrological studies of melt inclusions in phenocrysts from mantle-derived magmas: An overview of techniques, advantages and complications, Chem. Geol., Vol. 183, p. 5-24
- Danyushevsky, L. V. and P. Plechov, (2011). Petrolog3: integrated software for modeling crystallization processes. Geochemistry, Geophysics, Geosystems, Vol. 12
- Dasgupta, R. (2013). Rev. Mineral. Geochem. , Ingassing, Storage, and Outgassing of Terrestrial Carbon through Geologic Time, Vol. 75, p. 183 – 229
- de Leeuw, G. A. M., D. R. Hilton, T. P. Fischer, and J. A. Walker, (2007). The He-CO2 isotope and relative abundance characteristics of geothermal fluids in El Salvador and Honduras: New constraints on volatile mass balance of the Central American Volcanic Arc, Earth Planet. Sci. Lett., No. 258, p. 132-146
- Delmelle, P., P. Baxter, A. Beaulieu, M. Burton, P. Francis, J. Garcia-Alvarez, L. Horrocks, M. Navarro, C. Oppenheimer, D. Rothery, H. Rymer, K. St-Amand, J. Stix, W. Strauch, and G. Williams-Jones, (1999). Origin, effects of Masaya volcano's continued unrest probed in Nicaragua: Eos (Transactions, American Geophysical Union), Vol. 80, p. 575, 579, 581
- Demets, C., (2001). A New estimate for present-day Cocos–Caribbean plate motion: implications for slip along the Central American Volcanic Arc, Geophys. Res. Lett., No. 28 (21), p. 4043-4046
- Dengo, G., (1985), Mid America: tectonic setting for the Pacific margin from southern Mexico to northwestern Columbia. In: Nairn, A.E.M., Stechli, F.G. (Eds.), The Ocean Basins and Margins. Plenum Press, New York, p. 123-180
- De Vivo, B., and Bodnar, R.J. (2003) Melt inclusions in volcanic systems. Elsevier Sciences, Amsterdam.
- Duffell, H. J., C. Oppenheimer, D. M. Pyle, B. Galle, A. J. S. McGonigle, and M. R. Burton, (2003), Changes in gas composition prior to a minor explosive eruption at Masaya volcano, Nicaragua, Journal of Volcanology and Geothermal Research, Vol. 126, No. 3 - 4, p. 327 – 339

- Edmonds M., R.A. Herd, B. Galle, C.M. Oppenheimer, (2003). Automated, high time resolution measurements of SO2 flux at Soufrière Hills Volcano, Montserrat, Bull. Volcanol., Vol. 65, no. 8, p.578 – 586
- Ehrenborg, J., (1996), A new stratigraphy for the Tertiary volcanic rocks of the Nicaraguan Highland, Geol. Soc. Amer. Bull., No. 108, p. 830-842
- Eiler, J.M., M. J. Carr, M. Reagan, M., E. Stolper (2005). Oxygen isotope constraints on the sources of Central American arc lavas. Geochem. Geophys. Geosyst, 6
- Elkins, L.J., T.P. Fischer, D.R. Hilton, Z.D. Sharp, S. McKnight, J. Walker, (2006). Tracing nitrogen in volcanic and geothermal volatiles from the Nicaraguan volcanic front. Geochim. Cosmochim. Acta, Vol. 70, p. 5215 – 5235
- Fischer, T. P. , W. F. Giggenbach, Y. Sano, S.N., Williams, (1998). Fluxes and sources of volatiles discharged from Kudryavy, a subduction zone volcano, Kurile Islands, Earth and Planetary Science Letters, Vol. 160, Issues 1 - 2, p. 81 - 96
- Frezzotti, M.-L., (2001). Silicate-melt inclusions in magrnatic rocks: applications to petrology, Lithos 55, p. 273 - 299
- Galle B., M. Johansson, C. Rivera, Y. Zhang, M. Kihlman, C. Kern, T. Lehmann, U. Platt, S. Arellano, S. Hidalgo, (2010). Network for Observation of Volcanic and Atmospheric Change (NOVAC)-A global network for volcanic gas monitoring: Network layout and instrument description, J. Geophys. Res. 115, D05304
- Gans, P.B., G. Alvarado, W. Pérez, I. MacMillan, and A. Calvert, (2003), Neogene evolution of the Costa Rican Arc and development of the Cordillera Central: Geological Society of America Abstracts with Programs, v. 35, no. 4, p. 74
- Gazel, E., M.J. Carr, K. Hoernle, M.D. Feigenson, D. Szymanski, F. Hauff, P. van den Bogaard, (2009). Galapagos-OIB signature in southern Central America: mantle refertilization by arc–hot spot interaction. Geochemistry, Geophysics, Geosystems, Vol. 10, No. 2, Q02S11
- Gemmell, J. B., (1987). Geochemistry of metallic trace elements in fumarolic condensates from Nicaraguan and costa Rican volcanoes, J. Volcanol. Geotherm. Res., No. 33, p. 161 – 181
- Geirsson, H., M. Rodgers, P. LaFemina, M. Witter, D. Roman, A. Muñoz, V. Tenorio, J. Alvarez, V.C. Jacobo, D. Nilsson, B. Galle, M.D. Feineman, T. Furman, A. Morales, (2014). Multidisciplinary observations of the 2011 explosive eruption of Telica volcano, Nicaragua: Implications for the dynamics of low explosivity ash eruptions. J. Volcanol. Geotherm. Res., No. 271, p. 55 – 69
- Giggenbach, W.F., F. Le Guern, (1976). The chemistry of magmatic gases from Erta'Ale, Ethiopia, Geochim. Cosmochim. Acta, Vol. 40, p. 25 – 30
- Giggenbach, W.F., S. Matsuo, (1991). Evaluation of results from second and third IAVCEI field workshops on volcanic gases, Mt Usu, Japan, and White Island, New Zealand, Appl. Geochem, 6, p. 125 – 141
- Global Volcanism Program, National Museum of Natural History (GVP). Retrieved 2014,
- Gorman, P. J., D. M. Kerrick, and J. A. D. Connolly (2006). Modeling open system metamorphic decarbonation of subducting slabs, Geochem. Geophys. Geosyst., No. 7, Q04007
- Grevemeyer, I., C. R. Ranero, E. R. Flueh, D. Klaeschen, and J. Bialas, (2007), Passive and active seismological study of bending-related faulting and mantle serpentinization at the Middle America trench, Earth Planet. Sci. Lett., No. 258,
- p. 528-542

- Gualda, J., and M.S. Ghiorso, (2015). MELTS_Excel: A Microsoft Excel-based MELTS interface for research and teaching of magma properties and evolution. Geochemistry, Geophysics, Geosystems, 16: 315-324
- Halmer, M. M., H. U. Schmincke, H. F. Graf, (2002). The annual volcanic gas input into the atmosphere, in particular into the stratosphere: A global data set for the past 100 years, J. Volcanol. Geotherm. Res., Vo. 115, p.511-528
- Harris, D.M., and A.T. Anderson, Jr., (1984). Volatiles H2O, CO2, and Cl in a subduction related basalt, Contrib. Mineral Petrol., Vol. 87, p. 120 – 128
- Hauff, F., K. A. Hoernle, P. van den Bogaard, G. E. Alvarado, D. Garbe-Schönberg (2000). Age and geochemistry of basaltic complexes in western Costa Rica: contributions to the geotectonic evolution of Central America. Geochemistry, Geophysics, Geosystems 1, page number 1999GC000020
- Hauri, H. E., J. Wang, J. E. Dixon, P. L. King, C. Mandeville, S. Newman (2002). Chemical Geology, Vol. 183, p. 99 – 114
- Hauri, H. E., A. M. Shaw, J. Wang, J. E. Dixon, P. L. King, C. Mandeville (2006). Matrix effects in hydrogen isotope analysis of silicate glasses by SIMS, Chemical Geology, Vol. 235, p. 352 - 365
- Havlicek, P., P. Hradecky, M. Hrubes, B. Mlcoch, M. Opletal, J. Sebesta (CGU), N. Buitrago, W. Strauch, (1999). Estudio Geológico Y Reconocimiento De La Amenaza Natural - Zona Chinandega-Leon , Nicaragua. Praga-Managua 1999, Resumen Ejecutivo (Servicio Geológico Checo, CGU, en cooperación con Instituto Nicaragüense de Estudios Territoriales, INETER), 23 p.
- Havlicek, P., P. Hradecky, M. Hrubes, P. Kyel, B. Mlcoch, S. Mrazova, Z. Novak, M. Opletal, A. Prichystal, J. Sebesta, J. Seveik, M. Bustillo, Z. Rizo, (2000). Estudio Geológico Y Reconocimiento De La Amenaza Geológica En El Área De León - La Paz Centro Y Malpasillo, Praga-Managua 2000, Reporte Final (Servicio Geológico Checo, CGU, en cooperación con Instituto Nicaragüense de Estudios Territoriales, INETER), 244 p.
- Hazlett, R.W. (1977). Geology and Hazards of the San Cristobal Volcanic Complex, Nicaragua, Darmouth College, June 1977, 212 p.
- Hazlett, R. W. (1987). Geology of the San Cristobal volcanic complex, Nicaragua, Journal of Volcanology and Geothermal Research, No. 33, p. 223-230
- Hervig, R. L., and Williams, P. (1988). In Secondary Ion Mass Spectrometry, SIMS VI (Eds, Benninghoven, A., Huber, A.M. and H. W. Werner) J. Wiley and Sons, p. 961 – 964
- Heydolph, K., K. Hoernle, F. Hauff, P. van den Bogaard, M. Portnyagin, I. Bindeman, D. Garbe-Schonberg, (2012). Along and across arc geochemical variations in NW Central America: Evidence for involvement of lithospheric pyroxenite, Geochimica et Cosmochimica Acta, No. 84, p.459-491
- Hilton, D.R., T.P. Fischer, B. Marty, B., (2002). Noble gases and volatile recycling at sub-duction zones. In: Porcelli, D., Ballentine, C.J., Wieler, R. (Eds.), Noble Gases in Geochemistry and Cosmochemistry. In: Rev. Mineral. Geochem., Vol.47. Mineral. Soc. Am., Washington, DC, p.319–370
- Hoernle, K., Abt, D.L., K.M. Fischer, H. Nichols, F. Hauff, G.A. Abers, P. van den Bogaard, K. Heydolph, G. Alvarado, M. Protti, W. Strauch, (2008). Arc-parallel flow in themantle wedge beneath Costa Rica and Nicaragua. Nature, Vol. 451, p. 1094 – 1098
- Hoff R.M., and M.M. Millan, (1981). Remote SO2 mass flux measurements using COSPEC, J. Air Pollut. Control. Assoc., Vol. 31, No. 4, p. 381 – 384
- Hoernle, K., D. L. Abt, K. M. Fischer, H. Nichols, F. Hauff, G. Abers, P. van den Bogaard, G. Alvarado, J. M. Protti, and W. Strauch, (2008). Geochemical and

geophysical evidence for arc-parallel flow in the mantle wedge beneath Costa Rica and Nicaragua, Nature, No. 451, p. 1094-1097

- Houghton, B. F. and H. M. Gonnermann, (2008). Basaltic explosive volcanism: constaints from deposits and models, Chemie der Erde, Vol. 68, p. 117-140
- Hradecký, P., J. Šebesta et. al. (2007). Mapa de la Cadena volcánica Nicaragúense 1:200.000, Czech Geological Survey, iSBN 978-80-7075-671-3
- Humphries, S.D., A. R. Nehir, C. J. Keith, K. S. Repasky, L. M. Dobeck, J. L. Carlsten, L. H. Spangler, (2008). Testing carbon sequestration site monitor instruments using a controlled carbon dioxide release facility, Appl. Opt., Vol. 47, p. 548 – 555
- Johnson, E. R. (2008). Volatiles in basaltic magmas from central México: from subduction to eruption, Doctor of Philosophy Presented to the Department of Geological Sciences and the Graduate School of the University of Oregon, 183 p.
- Johnson, E. R., P. J. Wallace, K. V. Cashman, H. Delgado-Granados, and A. J. R. Kent, (2008). Magmatic volatile contents and degassing-induced crystallization at Volcán Jorullo, Mexico: Implications for melt evolution and the plumbing systems of monogenetic volcanoes, Earth Planet. Sci. Lett., Vol. 269, p. 477-486
- Johnson, E. R., P. J. Wallace, K.V. Cashma and, H. Delgado-Granados, (2010).Degassing of volatiles (H2O, CO2, S, Cl) during ascent, crystallization, and eruption at mafic monogenetic volcanoes in central Mexico, Journal of Volcanology and Geothermal Research, Vol. 197, Issues 1-4, p. 225-238
- Kamenetsky, V.S., A.J. Crawford, S. Eggins, R. Muhe (1997). Phenocryst and melt inclusion chemistry of near-axis seamounts, Valu Fa Ridge, Lau Basin: insight into mantle wedge melting and the addition of subduction components. Earth Planet Sci Lett, Vol. 151, p. 205 - 223
- Kent, A.J.R.,J.A. Baker, M. Wiedenbeck (2002a). Contamination and melt aggregation processes in continental flood basalts: constraints from melt inclusions in Oligocene basalts from Yemen, Earth Planet Sci Lett, Vol. 202, p. 577 - 594
- Kent, A.J.R., E.M. Stolper, D. Francis, J. Woodhead, R. Frei, J. Eiler (2004b) Mantle heterogeneity during the formation of the North Atlantic Tertiary Province: Constraints from trace element and Sr-Nd-Os-O isotope systematics of Baffin Island picrites, Geochem Geophys Geosys 5
- Kent, A.J.R. (2008). Melt inclusions in basaltic and related volcanic rocks. In K.D. Putirka, and F.J. Tepley, III, Eds. MInerals, Inclusions and Volcanic Processes, Vol. 69, p. 273-331. The Mineralogical Society of America
- Kulm, L. D., and E. Suess (1990). Relationship between carbonate deposits and fluid venting: Oregon accretionary prism, J. Geophys. Res., No. 95, p. 8899-8915
- La Femina, P. C., T. H. Dixon, and W. Strauch, (2002), Bookshelf faulting in Nicaragua, Geology, No. 30, p. 751 – 754
- LaFemina, P., T. H. Dixon, R. Govers, E. Norabuena, H. Turner, A. Saballos, G. Mattioli, M. Protti, and W. Strauch (2009). Fore-arc motion and Cocos Ridge collision in Central America, Geochem. Geophys. Geosyst., Vol. 10, Q05S14, p. 1 – 21
- Leeman W. P., M.J. Carr, J.D. Morris, (1994). Boron Geochemistry of the Central American Volcanic Arc: Constraints on the Genesis of Subduction-Related Magmas, Geochim. Cosmochim. Acta, No. 58, p. 149-168
- Lowenstern, J. B. (1995). Applications of silicate melt inclusions to the study of magmatic volatiles. In: Thompson JFH (ed) Magmas, fluids and ore deposits. Mineral Assoc. Canada Short Course 23, p. 71 - 99

- Lucic, G., J. Stix, B. S. Lollar, G. L.-Couloume, A. Munoz, M. I. Carcache (2014). The degassing character of a young volcanic center: Cerro Negro, Nicaragua, Bull. Volcanol., Vol. 76, p. 3 - 23
- MacKenzie, L., G. A. Abers, K. M. Fisher, E. M. Syracuse, J. M. Protti, V. Gonzales, and W. Strauch (2008), Crustal structure along the southern Central American volcanic front, Geochem. Geophys. Geosyst., No. 9, Q08S09
- Manning, C. E. (2014). A piece of the deep carbon puzzle, Nature Geosciences, Vol. 7, May 2014
- Marshall, J. S., D. M. Fisher, and T. W. Gardner (2000). Central Costa Rica deformed belt: Kinematics of diffuse faulting across the western Panama Block, Tectonics, Vol. 19, p. 468 - 497
- Mather, T. A. ,D. M. Pyle, V. I. Tsanev, A. J. S. McGonigle, C. Oppenheimer, A. G. Allen (2006). A reassessment of current volcanic emissions from the Central American arc with specific examples from Nicaragua. Journal of Volcanology and Geothermal Research, No. 149, p. 297-311
- McBirney, A., H. Williams, (1965). Volcanic history of Nicaragua. Univ. Calif. Publ. Geol. Sci. 55, p. 1-73
- Menyailov, I. A., L. P. Nikitina, V. N. Shaper, and V. P. Pilipenko, (1986). temperature increase and chemical change of fumarolic gases at Momotombo volcano, Nicaragua, in 1982 - 1985: Are these indicators of a possible eruption ?, Journal of geophysical Research, Vol. 91, No. B12, p. 12, 199-12, 214
- Metrich, N., and R. Clocchiatti, (1989). Melt inclusion investigation of the volatile behavior in historic alkali basaltic magmas of Etna. Bull .Volcanol., Vol. 51, p. 185 – 198
- Métrich, N., A. Bertagnini, P. Landi and M. Rosi, (2001). Crystallization driven by decompression and water loss at Stromboli Volcano (Aeolian Islands, Italy), Journal of Petrology, No. 42, p. 1,471-1,490
- Métrich, N., A. Bertagnini, P. Landi, M. Rosi, and O. Belhadj, (2005). Triggering mechanism at the origin of paroxysms at Stromboli (Aeolian archipelago, Italy): the 5 April 2003 eruption, J. Geophys. Res., No. 32, L10305
- Métrich, N. and P. J. Wallace, (2008). Reviews in Mineralogy and Geochemistry: Minerals, Inclusions And Volcanic Processes/Chapter 10. Volatile Abundances in Basaltic Magmas and Their Degassing Paths Tracked by Melt Inclusions, Vol. 69, p. 363-402
- Métrich, N. P. Allard, A. Aiuppa, P. Bani, A. Bertagnini, H. Shinohara, F. Parello, A. Di Muro, E. Garaebiti, O. Belhadj, and D. Massare, (2011), Magma and Volatile Supply to Post-collapse Volcanism and Block Resurgence in Siwi Caldera (Tanna Island, Vanuatu Arc), J. Petrology, No. 52, (6), p. 1077-1105
- Mooser, F., Meyer-Abich, H. and McBirney, A.R., (1958). Central America. Catalog of Active Volcanoes of the Moscow, Russia, p. 421- 444. (Unpublished transla-World, IAVCEI, V. 6, Rome, Italy, 146 p.
- Mori, T., K. Notsu, Y. Tohjima, and H. Wakita (1993). Remote detection of HCL and SO2 in volcanic gas from Unzen volcano, Japan, Geophys. Res. Lett., Vol. 20, p. 1355 - 1358
- Mori, T., and K. Notsu (1997). Remote CO, COS, CO2, SO2, HCl detection and temperature estimation of volcanic gas, Geophys. Res. Lett., Vol. 24, p. 2047 – 2050
- Mörner N. A. and G. Etiope (2002). Carbon degassing from the lithosphere, Global Planet Change, No. 33, p. 185-203
- Mysen, B.O., R.J. Arculus*, and D. H. Eggler, (1975). Solubility of Carbon Dioxide in Melts of Andesite, Tholeiite, and Olivine Nephelinite Composition to 30 kbar Pressure, Contrib. Mineral Petrol., Vol. 53, p. 227 - 239

- Navarro, M. C. (1994). Peligro volcánico, volcán Telica, MS, 73 p. INETER Managua
- Rivera, C., J.A. Garcia, B. Galle, L. Alonso, Z. Yan, M. Johansson, M. Matabuena, G. Gangoiti, (2009). Validation of optical remote sensing measurement strategies applied to industrial gas emissions, Int J Remote Sens., Vol. 30, (12), p. 3191 - 3204
- Navarro, M. C. (1994). Peligro volcánico, volcán Telica, MS, 73 p. INETER Managua
- Nielsen, R.L., P.J. Michael, R. Sours-Page, (1998). Chemical and physical indicators of compromised melt inclusions.Geochim Cosmochim Acta, Vol. 62, p. 831 - 839
- Novák, Z. and A. Přichystal, (2006). El área volcánica de Telica (Nicaragua) y sus peligros geológicos, in: Krystalinikum, Contribution to the geology and the petrology of crystalline complexes, Moravian Museum Brno, No. 31, 2006, p. 47-66
- Oppenheimer, C., P. Francis, M. Burton, A. J. H. Maciejewski, and L. Boardman, (1998), Remote measurement of volcanic gases by Fourier transform infrared spectroscopy, Appl Phys B, Vol. 67, No. 4, p. 505 – 515
- Papale, P., Moretti, R. & Barbato, D. (2006). The compositional dependence of the saturation surface of H2O-CO2 fluids in silicate melts. Chemical Geology, Vol. 29, p. 78 – 95
- Patino, L. C., M. J. Carr, and M. D. Feigenson, (2000). Local and regional variations in Central American arc lavas controlled by variations in subducted sediment input, Contributions to Mineralogy and Petrology, No. 138.3, p. 265-283
- Peiffer, L., (2011). Caracterización geoquímica y potencial geotérmico de los acuíferos del volcán El Chichón, Chiapas, México: Universidad Nacional Autónoma de México, PhD Thesis, 182 p.
- Peiffer, L., R. Bernard-Romero, A.Mazot, Y.A. Taran, M. Guevara, E. Santoyo, (2014). Fluid geochemistry and soil gas fluxes (CO2–CH4–H2S) at a promissory Hot Dry Rock Geothermal System: The Acoculco caldera, Mexico, Journal of Volcanology and Geothermal Research, Vol. 284, p. 122 - 137
- Peiffer, L., D. Rouwet, Y.A. Taran, (2015). Fluid Geochemistry of El Chichón Volcano-Hydrothermal System, In book: Active Volcanoes of Chiapas (Mexico): El Chichón and Tacaná, Chapter: 4, Publisher: Springer-Verlag Berlin Heidelberg, Editors: T. Scolamacchia, J.L. Macías, p.77-95
- Pérez N., G. Melian, J. Salazar, A. Saballos, J. Alvarez, F. Segura, P. Hernández, K. Notsu, (2000). Diffuse degassing of CO2 from Masaya Caldera, Nicaragua, Central America. EOS Trans, Am Geophys Union 81, (48), Fall Meet. Suppl.
- Plank, T., Langmuir, C.H., (1988), An evaluation of the global variations in the major element chemistry of arc basalts. Earth Planet. Sci. Lett., No. 90, p. 349-370
- Platt, U., (1994). Differential Optical Absorption Spectroscopy (DOAS). In: Sigrist, M.W. (Ed.), Monitoring by Spectroscopic Technique,. John Wiley & Sons Inc., New York, p. 27 – 76
- Platt U, Stutz J (2008) Differential optical absorption spectroscopy (DOAS), principle and applications. Springer Verlag, Heidelberg, 597 p.
- Portnyagin, M., Hoernle, K., Plechov, P., Mironov, N., Khubunaya, S., 2007. Constraints on mantle melting and composition and nature of slab components in volcanic arcs from volatiles (H2O, S, Cl, F) and trace elements in melt inclusions from the Kamchatka arc. Earth Planet. Sci. Lett., Vol. 255, Issue 1-2, p. 53 – 69
- Portnyagin, M. V., K. Hoernle, N. L. Mironov (2014). Contrasting compositional trends of rocks and olivine-hosted melt inclusions from Cerro Negro volcano (Central America): Implications for decompression-driven fractionation of hydrous magmas, International Journal of earth Sciences, October 2012, Vol. 103, Issue 7, p. 1963 – 1982

- Protti, M., F. Güendel, and K. McNally, (1994). The geometry of the Wadati-Benioff zone under southern Central America and its tectonic significance: Results from a high-resolution local seismographic network, Phys. Earth Planet. Inter., Vol.84, p. 271–287
- Rivera, C., J.A. Garcia, B. Galle, L. Alonso, Z. Yan, M. Johansson, M. Matabuena, G. Gangoiti, (2009). Validation of optical remote sensing measurement strategies applied to industrial gas emissions. Int. J. Remote Sens., Vol. 30, (12), p. 3191 – 3204
- Roberge, J., H. Delgado-Granados and P. J. Wallace, (2009). Mafic magma recharge supplies high CO2 and SO2 gas fluxes from Popocatépetl volcano, Mexico, Geology, Vol. 37, p. 107-110
- Rodgers, M., D.C. Roman, H. Geirsson, P. LaFemina, A. Muñoz, C. Guzman, V. Tenorio, (2013). Seismicity accompanying the 1999 eruptive episode at Telica Volcano, Nicaragua. J. Volcanol. Geotherm. Res. No. 265, p. 39–51
- Rodgers, M., C.D. Roman, H. Geirsson, P. LaFemina, S.R. McNutt, A. Muñoz, V. Tenorio, (2015). Stable and unstable phases of elevated seismic activity at the persistently restless Telica Volcano, Nicaragua, J. Volcanol. Geotherm. Res., No. 290, p. 63–74
- Rodrıiguez, L.A., I. M. Watson, W. I. Rose, Y. K. Branan, G. J. S. Bluth, G. Chigna, O. Matias, D. Escobar, S. A. Carn, T. P. Fischer, (2004). SO2 emissions to the atmosphere from active volcanoes in Guatemala and El Salvador, 1999-2002. Journal of Volcanology and Geothermal Research, No. 138, p. 325- 344
- Roedder, E., and P. W. Weiblen (1970). Silicate liquid immiscibility in lunar magmas, evidenced by melt inclusions in lunar rocks. Science, Vol. 167, no. 3918, p. 641 - 644
- Roedder, E., (1979). Silicate liquid immiscibility in magmas. In: Yoder H.S. (ed.). The evolution of the igneous rocks, fiftieth anniversary perspectives. Princeton Univ. Press, 15-57
- Roedder, E., (1984). Fluid Inclusions. Reviews in Mineralogy. Mineral. Soc. Amer., Vol. 12, 644 p.
- Roggensack, K., R. L. Hervig, S. B. McKnight, S. N. Williams, (1997). Explosive Basaltic Volcanism from Cerro Negro Volcano: Influence of Volatiles on Eruptive Style, Science, New Series, Vol. 277, No. 5332 (Sep. 12, 1997), p. 1639-1642
- Roggensack, K. (2001b). Crystals and their young melt inclusions Unraveling the 1974 eruption of Fuego volcano (Guatemala) with small, Geology 29, p. 911-914
- Rowe, M.C., A.J.R. Kent, and R.L. Nielsen, (2009).Subduction influence on basaltic oxygen fugacity and trace- and volatile-elements across the Cascade Volcanic Arc, Journal of Petrology, Vol. 50, Issue 1, p. 61 – 91
- Sadofsky, S. J., M. V. Portnyagin, K. Hoernle, and P. van den Bogaard, (2008). Subduction cycling of volatile and trace elements through the Central American Volcanic Arc: Evidence from melt inclusions, Contrib. Mineral. Petrol., Vol. 155, p. 433 – 456
- Sadofsky, S. J., M. Portnyagin, K. Hoernle and P. Van den Bogaard, (2008). Subduction cycling of volatiles and trace elements through the Central American volcanic arc: evidence from melt inclusions, Contributions to Mineralogy and Petrology, Vol. 155, p. 433-456
- Saginor, I., E. Gazel, M. J. Carr, C. C. Swisher iii, and B. Turrin, (2011a), New Pliocene-Pleistocene 40Ar/39Ar ages fill in temporal gaps in the Nicaraguan volcanic record.- J. Volcanol. Geotherm. Res. 202, p. 143-152
- Sawyer, G. M., G. G. Salerno, J. S. Le Blond, R. S. Martin, L. Spampinato, T. J.
- Roberts, T. A. Mather, M. L. I. Witt, V. I. Tsanev, and C. Oppenheimer (2011). Gas and aerosol emissions from Villarrica volcano, Chile, Journal of Volcanology and Geothermal Research, Vol. 203, no.1–2, p. 62 – 75

- Schiano, P. (2003). Primitive mantle magmas recorded as silicate melt inclusions in igneous minerals. Earth-Science Reviews, Vol. 63, No. 1-2, p. 121 – 144
- Shaw, A.M., D. R. Hilton, T. P. Fischer, J. A. Walker, G. Alvarado, (2003), Contrasting He–C relationships in Nicaragua and Costa Rica: insights into C cycling through subduction zones, Earth Planet. Sci. Lett., No. 214, p. 499-513
- Shaw, A.M., D.R. Hilton, T.P. Fischer, J.A. Walker, G.A.M. de Leeuw, (2006), Helium isotope variations in mineral separates from Costa Rica and Nicaragua: assessing crustal contributions, timescale variations and diffusion-related mechanisms, Chem. Geol., No. 230, p.124-139
- Shinohara, H., K. Fukui, K. Kazahaya, and G. Saito, (2003b). Degassing process of Miyakejima volcano: Implications of gas emission rate and melt inclusion data, in Advances in Volcanology Vol. 4, edited by B. de Vivo and B. Bodnar, p. 147- 161, Melt Inclusion s in Volcanic Systems, Elsevier
- Shinohara, H. (2005). A new technique to estimate volcanic gas composition: plume measurements with a portable multi-sensor system, Journal of Volcanology and Geothermal Research, No. 143, (4), p. 319-333
- Shinohara, H.K. (2013). A detailed evaluation of the fluxes from volcanoes in Japan, Journal of Volcanology and Geothermal Research, Vol. 268, no. 46 – 63
- Siebert L, Simkin T (2002) Volcanoes of the world: an illustrated catalogue of Holocene volcanoes and their eruptions. Smithsonian Institution, Global Volcanism Program Digital Information Series, GVP-3, http://www.volcano.si.edu/world/
- Signorelli, S. and M.R. Carroll (2000). Solubility and fluid-melt partitioning of Cl in hydrous phonolitic melts, Geochim. Cosmochim. Acta, no. 64, p. 2851 – 2862
- Simkin, T., L. Siehert, L. MeClelland, D. Bridge, C. Newhalt, and J.H. Latter (1981). Volcanoes of the World, Hutchinson Rose, Stroudsburg, PA, 232 p.
- Sisson, T.W., and G. D. Layne, (1993). H2O in basalt and basaltic andesite glass inclusions from four subduction-related volcanoes: Earth and Planetary Science Letters, Vo. 117, p. 619-635
- Snyder, G., R. Poreda, A. Hunt, and U. Fehn, (2001). Regional variations in volatile composition: Isotopic evidence for carbonate recycling in the Central American volcanic arc, Geochemistry, Geophysics, geosystems, G3, Vol. 2, p. 1 – 25
- Snyder, G. (2003). Sources of nitrogen and methane in Central American geothermal settings: Noble gas and 129I evidence for crustal and magmatic volatile components, Vol. 4, No. 1, p. 1 – 28
- Sobolev V. S., and V.P. Kostyuk, (1975). Magmatic crystallization based on a study of melt inclusions. In: Roedder E., Kozlowski A. (eds.). Fluid Inclusion Research 9, p. 182 – 253
- Sobolev, A.V., and M. Chaussidon, (1996). H2O concentrations in primary melts from supra-subduction zones and mid-ocean ridges: Implications for H2O storage and recycling in the mantle, Earth Planet.. Sci. Lett., Vol. 137, no. 1-4, p. 45 – 55
- Stoiber, R.E. and Jepsen, A., (1973). Sulfur dioxide contribution to the atmosphere by volcanoes. Science, No. 182, p. 577-578
- Stoiber, R.E., and M.J. Carr, (1973). Quaternary volcanic and tectonic segmentation of Central America: Bulletin of Volcanology, Vol. 37, p. 304 – 325
- Stolper, E. (1982). Water in silicate glasses: an infrared spectroscopic study, Contrib. Mineral Petrol., No 81, p. 1-17
- Symonds, R.B., T. M. Gerlach, M. H. Reed, (2001). Magmatic gas scrubbing; implications for volcano monitoring, J. Volcanol Geotherm Res., Vo. 108, p.303 -341
- Syracuse, E. M., and G. A. Abers, (2006), Global compilation of variations in slab depth beneath arc volcanoes and implications, Geochem. Geophys. Geosyst., No. 7, Q05017

- Tamburello, G., (2015). Ratiocalc: Software for processing data from multicomponent volcanic gas analyzers, Computers & Geosciences, Vol. 82, p. 63 – 67
- Taran, Y.A., T.P. Fischer, B. Pokrovsky, Y. Sano, M. A. Armienta, J.L. Macías, (1998). Geochemistry of the volcano–787 hydrothermal system of El Chichón Volcano, Chiapas, Mexico, Bull. Volcanol., No. 59, p.436 - 449
- Taran, Y.A., S. Inguaggiato, N. Varley, G. Capasso, R. Favara, (2002). Helium and carbon isotopes in thermal waters of the Jalisco block, Mexico, Geofísica Internacional (2002), Vol. 41, No. 4, p. 459 – 466
- Taran, Y.A., (2009). Geochemistry of volcanic and hydrothermal fluids and volatile budget of Kamchatka–Kuriles subduction zone, Geochim. Cosmochim. Acta, Vol. 73, p. 1134 - 1163
- Turner, H. L.III, P. LaFemina, A. Saballos, G. S. Mattioli, P. E. Jansma, and T. Dixon (2007). Kinematics of the Nicaraguan forearc from GPS geodesy, Geophys. Res. Lett., Vol. 34, L02302
- van Keken, P. E., Hacker, B. R., Syracuse, E. M., & Abers, G. A. (2011). Subduction factory: 4. Depth-dependent flux of H2O from subducting slabs worldwide. Journal of Geophysical Research: Solid Earth (1978–2012), Vol. 116 (B1)
- van Wyk de Vries, B., N. Kerle, D. Petley (2000). Sector collapse forming at Casita volcano, Nicaragua. Geology, Vol. 28, p.167 - 170
- Vaselli O., F. Tassi, E. Duarte, E. Fernández, R. J. Poreda and A. Delgado-Huertas, (2010), Evolution of fluid geochemistry at the Turrialba volcano (Costa Rica) from 1998 to 2008, Bull. Volcanol., no. 72, p. 397-410
- Vigouroux, N. (2011). Tracking the evolution of magmatic volatiles from the mantle to the atmosphere using integrative geochemical and geophysical methods, Thesis submitted in partial fulfillment of the requirements for the degree of Doctor of Philosophy, Department of earth Sciences, Simon Fraser University, 265 p.
- Wade, J. A., T. Plank, W. G. Melson, G. J. Soto, and E. H. Hauri, (2006). The volatile content of magmas from Arenal volcano, Costa Rica, J. Volcanol. Geotherm. Res., No. 157, p. 94-120
- Walker, J. A., L. C. Patino, J. C. Michael and M. D. Feigenson, (2001). Slab control over HFSE depletions in central Nicaragua, Earth and Planetary Science Letters, No. 192, p.533-543
- Walker, J.A., K. Roggensack, L. C. Patino, B.I. Cameron, O. Matias (2003).. The water and trace element contents of melt inclusions across an active subduction zone. Contrib Mineral Petrol, Vol. 146, p. 62 – 77
- Wallace, J.A., (2005). Volatiles in subduction zone magmas: concentrations and fluxes based on melt inclusion and volcanic gas data, Journal of Volcanology and Geothermal Research, Vo. 140, p. 217-240
- Walther, C. H. E., E. R. Flueh, C. R. Ranero, R. von Huene, and W. Strauch (2000). Crustal structure across the Pacific margin of Nicaragua: Evidence for ophiolitic basement and a shallow mantle sliver, Geophys. J. Int., Vol. 141, p. 759 – 777
- Wehrmann, H., K. Hoernle, M. Portnyagin, M. Wiedenbeck and K. Heydolph, (2012). Volcanic CO2 output at the Central American subduction zone inferred from melt inclusions in olivine crystals from mafic tephras, Geochemistry Geophysics Geosystems G3, Vol. 12, No. 6, p. 1 – 16
- Wehrmann, H., K. Hoernle, G. Jacques, D. Garbe Schonberg, K. Schumann, J. Mahlke, L. E. Lara, (2014). Volatile (sulphur and chlorine), major, and trace element geochemistry of mafic to intermediate tephras from the Chilean Southern Volcanic Zone (33–43S), Int. J. Earth. Sci., (Geol Rundsch), Vol. 103, p. 1945 - 1962

- Weinberg, R.F., (1992). Neotectonic development of western Nicaragua: Tectonics, Vol. 11, p. 1010 – 1017
- Werner, R., K. Hoernle, P. van den Bogaard, C. Ranero, R. von Huene, and D. Korich, (1999), Drowned 14-m.y. old Galapagos Archipelago off the coast of Costa Rica; implications for tectonic and evolutionary models, Geology, No. 27, p. 499-502
- Werner, R., K. Hoernle, U. Barckhausen, and F. Hauff, (2003), Geodynamic evolution of the Galápagos hot spot system (central east Pacific) over the past 20 m.y.: Constraints from morphology, geochemistry, and magnetic anomalies, Geochem. Geophys. Geosyst., No. 4, (12), p. 1108
- Weyl, R., (1980). Geology of Central America. Gebrüder Bornträger, Berlin. 371 p.
- Witham, F., J. Blundy, S. C. Kohn, P. Lesne, J. Dixon, S. V. Churakov, and R. Botcharnikov (2012). SolEx: a model for mixed COHSCL-volatile solubilities and exsolved gas compositions in basalt, Computers & Geosciences, Vol. 45, p. 87 - 97
- Williams, S.N., (1983). Geology and eruptive mechanisms of Masaya caldera complex, Nicaragua. Ph.D. thesis
- Williams-Jones , G., H. Rymer and D. A. Rothery, (2003).Volcanic hazards: Monitoring, prediction and mitigation Gravity changes and passive SO2 degassing at the Masaya caldera complex, Nicaragua, Journal of Volcanology and Geothermal Research, Vo. 123, Issues 1-2, 15 April 2003, p.137-160
- Wilson, M., (1989). Igneous Petrogenenis: A Global Tectonic Approach, 466 p.
- Witt, M. L. I., T. A. Mather, D. M. Pyle, A. Aiuppa, E. Bagnato and V. I. Tsanev, (2008). Mercury and halogen emissions from Masaya and Telica volcanoes, Nicaragua, Journal of Geophysical Research, Vo. 113, B06203
- Zimmer, M.M., T.P. Fischer, D.R. Hilton, G.E. Alvarado, Z.D., J.A. Walker, (2004). Nitrogen systematics and gas fluxes of subduction zones: insights from Costa Rica arc volatiles. Geochem. Geophys. Geosyst., Vol. 5, Issue 5

Notifications

The research leading to these results has received funding from the European Research Council under the European Union's Sev-enth Framework Programme (FP7/2007/2013)/ERC grant agreement n1305377. This study was initiated within the framework of the DECADE initiative of the Deep Carbon Observatory.

APPENDICE A

Int J Earth Sci (Geol Rundsch)
DOI 10.1007/s00531-014-1040-7

ORIGINAL PAPER

Measurements of volcanic SO_2 and CO_2 fluxes by combined DOAS, Multi-GAS and FTIR observations: a case study from Turrialba and Telica volcanoes

Vladimir Conde · Philippe Robidoux · Geoffroy Avard · Bo Galle · Alessandro Aiuppa · Angélica Muñoz · Gaetano Giudice

Received: 31 December 2013 / Accepted: 29 May 2014
© Springer-Verlag Berlin Heidelberg 2014

Abstract Over the past few decades, substantial progress has been made to overcome the technical difficulties of continuously measuring volcanic SO_2 emissions. However, measurements of CO_2 emissions still present many difficulties, partly due to the lack of instruments that can directly measure CO_2 emissions and partly due to its strong atmospheric background. In order to overcome these difficulties, a commonly taken approach is to combine differential optical absorption spectroscopy (DOAS) by using NOVAC scan-DOAS instruments for continuous measurements of crateric SO_2 emissions, and electrochemical/NDIR multi-component gas analyser system (multi-GAS) instruments for measuring CO_2/SO_2 ratios of excerpts of the volcanic plume. This study aims to quantify the representativeness of excerpts of CO_2/SO_2 ratios measured by Multi-GAS as a fraction of the whole plume composition, by comparison with simultaneously measured CO_2/SO_2 ratios using cross-crater Fourier transform infrared spectroscopy (FTIR). Two study cases are presented: Telica volcano (Nicaragua), with a homogenous plume, quiescent degassing from a deep source and ambient temperature, and Turrialba volcano (Costa Rica), which has a non-homogeneous plume from three main sources with different compositions and temperatures. Our comparison shows that in our "easier case" (Telica), FTIR and Multi-GAS CO_2/SO_2 ratios agree within a factor about 3 %. In our "complicated case" (Turrialba), Multi-GAS and FTIR yield CO_2/SO_2 ratios differing by approximately 13–25 % at most. These results suggest that a fair estimation of volcanic CO_2 emissions can be provided by the combination of DOAS and Multi-GAS instruments for volcanoes with similar degassing conditions as Telica or Turrialba. Based on the results of this comparison, we report that by the time our measurements were made, Telica and Turrialba were emitting approximately 100 and 1,000 t day^{-1} of CO_2, respectively.

Keywords DOAS · FTIR · Multi-GAS · Volcanic SO_2 and CO_2 fluxes

V. Conde (✉) · B. Galle
Department of Earth and Space Sciences, Chalmers University of Technology, Hörsalsvägen 11, 412 96 Göteborg, Sweden
e-mail: conde@chalmers.se

B. Galle
e-mail: bo.galle@chalmers.se

P. Robidoux · A. Aiuppa
Dipartimento di Scienzedella Terra e del Mare, Università degli Studi di Palermo, Via Archirafi, 22, 90123 Palermo, Italy
e-mail: philippe.robidoux@unipa.it

A. Aiuppa
e-mail: alessandro.aiuppa@unipa.it

G. Avard
Observatorio Vulcanológico y Sismológico de Costa Rica (OVSICORI-UNA), Apdo 2346-3000, Heredia, Costa Rica
e-mail: geoffroy.avard@una.cr

A. Aiuppa · G. Giudice
Istituto Nazionale di Geofisica e Vulcanologia, Sezione di Palermo, Via Ugo La Malfa, 153, 90146 Palermo, Italy
e-mail: gaetano.giudice@ingv.it

A. Muñoz
Instituto Nicaraguese de Estudios Territoriales (INETER), Apdo. Postal 2110, Managua, Nicaragua
e-mail: angelica.munoz@gf.ineter.gob.ni

Introduction

The increase of atmospheric CO_2 emissions leads to higher temperatures via the greenhouse effect, a natural process that has played a critical role during the different stages of

Published online: 12 June 2014

the earth's temperature record. After the industrial revolution, anthropogenic emissions became the dominant source of atmospheric CO_2 (IPCC 2007), leading to an increase of the global average temperature (Solomon et al. 2009). Despite the importance of estimating the budget of atmospheric CO_2, natural CO_2 emissions are still poorly constrained, thus making it difficult to quantify the extent of the anthropogenic signature in the atmosphere (e.g. Burton et al. 2013; Hazen and Schiffries 2013). Volcanoes constitute an important source of natural CO_2 emissions in the atmosphere; therefore, quantifying volcanic emissions is crucial in order to improve our knowledge of the atmospheric CO_2 budget.

In addition to their role in the atmospheric composition, quantifying volcanic gas emissions are an important parameter to quantify for evaluating magma-degassing processes, thus contributing to volcanic hazard assessment (e.g. Casadevall et al. 1983; Burton et al. 2007; Symonds et al. 1994). Water vapour, CO_2 and SO_2 are the most abundant volcanic gases (Symonds et al. 1994). In general, measuring volcanic gases is not a straightforward task; however, the difficulties for measuring SO_2 emissions have been successfully reduced with ground-based remote sensing techniques such as the correlation spectrometer (COSPEC) (Hoff and Millan 1981), mobile/scan differential optical absorption spectroscopy (DOAS) (Galle et al. 2002, 2010; Edmonds et al. 2003; Burton et al. 2009) and SO_2 cameras (Mori and Burton 2006). In contrast, volcanic CO_2 and water vapour are still hard to determine with similar techniques, partly due to the lack of suitable spectroscopic features in the ultraviolet (UV) spectral region and partly due to their abundant atmospheric background concentrations, which makes it difficult to distinguish the volcanic contribution from the standard atmospheric composition.

The volcanic CO_2 budget is still unconstrained for a number of degassing volcanoes (Burton et al. 2013), including Turrialba and Telica, two active volcanoes in Costa Rica and Nicaragua, respectively. Here, we present the results of a multidisciplinary experiment carried out in March 2013 with the aim of characterizing the gas composition of both volcanic plumes, with a particular focus on CO_2 and SO_2 emissions ratios. To overcome the difficulties of CO_2 flux measurements, we estimate the CO_2/SO_2 ratio of the volcanic plume by applying the Multi-GAS technique (Aiuppa et al. 2007; Shinohara 2005). Hence, the CO_2 flux is inferred by multiplying the CO_2/SO_2 ratio by parallel SO_2 flux measurements, which were made by using NOVAC scan-DOAS instruments (Galle et al. 2010). However, the CO_2/SO_2 ratio obtained by the stationary Multi-GAS instruments corresponds to an excerpt of the whole volcanic plume. In order to estimate how representative this ratio is compared to the bulk plume composition, cross-crater open-path (OP) Fourier transform infrared spectroscopy (FTIR) measurements (Oppenheimer et al. 1998; Sawyer et al. 2011; Duffell et al. 2003) were also made in parallel to stationary and mobile Multi-GAS measurements. The plumes of Turrialba and Telica volcanoes are easily accessible and are situated in regions with relatively stable wind direction and are therefore excellent test sites to apply and validate the combination of OP-FTIR, Multi-GAS and scan-DOAS techniques. This study represents the first systematic attempt to our knowledge to quantitatively compare results of two independent and widely used volcanic gas sensing techniques (Multi-GAS and OP-FTIR).

Turrialba volcano

Turrialba volcano is a basaltic-to-dacitic stratovolcano located approximately 15 km north of the city of Turrialba at 10.03°N 83.77°W (Fig. 1). It has an altitude of 3,340 m.a.s.l and is the easternmost of Costa Rica's Holocene volcanoes. The south-western end of the Turrialba edifice comprises an area of 800 m by 2,200 m, hosting three craters.

Historical natural hazards at Turrialba include landslides, pyroclastic flows, surges, lahars and ash falls and acidic volcanic gases. Reports from the 1864 to 1866 VEI 2 eruptions suggest ash fell as far as 125 km from the source (Reagan et al. 2006), which implies fallout from ash emissions may have been a problem in the Central Valley, the most populated and important economic area of Costa Rica. After 150 years of quiescence, a phreatic eruption, preceded by a gradual increase of activity, opened a new vent on the south-western side of the west crater on 5 January 2010 (Vaselli et al. 2010; Martini et al. 2010). The resulting new vent (Boca 2010) became the main contributor to the Turrialba plume. During the rainy season of 2011, the vent Boca 2011 opened. In 2012, another vent (Boca 2012) opened, emitting non-juvenile material on January 12 and 18 (OVSICORI-UNA 2012). Although Boca 2010 remained the main contributor to the Turrialba plume, the pair Boca 2011 and Boca 2012 added substantial additional gas input. The recent increase of activity of Turrialba has been accompanied by an increment of SO_2 emissions in the range of about 2,000–3,000 metric tonnes per day (t day^{-1}) at the onset of the eruptive event in January 2010 (Campion et al. 2012; Conde et al. 2013).

Telica volcano

Telica volcano is a basaltic-andesitic volcano located at 12.602°N 86.85°W. It has an altitude of 1,061 m.a.s.l. and is located north-west of the volcanic chain of Nicaragua. Telica features a typical stratovolcano shape; its summit is the highest point near the city of León and has a crater 700 m in diameter and 120 m deep (Smithsonian-Institution

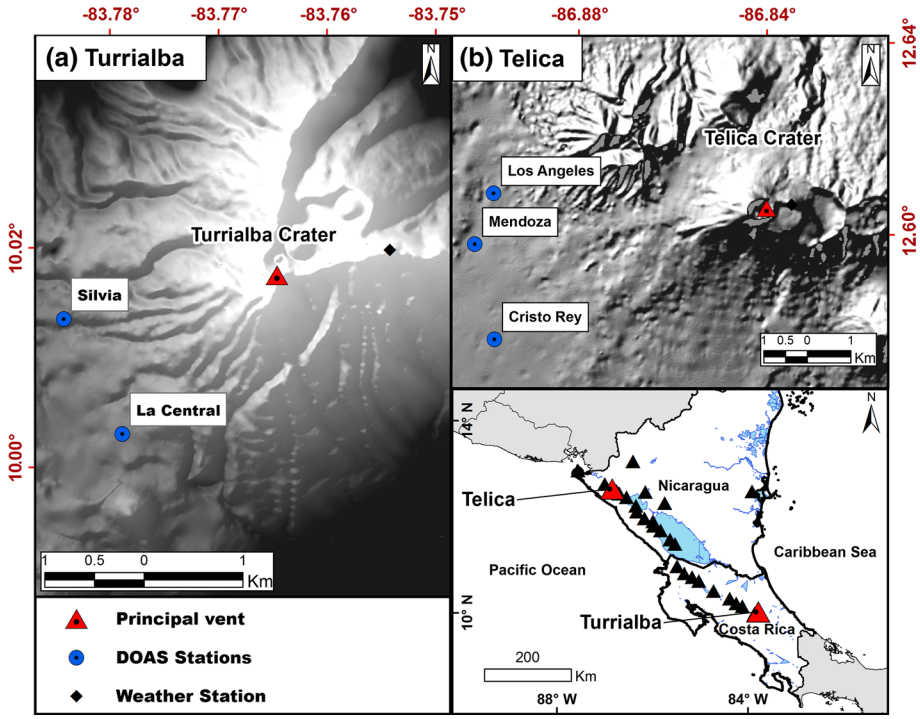

Fig. 1 Map showing the location of the NOVAC instruments surrounding the studied volcanoes **a** Turrialba volcano (Costa Rica). **b** Telica volcano (Nicaragua)

2013). The past eruptive story of Telica comprises at least ten important eruptions of vulcanian and strombolian styles since 1527, including the 1982 eruption that emitted a 3.7–4.3-km high column, from which ash fallout covered a distance of 37 km from the crater to the city of Corinto (Novák and Přichystal 2006). Currently, small explosive events are expected to take place every 1–5 years (Rodgers et al. 2013). For the past 5 years, SO_2 emissions have remained rather low, ranging between 70 and 200 t day^{-1}. This degassing rate has remained steady even during the last eruptive event, in May 2011 (Smithsonian-Institution 2011).

Measurements and methods

SO_2 flux measurements

Sulphur dioxide measurements were made by using NOVAC scan-DOAS instruments. This instrument acquires spectra which radiation source is UV-scattered sunlight in a vertical plane of 180° from one horizon to the other in angular steps of 3.6°. The spectra acquisition implemented by the NOVAC instrument consists of a motor-driven mirror or prism that redirects the scattered light from the sky collected through a telescope defining a field of view (FOV) of 8 mrad. From the telescope, light is redirected to a spectrometer (Ocean Optics®, S2000) by an optical fibre. More details about the NOVAC instruments can be found in Galle et al. (2010).

The instrument runs during daylight hours, adding 15 spectra in each step, and therefore improving the signal-to-noise ratio. The exposure time is automatically adjusted in order to avoid light saturation in the spectrometer detector. In view of the variable local weather conditions, this exposure adjustment is made every time a new scan measurement starts. Under clear sky conditions, a scan can be completed in <3 min. The SO_2 column amount was retrieved from the spectra for each angular step, applying DOAS (Platt and Stutz 2008). The spectra was evaluated in the wavelength region of 310–322 nm, which is less sensitive to scattering and stray light (Johansson 2009; Galle et al. 2010). The plume elevation, speed and direction are needed to determine the SO_2 flux. The SO_2 flux was obtained by multiplying the integrated gas columns by the plume (wind) speed.

At Turrialba, two NOVAC instruments were installed in the west flank of the volcanic edifice according to the predominant easterly wind direction, at a radial distance of about 2.3 km from the crater and a mean altitude of 2,600 m.a.s.l (Fig. 1). Similarly, a temporary installation of three NOVAC instruments was made at Telica, near a locality called Cristo Rey; this site is located at a radial distance of 6 km from the crater on the west side of the volcanic edifice and a mean altitude of 250 m.a.s.l. Plume direction and plume height were determined by triangulation, using the direction to the plume centre as simultaneously recorded by two instruments.

At Turrialba, during 18 and 19 March, plume speed was measured using an additional Dual-beam DOAS

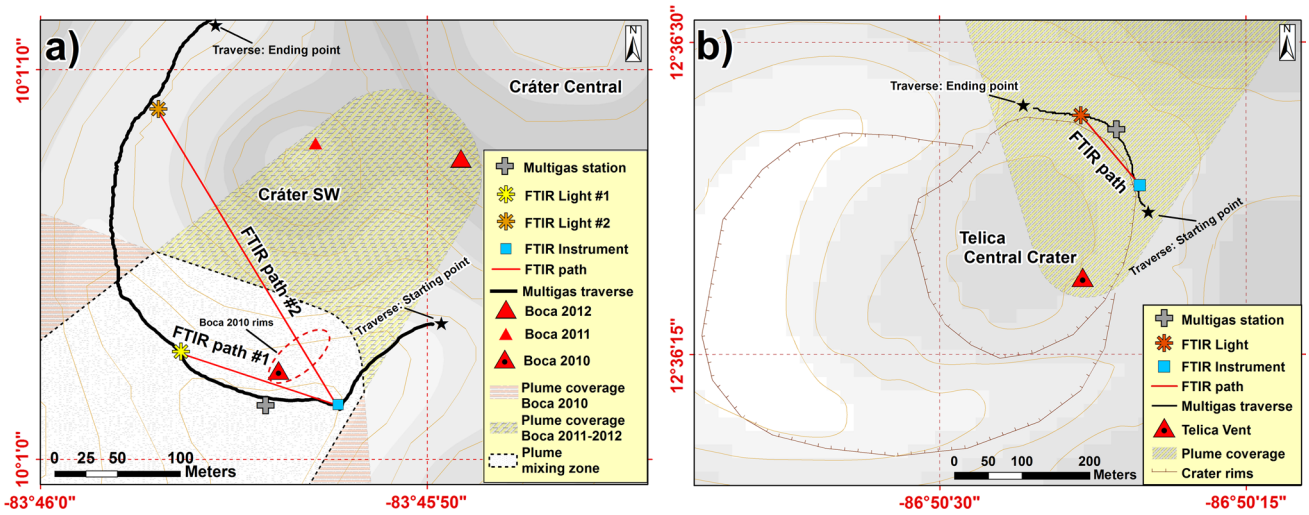

Fig. 2 Map of the area showing the spatial distributions of the volcanic plume, the location of the FTIR, the light sources and the stationary Multi-GAS stations. **a** Turrialba volcano. **b** Telica volcano

instrument located under the plume at a distance of about 3 km from the crater. This instrument measures simultaneously and with high time resolution the total column of SO_2 in the centre of the plume in a direction upwind and downwind. By correlating the time series, the time lag between different features in the plume can be determined and a plume speed can be derived. The method is described in detail in Johansson et al. (2009). The average plume speed was determined to be 5.3 and 5.9 m/s for 18 and 19 March, respectively, while for 17 March, the average of the two previous days, 5.6 m/s, was used. The plume direction and height averaged 260° and 3,340 m.a.s.l., respectively. At Telica, the plume speed was obtained from a meteorological station located on top of Telica, about 500 m east of the crater, and averaged 3 m/s. Although the plume at Telica typically hit the north wall of the crater rim, it was then typically dispersed further to the west, following the predominant wind direction, which during our field work averaged 268° with a height of 1,150 m.a.s.l.

FTIR measurements

FTIR allows to measure the columns of volcanic gas species that have spectral signatures in the infrared region (e.g. CO_2, SO_2, HCl, HF, CO, COS and H_2O). However, this study will be confined only to CO_2 and SO_2, since they can also be measured in parallel with a Multi-GAS instrument. The OP-FTIR measurements were made in the south-west sector of the crater of Turrialba from 17 to 19 March 2013, and north-east sector of Telica on the afternoon of 23 March 2013 using a FTIR spectrometer manufactured by Bruker, which has a Peltier cooled MCT detector and a ZnSe beam splitter. Spectra were collected in the range of 1,850–5,000 cm^{-1} with a resolution of 0.5 cm^{-1}. The spectrometer is equipped with an electric cooler, which avoids the difficulties of cooling down the detector by using liquid nitrogen. In order to reduce the signal-to-noise ratio, 16–64 spectra were averaged for every individual measurement, yielding a time resolution between 75 s and 5 min. An incandescent lamp stabilized with a DC/DC converter placed across the crater provided the source of artificial infrared radiation.

At Turrialba, the lamp was placed at two different positions, leading to two different light paths: path 1 and path 2, with lengths of 136 and 275 m, respectively (Fig. 2a). Each light path assesses the contribution of the main vents (Boca 2010 and the pair Boca 2011 and Boca 2012) to the total volcanic plume composition as shown in Fig. 3b. At Telica, the plume has a single origin; thus, the lamp remained fixed during the period of measurements (Fig. 2b).

The spectra were recorded in a portable computer and later evaluated using the software MALT (Multiple Atmospheric Layer Transmission) (Griffith 1996), which retrieves gas concentrations by implementing a nonlinear least square (NLLS) fitting of the measured spectra with a modelled synthetic spectrum retrieved from the molecular spectroscopy database HITRAN (Rothman et al. 2009), jointly with the estimated values of the atmospheric pressure and plume temperature. These last two parameters were obtained from the Multi-GAS instruments as explained in the following section. Different spectral regions were selected in order to retrieve the gas species: 2,100–2,248 cm^{-1} for CO_2 and 2,470–2,535 cm^{-1} for SO_2. In addition, other ambient species, N_2O, CO and H_2O, were included in the NLLS fitting.

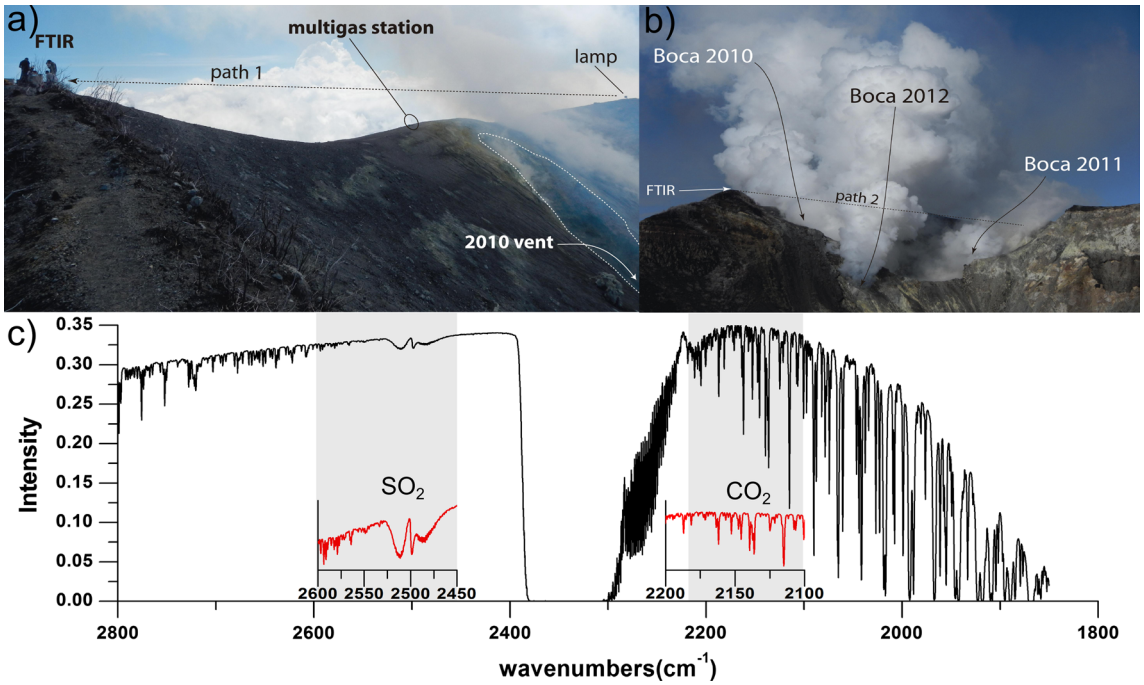

Fig. 3 Measurements at Turrialba and Telica volcano. **a** Location of the FTIR, incandescent lamp (path 1) and Multi-GAS at Turrialba. **b** Path 2 of Turrialba, through the main vents (Boca 2010, Boca 2011 and Boca 2012). **c** Example of a FTIR spectrum measured at Telica volcano on 23 March 2013

Due to the relatively short distance of the light paths and fairly high intensity of the incandescent light, good quality spectra were acquired at both volcanoes, for example the spectrum shown in Fig. 3c. Spectra with zero-base offset around the line 2,350 cm^{-1} and/or strong attenuation due to the occasional heavy condensation were discarded; however, only 20 % of the total spectra were considered to be of bad quality. The continuous background spectrum was modelled by using a fourth-order polynomial both for CO_2 and SO_2.

In addition to the gas concentration retrieval, the spectrum analysis also reports an evaluation fitting error; however, it has been demonstrated that the reported error largely underestimates actual measurement errors (Smith et al. 2011). Independent studies quantifying the error budget of the gas concentration retrievals have estimated that for a SO_2 concentration of 250 ppm, the choice of the background polynomial and inaccuracies in the instrumental line shape account for an uncertainty of 1.2 and 1.5 %, respectively (Horrocks et al. 2001). Similarly, Smith et al. (2011) estimated that for a CO_2 concentration of 280 ppm, the choice of the polynomial and FOV variations of the instrument account for an uncertainty of 1.7 and 5.2 %, respectively. All these uncertainties can be critical when measuring absolute gas columns/concentrations, while for measuring ratios between two gases, these uncertainties tend to cancel out and become less significant. Nevertheless, in a typical field situation with variable ambient conditions, the measured ratios may be significantly affected by an incorrect assumption of the plume temperature and pressure.

Multi-GAS measurement

The concentrations of major volcanic gas species (H_2O, CO_2, SO_2, H_2S) were also characterized using a multi-component gas analyser system (Multi-GAS) (Aiuppa et al. 2005, 2007; Shinohara 2005). A fully automated Multi-GAS instrument, developed at the Istituto Nazionale di Geofisica e Vulcanologia (INGV), Sezione di Palermo, was temporarily deployed from 17 to 19 March 2013 at a fixed site on the southern rim of the active west crater of Turrialba, about 10 m south-west from Boca 2010. A similar deployment was made on the north rim of the active crater of Telica on March 23 and during the period from March 27 to April 8.

The instrument integrates an infrared spectrometer for CO_2 measurement (Gascard II, calibration range 0–3,000 ppmv; accuracy ±2 %; resolution, 0.8 ppmv), along with specific electrochemical sensors for the measurement of SO_2 (CityTechnology, sensor type 3ST/F; calibration range, 0–200 ppmv; accuracy, ±5 %; resolution, 0.1 ppmv) and H_2S (SensoriC, sensor type 2E; calibration range, 0–200 ppmv; accuracy, ±5 %; resolution,

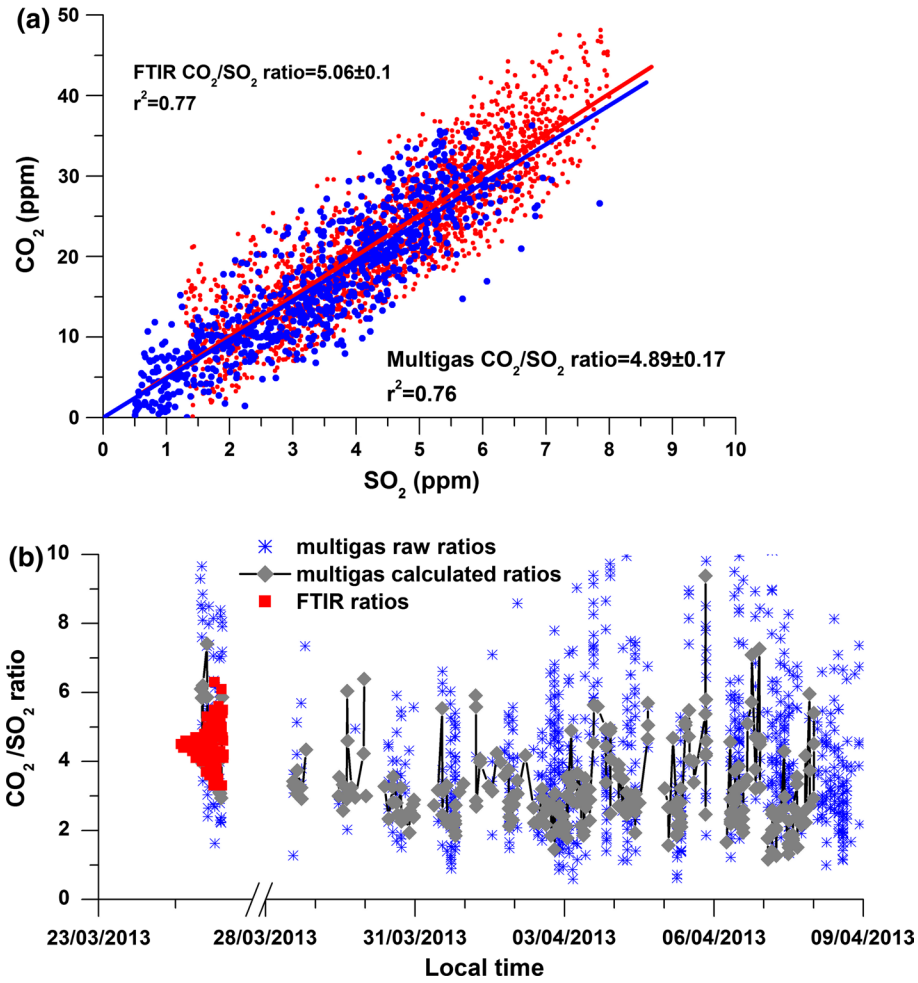

Fig. 4 Scatter plots of the CO_2/SO_2 ratios measured by FTIR (*red*) and Multi-GAS (*blue*) at Telica. The CO_2 concentration background has been removed from both data sets. **a** FTIR and Multi-GAS measurements on March 23 (13:00–19:00, local time). **b** CO_2/SO_2 ratio measured by Multi-GAS (*blue* and *grey dots*) and FTIR (*red dots*) on 23 March and from 17 March to 8 April 2013

0.1 ppmv). H_2O concentrations were also calculated from records of temperature and relative humidity (Galltec sensor; measuring range, 0–100 % Rh; accuracy, ±2 %), using a time-average pressure of 670 mBar at Turrialba and 912 mbar at Telica.

The Multi-GAS was set to perform measurements during sampling periods of 30 min to 2 h. During each measurement, the plume gas was steadily pumped into the sensor's housing and a data-logger board captured the output signals from the sensors at a rate of 0.1 Hz. The Multi-GAS was powered by a 12-V lead battery connected to a photovoltaic module, and the main box with sensors was protected inside a waterproof wallet (30 × 20 × 15 cm). At the end of each cycle, the data are automatically transferred via a radio link from the remote Multi-GAS to a temporary base station on the flank of the volcano.

In addition to the static measurements, a small, compact, portable version of the Multi-GAS instrument was used to perform sequences of walking transects around the outer rim of the western Turrialba Crater. During the walking traverses, the inlet tube of the Multi-GAS was kept 50 cm from the ground to capture plume gas while avoiding any soil contribution. In total, 12 traverses were done between March 9 and 19.

The acquired concentration data (from both fixed and portable Multi-GAS instruments) were processed using custom-made Ratiocalc software (Tamburello 2013), which automatically runs the retrieval methodology described in Aiuppa et al. (2005, 2006, 2009). Air-background-corrected concentrations were first calculated by subtracting ambient air concentrations of ~25,000 ppmv for H_2O and ~390 ppmv CO_2 from the raw data. Any temperature-dependent sensors' baseline drift was also removed by simple baseline fitting with polynomial functions. These corrected data were then used to derive gas–gas scatter plots and finally to derive CO_2/SO_2 molar ratios in the plume by taking the gradient of the best-fit regression lines (e.g. Fig. 4a). To explore the time variability of plume compositions, a number of such scatter plots were sequentially created by Ratiocalc (by scanning the available data set), each from data acquired during individual time windows of a few minutes. A time series for such "time-averaged" CO_2/SO_2 gas ratios is shown in Figs. 4e and 6b. Measurement intervals were discarded (e.g. no

ratio was calculated) when CO_2 and SO_2 concentrations were below fixed threshold values (e.g. air-corrected $CO_2 < 300$ ppmv; $SO_2 < 3$ ppmv). In such diluted plumes, the error in gas ratios has been observed to be larger than the error typically (±20 %) obtained in denser plumes (Aiuppa et al. 2006, 2009). The short-term (0.1 Hz) variability of CO_2/SO_2 ratios was also explored by calculating the point-to-point ratio between simultaneously measured CO_2 and SO_2 concentrations (e.g. Métrich et al. 2011). While the error in such higher frequency measurements can be as high as 20 %, we still observe an overall good match between point-to-point and time-averaged results (e.g. Figs. 4e, 6b). Overall, the instrument acquired a total of 12.5 h of observations, in ~20 % of which the plume was dense enough at the measurement site to allow accurate retrieval of plume composition.

Results

Comparison of CO_2/SO_2 ratio between Multi-GAS and FTIR at Telica

The simultaneous CO_2/SO_2 measurements made with FTIR and Multi-GAS at Telica are shown in the scatter plot of Fig. 4a. Both data sets exhibit linear trends that can be modelled as a simple regression line:

$$Y_k = rX_k + b \tag{1}$$

where the pair X_k and Y_k correspond to the fitted SO_2–CO_2 data points, while r and b correspond to the concentration ratio and the background CO_2 concentration, respectively.

In order to quantify the alikeness between FTIR and Multi-GAS, it is necessary to calculate independently their concentration ratios while taking into account their most significant uncertainties, which normally can be made with a simple least-squares line fitting. However, SO_2 and CO_2 measurements contain independent uncertainties; thus, fitting a line is not straightforward. Although several methods have been proposed to deal with this problem (e.g. Deming 1943; Reed 1989; Pearson 1901; York et al. 2004), the approach considered in this study is the one formulated by Deming (1943), as shown in Eq. (2):

$$S^2 = \sum_{k=1}^{N} \left[\left(\frac{x_k - X_k}{\sigma_{xk}} \right)^2 + \left(\frac{y_k - Y_k}{\sigma_{yk}} \right)^2 \right] \tag{2}$$

Equation (2) assumes that the best fitted lines X_k and Y_k (Eq. 1) are those minimizing the sum of the orthogonal distances (S^2) of the N pairs of SO_2–CO_2 (x_k and y_k) measurements with their respective uncertainties σ_{xk} and σ_{yk}.

The main source of FTIR retrieval uncertainties is the inability to obtain accurate values of atmospheric pressure and temperature for each spectrum. However, during the measurement period at Telica, the pressure was rather invariable with an average of 914 ± 1.5 mbar; thus, its contribution to the measurements' uncertainties can be assumed to be negligible (Smith et al. 2011; Horrocks et al. 2001). On the other hand, it was estimated that plume temperature ranged more widely (21–25 °C) and was, therefore, the predominant source of uncertainties in the gas concentration retrievals.

In Eq. (2), x_k and y_k correspond to the retrieved CO_2 and SO_2 concentrations assuming the mean temperature value (23 °C). Their uncertainties σ_{xk} and σ_{yk} were constrained by repeatedly retrieving the concentrations, assuming temperatures varying in the 21–25 °C range in steps of 1 °C, and further calculating the standard deviation:

$$\sigma(x_{23}) = \sigma_k(x_{23}) = \sqrt{\frac{\sum_{k=1}^{N} \sum_{T=\mathrm{ti}}^{\mathrm{tf}} \left(x_{23,k} - x_{T,k} \right)^2}{N(\mathrm{tf} - \mathrm{ti} + 1) - 1}} \tag{3}$$

whereas $x_{T,k}$ is the kth gas concentration data point assuming a temperature T; ti and tf are the limits of the considered temperature range (21–25 °C). Hence, σ_{xk} and σ_{yk} are estimated to be ±0.05 and ±4.65 ppm for SO_2 and CO_2, respectively. At first glance, these values appear to be of minor importance; nevertheless, their contribution to the uncertainty of the concentration ratios is significant, as will be further discussed.

The chosen procedure for minimizing Eq. (2) is based on a weighted total least-squares (WTLS) algorithm, which has been proved to be robust, and considers the orthogonal distance between the fitting line and the data points, by taking into account the reciprocal of the uncertainties as a "weight" (Krystek and Anton 2008). Hence, the estimated FTIR CO_2/SO_2 ratio (r_F) is 5.06, with a standard deviation (σ_F) of 0.1.

A similar procedure was followed in order to obtain the Multi-GAS parameters, but in this case, the main source of uncertainties σ_{xk} and σ_{yk} are linked to the sensors' accuracy, which, as described in the previous section, is proportional to the individual measured concentrations by a fraction of 2 % for CO_2 and 5 % for SO_2. From Eq. (2) and applying a WTLS fitting to the measurements and its uncertainties, the estimated Multi-GAS concentration ratio (r_M) is 4.89, with a standard deviation (σ_M) of 0.17.

Finally, the alikeness between FTIR and Multi-GAS ratios is statistically tested by measuring the 95 % confidence interval (CI) of the difference of both ratios relative to the Multi-GAS ratio:

$$\mathrm{CI}\,[\%] = \frac{(r_F - r_M) \pm t_{\alpha/2} \sqrt{\sigma_F^2 + \sigma_M^2}}{r_M} \times 100 \tag{4}$$

whereas $t_{\alpha/2}$ (1.96) is the 95 % T.

Table 1 Comparison of the CO_2/SO_2 ratio obtained by FTIR and Multi-GAS at Telica

Measurement period	Technique	CO_2/SO_2 ratio	R^2	95 % confidence interval (CI) of the ratio differences (%)
23 March 2013, 12:30–19:30	FTIR	5.06 ± 0.1	0.77	−4.11
	Multi-GAS	4.89 ± 0.17	0.76	

The CI of the measurements at Telica (Table 1) has an overlap of −4 to 11 %, which indicates that both ratios are statistically equivalent, with a typical discrepancy between Multi-GAS and FTIR of a factor ~3.5 %. Considering the scatter plot of the simultaneous measurements (Fig. 4a), the statistical alikeness between both techniques was expected.

Comparison of CO_2/SO_2 ratio between Multi-GAS and FTIR at Turrialba

The simultaneous measurements of CO_2/SO_2 ratios made with Multi-GAS and FTIR through the path 1 (March 17, 18) at Turrialba are shown in the scatter plot of Fig. 5a, b. The atmospheric pressure did not vary during the two measurement periods (664 ± 2 and 680 ± 4 mbar), while temperature, which ranged 30–40 °C with a mean value of 35 °C, remained as the main source of uncertainties. The alikeness between both techniques was quantified by applying the same procedure described in the previous section. From Eq. (2), x_k and y_k correspond to the SO_2 and CO_2 concentrations measured either with FTIR or Multi-GAS. For FTIR, the concentrations were retrieved by assuming the mean temperature value (35 °C), while their uncertainties (σ_{xk} and σ_{yk}) were calculated as shown on Eq. (3), with ti = 30 and tf = 40. On March 17, the estimated σ_{xk} and σ_{yk} are ±1.107 and ±8.72 ppm, respectively, while on March 18, σ_{xk} and σ_{yk} are ±1.35 and ±8.54 ppm, respectively. For Multi-Gas, the uncertainties were calculated based on the accuracy of the sensors (2 % for CO_2 and 5 % for SO_2). The concentration ratios and their standard deviations both for FTIR and Multi-GAS were calculated by applying WTLS fitting, yielding the results shown in Table 2.

From Eq. (4), the 95 % CI of the difference between the ratios on March 17 ranges between 20 and 30 %. On March 18, the 95 % CI of the difference between the ratios is found to be between 11 and 16 %. The results of these statistical tests suggest that in comparison with the general agreements observed at Telica volcano, the Multi-GAS and FTIR measurements at Turrialba differ by factors of 25 and 13 %, respectively.

The FTIR measurements through the path 2, corresponding to the secondary vents (Boca 2011 and 2012), were made on the afternoon of March 18 and the morning of March 19. The estimated CO_2/SO_2 ratios are 1.19 and 1.11 (Fig. 5c, d), which are approximately half of the ratio measured through path 1. The systematically lower ratios at Boca 2011 and Boca 2012, relative to the bulk plume (essentially contributed by Boca 2010; see Fig. 5), demonstrate a chemical vent-to-vent heterogeneity of gas emissions at Turrialba. This vent-to-vent variability likely reflects different vent temperatures, which were ~800 °C (Boca 2012) and ~400 °C (Boca 2010) during our survey (OVSICORI-UNA 2013). High temperatures at Boca 2012 likely resulted in larger extents of sulphur(S) remobilization (and consequently, in lower CO_2/SO_2 ratios).

SO_2 emissions

By the time of our measurements, NOVAC instruments measured the average SO_2 flux from Turrialba to be 840 ± 120 t day^{-1}, as shown in Fig. 6a and Table 3. These results are within the range of variability of the SO_2 flux since 2012 (OVSICORI-UNA 2012). Similarly, the SO_2 flux from Telica averaged 64 ± 34 t day^{-1}, within the range of typical values expected for this volcano (Smithsonian-Institution 2011).

Discussion

Our results are the first to our knowledge for the CO_2/SO_2 compositions of the volcanic plumes issuing from two persistently degassing volcanoes in Central America. Our inferred CO_2/SO_2 ratios for Telica and Turrialba (Tables 1, 2) compare well with the compositional signature of volcanic arc gases, the majority of which typically exhibit CO_2/SO_2 ratios in the 1–5 range (Hilton et al. 2002; Fischer et al. 2009). More specifically, our results are qualitatively consistent with the CO_2/SO_2 ratio of 2.7, proposed by Hilton et al. (2002) as representative of volcanic gas emissions in the Central American Volcanic Arc (CAVA). A slightly lower CO_2/SO_2 ratio (1–2.2) was proposed for CAVA by (Mather et al. 2006), which is still within the range of variation of our results.

Apart from adding a new piece to the puzzle of the still-growing database of volcanic gas emissions, our results pave the way to the first quantitative intercomparison between Multi-GAS- and FTIR-derived CO_2/SO_2 ratios, as detailed below.

CO_2/SO_2 ratios: FTIR and Multi-GAS matching

The statistically good match between CO_2/SO_2 ratios measured at Telica, as shown by the 95 % CI statistical test, results from favourable measuring conditions at this crater. At Telica, the plume is emitted by only one major vent

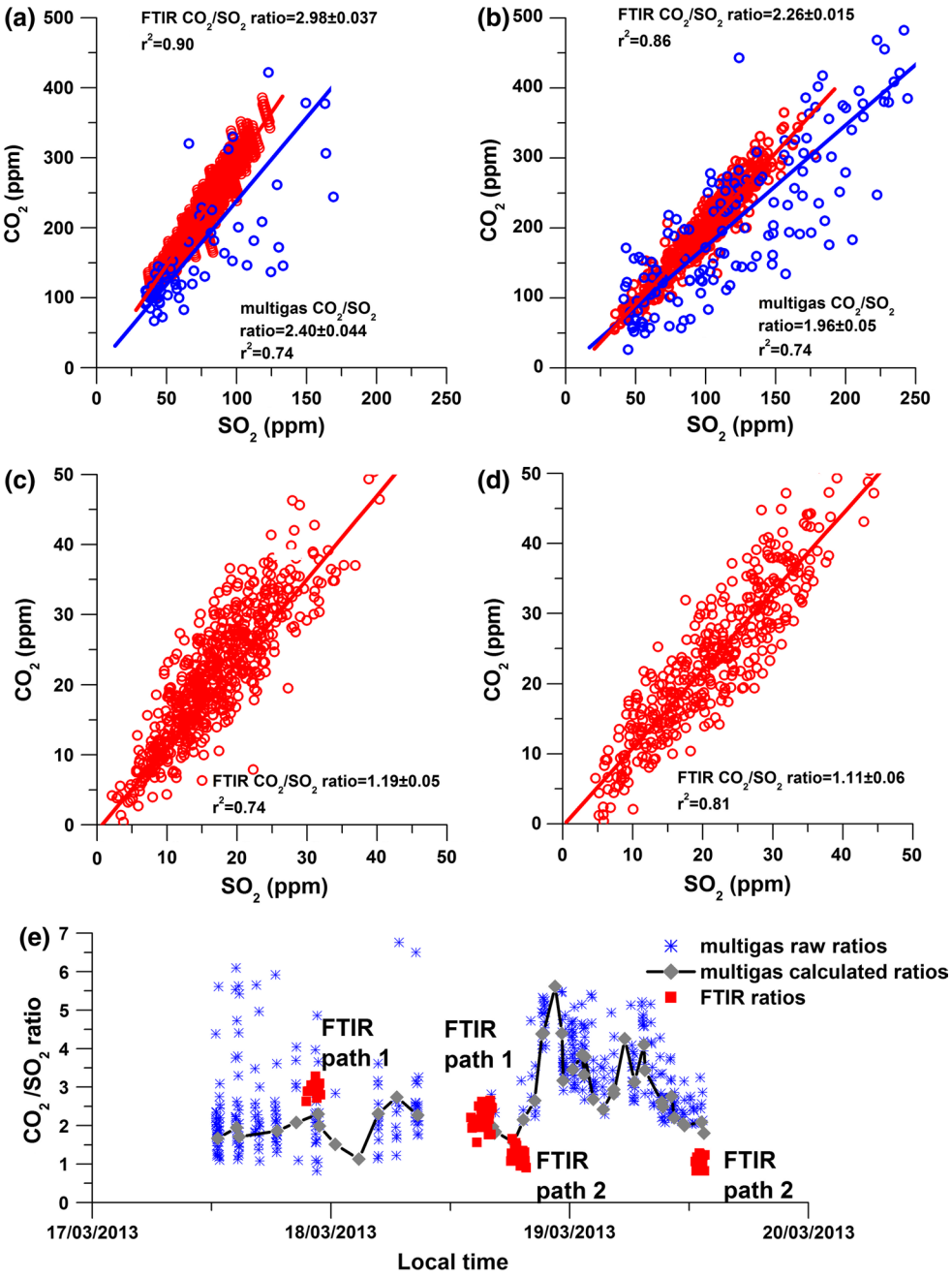

Fig. 5 Scatter plots of the CO_2/SO_2 ratios measured simultaneously by FTIR (*red*) and Multi-GAS (*blue*) at Turrialba in March 2013. The CO_2 concentration background has been removed from both data sets. **a** FTIR and Multi-GAS measurements through the vent Boca 2010 (path 1) on March 17 (21:30–23:00, local time). **b** FTIR and Multi-GAS measurements through the vent Boca 2010 (path 1) on March 18(14:30–16:00, local time). **c** FTIR measurements through the vents Boca 2011 and Boca 2012 (path 2) on March 18 (18:00–20:00, local time). **d** FTIR measurements through the vents Boca 2011 and Boca 2012 (path 2) on March 19 (12:30–13:30, local time). **e** CO_2/SO_2 ratio measured by Multi-GAS (*blue* and *grey*) and FTIR (*red*) during 17–19 March 2013. The measured FTIR ratios through path 2 are approximately half of the ratio measured through path 1

Table 2 Comparison of the CO_2/SO_2 ratio obtained by FTIR and Multi-GAS at Turrialba

Measurement period	Technique	CO_2/SO_2 ratio	R^2	95 % confidence interval (CI) of the ratio differences (%)
17 March 2013, 21:30–23:00	FTIR	2.98 ± 0.037	0.9	20.30
	Multi-GAS	2.40 ± 0.044	0.76	
18 March 2013, 14:30–16:00	FTIR	2.26 ± 0.015	0.86	11.16
	Multi-GAS	1.96 ± 0.05	0.74	

that is ≈120 m deep inside the crater. Because of transport through the atmosphere to the rim, the temperature of the plume was approximately the same as the ambient temperature, further supporting thorough mixing and homogeneity.

At Turrialba volcano, on the other hand, there is still reasonable correspondence of CO_2/SO_2 ratios observed by the two independent techniques, although to a lower degree than at Telica. The CO_2/SO_2 ratio measurements, made with the mobile Multi-GAS for traverses, indicate a distinct lateral heterogeneity of the Turrialba plume (Fig. 7). In all these traverses, made perpendicular to the plume transport

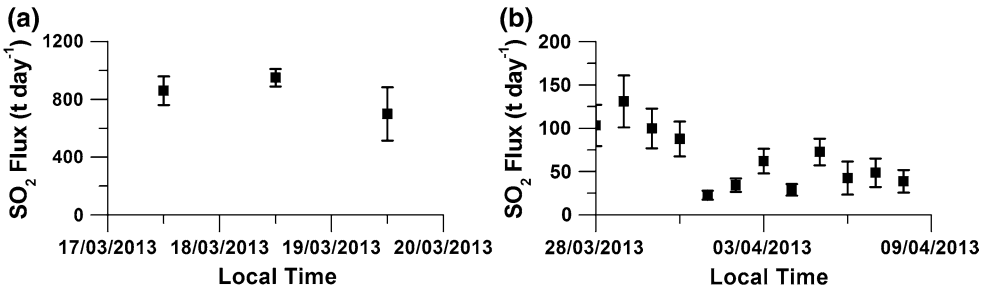

Fig. 6 Daily SO_2 emissions measured at Turrialba and Telica volcano by the NOVAC instruments. **a** Turrialba: 17–19 March 2013. **b** Telica: 27 March–8 April 2013. The error bar indicates the daily variability

Table 3 Daily average of SO_2 and CO_2 emissions at Turrialba during 17, 18 and 19 March

Day	Mean SO_2 flux (t day^{-1})	Standard deviation SO_2 flux (t day^{-1})	Mean CO_2 flux (t day^{-1})	Standard deviation CO_2 flux (t day^{-1})
17 March 2013	860	100	1,000	150
18 March 2013	950	60	1,350	150
19 March 2013	700	185	1,000	511

direction, the ratios are systematically higher (a factor of 10–40 %) in the centre of the plume than on its boundary. The variation of the ratio, observed along such relatively short distance (~10 m), is comparable to the differences estimated by the previous statistical tests. In the light of our FTIR results (Fig. 5), we suggest these deviations reflect gas contributions to the plume that come from three compositionally distinct sources (Boca 2010, Boca 2011 and Boca 2012). The FTIR measurements made through path 2 allow characterizing the gas contributions from Boca 2011 and Boca 2012 vents and indicate a CO_2/SO_2 ratio that is approximately half of the ratio measured through path 1. The CO_2-richer gas columns measured through path 1 instead are more likely to have their prevalent contribution from the Boca 2010 gas, due to the proximity of this vent to the south-west sector of the crater rim (≈25 m). In contrast, the boundaries of the plume are more likely to contain a mixed contribution of gas concentrations from the three vents, justifying the CO_2-poorer compositions observed during Multi-GAS traverses. The implication of these results is that a fixed Multi-GAS instrument is fairly sensitive to slight angular variations of the plume/wind direction, as can be observed by the broad dispersion of individual measurements in the time series and the scatter plots shown in Fig. 4.

CO_2 fluxes

Synchronized SO_2 flux and Multi-GAS measurements allowed monitoring of CO_2 flux emissions at Telica and Turrialba during our campaign. At Telica, these measurements were made continuously during a period of 13 days, and at Turrialba, for a period of 3 days (Figs. 4b, 5d). Combining the Multi-GAS CO_2/SO_2 ratios with the NOVAC-based SO_2 fluxes, the first estimates of CO_2 emission rates for Turrialba

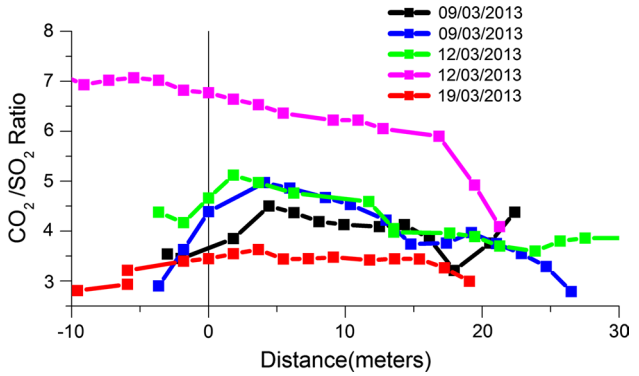

Fig. 7 Multi-GAS CO_2/SO_2 ratios measured by walking transects on the southern sector of the crater rim of Turrialba. The distance 0 is the reference point, where the walking transect was closest to the fixed Multi-GAS instrument

and Telica were derived, as shown in Fig. 8a, b, respectively. The averaged CO_2 emissions rates are 1116 ± 164 t day^{-1} for Turrialba and 166 ± 76 t day^{-1} for Telica.

When compared to the typical levels of CO_2 emissions from subaerial volcanoes, which range from 18 to 52,000 t day^{-1} (Burton et al. 2013), our derived CO_2 outputs can be ranked as moderate (Turrialba) to low (Telica). Our results indicate that along with Masaya volcano in Nicaragua (Burton et al. 2000; Martin et al. 2010), Turrialba is the strongest punctual source of volcanic CO_2 in the Costa Rica–Nicaragua segment of the CAVA.

Conclusions

The aim of this study was to determine CO_2 emissions from the volcanoes Turrialba and Telica and to compare CO_2/

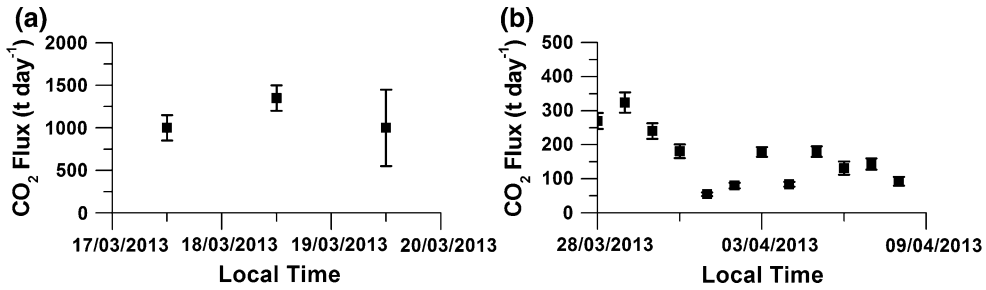

Fig. 8 Daily CO_2 emissions at Turrialba and Telica volcanoes, estimated by the product of the SO_2 flux with the calculated mass ratio measured by Multi-GAS. **a** Turrialba: 17–19 March 2013. **b** Telica: 27 March–8 April 2013. The error bar indicates the daily variability

SO_2 ratios obtained from two independent measurement techniques, FTIR and Multi-GAS, with a focus on their different spatial resolutions. The active OP-FTIR technique provides concentration averages across the entire plume, while the Multi-GAS instrument provides measurements from a fixed point in the plume. Telica volcano, with only one deep vent providing a well-mixed plume at the measurement site, represents an easy case of Multi-GAS–FTIR intercomparison. Results demonstrate a very good match between the two techniques, with the independently estimated CO_2/SO_2 ratios differing by only 3 %. This is within the calibration errors of the two methods. However, at Turrialba volcano, instead, the presence of 3 distinct active vents, for which there is FTIR evidence of CO_2/SO_2 ratio diversity, makes results of the intercomparison more difficult to interpret. The Multi-GAS instrument showed large fluctuations in the CO_2/SO_2 ratio over shorter time scales, while the FTIR showed a more constant ratio. This reflects the fact that the plume composition varied over its cross-section. Over time scales of several hours, the Multi-Gas ratio stabilized at a CO_2/SO_2 ratio 13–25 % lower than the FTIR average.

Our results show that for well-mixed plumes and single-vent emissions, the Multi-GAS instrument gives representative values of the CO_2/SO_2 ratio. For more complex cases, the method can still give representative results, but additional care should be taken in locating the instrument in the core of the plume and farther downwind from the vents (where the plume will be more mixed). Long-term deployments might also be required to obtain robust estimates of time-averaged CO_2/SO_2 ratios. Finally, this study demonstrates that CO_2/SO_2 ratios measured by the Multi-GAS instrument provide an acceptable representation of the bulk volcanic plumes' composition, and its combination with NOVAC instruments is a suitable strategy for measuring crateric CO_2 emissions at volcanoes with similar degassing styles. In the specific case of Turrialba and Telica, typical CO_2 emissions of 1,100 and 160 t day^{-1} are estimated, respectively, in the field studies reported here.

Acknowledgments This work was supported by the Swedish International Development Agency (SIDA), and the DECADE initiative in coordination with OVSICORI-UNA and INETER. The research leading to these results received funding from the European Research Council under the European Union's Seventh Framework Programme (FP7/2007/2013)/ERC grant agreement n1305377 (PI Aiuppa). We would like to thank the reviewers and the editor of this paper for their constructive comments. We thank the staff from OVSICORI and INETER for all their friendly support. Special thanks for the logistical assistance provided by the staff of Turrialba National Park and the civil defence of León.

References

Aiuppa A, Federico C, Giudice G, Gurrieri S (2005) Chemical mapping of a fumarolic field: La Fossa Crater, Vulcano Island (Aeolian Islands, Italy). Geophys Res Lett 32(13):1–4

Aiuppa A, Federico C, Giudice G, Gurrieri S, Liuzzo M, Shinohara H, Favarra R, Valenza M (2006) Rates of carbon dioxide plume degassing from Mount Etna volcano. J Geophys Res 111:B09207. doi:10.1029/2006JB004307

Aiuppa A, Moretti R, Federico C, Giudice G, Gurrieri S, Liuzzo M, Papale P, Shinohara H, Valenza M (2007) Forecasting Etna eruptions by real-time observation of volcanic gas composition. Geology 35(12):1115–1118

Aiuppa A, Federico C, Giudice G, Giuffrida G, Guida R, Gurrieri S, Liuzzo M, Moretti R, Papale P (2009) The 2007 eruption of Stromboli volcano: insights from real-time measurement of the volcanic gas plume CO_2/SO_2 ratio. J Volcanol Geotherm Res 182(3–4):221–230

Burton MR, Oppenheimer O, Horrocks LA, Francis PW (2000) Remote sensing of CO_2 and H_2O emission rates from Masaya volcano, Nicaragua. Geology 28(10):915–918

Burton M, Allard P, Mure F, La Spina A (2007) Magmatic gas composition reveals the source depth of slug-driven strombolian explosive activity. Science 317(5835):227–230. doi:10.1126/science.1141900

Burton MR, Caltabiano T, Murè F, Salerno G, Randazzo D (2009) SO2 flux from Stromboli during the 2007 eruption: results from the FLAME network and traverse measurements. J Volcanol Geotherm Res 182(3–4):214–220. doi:10.1016/j.jvolgeores.2008.11.025

Burton MR, Sawyer GM, Granieri D (2013) Deep carbon emissions from volcanoes. Rev Miner Geochem 75(1):323–354. doi:10.2138/rmg.2013.75.11

Campion R, Martinez-Cruz M, Lecocq T, Caudron C, Pacheco J, Pinardi G, Hermans C, Carn S, Bernard A (2012) Space- and

ground-based measurements of sulphur dioxide emissions from Turrialba Volcano (Costa Rica). Bull Volcanol 74(7):1757–1770. doi:10.1007/s00445-012-0631-z

Casadevall T, Rose W, Gerlach T, Greenland LP, Ewert J, Wunderman R, Symonds R (1983) Gas emissions and the eruptions of Mount St. Helens through 1982. Science 221(4618):1383–1385

Conde V, Bredemeyer S, Duarte E, Pacheco J, Miranda S, Galle B, Hansteen T (2013) SO_2 degassing from Turrialba Volcano linked to seismic signatures during the period 2008–2012. Int J Earth Sci (Geol Rundsch) :1–16. doi:10.1007/s00531-013-0958-5

Deming WE (1943) Statistical adjustment of data. Chapman and Hall Ltd, New York. Accessed from, http://nla.gov.au/nla.cat-vn1622338

Duffell HJ, Oppenheimer C, Pyle DM, Galle B, McGonigle AJS, Burton MR (2003) Changes in gas composition prior to a minor explosive eruption at Masaya volcano, Nicaragua. J Volcanol Geotherm Res 126(3–4):327–339. doi:10.1016/S0377-0273(03)00156-2

Edmonds M, Herd RA, Galle B, Oppenheimer CM (2003) Automated, high time resolution measurements of SO2 flux at Soufrière Hills Volcano, Montserrat. Bull Volcanol 65(8):578–586

Fischer TP, Burnard P, Marty B, Hilton DR, Füri E, Palhol F, Sharp ZD, Mangasini F (2009) Upper-mantle volatile chemistry at Oldoinyo Lengai volcano and the origin of carbonatites. Nature 459(7243):77–80

Galle B, Oppenheimer C, Geyer A, McGonigle AJS, Edmonds M, Horrocks L (2002) A miniaturised ultraviolet spectrometer for remote sensing of SO2 fluxes: a new tool for volcano surveillance. J Volcanol Geotherm Res 119(1–4):241–254

Galle B, Johansson M, Rivera C, Zhang Y, Kihlman M, Kern C, Lehmann T, Platt U, Arellano SR, Hidalgo S (2010) Network for Observation of Volcanic and Atmospheric Change (NOVAC)—a global network for volcanic gas monitoring: network layout and instrument description. J Geophys Res 115(D5):D05304. doi:10.1029/2009jd011823

Griffith DWT (1996) Synthetic calibration and quantitative analysis of gas-phase FT-IR spectra. Appl Spectrosc 50(1):59–70

Hazen RM, Schiffries CM (2013) Why deep carbon? Rev Miner Geochem 75(1):1–6. doi:10.2138/rmg.2013.75.1

Hilton DR, Fischer TP, Marty B (2002) Noble gases and volatile recycling at subduction zones. Rev Miner Geochem 47(1):319–370. doi:10.2138/rmg.2002.47.9

Hoff RM, Millan MM (1981) Remote SO2 mass flux measurements using COSPEC. J Air Pollut Control Assoc 31(4):381–384

Horrocks LA, Oppenheimer C, Burton MR, Duffell HJ, Davies NM, Martin NA, Bell W (2001) Open-path Fourier transform infrared spectroscopy of SO_2: an empirical error budget analysis, with implications for volcano monitoring. J Geophys Res: Atmos 106(D21):27647–27659. doi:10.1029/2001JD000343

IPCC (2007) Climate Change 2007—the physical science basis: working group I contribution to the fourth assessment report of the IPCC. Cambridge University Press

Johansson M (2009) Application of passive DOAS for studies of megacity air pollution and volcanic gas emissions. PhD thesis Chalmers University of Technology

Johansson M, Galle B, Zhang Y, Rivera C, Chen D, Wyser K (2009) The dual-beam mini-DOAS technique—measurements of volcanic gas emission, plume height and plume speed with a single instrument. Bull Volcanol 71(7):747–751. doi:10.1007/s00445-008-0260-8

Krystek M, Anton M (2008) A weighted total least-squares algorithm for fitting a straight line. Meas Sci Technol 19(7):079801

Martin RS, Sawyer GM, Spampinato L, Salerno GG, Ramirez C, Ilyinskaya E, Witt MLI, Mather TA, Watson IM, Phillips JC, Oppenheimer C (2010) A total volatile inventory for Masaya Volcano, Nicaragua. J Geophys Res: Solid Earth 115(B9):B09215. doi:10.1029/2010JB007480

Martini F, Tassi F, Vaselli O, Del Potro R, Martinez M, del Laat RV, Fernandez E (2010) Geophysical, geochemical and geodetical signals of reawakening at Turrialba volcano (Costa Rica) after almost 150 years of quiescence. J Volcanol Geotherm Res 198(3–4):416–432

Mather TA, Pyle DM, Tsanev VI, McGonigle AJS, Oppenheimer C, Allen AG (2006) A reassessment of current volcanic emissions from the Central American arc with specific examples from Nicaragua. J Volcanol Geotherm Res 149(3–4):297–311. doi:10.1016/j.jvolgeores.2005.07.021

Métrich N, Allard P, Aiuppa A, Bani P, Bertagnini A, Shinohara H, Parello F, Di Muro A, Garaebiti E, Belhadj O, Massare D (2011) Magma and volatile supply to post-collapse volcanism and block resurgence in Siwi caldera (Tanna Island, Vanuatu arc). J Petrol 52(6):1077–1105

Mori T, Burton M (2006) The SO_2 camera: a simple, fast and cheap method for ground-based imaging of SO_2 in volcanic plumes. Geophys Res Lett 33(24):L24804. doi:10.1029/2006GL027916

Novák Z, Přichystal A (2006) El área volcánica de Telica (Nicaragua) y sus peligros geológicos. In: Přichystal A (ed) Krystalinikum, Contributions to the geology and petrology of crystalline complexes, vol 31. Moravian Museum Brno, pp 47–66

Oppenheimer C, Francis P, Burton M, Maciejewski AJH, Boardman L (1998) Remote measurement of volcanic gases by Fourier transform infrared spectroscopy. Appl Phys B 67(4):505–515. doi:10.1007/s003400050536

OVSICORI-UNA (2012) Volcanic activity in Costa Rica

OVSICORI-UNA (2013) Estado de los volcanes de Costa Rica 2013—Resumen anual oficial

Pearson K (1901) LIII. On lines and planes of closest fit to systems of points in space. Philos Mag Ser 62(11):559–572. doi:10.1080/14786440109462720

Platt U, Stutz J (2008) Differential optical absorption spectroscopy (DOAS), principle and applications. Springer Verlag, Heidelberg. doi:10.1007/978-3-540-75776-4

Reagan M, Duarte E, Soto GJ, Fernández E (2006) The eruptive history of Turrialba volcano, Costa Rica, and potential hazards from future eruptions

Reed BC (1989) Linear least-squares fits with errors in both coordinates. Am J Phys 57(7):642–646. doi:10.1119/1.15963

Rodgers M, Roman DC, Geirsson H, LaFemina P, Muñoz A, Guzman C, Tenorio V (2013) Seismicity accompanying the 1999 eruptive episode at telica volcano, nicaragua. J Volcanol Geotherm Res 265:39–51. doi:10.1016/j.jvolgeores.2013.08.010

Rothman LS, Gordon IE, Barbe A, Benner DC, Bernath PF, Birk M, Boudon V, Brown LR, Campargue A, Champion JP, Chance K, Coudert LH, Dana V, Devi VM, Fally S, Flaud JM, Gamache RR, Goldman A, Jacquemart D, Kleiner I, Lacome N, Lafferty WJ, Mandin JY, Massie ST, Mikhailenko SN, Miller CE, Moazzen-Ahmadi N, Naumenko OV, Nikitin AV, Orphal J, Perevalov VI, Perrin A, Predoi-Cross A, Rinsland CP, Rotger M, Šimečková M, Smith MAH, Sung K, Tashkun SA, Tennyson J, Toth RA, Vandaele AC, Vander Auwera J (2009) The HITRAN 2008 molecular spectroscopic database. J Quant Spectrosc Radiat Transfer 110(9–10):533–572

Sawyer GM, Salerno GG, Le Blond JS, Martin RS, Spampinato L, Roberts TJ, Mather TA, Witt MLI, Tsanev VI, Oppenheimer C (2011) Gas and aerosol emissions from Villarrica volcano, Chile. J Volcanol Geotherm Res 203(1–2):62–75. doi:10.1016/j.jvolgeores.2011.04.003

Shinohara H (2005) A new technique to estimate volcanic gas composition: plume measurements with a portable multi-sensor system. J Volcanol Geotherm Res 143(4):319–333. doi:10.1016/j.jvolgeores.2004.12.004

Smith TEL, Wooster MJ, Tattaris M, Griffith DWT (2011) Absolute accuracy and sensitivity analysis of OP-FTIR retrievals of CO_2, CH4 and CO over concentrations representative of "clean air" and "polluted plumes". Atmos Meas Tech 4(1):97–116. doi:10.5194/amt-4-97-2011

Smithsonian-Institution (2011) http://www.volcano.si.edu/volcano.cfm?vn=344040&bgvn=1&rnum=region14&snum=nicarag&wvol=telica&tab=1

Smithsonian-Institution (2013) http://www.volcano.si.edu/volcano.cfm?vnum=1404-04=

Solomon S, Plattner GK, Knutti R, Friedlingstein P (2009) Irreversible climate change due to carbon dioxide emissions. Proc Natl Acad Sci USA 106(6):1704–1709. doi:10.1073/pnas.0812721106

Symonds R, Rose WI, Bluth GJS, Gerlach TM (1994) Volcanic-gas studies; methods, results, and applications. Rev Miner Geochem 30(1):1–66

Tamburello G (2013) https://sites.google.com/site/giancarlotamburello/volcanology/ratiocalc

Vaselli O, Tassi F, Duarte E, Fernandez E, Poreda RJ, Huertas AD (2010) Evolution of fluid geochemistry at the Turrialba volcano (Costa Rica) from 1998 to 2008. Bull Volcanol 72(4):397–410

York D, Evensen NM, Martínez ML, De Basabe Delgado J (2004) Unified equations for the slope, intercept, and standard errors of the best straight line. Am J Phys 72(3):367–375. doi:10.1119/1.1632486

APPENDICE B

Earth and Planetary Science Letters 407 (2014) 134–147

Contents lists available at ScienceDirect

Earth and Planetary Science Letters

www.elsevier.com/locate/epsl

Gas measurements from the Costa Rica–Nicaragua volcanic segment suggest possible along-arc variations in volcanic gas chemistry

A. Aiuppa [a,b,*], P. Robidoux [a], G. Tamburello [a], V. Conde [c], B. Galle [c], G. Avard [d], E. Bagnato [a], J.M. De Moor [d], M. Martínez [d], A. Muñóz [e]

[a] Dipartimento DiSTeM, Università di Palermo, Italy
[b] Istituto Nazionale di Geofisica e Vulcanologia, Sezione di Palermo, Italy
[c] Department of Earth and Space Sciences, Chalmers University of Technology, Sweden
[d] Observatorio Vulcanológico y Sismológico de Costa Rica (OVSICORI-UNA), Costa Rica
[e] Instituto Nicaragüense de Estudios Territoriales (INETER), Nicaragua

ARTICLE INFO

Article history:
Received 10 May 2014
Received in revised form 23 September 2014
Accepted 23 September 2014
Available online 13 October 2014
Editor: B. Marty

Keywords:
volcanic gases
CO_2 flux
arc volcanism
CAVA
Costa Rica
Nicaragua

ABSTRACT

Obtaining accurate estimates of the CO_2 output from arc volcanism requires a precise understanding of the potential along-arc variations in volcanic gas chemistry, and ultimately of the magmatic gas signature of each individual arc segment. In an attempt to more fully constrain the magmatic gas signature of the Central America Volcanic Arc (CAVA), we present here the results of a volcanic gas survey performed during March and April 2013 at five degassing volcanoes within the Costa Rica–Nicaragua volcanic segment (CNVS). Observations of the volcanic gas plume made with a multicomponent gas analyzer system (Multi-GAS) have allowed characterization of the CO_2/SO_2-ratio signature of the plumes at Poás (0.30 ± 0.06, mean $\pm$ SD), Rincón de la Vieja (27.0 ± 15.3), and Turrialba (2.2 ± 0.8) in Costa Rica, and at Telica (3.0 ± 0.9) and San Cristóbal (4.2 ± 1.3) in Nicaragua (all ratios on molar basis). By scaling these plume compositions to simultaneously measured SO_2 fluxes, we estimate that the CO_2 outputs at CNVS volcanoes range from low (25.5 ± 11.0 tons/day at Poás) to moderate (918 to 1270 tons/day at Turrialba). These results add a new information to the still fragmentary volcanic CO_2 output data set, and allow estimating the total CO_2 output from the CNVS at 2835 ± 1364 tons/day. Our novel results, with previously available information about gas emissions in Central America, are suggestive of distinct volcanic gas CO_2/S_T ($= SO_2 + H_2S$)-ratio signature for magmatic volatiles in Nicaragua ($\sim$3) relative to Costa Rica ($\sim$0.5–1.0). We also provide additional evidence for the earlier theory relating the CO_2-richer signature of Nicaragua volcanism to increased contributions from slab-derived fluids, relative to more-MORB-like volcanism in Costa Rica. The sizeable along-arc variations in magmatic gas chemistry that the present study has suggested indicate that additional gas observations are urgently needed to more-precisely confine the volcanic CO_2 from the CAVA, and from global arc volcanism.

© 2014 Elsevier B.V. All rights reserved.

1. Introduction

Characterizing the volcanic gas outputs along active volcanic-arc regions is crucial to quantifying the recycling of volatiles at subducting slabs and its consequences for arc magmatism (Hilton et al., 2002). The long-term (geological) volcanic-arc CO_2 budget (Wallace, 2005) is particularly critical to better constraining the relative C contributions from the slab, the mantle wedge, and the crust, and for predicting how arc degassing influences the atmospheric CO_2 budget and climate models (Berner and Lasaga, 1989).

In recent years a mass balance approach has been used to extensively investigate exchanges of volatiles at subduction zones (Fischer et al., 2002; Hilton et al., 2002). However, the global subaerial volcanic CO_2 flux, which is dominated by arc volcanism (Marty and Tolstikhin, 1998), remains poorly constrained, with current estimates ranging widely, from 65 to 540 Mt/yr (see review by Burton et al., 2013). CO_2 budgets for individual arc segments are also generally poorly understood (Hilton et al., 2002). In addition to estimates of the SO_2 output being incomplete and/or inaccurate, a major issue in deriving the CO_2 outputs from individual arcs is assigning a "representative" CO_2/SO_2 ratio to them. This remains problematic due to the limited data set of high-temperature volcanic gases that is available (Fischer, 2008), and the potentially

* Corresponding author at: Dipartimento DiSTeM, Università di Palermo, Italy.
E-mail address: alessandro.aiuppa@unipa.it (A. Aiuppa).

http://dx.doi.org/10.1016/j.epsl.2014.09.041
0012-821X/© 2014 Elsevier B.V. All rights reserved.

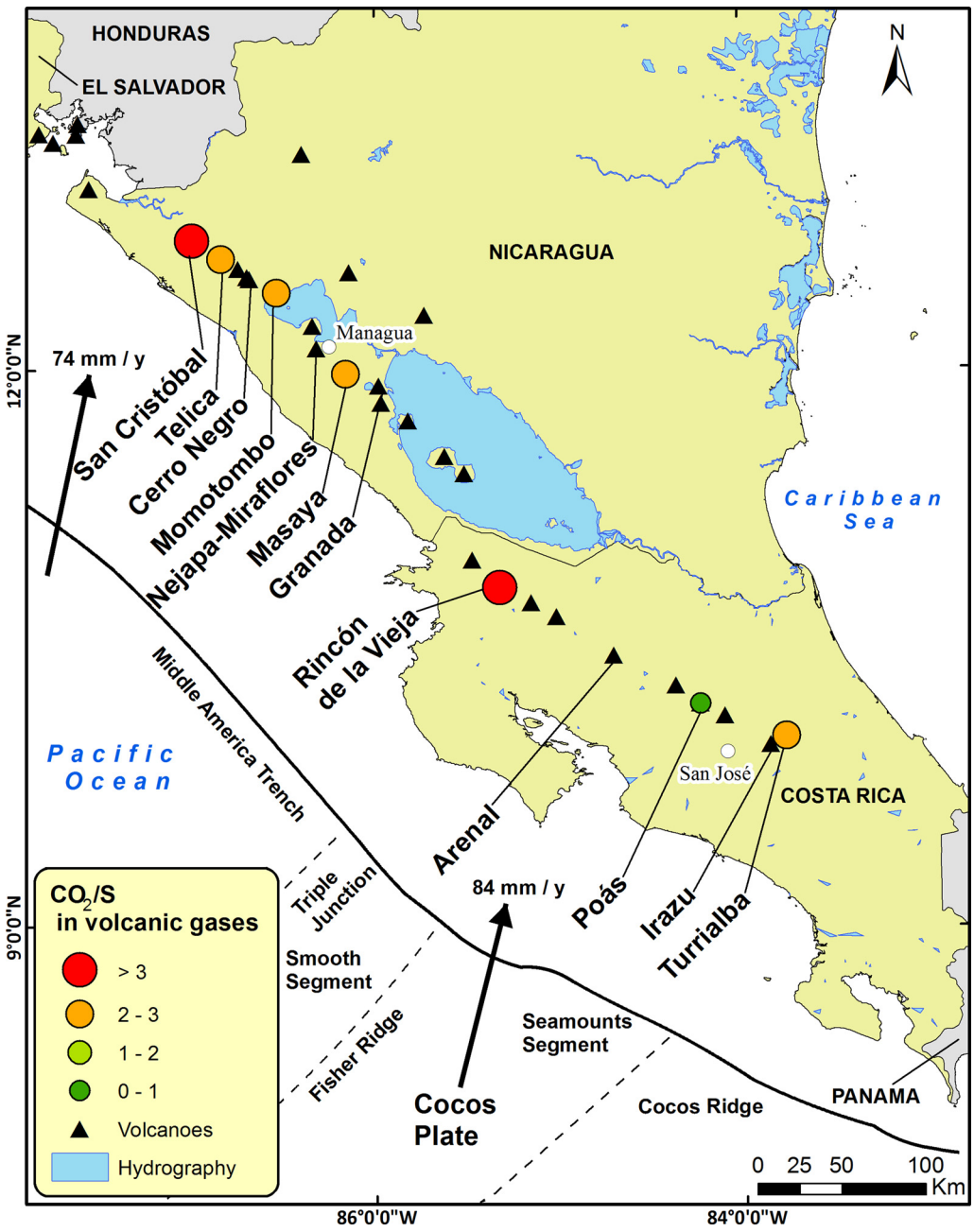

Fig. 1. Map of the subduction zone in Nicaragua and Costa Rica. Black arrows indicate the direction of motion of the Cocos Plate and the convergence velocities relative to the Caribbean Plate (in millimeters per year) after DeMets (2001). Plate segments and trench structures are interpreted from the bathymetry imagery in von Huene et al. (2000). The volcanic gas molar CO_2/S_T ratios indicated in the figure are from the present study except for Momotombo (Menyailov et al., 1986) and Masaya (Martin et al., 2010). CVS and NVS identify the Costa Rica and Nicaragua volcanic segments, respectively.

large variations in gas chemistry within a given arc segment, between different segments, and at individual volcanoes.

Herein we present experimental evidence for sizeable variations in the gas composition along the Costa Rica–Nicaragua volcanic segment (CNVS) of the CAVA (Fig. 1). Previous work in the region (Shaw et al., 2003; Zimmer et al., 2004; Elkins et al., 2006; Fischer et al., 2007) has concentrated on the chemical and isotopic systematics of poorly reactive (CO_2) or inert (N_2 and He) gases, with the majority of samples being low temperature. We concentrate here instead on determining the CO_2/SO_2 and H_2O/CO_2 ratios in the large, high-temperature emissions that generally dominate – and are therefore more appropriate to confine – the volcanic-arc CO_2 output (Shinohara, 2013). The CO_2/SO_2 signature of CAVA volcanism has been assigned constant values in previous CO_2 regional inventories (Hilton et al., 2002; Mather et al., 2006; Fischer, 2008), whereas the structural and magmatological complexities of the arc (Carr et al., 2003) make the existence of substantial along-arc variations highly plausible.

The results reported herein were obtained in the course of a gas survey conducted during March and April 2013 with the aim of characterizing the chemistry of the volcanic gas plume at five strong degassing volcanoes: Turrialba, Poás, and Rincón de la Vieja in Costa Rica, and San Cristóbal and Telica in Nicaragua. We combine our newly acquired data set with previous gas information in the region (i) to better confine the CO_2/SO_2 signature(s) of this arc segment, (ii) to derive a volcanic CO_2 budget for the region, and (iii) to infer new constraints on the (mantle vs. slab) origin of arc CO_2.

2. The Costa Rica–Nicaragua volcanic arc segment

Costa Rica and Nicaragua host an exceptionally well-studied arc segment (Fig. 1), which forms part of the CAVA (Fig. 1). The well-documented structural (Protti et al., 1995; MacKenzie et al., 2008) and geochemical (Carr, 1984; Carr et al., 1990, 2003; Patino et al., 2000; Sadofsky et al., 2008) variations that occur along the CNVS make it particularly suitable for investigating along-arc changes in volcanic gas chemistry. The entire arc segment is related to subduction (at a convergence rate of ~90 mm/yr; Protti et al., 1995) of the Cocos Plate beneath the Caribbean Plate (Fig. 1). However, the subduction angle of the slab is far steeper in Nicaragua (up to 84°) than in central Costa Rica (60°), which reflects different ages and thermal regimes of subducted oceanic crust (Protti et al., 1995). The steep subduction in Nicaragua and the extensive serpentinization of the subducted mantle are thought to allow a large influx of recycled slab fluids and a high degree of partial melting of a relatively small-volume mantle wedge (Carr et al., 1990; Abers et al., 2003). This would ultimately result in the influence of the slab on magma petrogenesis being larger in Nicaragua (e.g., the highest Ba/La, B/La, and $^{10}Be/^{9}Be$ ratios in CAVA lavas; Carr et al., 1990). In contrast, relatively low subduction fluxes of hemipelagic sediments and a dominant contribution of the mantle wedge to petrogenesis have been postulated for Costa Rica (Eiler et al., 2005). Underplating of hemipelagic sediment to the over-riding Caribbean plate has been invoked as one of the casual factors (Leeman et al., 1994).

A larger contribution of sedimentary slab fluids in Nicaragua relative to Costa Rica is also supported by along-arc geochemical variations in the compositions of volatiles (see review by Fischer et al., 2007). These studies have for instance found that the ratio of slab-derived C (from both limestones and organic sediments) to mantle-derived C is substantially greater in Nicaragua than in Costa Rica (Shaw et al., 2003; De Leeuw et al., 2007). The gases sampled in these studies were dominated by relatively low T emissions, thus, investigating the existence of such trends in volatiles also in high-temperature magmatic gases was one of the central objectives of the present study.

3. Methodology

We investigated the volcanic gas plumes of Turrialba, Poás, and Rincón de la Vieja (all in Costa Rica) and of San Cristóbal and Telica (both in Nicaragua) (Fig. 1) by using a custom-made multicomponent gas analyzer system (called Multi-GAS henceforth). The Multi-GAS, whose first volcano applications emerged in the mid-2000s (Aiuppa et al., 2005; Shinohara, 2005), is a compact unit constructed by assembling different commercial Infra-Red (for CO_2 and H_2O) and electrochemical (for SO_2 and H_2S) gas sensors. The same sensor assemblage as in Aiuppa et al. (2009, 2010, 2012) was used in the present study. We employed two distinct types of Multi-GAS. At Turrialba, Poás, San Cristóbal, and Telica, we temporarily deployed a fixed, fully autonomous version of the Multi-GAS, similar to the systems used in other permanent networks (e.g., Stromboli; Aiuppa et al., 2009). The fixed Multi-GAS, powered by a 12-V lead-acid battery connected to a photovoltaic module, ran unattended at Turrialba from March 12 to March 19, 2013; at Telica from March 22 to April 8, 2013; at San Cristóbal from April 11 to 16, 2013; and at Poás during April 16–18, 2013. The Turrialba and Telica data have been presented in Conde et al. (in press). In that paper, we focused on a comparison between FTIR and Multi-GAS results, and on the implications of combined DOAS–Multi-GAS data sets to quantification of the CO_2 output. We here discuss the observations of Conde et al. (in press) in a broader context of volcanic gas origin and variation along CAVA. At all volcanoes the fixed Multi-GAS was deployed at a location within the active crater(s) area, from tens to a few hundreds of meters from the main degassing vent(s), which ensured frequent fumigation by the plume (Fig. 2). The instrument was programmed to measure the concentrations of various gases (H_2O, CO_2, SO_2, and H_2S) in the plume at a sampling rate of 0.1 Hz, in cycles lasting for 30 min (four to eight daily cycles were performed, depending on power availability). Given the difficulty of accessing Rincón de la Vieja, a lighter (<2 kg) portable Multi-GAS (powered by an internal lithium battery) was used for a rapid survey performed on April 8, 2013, at which about 3 h of Multi-GAS data were acquired at 0.5 Hz. The same unit was used to repeat additional measurements at Turrialba during April 2–4, 2013. Table 1 summarizes Multi-GAS results.

The SO_2 output was measured at each volcano except Rincón de la Vieja (Table 2). SO_2 column columns were retrieved by applying differential optical absorption spectroscopy (DOAS) to spectra which source of radiation was ultraviolet (UV)-scattered sunlight (Platt and Stutz, 2008). At San Cristóbal and Turrialba, we used UV scanning spectrometers part of the NOVAC network (Galle et al., 2010); while at Telica a temporal installation of NOVAC instruments was set up (Conde et al., in press). At Poás the SO_2 flux was measured by traversing underneath the plume with a vertically pointed UV spectrometer.

4. Volcanic activity

The five volcanoes were all degassing strongly to moderately during our observations, but no eruptive activity was observed. Our observations are therefore representative of periods of "regular" degassing activity for all the volcanoes studied. Turrialba (Fig. 2a) was degassing intensively in March and April 2013 from two active vents inside the west crater (2010 vent and 2012 vent), which formed during the January 5, 2010 and January 12, 2012 vent-opening eruptions, respectively (OVSICORI-UNA, 2012). The vent temperatures ranged from 400 to 590 °C (at Vent 2010) up to 800 °C (at Vent 2012) (Table 1; data from OVSICORI-UNA, 2013). The 2011 vent (Fig. 2) was degassing more moderately during our measurements. Poás (Fig. 2b) was showing intense degassing in mid-April 2013 from a fumarole field between the shore of the crater lake and the dome (on the top of which the Multi-GAS was installed; Fig. 2b). The fumaroles of the dome, which had started a new heating cycle in early 2013, had a temperature of ~500 °C on April 16 (OVSICORI-UNA, 2013), and a total SO_2 output of 124 ± 33 tons was measured on the same day (average and SD of 8 walking traverses under the fumarolic plume). Given the high temperature of the dome during our sampling, and our measurement location right ontop of the dome itself, we can rule out any major influence from the lake. During our visit on April 6, 2013, Rincón de la Vieja (Fig. 2c) hosted a hyperacidic (pH ~ 0.1), warm (~36 °C), intracrateric volcanic lake, and several fumaroles at ~130 °C (temperature measured with IR camera). Both types of emission contributed to the bulk plume, which was measured by the Multi-GAS from the northern, outer rim of the summit crater. Telica (Fig. 2d) is a restless volcano in western Nicaragua, where persistent degassing is frequently interrupted by small explosions (VEI 1–3). Few studies have investigated plume gases at Telica (Witt et al., 2008; Conde et al., in press). The volcano has exhibited passive degassing during 2011–2014 at an average rate of 140 ± 100 tons/day SO_2 (Geirsson et al., 2014). Incandescence was observed during our survey in a major vent (with a peak temperature of 507 °C) located ~120 m deep inside the crater (INETER, 2013). San Cristóbal (Fig. 2e) has recently exhibited irregular degassing in response to eruptive activity (2 eruptive events/year on average during the past few years; INETER, 2013). The SO_2 flux (measured by NOVAC instruments) ranged from 2000 to 4000 tons/day at the time of the VEI 2 explosion on December 2, 2012. Immediately after this event

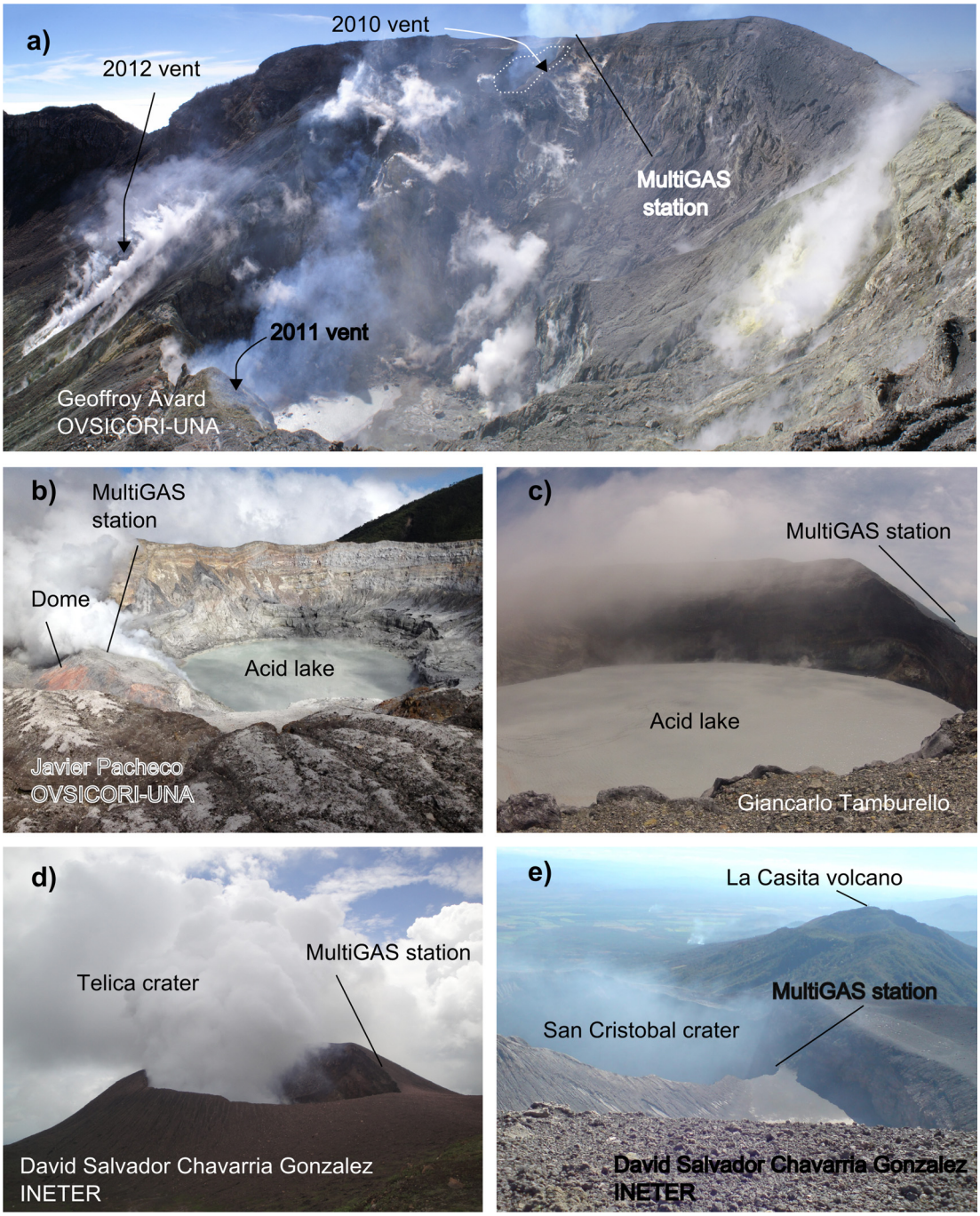

Fig. 2. Degassing activities at the summit craters of the five investigated volcanoes, and the positions of the Multi-GAS instrument: (a) Turrialba, (b) Poás, (c) Rincón de la Vieja, (d) Telica, and (e) San Cristóbal. The credits are shown in the figure.

Table 1
Time-averaged compositions of volcanic gas plumes at the five investigated volcanoes. The quoted ratios (all molar) are arithmetic mean±SD values for the data reported in Fig. 4 (except for Rincón de la Vieja, where only one acquisition was available). Vent temperatures were measured using portable IR cameras, and should be viewed as the minimum temperatures of the vents feeding the plumes (see Fig. 2).

Country	Date	Volcano	Peak vent temperature (°C)	CO_2/SO_2	H_2O/CO_2	SO_2/H_2S
Costa Rica	March 12–19, 2013	Turrialba	590 (vent 2010) to ~790 (vent 2012)[a]	2.2 ± 0.8	20.4	n.d.
Costa Rica	April 2–4, 2013	Turrialba	~500 (vent 2010) to ~800 (vent 2012)[a]	2.0 ± 0.3	32.0	n.d.
Costa Rica	April 8, 2013	Rincón de la Vieja	~130[a]	27.0 ± 15.3*	201	1.10 ± 0.15
Costa Rica	April 16–18, 2013	Poás	~500[a]	0.30 ± 0.06	175	9.9 ± 2.7
Nicaragua	March 27 to April 4, 2013	Telica	~507[b]	3.0 ± 0.9	21.7	n.d.
Nicaragua	April 11–16, 2013	San Cristóbal	500[b]	4.2 ± 1.3	22.0	n.d.

Data source: [a] OVSICORI-UNA (2013); [b] INETER (2013).
* This converts into a CO_2/S_T ratio of 14.2 ± 9.0, using a SO_2/H_2S ratio of 1.10 ± 0.15.

Table 2
SO_2 fluxes (measured by UV spectroscopy) and calculated CO_2 fluxes (from multiplication of SO_2 fluxes and time-averaged CO_2/SO_2 ratios). The same table also reports literature data from Momotombo and Masaya volcanoes, which we use for inferring total outputs from Costa Rica (CVS), Nicaragua (NVS) and the entire Costa Rica–Nicaragua volcanic arc segment (CNVS). See text for discussion.

Country	Date	Volcano	CO_2/SO_2	SO_2 flux (tons/day)	CO_2 flux (tons/day)
Costa Rica	March 12–19, 2013	Turrialba	[a]	840 ± 120[b]	1270 ± 700
Costa Rica	April 2–4, 2013	Turrialba	[a]	668 ± 308[c]	918 ± 560
Costa Rica	March–April 2013	Turrialba, mean	[a]	754 ± 214[b]	1094 ± 631
Costa Rica	April 16–18, 2013	Poás	[a]	124 ± 30[b]	25.5 ± 11.0
CVS		**Total output**		**878 ± 244**	**1120 ± 642**
Nicaragua	March 27 to April 4, 2013	Telica	[a]	64 ± 34[c]	132 ± 109
Nicaragua	April 11–16, 2013	San Cristóbal	[a]	181 ± 35[b]	523 ± 263
Nicaragua	1982–1985	Momotombo	2.6[d]	73[e]	130
Nicaragua	1998–2009	Masaya	2.6 ± 0.7[f]	690 ± 182[f]	930 ± 350[f]
NVS		**Total output**		**1008 ± 251**	**1715 ± 722**
CNVS		**Total output**		**1886 ± 495**	**2835 ± 1364**

Data source: [a] From Table 1 (this study); [b] This study; [c] This study and Conde et al. (in press); [d] Average of gas compositions reported by Menyailov et al. (1986); [e] From Andres and Kasgnoc (1998); [f] Time-averaged (1998–2009) flux and composition from Martin et al. (2010).

the SO_2 flux dropped to approximately 1000 tons/day, and by April 2013 it had decreased even further, to 181 ± 35 tons/day.

5. Results

The Multi-GAS-derived concentration data were post-processed to calculate the ratios of various volatiles using the procedure described by Aiuppa et al. (2006, 2010). Fig. 3a–e are scatter plots of CO_2 vs. SO_2 mixing ratios for the 5 explored volcanoes. We use raw data for SO_2 and background-corrected mixing ratios for CO_2. The latter were obtained from raw data by subtracting ambient air mixing ratios that were determined in "blank" sites upwind of the vents.

CO_2 vs. SO_2 compositions for the entire measurement intervals (open symbols in Figs. 3a–d) exhibited significant scatter at each volcano, implying substantial CO_2/SO_2 ratio variations over timescales of hours/days. Subsets of data acquired during shorter intervals, of 240–480 s each (examples of which are given by the populations of filled data-points in Figs. 3a–d), showed more restricted compositional ranges, instead. We therefore calculated the slopes of the best-fit regression lines in each of these subintervals (see examples in Fig. 3) to obtain the time-averaged (temporal windows of 240–480 s) CO_2/SO_2 ratios. No ratio was calculated during sub-intervals when there was excessive dilution of volcanic gases by atmospheric gases (e.g., for SO_2 mixing ratios <4 ppmv in (a) to (d)), or when a low correlation coefficient ($R^2 < 0.7$) was obtained. The procedure was optimized and automated by using the Ratiocalc software (https://sites.google.com/site/giancarlotamburello/volcanology/ratiocalc), which allowed to scan the entire data set and create sequences of scatter plots for distinct subintervals.

The so-obtained time series of CO_2/SO_2 ratios are shown in Fig. 4 for the volcanoes where the fixed Multi-GAS was deployed. At Turrialba (Fig. 4a) we obtained plume CO_2/SO_2 ratios ranging from 0.7 to 4.4 (all ratios quoted here and below are on a molar basis). Following Conde et al. (in press), we attribute this range of bulk plume compositions to the involvement of multiple, compositionally distinct gas sources. Using open-path FTIR, Conde et al. (in press) demonstrated that the level of CO_2 was lower at Vent 2012 ($CO_2/SO_2 \sim 1$) than at Vent 2010 ($CO_2/SO_2 \sim 3$). The majority of the 'bulk plume' Multi-GAS data are comprised between these end-member CO_2/SO_2 ratios. By taking an arithmetic mean of the data set of Fig. 4a, we infer that the overall CO_2/SO_2 ratio for Turrialba was 2.2 ± 0.8 (mean±SD) during March 2013. A slightly lower ratio was observed in early April (2.0 ± 0.3) (Table 1).

The CO_2/SO_2 ratios observed at Telica (3.0 ± 0.9; Fig. 4b) and San Cristóbal (4.2 ± 1.3; Fig. 4c) spread toward CO_2-richer compositions relative to those observed at Turrialba (Table 1). In contrast, a stable, C-poor composition (with a CO_2/SO_2 ratio of 0.30 ± 0.06) was captured by the Multi-GAS at Poás (Figs. 3d and 4d). Finally, the most-extreme CO_2/SO_2 ratios (27.0) in our data set were obtained at Rincón de la Vieja (Table 1 and Fig. 3e), where a very dilute plume ($SO_2 < 2$ ppm) was only detected (leading to smaller correlation – $R^2 = 0.6$ – and larger errors: ±15).

The plume SO_2/H_2S and H_2O/CO_2 ratios (Table 1) were determined using a similar procedure. H_2S was only detected at Poás and Rincón de la Vieja, which allowed for the SO_2/H_2S ratios to be quantified as 9.9 ± 2.7 and 1.10 ± 0.15, respectively. The derived CO_2/S_T ratio ($S_T = SO_2 + H_2S$) at Rincón de la Vieja was therefore 14.2 ± 9.0. Our inferred H_2O/CO_2 ratios for the plume varied over a restricted range (20.4–22.0) at Turrialba, Telica, and San Cristóbal (Table 1). In contrast, more-hydrous compositions (with H_2O/CO_2 ratios of 175–201) were obtained at Poás and Rincón de la Vieja, suggesting possible steam contribution from the active crater lakes.

The SO_2 flux from Turrialba, measured using scanning DOAS spectrometers of the local NOVAC network, was 840 ± 120 tons/day (mean ± SD) during March 12–19 (Table 2), in line with results of previous studies (Campion et al., 2012; Conde et al., 2013, in press). Our inferred SO_2 output from Poás (124 ± 30 tons/day) in 2013 was a factor ~15 larger than measured in 2001 (Zimmer et al., 2004), matching the increasingly active behavior of the volcano since early 2013. The SO_2 outputs from Telica and San Cristóbal averaged at 64 ± 34 and 181 ± 35 tons/day (Table 2).

6. Discussion

6.1. Identification of magmatic fingerprint for the CNVS

The compositional features of magmatic gases in the CNVS have been studied from direct sampling of fumaroles (Menyailov et al., 1986; Rowe et al., 1992; Zimmer et al., 2004; Elkins et al., 2006; Fischer et al., 2007) or via Fourier-transform infrared (IR; FTIR) spectroscopy (e.g., Masaya Volcano; Burton et al., 2000; Martin et al., 2010). The CO_2/S_T composition of these CNVS gases is reported in Fig. 5a, which includes both hot- and low-temperature crater fumaroles.

Low-temperature (<100 °C) fumarolic gases are a source of key information on inert (Zimmer et al., 2004; Elkins et al., 2006) and/or poorly reactive (e.g., CO_2) (Shaw et al., 2003) gases, but their deep CO_2/S_T magmatic fingerprint may in some cases be obscured by selective scrubbing of water-soluble S (Symonds et al., 2001): this is reflected by the high CO_2/S_T ratios (≫1000) in

some of the low-T crater gas manifestations (Fig. 5a). The Turrialba summit fumaroles of Vaselli et al. (2010) for example, being thought by those authors to sit at the hydrothermal–magmatic transition (temperatures of 86–282 °C), still show a large range of CO_2/S_T ratios (1.5–3803), particularly for the low-temperature samples (Fig. 5a). The same interactions of magmatic gases with lake and groundwater systems probably also explain the CO_2-rich signature of our Rincón de la Vieja gas (Table 1).

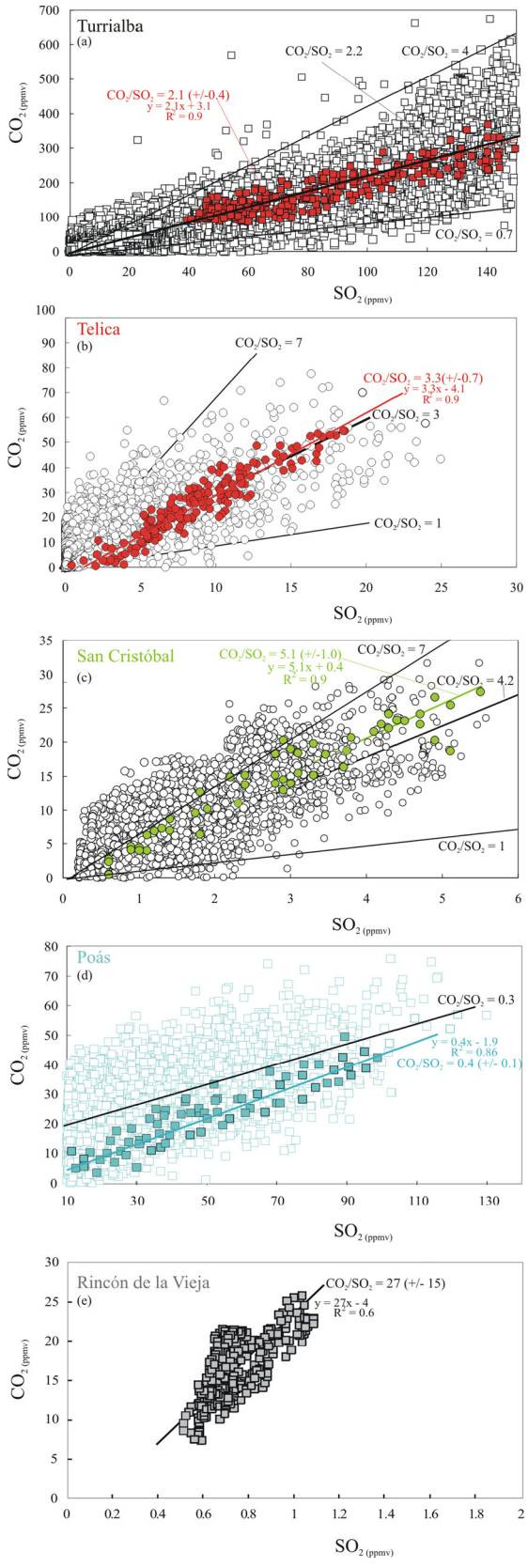

Our reported compositions (Table 1) show a restricted range of (relatively low) CO_2/S_T ratios (0.3–4.2; Fig. 5a). Also, given the relatively high emission temperatures of the gas manifestations, we consider that our gas composition was only marginally affected by secondary scrubbing processes. One possible exception is San Cristóbal, where a temperature of only 105 °C was reported during April 2013 (INETER, 2013); however, these observations were limited by poor visibility inside the crater. The persistence of perceptible sound irradiating from the crater (INETER, 2013), the lack of H_2S in the plume, and the reported temperatures being >500 °C only a few months previously support high-temperature, open-vent degassing activity during April 2013, and a minor effect of gas scrubbing processes.

Fig. 5 is also suggestive for that high-temperature gas samples from Costa Rica and Nicaragua (both our data and those of previous studies) plot along two distinct compositional domains. In Fig. 5b, which includes the subset of ≥185 °C gases, the temperature dependences of CO_2/S_T ratios from Nicaraguan and Costa Rican volcanic gas are shown by equations, along with their relative lower and upper 50% prediction bounds. The best-fit regression lines and their confidence intervals give rise to two distinct (and nearly parallel) compositional arrays. This suggests that, apart from some very minor overlap (see dashed area in Fig. 5b), the distinction between the two data clusters is statistically significant at 50% confidence level. The two data clusters remain distinct also if a higher cut off temperature (500 °C) is used to focus on 'truly magmatic' gases (Fig. 5c), which typically exhibit no temperature dependence. These trends converge at high temperatures to CO_2/S_T ratios of ∼3 and 0.5–1.0 for Nicaragua and Costa Rica, respectively, and are therefore suggestive of a distinct, CO_2-richer magmatic gas signature in Nicaragua relative to Costa Rica (Fig. 6a).

We caution that, given the paucity of data available and the (minor) data overlap in Fig. 5, we cannot entirely rule out coalescence of the fields as more data becomes available. To obtain more high-temperature gas information, especially in Costa Rica, clearly remains to be prioritized by future gas studies. We still observe that diffuse soil CO_2 degassing, which contributes to only 8% (Poás) to 16% (Turrialba) of crater plume emissions (De Moor J.M., pers. data), cannot compensate against the more C-poor gas signature in Costa Rica (relative to Nicaragua). We additionally argue that the melt inclusion (MI) record of the contents of volatiles in CNVS magmas (Fig. 6b, c) is well consistent with the volcanic gas information.

Fig. 3. Scatter plots of CO_2 versus SO_2 mixing ratios (in ppmv) for the five volcanoes investigated. CO_2 mixing ratios are after subtraction of background-air mixing ratios. In panels (a) to (d), we show with "open symbols" the complete data set of simultaneous CO_2–SO_2 detections collected during the entire Multi-GAS exposure period (we do not show results for measurement intervals with no plume). In each plot, the filled symbols demonstrate an example of the procedure used to calculate the CO_2/SO_2 (molar) ratio (shown in Fig. 4): a specific sub-subset of data (temporal window of 240–480 s) is selected, and the corresponding averaged CO_2/SO_2 ratio in that temporal interval is calculated from the slope of the best-fit regression line (color lines in panels (a) to (d); the same panels show equation of the regression lines, the correlation coefficients (R^2) and the errors of the CO_2/SO_2 ratio for the displayed sub-sets of data). The procedure was extended to the entire data set (using the software ratiocalc), but ratios are only displayed (in Fig. 4) for specific temporal intervals with high regression coefficients ($R^2 > 0.7$). The plots also show, for each volcano, the mean CO_2/SO_2 ratio (thick black line; arithmetic mean of the ratios displayed in Fig. 4a–d) and the minimum–maximum ratios obtained (thin solid lines; minimum and maximum ratios in Fig. 4a–d). For Rincón de la Vieja, the grey symbols refer to the entire data set acquired (regression line – color line – correlation coefficients (R^2) and errors of the CO_2/SO_2 ratio are also displayed).

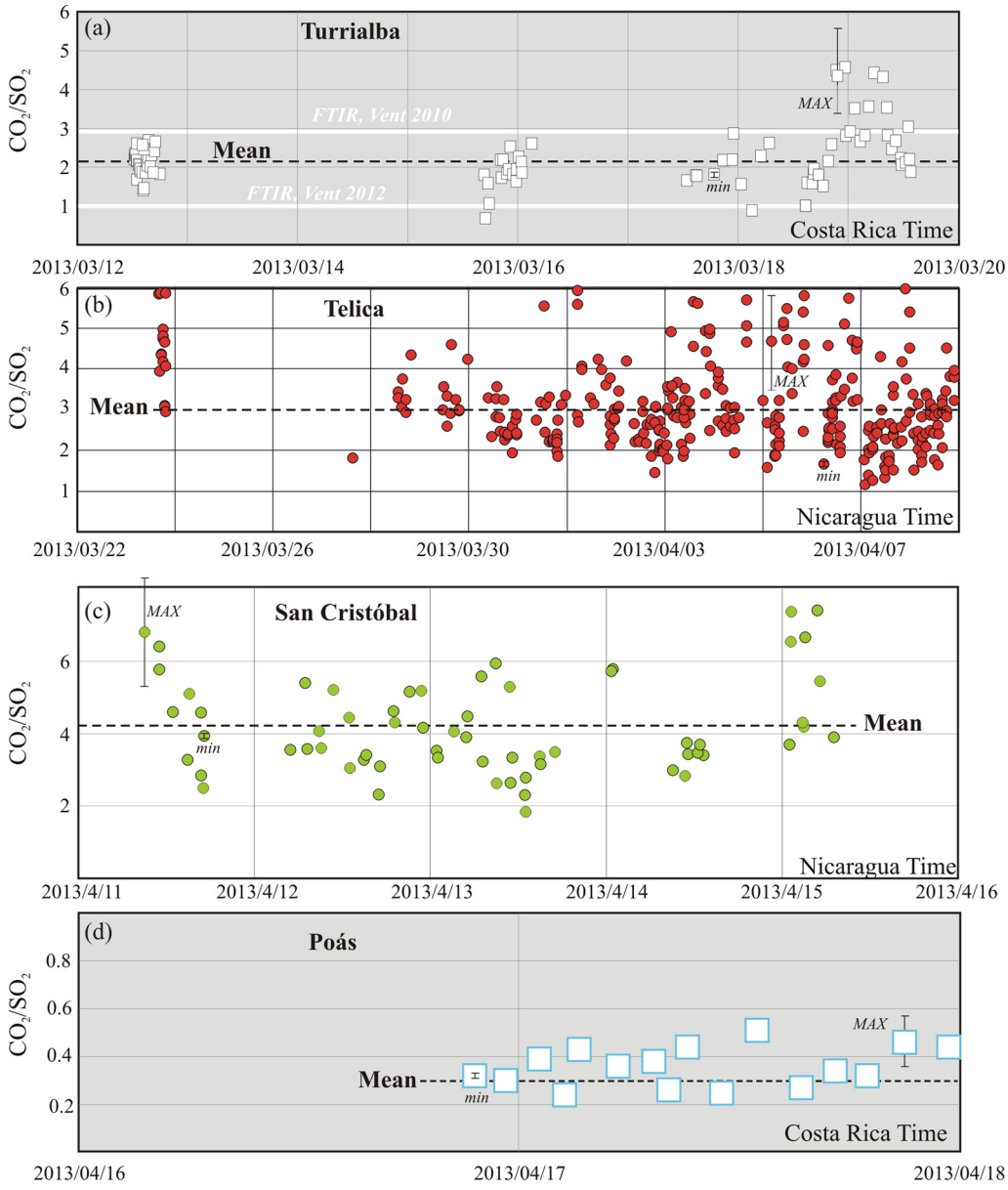

Fig. 4. Time series of the (molar) CO_2/SO_2 ratios recorded at the four volcanoes where the fully autonomous Multi-GAS was temporarily deployed. In each panel, each single data-point represents the time-averaged ratio obtained from sub-sets of data acquired within sub-intervals of 240–480 s (see examples of procedure for calculating the ratios illustrated in Fig. 3). The errors associated to each ratio are always lower $\leq$15% (minimum and maximum relative errors for each volcano data set are shown in the figure as error bars, labeled min and max, respectively). For Turrialba (panel a), we also show the inferred compositions for Vent 2012 ($CO_2/SO_2 \sim 1.1$) and Vent 2010 ($CO_2/SO_2 \sim 2.9$), as obtained by active open-path FTIR and reported in Conde et al. (in press). Most Multi-GAS data fall between these two extremes, indicating their spread of ratios reflect variable mixing between 2010 and 2012 gases. Higher (>3) ratios, particularly after March 19, probably reflect transient, sporadic gas contributions from other low-temperature gas sources such as fumaroles and steaming grounds. The time-averaged (mean) ratios, shown for each volcano and also reported in Table 1, are simple arithmetic mean values of the data reported in each panel.

Extracting from MIs information on CO_2 contents in source (mantle) magmas is complicated by a number of processes, including pre- and post-entrapment crystallization (Kelley et al., 2006, 2010), post-entrapment CO_2 sequestration into bubbles, and pre-eruptive CO_2 degassing (see Hartley et al., 2014 for an updated list of references). Of these, pre-eruptive degassing is more difficult to account for, so that measured CO_2 contents in MIs typically underestimate CO_2 contents in primitive (un-degassed) mantle melts. With these precautions in mind, we still observe that CO_2/S_T (molar) ratios in MIs from the CNVS (data from Wade et al., 2006; Benjamin et al., 2007 and Wehrmann et al., 2011) exhibit along-arc variations in all parallel to those shown by volcanic gases (Fig. 6b). The estimated parental magma CO_2 compositions (which we calculated from MIs using the procedure of Portnyagin et al., 2007 and Watt et al., 2013) also are consistent with such distinct CO_2-signatures (Fig. 6c).

In summary, although quantification of pre-eruptive CO_2 degassing remains an issue (for MIs) and more data are highly needed (for both gases and MIs) to corroborate our conclusions, we conclude that both volcanic gases and MIs concur to suggest that the CO_2/S_T-ratio signature for magmatic volatiles is higher for Nicaragua than for Costa Rica. It should be noted from Fig. 1 that the transition from CO_2-poor (Costa Rica) to CO_2-rich (Nicaragua) gases broadly corresponds to the Fisher Ridge, which is a structural discontinuity interpreted by Husen et al. (2003) as marking a compositional transition zone (distinct hydration states) in the mantle wedge. We return to the potential factors determining this compositional variability in Section 6.3.

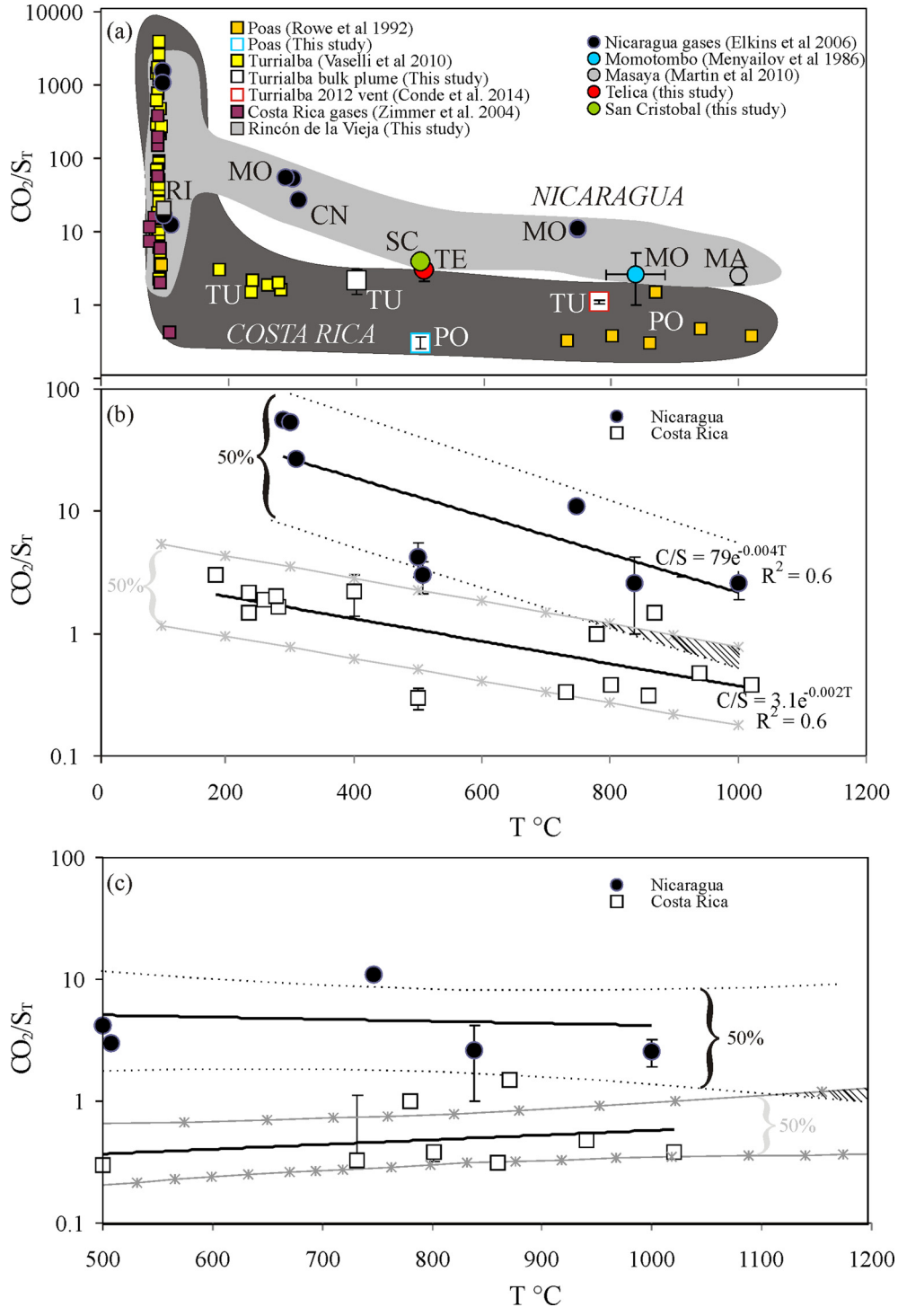

Fig. 5. (a) CO_2/S_T molar ratios of volcanic gases (from the literature) and plumes (this work) for Nicaragua (squares) and Costa Rica (circles), plotted versus the corresponding discharge temperatures. Where possible, a vertical error bar is displayed (one standard deviation of the mean value). S_T was calculated as the sum of measured SO_2 and H_2S (both for plumes and fumarolic gases). From the data sets of Zimmer et al. (2004) and Elkins et al. (2006), we only extracted their crater fumarole (FC type) samples and their (high-T) Momotombo power-plant samples. For the volcanic gas plumes, we used estimated temperatures of the source vents obtained using portable IR cameras. In the specific case of Turrialba, we show two independent compositions: (a) the composition of Vent 2012 measured by Conde et al. (in press) using FTIR (CO_2/S_T = 1.1; temperature = 790 °C) and (b) our own time-averaged bulk plume composition (CO_2/S_T = 2.2; Table 1), for which we assumed a source minimum temperature of 400 °C (the temperature of Vent 2010, which was clearly the source of most of the gas emitted). For San Cristóbal, we tentatively used the vent temperature (500 °C) measured in December 2012 (visibility was very low inside the crater during our April survey, which only allowed a minimum temperature of 105 °C to be determined). The diagram demonstrates a large spread of ratios in low-temperature gas manifestations, indicating the presence of secondary processes. High-temperature gases have a narrower range of CO_2/S_T ratios, and depict two distinct evolution trends for Nicaragua and Costa Rica; (b) a zoom of (a) for the selection of high-temperature (≥185 °C) gases. Nicaraguan and Costa Rican gases exhibit exponential decreases in CO_2/S_T ratios with increasing temperatures (see regression equations and R^2) that converge to distinct values of ≥3 (Nicaragua) and ≤1 (Costa Rica). The lower and upper 50% prediction bounds of the regression curves are also shown (see curves labeled "50%"). These intervals indicate that there is 50% chance that any new observation is actually contained within the lower and upper prediction bounds. The dashed area marks a small region of overall between the two distributions; (c) same as (b) but using a cut off temperature of 500 °C to specifically focus on magmatic gases.

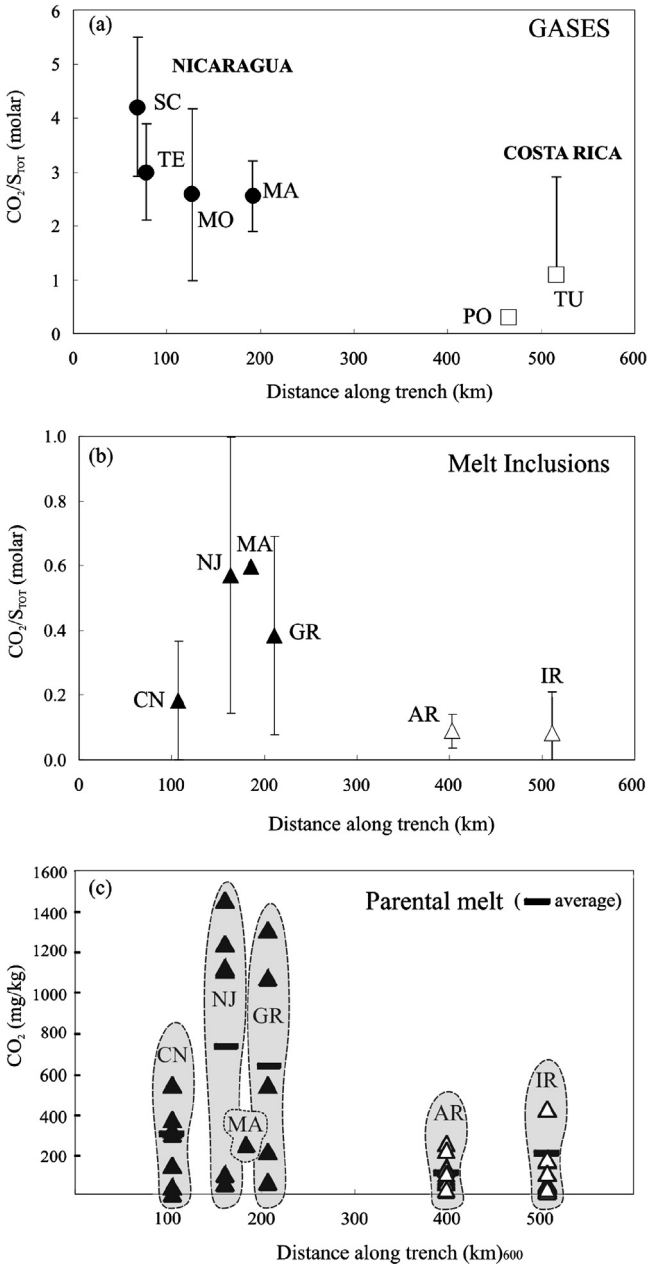

Fig. 6. (a) Along-arc variations of volcanic gas CO_2/S_T (molar) ratios. Distances along the arc are from north to south from the Cosigüina volcano in Nicaragua. This figures includes data for high-temperature (≥400 °C) gases only. Data for Poás (PO), Telica (TE) and San Cristóbal (SC) are mean ± SD from this study (Table 1). For Momotombo (MO) and Masaya (MA), we report averaged (mean±SD) compositions from Menyailov et al. (1986) and Martin et al. (2010), respectively. For Turrialba (TU), we show the mean gas composition for the 2012 vent (Conde et al., in press), which (given its high-temperature – 790 °C) is more representative of the magmatic gas signature. The vertical bar also includes the range of CO_2/S_T ratios measured in this study (2.2 ± 0.8). (b) Along-arc variations of CO_2/S_T (molar) ratios in MIs are displayed for comparison. Data on MIs (corrected for post-entrapment crystallization) are from Wade et al. (2006), Benjamin et al. (2007) and Wehrmann et al. (2011) (we omitted three evolved – SiO_2 > 57% – MIs from Irazù of Wehrmann et al., 2011, having unusually low S contents). Other volcanoes displayed are: CN = Cerro Negro; NJ, Nejapa; GR = Granada; AR = Arenal; IR = Irazú. (c) Along-arc variations in CO_2 contents in parental magmas from the CNVS. These were estimated correcting MI contents for pre-entrapment crystallization using the procedure of Portnyagin et al. (2007) and Watt et al. (2013). This involved adding olivine to the melt inclusion compositions until equilibrium with mantle olivine (Fo_{90}), using PETROLOG and the Ford et al. (1983) olivine model (fO_2 values from source MI data sets). The so-estimated parental magma CO_2 contents of figure (c) are likely under-estimates of the real CO_2 contents in source (mantle) magmas, since pre-entrapment CO_2 degassing is not accounted for. Still, the diagrams of (a) to (c) support a CO_2-richer composition of volcanism in Nicaragua relative to Costa Rica.

6.2. CO_2 output

The volcanic CO_2 output for each of our monitored volcanoes except Rincón de la Vieja was obtained by scaling the mean CO_2/SO_2 ratio to the co-acquired SO_2 flux data (Table 2). Our inferred CO_2 fluxes ranged from low (Poás: 25.5 ± 11.0 tons/day) to moderate (Turrialba: 918 to 1270 tons/day) (see Burton et al., 2013 for the typical CO_2 outputs from individual volcanoes). Our estimated CO_2 flux for Poás compares well with the CO_2 flux (33.6 tons/day) quoted by Zimmer et al. (2004) for March 2001, a time during which low SO_2 emissions (8.3 tons/day) were compensated by high CO_2/SO_2 ratios (5.9), presumably as a result of increased hydrothermal scrubbing of SO_2 during 2001 when fumaroles temperatures were also lower. Based on these values, Turrialba ranks as the largest volcanic CO_2 emitter in the CNVS, even exceeding the time-averaged contribution from Masaya (Martin et al., 2010). The CO_2 output for San Cristóbal is, for comparison, a factor ∼2 lower (523 ± 263 tons/day; Table 2).

6.2.1. Implications for the present-day CO_2 output from the CNVS

Our measurements reported here add new information to the currently incomplete volcanic CO_2 flux data set (Burton et al., 2013), and can serve as a basis for refining previous assessments of the volcanic CO_2 output from the CNVS. Hilton et al. (2002) reported on procedures for calculating the CO_2 output from individual arc segments based on extrapolation of available SO_2 flux data sets (Andres and Kasgnoc, 1998), and on the assumption that the distribution of SO_2 emissions follows the power law (Brantley and Koepenick, 1995). For the CAVA, they estimated a CO_2 output of ∼3600 tons/day. One possible source of uncertainty in the methodology of Hilton et al. (2002) is that a representative CO_2/SO_2 ratio for each arc segment has to be assumed in order to convert the SO_2 output into the CO_2 output. However, precise knowledge of these arc-averaged gas ratios is limited by the incomplete volcanic gas data set that is available, and by inadequate information on temporal and geographic (Fig. 6a) variability in the gas composition. Hilton et al. (2002) used a representative CO_2/S_T ratio of 2.7 for the CAVA, which, while close to our inferred magmatic signature for Nicaragua, appears unrepresentative (i.e., too rich in C) of Costa Rica gas (Fig. 6a). A lower CO_2/S_T ratio of 1.0–2.2 was proposed for the CAVA by Mather et al. (2006).

In light of the above-mentioned considerations, here we assess the total CO_2 output from the CNVS as a simple sum of the calculated CO_2 fluxes from individual volcanoes (Table 2). For Costa Rica, we infer a combined flux from Turrialba plus Poás of 1120 ± 642 tons/day (the average during March and April was used for Turrialba; Table 2). This value does not take into account emissions from Costa Rican volcanoes for which measurements are not available, or diffuse degassing from the flanks of volcanoes, and is therefore conservative in that it underestimates the total CO_2 output from CVS. The SO_2 flux was unfortunately not determined at Rincón de la Vieja, for example, so that the CO_2 contribution from this volcano remains undetermined. However, we consider that – at least in the conditions observed during March 2013 – Turrialba and Poás were the dominant sources of volcanic CO_2 in Costa Rica. Arenal Volcano, which has been degassing for years (Williams-Jones et al., 2001), was emitting <1 tons/day SO_2 during spring 2013 (OVSICORI-UNA, 2013). No visible plume was seen at any other volcano (e.g., Barva, Tenorio, Planatar) including Irazù, where only weak hydrothermal fuming persists (OVSICORI-UNA, 2013). We additionally note that our inferred total CO_2 output from CVS in 2013 is still larger than that (354–774 tons/day) measured by Zimmer et al. (2004) in 2001, when the (extrapolated) SO_2 flux was of only 191 tons/day (they used CO_2/S_T-ratio proxies for CVS of respectively 2.7 and 5.9) (Table 3).

Table 3
Summary of volcanic CO_2 output estimates for the NVS, CVS, and CNVS.

NVS CO_2 output (tons/day)	CVS CO_2 output (tons/day)	CNVS CO_2 output (tons/day)	Source	Procedure
Present-day fluxes				
–	–	3618	Hilton et al. (2002)	Gas composition (CO_2/S_T-ratio proxy of 2.7) + extrapolated SO_2 flux (3740 tons/day) for CAVA. The CAVA total CO_2 flux of 6932 tons/day of Hilton et al. (2002) was scaled to the total length of the CNVS (540 km) to obtain the CO_2 output for this arc segment.
–	354–774	–	Zimmer et al. (2004)	Gas composition (CO_2/S_T-ratio proxies for CVS of respectively 2.7 and 5.9) + extrapolated SO_2 flux (191 tons/day)
2411	–	–	Elkins et al. (2006)	From ^{3}He flux and arc length
14 500	–	–	Elkins et al. (2006)	Gas composition (CO_2/S_T ratio of 13) + extrapolated SO_2 flux (1700 tons/day)
		2296–5010	Mather et al. (2006)	Gas composition (CO_2/S_T ratio of 1.0–2.2) + extrapolated CAVA SO_2 flux (4360 tons/day). Note that the total CAVA flux of 4400–9600 tons/day reported by Mather et al. (2006) was scaled to the total length of the CNVS (540 km)
1715 ± 722	**1120 ± 642**	**2835 ± 1364**	**This study**	Sum of measured fluxes from individual volcanoes (from Table 2)
Geological fluxes				
–	–	1231	Wehrmann et al. (2011)	MI composition and magma eruption rate
319	26	345	Freundt et al. (in press)	MI composition and magma eruption+intrusion rate
3004	**180**	**3184**	**This study**	Combining the petrologically estimated S output of Freundt et al. (in press) (1457 tons/day and 261 tons/day for NVS and CVS, respectively) with our inferred magmatic gas compositional proxies of Nicaragua ($CO_2/SO_2 = 3$) and Costa Rica ($CO_2/SO_2 = 1$)

To calculate the CO_2 output for the NVS, we combined our Telica and San Cristóbal results with the recently reported CO_2 output from Masaya of 930 ± 350 tons/day (Martin et al., 2010). In our calculation we included a potential CO_2 contribution from Momotombo of 130 tons/day CO_2, calculated using the SO_2 flux of 73 tons/day reported by Andres and Kasgnoc (1998), and a CO_2/SO_2 molar ratio of 2.6 (the mean value of the Menyailov et al., 1986 data set; for comparison, a CO_2 flux of 120 tons/day was estimated for 1982 by these authors). Again we neglected the contributions from other volcanoes, since no visible plume or substantial gas manifestations were observed (INETER, 2013). Our calculated CO_2 output for the NVS of 1715 ± 722 tons/day is nearly one order of magnitude lower than that estimated by Elkins et al. (2006) (14 500 tons/day; Table 3), who adopted an high CO_2/SO_2 ratio of 13 in their calculations. According to our new data and calculations, the total CO_2 output from the CNVS during March and April 2013 was 2835 ± 1364 tons/day (Table 2), which is of the same range as the estimate of ∼3600 tons/day reported by Hilton et al. (2002) (Table 3).

6.2.2. CO_2 output from the CNVS over geological timescales

One obvious limitation of gas-based CO_2 output calculations is the relatively short observation period (days, in our specific case) on which they are based. To what extent campaign data – such as those presented here – can be extrapolated to long-term volcano degassing behavior remains questionable. For example, our finding of the CO_2 output for CVS being larger in 2013 than that measured in 2001 by Zimmer et al. (2004) clearly results from the present degassing unrest at Turrialba Volcano, which however only started in 2008 following more than a century of weak fumarolic activity (Vaselli et al., 2010; Campion et al., 2012; Conde et al., 2013). Therefore, the temporal stability of our estimate of ∼1200 tons/day for the CO_2 output from CVS remains uncertain.

Investigations of volatiles based on MI studies and long-term magma eruption rates (e.g., Wallace, 2005) cover time intervals ranging from years to tens of thousands of years, and are therefore in principle more suitable for inferring the long-term budgets of volatiles at arc segments. However, MI-based CO_2 output estimates are likely to be affected by pre-entrapment degassing, which can be very large for poorly soluble volatiles such as CO_2 (Papale, 2005). For example, Wehrmann et al. (2011) presented CO_2 compositional data for a suite of MIs from the CAVA, and calculated an arc-length-normalized CO_2 output of 2.6×10^{-2} g/m/s. In the very approximate assumption of a constant magma production rate (intrusive + extrusive) along CAVA, and for a ∼600-km-long CNVS, this would correspond to an average CO_2 output of 1230 tons/day, or a factor ≥3 lower than gas-based estimates (Table 3). An even lower CO_2 output (345 tons/day) can be inferred from the recent compilation of Freundt et al. (in press), who refined the earlier CO_2 output inventories by considering magma intruded in the crust in addition to magma erupted, and used specific CO_2/K_2O in MIs for the different arc segments (Wehrmann et al., 2011 used instead the Nicaraguan maximum CO_2/K_2O values for the entire volcanic front). Overall these results suggest that variable extents of pre-entrapment CO_2 degassing in MIs (Wehrmann et al., 2011) only allow for minimum estimates of the total CO_2 output to be inferred on the basis of petrology. Large pre-eruptive CO_2 degassing at depth, at conditions where S is mostly retained in the silicate melt, is also consistent with the CO_2/S_T ratios being far lower in CNVS MIs (Fig. 6b) than in the corresponding gases (Fig. 6a).

One possible method to resolve the conundrum of pre-entrapment CO_2 degassing is to combine petrologically estimated SO_2 outputs with our inferred magmatic gas CO_2/S_T proxies (Figs. 5 and 6a). Freundt et al. (in press) found that the long-term SO_2 output from the CNVS calculated on the basis of petrology – from the MI composition and the magma production rate – is 1718 tons/day (1457 tons/day and 261 tons/day for NVS and CVS, respectively; Table 3). We converted these SO_2 output fluxes into CO_2 output fluxes using our best estimates for the magmatic gas CO_2/S_T-ratio signature in Nicaragua and Costa Rica; values of 3 and 1, respectively, yielded a long-term CO_2 output of ∼3184 tons/day for the CNVS, with a dominant contribution from CO_2-rich volcanism in Nicaragua (∼3000 tons/day). We conclude that present-day (gas-based) and geological (petrology-based) CNVS CO_2 outputs are in very close agreement in our case (2835 ± 1364 vs. 3184 tons/day; Table 3). We additionally infer from Table 3 that, while total CNVS emissions are fairly similar in the two estimates, the present-day

(gas) emissions in Costa Rica (Nicaragua) are somewhat more (less) intense than the long-term (petrologic) time-averages.

6.3. Factors controlling along-arc variations in gas chemistry

It has been shown that there are large and systematic along-arc variations in several parameters at the CAVA, including the age and geometrical properties of the slab (Protti et al., 1994; Syracuse and Abers, 2006), the extent of serpentinization of the subducted mantle (Rüpke et al., 2004; Freundt et al., in press), and the crust thickness (MacKenzie et al., 2008). In response to such changing subduction conditions, the magma compositions also vary substantially along the arc (Plank and Langmuir, 1988; Carr et al., 1990, 2003; Patino et al., 2000; Rüpke et al., 2002; Eiler et al., 2005). Research (Sadofsky et al., 2008) has identified that multiple distinct slab (essentially sediments, altered oceanic crust, and serpentinized mantle) and mantle wedge components are involved in magma generation. However, the general consensus is that slab-derived fluids play the most-significant role in the generation of Nicaragua magmas (Plank and Langmuir, 1998; Plank et al., 2002), whereas a more MORB-type magmatism occurs in Costa Rica, possibly also due to underplating of the uppermost part of the sediment column beneath the overriding crust (Leeman et al., 1994). For example, high $^{10}Be/^{9}Be$, U/Th, and Ba/La ratios in lavas all point to a larger volume of trench sediments being subducted in Nicaragua, where the accretionary prism is also more significant (von Huene et al., 2000). These variable fluid contributions from the slab are also thought to control the along-arc variations in the signature of volatiles of CAVA magmas (Sadofsky et al., 2008; Wehrmann et al., 2011; Freundt et al., in press) and gases (Fischer et al., 2002, 2007; Shaw et al., 2003; Zimmer et al., 2004; Elkins et al., 2006), which all exhibit more sedimentary affinity in Nicaragua.

The present study is the first to attempt to extend the characterization of along-arc variations at the CAVA to major elements (CO_2 and S) in high-temperature magmatic fluids. The obtained results – although requiring additional measurements and studies – are suggestive of the existence of a distinct CO_2/S_T-ratio signature in magmatic gases of the CNVS (Fig. 6a), and likely imply involvement of different sources of volatiles in the two arc segments. Isotopic studies of CAVA cold-gas manifestations (Fischer et al., 2002, 2007; Shaw et al., 2003; Zimmer et al., 2004; Elkins et al., 2006) have revealed a more slab-like isotopic signature of the emitted N_2 and CO_2 in Nicaragua relative to the more-MORB-like signature of Costa Rica gas. In particular, Zimmer et al. (2004) and Elkins et al. (2006) used mass and isotopic balance considerations to calculate the fraction of slab-derived N_2 released from each of the major volcanic and geothermal systems in the CNVS. Fig. 7a indicates that our magmatic gas CO_2/S_T ratios are positively correlated with the calculated N_2 sedimentary fractions of Zimmer et al. (2004) and Elkins et al. (2006). Similarly, Shaw et al. (2003) and Hilton et al. (2010) used He–C systematics to calculate the relative contributions of slab-derived C (from both limestone and organic sediments) and mantle-derived C to the chemistry of Central American gas samples. Their calculated fractions of limestone-derived C, shown in Fig. 7b, are also consistent with our inferred magmatic gas CO_2/S_T ratios. We finally argue from these correlations that the transition from a CO_2-poor (Poás) to a CO_2-rich (San Cristóbal and Telica) volcanic gas composition is well explained by increasing additions of CO_2-rich slab fluids to the mantle wedge.

To explore this possibility further, we analyzed the discrepancy in the volcanic gas CO_2/S_T ratio between Nicaragua and Costa Rica in relation to the composition of the inputs of volatiles at the Central American subducting slab. An extensive compilation of these input flux data has recently been presented by

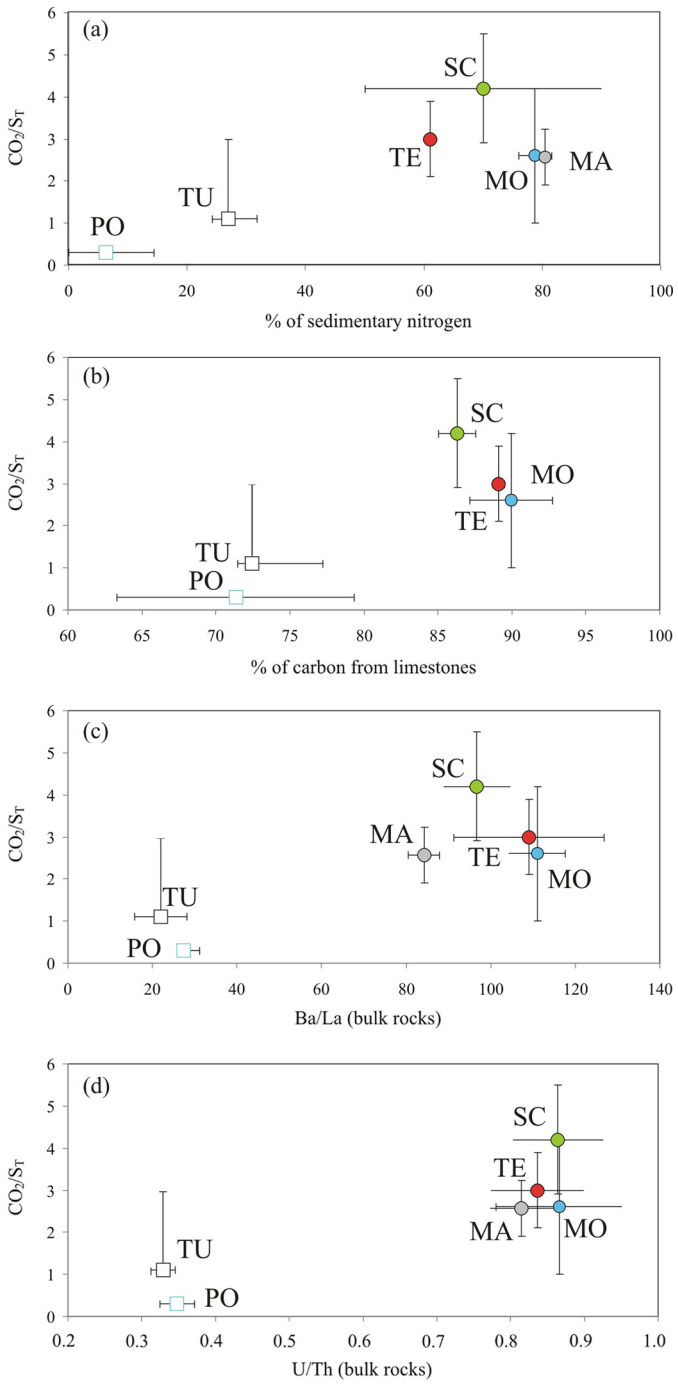

Fig. 7. Scatter plots displaying correlations between the magmatic gas CO_2/S_T-ratio signature of each volcano (same high-temperature gas data as in Fig. 6) and geochemical/petrologic tracers of slab-derived fluids. For each parameter, the mean ± 1 SD are shown. The considered proxies of slab fluid addition are (a) the percentage of sedimentary N_2, corresponding to the fraction of N_2 derived from the slab, calculated from $\delta^{15}N_{N_2}$ and the N_2/He ratios of volcanic gases (the values reported by Zimmer et al., 2004 and Elkins et al., 2006 were averaged for each volcano); (b) the percentage of C from limestone, corresponding to the fraction of C derived from subducted limestone, calculated from $\delta^{13}C_{CO_2}$ and the $C/^{3}He$ ratios of volcanic gases (the data reported by Shaw et al., 2003 and Hilton et al., 2010 for each volcano were averaged); and (c) Ba/La and (d) U/Th ratios in volcanic rocks (we averaged the whole-rock compositions listed in Carr, 1984; Reagan and Gill, 1989; Reagan et al., 1994; Carr et al., 1990; Leeman et al., 1994; Noll et al., 1996; Patino et al., 2000; Hoernle et al., 2008, and Bolge et al., 2009 for each volcano). See Fig. 5 and the caption of Fig. 6 for symbols.

Freundt et al. (in press), who found that the slab-derived fluids had similar CO_2/S_T ratios in Nicaragua (4.4) and Costa Rica (4.0); such a small difference is unlikely to explain the observed along-

arc variations in volcanic gas CO_2/S_{TOT} ratios. It is also noteworthy that the estimated CO_2 and SO_2 subduction input fluxes are larger in Costa Rica than in Nicaragua, which is due to higher rates of subduction erosion and faster convergence in the former arc segment (Freundt et al., in press). It is clear that this should lead to a result opposite to the south-to-north increase in CO_2 seen in both MIs and gases (Fig. 6). However, Freundt et al. (in press) also identified sizeable H_2O differences in slab fluids between the two arc segments. In particular, they revealed that the slab fluid was more hydrated in Nicaragua (H_2O = 84 wt%) than in Costa Rica (H_2O = 73 wt%), reflecting a larger extent of mantle serpentinization in Nicaragua (Abers et al., 2003; Grevemeyer et al., 2007). This reflects in the H_2O slab input fluxes being ~1.6-fold higher in Nicaragua (~62 Tg/Ma/m) than in Costa Rica (~39.5 Tg/Ma/m) (Freundt et al., in press).

Following Kerrick and Connolly (2001) and Schmidt and Poli (2003), we therefore assume that a pervasive upward flow of aqueous fluids produced at the "wet" Nicaraguan subducted mantle (Abers et al., 2003) leads to efficient C extraction from the upper slab sediments. This process would result in larger CO_2 release into the mantle wedge, and could ultimately cause the high CO_2/S_{TOT} ratios in both magmas and gases (Fig. 6). The contrasting more-anhydrous nature of the shallow subducting slab in Costa Rica (Protti et al., 1994) would result in lower C recycling (the C output at the volcanic arc was only 0.15–0.46% of the C input along the slab, compared to a CAVA average of 2% and 3.7–5.1% in Nicaragua; Freundt et al., in press). The resulting low CO_2/S_{TOT} ratios in magmatic gases would therefore result from a dominant contribution of volatiles from the mantle wedge, where a large fraction of the S arc output is typically produced (Wallace, 2005). We admit, however, that underplating of C-rich sediments in Costa Rica possibly plays an additional role.

If the above interpretation is correct, then a positive correlation should be expected between the degree of C enrichment in magmas/gases and petrologic tracers of slab-derived fluids. However, Wehrmann et al. (2011) noted that, while the H_2O contents in MIs are correlated with Ba/La, B/La, and U/Th ratios (Wade et al., 2006; Sadofsky et al., 2008), the CO_2 contents are not directly correlated with the same proxies for a slab-derived component. Although this decoupled behavior of H_2O and CO_2 could partially reflect the influence of the degree of sediment melting (controlled by slab temperature; Plank et al., 2009) on CO_2 recycling (Watt et al., 2013), it must be admitted that pre-entrapment CO_2 degassing, which is likely to have been highest in H_2O-rich Nicaragua magmas, may have complicated (or even obscured) any source-derived trend in MIs. In fact, our inferred magmatic gas CO_2/S_{TOT} ratios are positively correlated with any trace-element proxy for slab-fluids (e.g., Ba/La and U/Th; see Fig. 7c and d), providing additional support for our conclusion that slab-derived fluids are deeply implicated in the generation of CO_2-rich volcanic gases in Nicaragua.

7. Conclusions

Our novel CO_2/S_T ratio and CO_2 output results here contribute to extend the currently incomplete volcanic CO_2 flux data set (Burton et al., 2013). We show that CO_2:S_T compositions of high-temperature volcanic gases – where secondary (scrubbing) processes are insignificant – do vary over relatively restricted ranges (Shinohara, 2013), but still display measurable variations along a volcanic arc. While additional observations over longer measurement intervals are needed to strengthen our conclusions, our data presented here are suggestive of systematic and sizeable differences in volcanic gas signatures between Nicaragua ($CO_2/S_T \sim 3$) and Costa Rica ($CO_2/S_T \sim 0.5$–1.0). This CO_2-richer composition of Nicaraguan gas is consistent with (i) high CO_2 contents recorded in MIs, (ii) the more-positive (e.g., sedimentary) isotopic signatures of N_2 and CO_2 in gas manifestations, and (iii) high values of trace-element proxies for slab-derived fluids in magmas (e.g., high Ba/La, U/Th, and B contents in volcanic rocks). Based on these correlations, we provide additional support for the earlier theory relating CO_2-rich volcanism in Nicaragua to more-efficient C recycling along the "wet" (serpentinized) Nicaraguan slab. We also used our inferred and distinct compositional features for Costa Rica and Nicaragua gases to calculate that the long-term (e.g., based on the magma eruption rate) CO_2 output from the CNVS is ~3200 tons/day. This geological CO_2 output agrees well with the present-day CO_2 output (2835 ± 1364 tons/day) from the CNVS that we calculated from our gas observations made during March and April 2013.

Evaluating the general significance of along-arc variations in gas chemistry is presently restricted by the limited gas data set available. However, the heterogeneities observed in subduction geometry and conditions worldwide (Syracuse and Abers, 2006) suggest that the gas chemistry can vary substantially both within and between arc segments. Careful identification of the CO_2/S_T-ratio signature of each individual arc segment is key to improving the estimates of volcanic-arc CO_2 outputs at both regional and global scales.

Acknowledgements

The research leading to these results has received funding from the European Research Council under the European Union's Seventh Framework Programme (FP7/2007/2013)/ERC grant agreement n1305377. This study was initiated within the framework of the DECADE initiative of the Deep Carbon Observatory. Tobias Fischer (UNM) kindly provided the portable DOAS used for the Poás walking traverses. Constructive comments by David Hilton and two anonymous reviewers are acknowledged for improving the quality of the manuscript.

References

Abers, G.A., Plank, T., Hacker, B.R., 2003. The wet Nicaraguan slab. Geophys. Res. Lett. 30. http://dx.doi.org/10.1029/2002GL015649.

Aiuppa, A., Federico, C., Giudice, G., Gurrieri, S., 2005. Chemical mapping of a fumarolic field: La Fossa Crater, Vulcano Island (Aeolian Islands, Italy). Geophys. Res. Lett. 32 (13), L13309. http://dx.doi.org/10.1029/2005GL023207.

Aiuppa, A., Federico, C., Giudice, G., et al., 2006. Rates of carbon dioxide plume degassing from Mount Etna volcano. J. Geophys. Res. 111, B09207. http://dx.doi.org/10.1029/2006JB004307.

Aiuppa, A., Federico, C., Giudice, G., et al., 2009. The 2007 eruption of Stromboli volcano: insights from real-time measurement of the volcanic gas plume CO_2/SO_2 ratio. J. Volcanol. Geotherm. Res. 182, 221–230. http://dx.doi.org/10.1016/j.jvolgeores.2008.09.013.

Aiuppa, A., Bertagnini, A., Métrich, N., Moretti, R., Di Muro, A., Liuzzo, M., Tamburello, G., 2010. A model of degassing for Stromboli volcano. Earth Planet. Sci. Lett. 295, 195–204. http://dx.doi.org/10.1016/j.epsl.2010.03.040.

Aiuppa, A., Giudice, G., Liuzzo, M., et al., 2012. First volatile inventory for Gorely volcano, Kamchatka. Geophys. Res. Lett. 39 (6), art. no. L06307.

Andres, R.J., Kasgnoc, A.D., 1998. A time-averaged inventory of subaerial volcanic sulfur emissions. J. Geophys. Res. 103 (D19), 25,251–25,261.

Benjamin, E.R., Plank, T., Wade, J.A., Kelley, K.A., Hauri, E.H., Alvarado, G.E., 2007. High water content in basaltic magmas from Irazú Volcano, Costa Rica. J. Volcanol. Geotherm. Res. 168, 68–92. http://dx.doi.org/10.1016/j.jvolgeores.2007.08.008.

Berner, R.A., Lasaga, A.C., 1989. Modeling the geochemical carbon cycle. Sci. Am. 260, 74–81.

Bolge, L.L., Carr, M.J., Milidakis, K.I., Lindsay, F.N., Feigenson, M.D., 2009. Correlating geochemistry, tectonics, and volcanic volume along the Central American volcanic front. Geochem. Geophys. Geosyst. 10.

Brantley, S.L., Koepenick, K.W., 1995. Measured carbon dioxide emissions from Oldoinyo Lengai and the skewed distribution of passive volcanic fluxes. Geology 23, 933–936.

Burton, M.R., Oppenheimer, O., Horrocks, L.A., Francis, P.W., 2000. Remote sensing of CO_2 and H_2O emission rates from Masaya volcano, Nicaragua. Geology 28 (10), 915–918. http://dx.doi.org/10.1130/0091-7613(2000)28<915:RSOCAH>2.0.CO.

Burton, M.R., Sawyer, G.M., Granieri, D., 2013. Deep carbon emissions from volcanoes. Rev. Mineral. Geochem. 75 (1), 323–354.
Campion, R., Martinez-Cruz, M., Lecocq, T., Caudron, C., Pacheco, J., Pinardi, G., Hermans, C., Carn, S., Bernard, A., 2012. Space- and ground-based measurements of sulphur dioxide emissions from Turrialba Volcano (Costa Rica). Bull. Volcanol. 74, 1757–1770.
Carr, M.J., 1984. Symmetrical and segmented variation of physical and geochemical characteristics of the Central American volcanic front. J. Volcanol. Geotherm. Res. 20, 231–252.
Carr, M.J., Feigenson, M.D., Bennett, E.A., 1990. Incompatible element and isotopic evidence for tectonic control of source mixing and melt extraction along the Central American arc. Contrib. Mineral. Petrol. 105, 369–380.
Carr, M.J., Feigenson, M.D., Patino, L.C., Walker, J.A., 2003. Volcanism and geochemistry in Central America. In: Eiler, J.M. (Ed.), Inside the Subduction Factory. In: Geophys. Monogr., vol. 138, pp. 153–174.
Conde, V., Bredemeyer, S., Duarte, E., et al., 2013. SO_2 degassing from Turrialba Volcano linked to seismic signatures during the period 2008–2012. Int. J. Earth Sci. 1 (16). http://dx.doi.org/10.1007/s00531-013-0958-5.
Conde, V., Robidoux, P., Avard, G., Galle, B., Aiuppa, A., Muñóz, A., in press. Measurements of SO_2 and CO_2 by combining DOAS, Multi-GAS and FTIR: study cases from Turrialba and Telica volcanoes. Int. J. Earth Sci. http://dx.doi.org/10.1007/s00531-014-1040-7.
De Leeuw, G.A., Hilton, D.R., Fischer, T.P., Walker, J.A., 2007. The He–CO_2 isotope and relative abundance characteristics of geothermal fluids in El Salvador and Honduras: new constraints on volatile mass balance of the Central American Volcanic Arc. Earth Planet. Sci. Lett. 258, 132–146.
DeMets, C., 2001. A new estimate for present-day Cocos-Caribbean Plate motion: implications for slip along the Central American Volcanic Arc. Geophys. Res. Lett. 28, 4043–4046. http://dx.doi.org/10.1029/2001GL013518.
Eiler, J.M., Carr, M.J., Reagan, M., Stolper, E., 2005. Oxygen isotope constraints on the sources of Central American arc lavas. Geochem. Geophys. Geosyst. 6. http://dx.doi.org/10.1029/2004GC000804.
Elkins, L.J., Fischer, T.P., Hilton, D.R., Sharp, Z.D., McKnight, S., Walker, J., 2006. Tracing nitrogen in volcanic and geothermal volatiles from the Nicaraguan volcanic front. Geochim. Cosmochim. Acta 70, 5215–5235.
Fischer, T.P., 2008. Fluxes of volatiles (H_2O, CO_2, N_2, Cl, F) from arc volcanoes. Geochem. Int. 42, 21–38.
Fischer, T.P., Hilton, D.R., Zimmer, M.M., Shaw, A.M., Sharp, Z.D., Walker, J.A., 2002. Subduction and recycling of nitrogen along the Central American margin. Science 297, 1154–1157.
Fischer, T.P., Shaw, A.M., Hilton, D.R., 2007. Gas geochemistry of volcanic and hydrothermal fluids of Central America. In: Bundschuh, J., Alvarado, G.E. (Eds.), Central America: Geology, Resources and Hazards, vol. 2. Taylor and Francis, Leiden, The Netherlands, pp. 839–867.
Ford, C.E., Russell, D.G., Craven, J.A., Fisk, M.R., 1983. Olivine-liquid equilibria: temperature, pressure and composition dependence of the crystal/liquid cation partition coefficients for Mg, Fe^{2+}, Ca and Mn. J. Petrol. 24, 256–266.
Freundt, A., Grevemeyer, I., Rabbel, W., Hansteen, T.H., Hensen, C., Wehrmann, H., Kutterolf, S., Halama, R., Frische, M., in press. Volatile (H_2O, CO_2, Cl, S) budget of the Central American subduction zone. Int. J. Earth Sci.. http://dx.doi.org/10.1007/s00531-014-1001-1.
Galle, B., Johansson, M., Rivera, C., Zhang, Y., Kihlman, M., Kern, C., Lehmann, T., Platt, U., Arellano, S., Hidalgo, S., 2010. Network for Observation of Volcanic and Atmospheric Change (NOVAC) — A global network for volcanic gas monitoring: network layout and instrument description. J. Geophys. Res. 115, D05304. http://dx.doi.org/10.1029/2009JD011823.
Geirsson, H., Rodgers, M., LaFemina, P., Witter, M., Roman, D., Muñóz, A., Tenorio, V., Alvarez, J., et al., 2014. Multidisciplinary observations of the 2011 explosive eruption of Telica volcano, Nicaragua: implications for the dynamics of low-explosivity ash eruptions. J. Volcanol. Geotherm. Res. 271, 55–69.
Grevemeyer, I., Ranero, C.R., Flüh, E.R., Kläschen, D., Bialas, J., 2007. Passive and active seismological study of bending-related faulting and mantle serpentinization at the Middle America trench. Earth Planet. Sci. Lett. 258, 528–542.
Hartley, M.E., Maclennan, J., Edmonds, M., Thordarson, T., 2014. Reconstructing the deep CO_2 degassing behaviour of large basaltic fissure eruptions. Earth Planet. Sci. Lett. 393, 120–131.
Hilton, D.R., Fischer, T.P., Marty, B., 2002. Noble gases and volatile recycling at subduction zones. In: Porcelli, D., Ballentine, C.J., Wieler, R. (Eds.), Noble Gases in Geochemistry and Cosmochemistry. In: Rev. Mineral. Geochem., vol. 47. Mineral. Soc. Am., Washington, DC, pp. 319–370.
Hilton, D.R., Ramirez, C.J., Mora-Amador, R., Fischer, T.P., Füri, E., Barry, P.H., Shaw, A.M., 2010. Monitoring of temporal and spatial variations in fumarole helium and carbon dioxide characteristics at Poas and Turrialba volcanoes, Costa Rica (2001–2009). Geochem. J. 44, 431–440.
Hoernle, K.A., Abt, D.L., Fischer, K.M., Nichols, H., Hauff, F., Abers, G.A., Van Den Bogaard, P., Heydolph, K., Alvarado, G.E., Protti, M., Strauch, W., 2008. Arc-parallel flow in the mantle wedge beneath, Costa Rica and Nicaragua. Nature 451, 1094–1098.
Husen, S., Quintero, R., Kissing, E., Hacker, B., 2003. Subduction-zone structure and magmatic processes beneath Costa Rica constrained by local earthquake tomography and petrological modelling. Geophys. J. Int. 155, 11–32.
INETER, 2013. Monthly volcano monitoring reports, available at http://www.ineter.gob.ni/.
Kelley, K.A., Plank, T., Grove, T.L., Stolper, E.M., Newman, S., Hauri, E., 2006. Mantle melting as a function of water content beneath back-arc basins. J. Geophys. Res. 111, B09208. http://dx.doi.org/10.1029/2005JB003732.
Kelley, K.A., Plank, T., Newman, S., Stolper, E.M., Grove, T.L., Parman, S., Hauri, E.H., 2010. Mantle melting as a function of water content beneath the Mariana arc. J. Petrol. 51, 1711–1738. http://dx.doi.org/10.1093/petrology/egq036.
Kerrick, D.M., Connolly, J.A.D., 2001. Metamorphic devolatilization of subducted marine sediments and the transport of volatiles into the Earth's mantle. Nature 411, 293–296.
Leeman, W.P., Carr, M.J., Morris, J.D., 1994. Boron geochemistry of the Central American volcanic arc: constraints on the genesis of subduction-related magmas. Geochim. Cosmochim. Acta 58, 149–168.
MacKenzie, L., Abers, G.A., Fisher, K.M., Syracuse, E.M., Protti, J.M., Gonzáles, V., Strauch, W., 2008. Crustal structure along the southern Central American volcanic front. Geochem. Geophys. Geosyst. 9, Q08S09. http://dx.doi.org/10.1029/2008GC001991.
Martin, R.S., Sawyer, G.M., Spampinato, L., Salerno, G.G., Ramírez, C., Ilyinskaya, E., Witt, M.L.I., Mather, T.A., Watson, I.M., Phillips, J.C., Oppenheimer, C., 2010. A total volatile inventory for Masaya Volcano, Nicaragua. J. Geophys. Res. B, Solid Earth Planets 115 (9). http://dx.doi.org/10.1029/2010JB007480.
Marty, B., Tolstikhin, I.N., 1998. CO_2 fluxes from mid-ocean ridges, arcs and plumes. Chem. Geol. 145, 233–248.
Mather, T.A., Pyle, D.M., Tsanev, V.I., McGonigle, A.J.S., Oppenheimer, C., Allen, A.G., 2006. A reassessment of current volcanic emissions from the Central American arc with specific examples from Nicaragua. J. Volcanol. Geotherm. Res. 149, 297–311.
Menyailov, I.A., Nikitina, L.P., Shapar, V.N., Pilipenko, V.P., 1986. Temperature increase and chemical change of fumarolic gases at Momotombo Volcano, Nicaragua, in 1982–1985; are these indicators of a possible eruption? J. Geophys. Res. 91, 12,199–12,214.
Noll Jr., P.D., Newsom, H.E., Leeman, W.P., Ryan, J.G., 1996. The role of hydrothermal fluids in the production of subduction zone magmas: evidence from siderophile and chalcophile trace elements and boron. Geochim. Cosmochim. Acta 60, 587–611.
OVSICORI-UNA, 2012. Monthly volcano monitoring reports available at http://www.ovsicori.una.ac.cr/index.php?option=com_phocadownload&view=section&id=3&Itemid=73.
OVSICORI-UNA, 2013. Monthly volcano monitoring reports available at http://www.ovsicori.una.ac.cr/index.php?option=com_phocadownload&view=section&id=3&Itemid=73.
Papale, P., 2005. Determination of total H_2O and CO_2 budgets in evolving magmas from melt inclusion data. J. Geophys. Res. 110. http://dx.doi.org/10.1029/2004JB003033.
Patino, L.C., Carr, M.J., Feigenson, M.D., 2000. Local and regional variations in Central American arc lavas controlled by variations in subducted sediment input. Contrib. Mineral. Petrol. 138, 265–283. http://dx.doi.org/10.1007/s004100050562.
Plank, T., Langmuir, C.H., 1988. An evaluation of the global variations in the major element chemistry of arc basalts. Earth Planet. Sci. Lett. 90 (4), 349–370.
Plank, T., Langmuir, C.H., 1998. The chemical composition of subducting sediment and its consequences for the crust and mantle. Chem. Geol. 145 (3), 325–394.
Plank, T., Balzer, V., Carr, M., 2002. Nicaraguan volcanoes record paleoceanographic changes accompanying closure of the Panama gateway. Geology 30 (12), 1087–1090.
Plank, T., Cooper, L.B., Manning, C.E., 2009. Emerging geothermometers for estimating slab surface temperatures. Nat. Geosci. 2, 611–615. http://dx.doi.org/10.1038/ngeo614.
Platt, U., Stutz, J., 2008. Differential Optical Absorption Spectroscopy: Principles and Applications. Springer-Verlag, Heidelberg. 272 pp.
Portnyagin, M., Hoernle, K., Plechov, P., Mironov, N., Khbunaya, S., 2007. Constraints on mantle melting and composition and nature of slab components in volcanic arcs from volatiles (H_2O, S, Cl, F) and trace elements in melt inclusions from the Kamchatka Arc. Earth Planet. Sci. Lett. 255, 53–69. http://dx.doi.org/10.1016/j.epsl.2006.12.005.
Protti, M., Güendel, F., McNally, K., 1994. The geometry of the Wadati–Benioff zone under southern Central-America and its tectonic significance: results from a high-resolution local seismographic network. Phys. Earth Planet. Inter. 84 (1–4), 271–287.
Protti, M., Gundel, F., McNally, K., 1995. Correlation between the age of the subducting Cocos plate and the geometry of the Wadati–Benioff zone under Nicaragua and Costa Rica. Spec. Pap., Geol. Soc. Am. 295, 309–326.
Reagan, M.K., Gill, J.B., 1989. Coexisting calc-alkaline and high niobium basalts from Turrialba volcano, Costa Rica: implications for residual titanites in arc magma sources. J. Geophys. Res. B 94, 4619–4633.
Reagan, M.K., Morris, J.D., Herrstrom, E.A., Murrell, M.T., 1994. U series and Be isotope evidence for an extended history of subduction modification of the mantle below Nicaragua. Geochim. Cosmochim. Acta 58, 4199–4212.
Rowe Jr., G.L., Brantley, S.L., Fernández, M., Fernández, J.F., Borgia, A., Barquero, J., 1992. Fluid–volcano interaction in an active stratovolcano: the crater lake

system of Poás volcano, Costa Rica. J. Volcanol. Geotherm. Res. 49 (1–2), 23–52.

Rüpke, L.H., Phipps Morgan, J., Hort, M., Connolly, J., 2002. Are the regional variations in Central American arc lavas due to differing basaltic versus peridotitic slab sources of fluids? Geology 30, 1035–1038.

Rüpke, L.H., Phipps Morgan, J., Hort, M., Connolly, J., 2004. Serpentine and the subduction zone water cycle. Earth Planet. Sci. Lett. 223, 17–34.

Sadofsky, S., Portnyagin, M., Hoernle, K., van den Bogaard, P., 2008. Subduction cycling of volatiles and trace elements through the Central American volcanic arc: evidence from melt inclusions. Contrib. Mineral. Petrol. 155, 433–456.

Schmidt, M.W., Poli, S., 2003. Generation of mobile components during subduction of oceanic crust. In: Rudnick, R.L., Holland, H.D., Turekian, K.K. (Eds.), The Crust. Treatise on Geochemistry, vol. 3. Elsevier–Pergamon, Oxford, pp. 567–591.

Shaw, A.M., Hilton, D.R., Fischer, T.P., Walker, J.A., Alvarado, G.E., 2003. Contrasting He–C relationships in Nicaragua and Costa Rica: insights into C cycling through subduction zones. Earth Planet. Sci. Lett. 214, 499–513.

Shinohara, H., 2005. A new technique to estimate volcanic gas composition: plume measurements with a portable multi-sensor system. J. Volcanol. Geotherm. Res. 143, 319–333.

Shinohara, H., 2013. Volatile flux from subduction zone volcanoes: insights from a detailed evaluation of the fluxes from volcanoes in Japan. J. Volcanol. Geotherm. Res. 268, 46–63.

Symonds, R.B., Gerlach, T.M., Reed, M.H., 2001. Magmatic gas scrubbing: implications for volcano monitoring. J. Volcanol. Geotherm. Res. 108, 303–341.

Syracuse, E.M., Abers, G.A., 2006. Global compilation of variations in slab depth beneath arc volcanoes and implications. Geochem. Geophys. Geosyst. 7, Q05017. http://dx.doi.org/10.1029/2005GC001045.

Vaselli, O., Tassi, F., Duarte, E., Fernández, E., Poreda, R.J., Delgado Huertas, A., 2010. Evolution of fluid geochemistry at the Turrialba volcano (Costa Rica) from 1998 to 2008. Bull. Volcanol. 72 (4), 397–410.

von Huene, R., Ranero, C.R., Weinrebe, W., Hinz, K., 2000. Quaternary convergent margin tectonics of Costa Rica, segmentation of the Cocos Plate, and Central American volcanism. Tectonics 19 (2), 314–334.

Wade, J.A., Plank, T., Melson, W.G., Soto, G.J., Hauri, E.H., 2006. The volatile content of magmas from Arenal volcano, Costa Rica. J. Volcanol. Geotherm. Res. 157 (1), 94–120.

Wallace, P.J., 2005. Volatiles in subduction zone magmas: concentrations and fluxes based on melt inclusion and volcanic gas data. J. Volcanol. Geotherm. Res. 140, 217–240.

Watt, S.F.L., Pyle, D.M., Mather, T.A., Naranjo, J.A., 2013. Arc magma compositions controlled by linked thermal and chemical gradients above the subducting slab. Geophys. Res. Lett. 40, 2550–2556. http://dx.doi.org/10.1002/grl.50513.

Wehrmann, H., Hoernle, K., Portnyagin, M., Wiedenbeck, M., Heydolph, K., 2011. Volcanic CO_2 output at the Central American subduction zone inferred from melt inclusions in olivine crystals from mafic tephras. Geochem. Geophys. Geosyst. 12, Q06003. http://dx.doi.org/10.1029/2010GC003412.

Williams-Jones, G., Stix, J., Heiligmann, M., Barquero, J., Fernández, E., Duarte, E., 2001. A model of degassing and seismicity at Arenal Volcano, Costa Rica. J. Volcanol. Geotherm. Res. 108 (1), 121–139.

Witt, M.L.I., Mather, T.A., Pyle, D.M., Aiuppa, A., Bagnato, E., Tsanev, V.I., 2008. Mercury and halogen emissions from Masaya and telica volcanoes, Nicaragua. J. Geophys. Res. 113. http://dx.doi.org/10.1029/2007JB005401, art. no. B06203.

Zimmer, M.M., Fischer, T.P., Hilton, D.R., Alvarado, G.E., Sharp, Z.D., Walker, J.A., 2004. Nitrogen systematics and gas fluxes of subduction zones: insights from Costa Rica arc volatiles. Geochem. Geophys. Geosyst. 5. http://dx.doi.org/10.1029/2003GC000651.